IPNS
LIBRARY

SCHWEIZERISCHES INSTITUT FÜR NUKLEARFORSCHUNG

ICANS - IX

Proceedings of the 9th Meeting of the International Collaboration on Advanced Neutron Sources

Villigen, September 22 - 26, 1986

Editors: F. Atchison and W. Fischer

ISBN
3-907998-01-4
July 1987
SIN, Villigen

ICANS - IX

Proceedings of the 9th Meeting

of the International Collaboration

on Advanced Neutron Sources

Villigen, September 22 - 26, 1986

ISBN
3-907998-01-4

Produced in limited quantity by the Information Services.

ICANS-IX Proceedings are available from the

Public Affairs Office
Swiss Institute for Nuclear Research
CH-5234 Villigen/Switzerland

Phone : 056/99 36 66
Telex : 827419 sin ch
Telefax: 056/993294 SIN/IMP CH

7.87 180 40926

PREFACE

The ninth meeting of the ICANS collaboration was held at the Swiss Institute for Nuclear Research, Villigen, Switzerland from 22nd to 28th September 1986. There were 48 'full' participants from ten countries, representing 19 Institutes. The meeting opened with the traditional session containing status reports from the various participating laboratories, at the start of which the recent death of Yoshikazu Ishikawa, the ICANS representative from KEK Japan, was remembered; the text of the address given by Jack Carpenter is included in these proceedings immediately following this preface. The rest of the meeting was split into principal 'workshop' sessions on Targets, Moderators and (in parallel with these) Instrumentation. Further sessions on 'Common Problems' - which emphasised backgrounds - 'Boosters and New Concepts' and a 'Poster' session for instruments were also held. The final session consisted of summaries of what went on in the various worshops; these triggered lively discussion and also raised questions which hopefully may receive answers by the time of the next ICANS (possibly May-June 1988).

The written contributions have been grouped into nine sections, corresponding to the workshops, and within these groups roughly in the order in which they were presented in the session. Where available, the summary of the session is included at the start of the appropriate section. These summaries have been prepared here at SIN, from a recording taken on the Friday morning and the foils and notes of the summarisers. The aim has been to come as close as we can to a verbatim transcript but with some editing both by us and by the authors: to remove any figures used; to shorten somewhat the length; to include only a very brief summary of comments and discussion that occured during the actual presentation.

We should like to thank the session summarisers, Jack Carpenter, Alan Carne, Kent Crawford, Gary Russell and Gavin Williams. Our thanks also go to Mrs A. Bolsinger and to all those other people who helped in the organisation and running of the meeting and to Mrs S. Frigot for preparation of these proceedings.

Villigen, April 1987

F. Atchison
W.E. Fischer

IN MEMORIAM

YOSHIKAZU ISHIKAWA

On 28 February, 1986, our friend and colleague Yoshikazu Ishikawa died unexpectedly, after having suffered a subarachnoid hemorrhage ten days earlier. We all share a feeling of great loss, for he was one of the most vigorous members of the world community of neutron physicists, an excellent scientist, one of the pioneers of our field both in Japan and at large, the prime motivator for the development of the KENS pulsed spallation neutron source and its instrumentation, and was our gracious host at the marvelously successful ICANS IV meeting in Japan. He was a close personal friend and a vital collaborator of many of us.

Ishikawa was born on 24 October, 1930, in Yokohama, Japan. He studied at the University of Tokyo, where he received the Bachelor of Science degree in 1953, and the Doctor of Science in 1958. He became Lecturer in the Department of Applied Physics at the University of Tokyo in 1958, and Associate Professor of the Institute of Solid State Physics in 1959. Between 1964 and 1966, he was professor at Centre d'Energie Nucleaire in Grenoble, France. In 1969, he was appointed Professor of Physics at Tohoku University in Sendai, and was Joint Professor at the Laboratory for High Energy Physics (KEK) at Tsukuba, positions he held until his death.

Ishikawa was our ICANS representative in Japan, chairman of the Magnetism Commission of the International Union of Pure and Applied Physics, a member of the committee of the Science Academy of Japan, a member of the

advisory council for scientific policy and management, of the advisory committee for the Booster Synchrotron Utilization Facility, and chairman of the neutron scattering experiment advisory committee of KEK.

His scientific career began with the study of magnetism in Fe_3O_4-Fe_2TiO_4 mixed-phase systems and $FeTiO_3$ and $NiTiO_3$; he discovered ferrimagnetism in the hematite-ilmenite systems and clarified its origin. His interest in and contributions to the field of magnetism continued throughout his professional life. Early in his scientific career, he struck up collaborations with colleagues in Brookhaven National Laboratory in the United States, and CEN Grenoble. Later, he traveled frequently to use the spectrometers at the Institute Laue-Langevin in Grenoble. He maintained close connections with his colleagues in his scientific work, and was often abroad from Japan to extend his research; his colleagues acknowledge him as the "idea man" in much of this collaborative work.

Ishikawa's first encounter with pulsed neutrons was probably in 1967 when Motoharu Kimura constructed a large neutron diffractometer at the Tohoku linear accelerator in Sendai and persuaded him to support that project. When he arrived in Sendai in 1969, he took part with Kimura, Noboru Watanabe and others in the construction of instruments for the pulsed neutron source there, which was the first in Japan. After the successful work in Tohoku, Ishikawa proposed the KENS pulsed spallation neutron source project in Tsukuba, using the 500 MeV Booster Synchrotron of KEK. He led the nationwide project team in the construction and instrumentation of KENS, which was completed in March, 1980, only five years after the first proposal. Some of us remember the excited feelings of the members of that team when they reported their accomplishments at the mini ICANS meeting at the Rutherford Laboratory early in 1980.

His studies of spin dynamics in transition metals and their compounds and of Invar alloys were especially notable; in particular, his measurements on MnSi demonstrated the validity of Moriya's unified picture of band magnetism in itinerant magnetic systems. For this work, in 1983, Ishikawa was awarded the prestigious Nishina Memorial Medal.

His laboratory at Tohoku University trained many students in the field of neutron scattering in magnetism, and Ishikawa maintained a close interest in their subsequent careers. Several of them are continuing to push back the frontiers in this area at neutron centers in Japan.

Ishikawa was as frequent and expert a user of triple-axis instruments at the research reactors, as of time-of-flight instruments at the pulsed sources. Truly ecumenical in this as in many other ways, he spoke from a unique perspective when he observed in relation to the friendly conflict between steady source users and pulsed source users in other parts of the world, "In Japan, every neutron good neutron".

He was a leading force in arranging the United States-Japan Exchange Agreement on Neutron Scattering, which led to the construction of new instruments at the Brookhaven High Flux Beam Reactor and at the Oak Ridge High Flux Isotope Reactor, and provided those high-flux neutron facilities for use by Japanese scientists.

Yoshikazu Ishikawa was a most highly respected leader in pulsed neutron source development, in the use of neutron scattering methods for condensed matter research, and in condensed matter physics research in general. We admired him also for the great energy that he applied to all his work, and for his qualities as a sympathetic man. He acted in the best Japanese tradition as "nako-odo" for at least eleven couples, maintaining lifelong interest in their well-being. He was a sincere Christian, and volunteered much effort for his church. He loved the mountains; he climbed many mountains in the summertime, and enjoyed skiing in the winter. His charming wife, Hiroko, whom he married in 1959, accompanied him on many of his travels, and shared his affection for the French language and culture. She survives him in Sendai, as do his daughter, Mari, a student at Tohoku University, and his son, Tomoo, who studies at Tokyo Institute of Technology.

LIST OF PARTICIPANTS TO ICANS IX :

Dr. W.B. Amian	KFA	GERMANY
Dr. I.S. Anderson	SIN/NBS (USA)	SWITZERLAND
Dr Carla Andreani	Uni. Rome	ITALY
F. Atchison	SIN	SWITZERLAND
Dr. G. Bauer	KFA	GERMANY
Prof. Dr. J.P. Blaser	SIN	SWITZERLAND
Dr. T.A. Broome	RAL	UK
Dr. W. Bührer	ETHZ	SWITZERLAND
Dr. A. Carne	RAL	UK
Dr. J.M. Carpenter	ANL	USA
Dr. B.G. Chidley	AECL	CANADA
Dr. C. Coceva	ENEA	ITALY
Dr. R.K. Crawford	ANL	USA
Prof. Dr. L.A. de Graaf	IRI	NETHERLANDS
Dr B. Dreyfus	CENG	FRANCE
M. Dubs	SIN	SWITZERLAND
Dr. Yasuo Endoh	Uni. Tohoku	JAPAN
Dr. D. Filges	KFA	GERMANY
Dr. P. Fischer	ETHZ	SWITZERLAND
Dr. W.E. Fischer	SIN	SWITZERLAND
W. Francioni	EIR	SWITZERLAND
Dr. A. Furrer	ETHZ	SWITZERLAND
Dr. I.S.K. Gardner	RAL	UK
Prof. R. Geick	Uni. Würzburg	GERMANY
Dr R. Hardekopf	LANL	USA
Dr. M.W. Johnson	RAL	UK
Dr. Motoharu Kimura	Uni. Tohoku	JAPAN
Dr. W. Kley	ISPRA	ITALY
Prof. Dr. G. Kostorz	ETHZ	SWITZERLAND
Dr. A.T. Lucas	RAL	UK
Dr. F. Menzinger	Uni. Rome	ITALY
Dr. Masakatsu Misawa	KEK	JAPAN
Dr. F.A. Morse	LANL	USA
Dr. M. Pepin	SIN	SWITZERLAND
Dr. D.J. Picton	Uni. Birmingham	UK
Prof. Dr. H. Rauch	AOU	AUSTRIA
H. Robinson	LANL	USA
Dr. G.J. Russell	LANL	USA
Dr. U. Schryber	SIN	SWITZERLAND
Dr. P.A. Seeger	LANL	USA
Dr. G.C. Stirling	RAL	UK
Dr. Y. Takeda	SIN	SWITZERLAND
Dr. A.D. Taylor	RAL	UK
Dr. H. Tietze	Uni. Würzburg	GERMANY
Dr. Ch. Tschalär	SIN	SWITZERLAND
Dr. M. Victoria	EIR	SWITZERLAND
Dr. W.G. Williams	RAL	UK
Dr. R. Woods	LANL	USA

Nach
Klosterli-Arth-Gold

CONTENTS

STATUS REPORTS

Enhanced Target Moderator Concepts for ISIS 1
G.S. Bauer
Status Report on ISIS, the Spallation Neutron Source at RAL 23
D.A. Gray
Status Report on LANSCE, 1986 31
F.A. Morse
Status of the Intense Pulsed Neutron Source 45
B.S. Brown, J.M. Carpenter, R.K. Crawford and C.W. Potts
Status Report on the KENS Facility 65
N. Watanabe, Y. Endoh, K. Inoue and M. Misawa
Proton Storage Ring Commissioning at LANSCE 85
G.P. Lawrence, R.A. Hardekopf, A.J. Jason, B. Blind and T.W. Hardek
Status Report on SINQ, the SIN Neutron Source 101
W.E. Fischer
Performance of the Intense Pulsed Neutron Source Accelerator System 113
F. Brumwell, C.W. Potts, A. Rauchas, V. Stipp and G. Volk

INVITED PAPERS

Perfect Crystal and Magnetic Field Beam Tailoring 125
H. Rauch
Neutron Sources - Their prospects and their problems 141
G.S. Bauer
Common Problems 167
A.D. Taylor

TARGETS

Summary of Workshop on Targets 171
J.M. Carpenter
The LANSCE Target System 177
G.J. Russell, H. Robinson, G.L. Legate, R. Woods, E.R. Whitaker, A. Bridge, K.J. Hughes and R.D. Neef
Activation of the Heavy Water Coolant of the ISIS Target 245
G.H. Eaton, T.A. Broome and M.J. Bly
Thermofluid Dynamics of the SINQ Target
- A Natural Circulation Loop as a Target - 259
Y. Takeda

MODERATORS

Summary of Session on Moderators 271
J.M. Carpenter and G.J. Russell
Analysis of the Burping Behavior of the Cold Solid Methane Moderator at IPNS 279
J.M. Carpenter, U. Walter and D.F.R. Mildner
LANSCE Hydrogen Moderator System 304
H. Robinson and G.J. Russell
Operational Experience with the ISIS Cryogenic Moderators 305
A.T. Lucas
Deterioration of Performance of Neutron Moderators under Intense Irradiation 315
J.M. Carpenter, S.S. Cudrnak and C.M. DeCusatis

INSTRUMENTS - PART I

Summary of Instrument Session - Part I 343
W.G. Williams
HET: The High Energy Inelastic Spectrometer at ISIS 349
A.D. Taylor, B.C. Boland and Z.A. Bowden
Test of a Correlation Chopper at a Pulsed Spallation Neutron Source 365
R.K. Crawford, J.R. Haumann, G.E. Ostrowski, D.L. Price and K. Sköld
The NBS Neutron Time of Flight Spectrometer 383
I.S. Anderson, T.J. Udovic, J.M. Rowe, J.J. Rush and J. LaRock
The Rotating Analyser Crystal Spectrometer ROTAX 389
H. Tietze and R. Geick
The IPNS Resonance Detector Spectrometer 397
R.K. Crawford

INSTRUMENTS - PART II

Summay of Instrument Session - Part II 431
R.K. Crawford
The Low-Q Diffractometer at the Los Alamos Neutron Scattering Center ... 437
P.A. Seeger, A. Williams and J. Trewhella
The Determination of the Complete Neutron Scattering Law $S(\kappa,\omega)$ from Total Scattering Experiments using Computed Tomography 449
M.W. Johnson
New Developments of TOP Spectrometer 457
Y. Endoh, S. Itoh and S. Mitsuda
Data Acquisition and Analysis: A Forward Look 469
M.W. Johnson, W.C.A. Pulford and S.P.H. Quinton

INSTRUMENT POSTERS

Polarising Filter Developments at ISIS 477
J. Mayers, R. Cywinski, I.R. Harris, M. Hixon and W.G. Williams
CRISP, a Pulsed Source Neutron Reflectometer for Surface Studies 493
J. Penfold, R.C. Ward and W.G. Williams
High Resolution Molecular Spectroscopy Using TFXA at ISIS 505
J. Penfold and J. Tomkinson
Neutron Beam Shielding at ISIS 519
A.D. Taylor, T.A. Broome and D.J. Picton
The HET Background Suppressing Chopper 529
T.J.L. Jones, I. Davidson, B.C. Boland, Z.A. Bowden and A.D. Taylor
MARS - A Multi-angle Rotor Spectrometer at the Pulsed
Neutron Source ISIS 535
A.D. Taylor, R.C. Ward, W.G. Williams, Y. Endoh and N. Watanabe
Liquid and Amorphous Total Scattering Instrument at KENS - HIT 539
M. Misawa, T. Fukunaga, T. Yamaguchi and N. Watanabe

BOOSTERS AND NEW CONCEPTS

Summary of the Workshop on Boosters and New Concepts 551
A. Carne
Progress on the IPNS Enriched Uranium Booster Target 557
A.E. Knox, J.M. Carpenter, J.L. Bailey, R.J. Armani, R.N. Blomquist, B.S. Brown, D.R. Henley, A.G. Hins, B.A. Loomis, A.W. Schulke and H.R. Thresh
Studies of Low Enrichment Targets for ISIS 591
T.D. Beynon, D.J. Picton and T. Al-Sharify
A Concept for an eV Spallation Neutron Source 613
W.E. Fischer

CALCULATIONAL METHODS

Experimental and Theoretical Analysis of the High Energy Deep
Penetration Experiment at WNR - Los Alamos 627
(KfA/IRE - LANL/P9 Collaboration)
W.B. Amian, H. Schaal, V. Drüke, P. Cloth, D. Filges and N. Paul
The High-Energy Neutron background at SINQ 649
M. Pepin

AUTHOR INDEX 657

ICANS IX

INTERNATIONAL COLLABORATION ON ADVANCED NEUTRON SOURCES

22-26 September, 1986

Enhanced Target Moderator Concepts for ISIS

G. S. Bauer, KFA Jülich

for

The Members of the Target Group of the International ISIS Project Group

1. Introduction

With ISIS now well on its way to become the world's leading and most powerful pulsed neutron source and in particular in view of the fact that it will probably for a long time be Europe's only pulsed neutron source. It seems quite natural that questions are being discussed now, on how access to ISIS for an international community could be organized and what potential exists for future enhancement of its capabilities. These questions are being dealt with at present by a project group established under the Memorandum of Understanding which has been signed by Great Britain, France and Italy. This paper we report on the state of the discussion in the Target Section of the project group. Two distinctly different cases are considered, namely whether or not Rutherford Appleton Laboratory will be operating with a nuclear site license in the future.

2. The present situation

At present there exists one extracted beam line with a neutron target station at its end. The design of the accelerator, however, would allow a second beam to be

extracted approximately at right angles to the first one, i. e. in the direction where the old NIMROD Hall (Hall 1, or building R6) is located (fig. 1).

The present target station has 18 beam lines and will be able to accommodate an estimated total of 25 neutron scattering instruments. The beam lines are fed from four moderators of different characteristics and performance (fig. 2), located above and below the target, two ambient temperature water moderators (A, AP and D), a liquid methane moderator (CH_4) and a super-critical hydrogen moderator (H_2).

The target itself (fig. 3) consists essentially of a cylinder of depleted uranium, 34 kg in mass which is subdivided into 23 disks of three different thickness for cooling purposes. The disks are clad individually in zircaloy and mounted in a stainless steel support frame. The presurized D_2O-coolant is guided in a stainless steel manifold of quite elaborate design. At full proton current (≈ 180 μA), a total of about 230 kW of heat will be deposited in the target and its structural material, including the stainless steel pressure vessel in which the whole assembly is contained. Apart from a few components such as heat exchangers, which would have to be supplemented, the system could handle up to 1.5 MW, i. e. six times the present heat output. All pipework and the containment provided to avoid release of radioactivity from the target are designed and fabricated to meet the ASME standards required for a nuclear installation. The safety and control systems are similar to reactor practice.

3. Options for RAL operating without a nuclear site license

If RAL were to continue to operate without a nuclear site license, as is presently the case, the following potential for improving the neutron supply to the users can be seen:

3.1 Changes in the present target and moderator geometry

Research with respect to target-moderator optimization which has been carried out since important design parameters of the ISIS target had to be frozen has yielded

some clues on possible improvements that could be achieved from changes with respect to the present geometry.
There are two main points to be mentioned:

3.1.1 Improvement of geometric coupling into moderators by reducing the distance between target and moderator centre lines

Although great care was taken in designing the present target and its surroundings (fig. 4) to keep the target-moderator distance small, it may be possible to achieve even better geometric coupling by

(a) reducing the thickness of the stainless steel frame around the uranium,
(b) changing the shape of the pressure vessel in such a way that flat top and bottom sections can be avoided, which may allow a thinner wall thickness,
(c) scrutinizing the need for the 6 mm Boral layer between the target and especially for the cold moderator.

Taking all the possible gains from these measures together, an estimated improvement in neutron leakage from the moderators of the order of 10 % could be anticipated. It should be borne in mind, however, that moving the moderators closer to the target would make other changes necessary. This may include the centre section of the reflector and it requires an adjustment of the beam lines and instruments to the new moderator heights.

3.1.2 Change from cylindrical to "2-dimensional" target

Under the assumption, that the target would have a circular cross section, its optimum diameter was determined to be 9 cm (Atchison, 1981). Subsequent research done for a wheel-type high power target (Bauer et al, 1982) showed that, with a laterally extended target, important gains in target-to-moderator coupling can be achieved. Fig. 5 shows this effect for a set of uranium targets with an unreflected moderator. For comparison, the curve determined by Atchison (1981) for a reflected target with circular cross section is also shown. (This curve has been arbitrarily normalized to the one for a 10 cm wide target at 9 cm thickness.) The gain, that can be obtained by going from a 10 cm wide target to a 30 cm wide target is

about 30 %. Since the topology of Atchison's curve for the reflected case seems to agree well with the measured data for the unreflected case (showing the superiority even of a 10 cm wide target of thickness t over a circular one with diameter t for t < 9 cm), it may be anticipated that this gain could also be obtained in a reflected target.

Together with some of the measures described under 3.1.1 it may be assumed, that this provides a potential to improve the performance of a depleted uranium target by up to 35 to 40 % relative to the present one.

3.2 Second target station

Making use of the possibility to add a second extraction beam line to the ISIS synchrotron, the construction and operation of a second target station can be envisaged. Unless the accelerator characteristics change, the most likely way to operate with two target stations would be a pulse-switching mode, directing e. g. 1 out of 5 pulses onto the second target. Without making use of fissile material (see below), this would result in a relatively low time average power (≈ 50 kW with a depleted uranium target; ≈ 20 kW with a W-target) at a pulse rate of 10 Hz. The design of the second target station could provide for better target-to-moderator coupling than in the present high power case by taking advantage of these features and by placing cryogenic moderators with as high a hydrogen density as possible, at the optimum positions. The low pulse repetition rate makes this source particularly suitable for cold neutrons which, in turn, are easily transported through curved guides for efficient background and fast neutron suppression. In view of this fact one might even consider the use of slab moderators which have a 2 times better coupling to the target than wing moderators. Taking all these effects together, it is not unlikely that the useful cold neutron flux from this low power target would more or less match the one from the present cold moderators, especially since at 10 Hz there is no risk of frame overlap and each of the pulses could be used by all instruments. In this way target 1 could be freed from the cold neutron instruments and about 10 to 12 new beam lines for cold neutrons would become available at target 2, with

practically no loss in performance.

4. Options if RAL were to operate under a nuclear site license

In order to make possible more significant gains in neutron production than those discussed above, the possibility of using fissile material in the target has been examined both for the present and a new second target station.

The general problem in using fissile material, apart from the fact that a nuclear site license may have to be obtained, is that, with no special precautions taken, the pulses tend to be lengthened substantially. For a pulsed source it is therefore necessary to minimize thermal fission in the target by (a) preventing thermal neutrons from the moderator and reflector from diffusing back into the target and (b) allowing as little thermalization as possible within the target itself. Although it is essential to have very detailed calculations to assess the true source enhancement that can be obtained from any particular arrangement containing fissionable material, a crude estimate of the neutron production enhancement in the target can be attempted starting from the total energy dissipation in the target:

It is known, that in a non-fissile target, about 2/3 of the proton energy is dissipated inside the target and 1/3 is carried away by the particles leaving the target. The total neutron yield in a fissile target is taken as the sum of the yields from spallation and from subsequent fission processes. We set for the total energy dissipation per incident proton, E:

$$E = 2/3\ E_p + 190 \cdot (f/p) \qquad (1)$$

with (f/p) giving the number of fissions per proton and 190 MeV being the energy release per fission process. Taking into account, that each fission process adds about 1.4 neutrons to the overall production, we have for the number of neutrons produced:

$$n_{tot} = n_s + n_f = n_s + (f/p) \cdot 1.4 \qquad (2)$$

For the reference case of 800 MeV protons on depleted uranium it has been shown (Atchison, 1981), that about 1460 MeV are released in the target per incident proton, destroying about 4.9 nuclei by fission processes and producing a total of 26 $^{n}/_{p}$. Inserting these numbers in (1) and (2), we obtain from (1)

$$(^{f}/_{p}) = 4.8 \text{ in good agreement with the above result}$$

and from (2)

$$n_s = 19$$

Applying the same relations to a target of total power P_o (W) and assuming an incident current I (μA) we have

$$n_{tot} = 19 + (1.4/190)\,(P_o/I - 533) \qquad (3)$$

4.1 Use of enriched uranium on target 1

As mentioned before, the layout of the present target station is such, that no major amendments would be required from a technical point of view to operate it at a power level of about 1.5 MW. This amount of energy could be produced in a target of similar design to the present one but with the peak heat deposition of 770 W/cm³ of the present target ocurring throughout the target. This would require a target consisting of 32 plates, each 7.7 mm thick (as are the front ones of the present target) and a heat flux across the plate faces of ≈ 300 W/cm². This heat flux is close to what is presently considered the safety limit, but some increase in the pressure of the cooling system could be envisaged.

Let then P_o be 1.5 MW and I = 180 μA. So we have from (3)

$$n_{tot} = 76.5\ ^{n}/_{p}.$$

giving a total enhancement in neutron production of a factor 3 over a depleted uranium target. It should be noted, however, that (a) this enhancement is not uniformly distributed over the length of the target due to the need for

maintaining a flat power distribution and (b), more importantly, due to the spatial and spectral distribution of the neutrons produced from fission, target-to-moderator coupling as well as moderation efficiency of the moderator will be poorer than in the case of the depleted uranium target, especially since there is a need for decoupling the target to keep the pulses short. So, realistically, an enhancement for the thermal or cold neutron leakage of about 1.5 at the front moderators and 2.5 at the rear ones might be anticipated. These figures are also suggested from scoping calculations done within the present study work by D. Picton, University of Birmingham. These calculations indicate that the content in U-235 in such a target would have to vary between 0.2 % (centre of front plates) up to 60 % in different axial and radial zones.

4.2 Target 2 designed as a near-critical booster target

Assuming, as before, that ≈ 20 % of the proton beam (i. e. ≈ 36 μA) would be directed towards a second target station, a higher multiplication factor than above could be aimed for in a near-critical booster assembly.

4.2.1 Booster for short pulses using fast fission only

The reference model considered for initial scoping calculations in this case is shown in fig. 6. The booster consists of fuel plates, 30 cm wide and about 10 cm high which are stacked to a total depth of 35 cm and surrounded by a decoupling layer (≈ 10^{22} at.B_{10}/cm^2) to prevent thermal neutrons from the moderators from returning to the target. Slab water moderators were assumed on the two large faces of the target and the whole arrengement was surrounded by a reflector (Ni) except for the two moderators faces and the entrance face of the proton beam into the target. Although, initially, Na-cooling was assumed, it appears that, due to the small volume fraction of coolant in the target, also D_2O might be suitable.

The overall results of the calculations for Na-cooling are given in table 1, with the power in the target chosen to be 1.75 MW. The enrichment in the booster in U-235 was 65 % in an inner zone and 80 % in the outer zone resulting in an

average of 75 %. For comparison, the same arrangement has also been run for the case of natural uranium.

It can be seen that, while the source enhancement is 17 between a target of natural uranium and the booster, the leakage from the moderator faces is only enhanced by a factor of 12. It must be assumed, however, that the coupling of a small wing moderator would suffer more from the extended source than that of the large slab moderator used here.

The volume of the target is about 10 l with a uranium fraction of 80 %, leading to an average power density of 220 W/cm^3 which is relatively moderate. It should be noted, however, that it is assumed that the target will be operating at 10 Hz, thus depositing 175 KJ/pulse. This leads to a thermal cycling by about 10 K at each pulse. Work done by Krautwasser et al (1985) for the SNQ-project suggests that this should not be a problem from the point of view of thermal cycling growth, if U 10 % Mo is used. The concurrent effect of radiation damage can at present not be assessed.

The pulse shape to be obtained from this arrangement has also been investigated and is shown in fig. 7 together with the case for the reference target of natural uranium. Apart from the enhancement, both curves have equal characteristics and have a FWHM of about 100 μs. (Note, the thickness of the moderator is 7 cm, un-poisoned!) Also shown is the pulse for the case, where all delayed neutrons are included. From this it is obvious, that about 17 % of all neutrons produced will be spread out over the whole time between pulses. The delayed neutron background will therefore be about 0.2 ‰ of the pulse intensity.

Table 2 gives a comparison of some relevant data for D_2O cooling vs. Na-cooling. The pulse shapes for various energy groups are shown in fig. 8.

With its flux enhancement of about a factor 10, which might be expected in a real arrangement with wing moderators the booster target seems to be quite promising from a physics point of view, especially since reasonably short pulses would be obtained at a low repetition rate. It should not be overlooked, however, that the actual design and operation of such a target presents quite a challenge.

So far, in order to obtain a crude picture of the thermohydraulic situation, a reference target design has been looked at (Weisweiler, KFA) which is in principle similar to the present ISIS target (see fig. 9) and does not take into account any engineering or operational constraints. All 35 plates are of equal thickness (namely 7.7 mm including 2 x 0.25 mm cladding), and are seperated by 1.75 mm cooling channels. Temperature and coolant flow data for the cases shown in fig. 9a and b are compiled in table 3 for D_2O and Na-cooling.

As can be seen, D_2O-cooling (at 6 m/s flow velocity between the plates) in an arrangement according to fig. 9b results in very reasonable data although an optimization process might perhaps aim at reducing somewhat the flow rate, which is about five times higher than in the present target. It should be noted, however, that these data pertain to α-uranium. The metastable γ-phase, which might be required to reduce swelling due to thermal cycling, has poorer thermal conductivity.

While, as can be seen from table 2, the loss of coolant results in a negative void coefficient and therefore switching off the proton beam is an effective shutdown-mechanism in all situations. The heat production after shutdown is quite substantial - as in a 1.7 MW reactor (see fig. 10). Taking the decay heat as 3 % of the operating power over the first few minutes, with the dense packing of the material, little heat dissipation to the environment can be anticipated and a temperature rise of $\approx$ 3 K/s after a loss of coolant would result, making efficient emergency cooling mandatory.

A loss of the decoupling between the target and the moderators has to be avoided under all circumstances, since, as can be seen from table 2, this would result in k_{eff} exceeding 1 substantially. It is in particular these safety aspects, which require extensive further study, before the technical feasibility and cost of such a booster arrangement can be assessed. One possible conceptual design, which includes the decoupler (shrunk onto each target plate) in the pressure vessel to ensure adequate cooling as well as its rigid connection to the uranium in all cases is shown in fig. 11.

Since the burn up in the target is relatively low, the life-limiting factors will be radiation damage and target swelling. Efficient and independent means to monitor

this effect will have to be provided. Unfortunately a low burn up at the end of life results in high operating costs.

4.2.2 Booster allowing thermal fission

Some of the problems associated with a booster designed for short pulses could be alleviated, if the multiplication was allowed to result from thermal fission in the target. The immediate consequence of this would be a significant lengthening of the pulse decay constant. Calculations by Scherer (KFA) have shown that, with a source multiplication of about 10, only about a factor of 3 would be gained in pulse height and the rest would be in the long tail of the pulse. In this case also the moderator design could be different from the present one on ISIS, namely as developed for the SNQ-project (see e. g. Bauer et al, 1985). With such non-decoupled moderators and grooved surfaces, the time average thermal neutron yield at the same source strength is increased by almost a factor of 20 over the present design. Without exceeding a power level of a few MW in the target, it might become possible to devise an intensity modulated source of the type proposed in the German SNQ-project but with a 10 times lower time average flux (i. e. of the order of 10^{14} cm^{-2} s^{-1}). With the elaborate experimental techniques that have been proposed to exploit such a time structure another factor of 10 to 20 can be obtained in effective gain over a cw-source of the same time average flux, this might be an interesting option.

5. Conclusions

Without either introducing a fissile target or increasing the current in the accelerator, the improvements possible relative to the present design values are moderate (≈ 15 %) as far as the pulsed thermal and cold neutron intensities are concerned. Adding a second target station would increase the number of instruments that could be accommodated, but would hardly allow a new quality of experiments.

Under the assumption, that RAL were to operate under a nuclear site license, the present target station could be upgraded to operate with a fissile target with

relatively modest efforts, yielding an increase in neutron intensities between a factor 1.5 and 2.5 on the different moderators. If a second target station was to be built in this case, it would probably be wise to design for about 4 MW of total power. Depending on the outcome of future design study work, one of three options could then be realized:

(a) a fast booster for a pulsed source at a power level around 2 MW and at 10 Hz repetition rate,
(b) a thermal booster for an intensity modulated neutron source at 10 to 25 Hz repetition rate,
(c) a high power spallation target for either a pulsed or an intensity modulated source, if suitable amendments were made to the accelerator system. In this case, target 2 might take the bulk of the proton current, keeping target 1 around $2.5 \cdot 10^{13}$ ppp at 50 Hz.

The Members of the Target Group of the International ISIS Project Group:

P. Ageron (ILL), G. S. Bauer (KFA), T. D. Beynon (Birmingham Univ.), T. A. Broome (RAL), A. Carne (RAL), C. Coceva (ENEA), L. A. de Graaf (IRI), D. J. Picton (Birmingham Univ.), W. Scherer (KFA), G. C. Stirling (RAL) and A. D. Taylor (RAL).

References

Atchison (1981)
"A Theoretical Study of a Target Reflector and Moderator Assembly for SNS"
RL-81-006

Bauer, G.S.; Conrad, H.; Fischer, W.E.; Gompf, F.; Gründhagen, K.; Reichardt, W. and Spitzer, H. (1982)
"Ausfluß- und Zeitstrukturmessungen thermischer Neutronen aus Polyäthylen- und Schwerwassermoderatoren für Spallationsneutronenquellen"
SNQ 1 HG/BH 001

Bauer, G. S.; Conrad, H.; Filges, D. and Spitzer, H. (1985)
"The SNQ-Target and Moderator System for an Optimized Neutron Economy"
Proc. Int. Conf. on Neutron Scattering in the 90's; IAEA-CN-46/079

Carne, A. (1982)
"Progress on the SNS Target Station"
Proc. ICANS VI; ANL-82-80

Krautwasser, P.; Hoven, H. and Kirchhöfer, H. (1985)
"Thermal Cycling Growth of Uranium Alloys and Fabrication of SNQ Target Pins"
Proc. ICANS VIII; RAL-85-110

U-235 Enrichment

-inner: 65 % -outer: 80 % -average 75 %

Total Inventory

U-238: 38 kg U-235: 111 kg

Time for 1% Burn up: ≈ 600 days

Primary Proton Source 2.5 E14 p/s (≙ 40 μA)

Primary Spallation Source 5.7 E15 n/s

High Energy Power (> 14 MeV) 33 kW (≙ 820 MeV/p)

		natural U (0.7 %)	booster (75 %)
Low Energy Fission Power (< 14 MeV)	/kW	25	1 600
Low Energy Gamma Power	/kW	10	110
Total Power	/kW	≈ 70	≈ 1 750
Total Neutron Source	$/n \cdot s^{-1}$	8 E15	1.4 E17
Total Moderator Leakage J^+	$/n \cdot s^{-1}$	2.3 E15	2.9 E16

Enhancements	Booster: natural U
Power	25
Source	17
Output	12

Table 1 Some data for the booster target arrangement shown in fig. 6 (Na-cooled).
(Data by W. Scherer, KFA Jülich.)

	Na-cooled	D_2O-cooled
$K_{effective}$ (of assembly)	0.957	0.964
Source Multiplication		
(rel. to spallation yield)	23	28
Moderator Output per Source n		
- all energies	6.0	6.7
- < 0.5 eV	1.8	2.2
- < 0.01 eV	0.04	0.06
FWHM of Pulse (μs)		
- all energies	0.6	0.6
- < 0.5 eV	7.2	8.2
- < 0.01 eV	110	110
75 % of total n-emission (μs)		
- all energies	115	160
- < 0.5 eV	270	330
- < 0.01 eV	300	350
Loss-of-Coolant Reactivity (%)		
- in core	- 0.74	- 2.3
- in whole assembly	- 0.88	- 2.1
Loss-of-Decoupler Reaktivity (%)		
- total loss	+ 13	+ 12
- to reflector	+ 0.4	

Table 2 Comparison of Na and D_2O as coolant for the booster assembly of fig. 6.
(Data by W. Scherer, KFA Jülich.)

Target design (fig. 9)	a	b		present ISIS at full power
Coolant	Na	Na	D_2O	D_2O
Peak temperature in α-U (° C)	390	290	170	380
Coolant inlet (° C)	150	150	50	43
Coolant outlet (° C)	305	205	65	50
Pressure drop (bar)	1.8	0.9	1.05	1.36
Coolant flow rate (l/s)	11.3	34	34	7
Velocity in gaps (m/s)	6	6	6	5.5

Table 3 Thermal data for a reference booster design of α-uranium and at 2 MW total power (flat power distribution within the booster) with coolant flow channels arranged as shown in fig. 9 (a) and (b). For comparison the data for the present ISIS target at full power (270 kW) are also given.

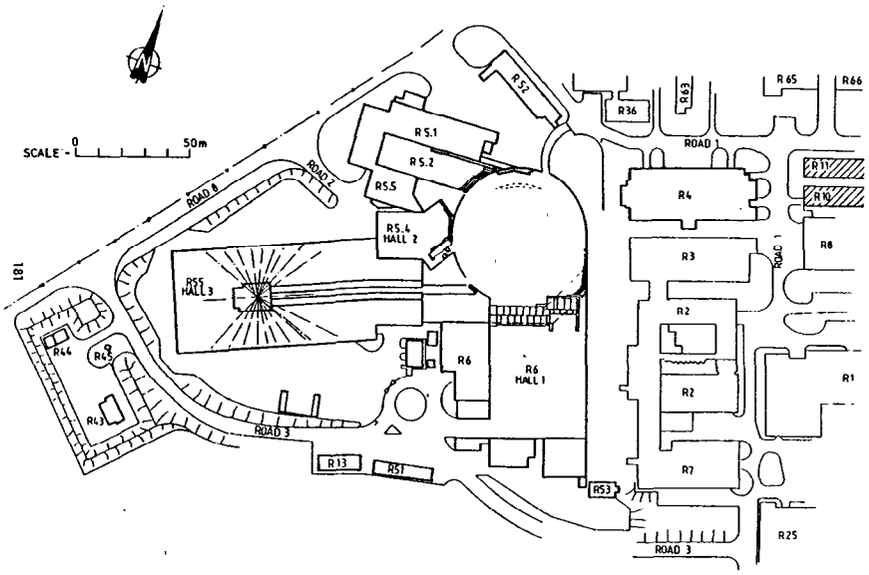

Fig. 1 The ISIS-site.

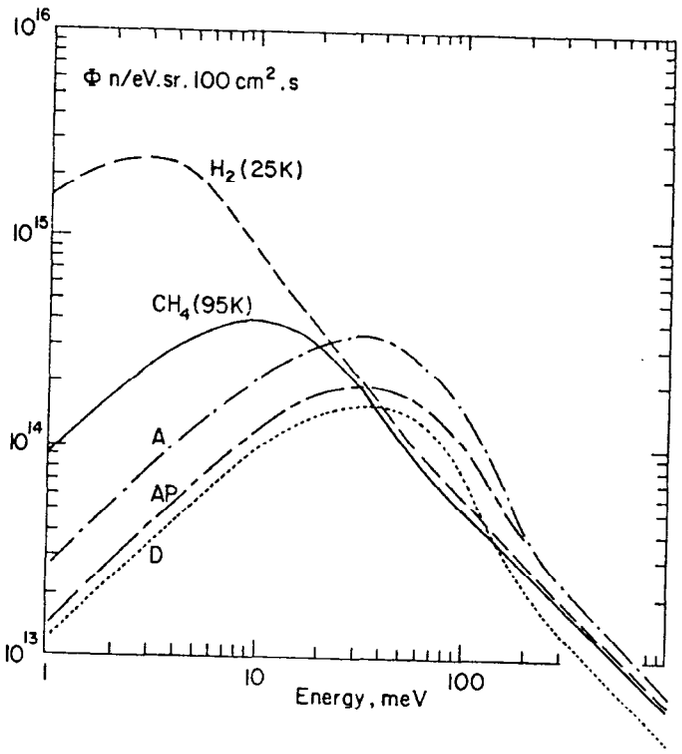

Fig. 2 The spectral distribution of neutrons from the six faces of the four ISIS-moderators CH_4 (two identical faces), D, A (ambient, one face poisoned, AP), and H_2.

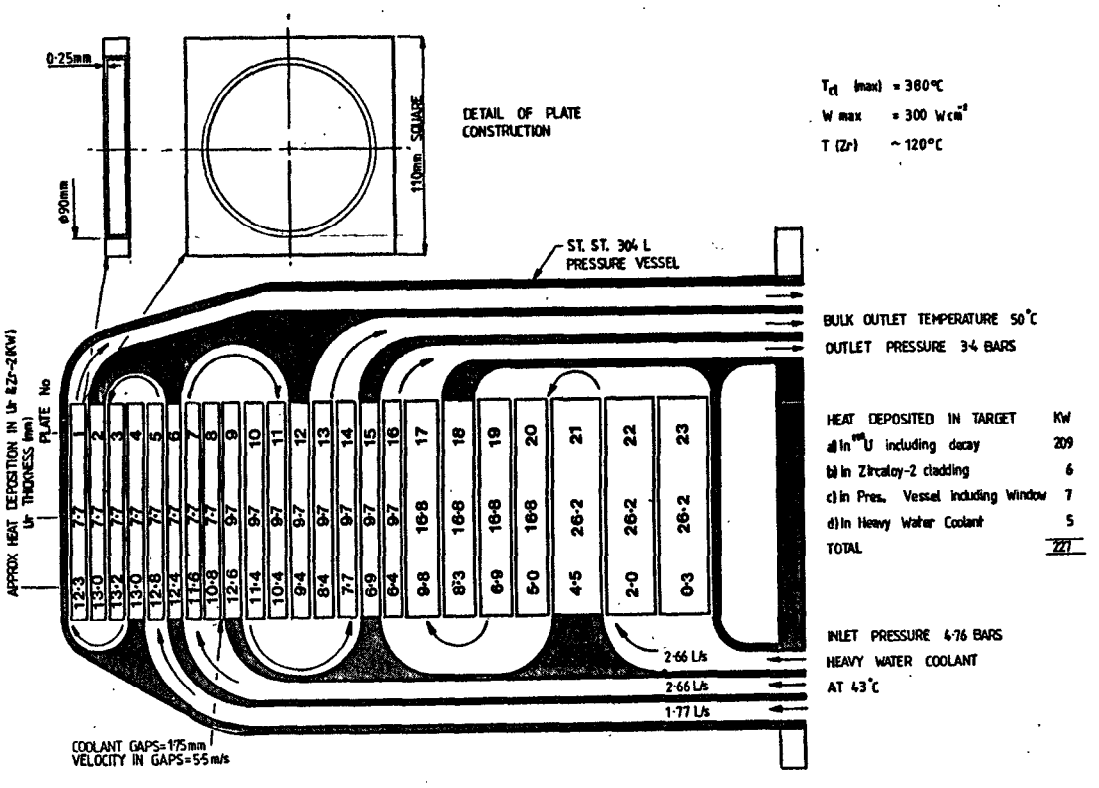

Fig. 3 Design schematic and target cooling parameters of the ISIS depleted uranium target (from Carne, 1982).

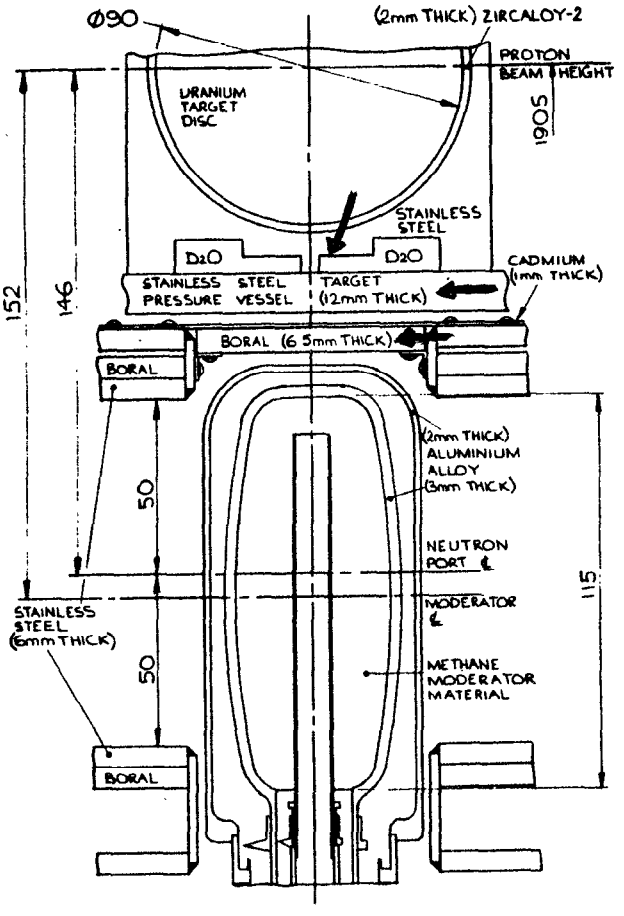

Fig. 4 CH_4 96 K-moderator location relative to the target. Areas where changes towards a reduction of the target-moderator distance might be possible are marked by arrows.

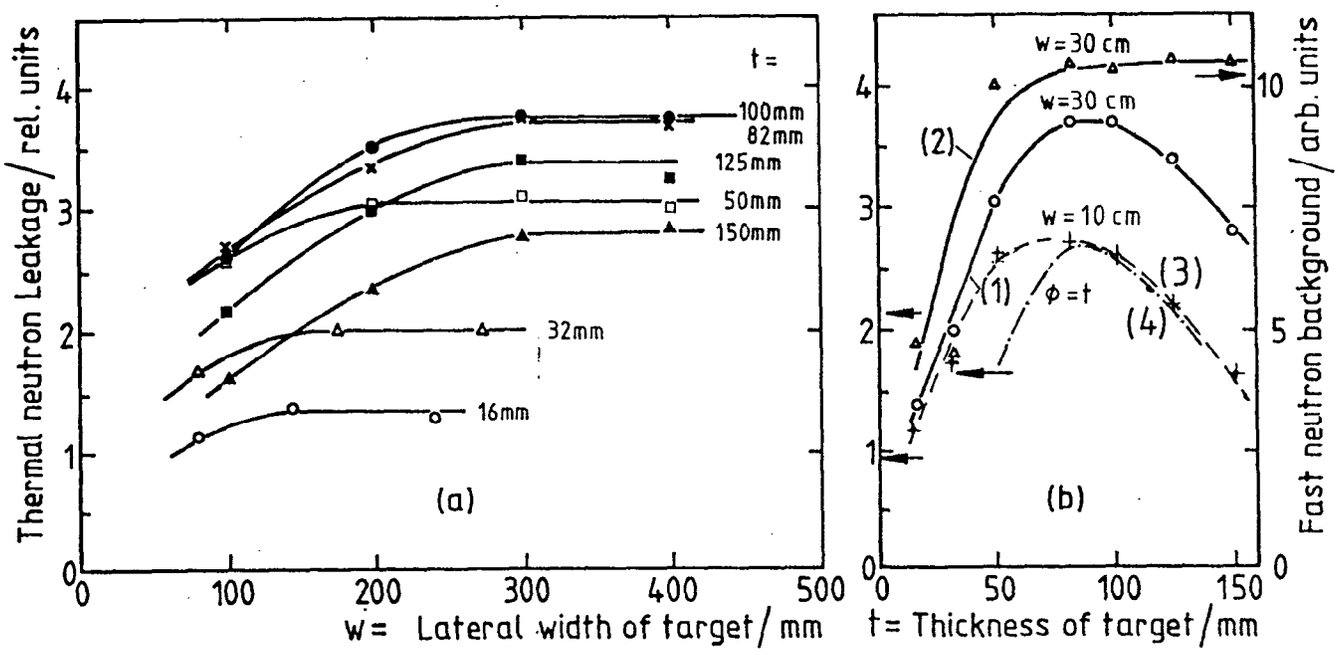

Fig. 5 Experimental results on thermal neutron leakage and fast neutron background from an unreflected polyethylene moderator as a function of the dimensions of a depleted uranium target (from: Bauer et al, 1982). Curve (4) in (b) is for a reflected arrangement with circular target cross section of diameter ϕ and has been arbitrarily normalized to curve (3) at t = 90 mm.

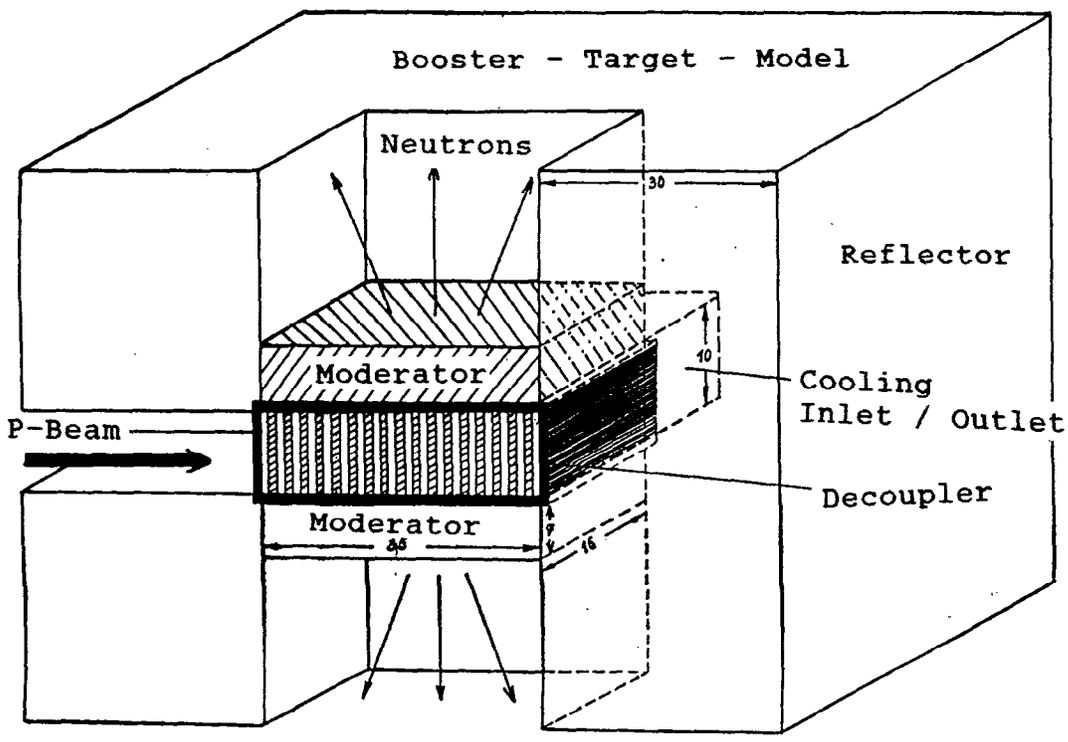

Fig. 6 Sketch of one half of the model used for the neutronic scoping calculations for the ISIS booster target.

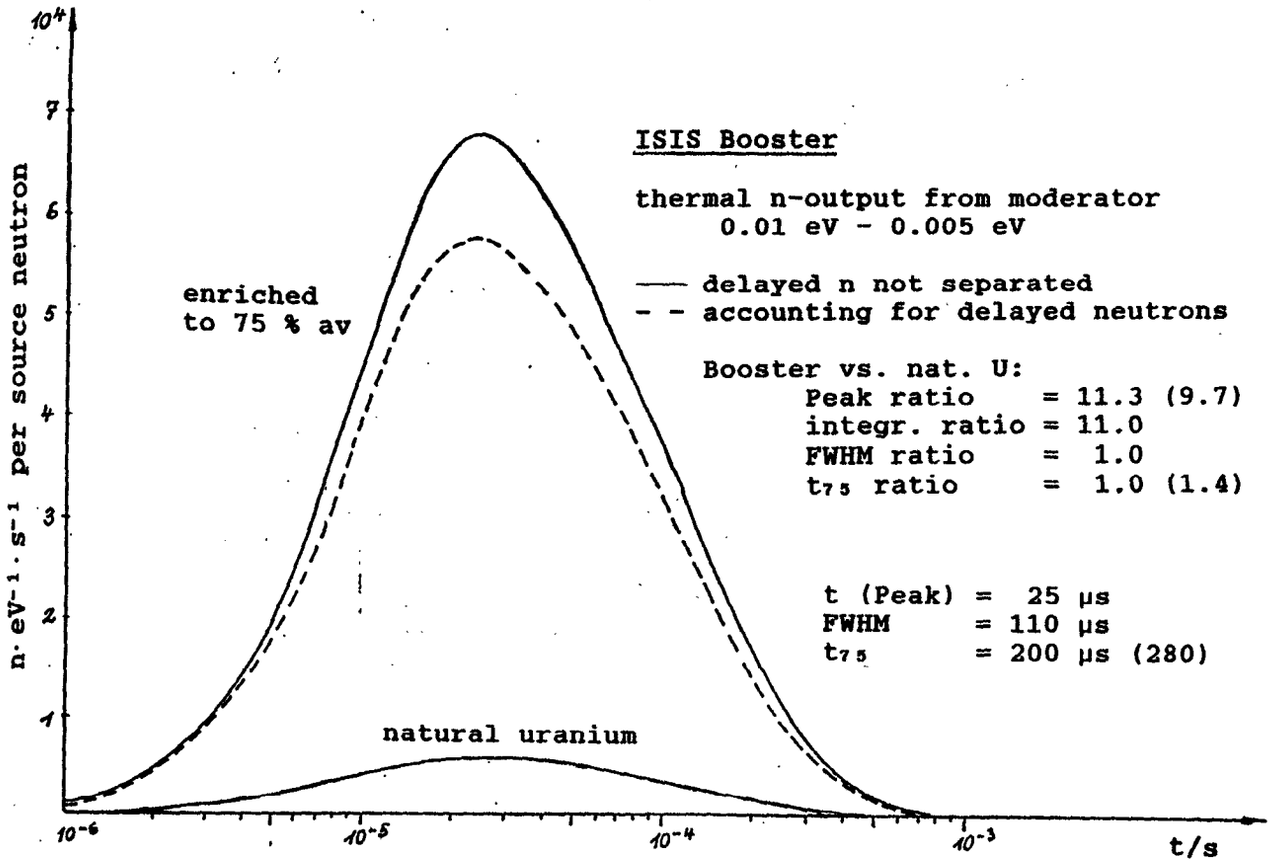

Fig. 7 Time dependence of the thermal neutron output from the arrangement shown in fig. 6 for a sodium cooled target of enriched and natural uranium.
The solid line includes all delayed neutron production in the peak.

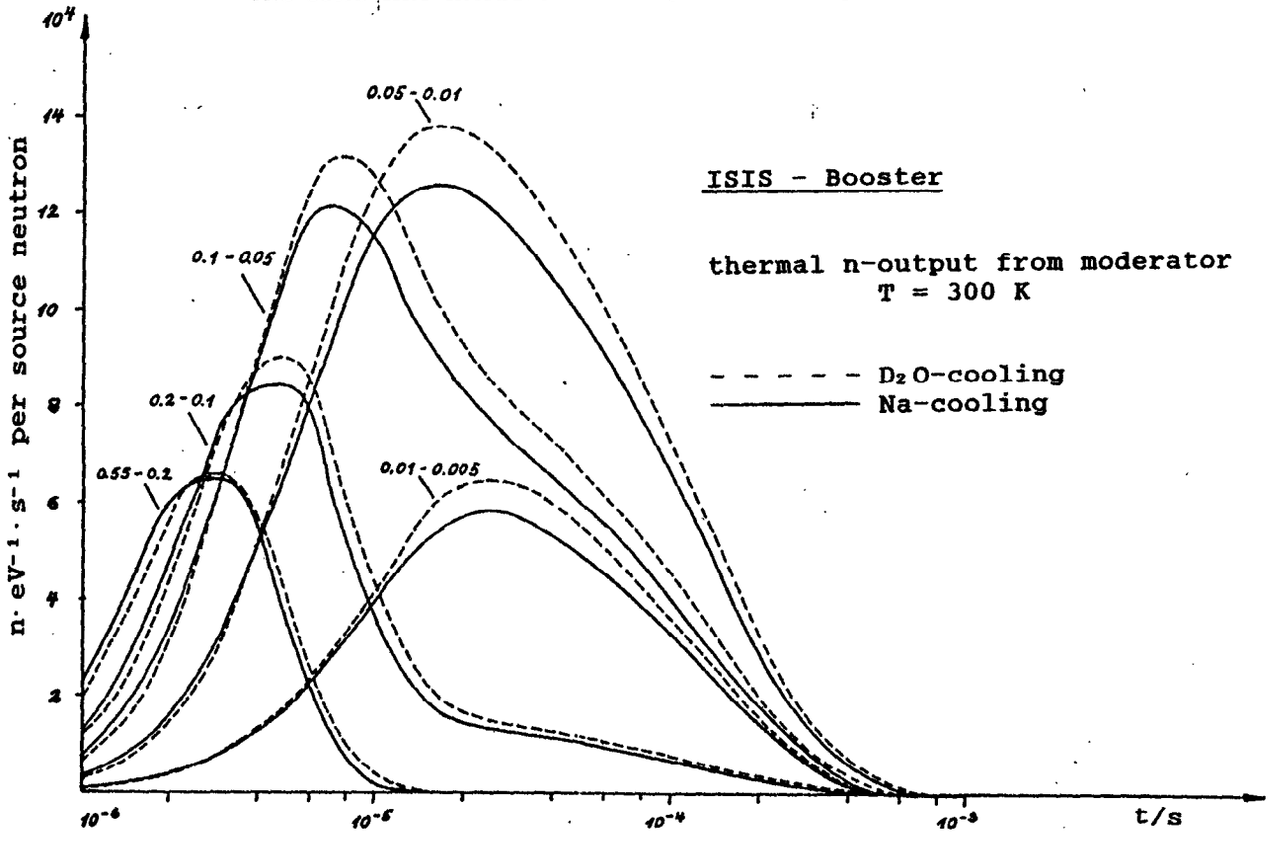

Fig. 8 Time dependence of the neutron output for various energy groups for an enriched uranium target cooled with Na (solid lines) and D_2O (dashed lines). The arrangement is as shown in fig. 6.

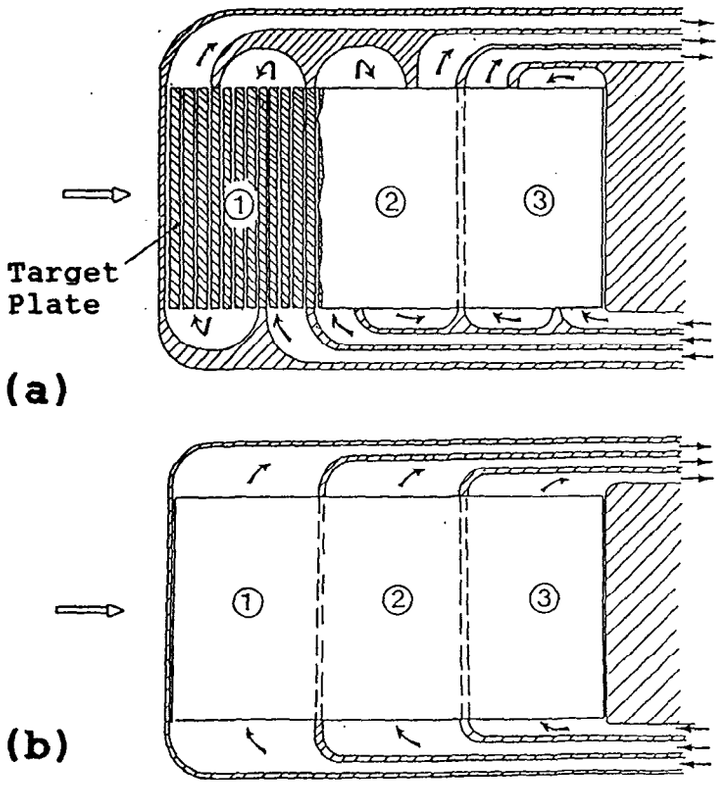

Fig. 9 Conceptual designs for the booster target used for the thermal studies. Plate thickness 7.7 mm with 2 x 0.25 mm Zr-2 cladding included, coolant gaps 1.75 mm in both cases.

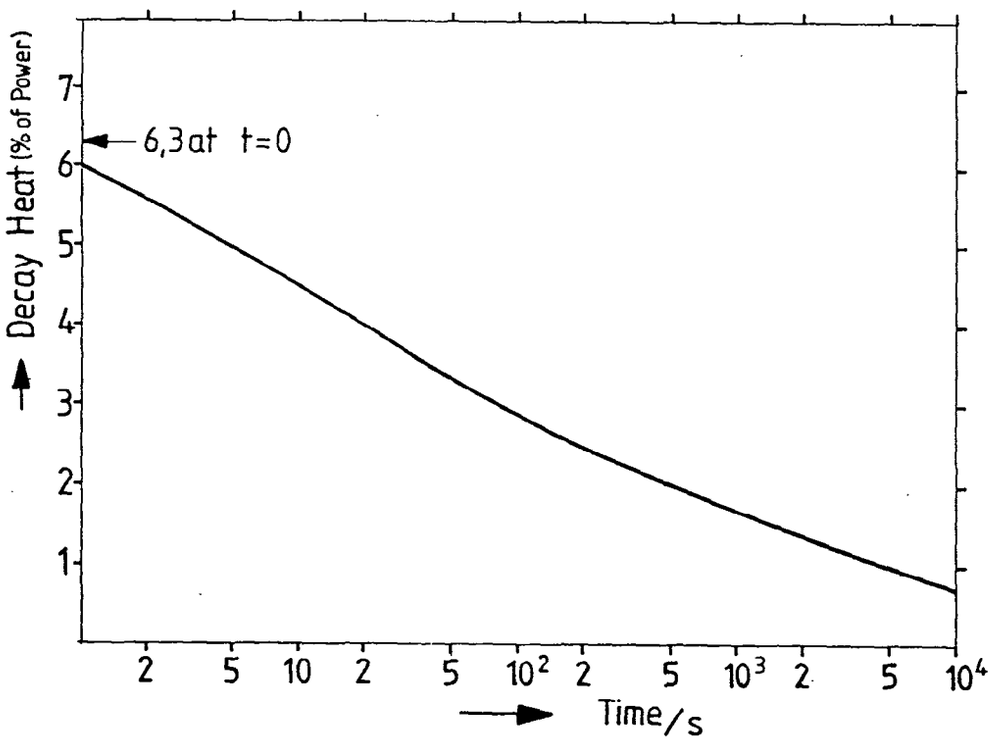

Fig. 10 Time dependence of the decay heat from the fission products of uranium given as a fraction of the operating power (after 30 days of operation).

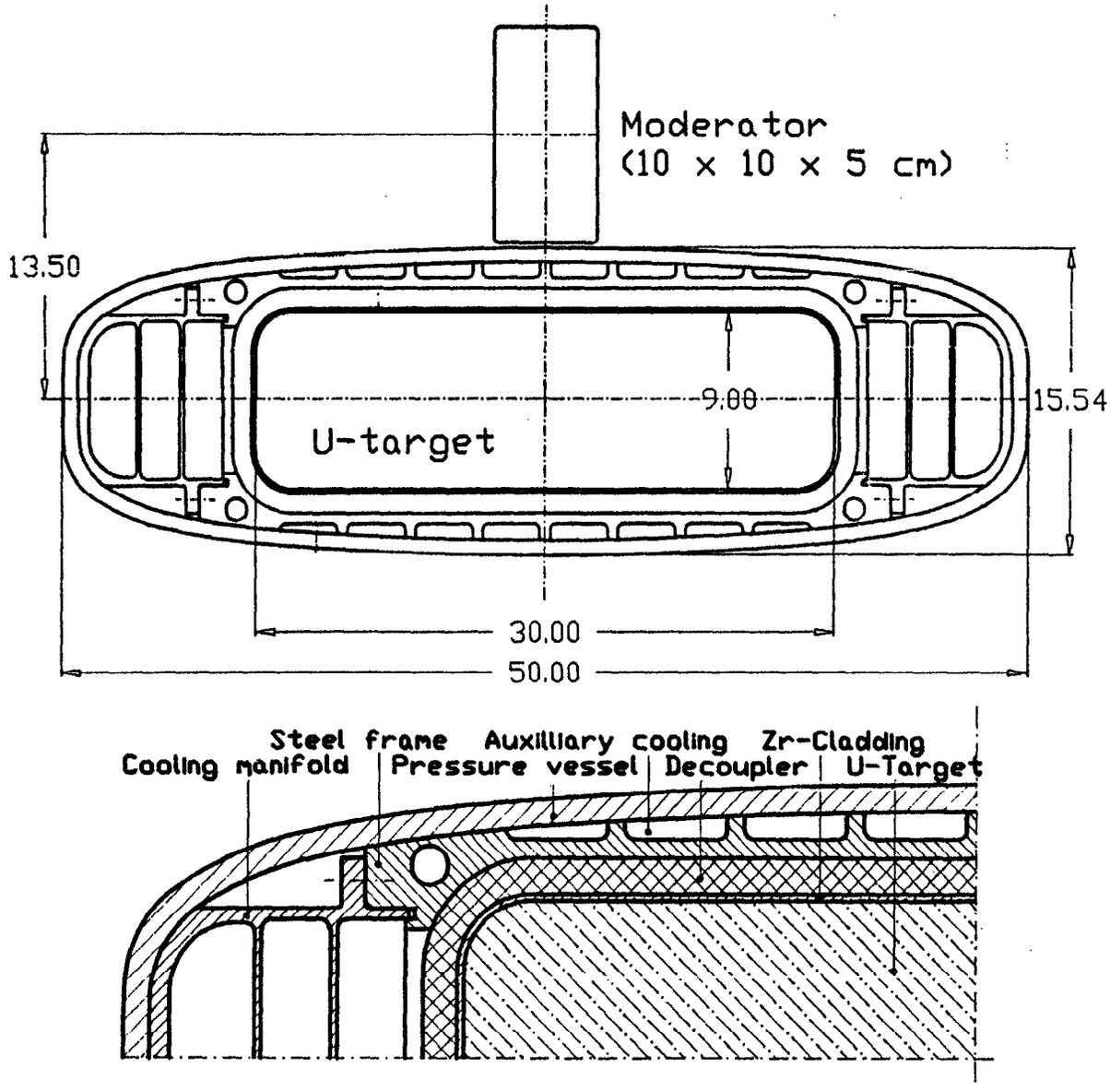

Fig. 11 Conceptual sketch showing a section through a booster target assembly with the decoupler shrunk on the target plates and included in the pressure vessel.

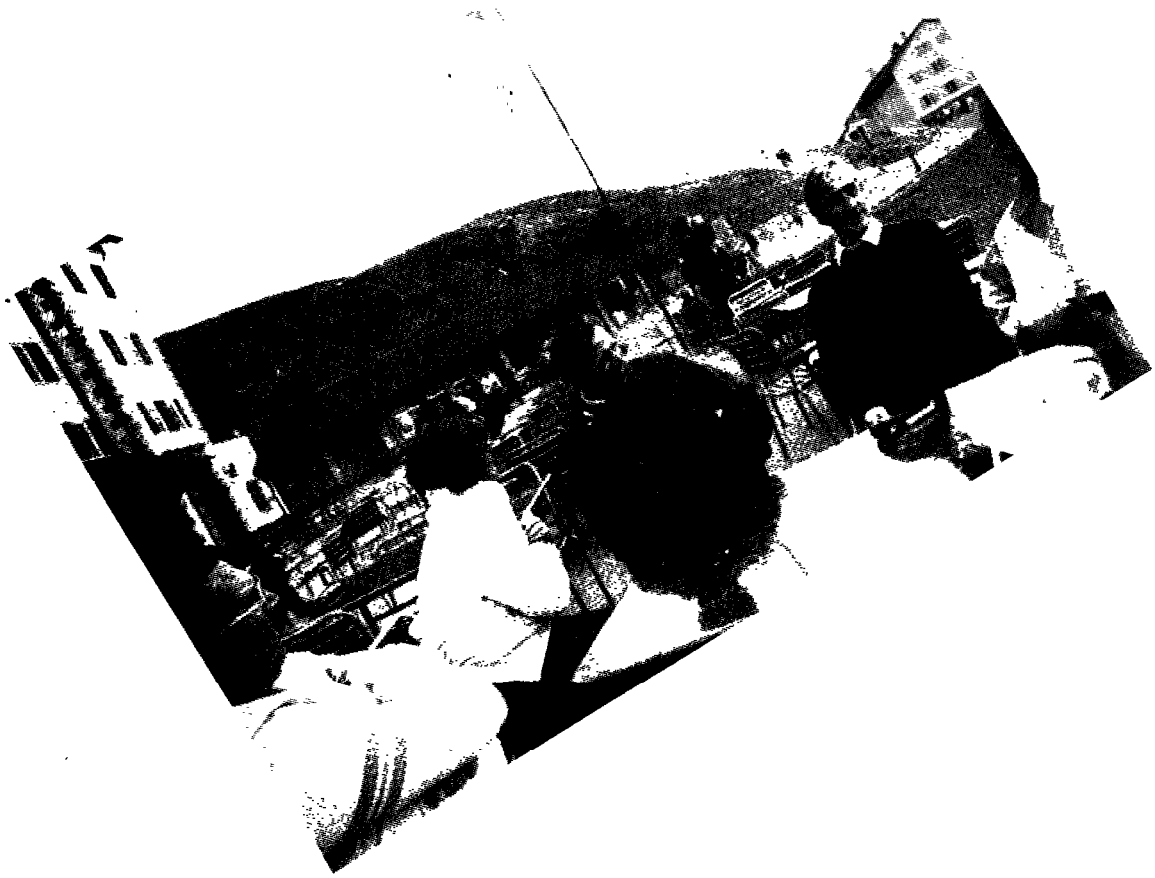

ICANS IX

INTERNATIONAL COLLABORATION ON ADVANCED NEUTRON SOURCES

22-26 September, 1986

STATUS REPORT ON ISIS, THE SPALLATION NEUTRON SOURCE AT RAL

D A Gray (presented by I S K Gardner)

1. INTRODUCTION

It was reported at the last ICANS meting (July 1985)[1] that the Spallation Neutron Source was being used at 50/16 Hz with 1.8×10^{12} protons per pulse on to target. Since that time the SNS has been renamed ISIS by the Prime Minister at an inauguration on 1 October 1985 and ISIS has been used for neutron production at 50 Hz with 3×10^{12} protons per pulse on target, a mean current of 24 μA. Details are given of running conditions and problems encountered during the period.

2. PROGRESS SINCE JULY 1985

A detailed report on ISIS and its experimental programme for the period 1 April 1985 to 31 March 1986 is available as a report RAL-86-061[2].

Covering the period until March 1986, all machine systems were run up to 50 Hz with the synchrotron energy at 550 MeV.

3. 70 MeV H^- INJECTOR

There were two main problems in achieving reliable running at 20 μA (10% of design performance). Firstly, the 665 kV pre-injector column sparked over at a rate dependent on the mean current passing through it. This caused electromagnetic pick-up on low level control electronics and subsequent damage to power supplies notably the pulsed quadrupoles for Tank 1 of the linac and to the supplies for the transfer line between the pre-injector and Tank 1. The second problem was one of unreliability of the hard-tube modulators for the linac RF system.

During the long shutdown which started in April 1986, the pre-injector column voltage gradient was modified so that instead of a breakdown every half-hour at 20 μA synchrotron current, there is now a breakdown every few hours at currents which would give about 100 μA in the synchrotron. The cause of the breakdown is believed to be due to electrons, stripped from the H^- beam in the column, being deflected transversely by the stray magnetic field from the ion source magnet. The deflected electrons are multiplied and charge the column insulators which then spark over. The provision of magnetic shielding is planned. The resultant trip puts the beam off for about a minute. Extra electromagnetic shielding and redesign of the power supplies has eliminated the problem.

Also during the long shutdown, a large amount of work has been done on the modulators for the linac RF system to improve reliability. The modulators now run to give a servo-controlled voltage waveform to the main RF valve (TH116) and the RF-level servo to the tanks has been improved. Major changes to the modulators include the changing of the modulator valve from a Maclett 8786 to two EE1600 valves in parallel, minimising the number of pulsed power supplies, reducing the number of interlocks and improvement of heater regulator units. Parasitics in the EE1600 system were cured using isolated carbon resistors near to the valve bases. The modulators now run much more reliably.

The main power supply reservoir capacitors which have frequently failed will be changed sequentially over the next months.

Cooling of the TH 116 valves has been improved to the stage where they have operated consistently with a 140 μs long beam pulse. Further improvement is needed to get to the design pulse length of 400-500 μs, especially in the cooling of the grid structure.

The ion source has run well. With an arc pulse length of 400 μs and 15 mA to 10 mA of H^- ions extracted (at least enough to give 10^{13} protons per pulse from the synchrotron) the source lasts several weeks. The beam pulse length is controlled by the ion source extraction voltage pulse length.

3.1 800 MeV Proton Synchrotron

The synchrotron has continued to run at 550 MeV using 4 of the eventual 6 RF cavities. The match of the beam from the transfer line to the synchrotron whilst not using theoretical beam sizes has produced an injection efficiency of 96% (maximum is 98% since 2% of H^- are not stripped to protons). There is a known protrubrance into the synchrotron aperture in one of the injection bump magnet boxes which will be cured at the next shutdown. It is anticipated that theoretical settings will then be used.

A watch is kept on the injected beam shape using a scintillator to look at the partially stripped H^0 particles.

The 0.25 micron alumina stripping foils are currently fitted individually through a vacuum trap. The most recent foils have operated to give about 1600 μA/hr of synchrotron current ie about 8 hours for a full intensity beam. An automatic foil change mechanism is being developed for fitting in the next shutdown.

The trapping efficiency with about 3×10^{12} protons per pulse injected is about 86% (design is for 50% at 2.5×10^{13} ppp trapped). Extraction efficiencies are 99% thus giving more than 80% of beam from the linac transfer line hitting the neutron producing target at the 3×10^{12} ppp level (24 μA). (See Fig 1). At this level the beam loss monitors (ionisation chambers along the linac and 70 MeV transfer line) operate a beam trip if on one pulse there is a beam loss of >0.05 μ coulomb at 70 MeV. Likewise for the synchrotron and 550 MeV transfer line to the target, the beam current toroid system trips the

beam if the losses are greater than certain preset values on any one pulse. This beam trip system is being refined.

The limitation on accelerated beam is currently the voltage induced in the RF cavities by the two proton bunches in the synchrotron. At about 2×10^{12} protons trapped the induced voltage is comparable with the voltage on the cavity during the trapping programme. A feed-forward system which looks at the fundamental frequency component of the bunch amplitude and feeds this to the cavity to overcome the fundamental induced voltage is in routine use. For a short period 5×10^{12} ppp were accelerated to 550 MeV. A laboratory trial has been completed to reduce the impedance of the cavity at the trapping frequency by resistive loading and has shown that the induced voltage can be reduced by a factor 5. This should allow the full beam intensity 2.5×10^{13} ppp to be accelerated without producing too large an induced voltage. Installation has started on a system for circulating copper sulphate solution to provide the resistive loading.

The RF phase loop is operated from trapping until 9.5 ms into operation. The radial beam position is controlled at the moment by programmed function generators to give reasonable stability. A radial beam loop is being developed.

With an untrimmed magnetic field configuration it was found that a coupling resonance was crossed which led to some blow-up in beam size. The computer-controlled trim quadrupole system has been used and betatron frequencies measured to find several satisfactory working points. One of these is used for operation. (See Fig 2).

With horizontal closed orbit positions corrected to about 2 mm using programmed horizontal steering magnets the lost 70-100 MeV beam collection system has worked well.

For extraction, a vertical beam bump puts the beam as near as possible to the vertically bending septum magnet for extraction.

Tuning of injection and extraction conditions is done using the beam loss monitors installed from linac, round the synchrotron and to within 20 m of the neutron target. Extraction from the synchrotron is triggered from the energy resolving chopper in the HET spectrometer neutron line.

Alignment of the extraction line is done by measuring the beam position using wire profile monitors. A segmented halo monitor of which the temperature is monitored is used as a final control of alignment of protons on to the neutron target.

3.2 Target Station

The target station has been run with facilities available to operate with at least 10% final beam levels. Installation of the helium ventilation system for the target void vessel and the ventilation system for the cooling of the shutter void vessel is under way. With the planned provision of the shielding at the top of the target

station and in the forward direction, this will complete the target station to cope with full power levels. A system for transporting used targets is being developed. The shutter system which cuts off neutrons to each line is still controlled from the target station control room. The modifications are in hand to provide control from the beam line control rooms.

More details of the target station operation will be given at this conference.

4. SHUTDOWN APRIL-AUGUST 1986

In addition to the work already mentioned the following major items were covered:

i) The remaining two synchrotron RF cavities were installed and run up to full power. The final phasing up is to be completed.

ii) The installation of the first stage of the low energy muon beam for μSR work was installed. This included the extracted proton beam components to make a waist in the beam at the muon producing target position, the target vacuum vessel, the necessary shielding modifications and trial installation of the muon collecting quadrupoles.

iii) The front end shielding for 3 new neutron lines was installed.

5. OPERATIONS

Reliability of operation has not been as good as hoped for at this stage but is improving. As shown in more detail in Reference 2, some 4300 μA hours was achieved up to March 1986.

Since the start of running in August 1986 about 2700 μA hours has been achieved with an average of 176 μA hours per day during the last 2 weeks of the run just completed. (See Fig 3).

It is planned to run until Christmas with 11 weeks scheduled for neutron production. The aim is to produce an average of 400 μA hr/day during this period.

Induced activity levels are high, about 50,000 μGy/hr in the injection straight caused by the need to steer around the protrubrance and 20,000 μGy/hr in straight No.5 caused by operation for a period with the beam collector system not being properly aligned. These levels are consistent with expectations for better operating routines at higher currents.

6. INTERNATIONAL ISIS PROJECT TEAM

As a result of a Memorandum of Understanding signed by Ministers from France, Italy, Sweden and the UK with interest shown from other countries, a project team has been set up to investigate possible

development of ISIS beyond its present full specification. Three international working parties have been set up to cover machine, target station and utilisation. A one-week meeting has been held, the second will be in November. A report is planned for early next year.

7. The report produced here is the result of the efforts of many people especially in ISIS Division of RAL to whom the author is grateful for their dedication.

REFERENCES

(1) D A Gray. ICANS-VIII. RAL-85-110, Vol 1, p65.

(2) ISIS 1986. RAL-86-061.

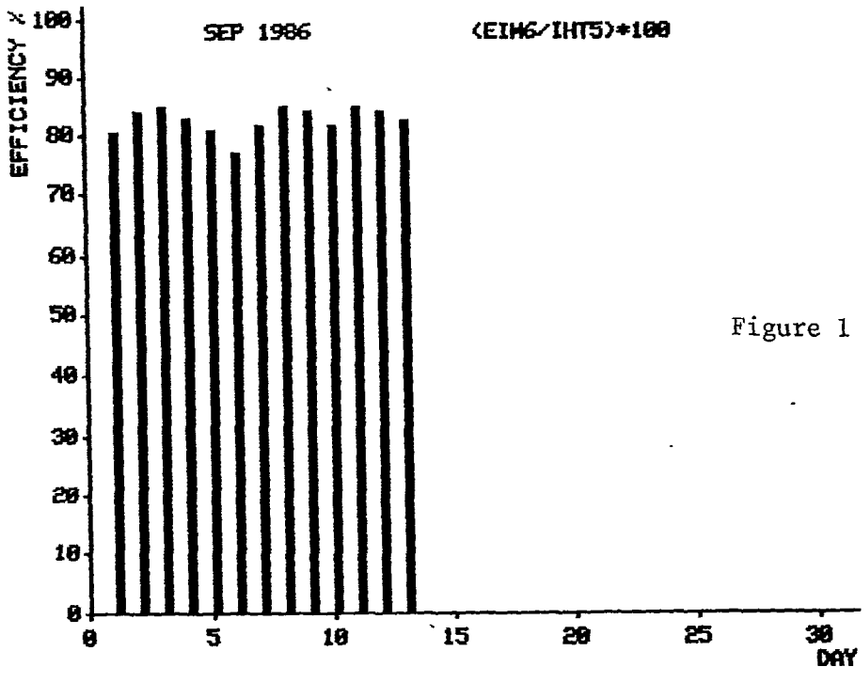

Figure 1

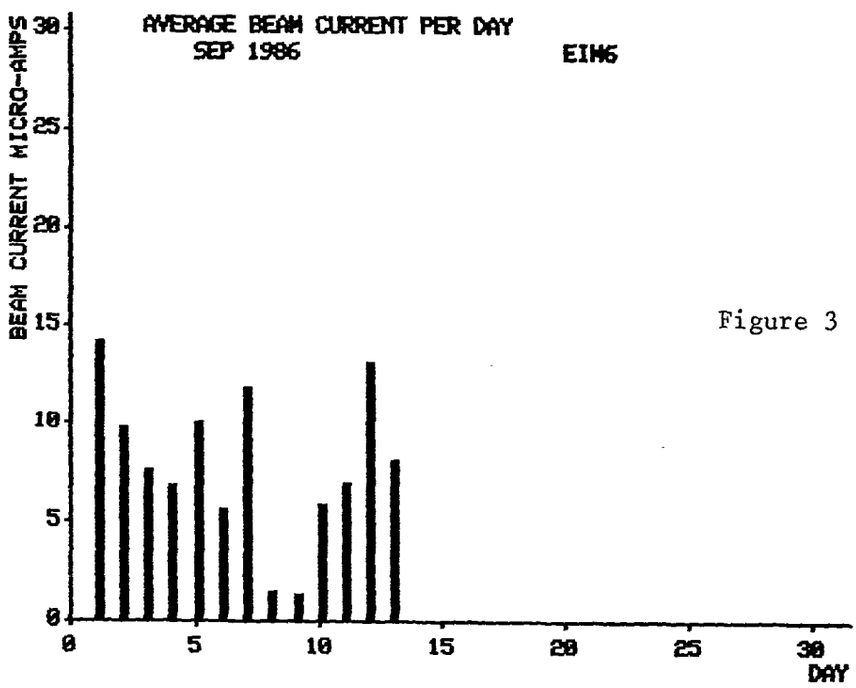

Figure 3

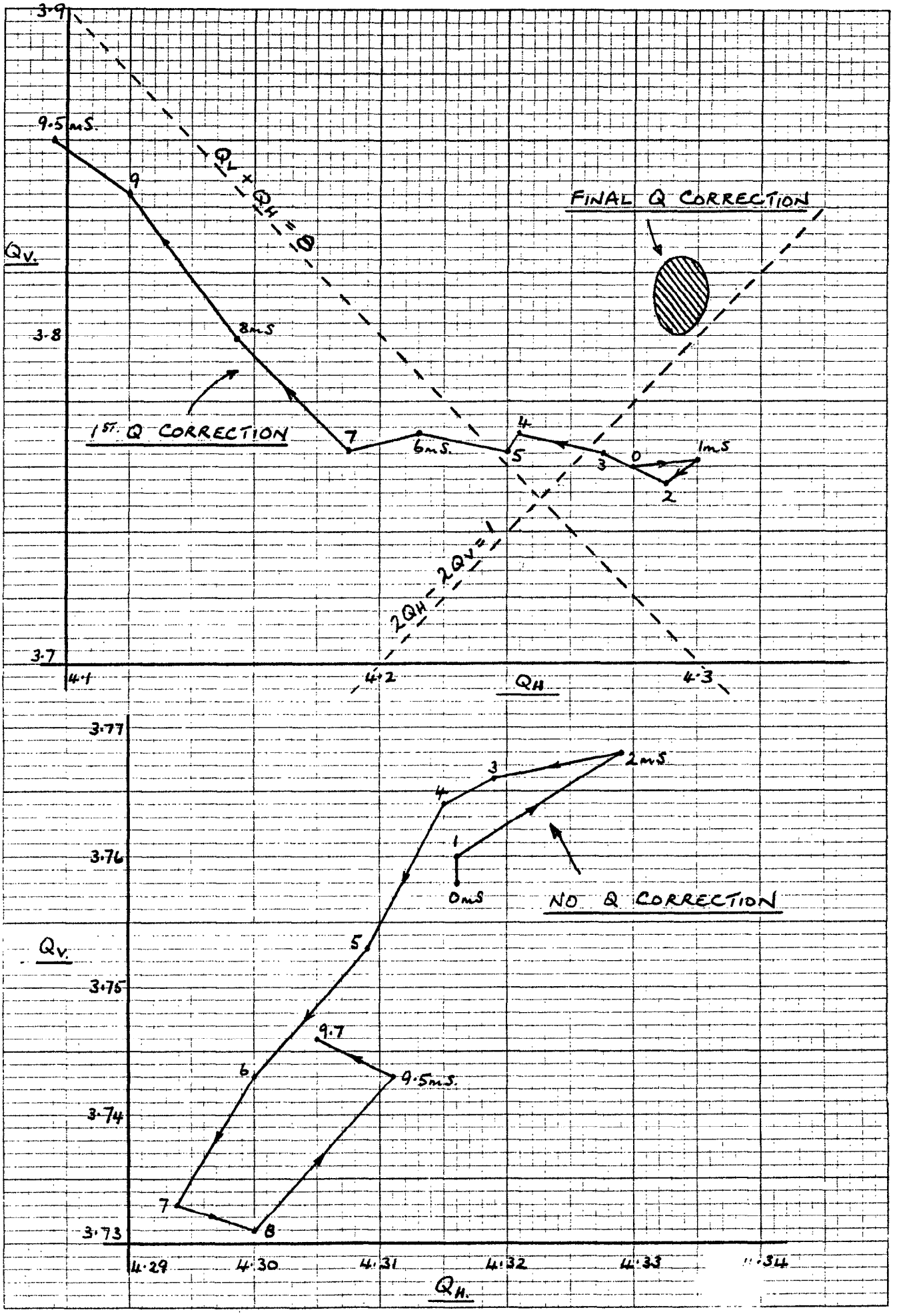

FIG. 2 : Q VALUES DURING ACCELERATION

ICANS IX

INTERNATIONAL COLLABORATION ON ADVANCED NEUTRON SOURCES

22-26 September, 1986

STATUS REPORT ON LANSCE, 1986

F. A. Morse

The most significant development at the Los Alamos Neutron Scattering Center (LANSCE) this past year has been the appointment of Roger Pynn as director.

Referring to Fig. 1, LANSCE is defined as the target/moderator and neutron scattering instrumentation complex. This area, previously known as Target 1 is part of a larger complex which has been known as WNR. The ion source and beam acceleration operations are still a part of LAMPF as before. The Proton Storage Ring (PSR) and the rest of the beam delivery system have been turned over to the LAMPF operations people as well. The other target areas serviced by the beam are still referred to as WNR.

Before presenting where we are in the commissioning of the PSR, let me remind you of our design goals, as given in Fig. 2. The remark about hands-on maintenance needs a little amplification. We desire to keep the hardware in the PSR as non-radioactive as possible and hoped for a total loss in the beam of from 100 to 1000 nA, knowing that maintenance would be simplified. The 100 nA figure was clearly an optimistic one. We are able to have hands-on maintenance but as you will see later, we would like to reduce the beam losses to simplify our maintenance problems. Our commissioning goals are shown in Fig. 3.

At the end of our last run cycle, December 1985, we reached 30 microamperes which was our goal for that cycle. That was a world record at the time. Figure 4 shows a TV monitor in the control room at the time. We were able to supply beam to local users at this rate for several experiments. On December 22 we reached about half the design goals in stable peak current.

As of this conference date, the 1986 run cycle has just begun and most of the time is spent in commissioning efforts. The latter half of this cycle we will emphasize reliable beam to users. Figure 5 indicates that we have reliable computer controls in cool weather; the other way to say that is, we found we have a cooling problem in hot weather. Other issues we are addressing in this phase of the commissioning are indicated in Fig. 6. So far we have been able to "tune" away from beam instabilities at the highest currents but they seem to remain just beyond us and we may have to add damping components before we reach full design.

We can now tune to 25 microamperes very quickly. We are able to supply 25 microamperes to users routinely. Though as mentioned, much of the time is actually spent exploring beam stability space. The ion source (by the end of the conference) is able to supply full design current of 100 microamperes.

The ring performance is good, though as shown in Fig. 7, we are concerned about beam losses. The evidence is that the losses are associated with the stripper foil, but in a way we do not yet understand.

Figure 8 details our instrumentation progress. The new data system is being added to the instruments most requiring it as soon as fabricated.

Beam losses are shown in Fig. 9. They are measured as contact readings shortly after beam shut down. The highest readings are near the septum magnet and the stripper foil as already mentioned. This question is more fully discussed in the talk by Bob Hardekopf.

The construction project for the new experimental hall and the support building is underway, at least in the sense that the architectural/engineering firm is under contract. Figure 10 shows the ground plot of the existing structure, and the location of the experimental hall and the support building. They are shown in the heavy dark outline. Figure 11 gives the construction schedule. We expect to begin to move our instrumentation into the building at the end of the 1987 run cycle.

In summary, our commissioning of the PSR is on schedule and the construction project is on schedule. I have indicated those areas we are working on, but hurry to remind you that the reason there is a commissioning period in all accelerator development projects is because there are always unknowns to deal with. So far we are finding only garden variety problems and have been able to deal with each of them as they arise.

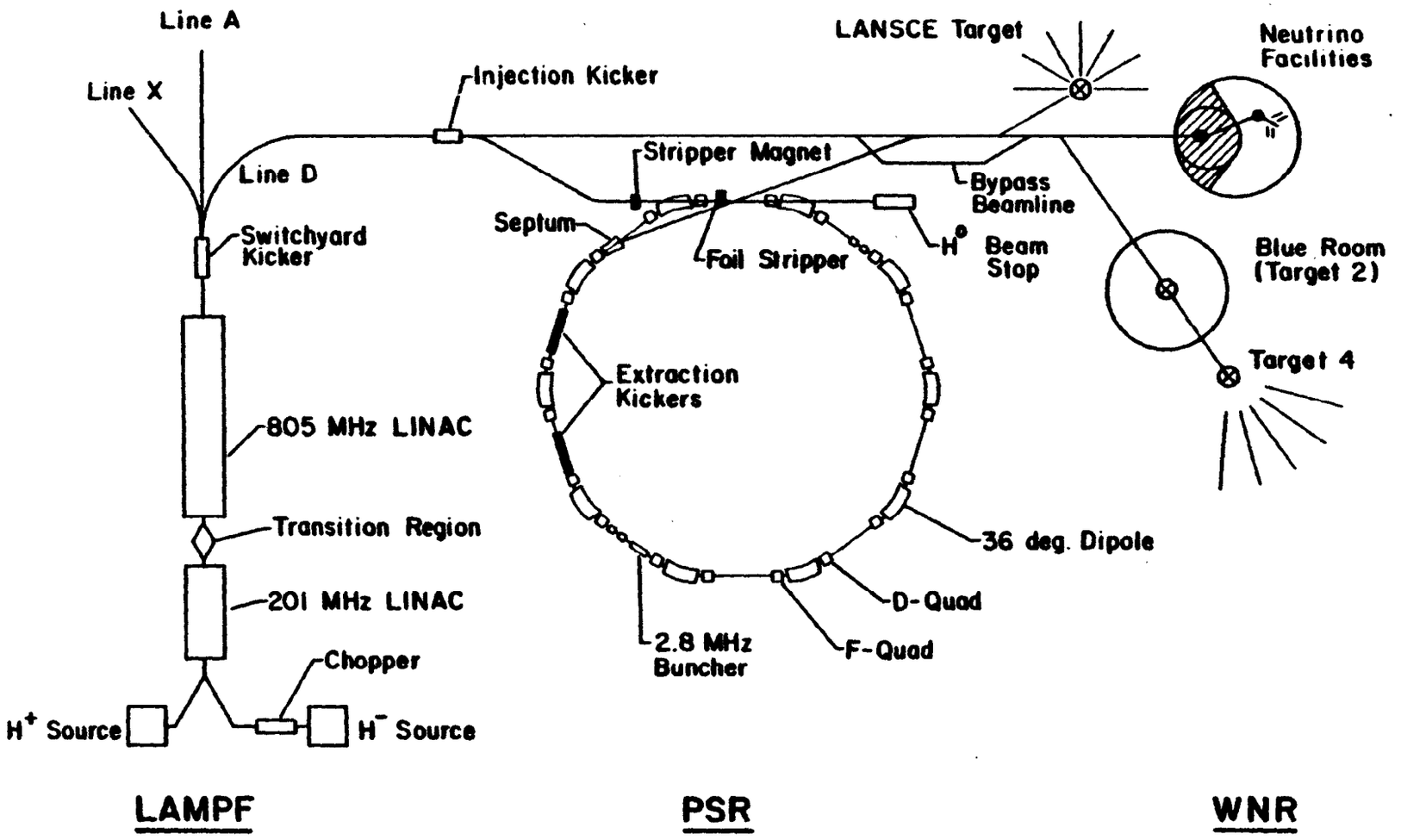
Line A
Line X
Line D
Switchyard Kicker
805 MHz LINAC
Transition Region
201 MHz LINAC
Chopper
H+ Source
H- Source
LAMPF
Injection Kicker
Stripper Magnet
Septum
Foil Stripper
Extraction Kickers
2.8 MHz Buncher
F-Quad
D-Quad
36 deg. Dipole
PSR
LANSCE Target
Bypass Beamline
H0 Beam Stop
Neutrino Facilities
Blue Room (Target 2)
Target 4
WNR

Fig. 1

PRIMARY DESIGN GOALS

- 5.2×10^{13} protons per pulse

  ➡ 46 A peak current

- 100 μA time averaged current (on target)

  ➡ 6.2×10^{13} protons/sec

  ➡ 12 Hz

- Hands on Maintenance

  ➡ Total loss ≤ $\underline{100}$ – 1000 nA

  ⬆

  {Taken as design goal}

Fig. 2

GOALS FOR LANSCE BEAM DELIVERY SYSTEM

FY–86

- Correct Known Problems
- Demonstrate 3.5 – 4 x 10^{13} ppp and 100 μA Ave. @ 18 Hz
- Operate at ≥ 20 μA for Users
- 40% Scheduled Production
- 70% Availability

FY–87

- Demonstrate 5.2 x 10^{13} ppp if Available from Ion Source
- Production at ≥ 50 μA for Users
- 50% Scheduled Production
- 75% Availability
- Consider New Source

FY–88

- 100 μA Production for Users
- 80% Scheduled Production
- 80% Availability

Fig. 3

PSR/WNR STATUS 15-DEC-1985 23:08

	BEAM	RATE	LENGTH	PSR CHOPPING PATTERN	
SRBG:	ON	12	770 us	Pattern Width:	255 ns
LEBG:	OFF	0	10 us	Countdown:	1
LDBG:	OFF	0	100 us	LBOG Width:	730 us

RUN PERMIT LINE-D MODE: PSR-1L
PSR MODE: WNR

LDCM01	-35.44 ua	RICM01	-36.09 ua
LDCM02	-35.50 ua	RICM02	-32.02 ua
LDCM04	-0.05 ua	RICM03	-0.09 ua
LDCM05	0.02 ua	RICM04	3.11 ua

30 MICROAMPERES REACHED---22:45 DEC 15, 1985---WORLD RECORD!!!

LANSCE PRODUCTION UNTIL 16:00 12/17

Dec. 22, 1986

-- 2.7×10^{13} ppp accumulated in the ring
and extracted to neutron target

Fig. 4

STATUS OF LANSCE COMMISSIONING

1985 — 30 μA for users 2 1/2 days

— 2.7×10^{13} protons/pulse for beam stability check in storage ring (→ 50 μA)

1986 (as of 9/13) — To date, run cycle just beginning

- Source improved, up 40%
- Storage Ring Set Points much better, near goal, operates readily at 25 μ.
- Computer controls reliable in cool weather

Fig. 5

ISSUES SO FAR:

BEAM AVAILABILITY POOR OWING TO

- Injector Reliability
- PSR Control System Bugs
- Beam Losses in Ring
- Beam Stability at Highest Intensities

Fig. 6

RING PERFORMANCE

- Injection Process Works as Expected
- Beam Size Well Within Ring Aperature
- Basic Parameters Check Out
  - Fractional Tune
  - Chromaticity ?
- Losses A Puzzle
  - Lifetime
  - Foil Scattering Implicated
  - Extraction
  - Activation
- Stability at High Intensity
  - Evidence for an Instability
  - Threshold Pushed Beyond 2.7×10^{13} pp

Fig. 7

INSTRUMENTATION

- Low Q Diffractometer—rebuilt and taking beam
- 4 Micro Vax — FastBus Systems in operation for both Powder Diffractometers
  - Low Q Diffractometer
  - Single Crystal Diffractometer

  Other instrumentation still using old Mod Com — CAMAC
- New rotating shutter with variable collimation on Low Q Diffractometer
- 32 Meter Powder Diffractometer fully rebuild and operational; new Sample Environment
- High Intensity Powder Diffractometer at 9 meters

CONTACT READINGS

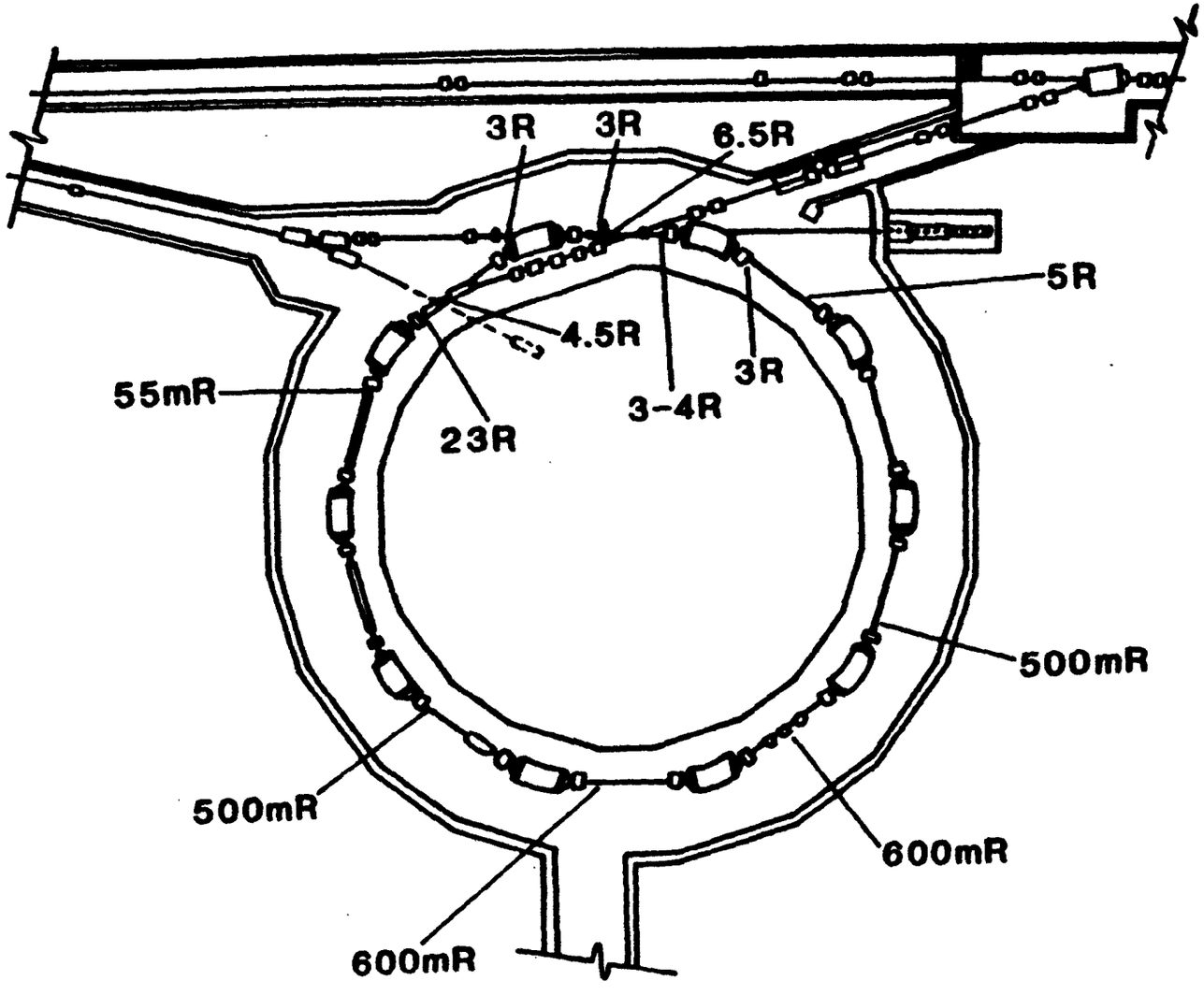

Los Alamos

Los Alamos National Laboratory/Operated by University of California

Fig. 9

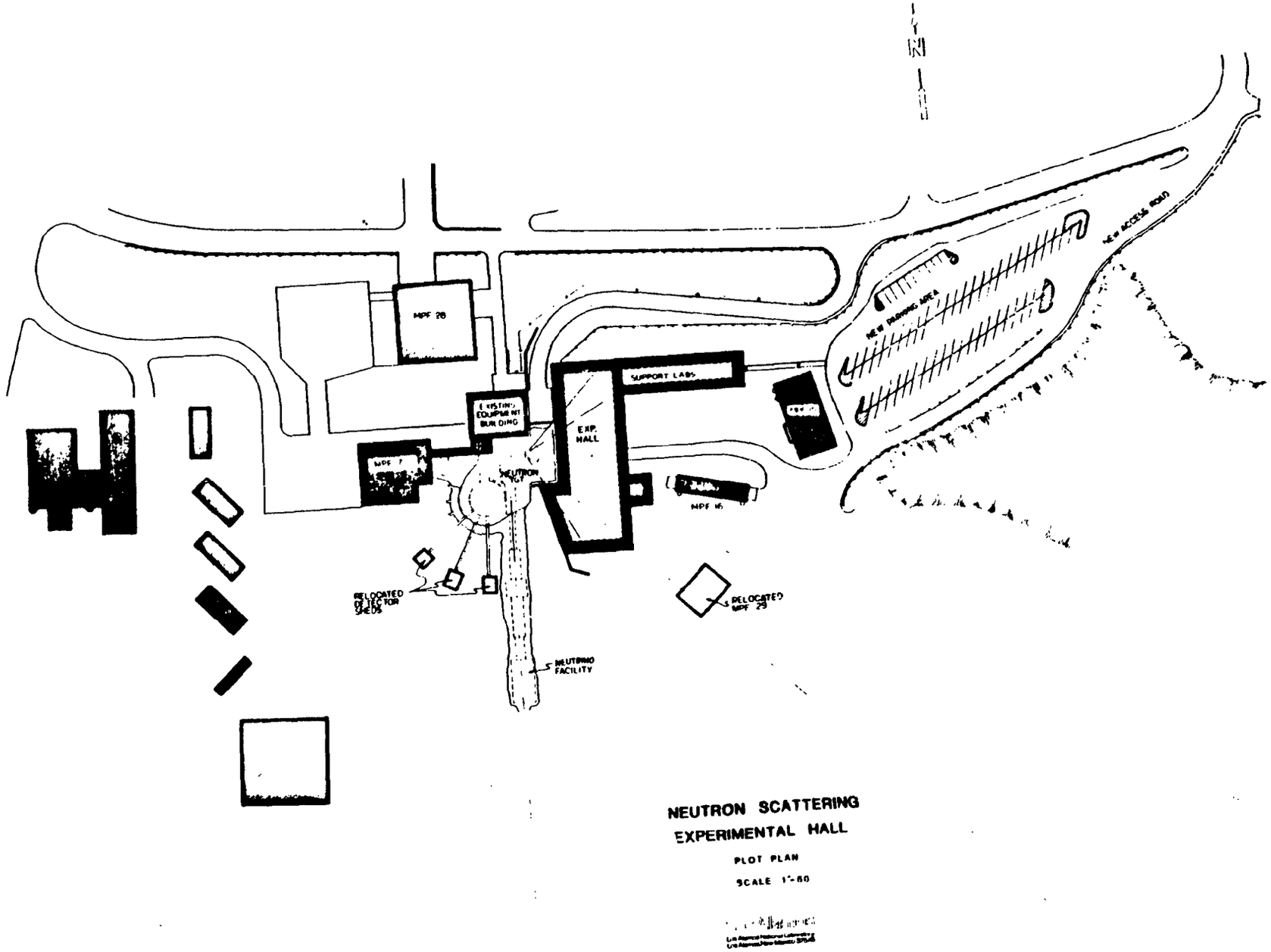
MPF 28
EXISTING EQUIPMENT BUILDING
MPF 7
NEUTRON
EXP. HALL
SUPPORT LABS
MPF 16
RELOCATED DETECTOR SHEDS
RELOCATED MPF 29
NEUTRINO FACILITY
NEUTRON SCATTERING
EXPERIMENTAL HALL
PLOT PLAN
SCALE 1"=60

Fig. 10

CONSTRUCTION PROJECT

Architecture—Engineer Design Complete	End 86
Hall Construction Contract Let	Mar 87
Support Building Construction Contract Let	Oct 87
Hall Construction Complete	End 87
Support Building Complete	Feb 89

** Assumes DOE goes along with the phased design and construction program.

Fig. 11

ICANS IX

INTERNATIONAL COLLABORATION ON ADVANCED NEUTRON SOURCES

22-26 September, 1986

STATUS OF THE INTENSE PULSED NEUTRON SOURCE*

B. S. Brown, J. M. Carpenter,
R. K. Crawford and C. W. Potts

Argonne National Laboratory
Argonne, Illinois 60439 USA

ABSTRACT

Since our last report, IPNS has continued to improve. We describe our recent experience and progress with the accelerator, targets, moderators, scattering instruments, data acquisition systems, ancillary equipment and the user program.

Operating Status of the IPNS Accelerator System

The IPNS Rapid Cycling Synchrotron just recently passed the ninth anniversary of the date when H^- ions were first circulated around the synchrotron. It is clearly improving with age! Of the 3892 hours scheduled since the last ICANS report, 93.2% were available. The average current over this interval was 13.39 μA. Since the last system improvement was completed in December 1985, current has averaged about 14.0 μA with weekly averages as high as 15.0 μA and peaks up to 16.7 μA. Figure 1 shows the weekly average current since user turn-on in 1981. Each point represents about 145 hours of scheduled operation.

There were no major system failures requiring cooldown before repair during this period, thus the large improvement in reliability of operation (see Figure 2). This factor has also allowed us to keep personnel exposure well under control. This smooth operation not only benefited the users but allowed IPNS accelerator personnel to participate in other ANL accelerator related activities. We discuss this briefly later.

As in the past, we have maintained a rigid beam loss limit of about 1.5 μA so necessarily the efficiency of trapping, acceleration and extraction have all improved slightly during the year. All but one of the system improvements responsible for the increased beam were discussed in our previous report.[1] The benefits of the most significant of these improvements, the new neutron chopper-accelerator synchronization system,[2,3]

Work Supported by the U.S. Department of Energy

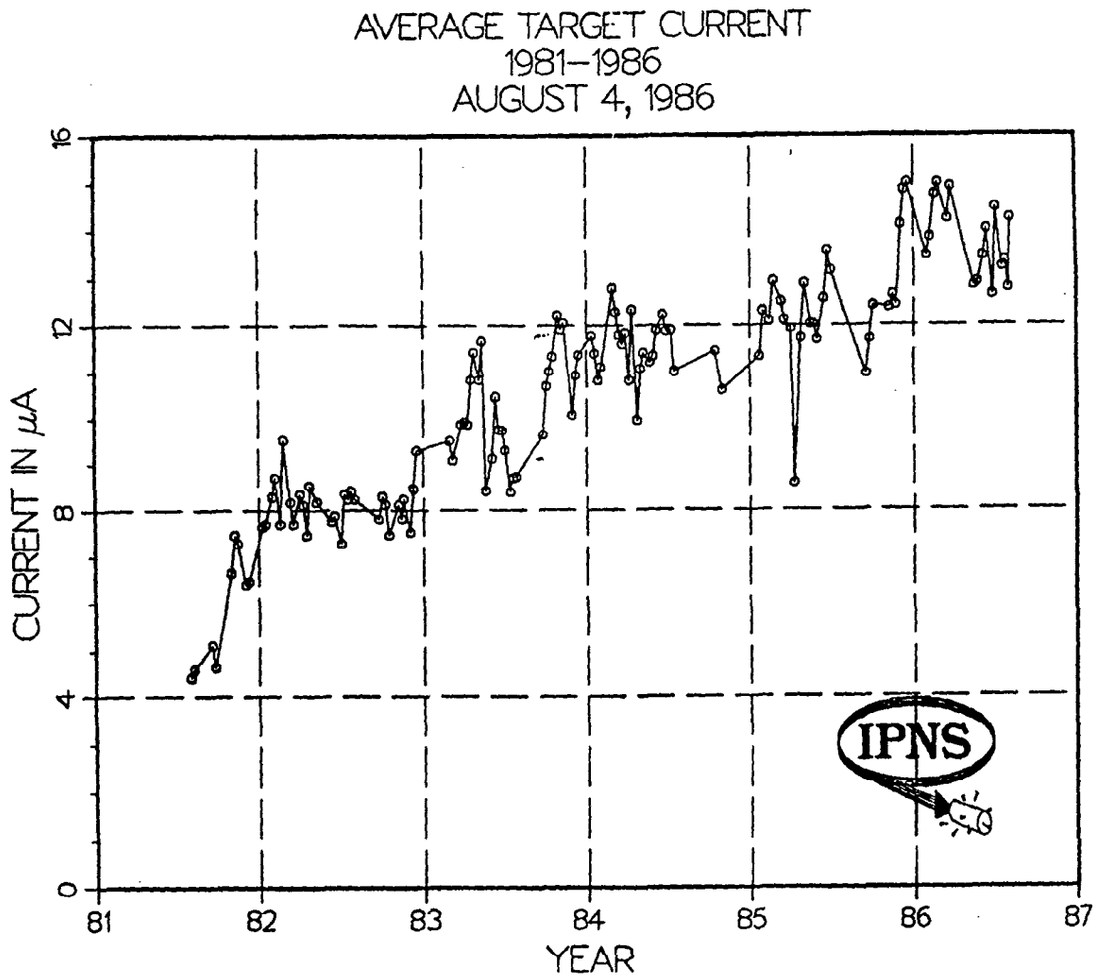

Figure 1: Average Target Current of IPNS

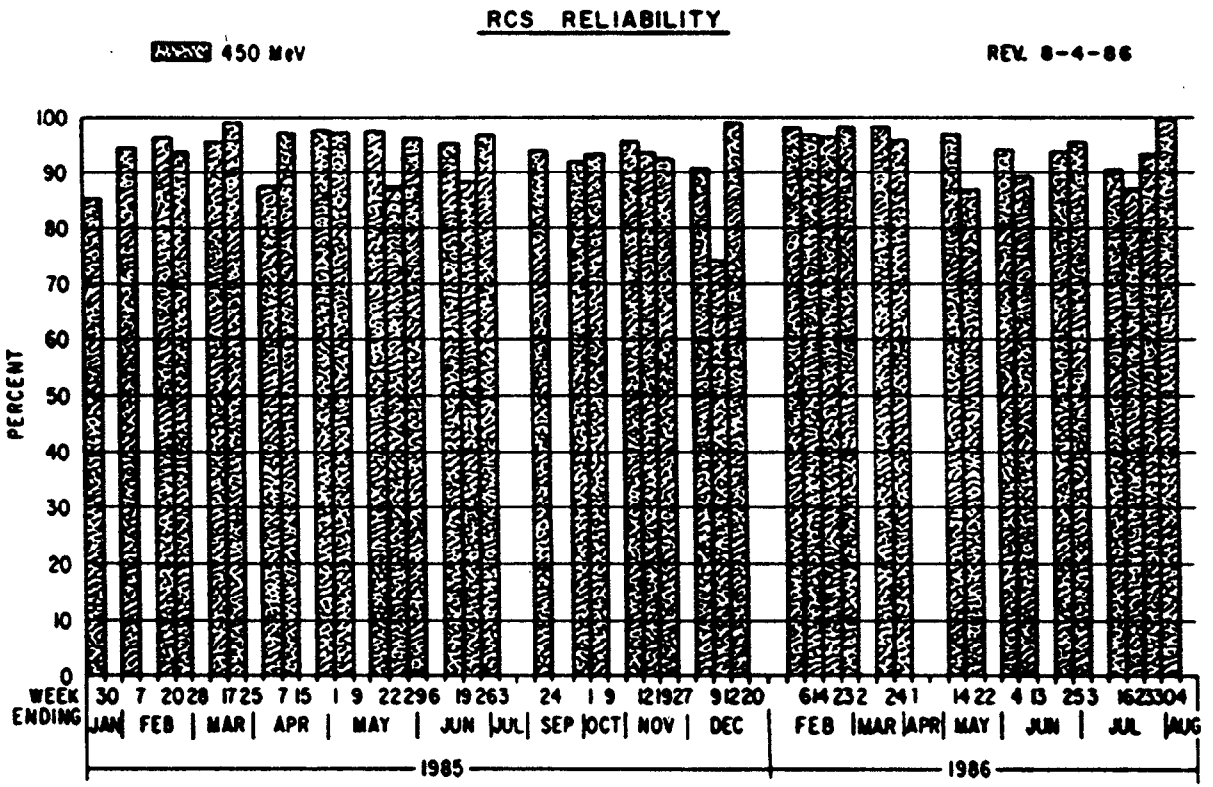

Figure 2: Reliability

were beginning to be harvested before the 1985 summer shutdown. This new synchronization scheme allowed about 0.8 μA increase in beam as expected but it had a side benefit in that it allowed us to study other systems more carefully while doing neutron science. A much improved regulator for the ring guide magnet power supplies resulted from these studies. This unit was installed in December of 1985 and was responsible for bringing the beam from the 14 μA to 15 μA level. This improved regulator is discussed in a companion paper[4] at this conference.

Both beam intensity and reliability were also enhanced by a complete switch over to commercially available 60-80 $\mu g/cm^2$ carbon stripping foils. Nine foils served us all year long. We estimate an average life of 42 million pulses per foil; about 5×10^{21} protons pass through each foil during its lifetime.

The reader will note from Figure 1 that beam improvement stagnated after January 1986. Due to the involvement of IPNS accelerator personnel in other ANL activities, accelerator research was less that 1% of scheduled time the remainder of the year.

Other Accelerator Activities

The most significant long-term activity was participation in the preparation of a proposal for a 6 GeV X-ray source to be built at ANL. The number of people involved was limited but their importance to accelerator improvement was great.

A far larger commitment in terms of personnel was IPNS involvement in the ANL portion of the U.S. Strategic Defense Initiative (SDI). Approximately one-half of our personnel have been working in this area since January 1986.

Neutral Particle Beam (NPB) systems are one facet of the SDI program. One goal of the program is to put a research 50 MeV H^- linac in space. The IPNS linac, though far from optimum for the NPB program, is the only operating 50 MeV H^- linac in the U.S. today and a large shielded beam hall exists nearby which formerly housed the Zero Gradient Synchrotron (ZGS). Since IPNS only runs about one-half time, the SDI program had an ideal opportunity - a H^- accelerator and a beam hall. The NPB program can only be run when the IPNS neutron operation is shutdown. Funding arrived in January to restore the beam line from the IPNS linac to the ZGS hall and to build two new test beams in the ZGS hall. The first of these test beams was brought into operation on April 30, 1986.

The SDI program is operated through the Engineering Division (ENG) at ANL but IPNS engineers and technicians took a leading role in the design and construction of the beam shown in Figure 3. Much of the equipment in this beam is IPNS and ZGS surplus. An effective collaboration between IPNS and ENG has been developed for the operation of this beam. A second beam, about three times as complex as the first, is now under construction and scheduled for completion in early 1987.

Some 1000 hours of NPB operation has now taken place with experiments on neutralization techniques, neutral beam sensing and target discrimination completed or underway. NPB users have come from industry, the military and other national laboratories and several ANL divisions. The second, yet to be completed beam, will perform similar experiments on large diameter beams as well as provide a test bed for specific prototype equipment evaluation.

Targets and Moderators

Most important among recent developments is the progress on the Enriched Uranium Booster Target. We have completed the design and the safety and security evaluations. The target and its various components and the needed facility modifications are nearing completion; we expect first operation this Fall. In its operating position, k_{eff} is 0.80; the enrichment is 77.5%. The new target will increase the intensity of all the neutron beams by a factor of about three. The expected increase in the primary source pulse width (to about 300 nanosec) will not significantly affect the performance of any existing IPNS instruments. We are assessing the impact of the increase in the fraction of delayed neutrons in the beams (to about 3%); most instruments will cope with this in data analysis software, but in addition we are designing choppers to reduce the effect in the powder diffractometers. Instruments will capitalize on the added flux by changing configuration to improve resolution, by concentrating on more difficult classes of measurements, or simply by accepting the higher data rates. Moderators are being changed to accommodate the greater nuclear heating power and the data acquisition systems are being upgraded to deal with higher data rates. We have recorded spectra from all the moderators under reproducible conditions, later to be compared with measurements with the Booster in place. With further modest improvements in the proton current delivered by RCS, we expect the Booster to elevate IPNS to a level of performance equivalent to that of a source with a 450. MeV, 48. μA proton beam and a depleted uranium target.

A separate report describes the Booster Target program in greater detail.[5]

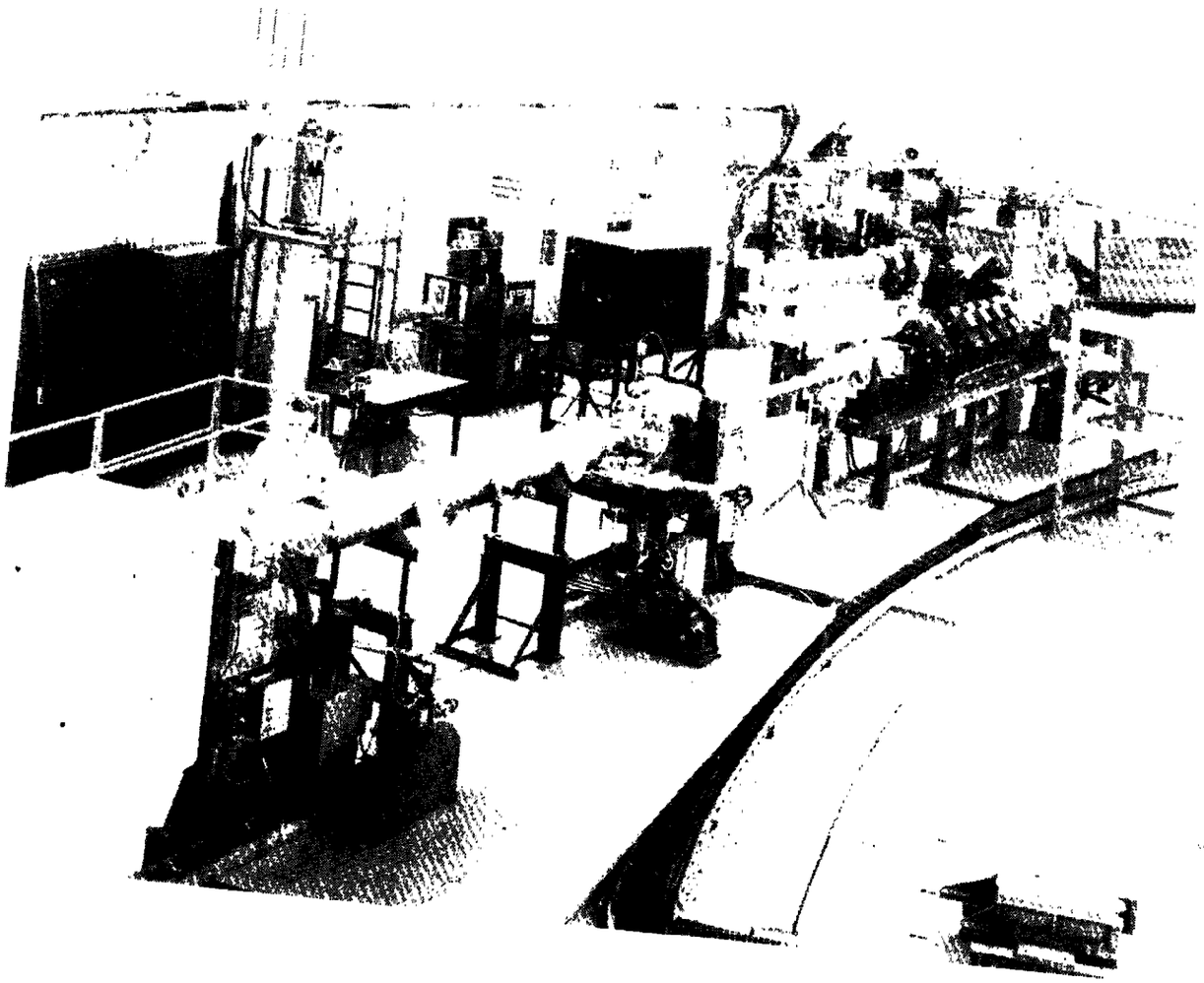

Moderators

Partly as a result of studies which quantified the deterioration of polyethylene moderators under irradiation and partly in anticipation of the higher nuclear heating power in the moderators, we replaced the two polyethylene moderators with circulating liquid methane systems in January, 1986. Both operate at temperatures of about 100 °K; both have nominal dimensions of 10. × 10. × 5. cm^3 and are decoupled with boron-aluminum composite. Both include gadolinium heterogeneous poison; "H" at 2.5 cm (like the ISIS moderators), "F" at 1.7 cm on both sides (more severe than the ISIS systems). Figure 4 shows the time average spectrum of the "F" moderator. The fitted functions (corrected for attenuation by Aluminum in the beam) has the form

$$C(t) \propto E\phi(E) \propto \left(\frac{\phi_{Th}}{\phi_{epi}}\right) \frac{E^2}{E_T^2} e^{-E/ET} + \left(\frac{E}{E_{ref}}\right)^{\alpha} \frac{1}{\left(1 + \left(\frac{E_{co}}{E}\right)^{s}\right)}$$

with E_T = 10.70 meV, ϕ_{Th}/ϕ_{epi} = 1.087, α = .0235, E_{co} = 69.4 meV, s = 1.76. For "H" moderator, the parameters are E_T = 8.024 meV, ϕ_{Th}/ϕ_{epi} = 1.622, α = .125, E_{co} = 24.1 meV, s = 3.79. The CH_4 circulating systems are the same as were used in 1982, and have operated quite reliably - we experience some minor problems with clogging of small orifices in the cold systems.

For purposes of powder diffraction profile analysis, we are accommodating the changes in the spectrum and pulse shape by using spectrum and pulse shape functions described elsewhere.[6]

We continue efforts to understand and control the "burping" behavior of the grooved, cold solid methane moderator, which results in high stresses in the CH_4 container and has caused three failures which we now believe that we understand. A new system of improved design will be installed this Fall. Studies will continue with the goal of providing the lowest spectral temperature and the highest intensity of long-wavelength neutrons, consistent with long-term stable operation. Our analysis of the burping behavior is the subject of a separate report.[7] On the basis of experience with the new cold CH_4 moderator, we are planning to design and install a cold solid methane moderator, without grooves for higher resolution, for installation in the H position next Spring.

Data Acquisition Systems

One major improvement has been the development of a new microprocessor system which increases histogramming speed by a factor of ten without

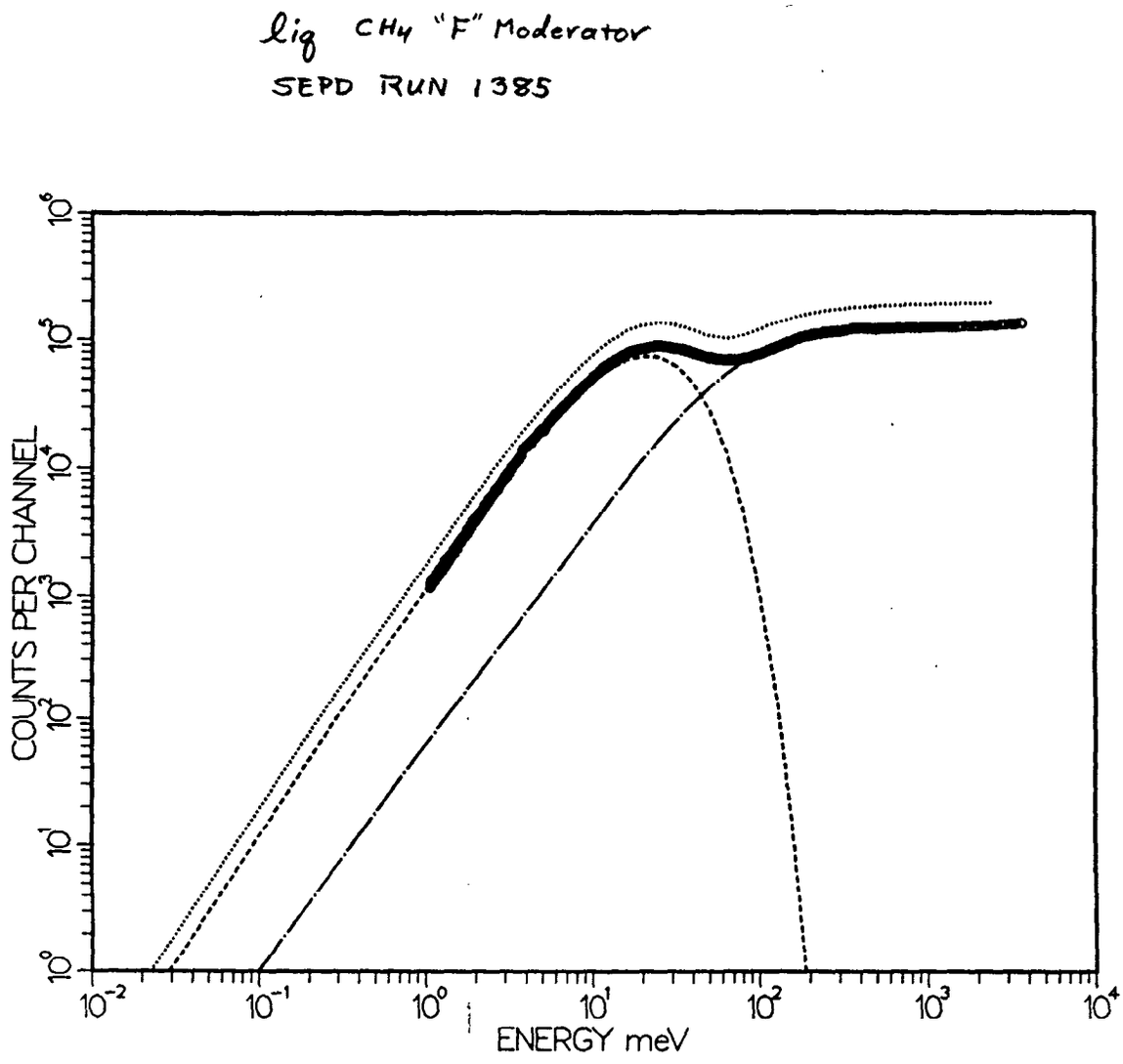

Figure 4: Time Average Neutron Flux Spectrum of the Liquid CH_4 "F" Moderator of IPNS

sacrificing any of the flexibility of the previous system. Refinements to the existing system include improvements in the interfacing of ancillary equipment to the instrument computers and to the VAXs, and the completion of networking of the instrument computers to the VAXs.

On the horizon are several other major developments. The instrument computer software will be converted to run on MicroVax computers, which will be used as the instrument computers on new instruments being developed. One of these new instruments (the glass diffractometer) will also require the development of encoding and histogramming hardware and software fundamentally different from that in use on current IPNS instruments, and this will involve a large fraction of the data acquisition effort over the coming year.

New Data Acquisition Microprocessor System

A multiprocessor data acquisition system has been developed and installed in all the IPNS instrument computer systems to replace the single microprocessor systems used earlier, in order to keep up with the data rates currently encountered on some of the instruments, as well as to cope with the large increase expected on all instruments as a result of the installation of the new booster target.

The old system used a dedicated Zilog Z8001 single board microcomputer on each instrument to histogram the data. Most of the histogramming operations were done in the software using this microcomputer. This permitted the on-the-fly time-focusing which has been so successful for the powder diffractometers and other instruments, as well as allowing a great degree of flexibility in the choice of channel widths, detector groupings, and other histogramming parameters. This flexibility was achieved at the expense of histogramming speed, which was limited to a maximum rate of about 3000 events/second. The new system maintains all this flexibility, and keeps all the histogramming algorithms used by the old system. However, this system uses improved hardware (National N32016 single board microcomputers instead of the Z8001) and the microcomputer software allows up to four microcomputers to be used in parallel. With these improvements the new system with a single microcomputer board can handle data rates a factor of 2.5 higher than the old system, a factor of 10 higher than the old system when four microcomputer boards are run in parallel. The new system has been running on several instruments since January, 1986, and installation in the remaining instruments is being completed in Fall, 1986.

Ancillary Equipment

Work has been continuing on the interfacing of ancillary equipment to the front end computer systems. Nearly all the instrument Displex systems now have controllers interfaced to the instrument computer systems, and the computer interfacing of some of the furnaces has now matured to the point where automated operation is becoming more useful. The sample changer interfacing works well, and the SEPD/GPPD changer is in such great demand that a second unit is being constructed. All the displex, furnace, and cryostat temperature controllers now can communicate with the VAXs as well, providing a means for device testing and development when the instrument computers are otherwise occupied. VAX software also provides communication with several multichannel analyzers and data loggers, permitting rapid transfer and storage of data from these devices.

Networking

All the instrument computer systems have now been connected to the Ethernet network, and can communicate with the VAXs via the DECNET software. This system is used primarily for transfer of data files, and for remote inquiry into the status of the instrument computer systems and/or the experiments running on them. The VAXs are connected to the ANL lab-wide system, thence to the outside world; they are called ANLPNS (780) and ANLPN2 (750).

Microvax Computers

All the instrument computer systems installed to date have been based on DEC PDP-11 computers (eight such computers currently support ten instruments). These computers have performed reliably and have met the needs of most of the instruments. However, two new instruments which are currently being considered at IPNS (glass diffractometer and new small angle diffractometer) have major needs for on-line computing capabilities and for greater disk storage capacity than is available on the current PDP 11/23 and 11/34 systems; we have selected DEC MicroVax-II computers for use with these instruments. We will soon begin to convert our instrument operating software for use on the MicroVax computers, and expect to have working MicroVax-based systems in 1987. In the longer term, it is expected that some of the existing instruments will be converted to MicroVax-based systems as well.

We are also exploring the use of MicroVax computers as part of the data analysis system, operating in a 2-4 user mode, dedicated to the analysis of data from a single class of instruments.

Data Acquisition for the Glass Diffractometer

This proposed new instrument, which is currently under development, will involve extensive use of linear position-sensitive detectors with different encoding requirements than any used in our present systems. Data rates on this instrument are potentially much larger than found on any of our other instruments, and will probably exceed the capabilities of even our new microprocessor system with the current histogramming algorithms. Thus this instrument will require a radically different approach to data encoding and histogramming than that used in all the current IPNS instruments. This approach will probably involve doing more in hardware and less in software than on the present systems, thus achieving speed at the expense of flexibility. This instrument will also involve very large data sets (preliminary estimates suggest something like 2-5 million channels), so the on-line data storage and analysis capability to be provided by the MicroVax computer will be very important. Data sets of this size may also require some serious rethinking of how the data analysis and archiving is to be handled.

Furnaces, Cryostats, Pressure Cells

Work on furnaces has concentrated on high temperatures and on controlled sample environments. A controlled-sample-environment furnace for SEPD and GPPD is now operating reliably to 1400 C. This furnace can be used with the sample in a vacuum or under different partial pressures of a variety of gases or gas mixtures. A controlled-sample-environment furnace has also been used on the SAD at temperatures up to ~ 1000 C. Table I summarizes currently-available equipment for special sample environments.

Table I

Equipment for Special Sample Environments at IPNS

Low Temperatures	
(Adaptable to most instruments)	
Displex Refrigerators	$T \geq 10K$
^{4}He Cryostat	$1.5 \leq T \leq 200K$
High Temperatures	
Diffractometer and Chopper Spectrometer Furnaces	$T \leq 1400$ C
Small-Angle Diffractometer Furnace	$T \leq 1000$ C

High Pressures

(Special Environment Powder Diffractometer, $2\Theta = 90°$)

	Pressure	Volume	Temperature
Piston-Cylinder	35 Kbar	0.25 cm^3	300 K
Gas-Pressurized Cells	6 Kbar	2.0 cm^3	10 K
Clamped Piston-Cylinder	25 Kbar	1.5 cm^3	10 K

(Single Crystal Diffractometer)

He Gas Pressure Cell	5 Kbar	1.5mm diam.	10K-300K

Scattering Instruments

We have rearranged the IPNS scattering instruments somewhat, partly as a result of introducing new ones, and partly as a result of phasing out the Ultralow Temperature Diffraction Experiment, formerly at the C3 beam. Figure 5 shows the new arrangement. The QuasiElastic Neutron Spectrometer (QENS) is a new instrument, located at the previously vacant H2 beam. It is the result of a collaboration between ANL, LANL, MIT, EXXON and Schlumberger-Doll Research. Figure 6 shows a diagram of the new machine. First tests show that the resolution is 65. μeV for quasielastic scattering about 3.7 meV, as designed. Background in the detectors is already acceptably low. The Single Crystal Diffractometer (SCD) is being moved from H1 to the F6 beam. There, with the higher resolution moderator and with the moderator-sample flight path increased to 9.5 m, the resolution will improve to about $\Delta Q = .03$ $Å^{-1}$. The overall data rate will increase by a factor around 1.4, and the instantaneous data rate will be about the same with the Booster as it was before. A new Glass Diffractometer (GLAD) is under design, in a collaboration between ANL, LANL, University of Houston and Willamette University to be placed at H1 beam. The instrument will feature a small angle detector array of moderate resolution, and a large array of detectors extending to 90.° scattering angle.

The Special Environment Powder Diffractometer (SEPD) will remain as is, but its capabilities for high pressure measurements are being enhanced by construction of new pressure cell. At the Low Resolution Medium Energy Chopper Spectrometer (LRMECS), the chopper shielding is being improved on the basis of better understanding of the origin of personnel background radiation. A new 10 meV chopper is being designed for use in LRMECS and in the High Resolution Medium Energy Chopper Spectrometer (HRMECS), to extend their ranges to lower energies and higher resolution.

IPNS
EXPERIMENT FACILITIES

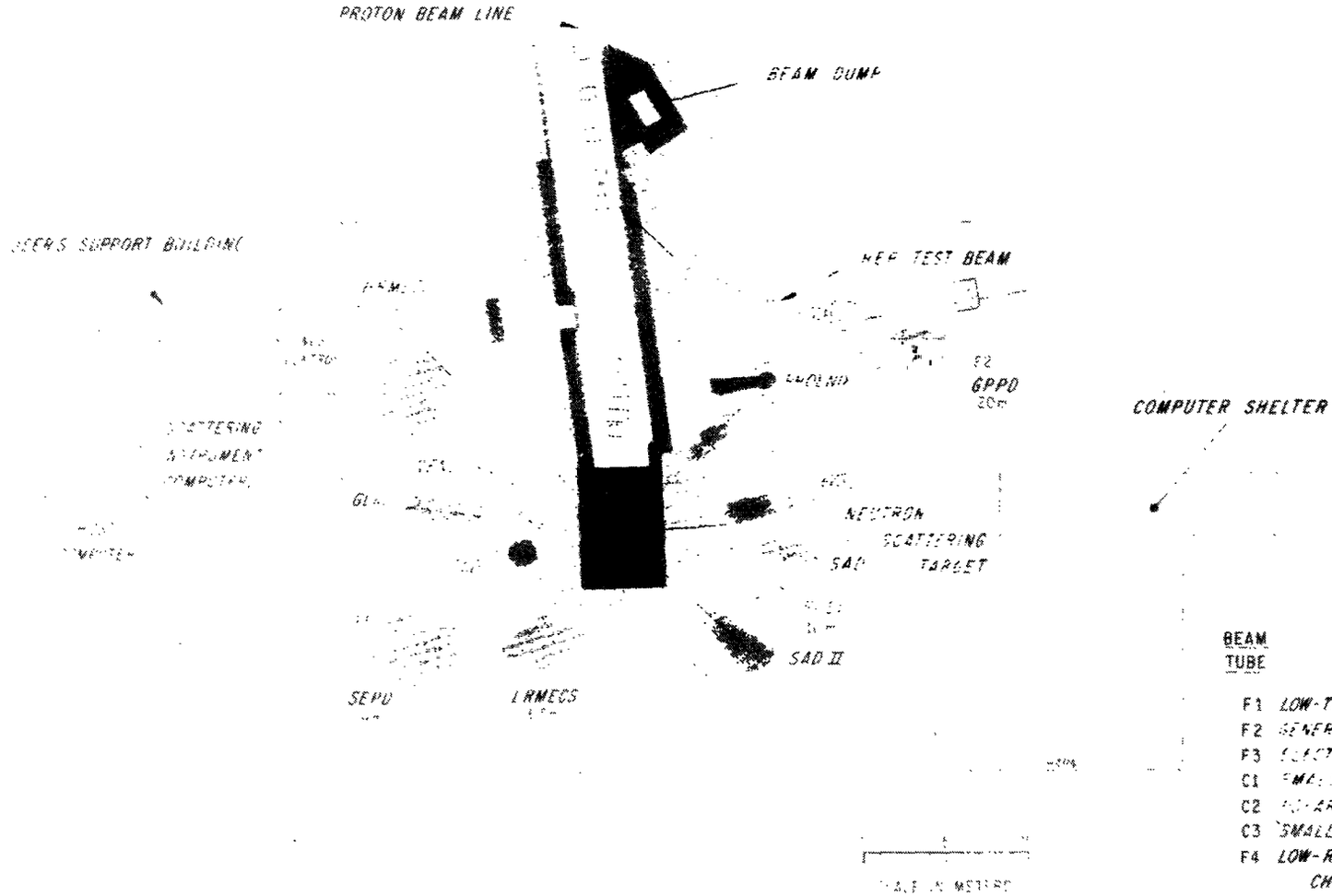

BEAM TUBE	UTILIZATION
F1	LOW-TEMPERATURE CHOPPER SPECTROMETER
F2	GENERAL PURPOSE POWDER DIFFRACTOMETER
F3	ELECTRON-VOLT SPECTROMETER
C1	SMALL ANGLE DIFFRACTOMETER
C2	POLARIZED NEUTRON REFLECTOMETER
C3	SMALL ANGLE DIFFRACTOMETER (PROPOSED)
F4	LOW-RESOLUTION MEDIUM-ENERGY CHOPPER SPECTROMETER
F5	SPECIAL ENVIRONMENT POWDER DIFFRACTOMETER
F6	SINGLE CRYSTAL DIFFRACTOMETER
H1	GLASS LIQUIDS AND AMORPHOUS DIFFRACTOMETER
H2	QUASIELASTIC NEUTRON SCATTERING SPECTROMETER
H3	HIGH-RESOLUTION MEDIUM-ENERGY CHOPPER SPECTROMETER

QENS

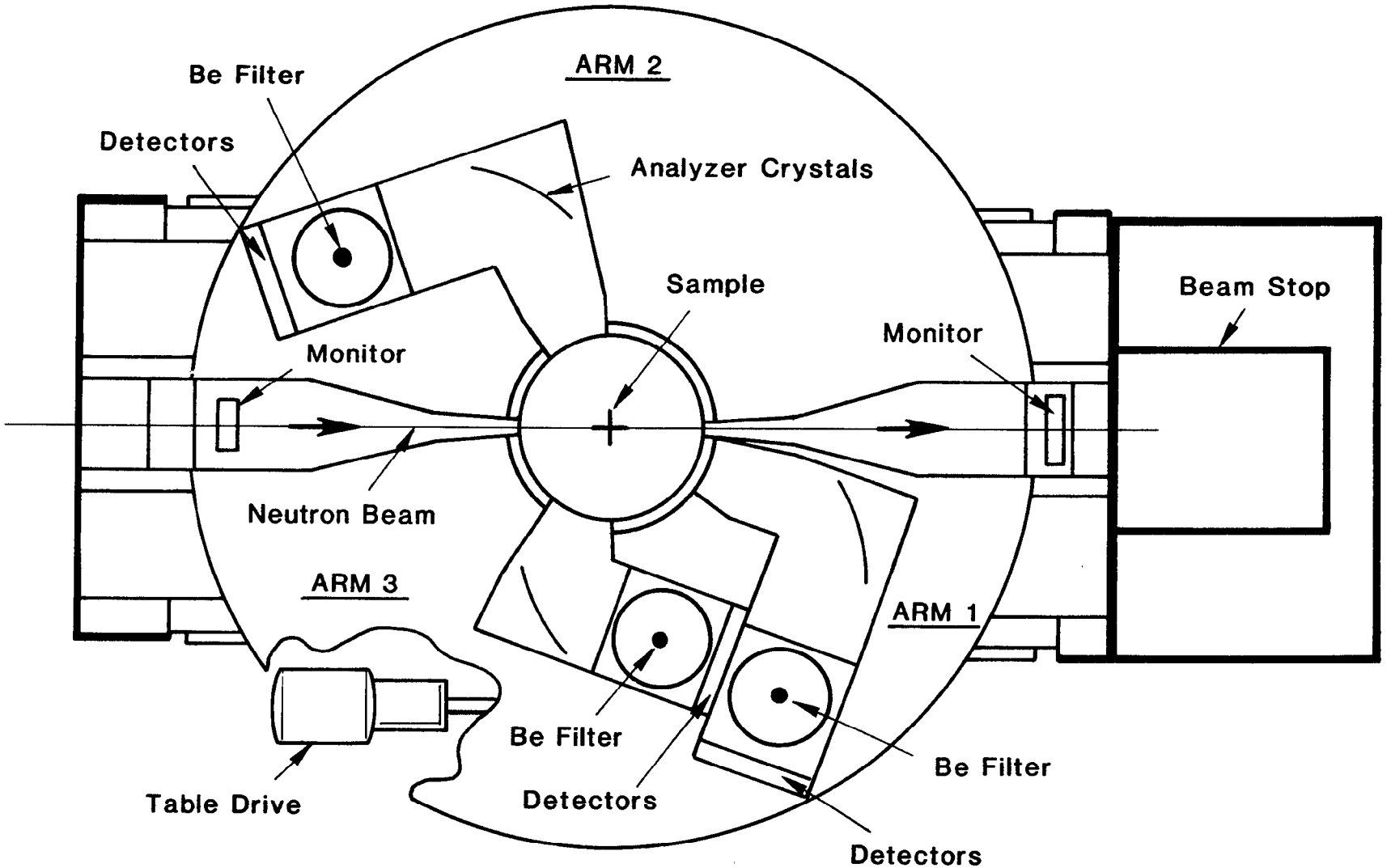
ARM 2
Be Filter
Detectors
Analyzer Crystals
Sample
Beam Stop
Monitor
Monitor
Neutron Beam
ARM 3
ARM 1
Be Filter
Be Filter
Table Drive
Detectors
Detectors

We plan to install a second Small Angle Diffractometer at the C3 beam; its detailed design depends on experience yet to be gained on the existing SAD. Meanwhile, we will install the Doppler shifter ultracold neutron apparatus, which is back from its round of experiments at Los Alamos. The Polarized Neutron Reflectometer at the C2 beam has developed into a highly productive instrument.[8] Figure 7 diagrams the instrument, while Figure 8 shows a recent measurement of the reflectivity of a layered, magnetically-biased permaloy structure. Recently, an electronic spin-flip chopper has been installed to improve the resolution and reduce the delayed neutron background.

The Small Angle Diffractometer (SAD) at C1 beam continues to improve. Recently we have installed a single crystal MgO filter which reduces the fast component of the delayed neutron background and the sensitivity to the prompt fast neutron and gamma flash. We are purchasing a new, larger (45 cm vs. 17 cm diameter) detector in the coming year. The Electron Volt Spectrometer (eVS) at F3 beam is the subject of a separate report.[9] The General Purpose Powder Diffractometer (GPPD) at F2 beam remains highly effective, especially for high temperature and residual stress measurements; no significant changes are envisioned for GPPD. We have replaced the Crystal Analyzer Spectrometer (CAS), formerly at F1 beam, with the QENS at H2, and have erected a new, special-purpose chopper spectrometer, the Pulsed High Energy Neutron Inelastic Chopper Spectrometer (PHENICS), dedicated to low temperature momentum distribution measurements. The new instrument uses the dilution refrigerator from the disassembled Ultralow Temperature Diffraction Experiment, formerly at C3, and has a single detector bank at a scattering angle of 150.°. The instrument is the result of a collaboration between ANL and Harvard University, and will begin operating at the time of the Fall startup. Table II summarizes the parameters of the present IPNS neutron scattering instruments.

User Program

The operating statistics shown in Table III clearly indicate an increase in the number of experiments and scientists at IPNS despite a small decrease in operating time. The increase from BY85 is due to the proton current increase and the coming to maturity of the Small Angle Diffractometer and the Polarized Neutron Reflectometer. The large increase in university users is due to the establishment of a number of groups consisting of faculty, post-doctoral appointees and graduate students which focus their research at IPNS. Particularly active research groups exist at Harvard University, University

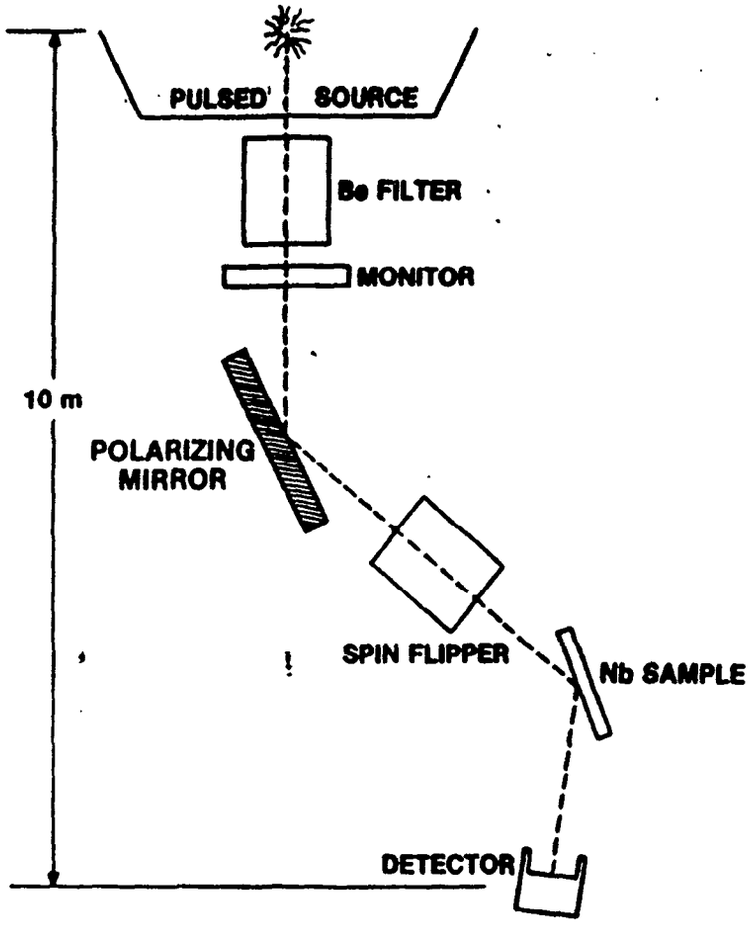

Figure 7: Schematic Diagram of the Polarized Neutron Reflectometer

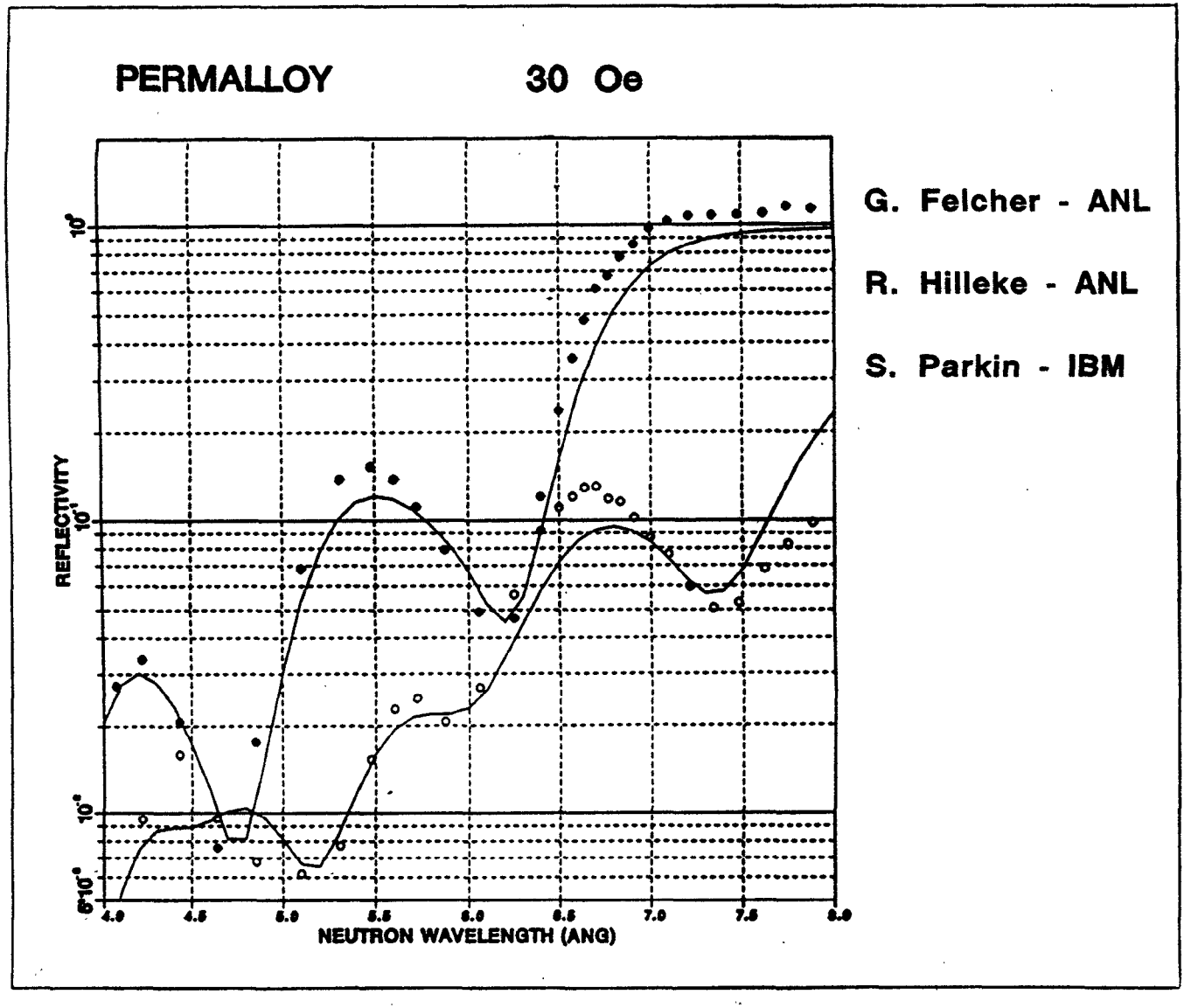

Figure 8: Polarized Neutron Reflection Spectrum of Magnetically Biased Permalloy

Table II
IPNS NEUTRON SCATTERING INSTRUMENTS

Facility (Instrument Scientist)	Assignment	Range • Wave-vector	Range Energy	Resolution Wave-vector	Resolution Energy
Special Environment Powder Diffractometer (J. D. Jorgensen/K. Volin)	F5	0.5–50 $Å^{-1}$	*	0.35%	*
General Purpose Powder Diffractometer (J. Faber/R. Hitterman)	F2	0.5–100 $Å^{-1}$	*	0.25%	*
Single Crystal Diffractometer (A. J. Schultz)	F6	2–20 $Å^{-1}$	*	2%	*
Low-Resolution Medium-Energy Chopper Spectrometer (C.-K. Loong)	F4	0.1–30 $Å^{-1}$	0–0.6 eV	0.02 K_o	0.05 E_o
High-Resolution Medium-Energy Chopper Spectrometer (D. L. Price)	H3	0.3–9 $Å^{-1}$	0–0.4 eV	0.01 K_o	0.02 E_o
Small-Angle Scattering Diffractometer (J. E. Epperson/P.Thiyagarajan)	C1	0.006–0.35 $Å^{-1}$	*	0.004 $Å^{-1}$	*

* No energy analysis
• Wave-vector, $K = 4\pi\sin\theta/\lambda$

NEUTRON BEAMS FOR SPECIAL EXPERIMENTS

Beam Tube	Current Use	Flight Path Length (m)
F3	eV Spectrometer	10.0
C2	Polarized Neutron Exp.	10.0
F1	n(p) Spectrometer	13.6
H1	Glass Diffractometer (planned)	10.0
H2	QENS Spectrometer	8.0
C3	Ultra-Cold Neutrons New SAD (planned)	10.0

Table III

IPNS USER PROGRAM

	FY83	FY84	FY85	FY86
WEEKS OF OPERATION	26	29	21	22
NUMBER OF EXPERIMENTS PERFORMED	110	210	180	212
VISITORS TO IPNS FOR AT LEAST ONE EXPERIMENT:				
DOE LABS - SAME SITE	41	49	44	52
DOE LABS - OTHER SITES	7	7	6	10
OTHER GOVERNMENT LABS	2	1	1	1
UNIVERSITIES	33	45	51	79
INDUSTRY	5	9	7	13
FOREIGN	18	39	34	27
	106	150	143	182

of Illinois, Northwestern University, Penn State University, University of Wisconsin, University of Chicago and University of Pennsylvania.

In addition to the basic research done for free under the proposed system, experimental time can be bought for proprietary research. Instrument time (primarily on the powder diffractometers) was sold this past year to Standard Oil (SOHIO), Amoco Oil, Canadian Hydro and Chalk River Nuclear Laboratory.

REFERENCES

1. A. Rauchas, F. Brumwell, C. Potts, V. Stipp and G. Volk, "Status of the Intense Pulsed Neutron Source Accelerator System," Proceedings of ICANS-VIII, Rutherford Appleton Laboratory Report RAL-85-110, Vol. I (July 8-12, 1985), 93.

2. L. Donley, "Phase Locking the IPNS Neutron Chopper to the 60 Hz Power Line," Proceedings of ICANS-VIII, Rutherford Appleton Laboratory Report RAL-85-110, Vol. III (July 8-12, 1985) 689.

3. G. Ostrowski, et al., "The IPNS Chopper Control and Accelerator Interface Systems," Proceedings of ICANS-VIII, Rutherford Appleton Laboratory Report RAL-85-110, Vol. III (July 8-12, 1985) 676.

4. F. Brumwell, C. Potts, A. Rauchas, V. Stipp and G. Volk, "Performance of the Intense Pulsed Neutron Source Accelerator System," proceedings of this conference.

5. A. E. Knox, J. M. Carpenter, J. L. Bailey, R. J. Armani, R. N. Blomquist, B. S. Brown, D. R. Henley, A. G. Hins, B. A. Loomis, A. W. Schulke and H. R. Thresh, "Progress on the IPNS Enriched Uranium Booster Target," proceedings of this conference.

6. J. M. Carpenter, A. D. Taylor, R. A. Robinson and D. J. Picton, Nucl. Inst. & Meth. in Physics Research A234, 542 (1985), also, J. M. Carpenter, S. S. Cudrnak and C. M. DeCusatis, "Deterioration of Performance of Neutron Moderators Under Intense Irradiation," proceedings of this conference.

7. J. M. Carpenter, U. Walter and D. F. R. Mildner, "Analysis of the Burping Behavior of the Cold Solid Methane Moderator at IPNS," proceedings of this conference.

8. G. P. Felcher, R. O. Hilleke, R. K. Crawford, J. Haumann, R. Kleb and G. E. Ostrowski, "The Polarized Neutron Reflectometer, A New Instrument to Measure Magnetic Depth Profiles," in preparation (1986).

9. R. K. Crawford, "The IPNS Resonance Detector Spectrometer," proceedings of this conference.

ICANS IX

INTERNATIONAL COLLABORATION ON ADVANCED NEUTRON SOURCES

22-26 September, 1986

Status Report on the KENS Facility

N. Watanabe, Y. Endoh*, K. Inoue** and M. Misawa

National Laboratory for High Energy Physic,
Oho-machi, Tsukuba-gun, Ibaraki-ken, 305, Japan

* Physics Department, Tohoku University,
Sendai 980 Japan

** Department of Nuclear Engineering,
Hokkaido University, Sapporo 060, Japan

1. Introduction

The pulsed spallation neutron source (KENS) at KEK has successfully been operated with a new uranium target system since last December. Due to improvements in the accelerator and the neutron target, the neutron-beam intensity has been increased by more than four times compared with the previous period in which a tungsten target was used.

Much effort has been devoted to the reinforcement of the biological shielding around spectromertors in order to keep the radiation level in the experimental hall at less than 2 mrem/h.

The beam time allocated to neutron-scattering experiments during the last fiscal year was 750 hours. About forty experiments were carried out successfully among the forty-nine proposals accepted.

This report summarizes the present status of the KENS-I'. The future project is discussed briefly.

2. KENS-I' Program

The KENS-I' Program was aimed at increasing the neutron-beam intensity from the pulsed spallation neutron source KENS-I by one order of magnitude by upgrading the neutron production target from the previous tungsten to depleted uranium, and by improving the performance of the existing proton accelerator (H^- injection as well as increasing the energy of the injector proton linac from 20 MeV to 40 MeV). The final goal for the proton-beam current is hopefully 10 μA at 500 MeV. The macroscopic pulse duration is maintained at about 50 ns at full width. Up to now, a proton beam intensity of about 1.5×10^{12} protons per pulse has already been achieved at a repetition rate 20 Hz as an instantaneous record, corresponding to about 5 μA in time-average current. The accelerators are continuously being tuned to increase the beam current so as to keep the beam loss at an accessible radiation level. At this moment the beam current in routine operation is about two thirds of the maximum value mentioned above in order to make maintenance easy.

The installation of a depleted uranium target system was completed last November; since then it has been operating satisfactorily. Figure 1 shows an illustration of the target assembly which consists of four blocks of depleted uranium enclosed in a bonded clad of zircaloy-2 alloy. The clad uranium blocks were fabricated at Argonne National Laboratory. The uranium core consists of depleted uranium with additions of carbon 450 wt ppm, iron 250 wt ppm and silicon 350 wt ppm. Each target block is a rectangular parallelepiped with partly rounded corners in order to avoid any possible concentration of the thermal stress. The dimension of the block is about 78 mm wide, 57 mm high and 30 mm thick.

The center temperature of the first target block is monitored by a thermocouple. The temperature increase is about 35°C at the rated flow of cooling water 60 ℓ/min for a proton-beam current of 2.5 μA as shown in Fig. 2. This corresponds to a center temperature of 175°C at the rated proton-beam current, well below the design value of 230°C in safety-side estimate by calculations and a mock-up test. At this temperature, thermal stress and thermal-cycling fatigue is no longer important, and we can expect a semi-infinite life of the target.

The gain factor of the neutron production of the depleted uranium target relative to the previous tungsten was measured by thermalized neutrons from the polyethylene moderator at ambient temperature. The

measured gain factor is shown in Fig. 3. The wavelength-dependence of the gain factor may be caused by the difference of the hydrogen density in the moderator, because the previous moderator had a lower hydrogen density (due to radiation damage) than the renewed one. A gain factor 1.9 ∿ 2.0 was confirmed from this data.

The cold neutron source, solid methane at about 20 K, has also been renewed. A flat moderator, 12 cm wide, 5 cm thick and 15 cm high, as illustrated in Fig. 4, was again adopted instead of the previous grooved moderator. The reason arises mainly from the limited cooling power of the present refrigerator system. Energy deposition in the previous grooved moderator at the rated beam power (500 MeV x 10 μA) was estimated to be about 50 W, including possible leakage proton bombardment, while the new flat moderator can reduce this value by about 40 %, since the latter has a smaller volume than the former. The new one has a heat exchanger inside the container wall (Fig. 4) instead of an overhead heat exchanger as in the previous system in order to improve the cooling efficiency. A lot of aluminium plates are inserted in the container in order to increase the effective heat conduction in the moderator. A typical moderator temperature in operation is also shown in Fig. 2 where vertical scale shifted by about + 2° K. The ratio of neutron spectrum from the new flat moderator relative to that from the previous grooved moderator is shown in Fig. 5. It is almost flat in the longer wavelength region. The result indicates that the new flat moderator is as good as the previous grooved modelator in the performance of cold neutron production.

One of the most important disadvantage in the use of a uranium target may be increase in the fast-neutron background caused by delayed neutrons. As the worst example, we show in Fig. 6 powder diffraction patterns (one measured with the uranium target and another with the tungsten). These data were obtained using longer-wavelength neutrons (approximately 7 A); the tail part of the spectrum results from the room-temperature moderator. Similar increase of the background was also observed on the WIT (small angle scattering instrument installed directly to the neutron beam hole from the room-temperature moderator). The results indicate that if we utilize longer wavelength neutrons far beyond the Maxwellian peak, the background caused by delayed neutrons becomes predominant. In the case of the inelastic machine the background problem is much more serious. Although the MAX (multi analyzer crystal spectrometer for coherent inelastic scattering) and the LAM-40 (quasielastic machine which is not

incorporated with a neutron guide tube) utilize the main part of the spectrum from the respective moderator, a considerable increase of the background was recognized in the data on these spectrometers. We understand that this is due to an inadequate shield around the incident beam path and insufficient beam collimation for fast neutrons. At KENS we realized a higher coupling efficiency of the target-moderator by adopting a target shape of a rectangular parallelepiped with a possible minimum distance between them. This configuration, however, is more susceptible to the background caused by delayed fast neutrons. A great deal of effort must be put to overcome this problem.

3. Improvements of Spectrometers

During the past two years a great effort was expended in developing a new type one-dimensional ^{6}Li-loaded-glass scintillation position-sensitive detector,[1] PSD, using a light-encode method. The detector system was completed last summer and installed at the four-circle single-crystal diffractometer (FOX). After electrical tuning, the detectors were successfully operated.

The layout of the PSD is shown Fig. 7. One detector element consists of 3 cylindrical scintillators (3 mm in diameter and 30 mm in hight). Flexible plastic optical fibres (3 mm in diameter) are connected to both ends of the scintillator. A total of 384 scintillator elements sit side by side in a semicircle 45 cm in radius. The PSD is divided into two sections, that is, right and left sections. Each section has 64 detector elements (192 scintillators), and they are covered by 12 PMs. Data in each section are further divided into 4 blocks. The positional resolution of the PSD was determined to be 9.7 mm. The resolution does not depend on the position since the shape of the PSD is semicircular and the scattered neutrons from the specimen never strike the detector elements obliquely.

One example of the raw data is shown in Fig. 8. The specimen is a well known material, $BaPb_{0.7}Bi_{0.3}O_3$, the size of which is 1 mm x 1 mm x 2 mm. The peak intensity of 200 reflections is 35,000 cts/10 μs for 4 hours. The analysis gave us a satisfactory parameters regarding structure refinement.

The construction of the thermal neutron small angle scattering instrument (WIT)[2] has partly been completed with a pilot detector system. The instrument has been installed at the H-2 neutron beam hole which

directly views the polyethylene moderator at room temperature. The schematic drawing is given in Fig. 9. The instrument is equipped with a two dimensional converging Soller slit and 12 annular ^{6}Li glass scintillation detectors. The FWHM of neutron beam size at the focusing point is observed as 9 mm x 9 mm without escape ghosts. The 12 annular detectors are located at the scattering angles between 0.46° and 4.88° and can cover the Q range from 0.008 A^{-1} to 1.34 A^{-1} by use of the wavelength between 0.4 Å and 6 Å. The construction will be completed by this year.

Change of the cold moderator from the grooved to the flat brought great advantage to the performance of the high-resolution powder diffractometer (HRP). The resolution $\Delta d/d$ was improved from 0.40 to 0.30 %. The simpler form of the peak shape function from the flat moderator made it possible to establish a Rietveld program[3] for analyzing powder patterns from the HRP. The HRP simultaneously utilizes a wide range of neutron spectrum 0.5-10 A. Correspondingly, the pulse shape function of neutrons significantly varies with neutron wave length : from a narrow and more symmetric one at the 1/E region to a broad asymmetric one at the Maxwellian region of cold neutrons, passing through a more complex shape at the transient region. It is very important to use a neutron shape function expressed by a unified set of parameters over the entire range of wavelength. We used a peak shape function of Cole and Windsor type,[4] but modified it based on a new pulse shape function by Ikeda and Carpenter.[5] The peak shape is described in terms of three separate regions: leading side with a Gaussian function, trailing side with another Gaussian function and trailing edge expressed by mixing two exponential functions. The mixing ratio changes with neutron wavelength; the steeply decaying exponential function is dominant in the short wavelength region, while the slowly decaying function becomes major with increasing wavelength. Figure 10 shows a diffraction pattern from Al_2O_3 together with calculated Rietveld profile. The pattern covers a d-range of 50 - 350 pm and includes 274 reflections. Final R-factors are R_{wp} = 7.1 %, R_p = 4.9 %, R_B = 1.9 % and R_F = 1.8 %.

The polarized epithermal neutron spectrometer (PEN) is one of the most challenging machine in our facility. The polarized epithermal neutrons with the polarization of 70 % or more are normally produced by a dynamically polarized proton filter.[6] As a unique use of the polarized

epithermal neutrons, measurements of parity non-conserving effect in nucleus were carried out. This is well demonstrated in Fig. 11 where helicity dependence of the resonance of the neutron radiative capture reaction of ^{139}La observed with the PEN[7] is shown. The preliminary result of asymmetry in the γ-ray intensity was obtained to be (9.5 ± 1.2) %.

The three LAM-Type quasielastic / inelastic scattering spectrometers (LAM -80, LAM-40 and LAM-D) are the busiest ones in our facility. About 1/3 of the proposals approved this year are allocated to these machines. One of the three machines, inelastic scattering spectrometer LAM-D, has only one analyzer mirror, but is scheduled to be upgraded. The new machine will have four analyzer mirrors as shown in Fig. 12. The machine can cover the range of energy transfer below 100 meV with a constant energy resolution of which typical value is about 0.3 meV for elastic scattering (4.3 meV).

Some of the interesting measurements recently done by use of these machines are (1) quasi-elastic scattering of a super cooled water measured with LAM-40, (2) quasi-elastic scatterings of polyethylene and polybtadiene measured with LAM-80 above their melting points, of which Q dependence were quite different with each other and (3) low energy excitations measured with LAM-40, which are commonly observed in various kinds of disordered states including organic amorphous polymers and inorganic glasses.

A series of chopper phasing experiments to the accelerator (500 MeV synchrotron) were carried out extensively with a newly developed phasing circuit. Since the frequency of the synchrotron is not exactly constant, it is an inevitable task to keep the chopper, with its high moment of inertia, sufficiently in phase with the synchrotron to achieve a better time-of-flight resolution. Within the acceptable time band (≃ 50 μs centered at peak field in the synchrotron magnet), the proton beam can be extracted according to the request from the chopper. If the request is outside the band, the beam is automatically extracted at the end of the band. Though the phase fluctuation of the chopper is about ± 20 μs at 400 Hz, we have achieved a phased extraction within a time accuracy of ± 0.4 μs with a duty cycle of more than 99 %. The performance is sufficiently good for a practical use. The design work on the chopper spectrometer

(INC) is now in progress.

The other instruments (HIT, SAN, MAX, RAT, TOP) run well as usual without great improvement of the instruments this year.

4. Future Program KENS-II

As a next generation neutron source in Japan we proposed an intense pulsed spallation neutron source so called KENS-II. The proposal included the construction of a high intensity proton synchrotron which was also supported by the μSR group. The whole project including a future program of the μSR as well as the name of the accelerator are then called GEMINI (a Generator of Meson Intense and Neutron Intense beam). For past five years the design studies of the accelerator system have extensively been performed.[8,9] The design goal of the synchrotron was 800 MeV with a time average beam current 500 μA and with a repetition 50 Hz. Recently scientists in the field of nuclear physics have proposed a future program so called Super Hadron Project aiming to produce intense kaon and anti-proton beam. Since then the both projects are being unified. Now KENS-II project is getting a wide range support among the Japanese scientists and expected to be authorized as a part of the Super Hadron Project.

The accelerator system in this program is still open, but may consist of a proton linac, a first ring accelerator for neutron and pion production which corresponds to the previous GEMINI part, with a storage ring for nuclear physics, and a 20 - 30 GeV ring accelerator for kaon and anti-proton factory. In the first phase of the project the existing 12 GeV proton synchrotron will substitute the 20 - 30 GeV ring accelerator after a necessary upgrading. Requirements for the first ring accelerator are of wide variety group by group. Neutron group requests pulsed proton beam with lower energies (<1.5 GeV) and a repetion rate not larger than 50 Hz but with possible highest beam current, while μSR people do with higher energies (>1.5 GeV), better emittance and with more frexibility in pulse width and repetition rate. The nuclear physics group requests higher energies 3 GeV or more and some times stretched beam, of course, with better emittance.

In order to make our standpoint more clear we performed a neutronic computor simulation for various proton energies in the range 0.5 - 3 GeV,

using a high energy transport code NMTC/JAERI.[10] As a model target, we assumed a cylindrical target, 10 cm in diam. and 32 cm (64 cm for 3 GeV) long, which consists of many disks of depleted uranium enclosed in a bonded clad of zirconium with proper cooling water gaps. Beam profile of protons incident upon the target was assumed to be cylindrical, 4.7 cm in diam. which may be typical for high intensity proton beam.

Figure 13 shows the total neutron yield for various proton energies. Neutron yield is almost proportional to the incident proton energy below 1 Gev, but there is no advantage for energies much greater than about 1 GeV. 3 GeV proton produces only two times as many neutrons as 0.8 GeV proton. Figure 14 shows axial distributions of source neutrons integrated over the radial direction. The maximum luminosity is almost unchanged with increasing proton energy. For reference, Fig. 15 shows spatial distributions of energy deposition in the target. Maximum heat load is also unchanged with proton energy.

Thermal neutron beam intensity was calculated using the TWOTRAN-II. In the two dimensional calculation, we assumed an annular water moderator, 10 cm wide and 5 cm thick, surrounding the target with a beryllium reflector 30 cm thick in the remaining part of the target cylinder, instead of a reference moderator 10 x 10 cm^2 x 5 cm thick as usual. Table I summarizes a rough estimate on relative intensity of thermal neutrons from the moderator for various proton energies.

We decided from the result that the acceptable maximum proton energy for pulsed neutron research, as a consequence of compromise with other group, is around 1.5 GeV.

The energy of the injector proton linac is another crucial point in the discussion. The nuclear physics group is keen to have a higher energy, hopefully 1 GeV, in order to obtain proton beam with better emittance from a synchrotron. The maximum energy of the injector, of course, depends on the total budget available. An injection energy of 100 MeV was considered in the original GEMINI, but higher injection energy is welcomed also in the first ring. Fox example 300 MeV injection will largely improve the performance of the first ring accelerator.

References

1) N. Niimura, J. de phys. (1986) in press ;
N. Niimura, K. Yamada, T. Kubota, M. Isobe, F. Okamura, I. Kawada, A. Masaki and H. Horiuchi, J. appl. Cryst. to be published.

2) N. Niimura, A. Ishida, M. Ueno, K. Yamada, M. Hirai and K. Aizawa, KENS-VI (1986) to be published.

3) F. Izumi: KENS Report-VI (1986) to be publoshed.

4) I. Cole and C. G. Windsor: Nucl. Instrum. Method, 171 (1980) 107.

5) S. Ikeda and J. M. Carpenter: Nucl. Instrum. Methods, A239 (1985) 536.

6) Y. Masuda, S. Ishimoto, M. Ishida, Y. Ishikawa, M. Kohgi and A. Masaike, submitted to Nucl. Instrum. Meth.

7) Y. Masuda, T. Adachi, S. Ishimoto, E. Kikutani, H. Koiso, K. Morimoto and A. Masaike: Hyperfine Insteractions to be published.

8) H. Sasaki and GEMINI study group : proc. ICANS-VII, AECL-8488 (1983) 50.

9) Y. Ishikawa and the KENS group : proc. ICANS-VIII, RAL-85-110 (1985) 17.

10) Y. Nakahara : J. Nucl. Sci. Technol., 20 (1983) 511.

Table I Thermal Neutron Yield

Ep (GeV)	Thermal Neut. yield (arb. unit)	Total No. of Source Neut.
0.8	59.8	3962
1.5	82.85	6010
2.0	96.97	7119
3.0	106.03	8199

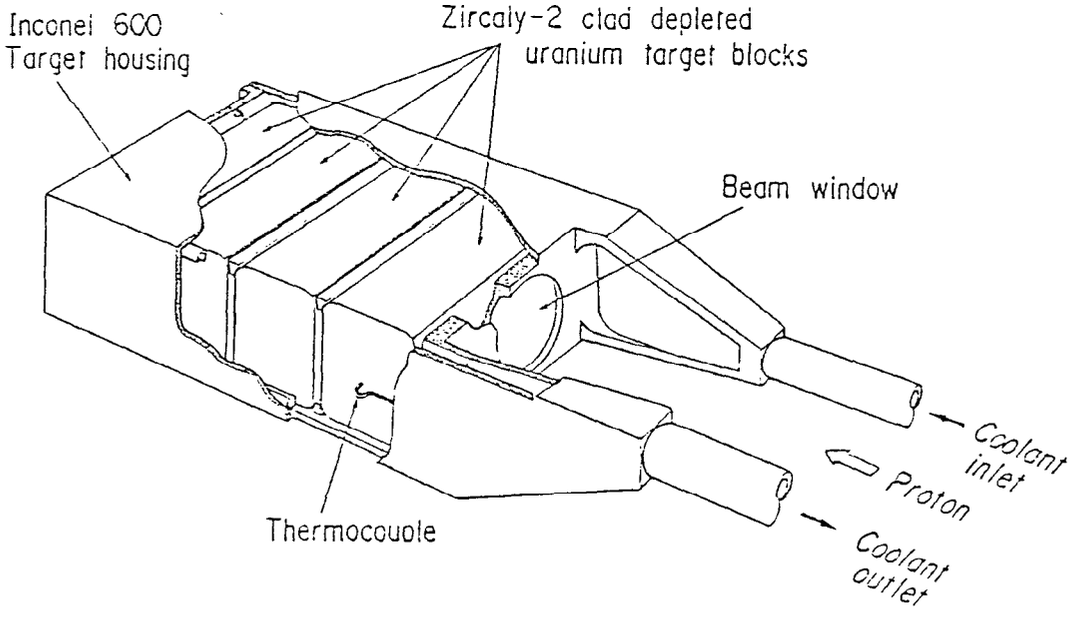

Fig. 1 Illustration of the target assembly which consists of four blocks of depleted uranium enclosed in a bonded clad of zircaloy-2 alloy. Target hausing is made of Inconel 600.

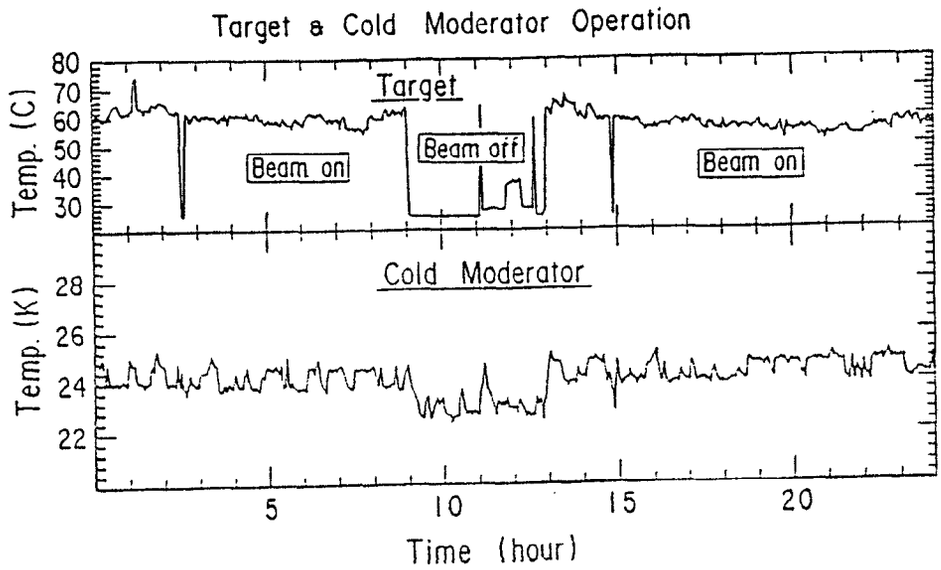

Fig. 2 Operational characteristics of the target and the cold moderator at a proton-beam current of 2.5 μA : center temperature of the first target block (upper figure), temperature of the solid-methane moderator (lower figure).

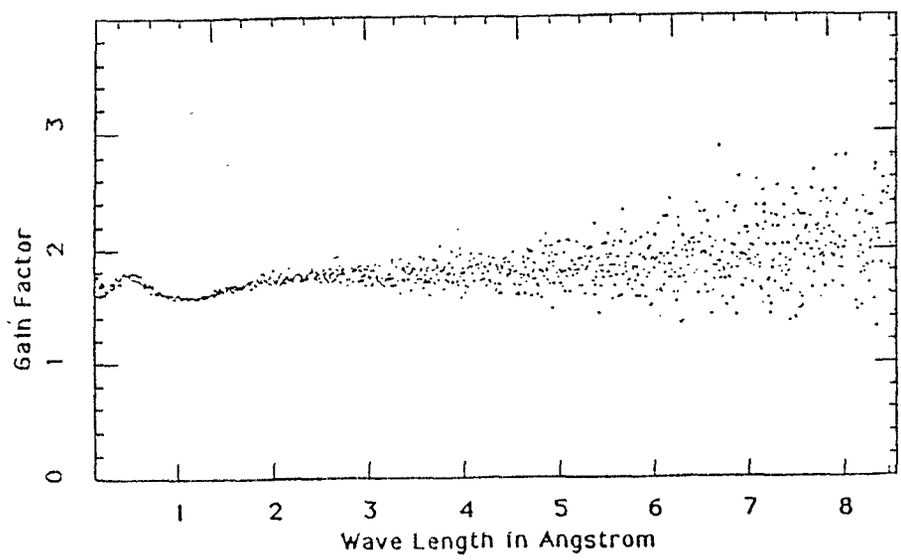

Fig. 3 Neutron gain factor of the uranium target relative to the previous tungsten determined by thermalized neutrons from the polyethylene moderator at ambient temperature.

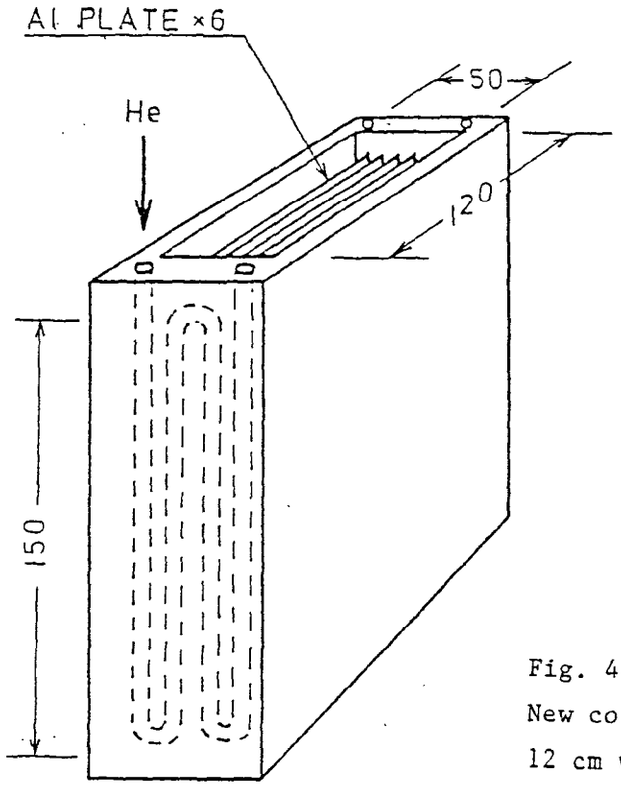

Fig. 4
New cold moderator container, 12 cm wide, 5 cm thick and 15 cm high.

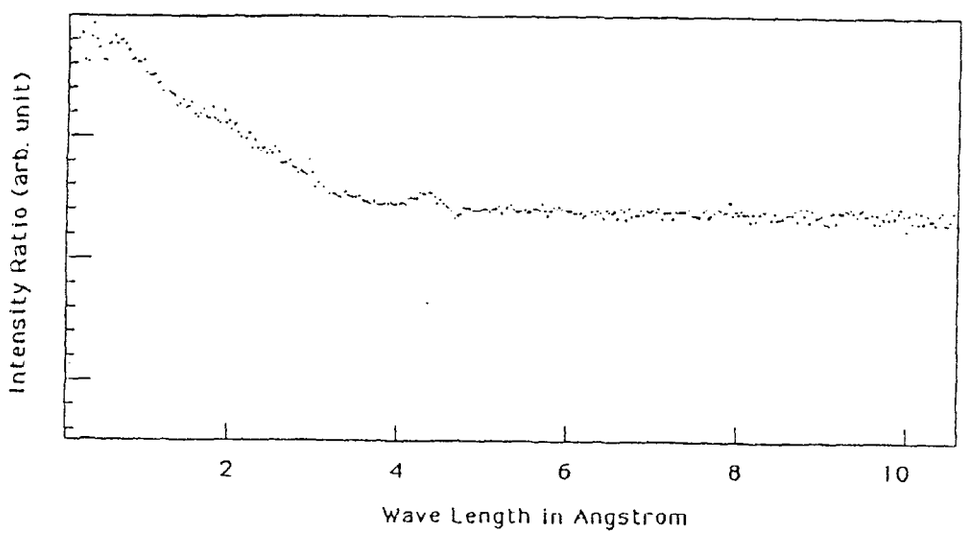

Fig. 5 Ratio of the cold-neutron spectrum from the new solid-methane moderator to that from the previous grooved one.

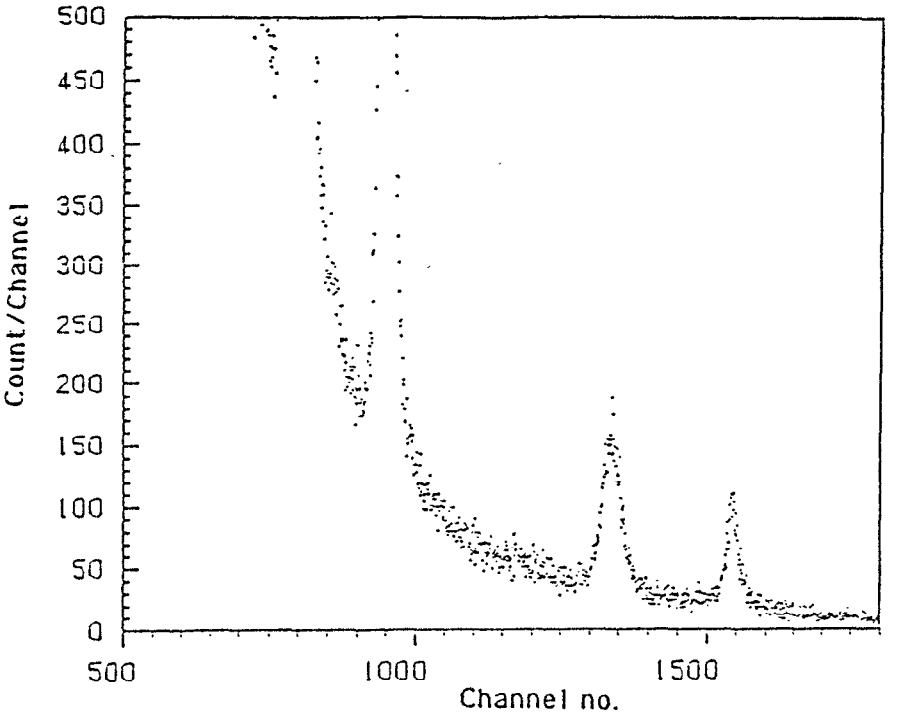

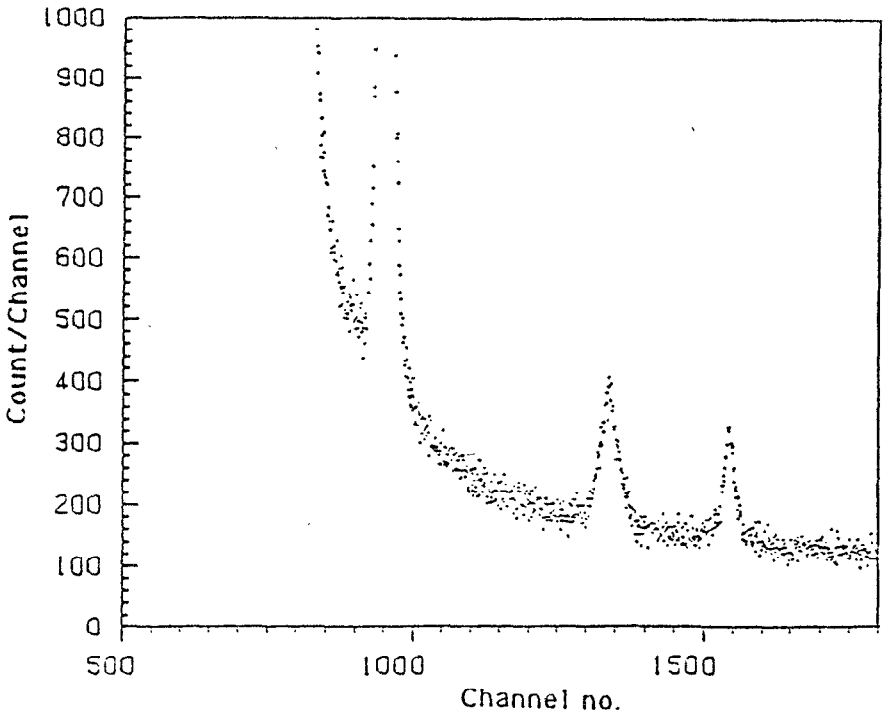

Fig. 6 Comparison of the background level in powder diffraction (worst example) : with a tungsten target (upper figure), with a uranium target (lower figure). The higher background in the uranium is due to delayed neutrons.

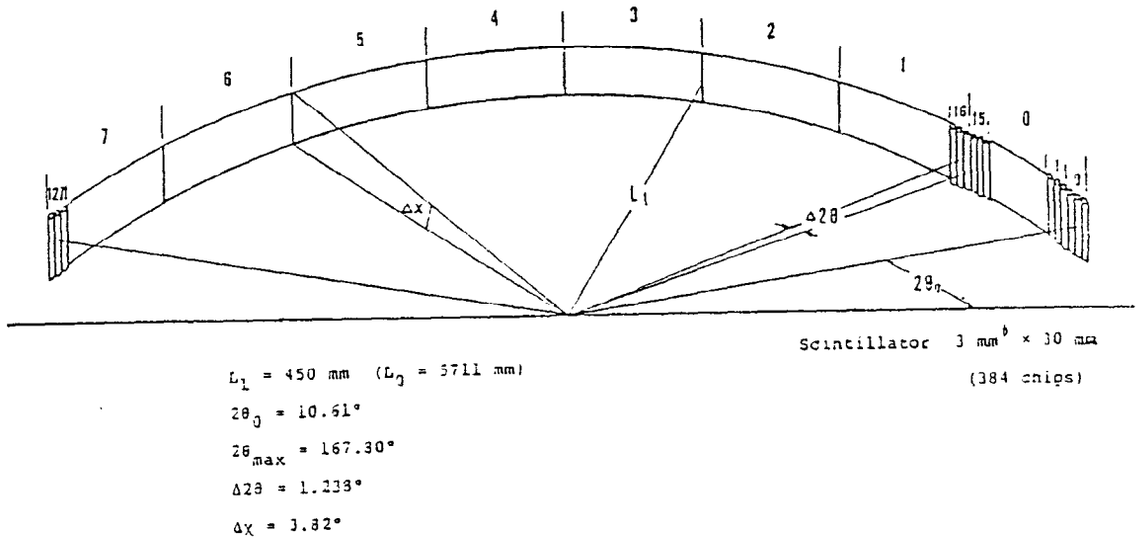

Fig. 7 Layout of a one-dimensional PSD using a ^{6}Li-glass scintillator installed at the single-crystal diffractometer FOX.

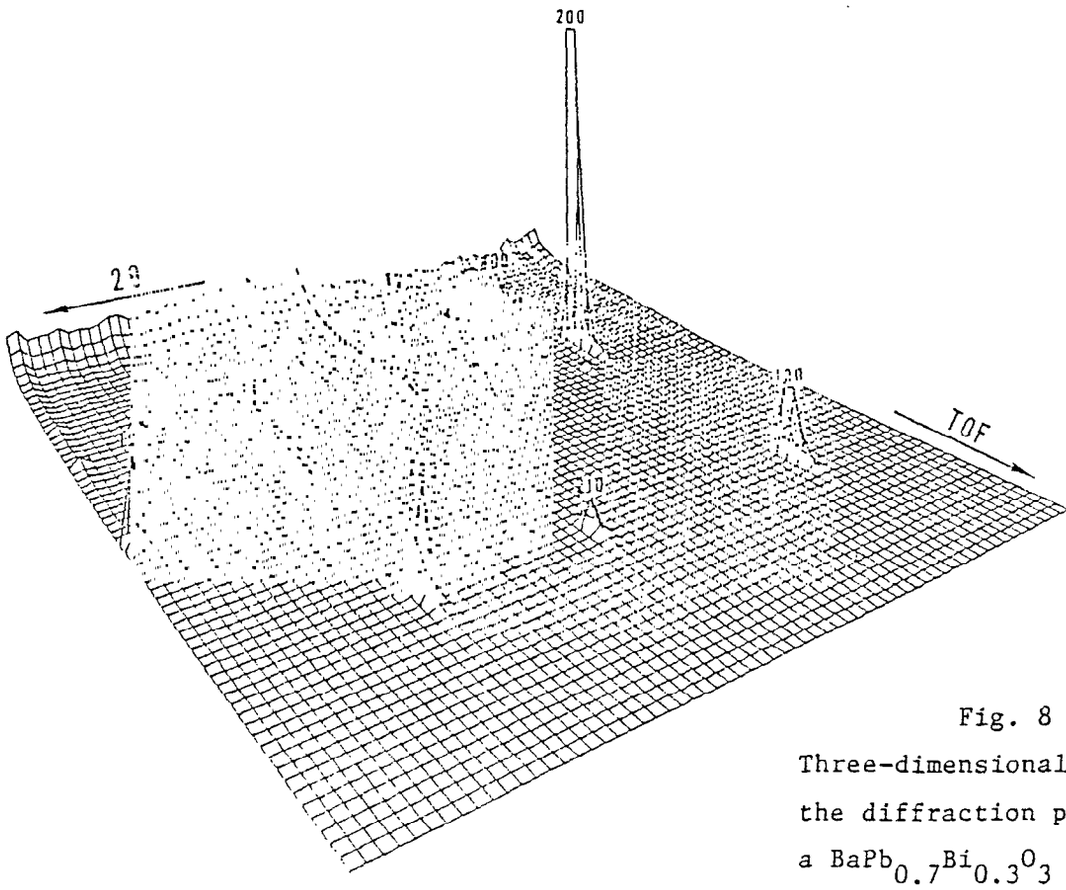

Fig. 8
Three-dimensional display of the diffraction pattern from a $BaPb_{0.7}Bi_{0.3}O_3$ crystal (1 mm x 1 mm x 2 mm).

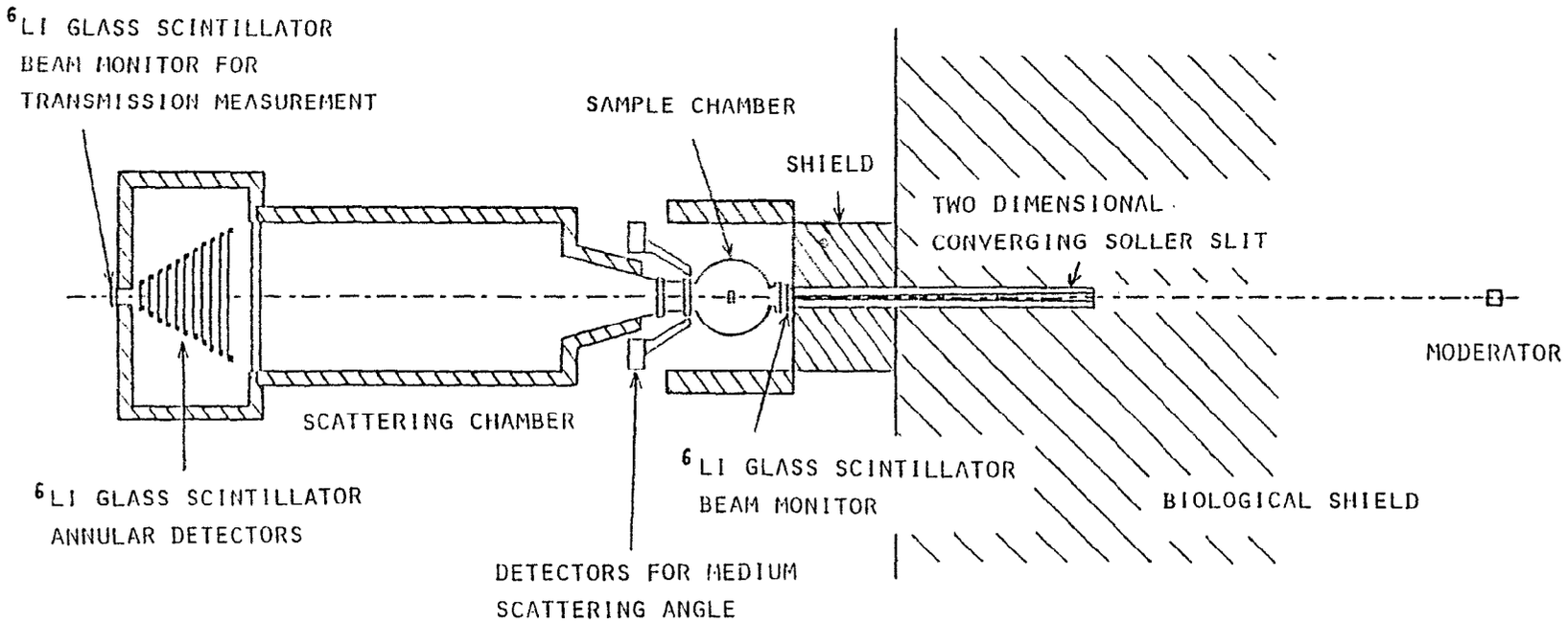

Fig. 9 Schematic layout of WIT.

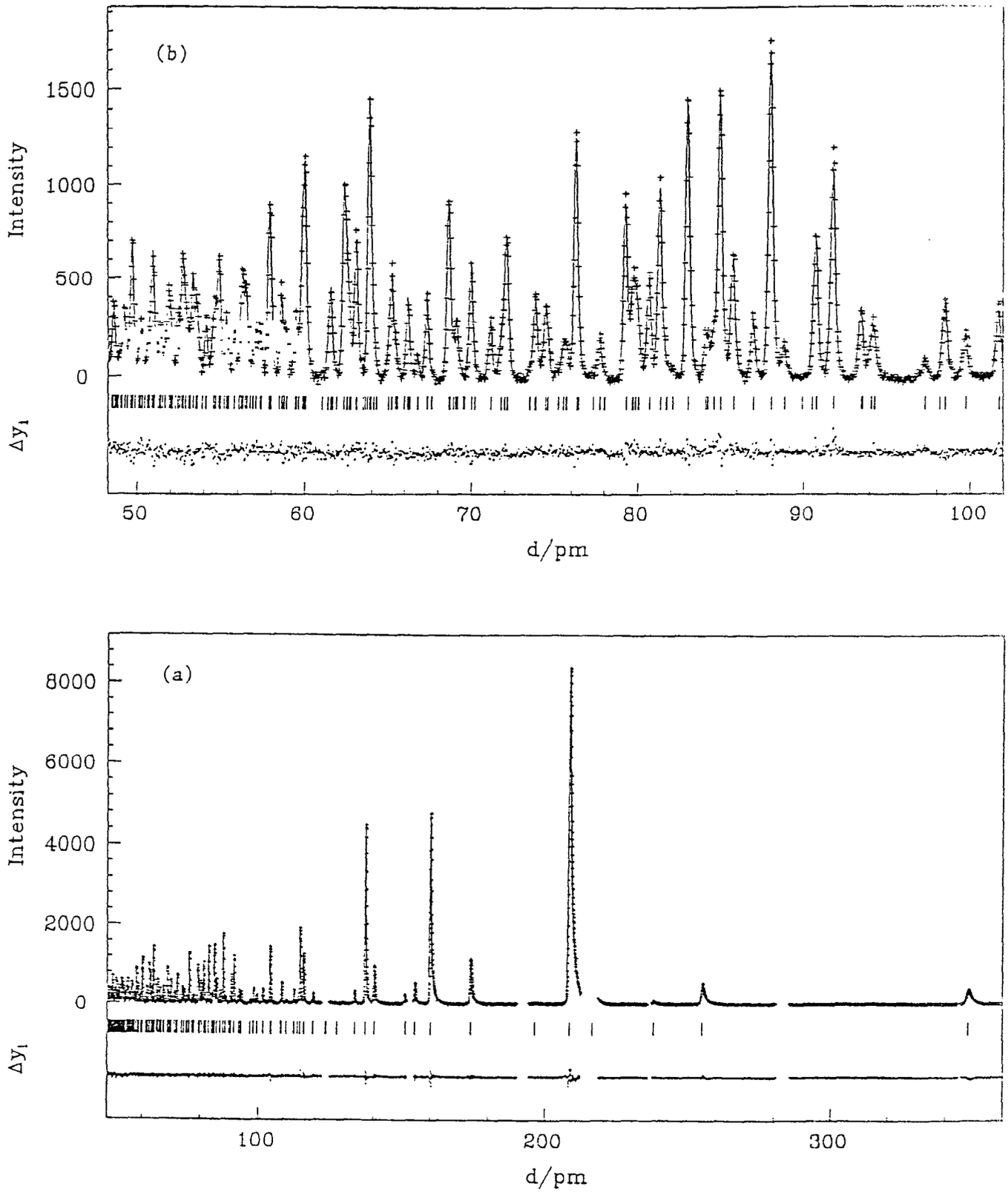

Fig. 10 (a) Neutron diffraction patter of Al_2O_3 observed with the HRP. Regions where Bragg reflections of the vanadium sample holder appear are omitted.
(b) Enlarged portion in the range d = 50 - 100 pm. Background is subtracted.

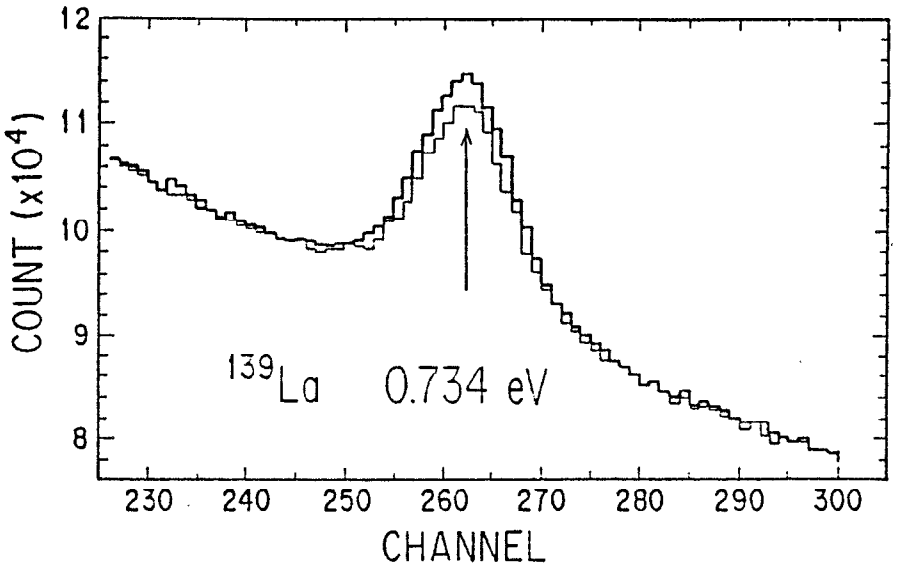

Fig. 11 TOF spectra around 0.743 eV resonance of ^{139}La observed with the PEN. The thick and thin lines are refer to the spectra for the parallel and antiparallel neutron polarization to the beam, respectively.

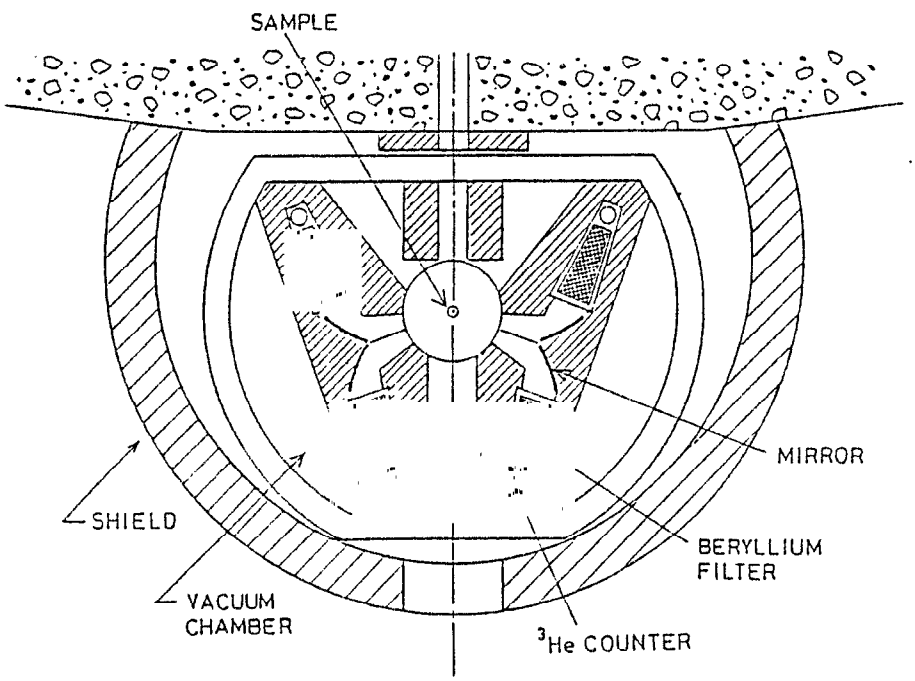

Fig. 12 Schematic layout of a new LAM-D.

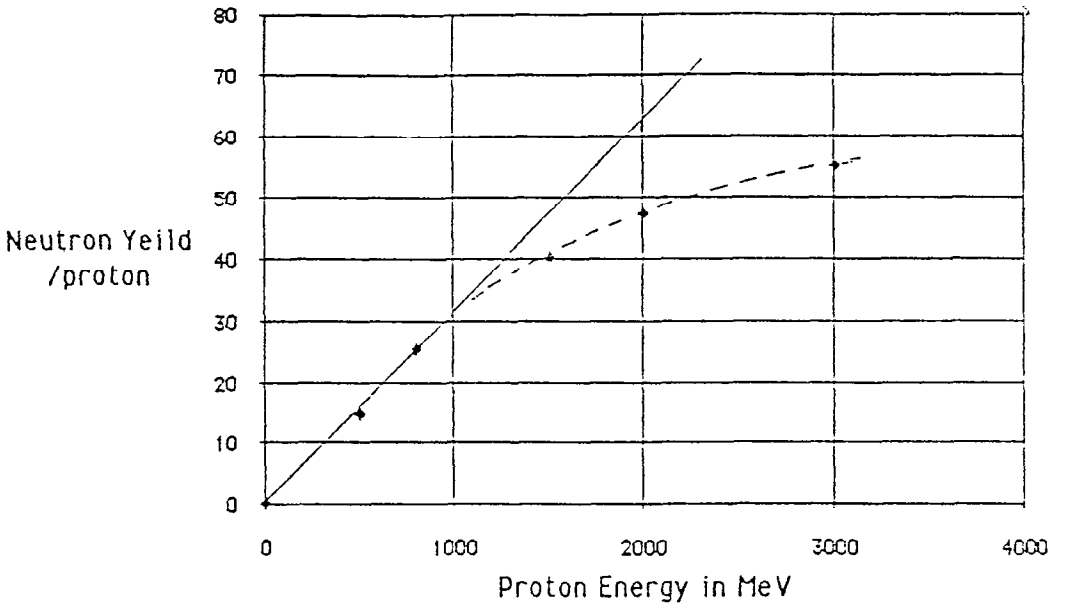

Fig. 13 Neutron total yield vs proton energy.

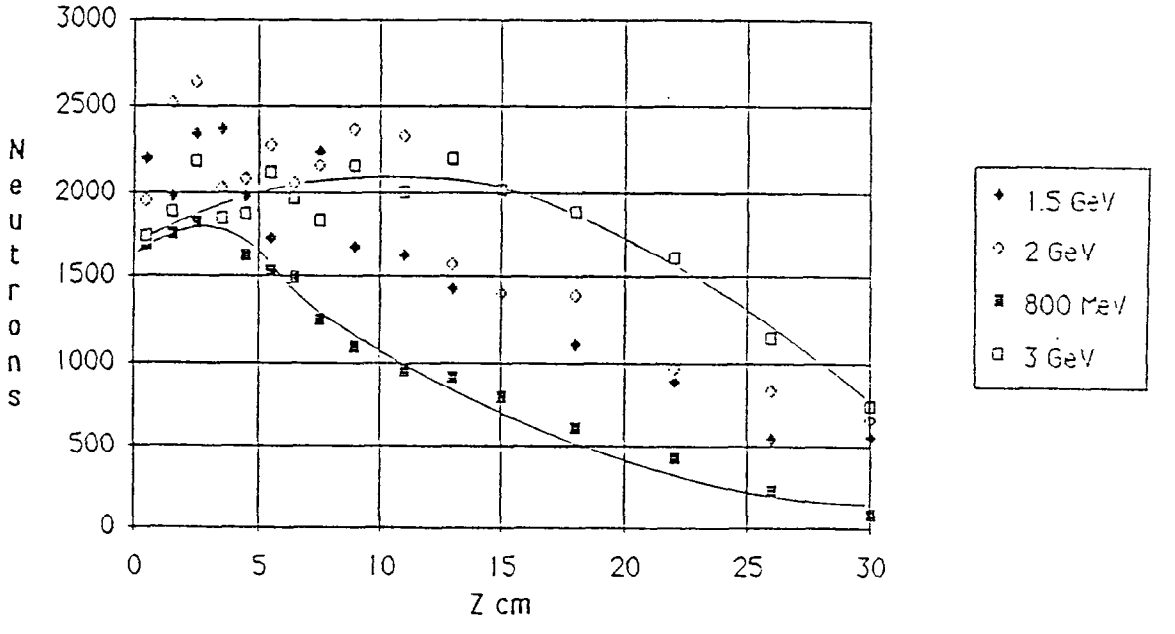

Fig. 14 Axial distribution of source neutrons for various proton energies.

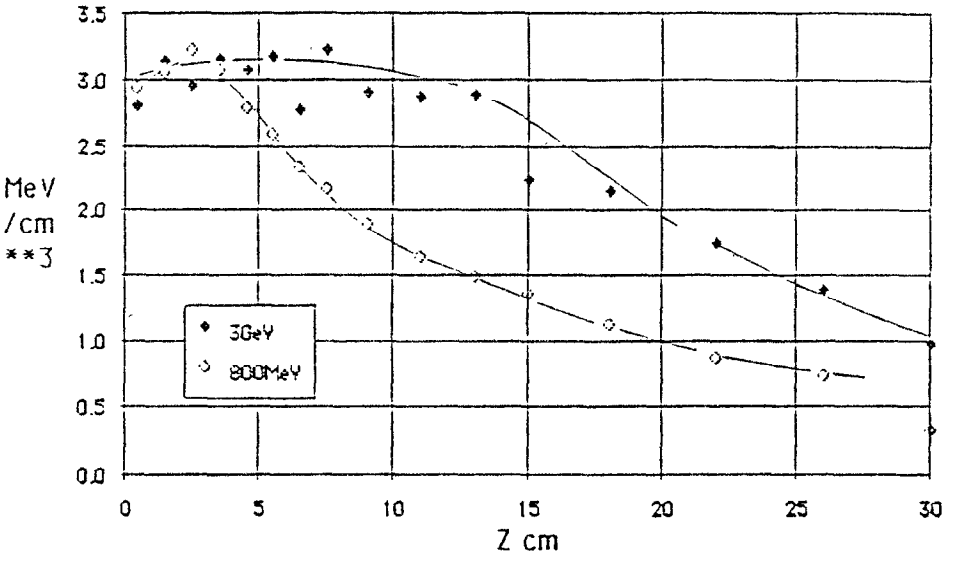

Fig. 15 Spatial distribution of energy deposition for different proton energies.

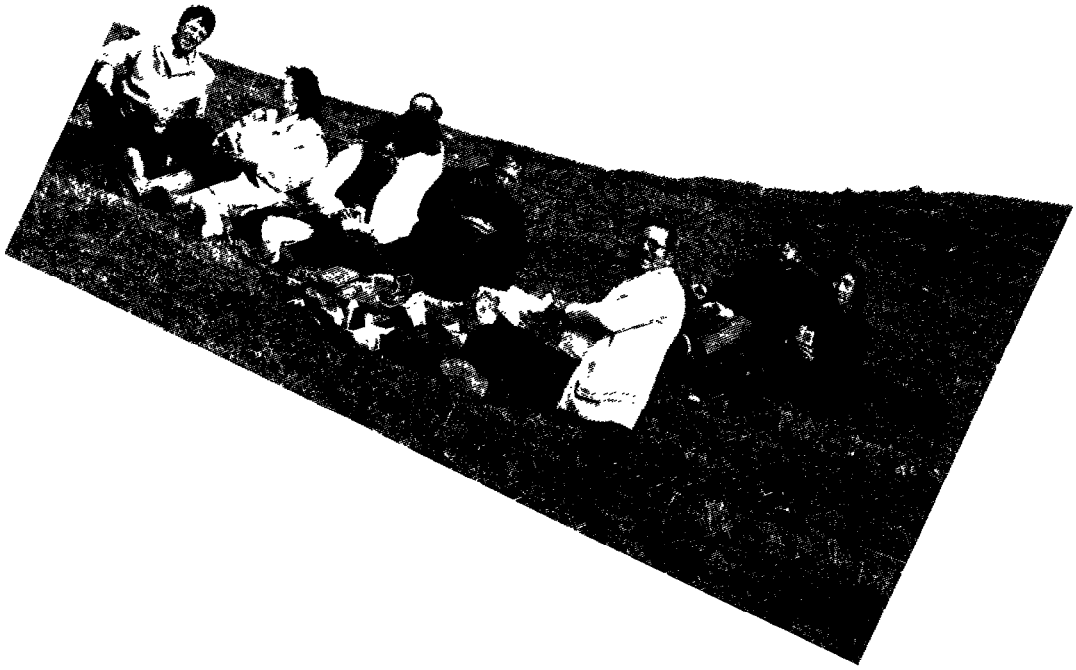

ICANS IX

INTERNATIONAL COLLABORATION ON ADVANCED NEUTRON SOURCES

22-26 September, 1986

PROTON STORAGE RING COMMISSIONING AT LANSCE*

G.P. Lawrence, R.A. Hardekopf, A.J. Jason
B. Blind, and T.W. Hardek, AT-3, MS H808
Los Alamos National Laboratory, Los Alamos, NM 87545 USA

INTRODUCTION

The Proton Storage Ring (PSR),[1] now being commissioned at Los Alamos, is a fast-cycling high-current accumulator designed to provide intense 800-MeV proton pulses for driving the Los Alamos Neutron Scattering Center (LANSCE) spallation source.[2] Although originally intended to operate in both a short-bunch accumulation mode (for fast neutron spectroscopy) and a long-bunch mode (for neutron scattering), the PSR as now implemented provides only a long-bunch output optimized for the requirements of a materials science research program using thermal neutrons. In this mode, the storage ring accumulates a long (up to 1000-μs) macropulse from the LAMPF linear accelerator into a short (270-ns) first-harmonic bunch and ejects it in a single turn. The design repetition rate is 12 Hz, which will provide 100 μA on the neutron-production target, assuming the design goal of 5.2×10^{13} protons from the linac in each macropulse. If beam losses can be sufficiently well controlled, the longer range plan calls for increasing the pulse repetition rate to at least 24 Hz, and perhaps to 48 Hz, to provide more current both for neutron scattering and proposed neutrino physics programs.

The PSR, which was built for a capital cost of about $22 million, was completed on schedule in late March 1985; first beam was circulated on April 25. Most of the remainder of 1985 was devoted to commissioning and developing an understanding of how the machine operated in practice. Particular attention was given to illumination of beam-loss mechanisms. By the end of 1985, the storage ring had operated briefly in production at 30-μA average current and had accumulated up to 2.6×10^{13} protons per pulse, about half the design goal. However, beam losses during accumulation and at extraction were considerably greater than estimated during design. The limitation on maximum charge accumulated in PSR in 1985 turned out to be the peak intensity available from the H^- ion source, although beam loss, apparently from a very fast instability, was observed under some conditions above 1.5×10^{13} protons per pulse (ppp). During the accelerator shutdown from January to July 1986, the 1985 commissioning results were assessed, and several improvements were made in PSR and its associated beam transport systems. The operating plan for the 1986 run

*Work supported by U.S. Department of Energy.

cycle has scheduled 40% of the available time for LANSCE beam production, 40% for continued commissioning of PSR, and the remainder split between machine maintenance and nuclear and neutrino physics programs sharing beamline-D. Major 1986 goals are to demonstrate 100-μA average current through PSR at 20 Hz and to investigate the high space-charge region up to about 4 x 10^{13} ppp. The existing H^- source has been improved during the shutdown, but it is expected that a new source design will be required to reach the goal of 5.2 x 10^{13} ppp.

So far this year the storage ring has operated routinely at 25 μA for LANSCE production, and machine physics experiments have reconfirmed both the short beam lifetime during accumulation and high extraction losses. Charge levels up to 3.3 x 10^{13} ppp have been accumulated during high-intensity machine development.

GENERAL DESCRIPTION

Beam Preparation

Figure 1 shows schematically the components in the PSR project and their physical relationship. The scale is distorted to highlight the storage ring. A summary of the design operating parameters is given in Table I; Tables II and III list the significant structural and dynamical parameters.

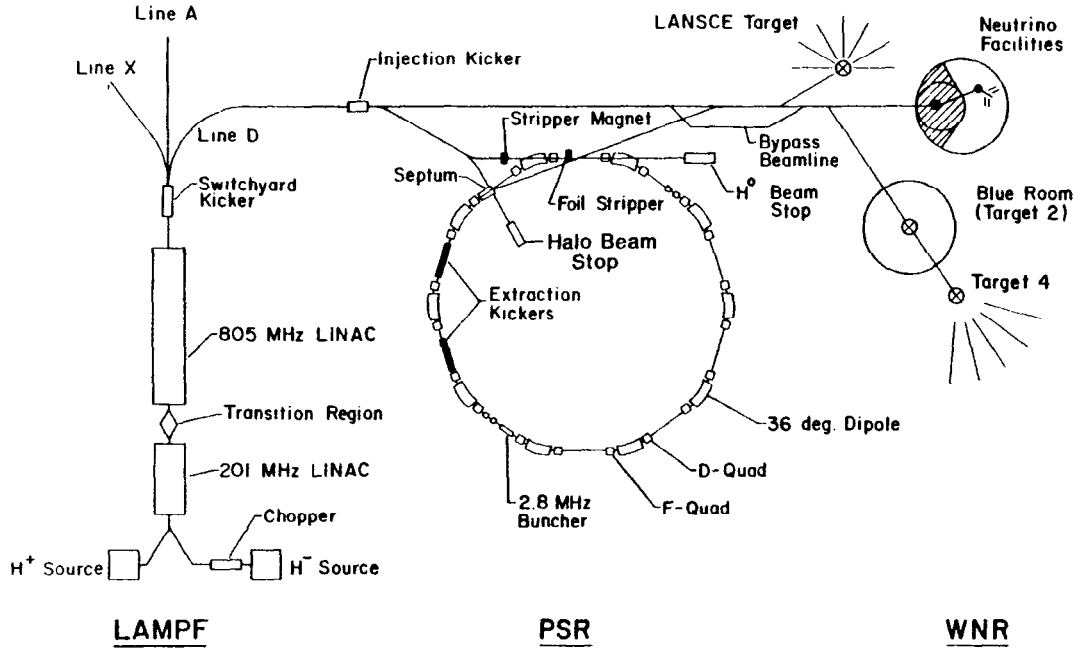

Fig. 1. Schematic drawing (not to scale) of the PSR project.

The PSR filling scheme requires multiturn injection by two-stage stripping of a high-intensity H^- beam. Design intensity of this beam is 13 mA at the output of the linac. About 6 mA was available for most of 1985, and up to 9 mA has been available so far in 1986.

TABLE I
PSR OPERATING PARAMETERS

Number of bunches in Ring	1	Injection rate	12 pps
Bunch length in Ring	270 ns	Filling time	750 μs
Buncher frequency	2.795 MHz	Extraction rate	12 pps
Protons/bunch accumulated	5.2×10^{13}	Peak circulating current	46.3 A
Accumulated turns	2100	Average current	100 μA

TABLE II
PSR STRUCTURAL PARAMETERS

Orbit circumference	90.2 m	Dipole field	1.20 T
Focusing structure	FODO	Bend radius	4.06 m
Lattice type	Separated function	Dipole aperture	10.5 cm x 28 cm
No. of periods	10	Quadrupole gradients	3.92, -2.33 T/m
Free straight section	4.51 m/cell	Quadrupole aperture	18.1 cm
Dipole length	2.55 m	Quadrupole length	0.47 m

TABLE III
PSR DYNAMICAL PARAMETERS

Circulation period	357.7 ns	$\delta p/p$ (injection/extraction)	±0.001/±0.003
Proton kinetic E	797.0 MeV	Emittance, injected beam	0.05 cm•mrad
Proton β, γ	0.842, 1.849	Emittance, extracted beam	2.0 cm•mrad
Proton rigidity	4.869 Tm	Phase advance/cell:	
Transition γ	3.02	Horizontal	115°
Tunes (Q_H, Q_V, nom)	3.2, 2.2	Vertical	79°

Considerable modification to the linac injector complex and switchyard was required to deliver H^- beam pulses to PSR while minimizing interference with other LAMPF experimental programs. The 750-keV H^- transport was completely rebuilt to accommodate multiplexing between the high-current H^- and polarized (P^-) beams and to provide the correct optics for slicing the PSR macropulse into 270-ns beam bursts every storage ring revolution period (360 ns). This is accomplished by a traveling-wave fast-rise-time electrostatic deflector (chopper).[3]

In the switchyard, totally reconfigured for PSR operations, the positive and negative beams are first separated vertically. Then the H^- macropulses for PSR are deflected horizontally into Line D by a kicker magnet and septum, whereas P^- pulses pass unperturbed into Line X. The kicker, which is driven by a high-current/low-voltage modulator, has a rise time short enough (40 μs) to permit macropulse splitting and a tightly regulated 1000-μs-long flat top.[4]

Injection

Beam is transported to PSR through the pre-existing Line D and the new injection line. All magnetic fields in this channel are below 4.0 kG to avoid field stripping the H^- ions. The injection line is skewed to permit bending in horizontal and vertical planes simultaneously.

Included in the injection line are seven pairs of remotely insertable foil strippers that are used to convert the H^- beam halo to H^+; the H^+ ions are sent to a beam dump under the ring floor. In principle, when the injection line is properly tuned, these beam scrapers should provide nearly complete rejection of all transverse phase space outside 3σ for a monochromatic beam. In practice we have found it essential to use these scrapers to reduce beam losses in the storage ring, but because momentum dispersion is nonzero in this part of the line, the trimming is not perfect.

At the end of the injection line, the H^- beam is completely converted to H^0 by a 1.8-tesla transverse magnetic field (stripper magnet). The neutral beam passes through a hole drilled in the yoke of a storage ring dipole and then contacts the (distorted) closed orbit while traversing a thin (200-μg/cm^2) carbon foil, where it is stripped to H^+ with about 90% efficiency. The unstripped H^0 beam leaves the ring through a hole in the next downstream ring dipole and is deposited in a well-shielded beam dump.

The magnetic stripping process implies an intrinsic emittance growth in the injected beam that depends on the magnet gap and horizontal beam size. A gap of one centimeter for the present stripper magnet adds a divergence of 0.36 mrad and for the chosen beam size causes a nearly threefold increase in emittance. This emittance growth severely constrains matching to the ring. A nearly homothetic match to the ring phase space can be accomplished in the vertical direction, but the horizontal match necessarily fills nearly the entire one-rms horizontal area alloted for a 2 cm-mrad beam. This situation is shown in Fig. 2.

The closed orbit is distorted (bumped) vertically during beam accumulation by a set of six pulsed magnets to allow control of phase space filling in that plane as well as minimization of beam-foil interaction. The distortion is a maximum at the beginning of accumulation and is programmed to zero by the end of the cycle. To maximize effectiveness of the orbit bump, the four quadrupoles at the end of the injection line are used to provide a good match to the storage ring in the y-y' phase plane.

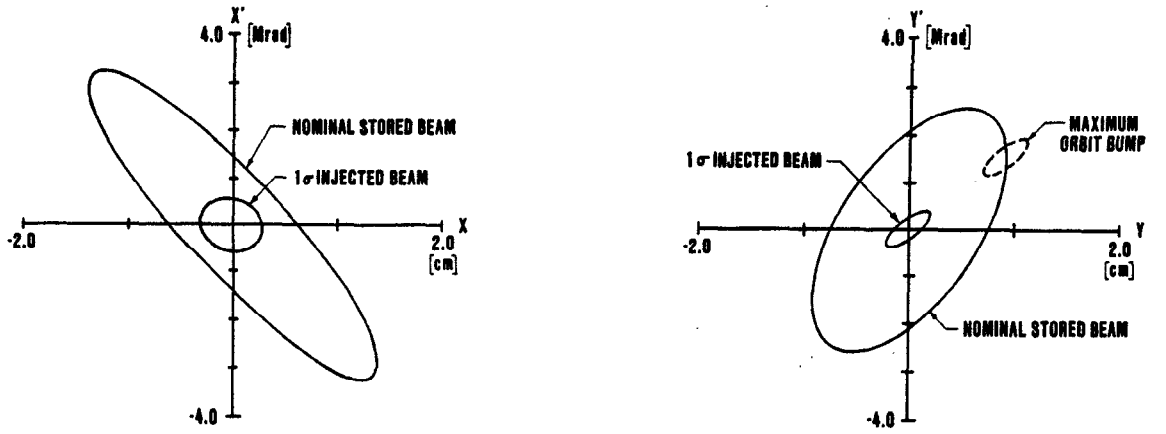

Fig. 2. Transverse phase space areas for PSR injected (small ellipses) and accumulated (large ellipses) beams. The accumulated beam emittance is taken to be 2 cm-mrad, corresponding to the Laslett tune-shift stability limit for the PSR operating parameters. The horizontal phase space area of the injected beam is shown in the left figure. The evident mismatch is necessitated by the stripper-magnet optics, which has also increased the beam emittance. In the right figure, the vertical injected beam (0.05 cm-mrad rms emittance) is shown dashed at the orbit bump trajectory extremum. The small mismatch shown is necessary to optimize transmission through the stripper magnet.

The Storage Ring

The ring design is basically a perfectly symmetric 10-cell FODO separated-function lattice. With a circumference of 90.2 m, the beam circulation period is 357.7 ns at the nominal linac energy of 797.0 MeV. For simplicity in discussion, we usually round these numbers to 360 ns and 800 MeV, respectively.

The 10 ring dipoles have parallel ends and are assembled from steel laminations. They are driven in series by a single power supply; transistor shunts are provided to allow adjustment of effective magnet lengths. Error multipoles are corrected in the integral sense by appropriately contoured solid steel pole end blocks. The F and D quadrupoles, fabricated from solid steel pieces, are identical except for their current excitation. Each set is driven by a separate power supply. The vacuum envelope is stainless steel, with each section pumped by two 600 ℓ/s ion-pumps. A pressure of less than 2×10^{-8} torr is maintained in the ring.

A single, first-harmonic rf buncher is provided in the storage ring to maintain a beam-free region for low-loss single-turn extraction. On each successive turn during accumulation, a new 270-ns beam bunch selected by the linac H^- injection line chopper is added synchronously and at zero relative phase to the previously inserted bunch stack in the rf bucket. The bucket amplitude is programmed to increase as accumulation proceeds

for space-charge confinement. A secondary function of the buncher is to increase the momentum spread of the stored beam, providing stabilization by Landau damping against wall-induced coherent motion at high space-charge levels. The buncher itself consists of a conventional single-gap, ferrite-loaded 1/4-wave coaxial cavity operating at 2.795 MHz. Because of the very large peak circulating beam currents (up to 46 A), the rf amplifier has been designed with an exceptionally low output impedance (20 Ω) to reduce beam loading to a negligible level.[5] Second and third rf harmonics have been added to the buncher system in 1986 to help homogenize the longitudinal density distribution and control the beam momentum spread.

Extraction

Single-turn extraction is achieved by two 4-m-long balanced strip-line kickers, each energized by thyratron-switched Blumlein pulse lines. The kickers generate 300-ns-long, ±45-kV pulses with 60-ns rise times. Working in combination with the lattice magnet elements, the kickers deflect the stored beam 8.5 cm horizontally into the throat of a 5-kG septum magnet, the first element of the extraction transport channel. The channel consists of regularly spaced, large-aperture quadrupole doublets; it delivers the extracted beam to Line D from where it is transported to the LANSCE neutron-production target. Several quadrupoles were added to this portion of the original beamline to facilitate good transmission of high peak-current beams. A vertically oriented dipole located a short distance along the extraction channel allows the beam to be switched to a separate beam dump so that the storage ring can be tuned at low average current before the extracted beam is directed to the target.

COMMISSIONING

Chronology

PSR construction was completed on schedule in late March 1985, and first beam was circulated on April 25. Beam was first extracted from PSR on May 24. The early summer was devoted to studying ring performance at low average currents and up to 2 x 10^{12} protons per pulse. Much of this period was devoted to debugging equipment and controls software and to improving operational reliability. The closed orbit was corrected to within 1 mm, using active shunts on the dipoles for horizontal plane correction. Displacement of quadrupoles was necessary for vertical plane correction.

From the beginning of the PSR design, it had been understood that keeping beam losses well below 1% would be a central requirement for operation at 100 μA. Within a few weeks after turn-on, it became apparent that fractional beam losses in PSR were considerably higher than anticipated. Average currents of 1-2 μA induced activation levels exceeding 3 rem/hr (contact) in some components, even after brief periods of operation. Machine experiments therefore quickly focused on trying to obtain a clear picture of beam losses and on studying the match from the injection line into the ring as one of the keys to understanding the loss mechanisms.

During the fall of 1985, a series of machine experiments exposed the main features of the beam loss. First beam (2 μA) on the LANSCE production target occurred on September 14. In November, with some improvements in instrumentation and tuning and also a decision to accept significant activation levels, trial three-day production runs were made at 10-μA and then 30-μA average currents. In mid-December, machine experiments were conducted at high peak intensities with a maximum of 2.6×10^{13} ppp being reached, about half the design goal. The peak accumulated charge in PSR was limited by the H^- intensity (about 7.5 mA) available at that time and the maximum macropulse length (1000 μs) allowed by the linac rf system. While tuning the ring at charge levels above 1.5×10^{13} ppp, some evidence of fast beam loss, possibly from coherent transverse motion, was observed.

Activation levels resulting from the 30-μA production run and the high-intensity machine experiments were high, especially at the extraction septum, where >30 rem/hr (contact) was measured shortly after beam shutdown. A few other locations had levels as high as 1-2 rem/hr (e.g., the foil stripper and the quadrupoles in the two following straight sections), but most of the storage ring had activation levels below 100-mrem/hr.

The PSR was shut down during the first six months of 1986, along with the linac, for the usual budgetary reasons. During the shutdown, improvements were made to several hardware systems, especially in the area of beam diagnostics. Procurement of sextupoles for chromaticity control was initiated, higher harmonics were added to the 2.8-MHz buncher, the VAX 11/750 control computer was supplemented by a microVAX and a software development console, and the neutral-beam transmission holes in the injection-section ring dipoles were enlarged to reduce losses from the injected beam halo.

Equipment Operation

Much of the initial work in the 1985 commissioning program was devoted to operational check-out of the many complex pulsed systems and to bringing the diagnostics into operation. The traveling-wave chopper, which provided variable-length bunches up to 300 ns long for injection into the ring, performed nearly flawlessly from the start. The flexibility of the pattern generator that drives the amplifiers has been invaluable for choosing the wide variety of pulse lengths and sequences needed for ring tuning studies.[6] Typically, ±500-V pulses having <5-ns rise times are needed to provide adequate chopping of the beam.

The switchyard kickers have also been relatively trouble-free and have easily provided the ultra-flat deflection pulses required. The two modulators have been tested up to 40 Hz at a pulse current of about 2000 A. We believe that pulse rates up to 60 Hz are possible with only minor modifications, which will allow multiplexing LANSCE with other Line D programs requiring different macropulse chopping sequences.

The extraction septum magnets[7] have operated reliably in spite of the activation of this region. The initial switchyard septum magnet experienced coil overheating problems that interfered seriously with commissioning during the early months. It was replaced by a septum with an improved coil design (parallel water circuits instead of one series connected loop) that has operated trouble-free.

The 2400-A transistorized pulse drivers[8] for the (six-unit) vertical orbit bump system have proved vulnerable to failures caused by imperfect protection against excess duty factor. Protection has been improved in 1986. The driver pulse shape has been easy to adjust through an interactive program using the console graphics/touch screens.

The 2.8-MHz rf buncher amplifier has functioned generally satisfactorily, except for minor control problems. Second and third rf harmonics are being added in 1986 to provide a linear bunching waveform over a wider phase range. This modification should reduce the peak longitudinal charge density in the accumulated bunch, decreasing the maximum space-charge tune shift at high currents. Because the cavity bandwidth is broad and the overall duty-factor is low, the harmonics can be applied directly at the same cavity gap as the fundamental.

The extraction kicker modulators have operated well and stably, considering their complex and unusual design.[9] They have provided suitably flat, 300-ns-long ±45-kV pulses to drive the two 4-m-long strip-line deflectors. The firing circuit for the modulators allows the operator to adjust the desired extraction time in 1-μs steps. A 1-ns resolution circuit then produces a beam-associated rotation delay that synchronizes the actual kick with the azimuthal position of the beam in the ring. Rotation delays were set correctly for each modulator by observing the stored bunch during its last revolution before extraction (using a beam transformer) and comparing it with the extracted bunch as seen by a similar transformer in the extraction line.

A gradual and significant increase in kicker-pulse rise time from the 50-ns design value has been observed, and is attributed to aging of the high-voltage switch thyratron. Troublesome circuit components have included the (copper-sulfate-cooled) line-terminating loads and the circuits used to charge the pulse forming networks.

Beam Diagnostics

The strip-line beam position monitor system, which is tuned to process the 200-MHz microstructure imposed by the linac, has been described in several publications.[10] It forms the backbone of the beam diagnostics both for the storage ring and the beam transport lines. It has performed efficiently and has provided us with vital data acquired during commissioning. In addition to its standard use for beam centering, it is also possible to observe fast and slow energy variation of the H^- beam with this system. In the storage ring, it is used specifically to measure the closed orbit, fractional betatron tunes, relative beam intensity, and fast coherent transverse beam motion.

The system competently handles the wide pulse-intensity range present during beam accumulation in the ring (10^3), but filtering is necessary for observing the extracted beam after the 200-MHz frequency component has washed out. The main drawback has been that all 60 detectors are multiplexed through a single position-processing system for each plane, which sometimes causes an operational bottleneck. The reed-relay multiplexers used in the ring (to assure wide dynamic range) have had lifetime problems because of the continuous use of the system to monitor the closed orbit. Terminating resistor contacts at the strip-line detectors

have also proved failure prone. Beam profile diagnostics in the transport lines consist of a mixture of wire-scanners, harps,[11] and Al_2O_3 viewing screens. In three-unit groups, the harps and wire-scanners are used to make on-line beam-emittance measurements. Although the harps have proved useful for determining the core width (1σ) of the beam profile, their noise background has been too large to yield good information about the profile tails. The wire scanners do somewhat better in this regard, but are not installed in all beamlines and are slow. They too cannot reveal details of intensity distributions below the 1% level. This kind of information is crucial for understanding and minimizing injection losses, but is not accurately determined by present PSR diagnostics.

A nonintercepting profile monitor is being developed to follow the transverse shape evolution of beam in the storage ring. This system, which relies on collection of electrons from the background gas atoms ionized by the circulating beam, may be available for use later this year. In the meantime, the time-dependence of the stored beam profile can be measured by ejection (at different accumulation times) onto an extraction channel wire-scanner or harp.

Other diagnostics[12] that have been important in commissioning are beam transformers for measuring the instantaneous stored current and longitudinal bunch profile, a wall-current monitor, and (in 1986) a split cylinder capacitive position pickup that can observe beam motion in the frequency range below 10 MHz. A time-of-flight beam-momentum detector installed in Line D is used to measure fast fluctuations and slow variations in the injected-beam energy and will eventually be part of a feedback loop to stabilize the accelerator energy.

Last, but far from least, are the beam loss monitors. In basic form these devices are liquid scintillators coupled to photomultipliers for observing beam loss at various points in the storage ring and beam transport lines. Some of the loss signals are integrated and fed to an automatic loss-limiting (fast-protect) system that shuts off beam when preset limits are exceeded. Other units are used for direct turn-by-turn observation of beam losses associated (at specific locations) with injection, accumulation, and extraction. The problems encountered with use of these loss monitors lie in quantitatively relating the loss-signal strength to actual beam loss, and (at high-peak-loss locations) obtaining sufficient dynamic range.

RESULTS

Experiments

From nearly the beginning of PSR commissioning, the concentration of experiments has been on understanding and minimizing sources of beam loss at intensities below the current level where space-charge effects would be important. We believe these losses are from single-particle effects, namely the interaction of individual beam particles with the physical environment, exclusive of the beam itself. Furthermore, the picture we have constructed distinguishes between single particle losses of several types, occurring at different times and locations. Although fast, coherent beam loss has been

observed briefly at very high accumulated charge levels (> 1.5 x 10^{13} ppp), not much investigation time has been devoted to such space-charge related phenomena.

Other machine measurements have been carried out, including the horizontal and vertical chromaticity, a map of the significant resonance lines in the betatron tune space near the normal operating point, determination of single-particle phase-space trajectories as a function of betatron amplitude, and observation of the longitudinal bunch shape as accumulation proceeds.

Injection Losses

Injection losses are due to long beam tails in x-x' and y-y' phase space, and also to tails of the $\delta p/p$ (relative momentum) distribution in finite-dispersion regions. The acceptance of Line D and the PSR injection line is large enough to transport the H^- beam with very small losses up to the stripper magnet. The beam is focused within the 1-cm vertical aperture of the stripper magnet to about a 1-mm (1σ) vertical waist. Steering or lens misadjustment errors at this location can cause significant beam to be scraped off vertically by the poles of this magnet, but proper insertion of the upstream halo strippers generally avoids this problem. A new halo stripper was installed in 1986 with orientation and longitudinal position chosen to image the stripper magnet gap, providing specific protection for this device.

During 1985, considerable injection loss was caused by beam halo scraping at the back-leg holes in the two ring dipoles traversed by incoming H^0 beam and outgoing unstripped H^0 beam. This situation has been remedied in 1986 by enlargement of these holes.

Observation of turn-by-turn losses during injection has made it clear that there are important losses in the storage ring during the first few revolutions caused by transverse phase-space tails and dispersed momentum tails scraping on limiting apertures. Absence of a homothetic match in the x-x' plane between incoming beam and the storage ring exacerbates the problem, and a momentum mismatch in the angular component of phase space at injection contributes by increasing the transverse displacement of momentum tails. Comparison of the time-dependence of loss signals at several ring locations indicates that such early-turn losses are greatest just downstream from the injection straight section and reduce to zero in about 10 turns. However, their absolute magnitude is hard to estimate.

These losses can be reduced by a factor 10 by inserting the injection-line halo scrapers (thus removing about 5% of the beam) and also by tuning the linac to minimize momentum tails. While the 1σ width of the H^- momentum distribution is normally about 0.05%, a poor accelerator tune can result in momentum tails exceeding 0.5%. Because the halo scraper configuration does not provide "clean" scraping in momentum space, at this time it is not possible to eliminate momentum tails in the injection line without excessive reduction of beam intensity.

An additional contribution to injection loss comes from angular dispersion introduced by the stripper magnet. This dispersion was measured

directly by comparing the H^0 beam profile with that of an unstripped H^- beam. As shown in Fig. 3, this dispersion, while basically in accord with prediction, has a larger-than-Gaussian tail that adds significantly to the magnitude of the x-x' phase space. Even a zero emittance beam passing through the stripper magnet would emerge with a finite angular distribution from this process. Early-turn losses in the ring were completely eliminated only in a special experimental configuration

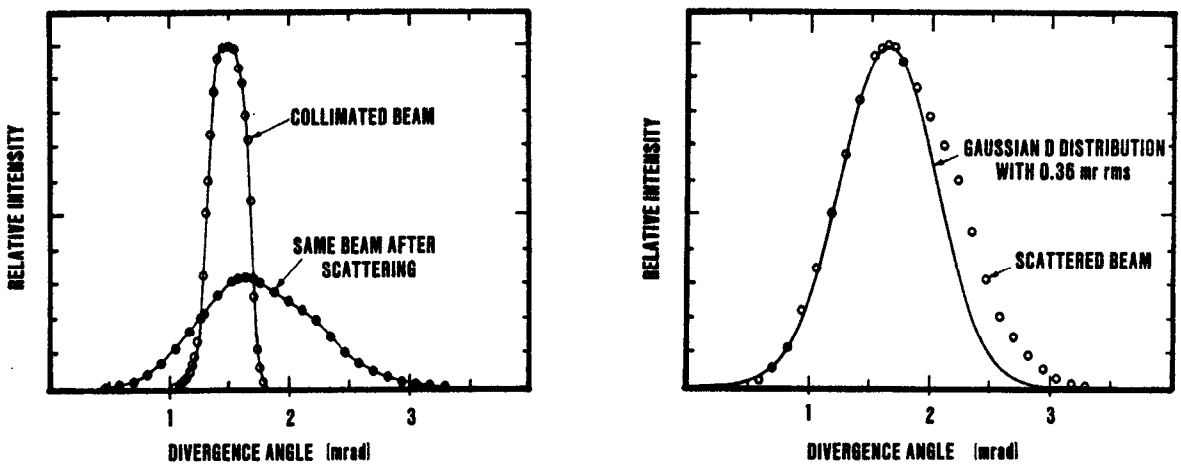

Fig. 3. Left Figure - Angular scattering of an initially collimated beam by the stripper magnet. Data were taken by allowing the beam to drift after magnetic stripping and measuring the horizontal distribution.

Right Figure - Comparison of stripper magnet scattering data with a Gaussian distribution of 0.36 mrad rms width, the expected rms divergence addition for the stripper magnet. The trailing edge of the distribution reflects the finite vertical beam width; off axis particles are stripped with less angular growth but are deflected further, hence producing a high divergence tail.

that employed a finely collimated H^- beam injected through a thin (60-$\mu g/cm^2$) stripper foil; the foil provided 50% conversion of H^- to H^0 and was temporarily substituted for the stripper magnet to permit a study of losses in the absence of the magnetic stripping. Because of its poor conversion efficiency, such an injection foil is not a practical operational option.

Accumulation Losses

By midsummer 1985, it became clear that significant beam loss occurred during accumulation as long as the circulating protons continued to intersect the stripper foil. Several sets of experiments outlined the general characteristics of this accumulation loss, which appears to arise from scattering at the foil and is much stronger than predicted in design calculations.

In one experiment, a small amount of beam was injected into the ring and its lifetime was determined (using a current transformer), as a function of

stripper foil thickness. The foils were inserted so that all protons intersected the foil on every turn, and lifetime was characterized by the time at which the stored beam intensity dropped to 1/e of its level at the end of injection. Results of this set of measurements are summarized in Fig. 4, which shows very clearly that beam lifetime is inversely proportional to stripper thickness. Concurrent beam loss measurements are also consistent with a scattering mechanism for beam loss.

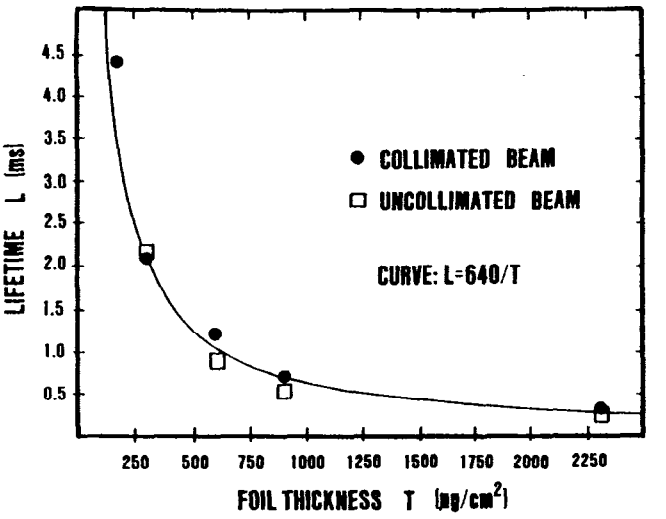

Fig. 4 Results of an experiment to determine the effect of stripper foil thickness on beam lifetime. As a result of this and other experiments, the foil thickness used for normal PSR operation has been reduced from 300 $\mu g/cm^2$ to 200 $\mu g/cm^2$.

A typical lifetime curve for a 300-$\mu g/cm^2$ stripper foil is shown in Fig. 5. This curve can be fitted fairly well by a function of the form $\exp[-(t/\tau)^{1.7}]$, where τ is the beam lifetime, suggesting that beam loss proceeds through growth in the transverse beam emittance resulting from multiple interactions with the stripper foil, rather than by direct removal of protons in single collisions. The latter kind of process (such as nuclear scattering) would produce a lifetime curve with a simple exponential decay, $\exp[-(t/\tau)]$, which looks very different from the observations.

Although beam loss from multiple scattering in the stripper foil was anticipated, the loss rate is much greater than was estimated during design. Recent particle tracking computations using a very accurate Monte Carlo representation of the Coulomb scattering in the foil have fallen short of simulating the observed beam-loss rate by more than an order of magnitude. Figure 6 shows the results of tracking a large number of particles around a linear version of the ring lattice, with an angular scattering function applied each turn to simulate the foil interaction. Fractional beam survival is plotted as a function of the number of revolutions for several effective limiting-aperture dimensions. The calculation assumed that particles were always lost at the extraction septum, known to be

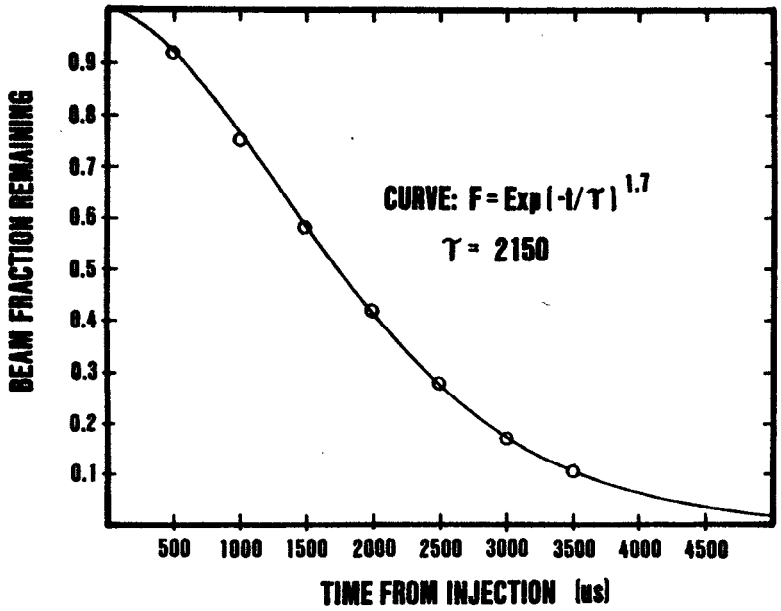

Fig 5. Lifetime curve for a 300 μg/cm^2 stripper foil. For this experiment, particles were allowed to circulate through the foil for several milliseconds after injection. Normal operation of the PSR extracts beam immediately after injection, but the injection period can last up to 1000 μs.

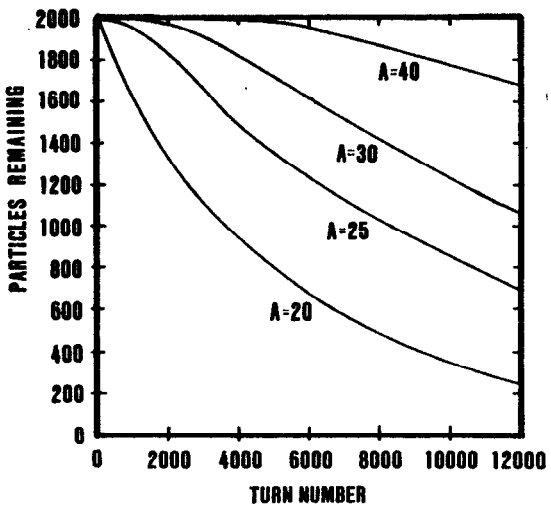

Fig. 6. Loss curves with a 300 μg/cm^2 foil for various assumed limiting half-apertures A. The simulation assumed 2000 initial particles with an initial Gaussian distribution of 16 mm horizontally and 8 mm vertically. It is assumed that all particles scattered by the stripper foil are lost when reaching a transverse amplitude of A (mm) at the septum. The curve for A = 25 mm is in best agreement with the measurements for the PSR.

the limiting aperture in the horizontal plane. The experimentally observed short lifetime can only be reproduced by supposing an effective aperture for the storage ring that is much smaller than the 4-cm physical half-aperture. A more sophisticated simulation using a nonlinear lattice description has been carried out with the Lie-Algebra code MARYLIE.[13] Even when a large sextupole is artificially inserted (at an F-quadrupole), the calculated beam lifetime is still much greater than has been observed.

The anomalously-short beam lifetime, presumably from scattering in the stripper foil, remains at present a mystery. Additional experiments are in progress to shed more light on this puzzle.

Extraction Losses

Beam losses in the extraction channel have been difficult to quantify because of saturation of the detectors during the short extraction pulse. The septum magnet is the most highly activated component in the ring, however, and it must be assumed that some of this activation is caused by less than optimum extraction efficiency. Additional diagnostic devices are being added in this region to study the extracted beam trajectory. Work is also under way to develop nonsaturating, quantitative beam loss monitors.

CONCLUSION

The first year of PSR commissioning has demonstrated that the basic machine design is sound and the equipment subsystems function according to specifications. Strong emphasis has been placed on increasing component and system reliability. Our primary goal, however, has been to study and reduce beam loss mechanisms so that activation remains sufficiently low to avoid remote handling during maintenance and upgrade operations. We have succeeded in this to a large extent by achieving one-third of the design average current and over half the design peak intensity with losses less than 5% and encountering no uncontrollable instabilities. The dominant loss mechanism is the accumulation loss that is likely caused by a virtual or real aperture restriction.

A series of runs for our user group has demonstrated PSR's utility as a spallation neutron source with the world's highest peak intensity. During these runs, component activition remained low enough so that "hands on" maintenance was possible after a short shut-down period. In forthcoming development our main priorities will be to increase the linac-source intensity as well as to understand and eliminate the anomalous beam loss observed. We feel confident that further machine experiments and improvements, especially in the area of diagnostics, will lead to attainment of the 100 μA goal while remaining within activation constraints.

REFERENCES

1. G. Lawrence, R. Hardekopf, A. Jason, P. Clout, and G. Sawyer, "Los Alamos High-Current Proton Storage Ring; A Status Report," Proc. 1985

Particle Accelerator Conf., IEEE Trans. Nucl. Sci. 32 (5), 2662 (1985).

2. D. Bowman, "Status Report on the WNR/PSR Pulsed Spallation Neutron Source at the Los Alamos National Laboratory, Proc. of International Collaboration on Advanced Neutron Sources (ICANS-VII), Report AECL-8488, 9 (1983).

3. J. S. Lunsford and R. A. Hardekopf, "Pulsed Beam Chopper for the PSR at LAMPF," Proc. 1983 Particle Accelerator Conf., IEEE Trans. on Nucl. Sci., 30, (4), 2830 (1983).

4. R. A. Hardekopf, E. Higgins, and J. Lunsford, "Ferrite Kicker Magnet for the LAMPF Switchyard Upgrade," Proc. 1985 Particle Accelerator Conf., IEEE Trans. Nucl.Sci. 32 (5), 3634 (1985).

5. T. W. Hardek, "A Low-Impedance, 2.8-MHz, Pulsed Bunching System for the Los Alamos Proton Storage Ring," Proc. of Sixteenth Power Modulator Symposium, IEEE Conf. Record 84-CH2056-0, 207 (1984)

6. R. A. Hardekopf, "PSR Beam-Pulsed Formation and Control," Proc. of International Collaboration on Advanced Neutron Sources (ICANS-VII) Report ACEL-8488, 134 (1983).

7. Alex Harvey and Andrew Jason, "DC Septum Magnets for the Los Alamos Proton Storage Ring," 9th Int. Conf. on Magnet Technology, Zurich, Switzerland, September 9-13, 1985, Swiss Institute for Nuclear Research (SIN) report ISBN 3-907998-00-6, 111 (1985).

8. A. J. Jason, E. F. Higgins, and A. R. Koelle, "The Los Alamos Proton Storage Ring (PSR) Injection Deflector System," Proc. 1983 Particle Accelerator Conf., IEEE Trans. on Nucl. Sci. 30, (4) 2941 (1983).

9. John F. Power, Barbara Blind, and Andrew J. Jason, "The Los Alamos Proton Storage Ring Fast-Extraction Kicker System," Proc. 1985 Particle Accelerator Conf., IEEE Trans. Nucl. Sci. 32 (5), 3021 (1985).

10. E. F. Higgins, and F. D. Wells, "A Beam Position Monitor System for the Proton Storage Ring at LAMPF," Proc. 1981 Particle Accelerator Conf., IEEE Trans. on Nucl. Sci. 28 (3), 2308 (1981).

11. D. M. Lee, D. Brown, R. A. Hardekopf, J. R. Bilskie, and O. B. van Dyck "Wide Dynamic Range Beam Profile Monitor" Proc. 1985 Particle Accelerator Conf., IEEE Trans. on Nucl. Sci. 32, (5) 1967, (1985).

12. P. N. Clout, "Proton Storage Ring (PSR) Diagnostics and Control System," Proc. of International Collaboration on Advanced Neutron Sources (ICANS-VII), Report AECL-8488, 128 (1983).

13. A. J. Dragt, Center for Theoretical Physics, Dept. of Physics and Astronomy, University of Maryland, College Park, MD, 20742, "Marylie 3.0, A Program for Charged Particle Beam Transport Based on Lie Algebraic Methods," User Manual (unpublished).

ICANS IX

INTERNATIONAL COLLABORATION ON ADVANCED NEUTRON SOURCES

22-26 September, 1986

STATUS REPORT ON SINQ, THE SIN NEUTRON SOURCE

(August 1986)

W.E. Fischer for the Project Group

INTRODUCTION

The main emphasis of the present work on SINQ is the production of a full engineering design for the source. The basic concept has not been changed but there has been (and will continue to be!) many modifications of details as we try to accommodate the necessary requirement that will make a system which can be built, operated and maintained. There is a continuing experimental program which includes materials testing (corrosion and radiation damage), thermofluid dynamics investigations and neutronic performance examinations of the cold source.

I. BUILDING WORK

The SINQ project includes the construction of two new buildings; the neutron hall, to house the spallation source and spectrometers located at beam tubes, and the guide hall. The floor areas are 34 x 51.5 m^2 and 24 x 50 m^2 respectively. Both buildings are to be equiped with cranes of capacity and hook clearance 60 t and 18 m for the neutron hall and 10 t and 6 m for the guide hall. An artists impression of the SIN site with these new buildings is shown in Fig. 1.

Figure 2 shows a plan of the SINQ area, the trench for the proton beam, an outline of the source and a tentative storage facility for irradiated targets are shown in the neutron hall, a cellar in the guide hall, containing active liquid storage tanks (again part of the upgrading of general SIN-facilities for high current operation) is shown with broken lines.

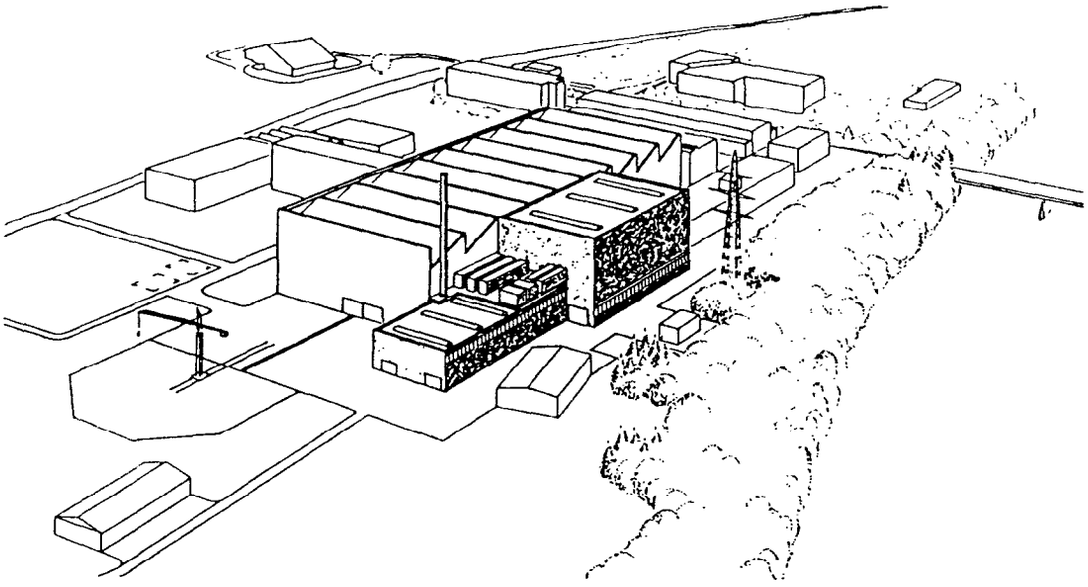

Fig. 1 Artists impression of the SIN-site with the new buildings for SINQ. The equipment on the roof of the guide hall is for the upgraded general SIN experimental ventilator system.

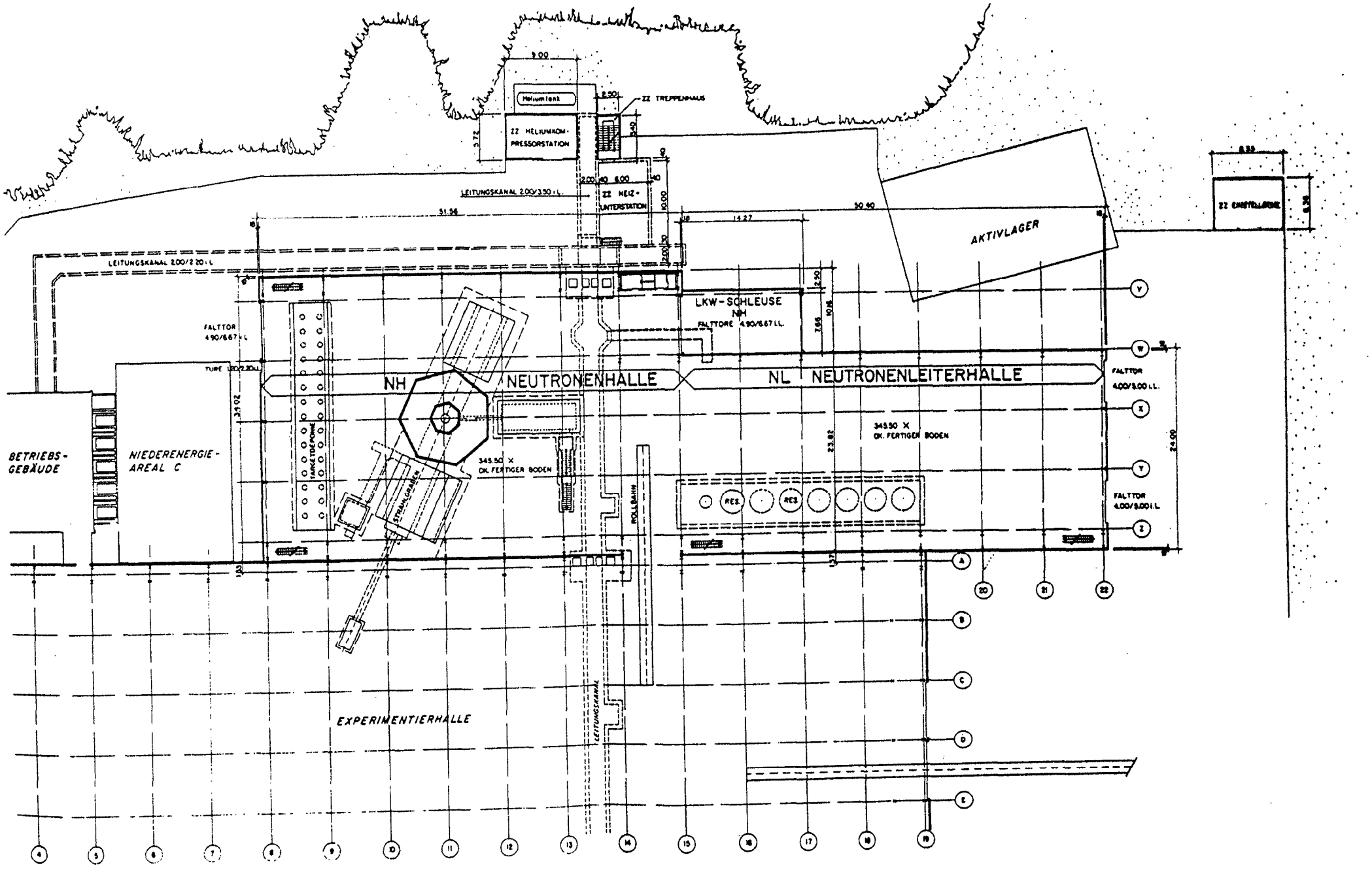

Fig. 2 Layout of the neutron hall and the guide hall. Contours of the trench for the proton beam and the shielding of the neutron source.

II. THE SPALLATION SOURCE - SINQ

i) Principle

As a reminder, we will briefly describe the principal features of SINQ. A vertical section through the central region of the source is shown in Fig. 3. The proton beam is deflected downwards to pass under the beam tube area, thence to the centre of the source, and finally pitched vertically upwards to the spallation target. The proton energy at the spallation target will range from 560 to 590 MeV with an initial intensity of 1 mA. The target consists of a "pot" of Pb/Bi eutectic mixture (molten) of inner diameter about 15 cm and 3 m high. Most of the beam power is deposited in the bottom 30 cm and natural convection is to be used to transport this heat to an exchanger mounted at the top and hence away from the source [1]. The active region of the target (the bottom 30 cm) is located at the centre of the D_2O moderator which has a diameter and height of about 2 m.

Figure 4 shows a plan of the "fixed" part of the source (note; the beam tubes are on two different levels with a vertical centre-line displacement of 230 mm). The beam tubes pass through the bulk shield in boxes. This allows the beam tubes (shielding, collimator, introduction of special equipment etc.) to be custom-built to the requirements of the individual instruments. It also makes it easier to make modifications as the source develops. Every beam tube will also have extra shielding outside the limit of the bulk shield which is most easily constructed onto flat faces; this extra shielding will normally contain the monochromator.

ii) Proton Beam Injection and the Window Problem

The optics of the primary-proton beam was discussed in some detail at the last ICANS-meeting [2]. An important feature of the design is the collimator close to the target window.

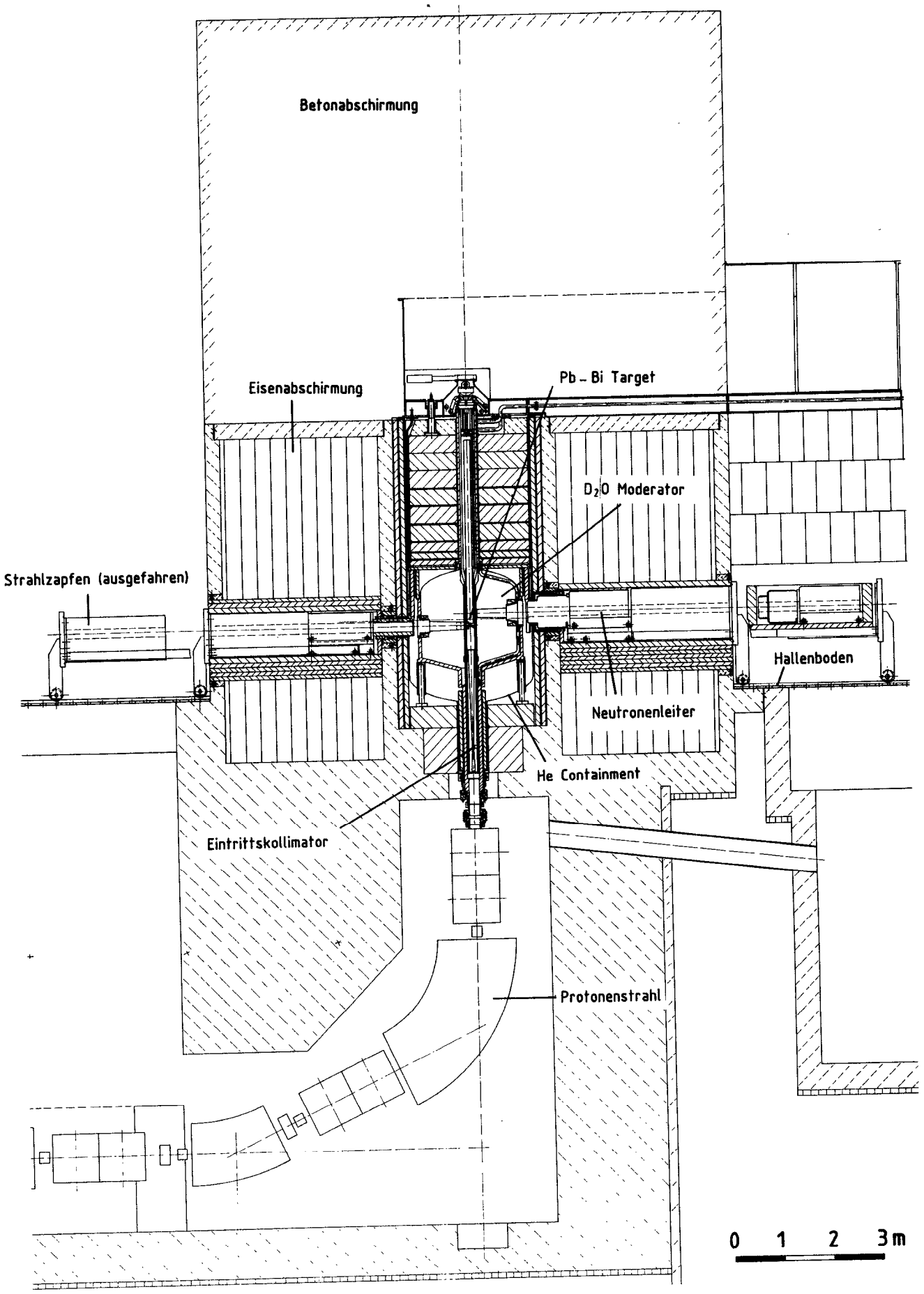

Fig. 3 Vertical section through the central region of the source showing the vertical beam injection into the spallation target.

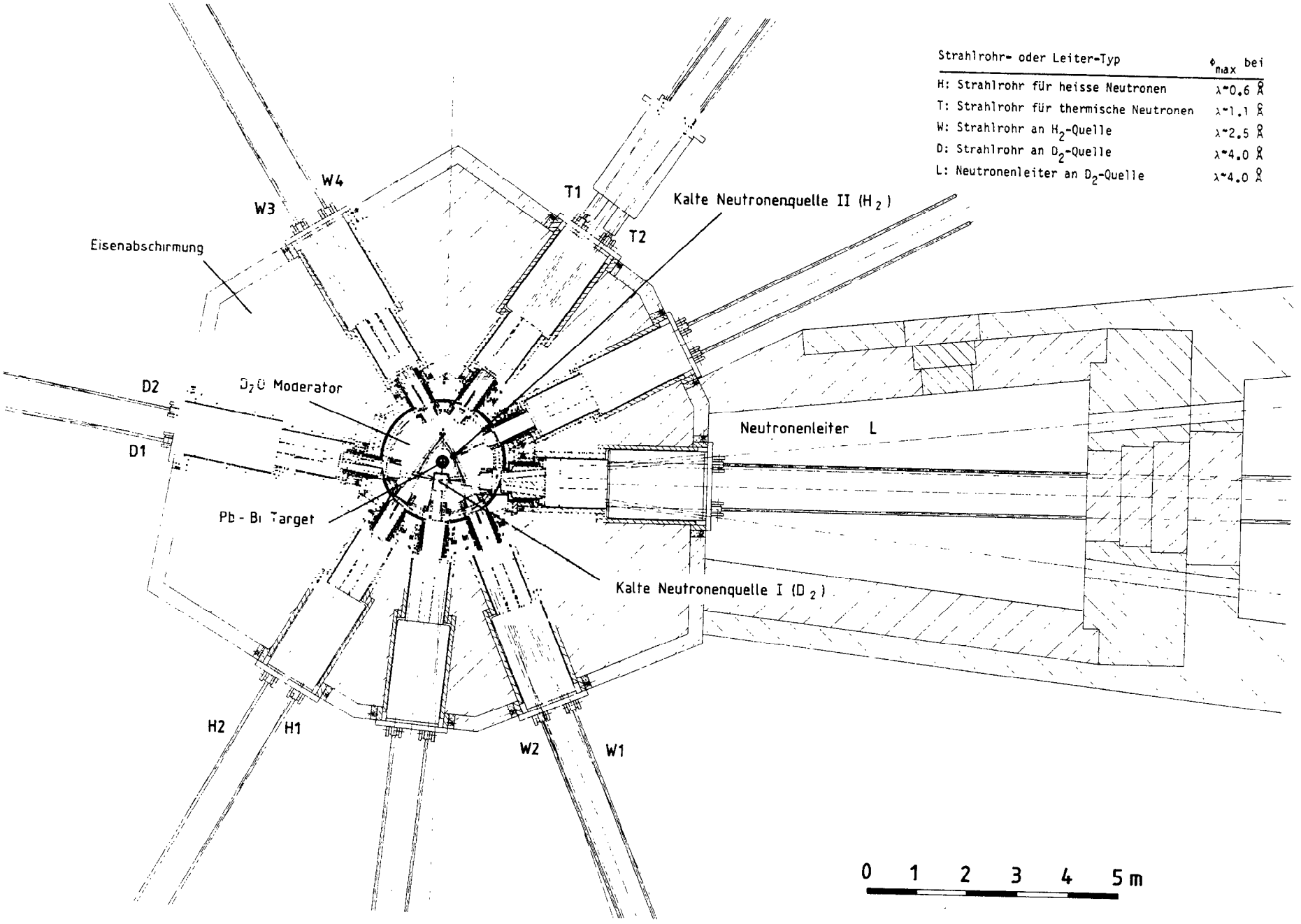

Fig. 4 Layout of the beam tube plugs and the insertions for the two cold sources.

This collimator enforces a double focus of the proton beam at a well defined position, presently 1.5 m in front of the target window (Fig. 3). With the given emittance of the beam, this produces a beam diameter at the target window which cannot be smaller than 6 cm. This is a necessary precaution in order to guarantee that the power density in the window material does not exceed ~ 130 w/grm.

Nevertheless, it is most likely that the beam window will be the limiting component on the target lifetime; we aim for this to be at least 1 year. In an experiment at the Los Alamos beam dump [3], the mechanical properties of various types of steel under proton irradiation were examined. The samples were also irradiated in contact with Pb/Bi to make a first attempt at seeing if there are any radiation induced corrosion effects.

Figures 5 and 6 show the strain-stress behaviour of pure iron and a 12 %Cr-1 %Mo (alloyed) steel, unirradiated and after being irradiated to fluences of 4.8×10^{19} and 5.4×10^{20} protons/cm^2. All the irradiations were made at a sample temperature of 400° C. The expected embrittlement of the pure iron was observed. The steel, however, retained its ductility up to the higher fluence. Although this steel seems a suitable candidate for the window material, the fluence used in the test is a factor of 6 to 7 below the expected operational value. Hence further tests are in progress.

The microscopic analysis of the samples for corrosion effects has not yet been made although macroscopically no signs of Pb/Bi induced corrosion have been observed.

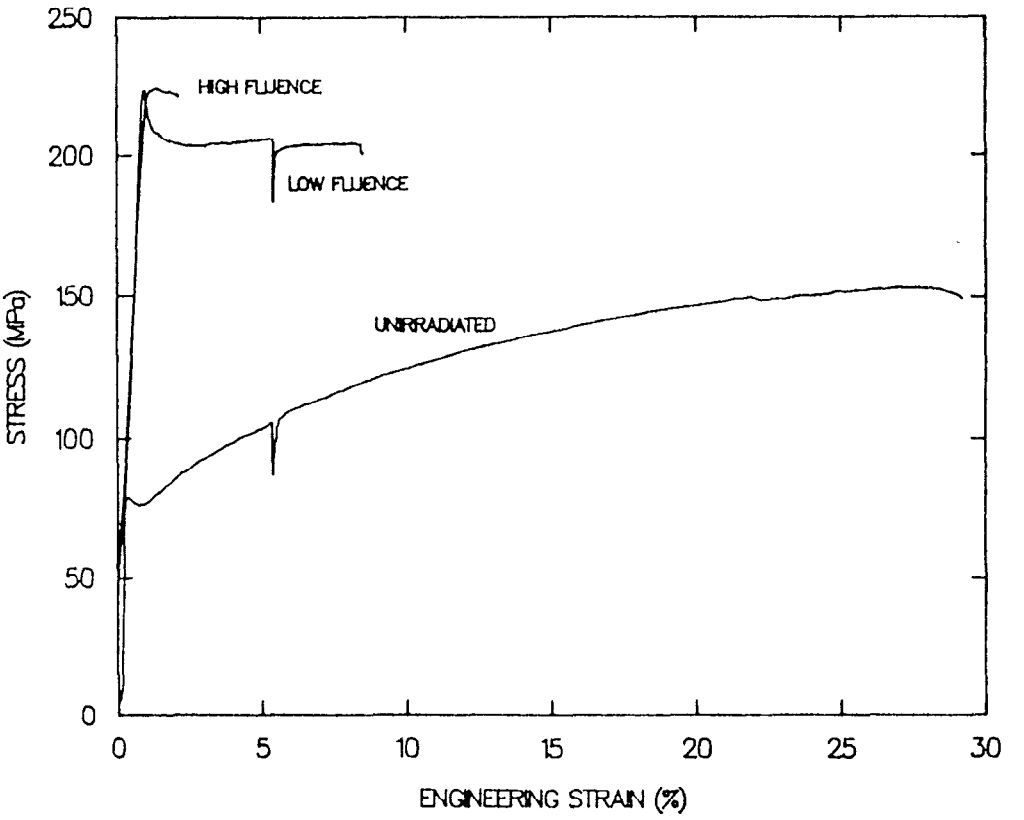

Fig. 5 Stress-strain behaviour of pure iron after irradiation with 500 MeV protons
Low fluence : 4.8 10 P/cm
High fluence: 5.4 10 P/cm
Sample temperature was 400 C

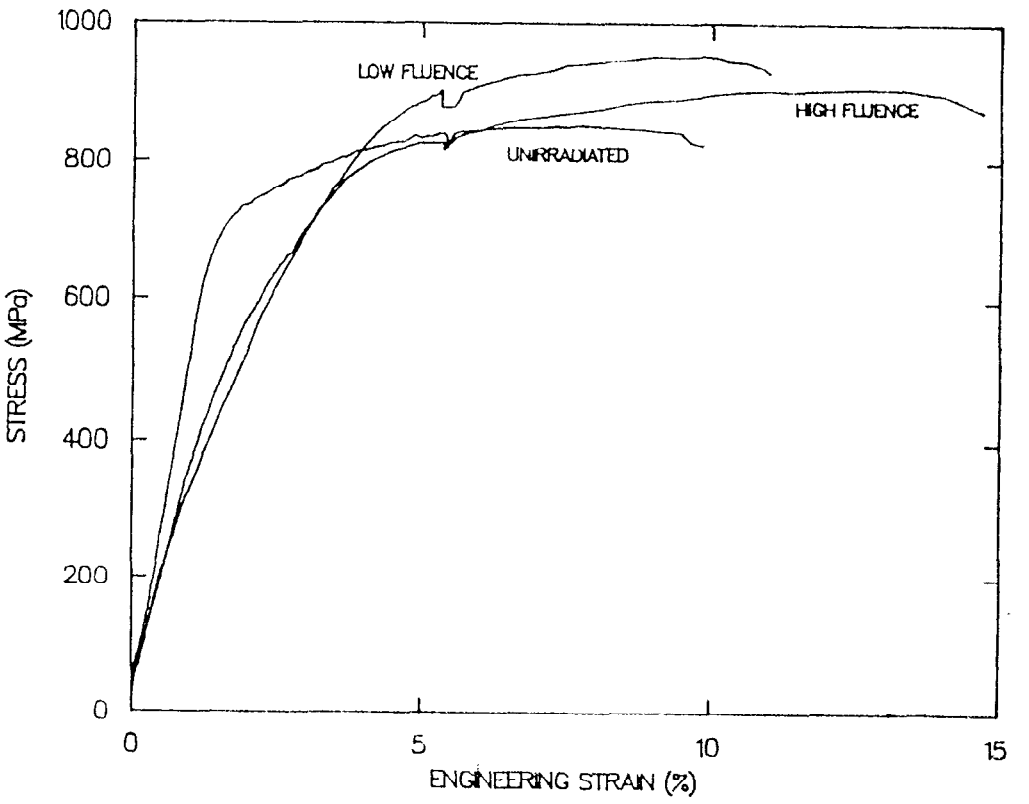

Fig. 6 Stress-strain behaviour of Fe-12Cr-1Mo steel after irradiation with 800 MeV protons
Low fluence : 4.8 10 P/cm
High fluence: 5.4 10 P/cm
Sample temperature was 400 C

iii) Cold Sources and Beam Layout

In order to optimize the performance of SINQ at longer wavelengths we plan to install two cold sources; a small H_2-source and a large (20 l) D_2-source. A vertical insert for the cryogenic thermosyphon-systems of these sources would interfere severly with the infrastructure of the spallation (target heat exchanger, secondary cooling circuits, and (possibly) a gas extraction system). Due to this we have decided on a solution with horizontal plugs inserted through the bulk shield. The height difference to the liquifiers needed to make the thermosyphon principle work (3 to 4 m for the D_2 source) can be obtained in a vertical shaft at the periphery of the bulk shield. According to the investigation for the second cold source at ILL [4] and the expected power deposition in the cold source and its container [5], this solution should be feasible.

The beam tube layout may be seen in Fig. 4. There are five neutron beam tubes, each of which provides two independant beam ports. Two of the equipment boxes are for the cryogenic infrastructure of the cold sources and there is a tube and box for the first sections of a guide system. The beam tubes are on two different levels; the two thermal neutron beams are not a "through tube" and so one of these can be used to provide a hot source.

There are four beam parts viewing the H_2-source which should provide a neutron spectrum in the region 80 to 100 K. The D_2 source will produce a neutron spectrum in the 20 to 30 K region and is viewed by two beam ports and the guide system.

Two guides are planned for the initial operation of SINQ; the option of installing a third is being built into the design. Guides of cross section 30x100 mm^2 are to be used and one will be split to provide two branches of 30x45 mm^2 cross section. Because of the high-energy neutron background we prefer to localise the beam loss in a single strongly shielded region and plan to include beam benders into all guides as the means of obtaining a good spread and hence sufficient room for the instruments in the guide hall. These benders and the splitter are to be mounted in a beam switch-yard at the laternal face of the bulk

shield. The benders would consist of 12 guidlets with a wall thickness of 0.5 mm and a gap of 2 mm. The parameters for bending angles of 2° and 4° are given in Table I. Since this ystem is rather similar to the concept of the new guide laboratory at KFA-Julich, our decision will depend on their operational experience.

Table I

Bending angle	2°	4°
Length (m)	3.5	4.0
Critical wave length (Å)	3.1	4.1
Bending radius (m)	107.0	57.2

The guides are assumed to be coated with ^{58}Ni, that is $k = 2.04 \times 10^{-4}$ rad $Å^{-1}$.

iv) SINQ-Performance

The design and performance of SINQ are based on results from an experimental program for the investigation of the neutronics. This program has been realized by a Jülich-SIN collaboration on a secondary proton beam at SIN with a one-to-one mock-up model of the source [6]. In later runs [7] several configurations of cold hydrogen sources and their spectra were examined. From these data we can estimate the spectral fluxes at monochromator (or velocity selector) positions of beam tubes and neutron guides. The spectral fluxes from the D_2-source have, however, not yet been measured at the mock-up and the fluxes presented here are based on the measurements made by Ageron et al. [8] for the development of the cold source at ILL.

The spectral fluxes are shown in Fig. 7. They are based on a primary beam current of 1.5 mA (1 Mw beam power) and beam tube tips of height

10 cm and width 5 cm. Fluxes for the three different guide arrangements as listed below, are also included:

a) a straight guide plated with Ni^{58}

b) the same guide as in a), but also including a Be-filter of 50 cm length at a temperature of 100° K

c) a guide which is plated with natural nickel and a 4°-bender.

All three systems are assumed to have a length of 40 m.

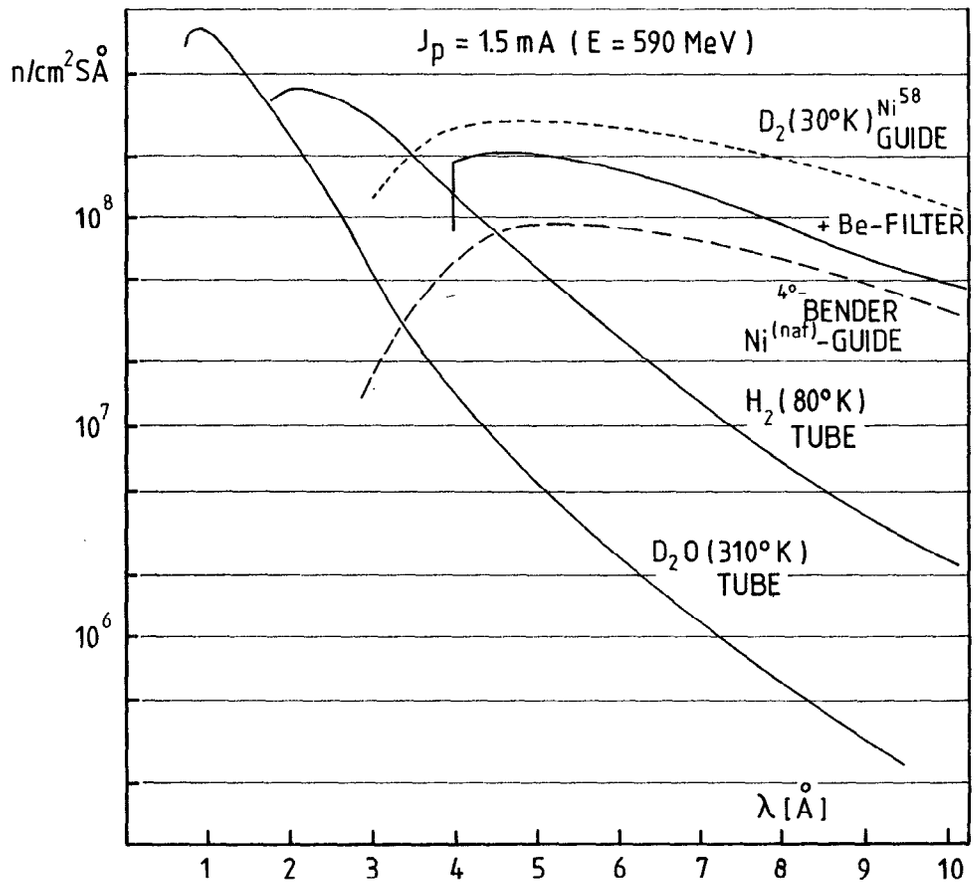

Fig. 7 Spectral fluxes at monochromator (or velocity-selector) positions at thermal beam tubes, cold tubes and neutron guides.

REFERENCES

[1] Y. Takeda
Proceedings

[2] F. Atchison, W.E. Fischer, M. Pepin, D. Renker, Y. Takeda, Ch. Tschalaer
Proc. ICANS VIII, Oxford (1985)

[3] R.D. Brown, M.S. Wechsler, Ch. Tschalaer
LA-UR-86-733
Submitted to 13th Int. Symp. on Effects of Radiation on Materials, June 23-25, 1986, Seattle Washington

[4] M. Hofmann
KfK-3630, February 1984

[5] W.E. Fischer, L. Moritz, H. Spitzer, I. Thorson
Nucl. Sc. and Eng. 93 273-282 (1986)

[6] G.S. Bauer, W.E. Fischer, F. Gampf, M. Kuechle, W. Reichardt, H. Spitzer
Proc. ICANS V, Julich (1981)

[7] G.S. Bauer, H. Conrad, W.E. Fischer, K. Gruenhagen, H. Spitzer
Proc. ICANS VIII, Oxford (1985)

[8] P. Ageron, Ph. de Beaucourt, H.D. Harig, A. Lacaze, M. Livolant
Cryogenics (February 1969) 42-50

ICANS IX

INTERNATIONAL COLLABORATION ON ADVANCED NEUTRON SOURCES

22-26 September, 1986

PERFORMANCE OF THE INTENSE PULSED NEUTRON SOURCE ACCELERATOR SYSTEM*

F. Brumwell, C. Potts, A. Rauchas, V. Stipp and G. Volk

Argonne National Laboratory
Argonne, Illinois 60439 USA

Introduction

The Intense Pulsed Neutron Source (IPNS) Accelerator System has had a banner year since the last ICANS meeting. Average beam current increased by 12% to 13.4 μA and our already excellent reliability increased by 2.1% to 93.2%. The reliability improvement came not from equipment improvement as much as from prudent operating practice. In the prior year, we had 66 hours of lost operation waiting for radiation cooldown before we could repair beam induced damage to our rf shielding liners. This year, thank the synchrotron gods, the liners stayed undamaged and no cooldown time was required.

Table I.

Accelerator Operating Summary

	Nov. 81-July 82	Oct. 82-July 83	Oct. 83-July 84	Oct. 84-June 85	Oct. 85-July 86
Average Current (μA)	8.02	9.21	11.46	11.94	13.39
Operating Efficiency (%)	88.9	90.2	90.4	91.6	93.2
Scheduled Hours	3358	3833	4750	2946	3892
Available Hours	2985	3458	4294	2699	3628
Pulses on Target x 10^8	2.94	3.33	4.23	2.81	3.80
Proton on Target x 10^{20}	4.44	6.39	10.12	7.00	10.63

*Work supported by the U.S. Department of Energy.

The submitted manuscript has been authored by a contractor of the U. S. Government under contract No. W-31-109-ENG-38. Accordingly, the U. S. Government retains a nonexclusive, royalty-free license to publish or reproduce the published form of this contribution, or allow others to do so, for U. S. Government purposes.

Operating Summary

Several completed modifications were discussed in last year's status report and the indications were clear that they had helped to increase beam on target without a concurrent increase in beam lost. These devices were primarily equipment feedback loops that helped correct for the power line phase slip that occurred when the neutron choppers[1] controlled the start time of the synchrotron operating cycle. Just before the summer shutdown in July of 1985, a new type chopper-accelerator-synchronization system[2] was brought into test operation. This unit drastically reduced the rate of phase slip as well as limiting the slip to $\pm 15^{o}$. The effect of this new equipment was twofold. First, there was an immediate increase in beam current of about 1 μA and second, with the increased phase stability, it was easier to identify other equipment that should be improved.

It was clear that the main culprit was the stability of the power supplies that power the main ring guide magnets. This instability was in effect making about 14% of the vacuum aperture unusable. An immediate assault on the regulator circuitry of these supplies was begun. This regulator improvement is described in some detail later in this paper. The problem with the regulator was a stubborn one. At first the "improved" regulator was worse than the previous unit and we ran six weeks averaging only about 11.5 μA. But the designer's persistence paid off and by the end of December we had our first weekly average current of 15 μA and had pushed the short-term best up to 16.7 μA. In fact, since the completion of the regulator improvements the current is almost 14 μA averaged over 280 million pulses. The target current graph (Fig. 1) shows the dramatic increase just before the beginning of 1986.

The viewer of Fig. 1 will note that beam current improvement leveled off for most of 1986. Two new factors had entered the equation of IPNS operation. All attempts at increasing beam current stopped and we just ran the machine with little if any accelerator research. The last five months the accelerator research was less than 1% of the scheduled running time--not a very healthy long-term situation.

The first of these new factors was IPNS accelerator personnel participation in preparation of the proposal for the X-ray source proposed

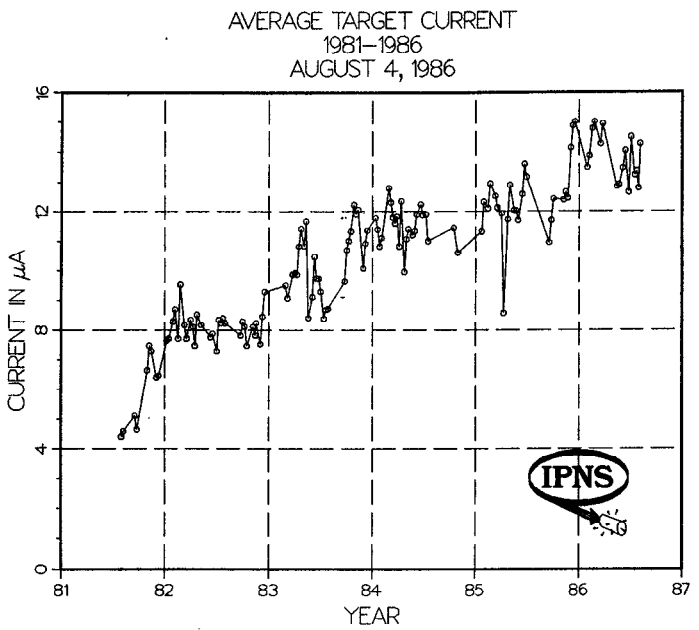

Fig. 1. IPNS Weekly Average Target Current Since Turn-on

for Argonne National Laboratory (ANL). The number of people diverted wasn't large but they were leaders in our beam improvement program. The second factor was IPNS accelerator personnel involvement in the Strategic Defense Initiative (SDI) Program at ANL. The SDI program asked ANL to build two test beams in the old Zero Gradient Synchrotron (ZGS) hall for Neutral Particle Beam (NPB) activities. This beam is derived from the IPNS 50 MeV H^- linac. IPNS accelerator personnel took a leading role in the design and construction of these test beams and are now assisting in the operation of these test beams as well as operating the linac for NPB studies. These studies have consisted primarily of methods of neutralizing H^- beams and sensing the direction, size, divergence, etc., of a neutral beam. In total, more than one-half of the accelerator group's effort has been diverted to other activities this fiscal year. This is great for the financial health of IPNS but there will be long-term consequences if this continues too long. A photograph of one of the NPB test beams is included as Fig. 7.

The point we have been trying to make is that this year's great performance is based on previous year's equipment improvements. However, our very experienced and skilled shift operators deserve a great deal of credit for taking advantage of the opportunities offered by the new equipment. As Fig. 2 shows, the beam losses have been held to about

1.5 μA. There are now 1.72 billion pulses on target and the residual radiation in the accelerator tunnel has not increased over the last year. We feel further increases in target current are possible when our personnel again are able to take a full time interest in the IPNS accelerator.

The reliability graph (Fig. 3) and trouble distribution graph (Fig. 4) document our comfortable feeling about machine reliability. The operation has been very smooth from the user's perspective. Most of the increase in ring magnet power supply (RMPS) trouble came during two long incidents of intermittent ground faults. Obviously, two thirty hour breakdowns are less of a user disturbance than ten three hour breakdowns. Most of the increase in kicker magnet trouble came from pushing the thyratron tubes for very long lifetimes. We got 560 million pulses out of one of the tubes. If our financial situation were improved we could probably decrease this source of trouble somewhat.

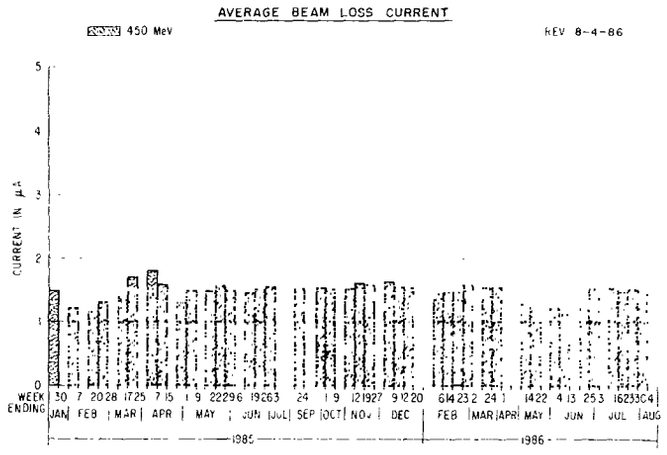

Fig. 2. Average Beam Current Lost in the Synchrotron

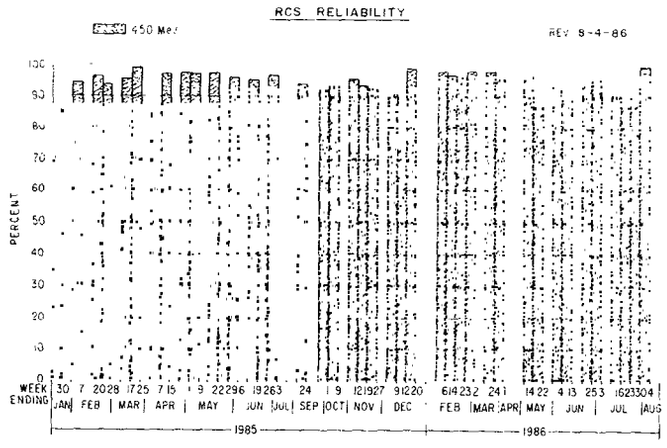

Fig. 3. IPNS Accelerator System Reliability

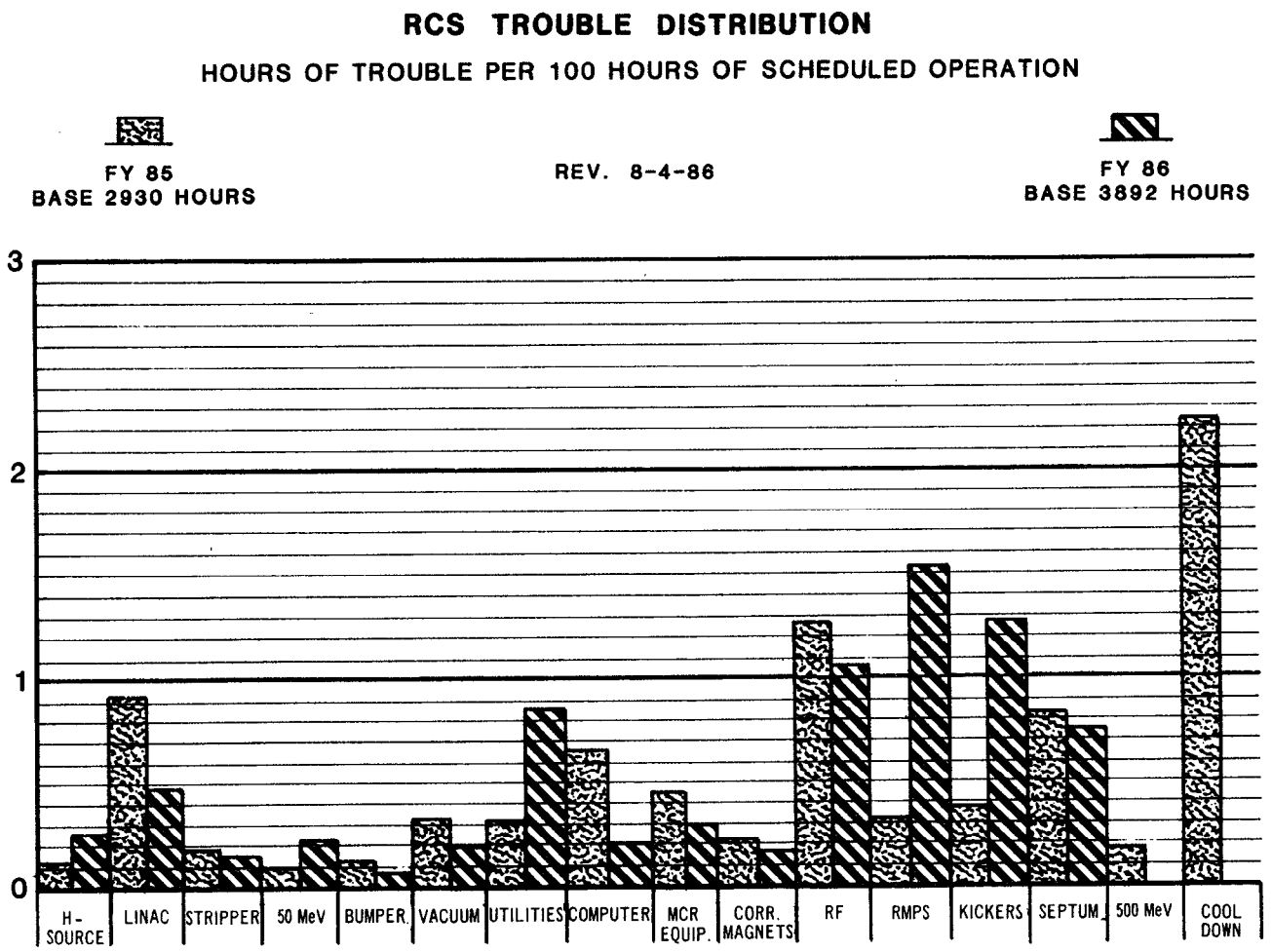

Fig. 4. IPNS Accelerator Subsystem Trouble Distribution

The following sections will provide brief comments on major accelerator subsystems.

H^- Ion Source and Preaccelerator

A grooved cathode magnetron H^- ion source[3,4,5] has now been supplying negative ions to the RCS since early 1983. As shown in Fig. 4, the H^- source reliability continues to be excellent with less than 0.3% of unscheduled downtime charged in FY 1986. This number not only reflects the ion source reliability but also includes the Cockcroft-Walton power supply, the high voltage column and all other ancillary equipment required to deliver 750 keV negative ions.

The nominal negative ion output as measured in the 750 keV terminal is 40 mA peak at the Rapid Cycling Synchrotron (RCS) repetition rate of 30 Hz.

There is no forced cooling on the ion source so the arc (beam) pulse width is limited by the source cathode temperature to approximately 80 μs. The source is removed and cleaned after three or four thousand hours of operation. The only component normally requiring replacement after that period of operation is the titanium anode cover plate from which the negative ions are extracted through a 1 cm x 1 mm slit. With about 4000 hours of 30 Hz operation, the focused ions from the cathode groove have eroded the anode cover plate by approximately 50%.

With the somewhat long (>1 m) 20 keV beam line separating the ion source from the high voltage accelerating column, it was decided we could operate without a refrigerated "cold box" to trap the cesium evolving from the source before it could have a chance to migrate into the column. However, after three years of operation it appears that cesium is indeed entering the column at certain times and can cause an increase in the column spark rate up to 3 or 4 times normal. The normal spark rate is 4 per hour. "Normal" sparks do not trip off the Haefly power supply but the beam is inhibited for 1 second each time a "normal" spark occurs. After lowering the cesium flow into the source, the column spark rate will return to normal but it may take up to two days to notice the results. This lower cesium flow condition may result in less than optimum source performance. A source with closer fitting components which allows less cesium to escape was recently installed. This did seem to have a positive effect but a refrigerated baffle is being designed which should allow us greater latitude in cesium flow adjustment.

Linac

The 50 MeV linac was originally designed to run at 10 Hz and for all the years it provided beam to the ZGS the average repetition rate was one pulse per three seconds. While operating at 30 Hz for the RCS, the overall linac reliability has been excellent. Figure 4 shows the total linac downtime in FY 1986 accounted for less than one-half of 1% of the scheduled operating time. The only component that has obviously had an increase in failure rate due to the increased duty cycle is the upper blocking capacitor for the final rf tube (RCA 7835). The manufacturer believes this problem could be eliminated by changing the capacitor dielectric from irrathane to teflon. However, since this would require some redesign of

the 7835 cavity and the failure rate is not much more than one per year, there are no plans for any modifications in the near future. The 7835 lifetime is nominally 15,000 hours and if anything, the average has increased with the higher duty factor. The high voltage modulator tube (Machlett 7560) was changed last November due to breakdowns from cathode to grid and it was noted to have accumulated over 43,000 hours.

Synchrotron

Ring Magnet Power Supply

The stability of the injection field is determined by the stability and response of the ring magnet power supply (RMPS) regulator. With the old regulator,[6] injection field variations as a function of the phase of the power main had been over ±8 gauss. Since the ring magnet power supply operates as a 24 phase dc rectifier, the variations had a frequency of the 720 Hz, a frequency beyond the full response of the regulator circuitry. Although the variable frequency master clock[2] was able to limit the variations of the phase of the power main to approximately $\pm 15^{o}$, this corresponds directly to a complete cycle of the 720 Hz injection field variation and therefore did not limit the variation of the minimum field. The improvements to the RMPS regulator system decreased the variation of the injection field by a factor of 2 to less that ±4 gauss and therefore the beam position variation during injection to less than ±3 mm. A block diagram of the new regulator is shown in Fig. 5.

The basic concept for the old and new designs is the same except for the manner in which the ac and dc components of the current feedback signal are separated. The old design separated these components with a combination of low pass and high pass active filters, which required hand selected components for proper alignment and ovens for stability, and with limited frequency response responded poorly to initial surges and transients. The new design separates the ac and dc components of the current feedback signal with ideal rectifiers and summing amplifiers. A detailed schematic of the process is shown in Fig. 6.

The current feedback signal is a 30 Hz ac sine wave offset by a dc level. This signal is peak rectified and filtered by an ideal rectifier to

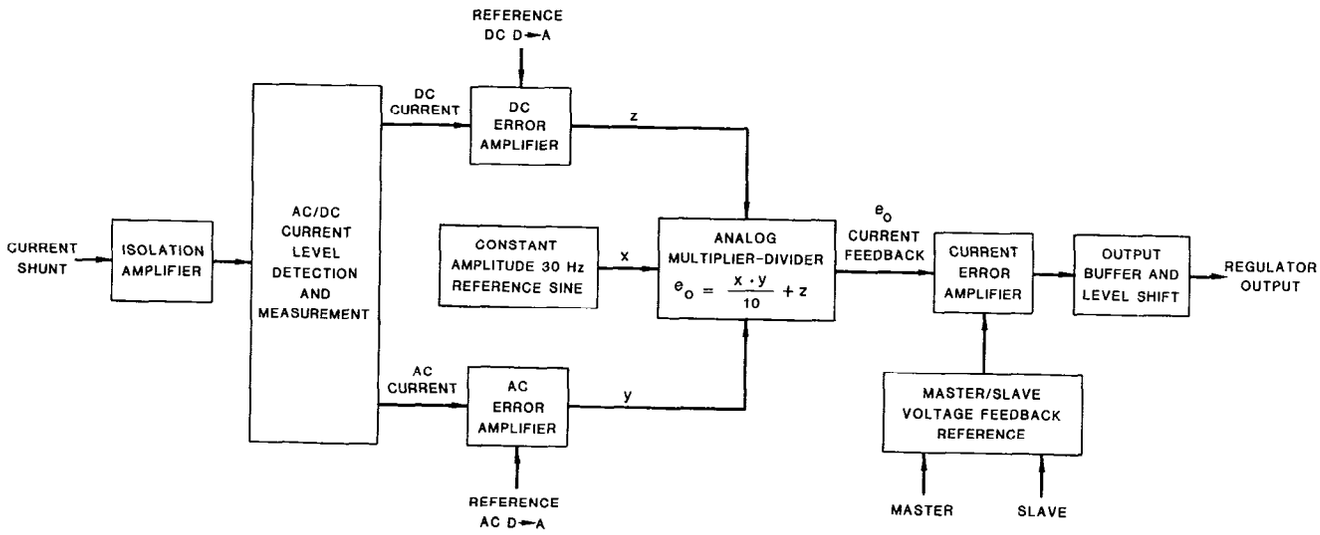

Fig. 5. RMPS Current Regulator Block Diagram

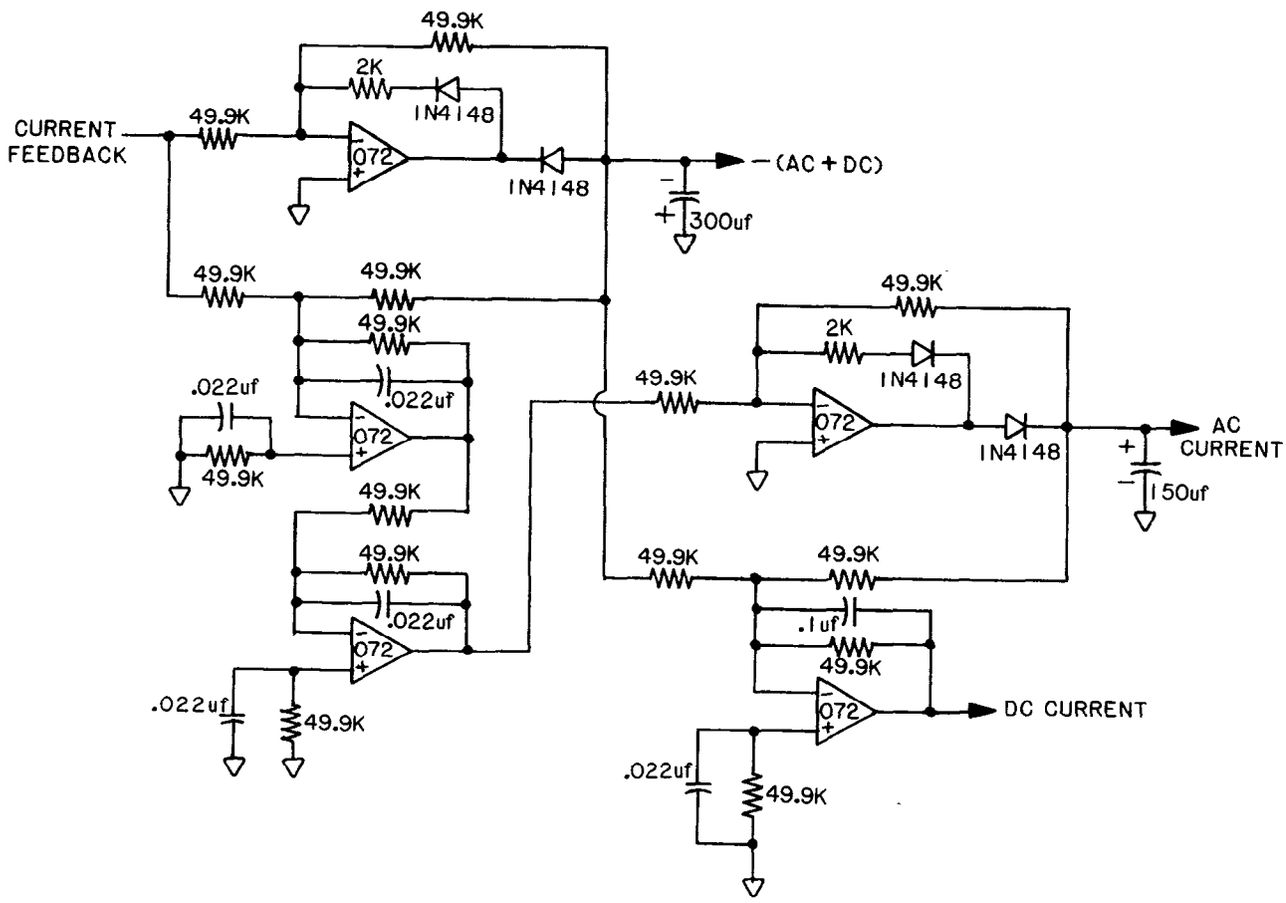

Fig. 6. AC/DC Current Level Detection Schematic Diagram

yield a dc level proportional to the peak of the current feedback (ac and dc). This rectified signal is combined with the original current feedback signal to provide an unbiased ac waveform which is again peak rectified and filtered to yield a dc level proportional to the ac component of the current feedback (ac current). The difference of the two rectified signals provides a dc level proportional to the dc offset of the current feedback (dc current). The dc levels proportional to the ac and dc components of the current feedback are used to generate the error signals for the remaining regulator circuitry which operates in the same manner as the old regulator design.

Master Oscillator Adjustments

The resultant increased injection aperture did not immediately manifest itself in increased accelerated intensities, however, it did provide beam intensity stability. As had occurred many times before, the accelerator operators were able to tune the accelerator under stable conditions and increase the intensity. The injection field stability also allowed other field dependent systems, such as the injection frequency to be optimized. The initial frequency program is derived from the $\dot{B}$ signal by integration. This yields a bipolar sinusoidal waveform which is offset by a stable reference to provide the required injection frequency from the voltage controlled oscillator. Correction of injection frequency for small variations of magnetic field are provided by sampling the field prior to injection, comparing the value to a fixed reference and applying this difference to the function going to the voltage controlled oscillator. Previously, this correction had not been able to be optimized with the relatively large variations of the injection field. After installation of the new ring magnet regulator, this circuitry was optimized, yielding an additonal measure of stability of the injected beam. These improvements contributed to the increase in current shown in Fig. 1.

H^- Stripping Foil

After several years of experimenting with stripping foils of various types we have settled on pure carbon of 60 to 80 $\mu g/cm^2$ thickness. These foils are commercially available in the U.S. The entire year's running described in this paper has been carried out with only nine of these foils.

The average life of each foil has been 42 million beam pulses which translates to about 500 hours of operation each. When thought of in terms of the protons and recirculations, a good guess is that each foil is struck about 5×10^{21} times. The failure mode is not total breakage but a shredding of the foil edge which effects stripping efficiency. These foils are brought up to essentially full beam current with only two hours of conditioning as opposed to at least six hours with the old plastic foils. Obviously this improved foil performance has helped create our average current increase.

Carbon has always looked like our best choice but mounting difficulties have precluded its use in the past. In late 1985, a small 2 axis manipulator was developed to draw the foil from the water floatation device onto the holder and then draw the mounted foil assembly out of the water. This manipulator avoided the "jerky" motion of the human hand. It was the "jerky" motion which frequently resulted in damage due to water surface tension. Temporarily supporting the free edge with a thin wire until the assembly was in a vertical position has always proved helpful. The success rate with these new techniques is about 50% when done by our most skillful man.

Other Synchrotron Activities

Many of the upgrades mentioned in last year's ICANS report did not get completed because of our SDI involvement but a few things are worth mentioning.

We did, as planned, remove the trim octupoles and replace them with a second set of programmable trim quadrupoles. We had hoped to reduce the β function distortion by applying smaller trim quadrupole correction in more than one location in the ring. The effect of the new apparatus on the beam was not beneficial although the ability of the new quadrupoles to shift the betatron tune was as expected. The new quadrupoles do not have the same beam effect as the old set located 120° around the ring nor are beam effects equivalent when each set operates at one-half current. From this behavior we conclude that the benefit from the old trim quadrupoles is not correction of tune shift but is orbit error correction.

A second set of remotely controlled protective vertical collimators has been installed in the synchrotron. Like the first set, these are adjusted during operation to just touch the beam then backed away about 0.05 inch. Their purpose is to protect the rf liners from beam damage and also localize radiation from the lost beam. Since we had no liner damage this year, they must be working!

Conclusion

This year we harvested the fruits of previous years' improvements and continued attention to reliability. Beam intensity continues to improve gradually which is about all that can be expected without major capital investments. Once the enriched target system becomes operational, perhaps the IPNS future will be more defined and significant accelerator upgrades can be considered.

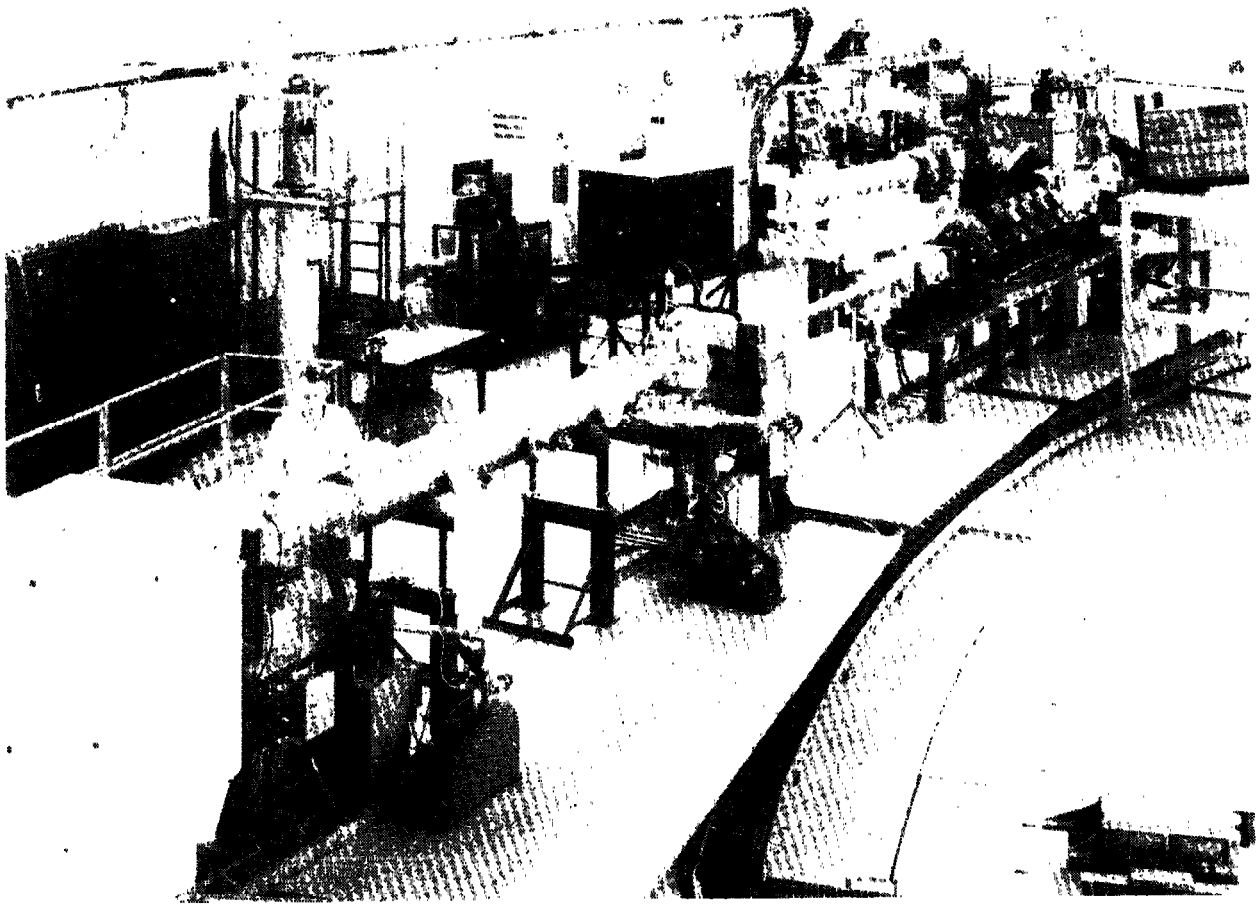

Fig. 7. Neutral Particle Test Beam A

References

1. G. E. Ostrowski, et al., "The IPNS Chopper Control and Accelerator Interface Systems," Proceedings of the Eighth Meeting of the International Collaboration on Advanced Neutron Sources (ICANS-VIII), Rutherford-Appleton Laboratory Report RAL-85-110 (July 1985) Vol. III, 676.

2. L. I. Donley, "Phase Locking the IPNS Neutron Choppers to the 60 Hz Power Line," Proceedings of the Eighth Meeting of the International Collaboration on Advanced Neutron Sources (ICANS-VIII), Rutherford-Appleton Laboratory Report RAL-85-110 (July 1985) Vol. III, 689.

3. V. Stipp, A. DeWitt and J. Madsen, "A Brighter H^- Source for the Intense Pulsed Neutron Source Accelerator System," IEEE Transactions on Nuclear Science, Vol. NS-30, No. 4 (August 1983) 2743.

4. J. G. Allessi and Th. Sluyters, "Regular and Assymetric Negative Ion Magnetron Sources with Grooved Cathodes," Review of Scientific Instruments, Vol. 51, No. 12 (December 1980) 1630.

5. V. Stipp and A. DeWitt, "Performance of the H^- Ion Source for the Intense Pulsed Neutron Source," IEEE Transactions on Nuclear Science, Vol. NS-32, No. 5 (October 1985) 1754.

6. W. F. Praeg and D. G. McGhee, "Ring Magnet Power Supply for a 500 MeV Synchrotron," IEEE Industry Applications Society - 1978 Annual Meeting Conference Record, 1118.

ICANS IX

INTERNATIONAL COLLABORATION ON ADVANCED NEUTRON SOURCES

22-26 September, 1986

PERFECT CRYSTAL AND MAGNETIC FIELD BEAM TAILORING

H. Rauch

Atominstitut der Österreichischen Universitäten, A-1020 Wien, Austria

Perfect crystals and magnetic fields are effective and coherent tools for beam tailoring. Moderate magnetic fields can cause shifts of the perfect crystal reflection curve of the order of its width, which provides the basis for gated crystal systems and for crystal resonators. Various systems for an extremely high energy or momentum resolution have been tested. They are based on an effective decoupling of the resolution from the intensity. It is shown how travelling magnetic waves can be used for an effective beam bunching from pulsed sources.

1. INTRODUCTION

Evidently the ICANS-meetings deal mainly with more intense primary neutron sources but it should be remembered that the quality of a diffraction experiment will still depend on the economy with which the available neutrons are used throughout the whole experiment. Unfortunately, at present, thermal neutrons can only be produced by a statistical slowing down process, where they become spread into a wide phase space which causes a very low density in the elementary phase space (Maier-Leibnitz 1966). There are no methods known for neutrons that give an increase of the phase space density as exist in charged particle physics (e.g. Sorenson et al. 1983, v.d.Meer 1985).

To compete with other techniques of condensed matter research, a very effective use of the available neutrons is required. The decoupling of the resolution from the intensity is an effective tool in this direction. A high resolution of one quantity - energy or momentum - is usually balanced by a worse resolution of the other. In certain cases the resolution in diffraction techniques has been increased up to a level where the objects and time scales under investigation are accessible to direct methods.

It will be shown, in separate chapters, that the combination of perfect crystal diffraction and the Zeeman energy shift due to magnetic fields can be used for novel beam tailoring devices. Although the phase space density remains unchanged, the intensity can be shifted into phase space elements which are of interest to specific experiments. Not all details can be treated in this article and the reader is referred to the cited literature.

2. RESOLUTION-INTENSITY DECOUPLING

2.1 Spin-echo systems

The spin-echo technique was established in 1972 (Mezei 1972) and is now widely used in neutron spectroscopy (Mezei 1980). It provides a decoupling of the energy resolution from the energy width of the beam by using the Larmor precession of the neutron spin to measrue the energy transfer. This method operates most effectively at small momentum transfers and reaches energy resolutions in the 10^{-4}eV range.

2.2 Nondispersive double perfect crystal systems

These systems provide in momentum space, an analog of the spin echo system which operates in energy space. The symmetrical Bragg reflection from a perfect crystal can be given in the form of the Darwin curve (e.g. Rauch & Petrascheck 1978, Sears 1978)

$$R(y) = 1 \qquad |y| \leq 1$$

$$R(y) = 1 - \sqrt{1 - \frac{1}{y^2}} \qquad |y| > 1 \tag{1}$$

$$y = \frac{\pi(\theta - \theta_B)\sin 2\theta_B}{\lambda^2 b_c N}$$

where θ_B, b_c and N are resprectively, the Bragg angle, the coherent scattering length and the particle density. The rocking curve of a double crystal system is given by the convolution of two such reflection curves

$$I(y) = \int R_1(y')R_2(y + y')dy' \tag{2}$$

and exhibits a width of about 2 seconds of arc. The tails can be reduced by channel-cut crystals (Bonse & Hart 1965). These systems can be used for investigations of small angle scattering from a sample placed in between the crystals (Fig.1). The related momentum transfer regime is much smaller

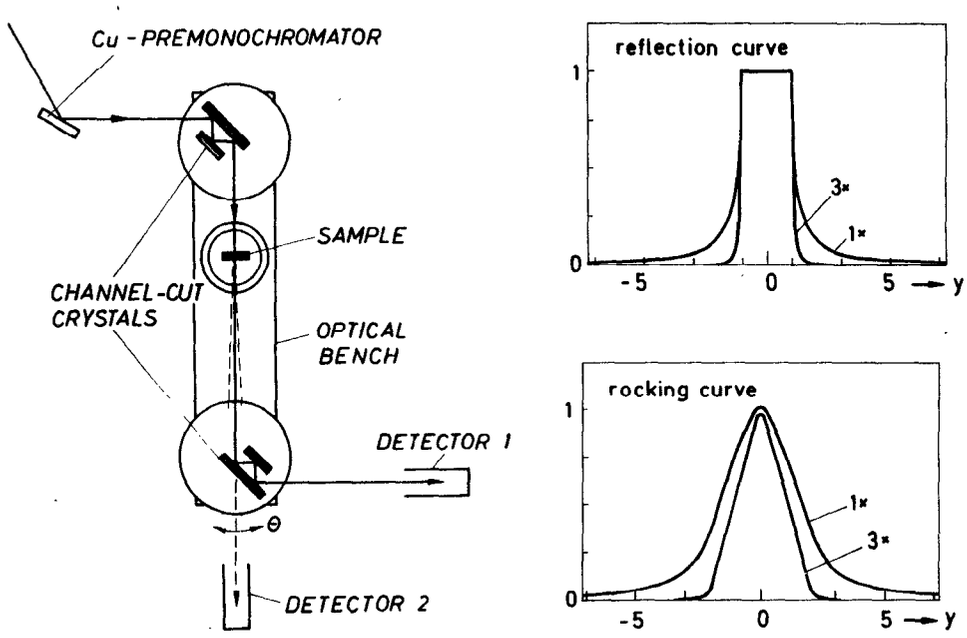

Fig.1: Experimental arrangement to demonstrate, and indication of, the action of channel-cut perfect crystals on the rocking curve of a double crystal system.

than in conventional small angle scattering instruments. The data evaluation has to take account of the slit-like geometry, as is often done in X-ray small angle scattering investigations (e.g. Glatter & Kratky 1982).

The typical momentum transfer regime ($Q = 2k\sin\theta/2 \sim k\theta$) becomes 10^{-5} Å^{-1} $\leq Q \leq 10^{-3}$Å^{-1} but the intensity remains rather high because - in principle - all neutrons reflected from the first crystal are also reflected from the second. From the accessible Q-range, follows that objects with dimensions of the order of μm can be investigated. Related experiments with neutrons using channel-cut perfect crystals can be found in the literature. Polymer blends and lamellar structures have been investigated (Schwahn et al. 1985).

An even more effective use of the available neutron intensity can be obtained by a multiple perfect crystal small angle scattering camera as shown in Fig. 2. The resolution can be varied by using symmetrical or asymmetrical cut crystals or perfect multiplate crystal systems (curved or with a temperature gradient). Intensity gains of up to a factor 100 seem to be feasible by using the full potential of this method.

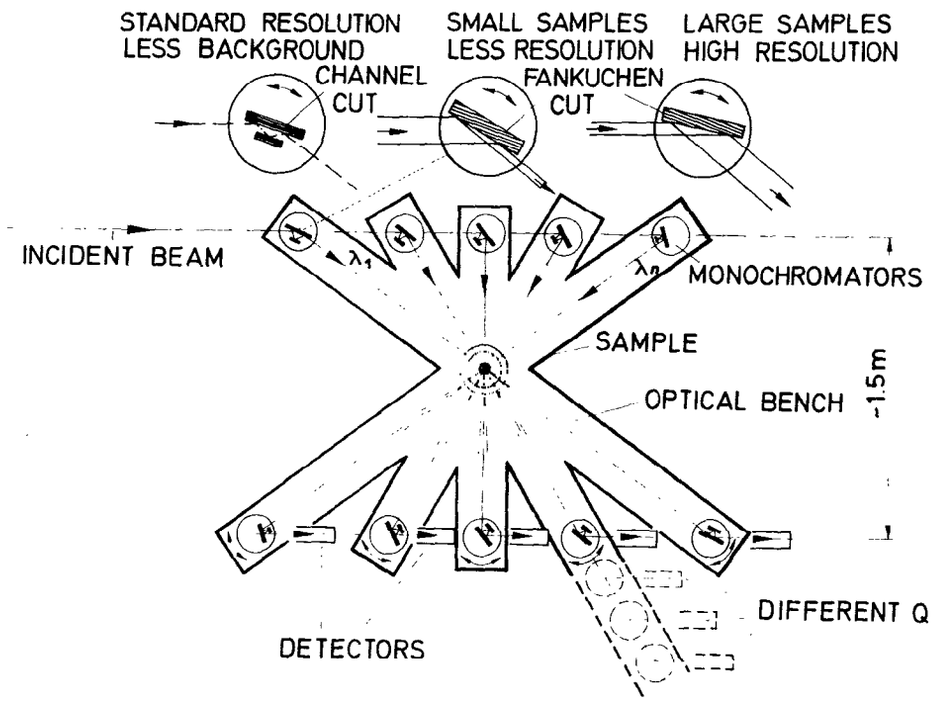

Fig.2: Proposed design of a multiple small angle scattering camera for stereoscopic investigation of samples.

2.3 Multiple Laue-Reflection (Diffraction focusing)

Even higher Q-resolutions can be achieved with a perfect crystal system when a monolithic multiplate system is used in the Laue position; that is where the lattice planes in the different plates are parallel (coherent) to each other and where the whole Pendellösung structure of the reflection curve has to be taken into account (e.g. Rauch & Petrascheck 1978, Sears 1978).

$$\frac{P_H}{P_0} = \frac{\sin^2 A\sqrt{1 + y^2}}{1 + y^2} \qquad (3)$$

$A = b_c \lambda N t/\cos\theta_B$ gives the reduced thickness of the crystal plates. This curve and the related rocking curve for a nondispersive arrangement are shown in Fig.3. The rocking curve exhibits a very narrow central peak whose width is determined by the ratio of the lattice constant divided by the thickness of the crystal ($\theta \sim d_{hkl}/t$), which is in the order of a thousandth of a second of arc (Bonse et al. 1977).

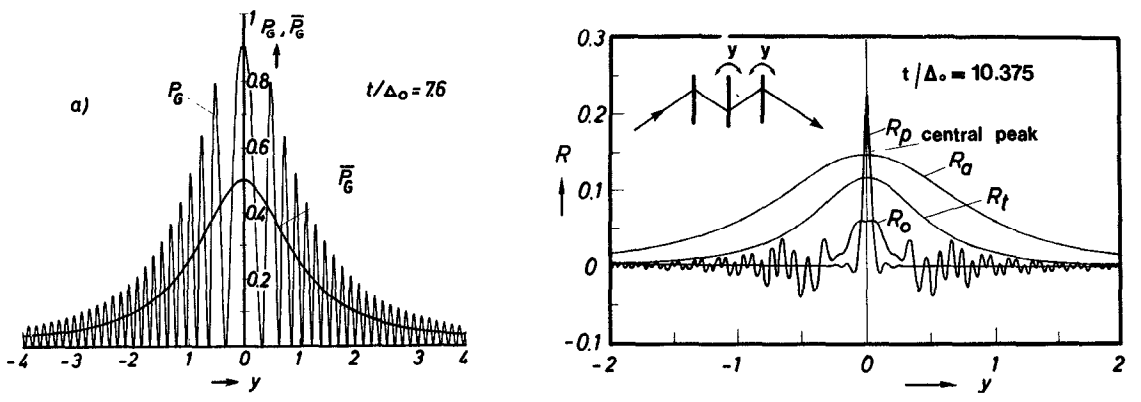

Fig. 3: Laue reflection curve and various contribution to a triple Laue rocking curve.

This effect was first observed for a monolithic two plate system (Bonse et al. 1979). In order to achieve the required high angular sensitivity for a precise rocking curve measurement a wedge was rotated around the beam axis. This produces for a wedge with an apex angle β, a beam deflection in the horizontal plane of

$$\delta = \frac{N\lambda^2 b_c}{\pi} \, tg\frac{\beta}{2} \sin\alpha. \qquad (4)$$

This trick causes a magnification factor of about 10^5 between the deflection angle δ and the rotation angle α of the wedge. The related rocking curves can also be calculated analytically, which is important for an application to small angle scattering (Petrascheck & Rauch 1984). This extremely high angular resolution can be used for small angle scattering measurements in the Q-range of $10^{-7}\text{Å}^{-1} \leqslant \Delta Q \leqslant 10^{-9}\text{Å}^{-1}$. A related measurement for the triple plate case has been reported (Rauch et al. 1983), where the diffraction of 1.8 Å neutrons at a single slit with a width of 5 mm has been observed (Fig.4).

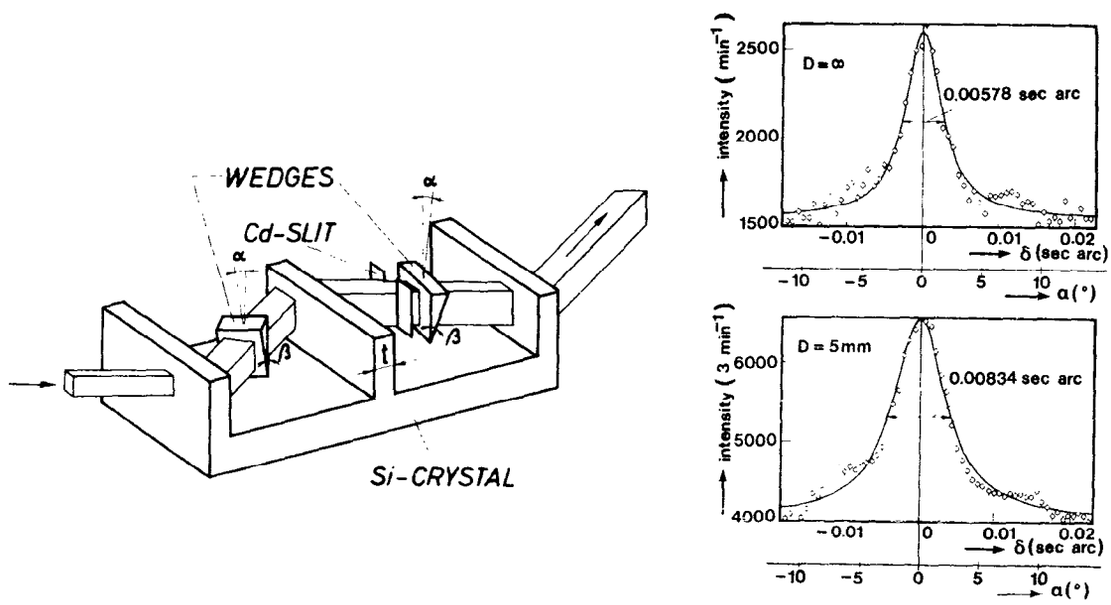

Fig.4: Sketch of the triple Laue rocking curve experiment and the measured broadening of the central peak due to single-slit diffraction from a 5 mm slit.

This behaviour can also be understood in terms of the Heisenberg uncer-

tainty relation $\Delta Q \Delta x \geq \hbar/2$. Therefore, perfect crystal extends small angle scattering investigations from the study of microscopic objects up to the observation of macroscopic systems. Applications to the investigation of macroscopic cracks or voids in bulk or for the observation of long range density fluctuations, can be envisaged.

The high angular sensitivity can also be used to give to a high energy resolution of the order of 10^{-9}eV (Zeilinger et al.1979).

2.4 Coherent magnetic resonance system

This device takes advantage of the high sensitivity achieved in neutron interferometry (Rauch et al. 1974, Bonse & Rauch 1979) and from the Zeeman energy exchange between the neutron and a Rabi-type resonance flipper (Alefeld et al. 1981). Here a real energy exchange between the neutron and the resonance flipper device takes place. This feature has been verified experimentally, using a backscattering instrument with an energy resolution ΔE better than the Zeeman energy transfer $2\mu B$. The kinetic energy changes at the entrance due to the Zeeman splitting. Inside the resonance coil, the energy quanta $\hbar\omega_1 = 2\mu B_0$ is exchanged which

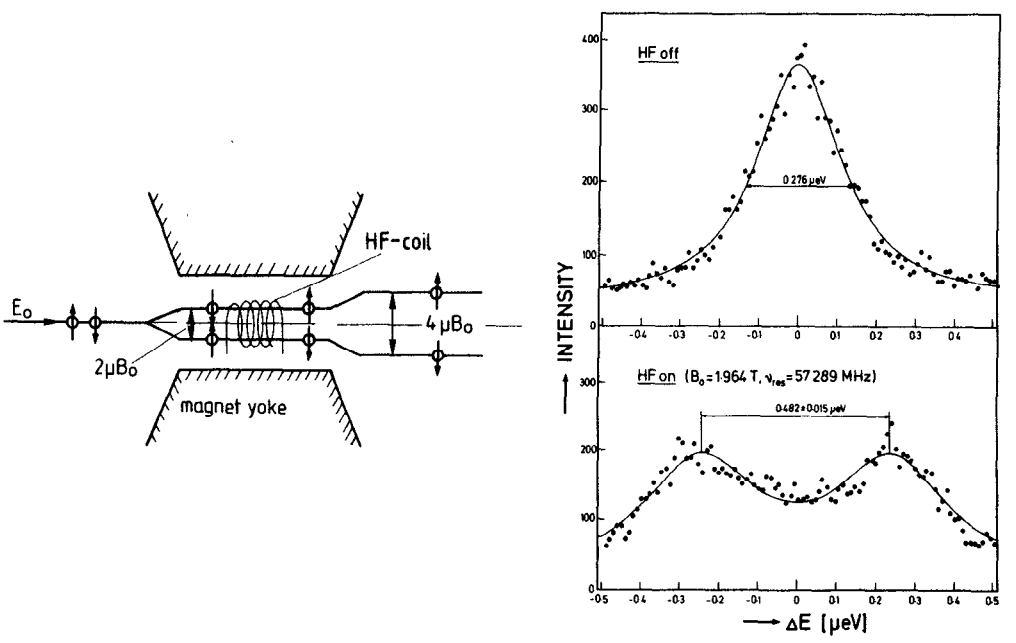

Fig. 5: Sketch of the neutron magnetic resonance system and the observed energy shift at resonance.

changes the potential (and total) energy of the neutron accordingly, and at the exit the Zeeman energy shift occurs in the same direction (Fig.5).

Inside a neutron interferometer, an energy transfer smaller than the apparent energy resolution of the system can be observed because properties of the wave function itself become measureable. In this case the total energy change and the two wave functions of both beams can be written as

$$\psi_0^{I} + \psi_0^{II} \rightarrow e^{i(\omega - \omega_{L_1})t} |-z\rangle + e^{i\chi} e^{i(\omega - \omega_{L_2})t} |-z\rangle \qquad (5)$$

This results in an intensity modulation of the beams behind the interferometer

$$I_0 \propto |\psi_0^{I} + \psi_0^{II}|^2 \propto 1 + \cos\,[\chi + (\omega_{L_1} - \omega_{L_2})t] \qquad (6)$$

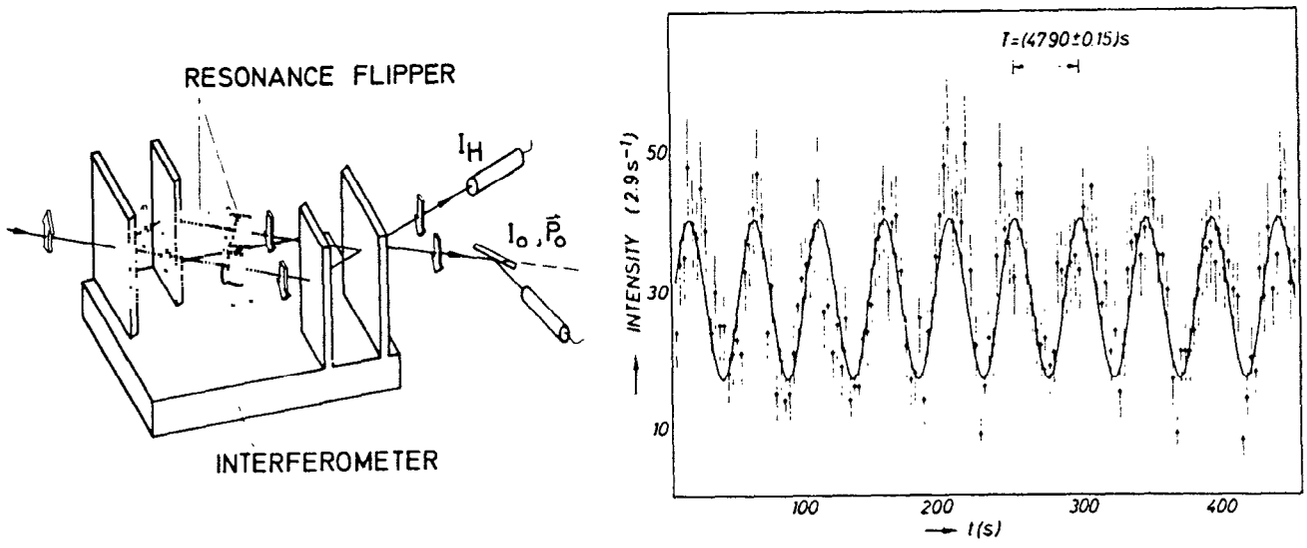

Fig.6: Experimental arrangement of the double coil quantum beat experimental which achieved an energy sensitivity of 2.7×10^{-19}eV.

where χ is a static (and hence unimportant) phase shift given by the index

of refraction. The energy transfer in both beams ($\hbar\omega_{L1}$ and $\hbar\omega_{L2}$) can be chosen to be different and then a time-dependent intensity modulation with a time constant $T = 2\pi/(\omega_{L1} - \omega_{L2})$ occurs. The result of a related experiment, where the frequency difference chosen was only 0.02 Hz and hence the beating period corresponded to an energy difference of $8.6 \cdot 10^{-17}$eV and to an energy sensitivity of $2.7 \cdot 10^{-19}$eV (Badurek et al. 1986), is shown in Fig. 6.

The extremely high momentum resolution discussed in chapter 2.3 and the extremely high energy resolution discussed in this chapter approach the limits of the uncertainty relation ($\Delta k \Delta x \geqslant \hbar/2$ and $\Delta E \Delta t \geqslant \hbar/2$).

Summarizing this general chapter: one gets three levels of energy and momentum resolution (ΔE_{exp}, ΔQ_{exp}), and in each case a strong decoupling from the energy and momentum width (ΔE_{beam}, Δk_{beam}) of the beam exists, which also means these instruments operate at a comparable intensity level.

These high resolution systems also have on the other hand distinct constraints concerning the accessible Q-range, which usually becomes more and more concentrated near Q=0.

Table 1

Resolution - Intensity Decoupling Systems

standard spectroscopy	$\frac{\Delta E_{exp}}{\Delta E_{Beam}} \sim 1$	$\frac{\Delta Q_{exp}}{\Delta k_{Beam}} \sim 1$
	crystal and time-of flight	
high resolution spectroscopy	$\frac{\Delta E_{exp}}{\Delta E_{Beam}} \sim 10^{-4}$ *spin-echo*	$\frac{\Delta Q_{exp}}{\Delta k_{Beam}} \sim 10^{-2}$ *non dispersive perfect crystals*
ultra high resolution spectroscopy	$\frac{\Delta E_{exp}}{\Delta E_{Beam}} \sim 10^{-12}$ *coherent double resonance system*	$\frac{\Delta Q_{exp}}{\Delta k_{Beam}} \sim 10^{-6}$ *multiple Laue reflection*

3. GATED CRYSTALS

The reflection curve of perfect crystals in the Bragg position has been discussed in chapter 2.1. As can be seen from equation (1), a particular situation exists for backreflection ($\Theta_B = \pi/2$) when the acceptance angle becomes rather large (the order of 1 degree). This provides the basis for back-scattering spectrometers which are used routinely for high resolution neutron spectrometry (e.g. Alefeld 1972). The Darwin curve of a perfect crystal in the reflection position can be shifted relatively either by changing the lattice constant (e.g temperature variation) or by applying a magnetic field to change the wavelength of the neutrons. This latter change can be calculated from energy conservation in the entrance field (see Fig.5)

$$H = \frac{\hbar^2 k^2}{2m} - \vec{\mu}\vec{B} \tag{7}$$

which caused the wavelength to change:

$$\lambda_{\pm} = \lambda(1 \mp \frac{\mu B}{2E}) \tag{8}$$

In the back-scattering position, where the acceptance angle becomes very large, the width of the reflection curve corresponds to a momentum transfer width of

$$\frac{\Delta k}{k} \approx 4N_c b_c |F| \frac{d_{hkl}}{\pi} \tag{9}$$

The shift due to a magnetic field can be written as

$$\Delta k_m = \pm \frac{\mu B m}{\hbar^2 k} \tag{10}$$

The magnetic field required to change the gate from the closed to the open position (i.e. a shift of 2 y-units) is 12.6 kG for the (111) back-reflection from silicon (λ = 6.275 Å). The proposed system and the shift of the reflection curve are shown in Fig.7. The system acts effectively only for a pulsed beam and when

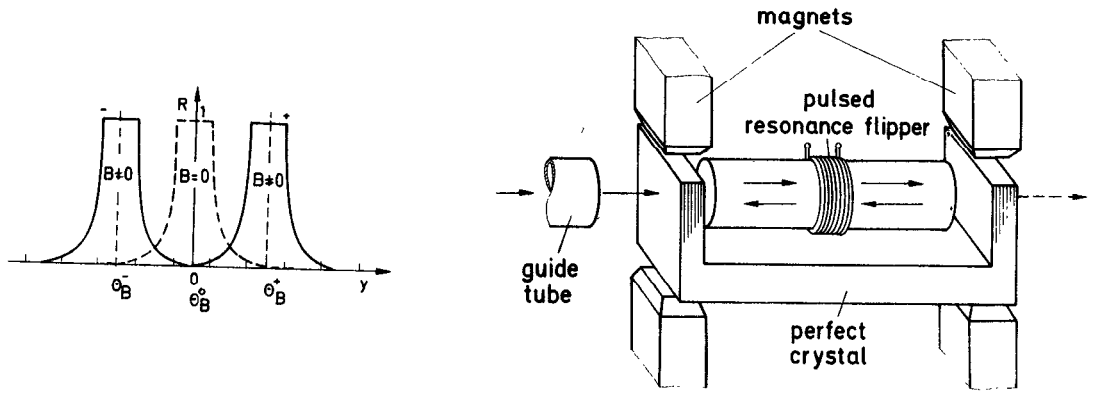

Fig. 7: Sketch of a proposed perfect crystal resonator and indication of the action of perfect crystals.

the magnetic field (or the resonance coil) is operated synchronously so as to catch neutrons between the perfect crystal plates. The version with the pulsed resonator flipper has the advantage that a stationary field at the crystal plates is sufficient. The performance of fast pulsed resonance flippers has been tested (Rauch et al. 1968, Freisleben & Rauch 1972).

The action of such a system can be increased by using a multiple backreflection crystal system as shown in Fig.8, where a temperature

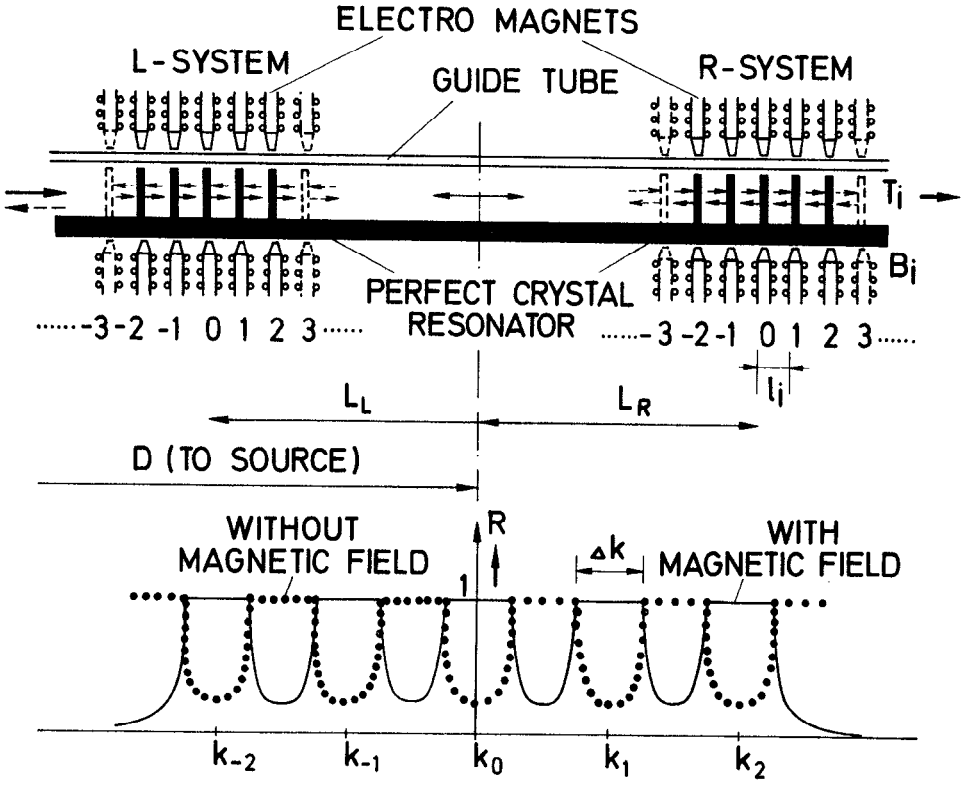

Fig. 8: The proposed multiple perfect crystal back-reflection resonator

difference is chosen to obtain a comb-shaped reflection curve which can be varied between an open and a closed position by a magnetic field (Rauch 1985). The temperature difference required for a shift of 2 in y-units (i.e. the whole width) is given as

$$\Delta T = \left[1 + \frac{\pi}{8N_c b_c |F| d_{hkl}^2}\right]^{-1} \frac{1}{\alpha} \tag{11}$$

where α is the linear expansion coefficient. The temperature difference for a (111) back-reflection from silicon is 8 K. Figure 8 shows a possible multiplate system, with a temperature gradient between the plates of 16°C and where the magnetic fields at the crystals can be varied in the required manner. Such devices can be used to good advantage at pulsed sources: neutrons can be caught temporarily between the crystal plates and then released under controlled conditions. Either fast switching magnets or a pulsed spin flipper between the crystal system can be used as the active element of the system. Similar systems, with a monochromatizing action, have also been discussed (Rauch 1985).

4. TRAVELLING MAGNETIC WAVE SYSTEM

The neutron magnetic resonance system, discussed in chapter 2.4 (Fig. 5), provides an energy shift of only the Zeeman energy ($2\mu B_0$). An alternative method, which so far has only been investigated theoretically, is to use a magnetic oscillator potential, with a fixed or an expanding width (w(t)), that moves along the path of a pulsed neutron beam (Fig. 9). In this arrangement, the gradient of the field acts more effectively than in the static case. Figure 9 shows a schematic layout for such a system, which could be installed along a neutron guide at a pulsed source (Rauch et al. 1985, Summhammer et al. 1986).

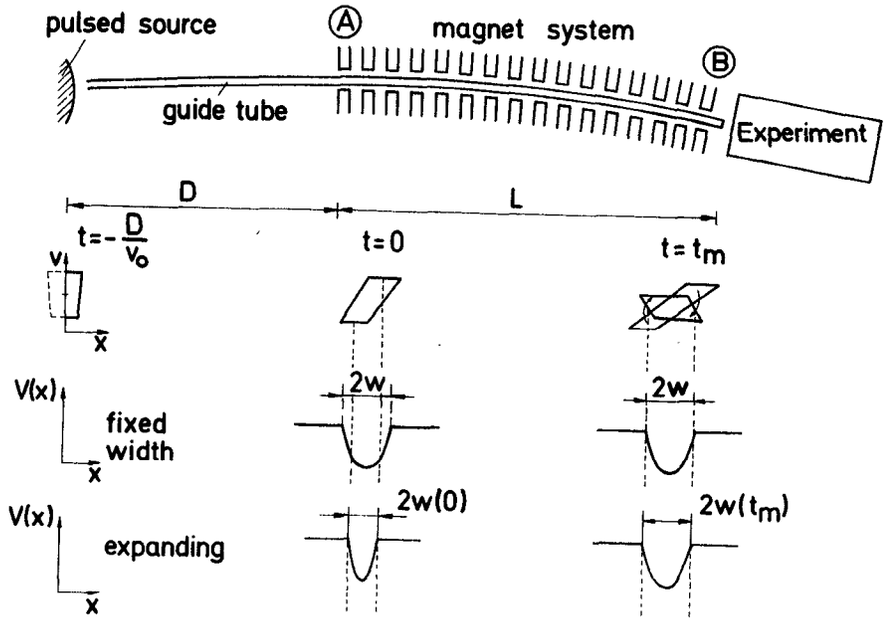

Fig. 9: Schematic layout of a travelling magnetic-wave system for beam bunching.

While passing along the beam path, the neutron feels a potential

$$V(x',t) = \pm\mu B_{max}\left(\frac{x'^2}{w^2(t)} - 1\right) \qquad |x'| \leq w(t)$$
$$= 0 \qquad |x'| \geq w(t) \tag{12}$$

where primed variables refer to quantities in the moving frame of the potential. Neutrons in the potential and within a specific velocity band, perform an oscillatory movement. The maximum escape velocity in the reference frame is given by

$$v_{esc} = \sqrt{\frac{2\mu B_{max}}{m}} \tag{13}$$

which reaches, for $B_{max} \sim 10$kG, a value of a few m/s and which is a factor of about 100 larger than the normal Zeeman splitting. The maximum gain factor for a fixed width potential can be written as

$$\rho = \frac{2w}{\tau V_0} \tag{14}$$

where τ is the pulse width of the source. By means of this method a reasonable intensity gain within the specific velocity band can be achieved, as is shown in the figure 10.

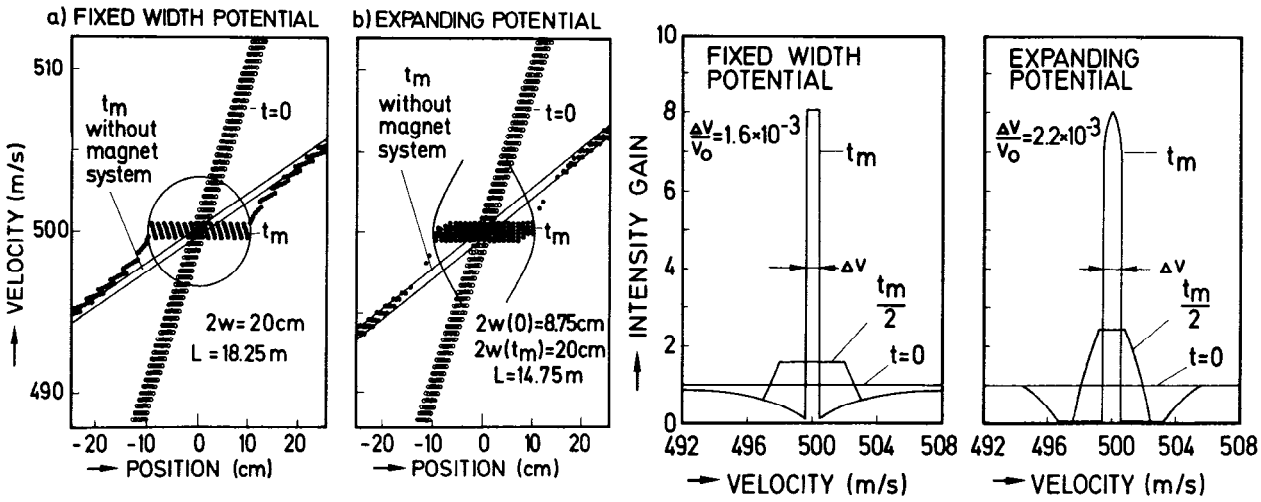

Fig. 10: Phase-space rotations of a pulsed beam for a fixed width potential and an expanding potential (left), and the related intensity gains (right) for feasible parameters (see text).

The results have been calculated for a source with a pulse width of 50μs located 5m in front of the travelling wave system, a maximum field strength of 10kG and a mean neutron velocity v_0 of 500m/s ($\lambda \sim 7.91$ Å) (which equals the velocity of the travelling wave). The action of the travelling magnetic potential corresponds to a rotation of the pulse in the x,v-phase space, hence the phase space density remains constant. Such systems will be expensive but they permit a very general tailoring of the beam pulse. Further details may be found in the references given.

The contributions of my colleagues in our institute, who are cited in the references, are gratefully acknowledged. Most of the investigations discussed in this paper were supported financially by Fonds zur Förderung der wissenschaftlichen Forschung (project S4202).

References:

Alefeld G., Kerntechnik 14(1972)15

Alefeld B., Badurek G., Rauch H., Z.Physik B41(1981)231.

Badurek G., Rauch H., Tuppinger D., Phys.Rev.A34(1986)2600.

Bonse U., Hart M., Appl.Phys.Lett.7(1965)238.

Bonse U., Graeff W., Teworte R., Rauch H., phys.stat.sol.(a)43(1977)487.

Bonse U., Graeff W., Rauch H., Phys.Lett.69A(1979)420.

Bonse U., Rauch H., (Eds.) "Neutron Interferometery" Clarendon Press Oxford, 1979.

Freisleben H., Rauch H., Nucl.Instr.Meth. 98(1972)61.

Glatter O., Kratky O., "Small Angle X-Ray Scattering", Academic Press, N.Y.1982.

Maier-Leibnitz H., Nukleonik 8(1966)5.

Meer van der, S. Rev.Mod.Phys.57(1985)689.

Mezei F., Z.Physik 255(1972)146.

Mezei F., (Ed.), "Neutron Spin Echo", Lect.Notes Physics 128, Springer Verlag, 1980.

Petrascheck D., Rauch H., Acta Cryst. A40(1984)445.

Rauch H., Harms J., Moldaschl H., Nucl.Instr.Meth.58(1968)261.

Rauch H., Treimer W., Bonse U., Phys.Lett.A47(1974)369.

Rauch H., Petrascheck, in "Neutron Diffraction (Ed.H.Dachs), Top. Current Physics 6,303, Springer Verlag 1978.

Rauch H., Kischko U., Petrascheck D., Bonse U., Z.Phys.B51(1983)11.

Rauch H., in "Neutron Scattering in the 90-ties", p.35, IAEA-Vienna 1985.

Rauch H., Summhammer J., Weinfurter H., in "Neutron Scattering in the 90-ties", p.53, IAEA-Vienna, 1985.

Schwahn D., Miksovsky A., Rauch H., Seidl E., Zugarek G., Nucl.Instr. Meth.A239(1975)229.

Sears V.F., Can.J.Physics, 56(1978)1261.

Sorenson A.H., Bonderup E., Nucl.Instr.Meth.215(1983)27.

Summhammer J., Niel L., Rauch H., Z.Physik B62(1986)269.

Zeilinger A., Shull C.G., Phys.Rev.B19(1979)3957.

ICANS IX

INTERNATIONAL COLLABORATION ON ADVANCED NEUTRON SOURCES

22-26 September, 1986

Neutron Sources
— Their Prospects and Their Problems —

G. S. Bauer

Kernforschungsanlage Jülich, FRG

1. How Advanced is Advanced?

When this "International Collaboration on Advanced Neutron Sources" was first agreed upon, today's most powerful research reactors were already in operation and were obviously considered as conventional installations. Today, almost ten years later, our advanced sources are still thriving (although with notable progress) to match in performance those conventional "oldies" and it might well be that the organizers of this meeting had something like this in mind, when they asked me to give some thoughts to the problems and prospects of neutron sources in general.

Neutron scattering is a scientific tool and obviously, the better our tools, the more sophisticated questions will one be able to solve. It is therefore natural that continuing thought is given to the question, how the neutron sources and the instruments that go with them can be improved. This will also remain so with the very powerful sources of light and X-rays which can now be built on electron storage rings although there may be a shift of the border line between the domains of X-ray and neutron scattering. This question will not be given further consideration here. Instead, we will focuss on the more technical questions of the topic. Also, the two types of neutron sources - steady state and pulsed - with their characteristics being different, have their respective scientific justifications and don't need to be weighed against each other. It is therefore the aim of this paper to point out, where we stand today, and what potential for future growth one can see.

2. Continous Sources – A Never Ending Stream?

The impressive development in nuclear research reactors, leading within a span of less then 25 years from the first controlled chain reaction ever to the elaborately designed HFIR in Oak Ridge, did not only happen in a period of general enthusiasme for new technologies, it was also strongly motivated by the military and commercial interest in this new field. If at all, neutron scattering was only a side aspect in the design and use of most research reactors and there are but a few reactors which have been built with neutron scattering as the main motivation.

Although the quality of the beams in therms of fast neutron and gamma ray background is important, the prevailing quality criterion for a continous reactor is its time average thermal flux outside the core where the beam tubes end. It has been sitting at a value of 10^{15} $cm^{-2}s^{-1}$ for more than twenty years now with no ongoing new project in sight that would promise any significant progress.

2.1 Hopes and Horizons

A recent conference at the US National Bureau of Standards, organized to review the issue of an advanced steady-state neutron facility has produced some evidence, that an increase in flux by one order of magnitude might be feasible with present technology, although not without an extensive R+D programme to preceede such an attempt.

Under some simplifying assumptions, it is not difficult to see (Difilippo et al. 1986), that the flux outside the reactor core is approximately proportional to $P^{1/3} \cdot \rho^{2/3}$, where P is the thermal power and ρ is the power density in the core. This means that, although some geometric optimization is possible (see e. g. Böning et al. 1985), the essential quantity that determines the useful flux in the moderator is the average power density in the core. This has several consequences

(1) It means that the volume fraction of coolant should be low, requiring high coolant mass flow and/or high outlet temperatures and pressure.

(2) The result is a strongly undermoderated core relying on thermal neutrons from the moderator/reflector to diffuse back into the core region. The resulting thermal flux gradiend across the fuel zone would lead to strong power peaking at the edges, unless variable U-235 content is applied.

(3) At the same time, since the neutrons have to cross a thick uranium layer before being moderated, resonance absorption becomes more likely and k_{eff} is reduced. This can only be compensated by a high uranium enrichment. At least outside the US this conflicts with the general US policy to push for the use of less than 20 % enriched uranium in research reactors.

(4) In cores using the standard fuel plate technology, the heat load on the plate surface increases. This leads to an enhancement of the formation of a thermally insulting oxide layer on the aluminium cladding and, as a consequence, to unacceptably high fuel temperatures.

Especially the last point is a concern for the reactor designers, because the conditions affecting the growth of the oxide layer are not well understood, it seems, however, that the growth rate depends on the heat flux as well as on the exposure time, the surface temperature and the quality of the cooling water (Gambill, 1986).

The various constraints are illustrated in Fig. 1 which shows the relation between power and power density for two flux levels, namely $5 \cdot 10^{15}$ $cm^{-2}s^{-1}$ and 10^{16} $cm^{-2}s^{-1}$. Also indicated is the maximum power density at which a reactor of a certain power can be operated to allow a 15 day core life, if a U_3Si_2-content of 30 % in the fuel matrix is assumed. The hatched area is where the design parameters must lie, if a flux between $5 \cdot 10^{15}$ and 10^{16} $cm^{-2}s^{-1}$ and a minimum of 15 day core life is to be achieved. If the oxide formation cannot be suppressed, $\approx$ 4 MW/l is an upper limit and no flux level higher than $5 \cdot 10^{15}$ $cm^{-2}s^{-1}$ is possible with this technology.

It should be noted, that the high power density during operation results in a substantial decay heat density also after shut down. It can not be expected that such a core could be cooled by convection soon after the reactor was switched off. Since D_2O is used as coolant, this makes core replacement not easy, because the transfer from D_2O to H_2O for core storage requires a certain minimum time for the

core to be gas-cooled, unless substantial losses of D_2O at each transfer are accepted.

The core design proposed for a new CNR (Centre of Neutron Research) by the Oak Ridge Group, which is based on these considerations is shown in Fig. 2. Depending on whether or not a method can be found to suppress the oxide formation, it should operate at a power level of 135 or 270 MW, giving a thermal flux of $5 \cdot 10^{15}$ or 10^{16} $cm^{-2}s^{-1}$ respectively.

Some of the design parameters of the CNR-core are listed in Table 1, together with those for another design (UHFR) developed at the Idaho National Engineering Laboratory and shown in Fig. 3.

This concept uses much thinner fuel plates, only 0.89 mm thick with 0.39 mm meat thickness. This results in a heat flux of 13.5 MW/m^2. The plenum between the two halfs of the core allows mixing of the coolant to suppress hot stream lines. The U-235 concentration varies across each fuel plate to avoid excessive heat peaking (see Fig. 4). The thermal flux in the moderator around the central region has been calculated as $1.1 \cdot 10^{16}$ $cm^{-2}s^{-1}$ at a reactor power of 355 MW.

A completely different design (HFPBR),also included in Table 1 and shown in Fig. 5, which was proposed by the Brookhaven Group is quite interesting, although perhaps even more remote: Directly water cooled coated particles arranged in a thin annulus. Although the coated particles are well developed and commercially available, they do not seem to have been used with direct water cooling so far.

Nevertheless, the concept would present some attractive features. Among them are:

(1) No aluminium oxide formation because the coating of the particles is of pyrolytic graphite and the residence time is small.

(2) Large surface to volume ratio due to spheric shape (≈ 750 μm diameter) and small U-content.

(3) Use of uranium oxide or carbide allows high fuel temperature.

(4) High power density of 10 MW/l or more can be achieved.

(5) Fuel loading in the core is small (≈ 2 kg U-235).

(6) Low enriched uranium can be used.

Although this concept has not yet been developed very far, it has a basic potential to break through the limits that hamper present plate fuel technology. However, a large number of problems would have to be solved, among them on line fuel replacement, fission product retention in the particles, particle surface erosion etc.

2.2 Reactor Realities

Considering the amount of research required before such a very high flux reactor can be built, the tedious licensing procedure it would have to undergo and the amount of money required for its construction, there seems to be little hope that the present decade, and probably even the present century (or millenium) will see a steady state neutron source become operational which would constitute such a decisive step forward from what is presently available at the HFR Grenoble.

On the other hand, as can be seen from the data compiled by R. Moon (1985), there are several less ambitious projects on their ways, like e. g. the replacement of the JRR-3 at JAERI (Japan), the MPR-30 in Indonesia, which is presently being commissioned and, most notably, the light water cooled PIK-reactor at Leningrad which is under construction. Although not particularly outstanding in its peak flux to power ratio ($1.3 \cdot 10^{15}$ $cm^{-2}s^{-1}$ at 100 MW) because, like the HFIR in Oak Ridge, PIK is designed to provide a flux trap in its centre, it is quite remarkable with its outer diameter of only five metres (see Fig. 6). This is based on the fact that the shielding around the instruments will add to the overall shielding and reinforcements can be provided where necessary. Some parameters of this reactor are listed in Table 2 in comparison to the HFR at ILL. Also included in this table for easier comparison are two of the advanced desigs of Table 1 and a new proposal for an FRM-II forwarded by the Technical University at Munich (Böning et al, 1985). The latter excells by its high flux-to-power ratio, made possible by the use of high density, highly enriched fuel (as in the advanced concepts described

above) and a small core diameter. Development work for this core is funded by the German Ministry for Research and Technology under its nuclear development programme.

Medium flux research reactors, which have mostly been designed as multipurpose reactors and therefore often do not provide adequate conditions for frontier neutron scattering have nevertheless played an important role in the past as far as training of young scientists and development of methods and instruments was concerned. With materials testing on these reactors becoming less important, there is, however, growing concern about the relatively high operating costs of these facilities in relation to their scientific output. In West Germany two such reactors, at Karlsruhe and Jülich, have been shut down permanently for this reason. Plans for upgrading existing facilities are being developed in several places. One basic problem, which may become even more serious, as public concern over the nuclear issue in general increases, is the following: Shutting such a reactor down for a major change will mean that its operating license expires and a new one will have to be obtained under the rather more stringent regulations now in effect. This may prove expansive in some cases and almost impractical in others. At present, it is almost impossible to predict, what exactly would be required for the renewal of an operating license for a modified older reactor.

2.3 If not Reactors, what else?

It started out as a big deal 25 years ago: 10^{16} $cm^{-2}s^{-1}$ was the goal; spallation was the clue! Chalk River's ING project, when proposed in the early 1960's (Bartholomew and Tunnicliffe, 1966, was sufficiently ambitious that it doesn't fail to amaze people even today: a 1 GeV - 65 mA cw-proton linac would produce enough neutrons in a flowing liquid lead-bismuth target that the flux goal could be achieved in a D_2O moderator around the target. The numbers were correct but - pitiful enough - there was no suitable accelerator which could be tapped, nore was there the money available to develop one. The project died after 5 years.

Today, twenty years later, this is where we stand:
$1.5 \cdot 10^{14}$ $cm^{-2}s^{-1}$ is the goal, the method is still spallation, the accelerator is (almost) there and the prospect for getting the money for the target station is good: the SINQ-project. The target station of this spallation neutron source

(Fig. 7) resembles closely a reactor, since it will operate in a continuous fashion and relies on a high time average flux.

The fact, that SINQ will be built is more than just the birth of another medium flux neutron source, it is a major step forward in a new technology and it is the test case for the question, how well spallation sources can be utilized. It is well known that, while being attractive for its low heat release, γ-radiation level and inventory of hazardous fission products, a spallation neutron source tends to produce a high energy component in its neutron spectrum, which is quite difficult to shield. At the very least, a more massive shield than for a reactor is required. In fact, the shield designed for the SINQ has about twice the diameter of that of the PIK-reactor which has a ten times higher thermal flux. Obviously, at the first glance this is a drawback as far as beamhole experiments are concerned. It is not quite so serious on the long run, however: Firstly, the shield thickness would not have to increase in proportion to the flux if more proton current was available, secondly, at a heavily used source a larger circumference allows more instruments to be accommodated and, last but not least, the cold neutrons, which are much in demand at present, can be easily guided away from the source over quite long distances. The effect of high energy contamination in the extracted beam on the quality of the experiments is extremely difficult to predict (Atchison, 1985). It should not be overemphazised, however, since also the scattering power of the monochromator (or sample) for these neutrons will be quite low. Of course, a carefully designed beam path and beam stopper at its end as well as adequate detector shielding will be essential. The question what the future potential of sources of this type really is can only be answered by trying it. SINQ offers the opportunity!

Another medium flux spallation source is under construction at the Moscow Meson Factory in Troitsk (USSR) (see Table 3) which is designed for operation in a quasi continuous mode or as a pulsed source. For this purpose two target locations are incorporated in the shielding (Fig. 8), which can be fed with protons either from the linac directly or via a pulse regrouping ring. There is also a proposal to build a rather more powerful one for fusion materials test purposes (Kley and Bishop, 1985).

3. Pulsed Beams - Salvation by Concentration?

The idea is quite simple and can be told in many different ways. Here is one: From the early days of neutron scattering on reactors, two methods of determining the neutron energy have been known: monochromatisation by Bragg scattering and time-of-flight measurements. Since each neutron can only be detected once (thus terminating its existence as a free neutron), time-of-flight measurements are only possible, if the starting time of the neutron can be defined by other means, e. g. if all neutrons start in a bunch from a known location. Although the choppers, which have to be used to impose this condition on a continuous beam reduce the average beam intensity often by more than 99 %, the technique managed to remain competitive on reactor sources for certain types of investigations, where large spectral width and large data collection angles around the sample could be used simultaneously to make up for the chopper losses. What a thought to have all the neutrons produced in the source concentrated in those time bins which would be transmitted by the chopper (and thus perhaps do away with the chopper altogether)! A closer inspection shows that such a source has a number of other attractive features which can be exploited to collect scientific information, in particular a large fraction of epithermal neutrons, which are generated in pulses suitable for time-of-flight measurements.

3.1 Tricks and Tradeoffs

Unfortunately it turns out that it is not easy to devise a neutron source which delivers a time average flux even of a medium flux reactor in pulses of one or a few microseconds duration and with a suitable repetition rate. The fundamental problem is, that neutrons are not born at the energies the scientists desire but have to be slowed down by about eight orders of magnitude in energy by collisions with the atoms of a moderator. It is not so much that this takes time to happen (of the order of a few to a few tens of microseconds) as it is the fact that, once thermalized, the neutrons take their time to diffuse out of the moderator, which causes trouble. Obviously, this makes the main trick, which is used on cw-sources to obtain a high flux of thermal neutrons, namely a large moderator in which neutrons have a long lifetime, impossible. On the contrary, even small moderators have to be decoupled from the reflector and internally poisoned to obtain pulses of the desired shortness. With respect to an assembly designed for optimum time

average thermal neutron output this may result in a loss in time average flux up to a factor of 20 (see Fig. 9). Also the peak flux is reduced, although only of the order of some 20 to 30 percent (Bauer et al, 1981). This is the main tradeoff one has to pay. Others result from the cyclic thermal load on the neutron producing zone and from the extra effort and cost to produce short bursts of fast neutrons in the first place. Pulsed reactors and proton beam driven spallation sources are the main options and we will limit our discussion to these. A nice feature common to all pulsed sources (at least to a certain extent) is the fact, that the fast neutrons and γ-radiation flash have disappeared from the beam when the signal neutrons arrive at the detectors. Although this doesn't affect the need for appropriate bulk shielding, it helps to keep the experimental conditions clean.

3.2 The Reactivity Roulette

Pulsing a reactor means to change its reactivity periodically from a value of k_{eff} well below one to slightly above one, to build up a high neutron population for short times. This can be done by moving part of the core or part of the reflector. While the first method may be more efficient, only the second one is possible at higher power levels because of cooling problems. The Mekka of pulsed reactor technology undoubtedly is the Joint Institute of Nuclear Research in Dubna, where the first pulsed reactor for beamhole research became critical in 1960 and the world's most powerful one, the IBR II, is presently being commissioned, operating at 2 MW, which is 50 % of its design power.

Figs. 10 and 11 show a cutaway view and a horizontal section of the core and reflector arrangement. While the reflector is stationary on five sides of the hexagonal core, two moving reflector arms are arranged on the sixth side. The three-forked auxiliary reflector rotates at 5 Hz while the solid main reflector rotates in opposite direction at 25 Hz. Each time both reflectors meet in front of the core, the main pulse is produced, while satellite pulses which are about 0.03 % in height of the main pulse are produced when the auxiliary reflector alone passes in front of the core (Fig. 12). The background level from delayed neutrons between the pulses is quite low, 0.006 % of the peak height, which is due to the low reactivity with the reflectors removed.

Obviously, in order to obtain short pulses, the core has to be prompt supercritical during the pulse. The core is made up of PuO_2 fuel, arranged in hexagonal packs of fuel rods. The cooling medium is Na to avoid thermalization inside the core and to allow high fuel temperatures. Table 3 gives some data of the IBR II in comparison with other high performance neutron sources (see also below). The pulse duration is about 150 μs for the primary pulse as well as for the thermal neutrons emerging from the moderators. This makes it necessary to use choppers for many experiments. These choppers can be accommodated in an annular space within the main reactor shield. As a rule, their rotation axes have to be parallel to the beam lines.

IBR II had been under construction for about 15 years with many problems to be solved before it started operating in 1982.

With its complicated technology and its restrictions with respect to pulse length and spectral tailoring it is likely that it also marks the end of a development line although the engineering that went into it deserves utmost admiration.

3.3 The Pulsed Proton Poker

While older than reactors, in principle, accelerator based pulsed neutron sources are only gradually making their way into routine application to thermal and cold neutron scattering. The one type which really has a prospect for growth and development are neutron sources using the proton-induced spallation reaction. These sources depend on the availability of proton accelerators in an energy regime of about 1 GeV to make the targets radiate with neutrons. Such machines have been built in the past as boosters for high energy accelerators and as drivers for meson factories. Parasitic use for neutron sources was gracefully granted. KENS, WNR and IPNS were all born in this craddle, although, with IPNS leading the way, they are gradually maturing into neutron scattering facilities of their own right: The old AGS Booster synchrotron has been upgraded and is operating for the sole purpose of keeping IPNS ablaze, WNR has been supplied with a proton storage ring recently and KENS was an important factor in the planning of future medium energy accelerators at KEK right from the beginning.

The only member in this family of accelerators which, although thriving on existing buildings and equipment, was designed as a neutron source driver from the very beginning is the 50 Hz ISIS Synchrotron at the Rutherford Appleton Laboratory, which is presently working its way up to its design specifications. These specifications reached, the facility will be competitive and, due to a suitably designed set of instruments in some cases even significantly superior to the HFR at the ILL Grenoble. This is true in all cases, where the pulse structure can be exploited beneficially to collect the desired information and it is especially true for energies in the slowing down regime where the spectral fraction at the ILL is low and where the pulses on ISIS are short and time-of-flight is the only viable technique for energy determination.

On the other hand, the need for keeping the pulses short for good time resolution results in a disapointingly low time average flux and makes some well established and important techniques such as triple axis spectroscopy impossible. This is one of the tradeoffs that have to be accepted on pulsed sources.

Another problem with accelerators is their technical complexity, which unfortunately leads to more or less frequent failures. This is not only a nuisance to the neutron users, it also has the effect of thermally quenching the target, thus reducing its life time. This is the more serious, the higher the power on the target and hence its operating temperature is. The temperature in a spallation source target will always be a problem because, in order to produce a "bright" source of fast neutrons, the metal density in the target should be high and hence cooling channels are undesirable (but can, of course, hardly be avoided). Also, the very inhomogeneous heat distribution inside the target resulting from the intensity profile of the beam and its exponential decrease along the target axis poses problems: The coolant flow has to be able to handle the power density at the hot spot and thermal stresses within the individual target plates may become considerable.

Part of these stresses are cyclic and follow the pulse repetition rate of the protons. Here comes one of the main problems with these targets: The temperature rise in each pulse is determined by the power density in the target plate and because of the shortness of the pulse and the need to keep the beam size within the order of a few centimeters, the heat load becomes considerable as one tries to

go up in beam power. Also, there is no way to reduce the power density within the materials.

While it is just to say that today's spallation sources are not yet probing the limits of target technology, not even at ISIS when its full design current will be reached, the rapid cycling ISIS synchrotron will be more or less at the limits of what one can do with this technique.

Trying, as we did with the reactors, to take a look at the future development protential of spallation sources in general, there doesn't seem to be such a clear cut limit, but, of course, much less experience is available, too. In the accelerator field, two routes seem to be feasible to achieve more intense but still short pulses: The FFAG's on the one hand and linacs with pulse compressors on the other. The first route has been proposed for Argonn's next generation neutron source, the ASPUN, aiming at a time average current of 3 800 μA at 1 500 MeV (as compared to 200 μA at 800 MeV for ISIS). At this level, a number of problems have to be dealt with also on the target side and certainly engineering constraints will prevent the flux from the moderators to increase in proportion to the target source strength.

The combination of a linac with a compressor ring is being pioneered at LAMPF/LANCE and the Moscow Meson Factory has similar plans. The idea here is, to inject into the ring at full energy and at a phase space density which is much higher than at the low injection energy into a synchrotron. The long pulses of a linac can be injected over many turns and extracted during one single revolution of the protons. The current amplification is then approximately given by the ratio of the linac pulse length to the revolution time in the ring. In the German IKOR study (Schaffer ed., 1981) this factor was to be about 650, starting with a 100 mA in the linac and delivering a time average current of 4.5 mA at 1 100 MeV.

Pulsed sources at this sort of intensity level would certainly not only be a tremendous engineering challenge in accelerator as well as target technology, they

3.4 The Enchantment of Enrichment

In the absence of the high current accelerating systems mentioned above, one is of course tempted to enhance the neutron production in the target by going back to good old fission as long as the heat removal system can cope with the power deposition. This route is being taken by IPNS (see e. g. Schulke, 1985) and similar considerations are under ways at ISIS . The basic concept is, to produce a more or less flat heat distribution over the whole target volume by increasing the content in fissile material in those regions, where the power density would otherwise be low. The options considered for ISIS are reported in a different paper in this meeting (Bauer, 1986). Although the work is still in an early stage, it is clear, that a decoupler has to be used around the target to avoid thermal fission and the resulting pulse degradation. This means, that a relatively large quantity of material is required to reach the desired enhancement factor of 10 or more in the leakage from the moderator. With a beam current of 40 μA time average, and at an overall thermal power of 1.75 to 2 MW in the booster, the amplification of source neutrons relative to a target of depleted uranium would be about a factor of 20, while the power is increased by a factor of 30. Not allowing for any engineering constraints, the thermal flux from a slab moderator would be increased by about a factor of 12 to 15, but since a wider target had to be assumed to achieve the necessary k_{eff}, the coupling into a wing moderator will be poorer than in the present ISIS arrangement and the goal of a factor 10 in enhancement will rather be an optimistic estimate.

It is worth noting, that at this power level the ISIS-target will be in the same regime as the IBR II pulsed reactor although, of course with less sophisticated technology. However, in contrast to a pulsed reactor, a booster target will in general not be reactivity modulated. As a consequence, delayed neutron background will constitute much more of a problem; the worse, the higher the multiplication (k_{eff}) is. It may well become necessary to devise quite sophisticated equipment (such as choppers close to the target) to control this problem.

In general it is probably fair to say, that a booster is a viable solution if the time average proton current is of the order of a few tens of microamperes but will probably not be an option if a current in the milliampere regime is available.

3.5 Abandoning Abortion

It is a pity to see that, in a pulsed source, 80 % of all neutrons which could leak from a suitably optimized moderator are killed in order to keep the pulses short (Fig. 9). This is even more a problem with a booster assembly, which has to suppress thermal fission to keep the pulses reasonably short. For a well coupled moderator designed for maximum neutron leakage the pulse duration is of the order of 100 μs even for very short proton pulses and increases as the duration of the source pulse reaches the same order of magnitude. If a proton current of the order of 1 mA time average can be devised, such a moderator could yield a time average flux of the order of $2 \div 3 \cdot 10^{14}$ $cm^{-2}s^{-1}$, thus lying well inside the regime of medium flux reactors, but with the added advantage of having the neutrons concentrated in bursts. Such a source has been termed "intensity modulated" in contrast to the pulsed sources discussed above. During the study work for the German SNQ project, substantial effort has been devoted to the question, how such a time structure could be optimally exploited (see e. g. Scherm and Alefeld, 1985). The net result of a very careful evaluation is that, relative to a cw-source of equal time average flux, there is not a single technique which could not benefit in one way or the other from such a time structure. While in some cases only nominal gains (as defined as the time required to obtain a certain information) of the order of 2 would be expected, the average was found to be at least an order of magnitude, with some special cases being able to profit from the full peak-to-average flux ratio, which was 35 in this case, but could be higher for shorter proton pulses.

No such source exists or is planned at present, but with the limitations that can be seen for cw-reactors on the one hand and for pulsed sources on the other, this intermediate route might constitute another way to improve conditions for neutron scattering in the more distant future. It would help, if an interest in high intensity accelerators builds up also for other reasons.

References

Ananiev V D, Kozlov Zh A, Luschikov V I, Ostanevich Yu M, Shabalin E P and Frank I M
"Pulsed Reactor IBR-2 in the `Nineties"
Proc. Conf. "Neutron Scattering in the `Nineties", IAEA, Vienna 1985, p. 63 - 73, paper IAEA-CN-46/85

Atchison F (1985)
"Considerations on Backgrounds at SINQ"
Proceedings of the Eighth Meeting of the International Collaboration on Advanced Neutron Sources (ICANS-VIII), 8 - 12 July 1985, Rutherford Appleton Laboratory, report RAL-85-110, p. 648 - 658

Bartholomew G A and Tunnicliffe P R (1966)
"The AECL Study for an Intense Neutron-Generator
AECL 2600, Atomic Energy of Canada Limited, Chalk River, Ontario

Bauer G (1986) (presenter)
"Enhanced Target Moderator Concepts for ISIS"
This conference

Bauer G, Conrad H, Filges D, and Spitzer H (1985)
"The SNQ Target and Moderator for an Optimized Neutron Economy"
Proc. Conf. "Neutron Scattering in the Nineties", IAEA, Vienna 1985, p. 267 - 278, paper IAEA-CN-46/79

Böning K, Gläser W, Meier J, Rau G, Röhrmoser A and Zhang L
"Upgrading of the Munich Reactor with a Compact Core"
Proc. Conf. "Neutron Scattering in the `Nineties", IAEA, Vienna 1985, p. 165 - 170, paper IAEA-CN-46/53

Bulkin Yu M, Gratshev M I, Kolmytshkov N V, Lobashov V M, Sidorkin S F, Stavissky Yu Ya, Chmelstshikov V V and Chrjastov N A (1985)
"Assembly of Neutron Sources Based on Proton Beams of the Moscow Meson Facility"
Proc. Conf. "Neutron Scattering in the `Nineties", IAEA, Vienna 1985, p. 369 - 376, paper IAEA-CN-45/52

Difilippo F C, Gambill W R, Moon R M, Primm R T and West C D (1986)
"A Preliminary Reactor Design for the Center of Neutron Research"
Nucl. Inst. Meth. A 249, p. 58 - 65

Gambill W R (1986)
"Thermal-Hydraulic Constraints on Water-Cooled Research Reactor Performance"
Nucl. Inst. Meth. A 249, p. 53 - 57

Kley W and Bishop G R (1985)
"The JRC Proposal for a European Fusion Reactor Materials Test and Development Facility"
Proceedings of the Eighth Meeting of the International Collaboration on Advanced Neutron Sources (ICANS-VIII), 8 - 12 July 1985, Rutherford Appleton Laboratory, report RAL-85-110, p. 100 - 137

Konoplev K A (1986)
" High Neutron Flux Research Reactor PIK"
Report IAEA Consultative Meeting on "Properties of Neutron Sources and Nuclear Data", Leningrad, June 9 - 13, 1986

Lake J A, Parsons D K, Liebenthal J L, Ryskamp J M, Fillmore G N and Deboisblanc D R (1986)
"Ultrahigh Flux Research Reactor Design Probing the Limits of Fuel Plate Technology"
Nucl. Inst. Meth A 249, p. 41 - 52

Moon R M (1985)
"A Review of Current and Proposed Reactor Upgrades"
Proc. Conf. "Neutron Scattering in the `Nineties", IAEA, Vienna 1985, p. 119 - 134, paper IAEA-CN-46/28

Powell J R, Takahashi H and Horn F L (1986)
"High Flux Research Reactor Based on Particulate Fuel"
Nucl. Inst. Meth. A 249, p. 66 - 76

Schaffer G, ed. (1981)
"An Isochronous Pulse Compressor Ring for Proton Beams"
Jül-Spez-114, Juni 1981, KFA Jülich

Scherm R and Alefeld B (1985)
"Instruments for High-Flux Sources with Time Structure of Neutron Flux"
Proc. Conf. "Neutron Scattering in the `Nineties", IAEA, Vienna 1985, p. 247 - 259, paper IAEA-CN-46/80

Schulke A W, Jr. (1985)
"IPNS Enriched Uranium Booster Target"
Proceedings of the Eighth Meeting of the International Collaboration on Advanced Neutron Sources (ICANS-VIII), 8 - 12 July 1985, Rutherford Appleton Laboratory, report RAL-85-110, p. 231 - 238

Reactor concept	CNR Baseline	CNR Enhanced	UHFR ("double donut")	HEPBR ("particle bed")
Peak thermal flux ($cm^{-2}s^{-1}$)	$5 \cdot 10^{15}$	$1 \cdot 10^{16}$	$1.1 \cdot 10^{16}$	$6 \cdot 10^{15}$ ($1.2 \cdot 10^{16}$)
Thermal power (MW)	135	270	355 → 300	163 (350)
Fuel enrichment (% U-235)	93	93	93	20
Type of fuel	U_3Si_2	U_3Si_2	U_3Si_2	UO_2
Core volume (l)	35	35	50	27.6 (35.3)
Core fissile loading (kg)	18	18	26.5	≈ 2
Plate thickness (mm)	1.27*1	1.27*1	0.89*1	≈ 0.75*4
Coolant channels (mm)	1.27	1.27	0.76	---
Peak heat flux (MW/m^2)	9.77	19.55	13.5	
Coolant velocity (m/s)	27.4	27.4	16	
Coolant flow (l/s)				400 (580)
Coolant pressure*2 (bar)	55.7	55.7	41	80 (100)
Pressure drop*3 (bar)	13.7	13.7	7	6 (15)
Coolant exit temp. (° C)	70.6	91.7	123	130 (180)
Reactor cycle length (d)	23	14	14	2 (1)*5

*1 including 2·0.25 mm cladding; *2 at core inlet; *3 across core only; *4 particle diameter; *5 continuous refuelling desirable.

Table 1 Some characteristic data of proposed advanced US beamhole reactor concepts. The coolant is D_2O in all cases.

Reactor	HFR, ILL	PIK	FRM-II	CNR (Design 25)	(UHFDD) UHFR	Dim.
Max. thermal flux Φ_{th}^{max}	1.5	1.3	0.8	10	10	$x10^{15}$ $cm^{-2}s^{-1}$
Thermal power	57	100	20	270	355	MW
Av. power density	1.15	2	1.18	7.7	8.9	MW/l
Power peaking factor	2.9	2.1	< 3	1.6	1.5	---
Core dimensions $R_a/R_i/H$	19.5/14/80	19/6/50	10.8/6.7/70	22/7/35	21/5/2x15	cm/cm/cm
U-235 loading	8.6	27.5	6.64	18	26.5	kg
Fuel	UAL_x	UAL_x (?)	U_3Si_2	U_3Si_2	U_3Si_2	---
Enrichment	93	90	93	93	93	%
Coolant	D_2O	H_2O	H_2O	D_2O	D_2O	---
Pressure (outlet)	---	4	---	4.1	3.4	MPa

Table 2: Selected Reactor Parameters

Accelerator:

Maximum energy 600 MeV
Proton macropulse duration 100 μs
Injection: dc-preacceleration to 750 keV
100-600 MeV: disk-and-washer, 1000 MHz
Total power consumption 25 MW

Repetition rate 100 Hz
Peak proton current 50 mA
750 keV-100 MeV: Alvarez structure 200 MHz
Active time of rf-structure: 200 μs/pulse

The proton pulse regrouper: Ring equipped with a 200 MHz rf-cavity

Mode of operation	pulse duration	rep. rate	Protons per pulse
40 buckets filled	200 ns	100 Hz	$3x10^{13}$
1 bucket filled	5 ns	100 Hz	$7.5x10^{11}$
4 buckets filled	5 ns	400 Hz*	$7.5x10^{11}$
4 x 5 buckets filled	25 ns	400 Hz*	$3.75x10^{12}$
5 linac pulses stored	200 ns	1 Hz**	$1.5x10^{14}$

* storage and pulse-by-pulse extraction
** limited by activation of ring, because losses are more serious in storage mode than in compression mode

Table3: THE MOSCOW MESON FACTORY AT TROITSK

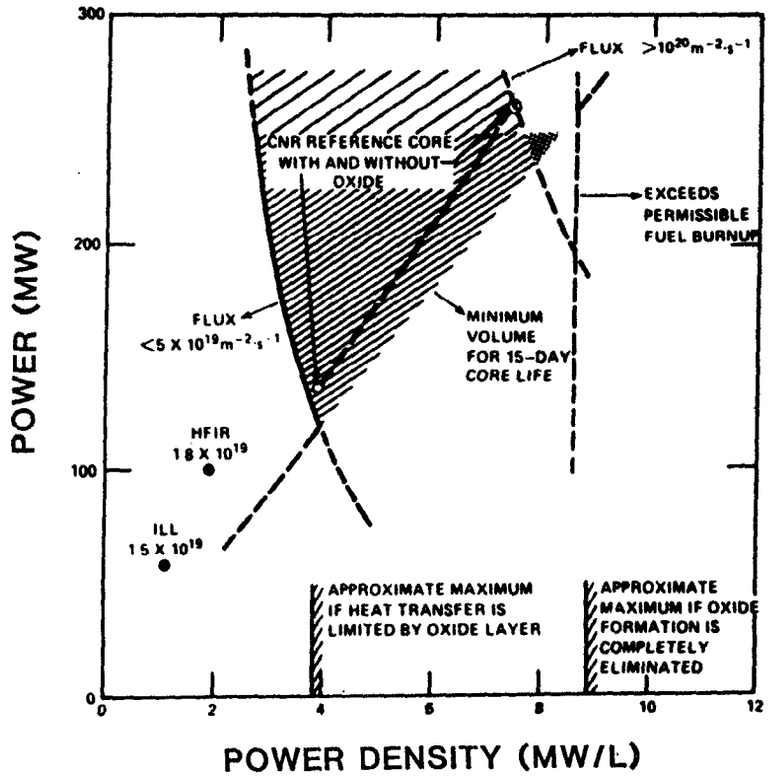

Fig. 1 Constraints for the power density for 30 vol % of U_3Si_2 fuel in an aluminium matrix with aluminium cladding. The request to have a minimum of 15 days core life leads to a minimum volume required to accommodate the necessary fissile material at a given volume fraction. Together with the operating power this determines a maximum allowable power density. Other constraints see text (from Difilippo et al, 1986).

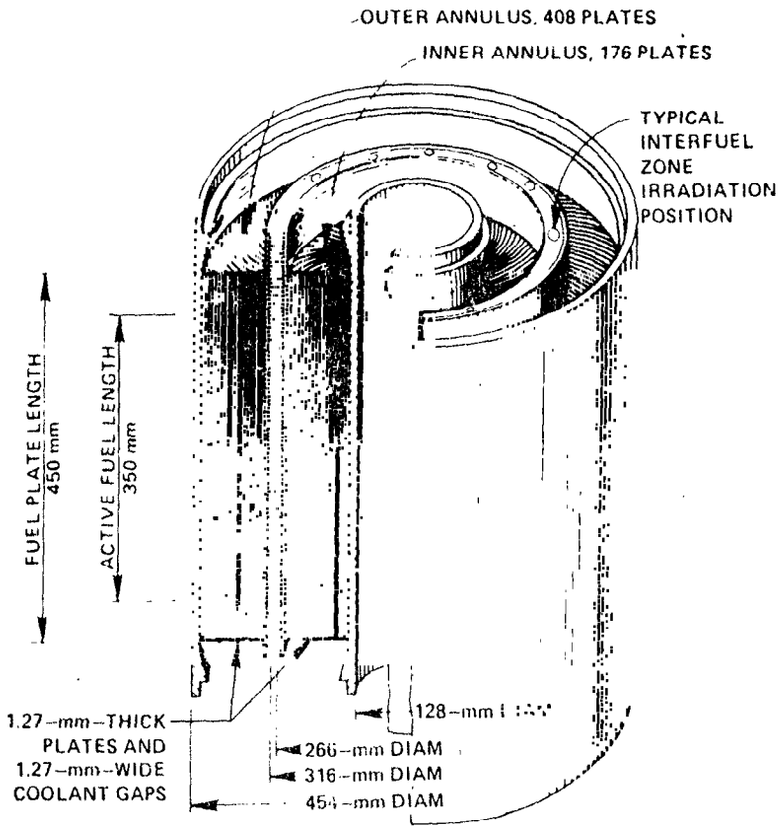

Fig. 2 Schematic of the CNR fuel element proposed by the Oak Ridge design team. The design is based on the present HFIR fuel element with irradiation positions located between the two annular fuel zones (from Difilippo et al, 1986)

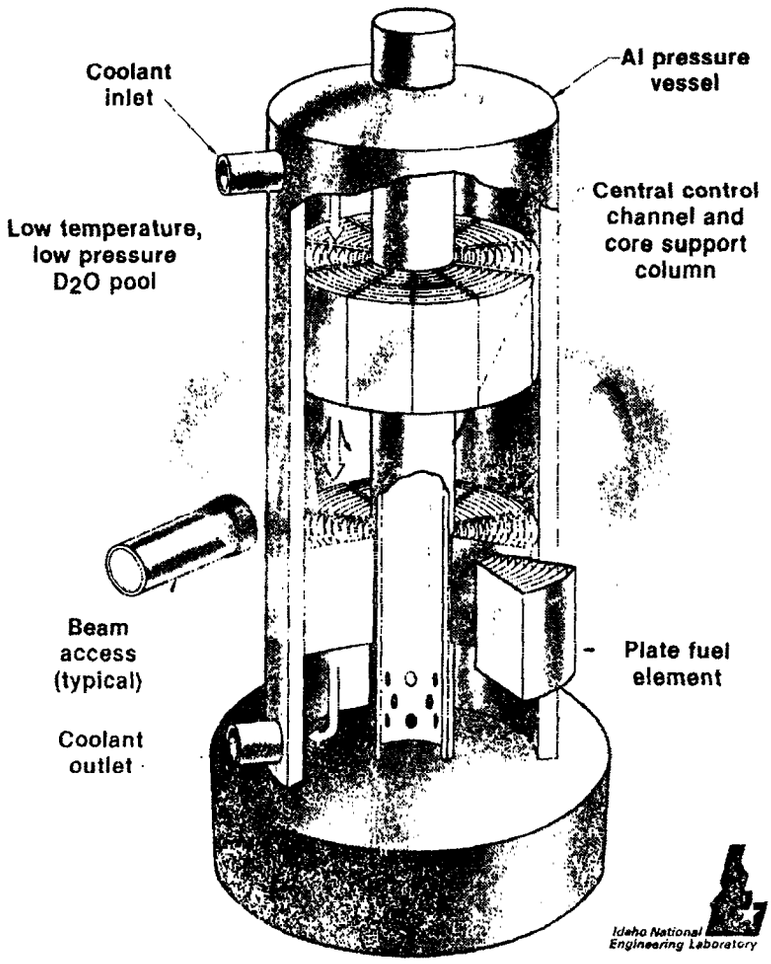

Fig. 3
The "double donut" core concept developed at the Idaho National Engineering Laboratory for an Ultrahigh Flux Reactor (from Lake et al, 1986).

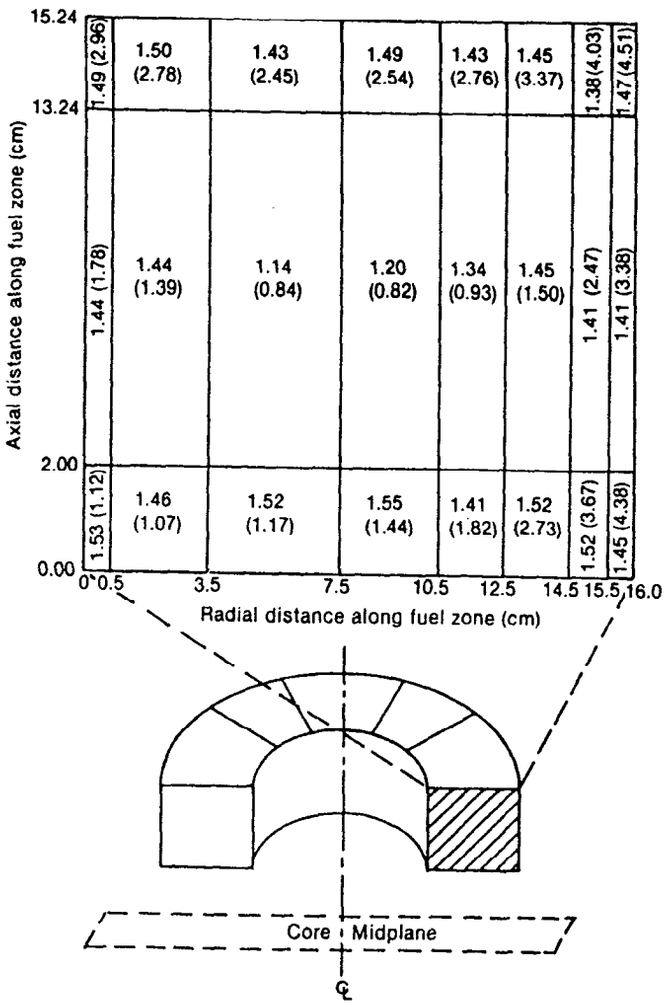

Fig. 4
Power peaking factors for the core design of fig. 3 for the cases with variable and (in parentheses) with uniform fuel loading. Fuel loading is varied both, axially and radially (from Lake et al, 1986).

Legend

1.38 = F_R^N with variable U^{235} loading

(4.03) = F_R^N with uniform U^{235} loading

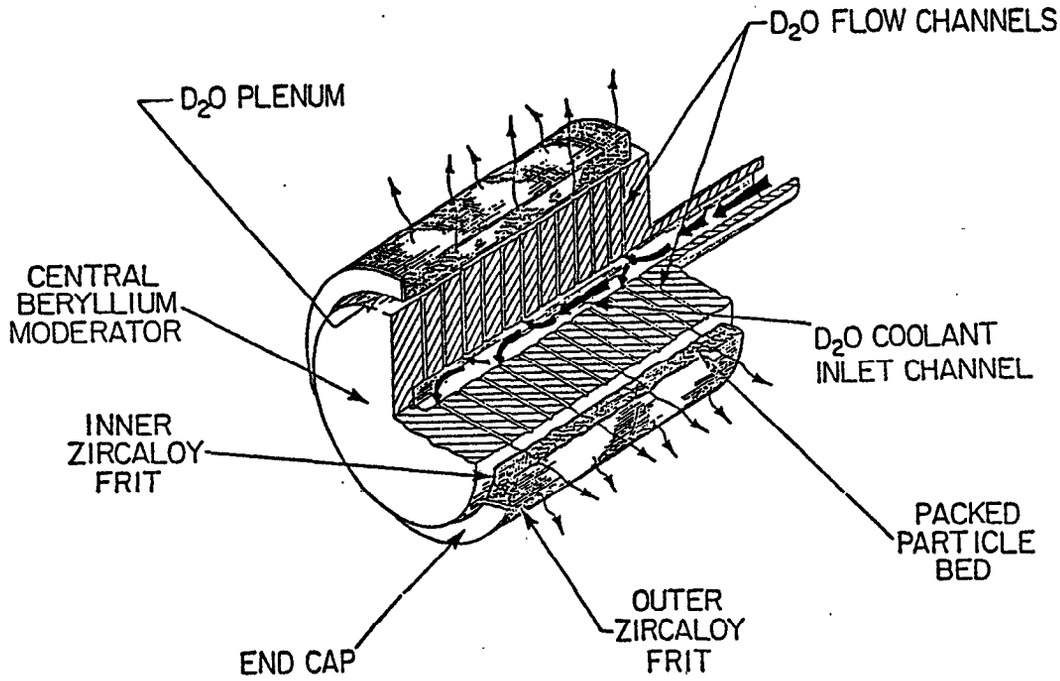

Fig. 5 A conceptual design for a High Flux Pebble Bed Reactor (HFPBR) proposed by Brookhaven (from Powell et al, 1986).

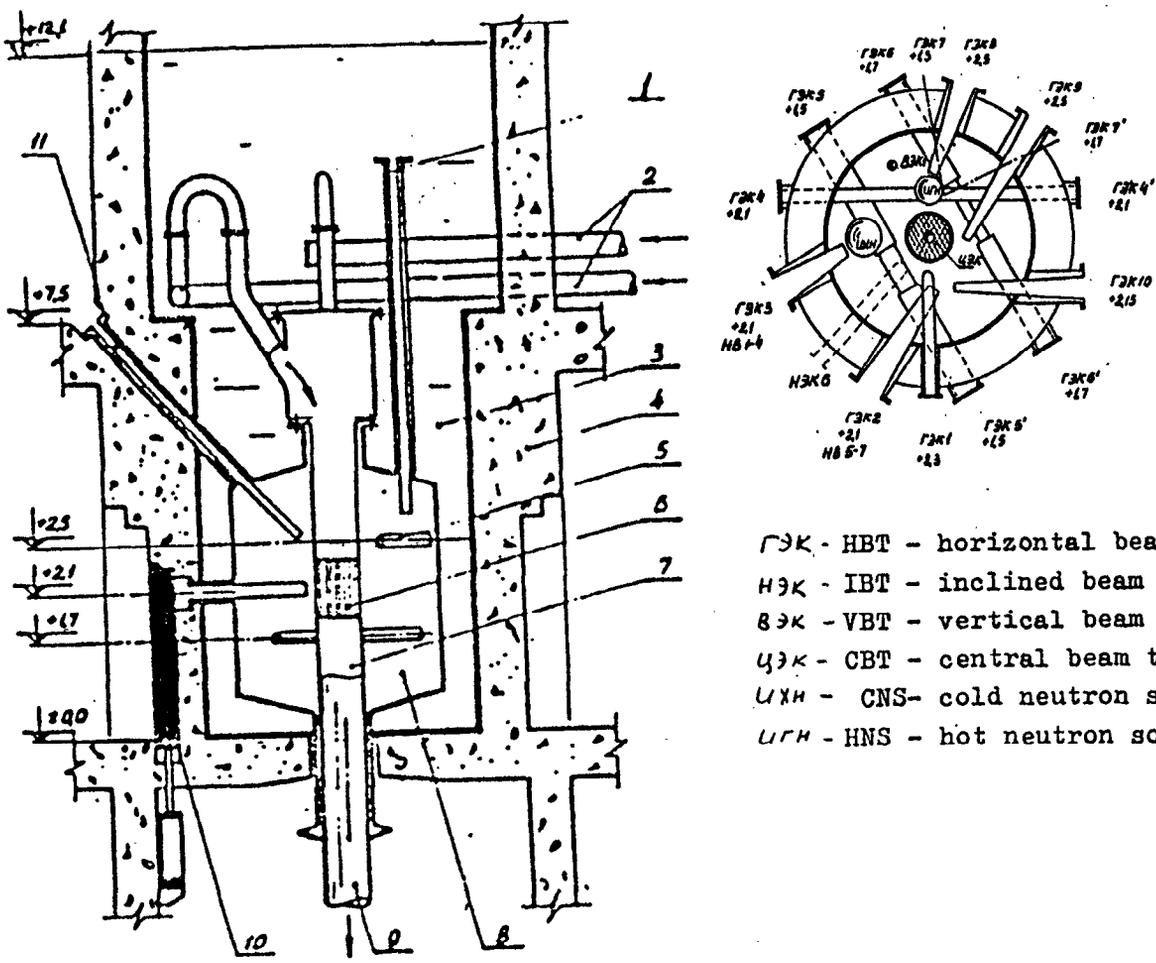

Fig. 6 The PIK reactor (schematic) under costruction at Leningrad (from Konoplev, 1986).
1- vertical tube; 2- coolant inlet; 3- well with water; 4- biological shielding; 5- horizontal beam tube; 6- core; 7- replaceable vessel; 8- heavy water reflector; 9- coolant outlet; 10- gate; 11- inclined beam tube. Given on the left are distances from experiment floor in meters.

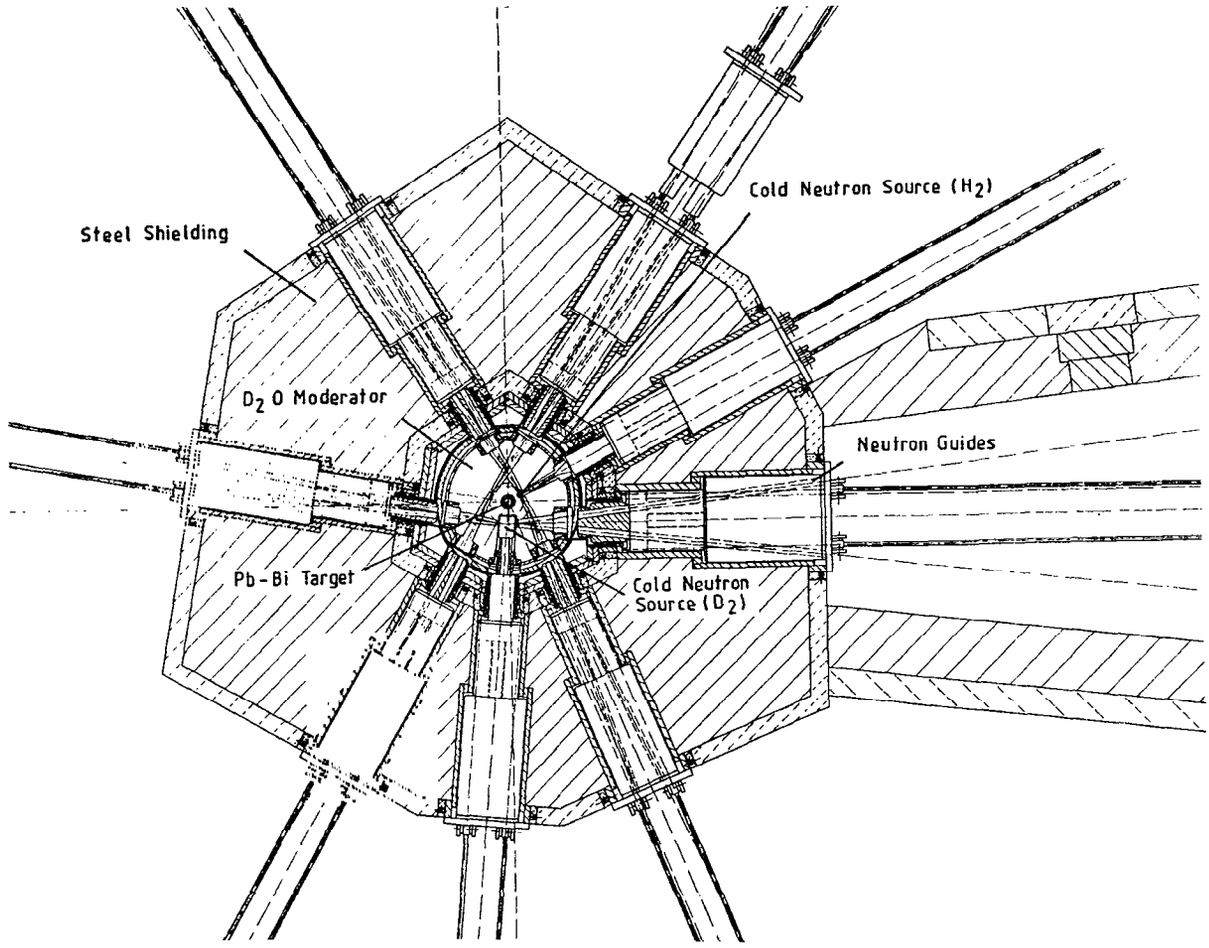

Fig. 7 Horizontal section through the target station of SINQ. A large D_2O tank surrounding the cylindrical target and in which the beam tubes end will accommodate two cold neutron sources

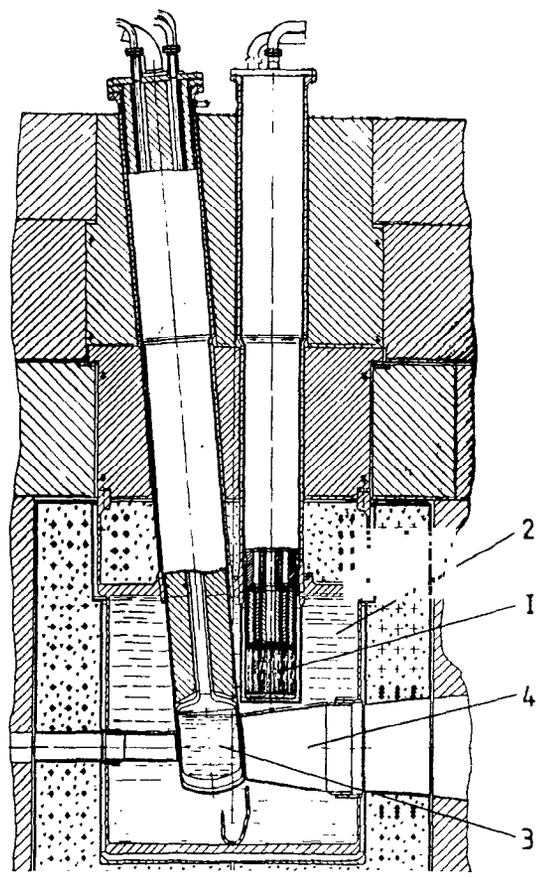

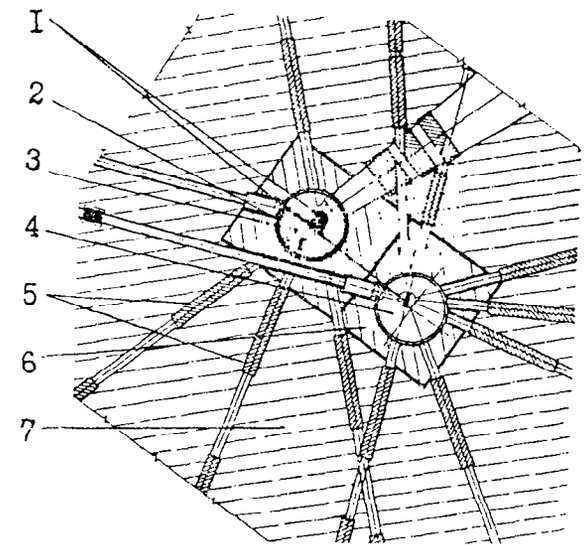

1 Neutron target
2 Heavy water vessel
3 D_2 - cold source
4 Vacuum vessel
5 Beam ports
6 Thermal shield
7 Heavy concrete block

Fig. 8 Target station of the Moscow Meson Factory spallation neutron source. (from Bulkin et al. 1985).

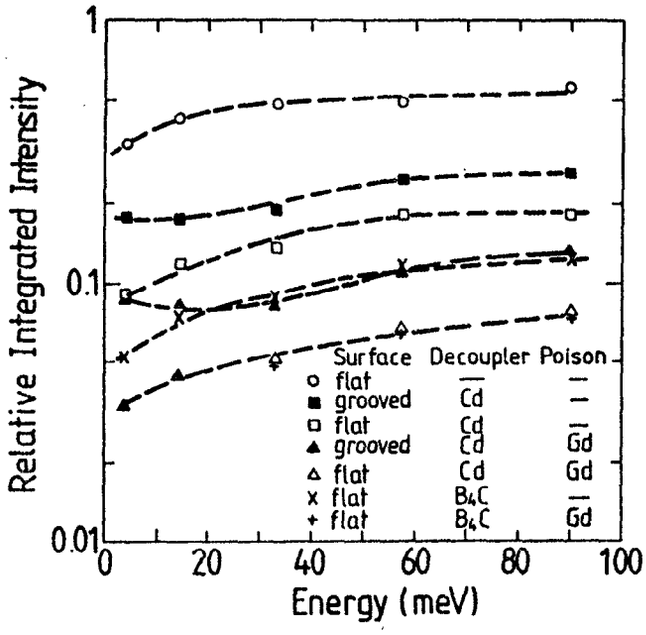

Fig. 9 Tradeoffs in integrated intensity resulting poisoning and decoupling the moderator for short thermal neutron pulses. The reference value (1) is the intensity obtainable from a well coupled moderator as proposed for the German SNQ-project (from Bauer et al, 1985).

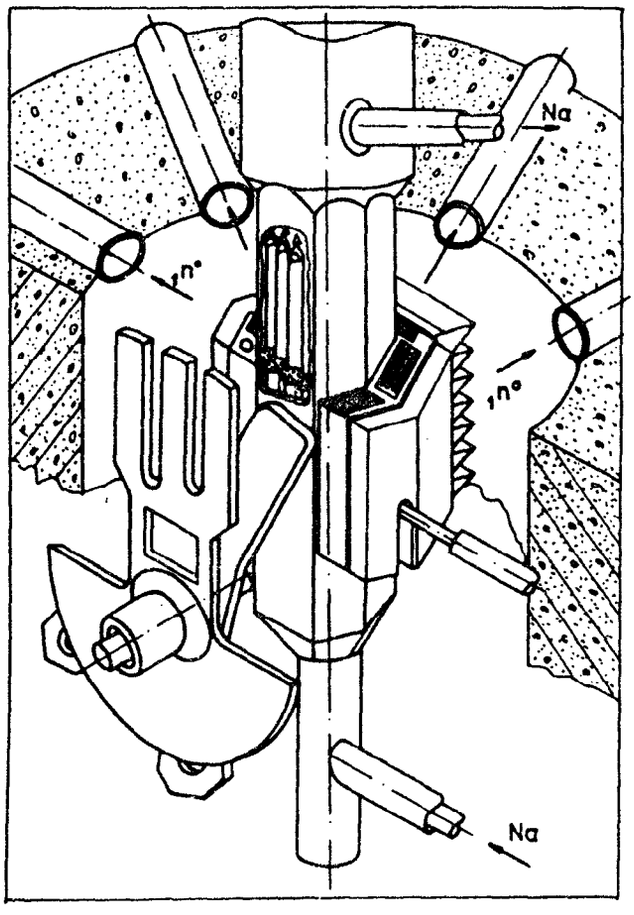

Fig. 10 Schematic of the IBR-II core region (from Ananiev et al, 1985).

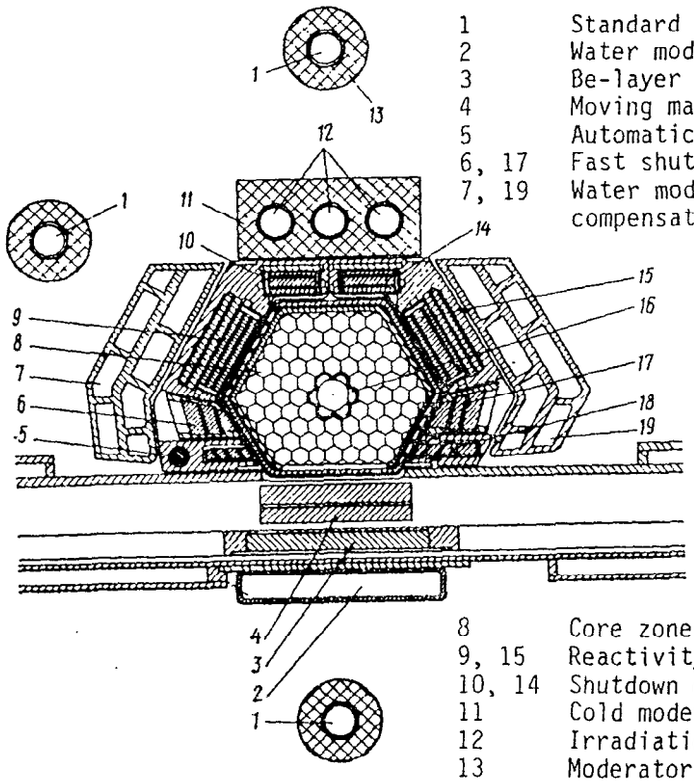

1	Standard fission chamber
2	Water moderator for moving reflector
3	Be-layer of the auxilliary reflector
4	Moving main reflector
5	Automatic control rod
6, 17	Fast shutdown equipment
7, 19	Water moderator for reactivity compensator
8	Core zone (PuO_2-fuel elements)
9, 15	Reactivity compensator
10, 14	Shutdown equipment
11	Cold moderator mockup
12	Irradiation positions
13	Moderator for standard fission chambers
16	Central irradiation position
18	Intermediate control equipment

Fig. 11 Horizontal section through the IBR-II core region

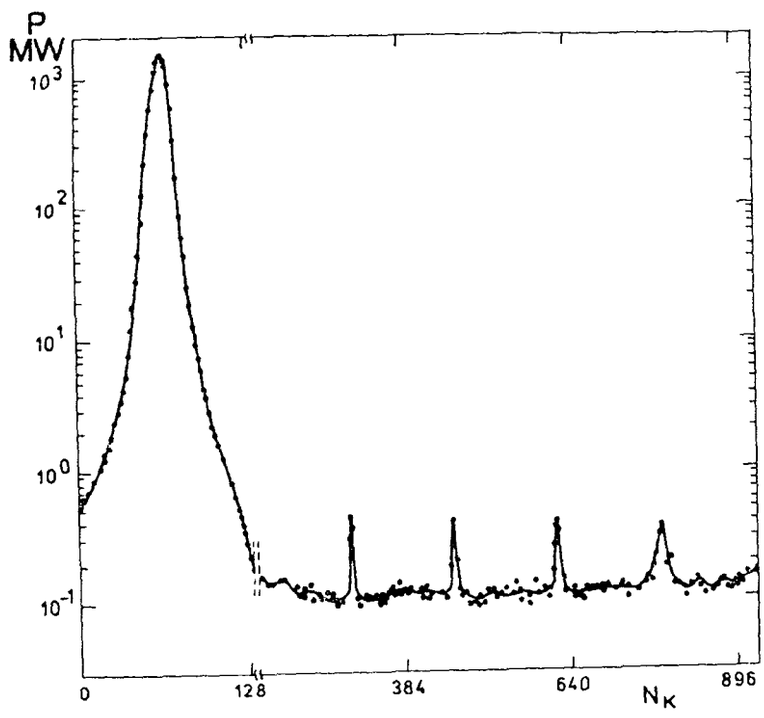

Fig. 12 Time structure of the IBR-II reactor power spectrum. In the Interval 0 - 128 the scaling is 32 μs/channel, in the later ones - 256 μs/channel. The narrow peaks on residual background result from the fast main reflector. (From Ananiw et al, 1985)

ICANS IX

INTERNATIONAL COLLABORATION ON ADVANCED NEUTRON SOURCES

22-26 September, 1986

COMMON PROBLEMS

A D Taylor

Rutherford Appleton Laboratory, Chilton, Didcot, Oxfordshire UK

INTRODUCTION

The ICANS collaboration has provided an excellent forum for the discussion of problems common to the development of spallation neutron sources for condensed matter research. The growth in the volume of each subsequent proceedings stands as a testimony to its usefulness for sharing information, much of which would be inappropriate to publish elsewhere. The ICANS meetings in particular provide an opportunity to discuss the neutronic and engineering aspects of target-moderator systems, source-instrument interactions, beam quality effects and novel neutron scattering instrumentation and techniques (especially those concepts unique to pulsed sources). The following summary of recent and potential problem areas may be regarded as a personal agenda for future ICANS meetings.

ACCELERATORS

The accelerators used are sufficiently different to make this the least common aspect. However, some problems are general, such as beam loss, activation of components, and the need for remote handling. Such problems will ultimately limit the performance of each accelerator.

TARGETS

The debate between non-fissile targets, fissile targets and ultimately boosted targets is far from reaching a consensus. It may be that fissile and boosted targets are appropriate only on low current sources. Non-fissile targets on present and projected sources are still a long way from their thermo-mechanical limit, although some limiting problems may soon be encountered in the design of the proton beam window. Fissile targets have been designed for 200 μA operation, but the acceptability from an instrumental point of view of the contamination due to delayed neutrons has not yet been fully evaluated. It may be necessary to employ background-suppressing choppers buried deep in the bulk shield to minimise delayed neutron contamination. Booster concepts are in their infancy and metallurgical problems have been encountered even for low current (10 μA) designs. It is probable that a fuel validation study would be required before a highly enriched, high power booster could be operated; some indications already exist from SNQ studies at LAMPF that the irradiation damage behaviour and embrittlement in proton beams is significantly different from that in high neutron fluxes.

MODERATORS

Ambient temperature water moderators and 100 K liquid methane moderators perform well physically and are well understood neutronically. The neutronic behaviour of liquid hydrogen moderators is not so well described and an experimental and computational programme to study their behaviour would be appropriate. Low temperature solid methane is a significantly better moderator than liquid hydrogen but, for radiation damage reasons, can only be used on low-power sources. The development of a good high hydrogen density, low temperature moderator for use on intense sources would be a major advance. The use of polyethylene or solid methane slurrys suspended in flowing liquid hydrogen has been suggested, but feasibility studies of the cryogenic engineering have not been carried out.

INSTRUMENTS

The first generation of pulsed source **spectrometers** were in general analogues of existing reactor-based instruments. Several new and innovative designs have emerged but, as the SNQ study showed, there are many advanced concepts involving focusing and phase space transformations which remain to be evaluated. The need still remains for low-cost,low-noise, multipixel **detectors. Data acquisition systems** need to respond to the trend towards high data-rate multidetector arrays. Systems using 2 MBytes are currently in operation, but there is already a need for 20 MByte memories. With such large data arrays, sophisticated analysis 'on the fly' becomes almost essential. **Sample environment** development projects have traditionally been underfunded, and would probably yield a significant return on investment by opening up new areas of physics, particularly in the field of high pressure studies.

CONCLUSION

There are sufficient problems common to our various laboratories to guarantee the need for many future ICANS meetings !

ICANS IX

INTERNATIONAL COLLABORATION ON ADVANCED NEUTRON SOURCES

22-26 September, 1986

SUMMARY OF WORKSHOP ON TARGETS.

J.M. CARPENTER

Gary Russell and I were co-chairmen of the session on Targets and Moderators held on Tuesday. I thank Tim Broome and Dave Picton for recording summaries of the discussion and the contents of the talks. We divided our discussions into two halves; target systems and moderator systems. For the target session we had three reports, one on the LANSCE target system by Gary Russell, another on the ISIS target cooling water activation by Tim Broome and a third by Fritz Takeda on the SINQ target thermofluid dynamics.

I just want to summarise some of the points that came up and invite you all to comment further. I have actually a second motive in making this summary: to get people to commit themselves to collaborate on several of these matters - that is another function of these ICANS meetings. I shall start by relating some of the issues raised.

One of them has to do with the method of cooling decouplers, particularly boron and lithium which capture neutrons by (n, α) reactions and therefore deposit heat locally at the site of the neutron interaction (compared to the broader distribution for gamma capture). We need to have better information on the relationship of heating (say) to proton beam power on the target, and on that basis to devise methods for cooling these decouplers (which we can at least imagine will get rather warm). I don't think that we have much data on this. The burden may lie on the Target/Moderator/Reflector designers simply to work it out by a combination of calculation and measurement. I hope that by the time we meet again, we will have more information on decoupling materials and their cooling in particular.

Gary Russell showed some calculated results that more or less confirm a trend to decouple at lower and lower energies. One of the first thoughts which Günter Bauer has disabused us of is to decouple moderators from their surroundings at some very high energy, like a keV, just to guarantee that the pulses will be unbroadened due to interaction with the reflector. As time goes on, we decouple at lower and lower energies (we abort fewer neutrons), but we still have not fully gone over to Günter's point, namely, "To use all the neutrons, don't throw any away".

There was another set of issues raised, namely - What are appropriate coolants for high power (fixed) targets? Water (H_2O) is a convenient coolant but in booster targets this extends the response time, so that we are led to think in terms of D_2O. Both have similar heat transfer properties, although D_2O is about 10% worse than H_2O. It's actually in some way contrary to what we think, that D_2O is a good moderator; it's only good when we have huge volumes used as a coolant. Where volumes are tiny (the ISIS target is cooled with D_2O) it is an inferior moderator and leads to shorter response times. I don't think that this issue is so important in a non-multiplying target.

A further question arises: If we push harder and harder on power densities, when is it necessary to go away from water as coolant and adopt, for example, liquid sodium or sodium/potassium eutectic? Günter Bauer has done some analysis of this kind and in the IPNS-II design (pursued long ago) the target was intended to be cooled by Na-K eutectic. The next stage questions that apply to even higher power densities are: When is it necessary to move the target material? When can we no longer get away with keeping it one piece standing still? The SNQ wheel-design is one method of moving the target material and spreading out the heat, the SINQ naturally-circulating Pb/Bi eutectic is another. So there are the questions: at what level of beam power must you go from one technology to another (or when must one cooling method be given over in favour of a more difficult one) and when must fixed targets be replaced by moving targets? Eventually, I think, we will have a more general understanding of this, but just now it's an issue that lies before us.

Further, when we address sources of higher power, comes the question in solid target materials of the levels at which thermal elastic shock becomes an important problem. We are capable of delivering pulses that are much

shorter than the sound transit time across a typical dimension of a target. When a significant amount of heat is delivered (either uniformly or non-uniformly) to a part (say a disk in a fixed target), it will want to expand, but it cannot in the time that all the energy is delivered, so that after the heating impulse a sound wave will propogate and ring within the part. This gives rise to a number of stress cycles. The question is, when does this thermal elastic stress wave become significant in determining the performance of target parts, not only fuel parts but also windows? There have not been many analyses which relate to our particular technology.

> *A point raised in discussion concerned the problem due to stress cycling from irregularities in accelerator operation or from heat-up and cool-down. This was not considered to be a problem and anyway can be estimated by standard methods. It was suggested that it is relatively benign. We were reminded that the thermal stress is at its maximum in the steady state.*

We surfaced the issue of radiation damage in target parts and windows. A window test has been made in a collaboration between SIN and LANL. There is the question, what does a good window look like and how long will it last? Another problem we are now addressing in the IPNS booster target design is how to characterise the radiation and thermal cycling growth in uranium targets. The IPNS booster target uses the (anisotropic) α-uranium. Might it be better to go over to the cubic gamma stabilised phase? In practical materials with some preferred orientation among the grains - α-uranium grows in a preferred direction and shrinks in another - if the grains are not randomly orientated there will be large scale growth in a particular direction. A related point is that non-uniform irradiation will lead to localised growth and hence stress. This leads to - How do radiation and thermal cycling growth for our temperatures and our alloys depend on stress? This is a highly qualified question, and I think beyond us to answer: somehow we need to learn something about this.

Gary Russell has developed a very innovative split-target design. The basic motive is to provide a region that one can look into through the neutron beam holes, behind which there is no target (source of very high energy neutrons). An early question was whether the presence of this void between the moderators causes significant pulse broadening. This issue has

been resolved by the results of various studies that Gary Russell has shown. The void does not significantly broaden the pulse.

In connection with this split target design, we need better understanding of how the moderator couples to the primary neutron source. To get neutron beam currents in absolute terms in relation to proton beam currents maybe not so difficult but you cannot just do measurements cavalierly. I tried them at Argonne and we were left with an uncertainty of a factor of 2; the lower limit says the calculation is good, the upper limit says the calculation is a factor of two too low. We found problems due to collimation elements in the beam lines which were misaligned (makes the measured neutron intensity lower), but somewhere there are still errors in our measurements which have not yet been traced. We should remember that both measurement and calculation are very difficult; the success rate for Monte-Carlo is very low.

The following points arose in a general discussion:

- *No real problem (excepting blunders in the representation!) come from the Monte-Carlo modelling. Mostly a reasonable approximation to the geometry will do.*
- *Proton beam measurements should be able to be made to 10% or better.*
- *It was suggested that maybe the neutron part is perhaps the easier of the two. Care has to be taken to ensure that the proton beam current measurement determines what actually strikes the target. In the early days at ISIS, 50% changes were found in the number of neutrons per proton. This was cleared up with a better monitor of what goes onto the target.*
- *Gary Russell said that (despite several difficulties) they were planning a measurement of the LANSCE system in the very near future.*

One of the motives for the split-target is to produce a lower background of the very high energy neutrons. Somehow one needs to know the extent

to which this design really works. It's rather difficult to make the comparison between this target and a solid target, nevertheless it would still be interesting to know if the flux trap geometry does work to produce a low background of very high energy neutrons. A secondary question: here is this hole - should we leave it empty or put something in there? If you put in tungsten or uranium it's no longer a split target! But what about D_2O or beryllium, is this good or harmful? There are questions of how to cool it. That would be an interesting study! Another question for split targets is, should the pieces be of the same material? (eg the front half [where the power density is the highest] of tungsten and then use a high gain material [like Uranium] at the back). These are the questions which it would be hoped would be answered by the time of the next ICANS.

There are some resolved issues. We know that the split targets are feasible: maybe there were no doubts, but now there has been one run, we know it works! The question of the pulse broadening (I say) has been resolved by Gary's calculations. In a separate report, we found that codes now exist to calculate satisfactorily the activity in water coolant and in fact in complex loops of cooling systems; that has been checked out on ISIS and the procedure seems to work. Fritz Takeda showed great progress on the understanding of the systematics of naturally circulating liquid metal target systems. There have been new methods developed which are being employed to refine the design, so that is a resolved issue, but there are still many unresolved design questions.

ICANS IX

INTERNATIONAL COLLABORATION ON ADVANCED NEUTRON SOURCES

22-26 September 1986

THE LANSCE TARGET SYSTEM

G. J. Russell, H. Robinson, G. L. Legate, R. Woods, E. R. Whitaker,
A. Bridge, and K. J. Hughes

Los Alamos National Laboratory
P.O. Box 1663
Los Alamos, New Mexico 87545 U.S.A.

and

R. D. Neef

Institüt für Reaktorentwicklung
KFA, D-5170
Jülich, West Germany

ABSTRACT

During the summer of 1985, we replaced the WNR T-shaped target/moderator scheme with the LANSCE split-target/flux-trap-moderator design. The intent of this 'LANSCE upgrade' was to increase (to 12) the number of neutron beam lines serviced simultaneously, and to enhance the target area shielding and target system to accept 200 μA of 800-MeV protons. The four LANSCE moderators consist of three (chilled) water moderators, and a liquid hydrogen (20 K) moderator. The LANSCE target is machinable tungsten.

INTRODUCTION

The Los Alamos Neutron Scattering Center (LANSCE)[1] consists of the Proton Storage Ring (PSR)[2], and the high-current target area of the 'old' Weapons Neutron Research (WNR) facility[3] (see Fig. 1). As can be seen in Fig. 1, the LANSCE target area has vertical proton insertion; the layout of the neutron flight paths is shown in Fig. 2. This particular combination of vertical proton insertion and four flight path clusters at 90 degrees to each other (three flight paths per cluster) provides peculiar challenges for target/moderator design. Our split-target/flux-trap-moderator concept (see Fig. 3) provides an innovative and excellent solution to these particular design constraints. The four flux-trap moderators shown in Fig. 3 exist; the two 'future' upper moderators (depicted in wing-geometry) will accommodate additional flight paths constructed specifically to service the new expanded experimental hall.[1] We will do further studies to determine if the upper moderators should be in wing- or slab-geometry.

The LANSCE target system has four unique features:

- There is **no crypt** per se (a void region) surrounding the target-moderator-reflector-shield (TMRS).

- The target is **not in one piece**, but is split into two unequal segments separated by a void.

- Moderators are **not** located adjacent to the target as in conventional wing-geometry design. In the LANSCE TMRS, moderators are located between the target elements next to a void region (flux-trap) between the target elements.

- A conventional all beryllium reflector is **not used**; instead, a composite beryllium/nickel reflector/shield is employed.

For ease of installation and to retain flexibility, we built the LANSCE TMRS in two distinct sections: a) an inner region housing the targets, moderators, and the start of the beryllium/nickel reflector/shield, and b) an outer nickel reflector/shield zone. We cool both regions with light water.

When a reflector is used to enhance neutron production, there is no reason to surround the reflector with a void region. This space is better utilized for shielding purposes. For the LANSCE upgrade, we removed everything from the 2-m-diam by 2-m-high WNR crypt[3], and reinstalled the LANSCE TMRS plus additional iron shielding in the forward, backward, and radial directions. By using a split-target with four moderators around the void region between the targets, we are able to neutronically service all 12 LANSCE flight paths simultaneously.

The layout of the LANSCE flux-trap moderators is further illustrated in Fig. 4. The poison defines an 'effective' volume for thermal or cold neutron production. The decoupler neutronically isolates a moderator from the reflector/shield. The liner eliminates neutron 'crosstalk' between the moderator surface viewed by a flight path and the reflector/shield. The energies at which poisons, decouplers, and liners are effective in tailoring neutron pulses depend on the material used. By employing various combinations of poison, decoupler, and liner materials, we customize the neutronics of each moderator to meet specific experimental requirements. By combining beryllium and nickel in a reflector/shield configuration, we enhance both our thermal neutron production and neutron shielding capabilities.[4]

We will now describe what we did during the LANSCE upgrade, review neutronic calculations done to support our liquid hydrogen moderator design, discuss our operating experiences with the liquid hydrogen moderator, and examine further improvements to LANSCE.

LANSCE UPGRADE

Shielding

Everything in the 'old' WNR crypt (including the borated water tank) was removed in preparation for the LANSCE upgrade. We enhanced the neutron shielding in the forward direction to the proton beam by installing a water cooled stainless steel shield designed to remove two kW of heat. Primary protons are completely stopped in the LANSCE TMRS, and do not contribute to this heat load. The stainless steel shield (shown in Fig. 5) was the first element installed in the LANSCE upgrade, and added about 50 cm of iron shielding. Besides this new shield component, the LANSCE lower tungsten target provides additional neutron shielding in the extreme frontal direction to the proton beam.

We also enhanced the neutron shielding in the backward direction to the proton beam. Progressing out from the TMRS center, this rearward shielding now consists of 30 cm of nickel (provided by the TMRS) and 150 cm of iron. We also have 10 cm of poleythylene above the iron layer to mitigate the 'iron window' effect. Cadmium (0.8 mm thick) is placed on the service cell side of the polyethylene to help reduce thermal neutron activation in the service cell. The service cell is the area above the TMRS that houses the 90-degree-bending-magnet assembly for the proton beam and various TMRS support and remote handling systems.

The shielding added in the radial direction (illustrated in Fig. 2 and shown in Fig. 6) consists of two parts: a) an iron layer 30 cm thick placed between the crypt wall and the LANSCE TMRS, and b) the TMRS itself. In the TMRS, the nickel layer not only serves as a neutron shield, but is also an integral part of the reflector system. The overall radial thickness of the nickel in the TMRS is 30 cm. The composite beryllium/nickel reflector/ shield is neutronically better (in the 10-20% range) for thermal neutron

production than an all beryllium reflector,[4] with the added benefit of the additional shielding provided by the nickel. The inner portion of the TMRS is shown in Fig. 7.

The shielding enhancements described above were designed to allow for LANSCE operation with 200 μA with 800-MeV protons.

Targets and Moderators

The LANSCE split target is shown disassembled in Fig. 8 and assembled in Fig. 9. The target consists of two solid pieces of tungsten surface-cooled with light water. The upper target is 10 cm in diameter and 7.25 cm long; the lower target is 10 cm in diameter and 27 cm long; the flux-trap region between them is 10 cm in diameter and 14 cm long. We designed the target to accept 100 μA of 800-MeV protons. The target is simple and relatively inexpensive to build. In Fig. 10, where we compare the LANSCE and ISIS[5] target designs, one can see how the basic neutron production advantage of depleted uranium (as in the ISIS target) compared with 'solid' tungsten, is significantly compromised in 'engineered' targets. This occurs primarily because the depleted uranium target must be severely segmented for cooling purposes, and each segment must be clad to contain fission products. Because of the necessity to deal aggressively with cladding and containment requirements, fission products, and potential radiation damage problems, a fissile target is much more costly to build and operate than a pure spallation target, such as tungsten or tantalum.

Light water (chilled to 10 C) was chosen for three of the four LANSCE flux-trap moderators, and liquid para-hydrogen at 20 K for the fourth moderator. The water moderators are kept chilled for better temperature stability. We chose liquid hydrogen for our initial cold moderator for the following reasons: a) the availability of local expertise in extensive use of liquid

hydrogen, b) access to a refrigeration system capable of meeting our needs, c) consideration of a properly developed liquid hydrogen moderator as a true high-power, high-intensity cold neutron source, and d) recognition that other practical cold moderator candidates, i.e., liquid and solid methane, being developed at other laboratories (ISIS,[6] IPNS,[7] and KENS[8]) may suffer from radiation damage at high-power (>100 μA) operation.

The physical moderator sizes and our choices of poisons, decouplers, and liners are summarized in Table I. We designed two of our water moderators for high intensity and moderate resolution by placing a gadolinium poison layer at 2.5 cm from the output face, and using cadmium decouplers and liners. We designed the third water moderator for high resolution by placing gadolinium poison at 1.5 cm, using elemental boron-10 as the decoupler, and employing a boral liner. The boron compounds decouple (1/e) at an energy of about 3 eV. For our initial liquid hydrogen moderator design, we are mainly interested in intensity and not too concerned with neutron pulse widths. Accordingly, we did not poison, decoupled with gadolinium, and used cadmium liners. Disassembled and assembled light water moderators are shown in Figs. 11 and 12, respectively. The liquid hydrogen moderator is shown in Fig. 13. Exclusive of the void region between the targets, there is about 10 cm of beryllium between the moderators and the nickel reflector/shield.

Support Systems

In addition to modifying the shielding and neutron production schemes, we also upgraded the LANSCE support systems. These support systems include the ventilation, moderator cooling, and target/reflector cooling systems.

Ventilation

During the LANSCE upgrade, we did not modify the ventilation scheme. However, we did recognize two potential changes: a) modifications will be required if a depleted uranium target is installed, and b) instead of evacuating the LANSCE crypt, we may want to fill it with helium. We presently evacuate the crypt to about 20 microns, and have found the crypt vacuum to be an extremely useful diagnostic for monitoring the integrity of the target system inside the crypt. We continually watch crypt vacuum, and have it tied into the LANSCE 'run permit'.

Moderator Cooling Loop

We designed this system to provide (chilled) 5 ± 0.3 C demineralized (processed) water to the moderator canisters, and presently operate the loop at a nominal 10 C. Except for the aluminum moderator canisters, the system has all stainless steel components, and is shown schematically in Fig. 14. We designed the loop to remove 4 kW of heat. The system volume is 1000 liters.

We maintain the moderator water temperature with a water cooled freon-12 chiller system to cool the 880 liter process water storage tank. A centrifugal pump circulates the processed water through a closed loop to the moderator canisters. In a bypass polishing loop, we flow 15 ℓ/min through a set of demineralizer resin beds to maintain a resistivity of about 5 megohms in the main loop. Makeup water is automically added to the storage tank from the LANSCE demineralized water supply.

Target/Reflector Cooling Loop

We have a separate system for cooling targets, reflector, beam stop, and 'future' high-power liners. This cooling loop is shown schematically in Fig. 15. We used all stainless steel components in the crypt, service cell, and beam channel areas. Because of cost considerations, we used some brass and copper components in the service area; these brass and copper components will be removed in the near future. We designed the system with the capacity to cool a 'future' depleted uranium target bombarded by 200 μA of 800-MeV protons; we can remove 500 kW of heat at a flow rate of 22.7 ℓ/s at a pressure of 100 psig. For a depleted uranium target, we will need multiple flow channels through the target and provisions for removing decay heat (see Fig. 15).

We built the system on four separate skids, and interconnected them with piping. The pump, heat exchanger, expansion tank, demineralizer, and valving are on skids in the service area. A valve gallery skid containing valves, flow, and pressure monitoring components is located in the service cell.

We circulate the water with a single 60 HP centrifugal pump to the valve gallery where it divides to cool all components. We monitor the input and output temperature, flow, and pressure for each of the three target cooling subloops. The target cooling circuit also contains provisions for a 'future' emergency decay cooling section using a pump powered by a motor-generator set. If necessary, this latter pump is backed up with the provision for single pass flow of industrial water. We monitor the output side of reflector, beam stop, and liners for temperature, flow, and pressure. The volume of the cooling system is about 1000 liters.

The system has an air separator for removing entrained air through a HEPA filter. We make the heat exchange through a plate type heat exchanger

cooled by facility tower water. Makeup water is added automatically from the LANSCE demineralized water supply. We strip off about 0.3 ℓ/s of water from the main flow, drop its pressure to 40 psig, and flow this bypass stream through a demineralizer tank containing a mixed resin bed and an oxygen scavenger resin. We continually monitor the resistivity and pH of the main cooling loop.

All flow circuits can be purged with dry helium to force the residual water into radioactive waste storage tanks. All skids have drip pans to catch and drain lost water into radioactive waste storage tanks. Water from the cooling system is routinely monitored for radioactivity by the Laboratory's Accelerator Health Protection Group.

TARGET/MODERATOR NEUTRONICS

The LANSCE neutron production scheme, consisting of a split-target with moderators located around the void space between targets, is **an unconventional spallation neutron source target system design.** We have had to convince both ourselves and our colleagues of the viability of this approach. Accordingly, we have done extensive Monte Carlo neutronic simulations of the LANSCE TMRS concept. We also have a comprehensive experimental effort to support our general understanding of spallation neutron source neutronics.[9-11] We combined both these endeavors to bolster the unique LANSCE TMRS design.

Split-Target Performance

We have gone through a comprehensive series of Monte Carlo neutronic calculations for the LANSCE TMRS. We were primarily looking for neutron

intensity shortcomings, and any degradation in neutron pulse widths due to the void space between the targets. Compared to a conventional wing-geometry system (where moderators are placed close to targets for 'good' geometric and neutronic coupling), the LANSCE TMRS appears to suffer a 15-20% reduction in thermal neutron intensity. This is an acceptable compromise for serving the twelve LANSCE flight paths simultaneously. In contrast to the aft moderators in a multi-moderator, wing-geometry design (where the forward moderator intensity is about twice that of the rearward moderators), **all LANSCE flux-trap moderators are 'high intensity'**. We see no evidence of any degradation in **thermal neutron pulse widths** from the LANSCE flux-trap moderators.

Water Moderator Neutronics

As can be seen in Fig. 16, flux-trap moderator performance is strongly tied to the thickness and type of liner (and decoupler) used. As a 'rule of thumb', one wants to get as much neutron intensity from a moderator as possible with little or no attendant degradation of the neutron pulse width. This is obviously an over simplification because it is an energy dependent consideration; we are concentrating on 'thermal neutrons' in Fig. 16. Referencing 1 cm of sintered $^{10}B_4C$ as a neutronically 'thick liner', one can get at least a factor of 5 relative increase in neutron intensity (without a neutron pulse width penalty) if a 0.05 cm-thick $^{10}B_4C$ liner is employed (see Fig. 16). The same effect can be achieved using 0.0762 cm (30 mils) of Cd.

The importance of a reflector in the LANSCE TMRS concept is also illustrated in Fig. 16, where it can be seen that the reflector enhances the thermal neutron production by about a factor of 100 compared to the 'no reflector' case. This relative gain is obtained by referencing the

intensity with a 1-cm-thick $^{10}B_4C$ liner (which essentially negates the effect of a reflector) to that of a liner of zero thickness (a coupled system). Such a large reflector gain does not occur for the T-shape, wing, and slab moderator configurations. For our two 'high-intensity' water moderators, we chose 0.0762 cm of Cd for both the decouplers and liners. For our 'high-resolution' water moderator we use elemental ^{10}B for the decoupler, and boral for the liner. The neutron decoupling energy for these two boron compounds is about 3 eV.

Overall moderator thickness determines epithermal neutron performance; we chose the thickness of our water moderators using the data given in Fig. 17. In this figure, we show 'figure-of-merit' (defined as neutron intensity divided by the square of the neutron pulse width) versus moderator thickness. Using the data in Fig. 17, we selected overall moderator thicknesses of 3.5 cm for two moderators, and 4.0 cm for the third. We would have made all three moderators 3.5 cm thick, but could not because of an early decision required on moderator field-of-view locations. This early determination was needed so that neutron collimation systems could be designed.

The poison material, thickness, and depth from the viewed surface determine the thermal neutron performance of a moderator. We chose gadolinium as our poison material; the thickness of the gadolinum poison ranges from 0.00381 to 0.00508 cm (1.5 to 2.0 mils). For the two high intensity moderators, we set the poison depth at 2.5 cm; for the high resolution moderator, the poison depth is at 1.5 cm.

As mentioned above, the effect of a reflector on enhancing moderator neutronics is **strongly dependent** upon the geometry of the target/moderator/reflector system. For our flux-trap system, the reflector enhancement is about 100! For wing-geometry, the embellishment is more like a factor of 3-4.[9] For slab-targets and slab/moderators[12,13] or a

hybrid system,[14] reflector augmentation of moderator neutron intensity is around a factor of 2. The reason is that **slab systems in general are intrinsically neutronically efficient**, and the addition of a reflector has a minimal (but significant) effect on moderator neutronic performance. The effects of a reflector and liner thickness on a hybrid moderator system are shown in Figs. 18-20.

Cold Hydrogen Neutronics

Monte Carlo techniques are generally used for doing the complex neutronic calculations required in spallation neutron source design. The complicated geometries of these sources are (more-or-less) adequately handled by Monte Carlo methods. However, it is not sufficient to just treat the geometry correctly; the physics of the problem (which is even more involved) must also be dealt with properly. The physics comes in via the neutron cross sections used. A particularly weak link at low energies is the availability and adequacy of scattering kernels to describe these cross sections.

This could be a particular problem for liquid hydrogen, where there may be serious deficiencies in pertinent data and adequate theoretical kernel formalisms. In particular, theoretical scattering kernels for liquid hydrogen should: a) model 'liquid' effects properly, and b) adequately account for the different cross sections of ortho- and para-hydrogen. We have not made any effort to find the most recent experimental data for liquid hydrogen cross sections or the latest theoretical kernel formalisms. Instead, we obtained from our Jülich colleagues[15] a **cold molecular-hydrogen gas** kernel formulated by Young and Koppel.[16] This kernel should be applicable to liquid hydrogen for input neutron energies above 7 meV. This latter qualification is not too comforting; however, the severity of the restriction depends on how important 'liquid' effects are below 7 meV in a

particular application. We implemented this kernel at Los Alamos and used it in all neutronic calculations supporting our liquid hydrogen moderator design.

As mentioned above, Young and Koppel (in 1964) published a formalism for calculating neutron cross sections for **cold molecular-hydrogen gas.** Their calculated total cross sections for both para-hydrogen and ortho-hydrogen gas at 20.4 K agreed reasonably well with the limited experimental data available at that time. Their calculated results and comparison with experimental data are shown in Fig. 21. A pronounced rise in the para-hydrogen cross section can be seen at roughly 10 meV. In their paper, Young and Koppel also gave a simplified cross section formalism where vibrations were not considered. It was this latter formalism which we received from our Jülich collaborators (in coded form) and implemented on the Los Alamos computers. In Fig. 21, we also show the cross sections as calculated at Los Alamos using the kernel obtained from Jülich. The difference between the results obtained using the approximate formalism compared to the more complete treatment, as calculated by Young and Koppel, are evident. The effect of these differences on an applied calculation of spallation neutron source neutronics is difficult to quantify.

The 'normal' concentration of hydrogen at 300 K is 25% para-hydrogen and 75% ortho-hydrogen; at 20 K the concentration is 100% para-hydrogen. If neutronically wise and physically possible, we would like to take advantage of the larger ortho-hydrogen cross section in designing liquid hydrogen moderators. Because of the rapid changes in the para-hydrogen cross section in the region around 10 meV, we binned the data from our Monte Carlo calculations into the following energy ranges: a) $E \leq 10$ meV, b) 10 meV $\leq E \leq 100$ meV, and c) $E \leq 100$ meV. By binning the results in these energy ranges, one should get a feel for the relative importance of para- and ortho-hydrogen cross sections on hydrogen moderator neutronics.

In Fig. 22, we show calculated results of moderator neutron leakage versus moderator thickness for two different para-hydrogen concentrations. The computations were for a coupled moderator, that is, no decoupler/liner. For 100% para-hydrogen and 'cold' neutrons (defined here to be neutrons with energies below 10 meV), the neutron leakage reaches a 'plateau' at a moderator thickness of about 3 cm. The maximum neutron leakage for 'epicold' neutrons (defined here to be neutrons in the energy range 10 meV $\leq E \leq$ 100 meV) is between 1 and 2 cm. The situation is somewhat different for the 'normal' (25% para- and 75% ortho-) hydrogen concentration where there is no plateau effect for the cold neutrons. For normal hydrogen, cold neutron leakage has broad maximum around 4 cm, and epicold neutron leakage peaks just below 1 cm. Note that the **maximum neutron leakage intensity** from a pure para-hydrogen moderator exceeds that from a normal hydrogen moderator! One must remember, however, that all hydrogen moderator neutronic calculations reported here use Young and Koppels' approximate **cold molecular-hydrogen gas** kernel at 20 K.

We show the same type of data for a decoupled system in Fig. 23. The gadolinium decoupler/liner was 0.00381 cm thick (1.5 mils). Comparing the data in Figs. 22 and 23, we see that the shapes of the curves are different for the coupled and decoupled cases. This just emphasises the complexity of what is going on in the physical process of producing cold neutrons. For these calculations, moderator neutron leakage is strongly dependent on the energy distribution of the neutrons 'feeding' the moderator. The differences in absolute neutron intensities between coupled and decoupled moderators (Figs. 22 and 23) are indicative of the penalties paid when neutron pulses are shaped with decouplers and liners. Using the data in Fig. 23, together with the criteria of keeping energy deposition minimal, we set the LANSCE liquid hydrogen moderator thickness at 5 cm. The calculated energy deposition in a coupled cold hydrogen moderator as a function of moderator thickness is depicted in Fig. 24.

In Fig. 25, we show neutron leakage versus para-hydrogen content for a 5-cm-thick decoupled and coupled hydrogen moderator. The neutron leakage intensities do not vary dramatically, have different shapes depending on whether the moderator is decoupled or coupled, and, for the decoupled case, are essentially flat. For a coupled moderator, our data show cold neutron leakage increasing linearly with para-hydrogen concentration. This is in slight difference to the results given in Ref. 17, which, for a coupled system, show an intensity peak at a hydrogen concentration of 90% para and 10% ortho. However, the referenced data do not vary by more than 25%, and quote neutron leakage intensities in the 5-6 Å range compared to our integral results which are for neutron wavelengths greater than 3 Å. Deviations in the details of data reporting probably account for the minor disparances between the two calculational results.

In Figs. 26 and 27, we show calculated neutron leakage intensities and pulse widths for a 5-cm-thick moderator; this is the thickness of the LANSCE cold source. The intensity penalty for using decouplers and liners is evident. However, the degradation in neutron pulse widths below the cutoff energy of the decoupler/liner (about 0.2 eV for the Gd used here) can be severe. Depending on the application, neutron choppers can be used to better shape the neutron pulses from a coupled moderator. In Figs. 26 and 27, there is very little difference in the energy distribution and intensity of neutrons from a 100% para-hydrogen moderator compared to a 25% par- and 75% ortho-hydrogen one. This is independent of whether the moderator is decoupled or coupled. This should not be too surprising because we deliberately chose the thickness (5 cm) of the LANSCE cold hydrogen moderator to minimize the effects of differing para-hydrogen concentrations. To take advantage of any gain attributable to ortho-hydrogen, one must design a specialized moderator canister (for example, a re-entrant canister).

For the LANSCE hydrogen moderator thickness of 5 cm, we directly compare leakage neutron spectrum from a 100% para-hydrogen moderator to that from a

25% para- and 75% ortho-hydrogen one in Fig. 28. As can be seen, there is little quantitative difference predicted by the Young and Koppel **cold molecular-hydrogen gas** kernel. For 100% para-hydrogen, there are a few more neutrons in the 5-50 meV range. The presence of ortho-hydrogen produces a slightly 'cooler' spectrum. The enchancement of 'cold' neutron production from a cold source compared to an ambient temperature moderator is dramatic.

For a 100% para-hydrogen moderator 6 cm thick, the penalties for shaping neutron pulses with decouplers and liners are further illustrated in Fig. 29. Here we see that cold neutron production increases by a factor of about six when going from a decoupled to a coupled moderator. For a pulsed spallation neutron source, not all this gain is useful because a significant fraction of the neutrons are produced in the 'tails' of the neutron pulses. If one assumes that neutrons produced in the first 200 μs of a pulse are useful, the cold neutron intensity gain of a coupled compared to a decoupled moderator is about 2.3. To take advantage of this latter intensity increase, one would use a neutron chopper to produce neutron pulses from a coupled system. In Fig. 29, the relative importance decouplers and liners have on neutron leakage intensity can be seen. The impact on neutron pulse widths should be more pronounced for liner removal than decoupler removal. As shown in Fig. 29, the effects of decoupling and coupling on neutron leakage intensity are energy dependent, again demonstrating the complexity of the physical processes going on during moderation. As can be seen in Fig. 29, neutron leakage intensity is not too sensitive to the type of material used for decouplers and liners.

LIQUID HYDROGEN MODERATOR SYSTEM

We installed the LANSCE liquid hydrogen moderator system during the 1985 LANSCE upgrade, and reported on it at ICANS-VIII,[18] and more recently at

the 1986 annual meeting of the American Institute of Chemical Engineers.[19] While the system has remained operational since ICANS-VIII, we have been limited to approximately 2500 hours of operation at proton beam currents up to 35 μA. This running time has primarily been influenced by: a) PSR commissioning, where high priority has been given to understanding PSR operation in lieu of production time, and b) delays in design, fabrication, and installation of the small angle scattering instrument which utilizes the cold moderator.

System Description

We flow liquid hydrogen to and from the moderator canister. The system consists of the following major components: a) a KOCH model 1430 liquid helium refrigerator, b) the helium-to-hydrogen heat exchanger, c) a resistance heater, d) the liquid hydrogen circulating pump, and e) the moderator canister. The layout of these components is shown in Fig. 30. The KOCH unit is powered by three reciprocal compressors and has a capacity of 500 Watts at 20 K.

Through cryogenic transfer lines, we circulate cold helium gas from the refrigerator to the helium-to-hydrogen heat exchanger. As the hydrogen loop cools down, we add hydrogen at a pressure of 15 atm. When full, the volume of liquid hydrogen in the hydrogen loop is about 6 liters. Using a centrifugal pump, we circulate liquid hydrogen to the moderator canister through cryogenic transfer lines. A schematic of the liquid hydrogen system is shown in Fig. 31.

In addition to nuclear heating during operation, we deliberately add heat to the hydrogen loop through the resistance heater. We do this to maintain a steady heat load for the refrigerator, and a moderator temperature variation of ± 1 K. The moderator, pump, and heat exchanger are in an

evacuated space. We continually monitor the moderator temperature using a hydrogen vapor bulb thermometer and the heat exchanger temperature with silicon diodes. Pressure transducers are located throughout the system to monitor hydrogen pressure.

System safety is assured through multiple overpressure relief devices which vent the hydrogen into an exhaust stack when overpressure occurs. A solenoid 'dump' valve (controlled by relay logic with inputs from combustible gas detectors, vacuum gauges, and pump and refrigerator status) is also connected into the vent stack.

System Problems

The helium-to-hydrogen heat exchanger is presently located in the service cell, an area which may experience radiation levels as high as 50 Rem/h at 100 μA of proton current. At this current, we estimate 30 Rem/h at the location of the pressure transmitter for the vapor bulb thermometer. One potential problem associated with such relatively high radiation levels is premature failure of the signal conditioning electronics for the pressure transmitter. At the nominal proton currents of 20-25 μA run to date, we may have begun to experience temperature drifts attributable to the onset of radiation damage in the pressure transmitter electronics.

Several power failure problems have caused our safety rupture diaphragm to do its job and burst. We designed the vent valves to open on a power failure and leave the loop in a safe state after unscheduled power outages. The breaking of the rupture diaphragm occurred when the valve opened starting a flow of liquid hydrogen, and, when the power returned shortly thereafter, liquid hydrogen was trapped in warm lines. This trapped liquid hydrogen rapidly turned to gas causing an overpressure and breaking of the rupture disk. This failure mode has been eliminated by modifying the power supply electrical operation to carry us through 'short' power glitches.

On the positive side, the liquid hydrogen system has performed as expected with no active controls being required.

Short-Term Improvements

During the upcoming cycle break starting roughly mid-December and lasting through about mid-June of 1987, we will relocate the vapor bulb thermometer electronics from the service cell to the service area. This will essentially mitigate any radiation damage problems to this unit.

Our present startup and cool down procedures require personnel to be in the service area to do the needed tasks. This requirement, in turn, prohibits proton beam from being delivered to LANSCE. We will eliminate this unnecessary perturbation to the already precious LANSCE production time by extending the charge piping for the hydrogen loop to an area accessible when LANSCE is operating. This will reduce LANSCE downtime during the cool down period for the hydrogen moderator system.

Long-Term Modifications

Our long range plans include moving the helium-to-hydrogen heat exchanger unit from the service cell to the service area. The service area has a much lower radiation level, essentially eliminating any radiation damage concerns. Relocating the heat exchanger and helium refrigerator units outside the service area is an option we will also consider.

The present hydrogen moderator canister is a 'flat plate' design. With help from our colleagues at the Rutherford Appleton Laboratory, we intend to fabricate and have on hand a 'spherical sided' hydrogen moderator canister. This will improve the safety factor for materials failure at our

present operating pressure of 15 atm. This improved canister design will also allow us to fabricate the canister with thinner walls.

Finally, we are investigating methods to maintain and monitor a liquid mixture of 25% para and 75% ortho hydrogen. As noted in the cold hydrogen neutronics section, we would have to neutronically optimize the target canister design to take full advantage of this capability.

FUTURE IMPROVEMENTS TO LANSCE

In addition to the specific betterments to the liquid hydrogen moderator system discussed above, we will continue to enhance the neutron production and understand the performance of LANSCE. The improvements will primarily be in the following areas (arranged roughly according to priority):

- optimization of the TMRS materials and geometry,
- maximization of moderator neutronic performance to experimental requirements,
- implementation of more cold moderators,
- application of a fissile depleted uranium target, and
- if technologically feasible and warranted, utilization of a fissile (^{235}U, ^{239}Pu, etc.) booster target.

For Los Alamos spallation target system designs, we have always emphasized optimal neutron production and efficient neutron utilization. This can easily be as important in useful neutron production for experiments as making more neutrons by using advanced targets such as depleted uranium. We are taking both approaches (optimal neutron usage and implementation of advanced targets and moderators) in our upgrades to the LANSCE target system. This involves: a) proper choice of target, moderator, reflector, poison, decoupler, liner, structural, and cooling materials, b) placing these materials in an optimal geometry, c) matching source neutronics to

instrument requirements, and d) engineering the system to operate at high-power for a useful period of time. In addition, we need to better understand LANSCE shielding requirements, and improve the LANSCE target area remote handling capabilities. **We must also look to the next generation of LANSCE.**

If one considers materials like tungsten, tantalum, and 'lead' to be pure spallation targets, then depleted uranium is a spallation/fission target, and a booster target is a fission/spallation target. We 'sorted' the targets according to the importance fission plays in neutron production. This ordering automatically ranks the targets according to cost and complexity, with the booster target being the most expensive and difficult to implement. We put lead in quotes because at proton energies of 800-MeV and higher, even a lead target fissions slightly.

For a LANSCE target designed to handle 100 μA of 800-MeV protons, we have calculated the gain in useful neutron beam flux from an engineered depleted uranium target to be 1.4-1.5 that from an engineered tungsten target.[4] We consider this gain to be significant, but only one of the many issues which must be addressed to employ a fissile target. Other important considerations are safety, cost, complexity, and **the 'quality' of the neutron beams delivered to the users.** This latter consideration must include such effects as delayed neturons, delayed fissions (as they contribute to neutron pulse broadening), and additional gamma-ray contamination of the neutron beams. However, depending on funding support and user input, we are including a depleted uranium target in the plans for the future betterment of LANSCE, and have started considering some initial detailed issues necessary for implementing a LANSCE depleted uranium target system.

One such item is the induced radioactivity and afterheat production for such a target.[20] Detailed procedures to calculate the time behavior of

radioactivity, thermal power, nuclide production, etc. from proton bombardment of a spallation target have been devleloped by Atchison[21] and Schaal.[22] At Los Alamos, we developed a similar capability by coupling our Monte Carlo code package[23] with the KFA/Jülich version of ORIHET and ORIGEN. We adapted the Jülich ORIGEN code to accept the expanded Los Alamos ORIGEN library. It is not possible for the ORIGEN code to calculate the time behavior of all nuclides produced by spallation reactions because the cross section libraries of the ORIGEN code are based on fission reactor applications. Also, calculational procedures do not account for nuclide burnup, and Atchison's ORIHET data libraries do not contain nuclides with mass numbers below 40. Shaal extended these libraries into the mass number range $A < 40$, but still the libraries are incomplete.

For LANSCE depleted uranium target, an irradiation time of two years is foreseen with two half-year operating periods. We did a calculation of induced radioactivity and afterheat for a split-target imbedded in the LANSCE TMRS. We assumed an irradiation time of one year without any shutdown; this assumption leads to pessimistic values of target radioactivity and afterheat. The results of the computation are shown in Figs. 32 and 33 and in Tables II and III. We used this type of data to determine the capacity of our target cooling system, and to size the emergency backup cooling loop. The data are also necessary for safety considerations.

To assure ourselves that our innovative flux-trap design is competitive with the more 'classical' wing-moderator approach, we calculationally compared thermal neutron production from flux-trap and wing-geometry moderators. We did the computations for two 'viewed' moderator surfaces; the geometries used are illustrated in Fig. 34. We further quantified the intercomparison by using IPNS, ISIS, and LANSCE 'as built' target designs and proton beam characteristics. The results of the calculations are shown in Figs. 35 and 36. We believe these intercomparisons between facilities

to be the best **relative** comparisons that exist to date; and demonstrate our resolve to keep LANSCE at the forefront of the world's pulsed spallation neutron sources. The moderator, poison, decoupler, and liner materials, and poison depth from the moderator viewed surface were the same in all the computations. The reflector material was that used at each facility. We did not account for either reflector coolant nor (with the exception of the target itself) for any particulars associated with real engineered systems. **As can be seen in Fig. 36, LANSCE (when operating at design specifications) will be the most intense pulsed spallation source in the world.**

If we denote the existing LANSCE facility as **LANSCE-I**, then **LANSCE-II** designates a target area at the proposed Los Alamos Advanced Hadron Facility (AHF).[24] As presently envisioned, LANSCE-II would be a 'world class' cold neutron facility for materials science research; we are attempting to integrate LANSCE-II with a neutrino facility. Preliminary LANSCE-II proton beam characteristics are 500 μA of 1-2 GeV protons in 1 μs bursts at 12 Hz. The LANSCE-II target area concepts are just evolving as well as the proton beam properties. Our preliminary thinking should become firmer in about a year's time.

CONCLUSIONS

The LANSCE upgrade involved **major changes** to the 'old' WNR high-current target area. We are glad the enhancements of the target area shielding, and the installation of the unique split-target/flux-trap-moderator system (including upgrades to support systems) are behind us. The successful implementation of a liquid hydrogen moderator is particularly gratifying given the minimal resources we had to devote to the effort.

Initial indications are that the neutronic performance of the LANSCE TMRS is as expected. However, during the next few months, we will make detailed neutronic measurements of moderator performance, and compare the results

with calculations of the 'as built' LANSCE TMRS. We need a definitive measurement of the neutron leakage spectrum from the LANSCE hydrogen moderator to compare with our calculations.

ACKNOWLEDGEMENTS

We acknowledge the efforts of Bob MacFarlane in implementing the cold hydrogen kernel on the Los Alamos computer system, and for useful discussions concerning the limitations of the kernel. We appreciate Dick Prael's help in integrating the cold hydrogen kernel into the Los Alamos Monte Carlo code package. We are indebted to Teri Cordova for her typing help. Special thanks to Francis Atchison for being so patient, and to the 'SINQ crew' for a successful ICANS conference, and for a very special day at the 'Rigi'.

This work was performed under the auspices of the U. S. Department of Energy, Office of Basic Energy Science.

REFERENCES

1. F. A. Morse, "LANSCE Overview," ICANS-IX, Proc. of the Ninth Meeting of the International Collaboration on Advanced Neutron Sources, Villigen, Switzerland, 22-26 September 1986 (this conference), LA-UR-86-3227, Los Alamos National Laboratory (1986).

2. G. P. Lawrence, R. A. Hardekopf, A. J. Jason, B. Blind, and T. Hardek, "Proton Storage Ring Commissioning at LANSCE," ICANS-IX, Proc. of the Ninth Meeting of the International Collaboration on Advanced Neutron Sources, Villigen, Switzerland, 22-26 September 1986 (this conference), LA-UR-86-3971, Los Alamos National Laboratory (1986).

3. G. J. Russell, P. W. Lisowski, S. D. Howe, N. S. P. King, and M. M. Meier, "Characteristics of the WNR - a Pulsed Spallation Neutron Source," Nucl. Data for Sci. and Tech., pp. 831-835, K. H. Bockhoff, Ed. (1983).

4. G. J. Russell, C. D. Bowman, E. R. Whitaker, H. Robinson, and M. M. Meier, "LANSCE High-Power (200 μA) Target-Moderator-Reflector-Shield," ICANS-VIII, Proc. of the Eighth Meeting of the International Collaboration on Advanced Neutron Sources, Oxford, England, 8-12 July 1985, RAL-85-110, pp. 272-293 (1985).

5. A. Carne, "Review of SNS Target Station," ICANS-IV, Proc. of the Fourth Meeting of the International Collaboration on Advanced Neutron Sources, Tskuba, Japan, 20-24 October 1980, KENS Report II, pp. 136-153 (1981).

6. A. D. Taylor, SNS Moderator Performance," ICANS-VIII, Proc. of the Eighth Meeting of the International Collaboration on Advanced Neutron Sources, Oxford, England, 8-12 July 1985, RAL-85-110, pp. 319-328 (1985).

7. J. M. Carpenter, A. W. Schulke, T. L. Scott, D. G. Wozniak, B. E. Benson, and B. D. Leyda, "The IPNS Grooved, Solid Methane Moderator," ICANS-VIII,

Proc. of the Eighth Meeting of the International Collaboration on Advanced Neutron Sources, Oxford, England, 8-12 July 1985, RAL-85-110, pp. 311-318 (1985).

8. Y. Ishikawa, M. Furusaka, S. Itoh, S. Ikeda, N. Watanabe, K. Inoue, and H. Iwasa, "Mock-up Experiments for KENS-I Cold Moderator," ICANS-VIII, Proc. of the Ninth Meeting of the International Collaboration on Advanced Neutron Sources, Oxford, England, 8-12 July 1985, RAL-85-110, pp. 329-343 (1985).

9. G. J. Russell, M. M. Meier, J. S. Gilmore, R. E. Prael, H. Robinson, and A. D. Taylor, "Measurements of Spallation Target/Moderator/Reflector Neutronics at the Weapons Neutron Research Facility," ICANS-IV, Proc. of the Fourth Meeting of the International Collaboration on Advanced Neutron Sources, Tsukuba, Japan, 20-24 October 1980, KENS Report II, pp. 210-241 (March 1981).

10. G. J. Russell, M. M. Meier, H. Robinson, and A. D. Taylor, "Preliminary Neutronics of a 'T'-Shape Premoderator/Moderator for the Weapons Neutron Research Facility," ICANS-V, Proc. of the Fifth Meeting of the International Collaboration on Advanced Neutron Sources, Jülich, West Germany, 22-26 June 1981, Jülich-Conf-45, ISSN-0344-5789, pp. 389-416 (October 1981).

11. G. J. Russell, "Applied Spallation Physics Research at Los Alamos," LA-UR-84-778, Los Alamos National Laboratory (1983).

12. G. J. Russell, P. A. Seeger, and R. G. Fluharty, "Parametric Studies of Target/Moderator Configurations for the Weapons Neutron Research (WNR) Facility," LA-6020, Los Alamos Scientific Laboratory (1977).

13. G. J. Russell, P. A. Seeger, and R. G. Fluharty, "Monte Carlo Studies of Target/Moderator Configurations for the Weapons Neutron Research Facility," Trans. Am. Nucl., Soc., 22, 715-716 (1975).

14. G. J. Russell, "Inital Target/Moderator Configuration for the Weapons Neutron Research Facility," Trans. Am. Nucl. Soc., 27, 861-862 (1977).

15. D. Filges, KFA Jülich (private communication).

16. J. A. Young and J. U. Koppel, "Slow Neutron Scattering by Molecular Hydrogen and Deuterium," Phys. Rev., 135, No. 3A, A603-A611 (1964).

17. R. D. Neef and H. Schaal, "Evaluation of Hydrogen Data for Cold Neutron Sources and Their Application to Source Design Studies, KFA Jülich (unpublished).

18. H. Robinson, G. J. Russell, E. D. Tucker, E. R. Whitaker, K. D. Williamson, Jr., and F. J. Edeskuty, "LANSCE Liquid Hydrogen Moderator System Hardware-Characteristics-Operation," ICANS-VIII, Proc. of the Eighth Meeting of the International Collaboration on Advanced Neutron Sources, Oxford, England, 8-12 July 1985, RAL-85-110, pp. 294-310 (1985).

19. H. Robinson, G. J. Russell, K. D. Williamson, Jr., and F. J. Edeskuty, "The Los Alamos Liquid Hydrogen Neutron-Moderator System," Proc. of Symp. on Cryogenic Properties, Processes and Applications 1985, AICHE 251, 82, 172-176 (1986).

20. R. D. Neef, "Calculation of Initial Induced Radioactivity and Afterheat Production for a LANSCE Depleted Uranium Target, "Los Alamos National Laboratory (1986) (unpublished).

21. F. Atchison, "A Theoretical Study of a Target Reflector and Moderator Assembly for SNS," RL-81-006, Rutherford and Appleton Laboratories (1981).

22. H. Schaal and G. Sterzenbach, SNQ 3 J../BH 27 11 84, KFA Jülich (1984).

23. R. E. Prael and H. Lichtenstein, "User Guide to the HETC Code System," Los Alamos National Laboratory (1986) (unpublished).

24. H. A. Thiessen, "An Advanced Hadron Facility: A Combined Kaon Factory and Cold-Neutron Source," Los Alamos National Laboratory (unpublished).

TABLE I

LANSCE MODERATOR CHARACTERISTICS

Moderator Type	Material	Width (CM)	Height (CM)	Thickness (CM)	Poison Depth (CM)	Poison Material	Decoupler	Liner
high-resolution	H_2O	13.0	13.0	3.5	1.5	Gd	^{10}B	Boral
high-intensity	H_2O	13.0	13.0	3.5	2.5	Gd	Cd	Cd
high-intensity	H_2O	13.0	13.0	4.0	2.5	Gd	Cd	Cd
cold	liquid H_2	13.0	13.0	5.0	---	none	Gd	Cd

TABLE II

GASEOUS ELEMENT PRODUCTION IN A LANSCE DEPLETED URANIUM TARGET

	Amount (g)			
	Spallation		Low-Energy Neutron Flux	
Element	t = 0	t = 10 yr	t = 0	t = 10 yr
He	1.04×10^{-2}	1.43×10^{-2}	1.21×10^{-5}	2.69×10^{-4}
Cl	3.78×10^{-8}	0.0	0.0	0.0
Ar	4.41×10^{-4}	3.85×10^{-4}	0.0	0.0
Br	7.60×10^{-2}	7.58×10^{-2}	1.27×10^{-2}	1.27×10^{-2}
Kr	3.75×10^{-1}	3.73×10^{-1}	2.47×10^{-1}	2.39×10^{-1}
I	3.85×0^{-1}	3.83×10^{-1}	1.88×10^{-1}	1.75×10^{-1}
Xe	1.00×10^{0}	1.01×10^{0}	3.11×10^{0}	3.11×10^{0}
Rn	3.35×10^{-5}	1.12×10^{-8}	2.34×10^{-15}	4.45×10^{-14}
Total	1.85	1.86	3.56	3.54

TABLE III

SPECIAL GASEOUS NUCLIDE PRODUCTION

IN A LANSCE DEPLETED URANIUM TARGET

	Amount (g)			
	Spallation		Low-Energy Neutron Flux	
Nuclide	t = 0	t = 10 yr	t = 0	t = 10 yr
^{85}Kr	2.52×10^{-2}	1.32×10^{-2}	1.60×10^{-2}	8.41×10^{-3}
^{85m}Kr	3.78×10^{-5}	0.0	6.02×10^{-5}	0.0
^{90}Sr	1.07×10^{-1}	8.36×10^{-2}	3.55×10^{-1}	2.77×10^{-1}
^{131}I	4.88×10^{-3}	0.0	1.52×10^{-2}	0.0
^{133}Xe	3.62×10^{-3}	0.0	2.01×10^{-2}	0.0
^{137}Cs	1.21×10^{-1}	9.62×10^{-1}	9.03×10^{-1}	7.17×10^{-1}

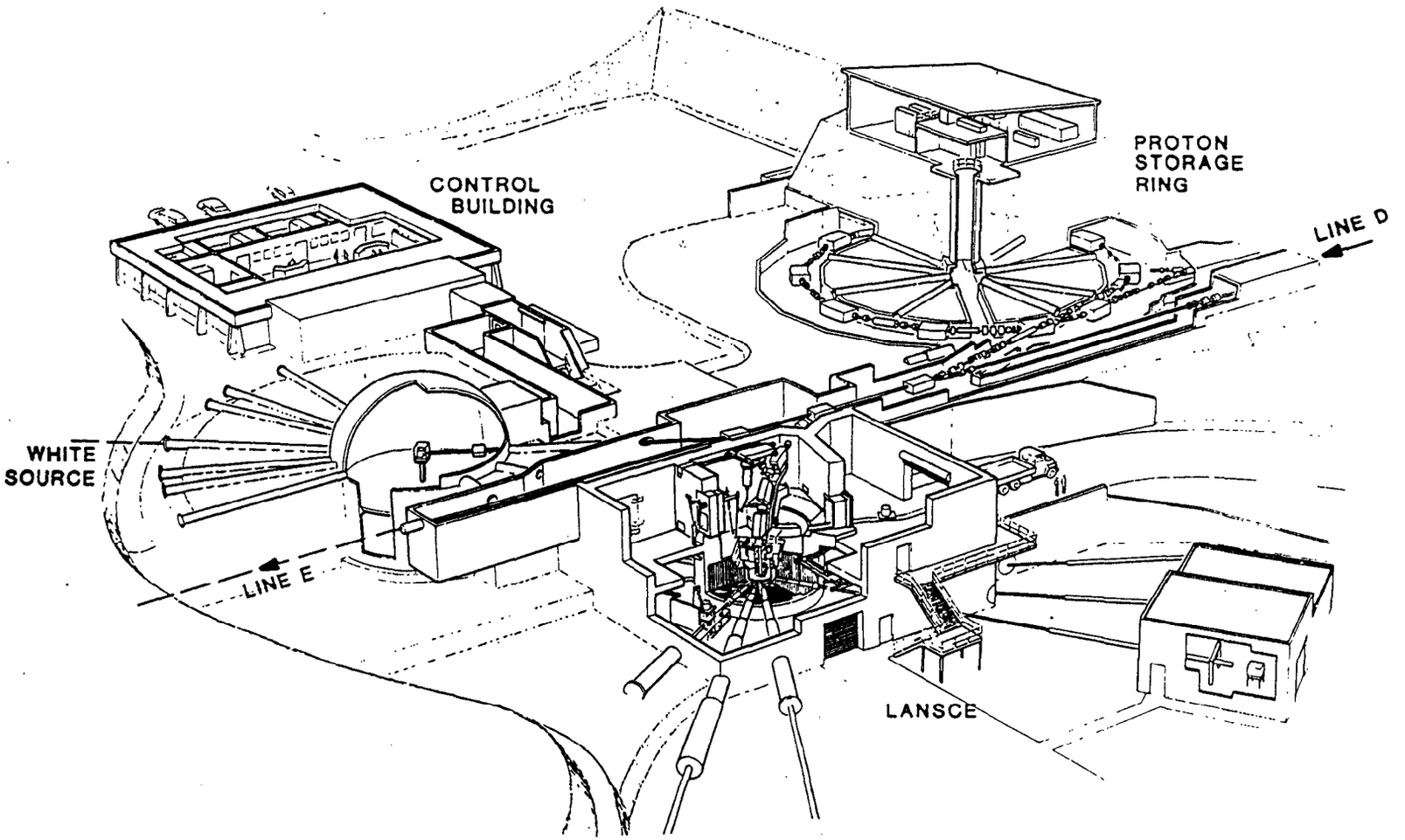

Fig. 1. General layout of the LANSCE/WNR complex. The new Neutron Scattering Experimental Hall, under construction in 1987, will surround the present LANSCE experimental hall (shown in the foreground) and will greatly enhance the LANSCE experimental area.

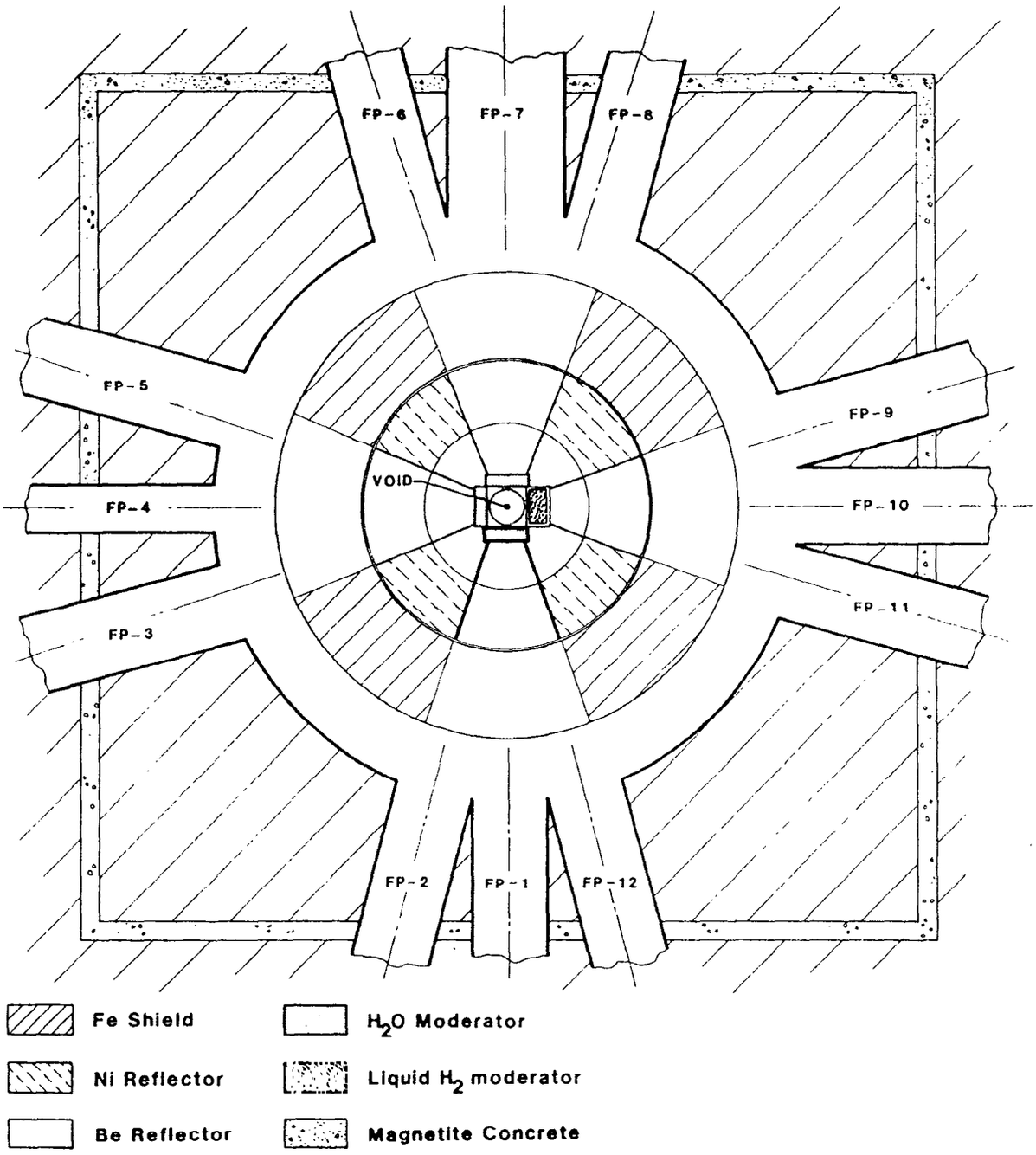

Fig. 2. Plan view of the LANSCE moderator and flight path arrangement.

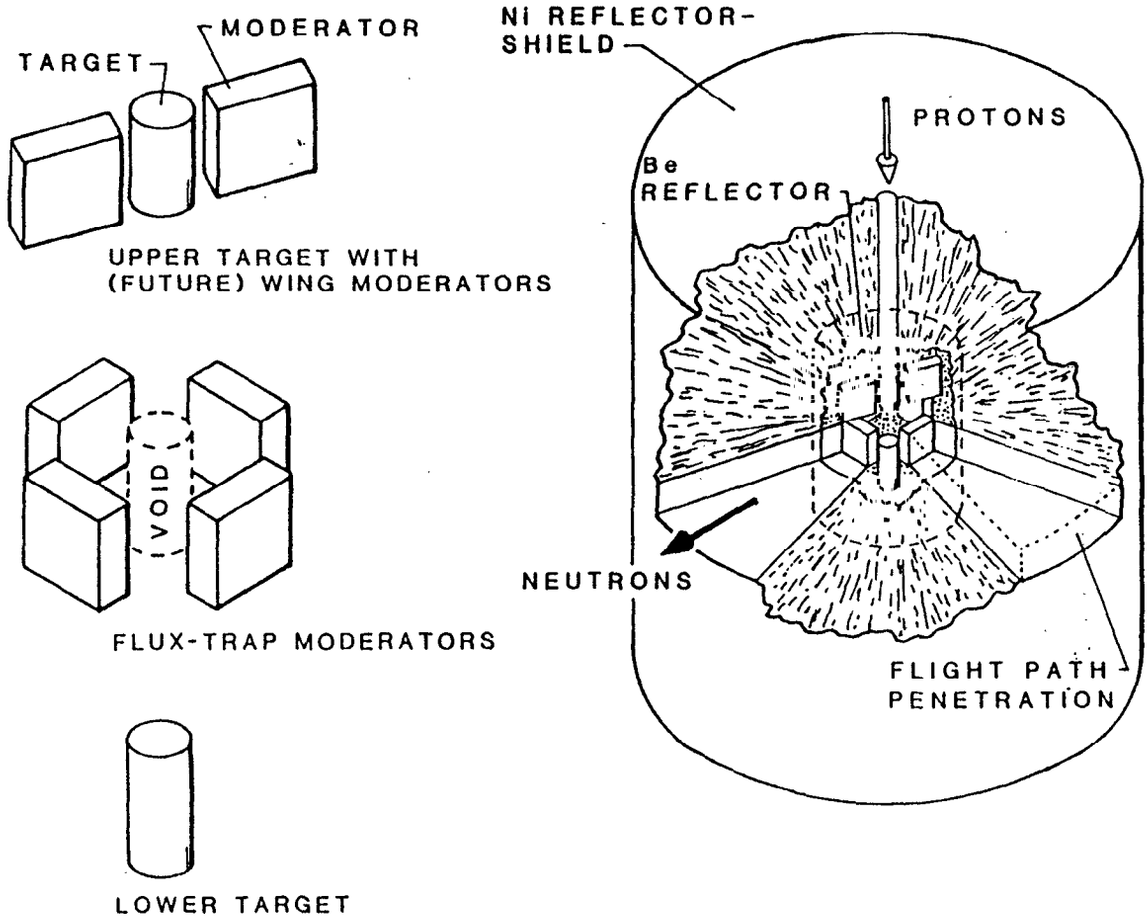

Fig. 3. Illustration of the LANSCE target system consisting of a split-target, an inner beryllium/nickel reflector region, and an outer nickel reflector/shield. Three water moderators and a liquid hydrogen moderator are in flux-trap geometry between the two tungsten targets. The system is one meter in diameter and one meter high.

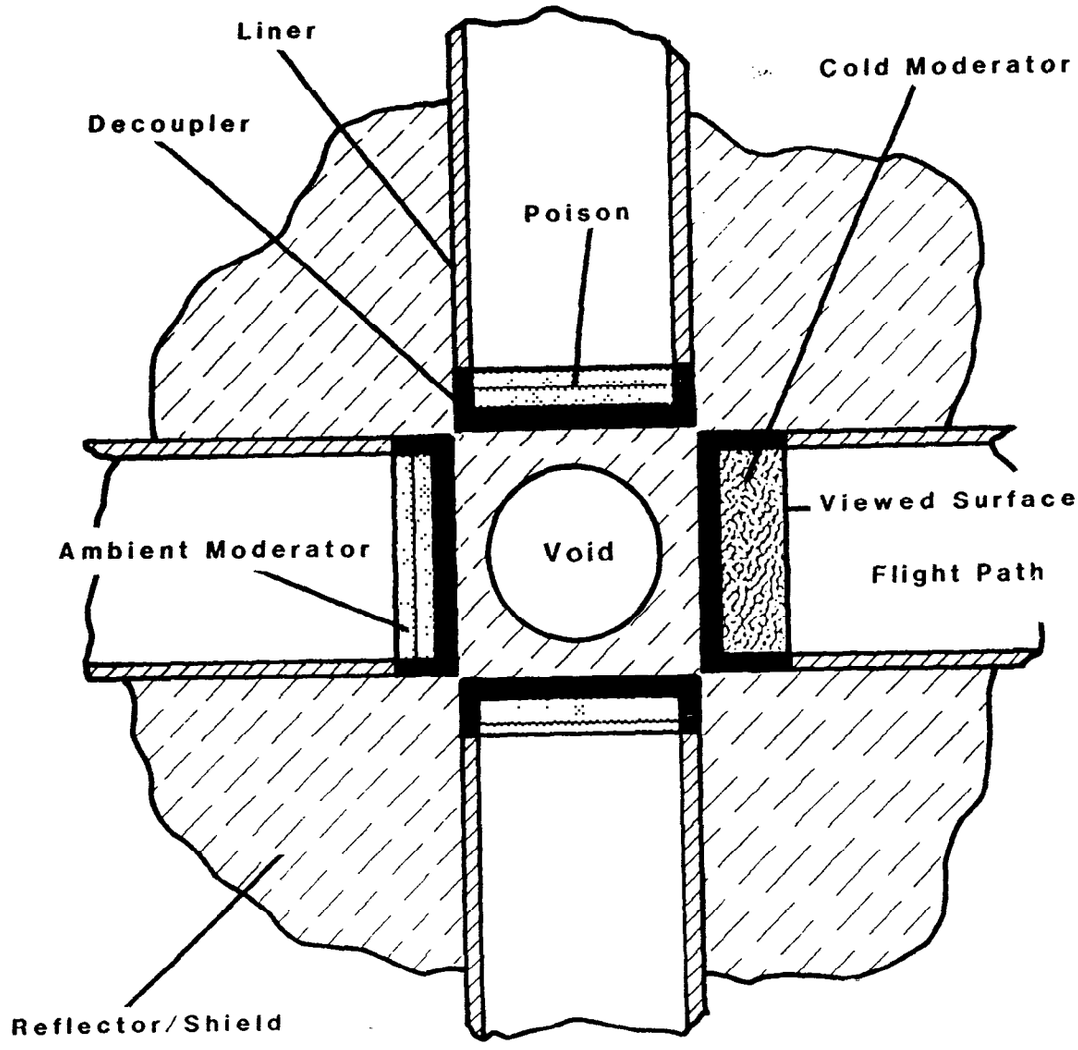

Fig. 4. Expanded plan view schematic of the LANSCE target/moderator arrangement. The liquid hydrogen moderator is depicted on the right side.

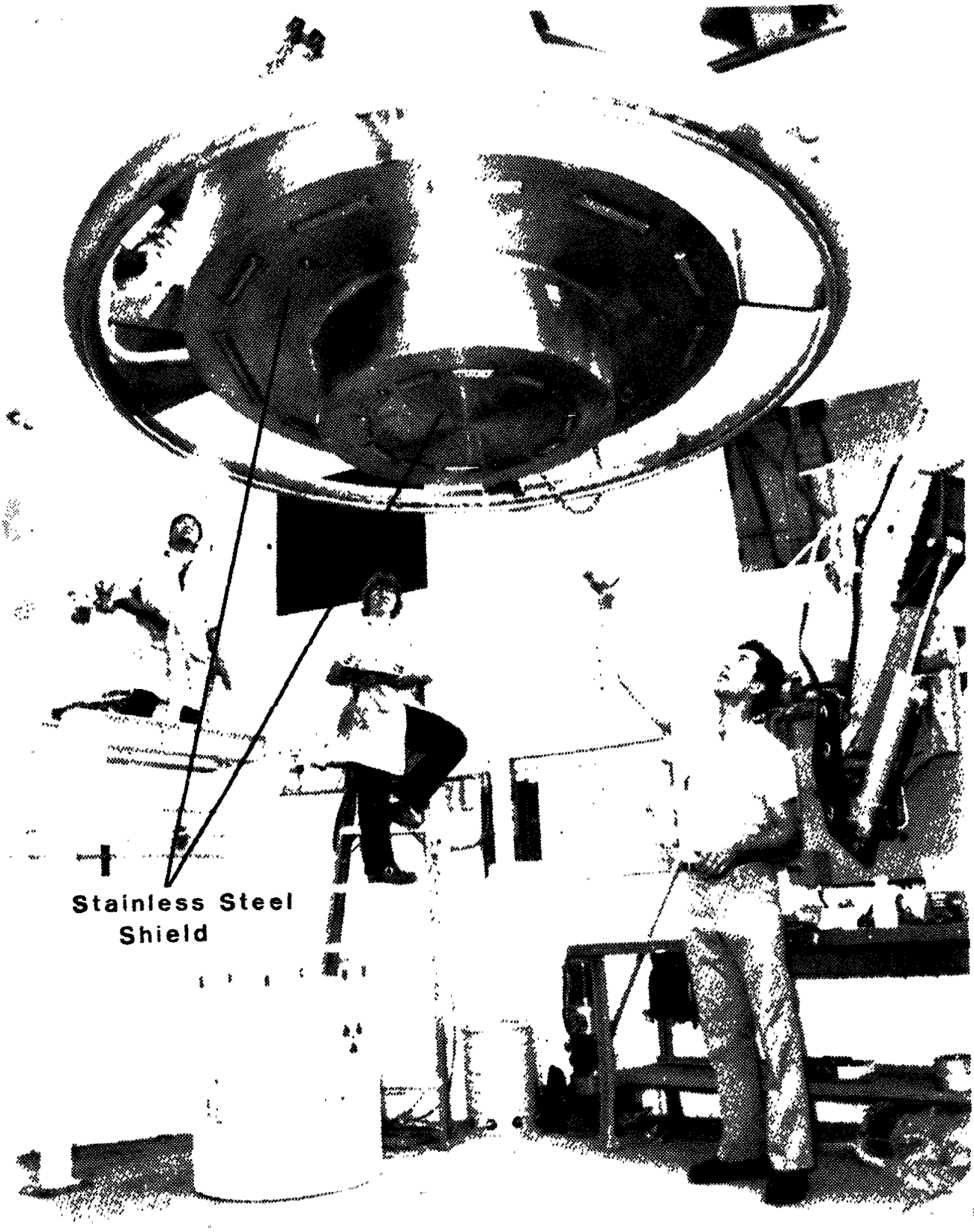

Fig. 5. Forward shield being lowered in place. The shield is shaped to fit the concave LANSCE target cavity and has a tubular support and centering ring.

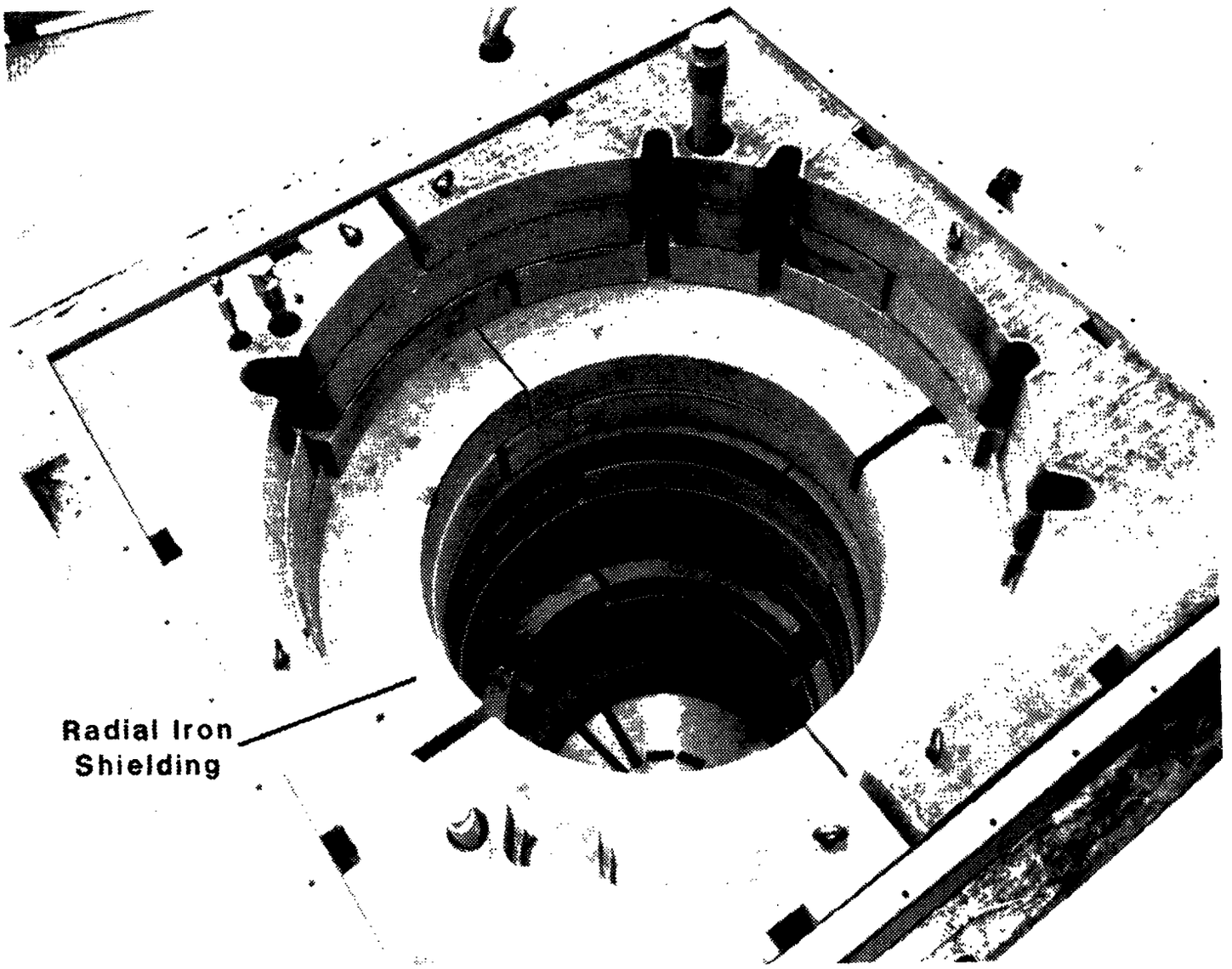

Fig. 6. Iron shielding as installed in the LANSCE target cavity. The forward stainless steel shield is visible at the bottom. Cooling and purge lines extend to the top of the shielding through offset holes in the shield elements.

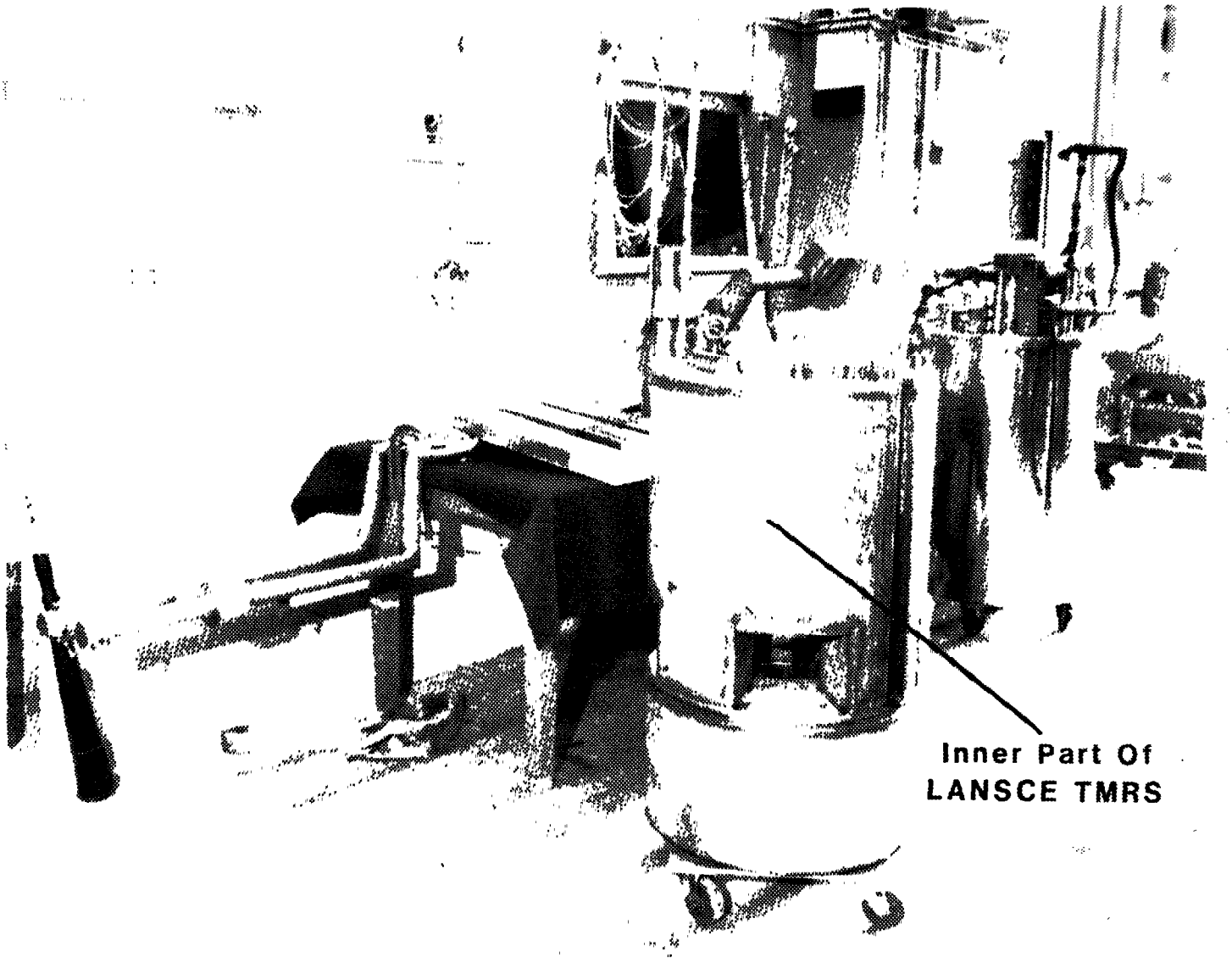

Fig. 7. Inner portion of the LANSCE TMRS showing neutron flight windows in the upper section.

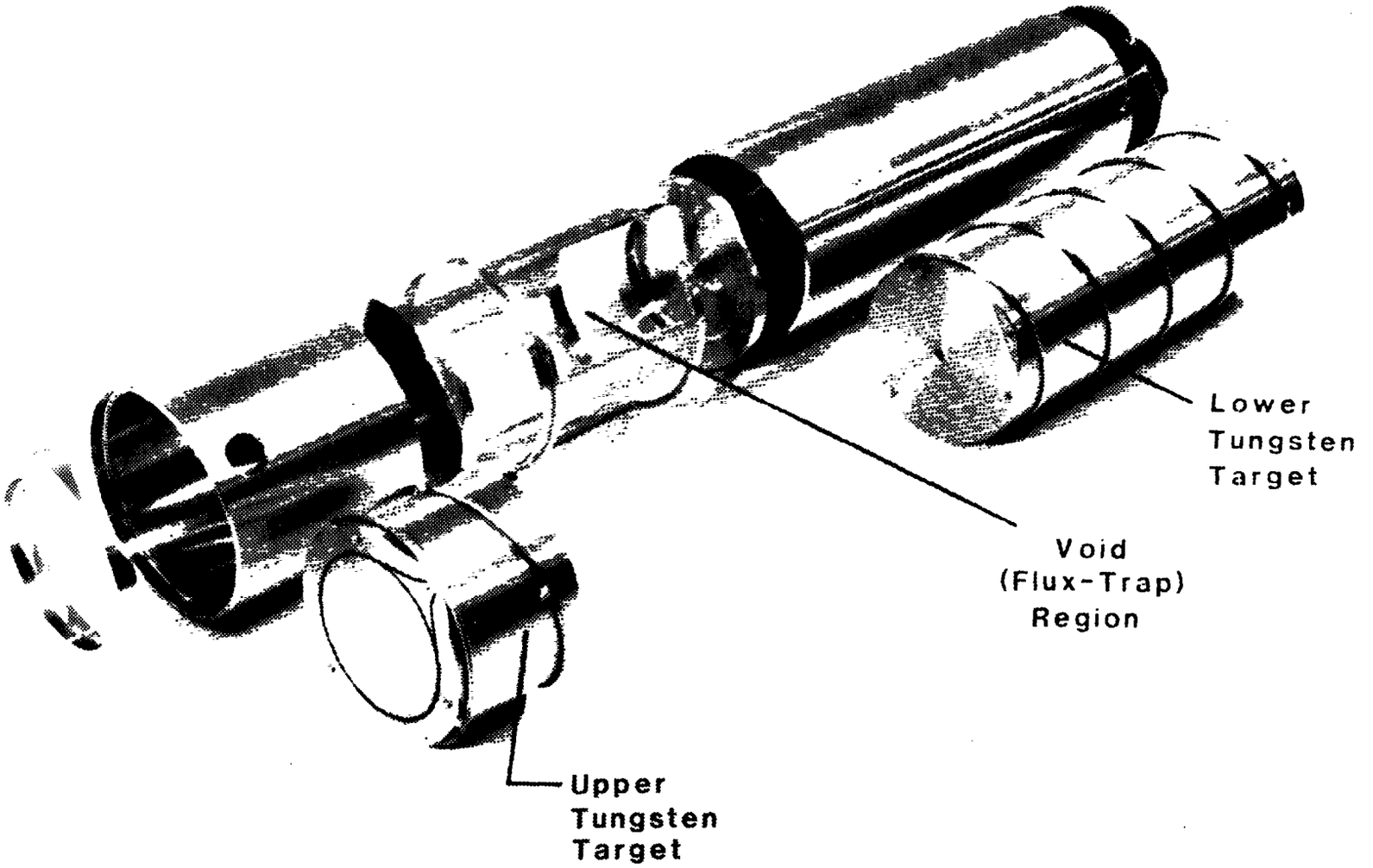

Fig. 8. Disassembled LANSCE target pressure vessel and targets, showing the spiral guides for target cooling.

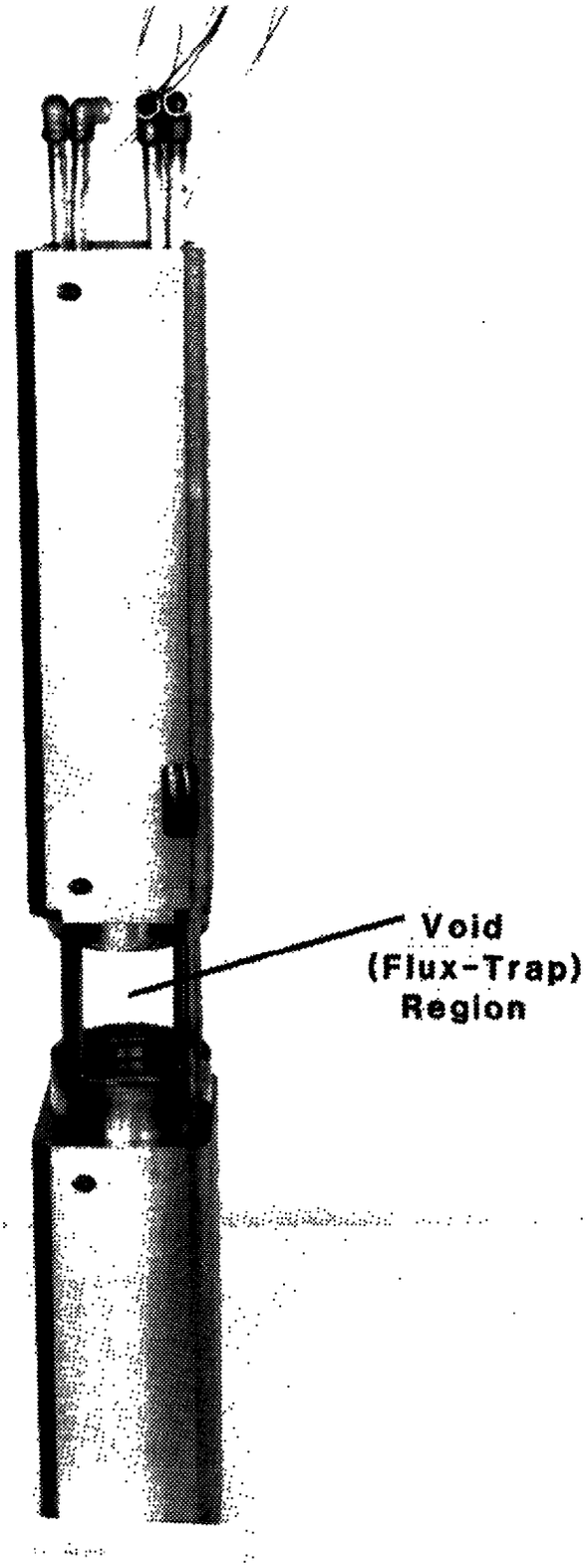

Fig. 9. Assembled LANSCE target with beryllium jackets installed.

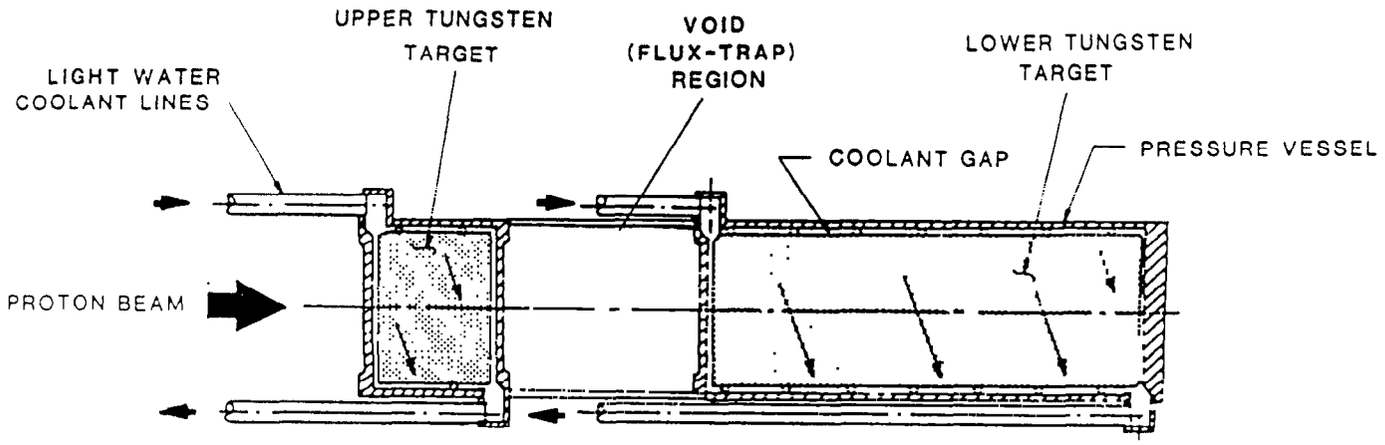

LANSCE TARGET

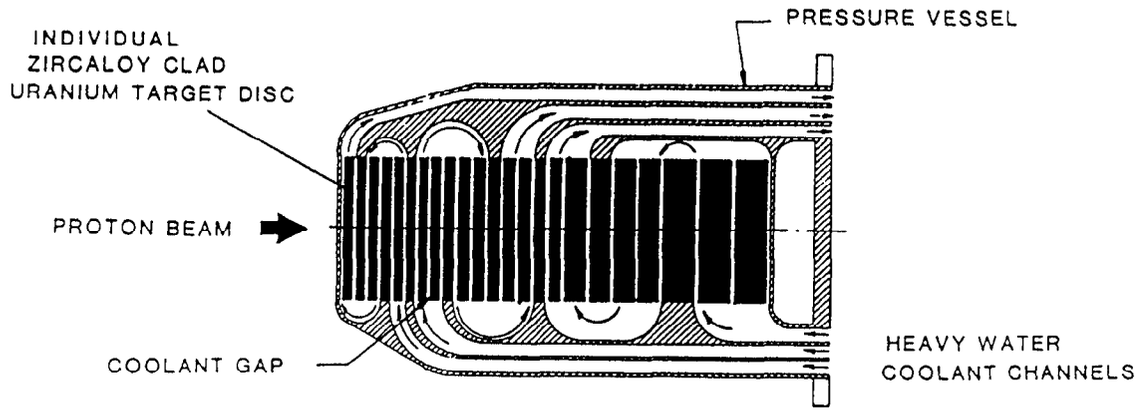

ISIS TARGET

Fig. 10. Intercomparison of LANSCE and ISIS targets, overall target designs, and the different cooling approaches. Note the two solid LANSCE tungsten target elements compared to the multiply segmented ISIS depleted uranium target plates.

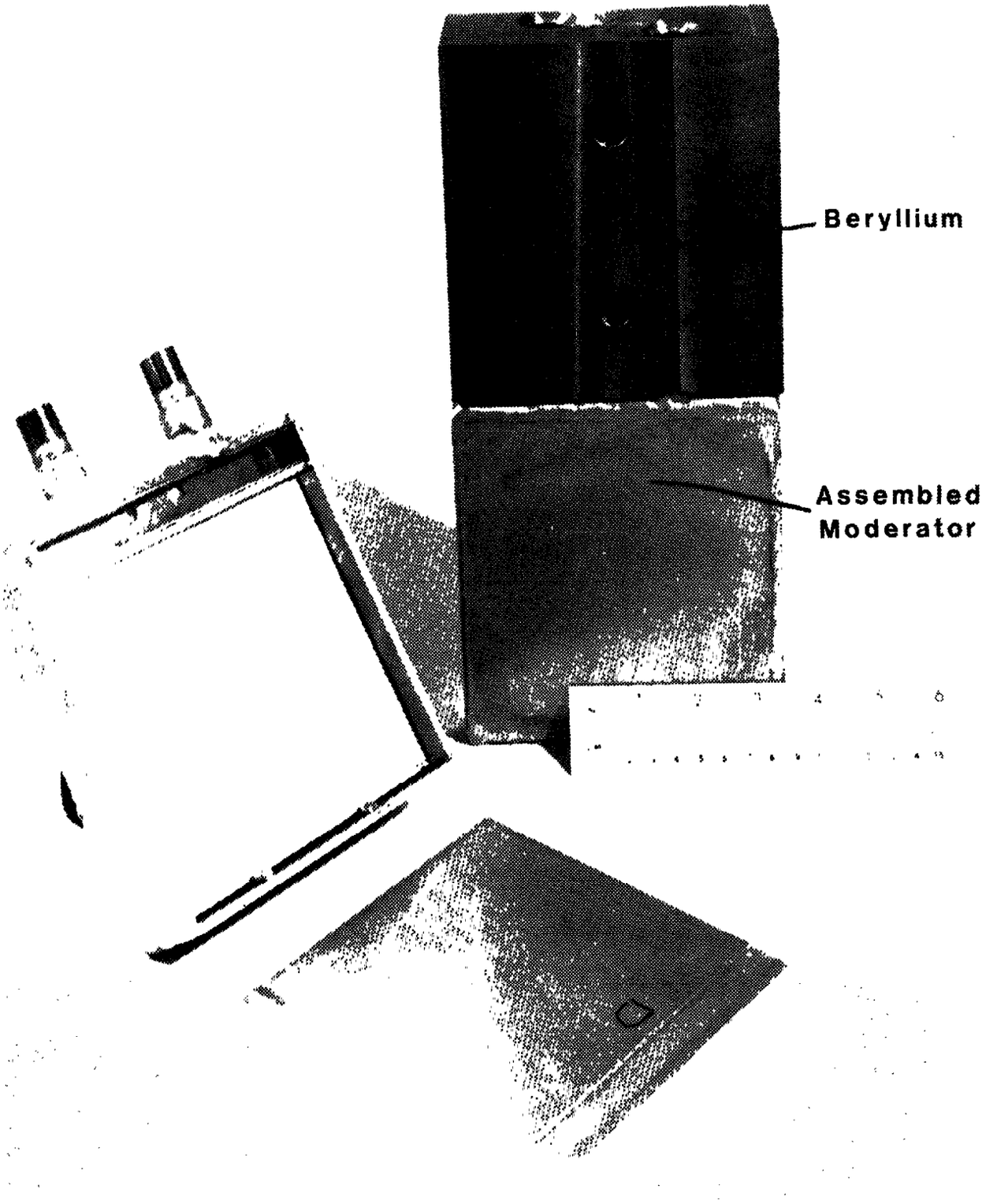

Fig. 11. Disassembled LANSCE light water moderator, showing the gadolinium poison insert behind the output face. An assembled moderator, with the beryllium reflector block, is shown in the background.

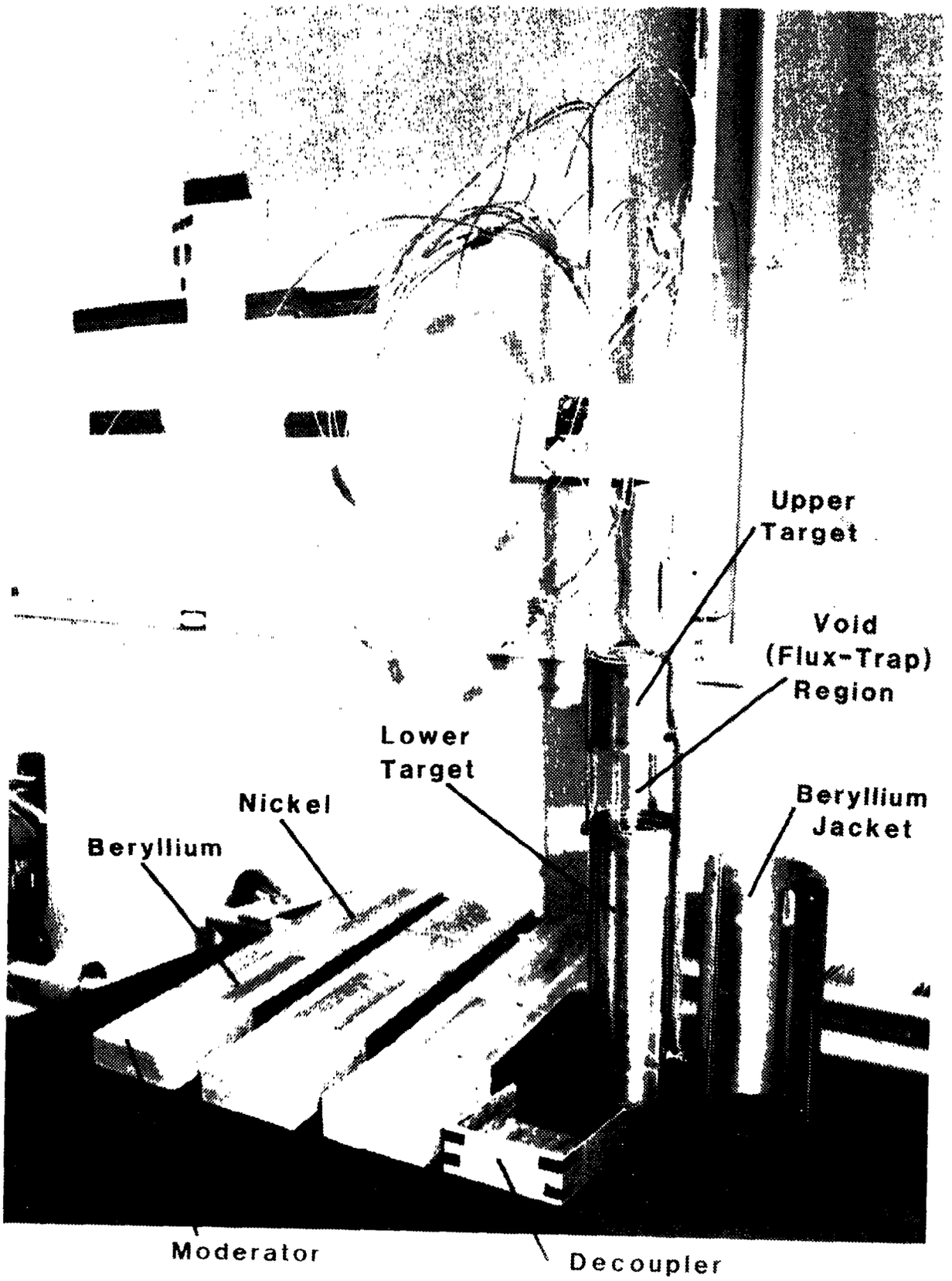

Fig. 12. Assembled LANSCE water moderators with beryllium reflector blocks, nickel reflector/shield blocks, a cadmium decoupler, and the assembled target (with beryllium jackets removed).

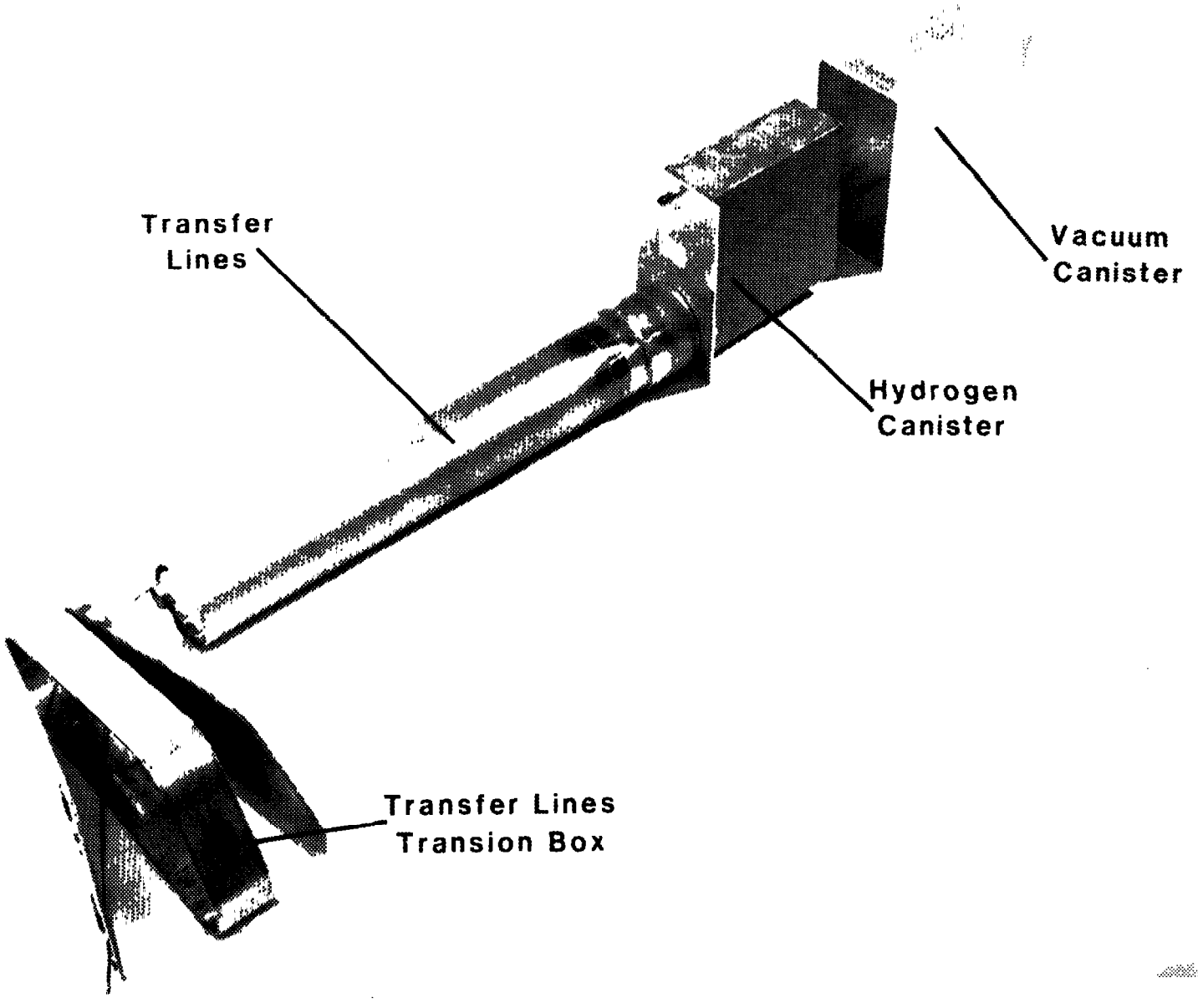

Fig. 13. LANSCE liquid hydrogen moderator with vacuum jacket removed.

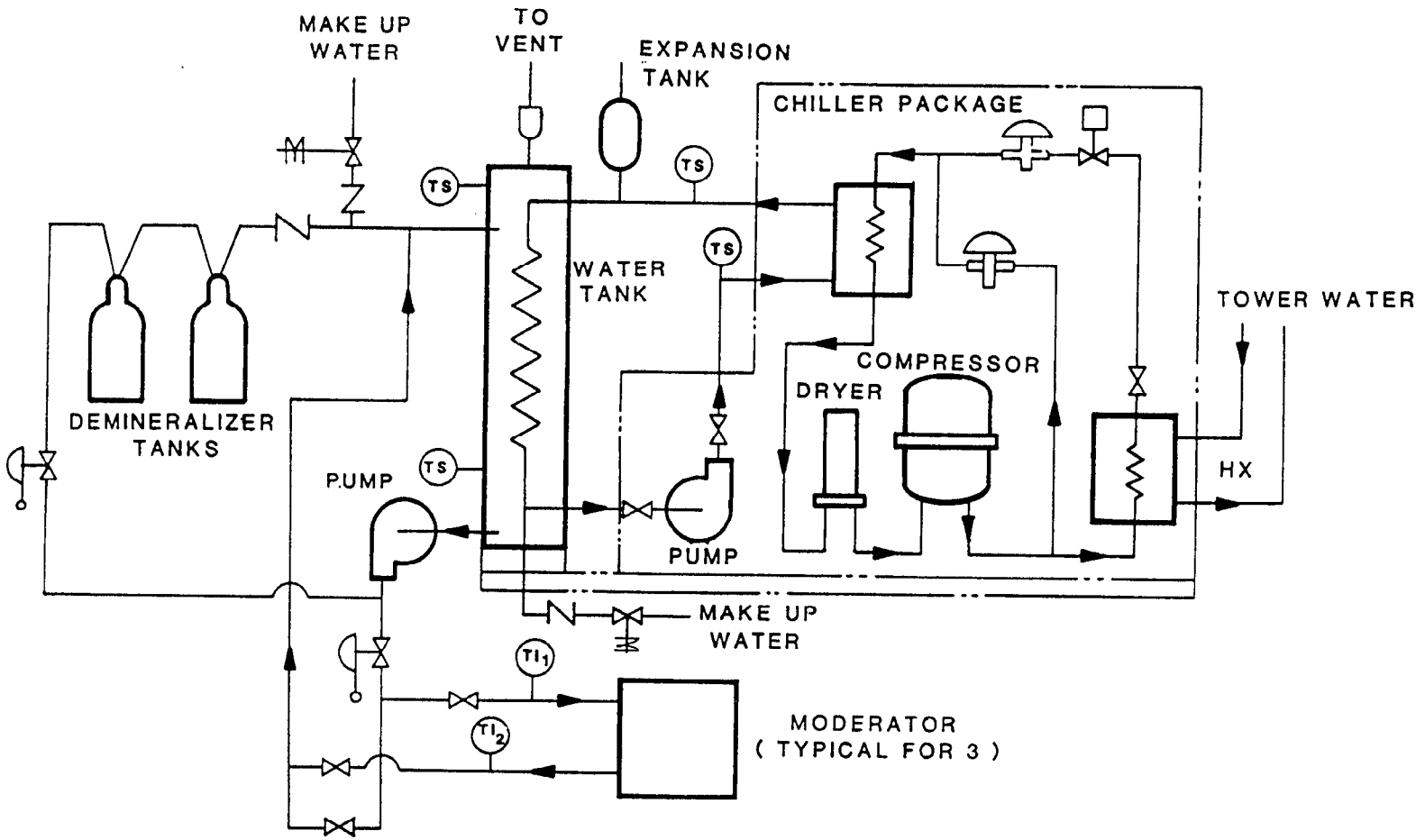

Fig. 14. Schematic of LANSCE (chilled) water moderator cooling system.

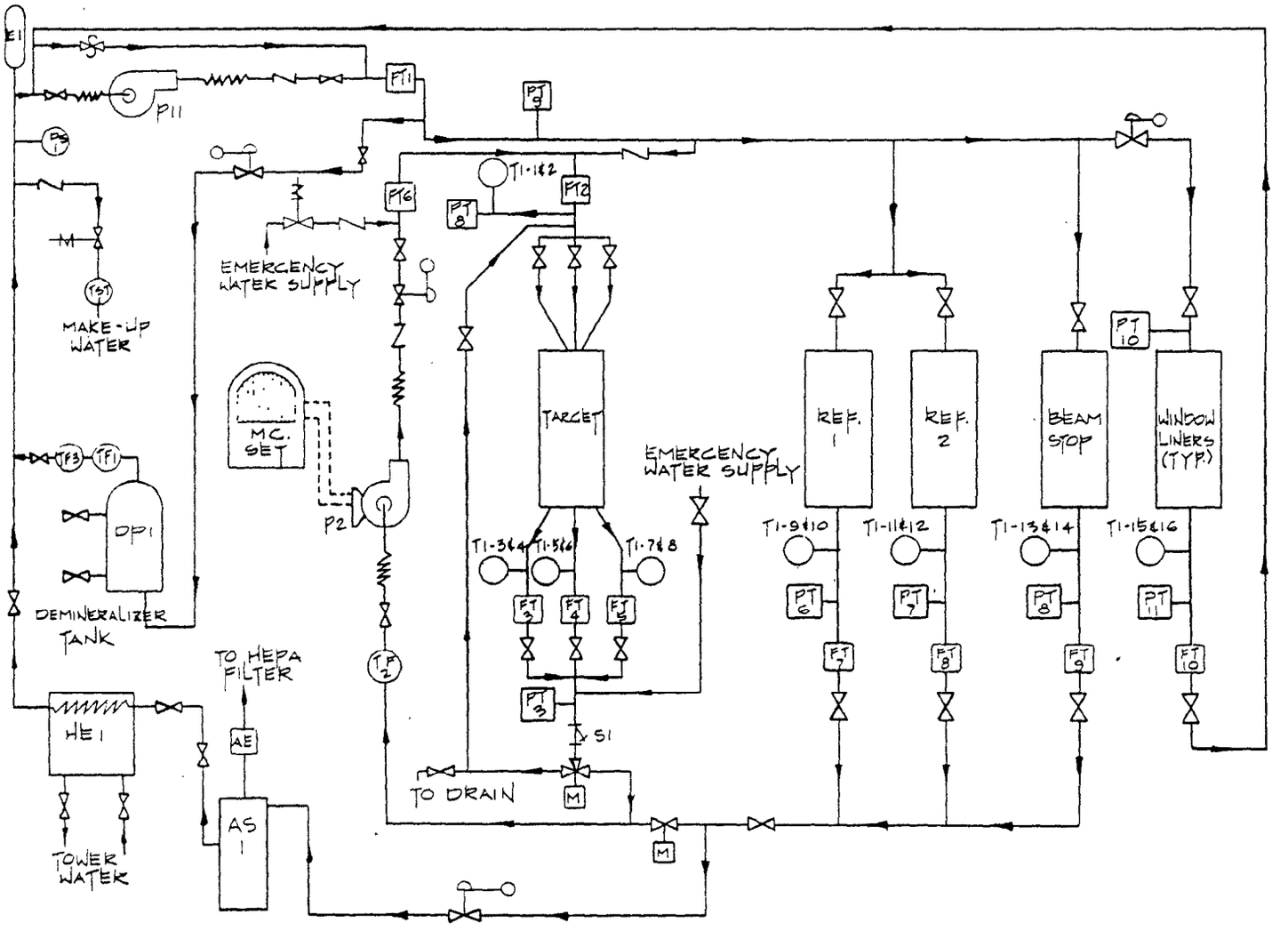

Fig. 15. Simplified schematic diagram of the LANSCE target/reflector cooling system.

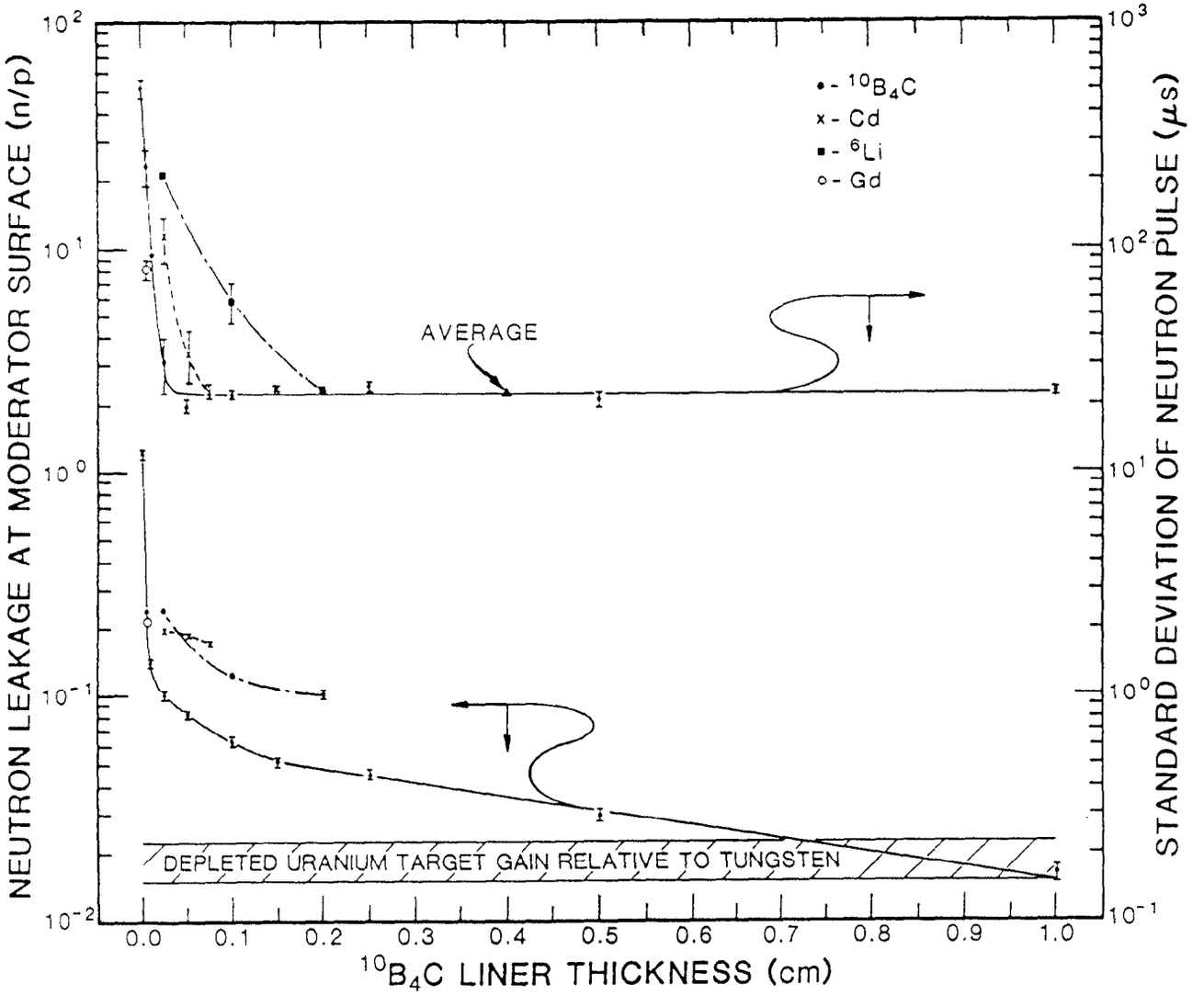

Fig. 16. Moderator performance as a function of liner thickness and type. The moderator used in the computations was a 2.5 by 13 by 13 cm water slab in flux-trap geometry. A beryllium reflector was used; the moderator was not poisoned.

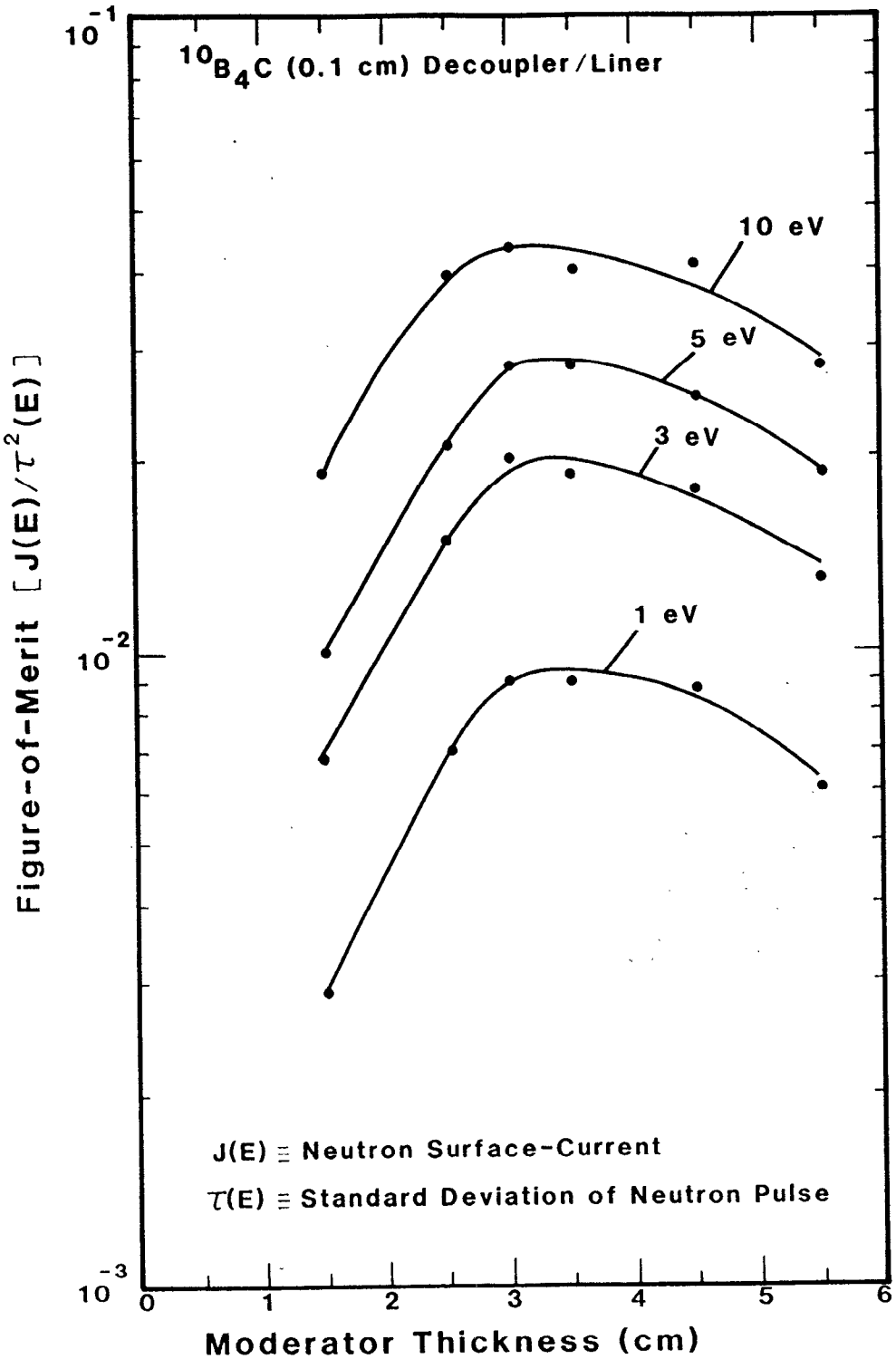

Fig. 17. Study to find the optimum thickness for epithermal neutron production from a water moderator in flux-trap geometry.

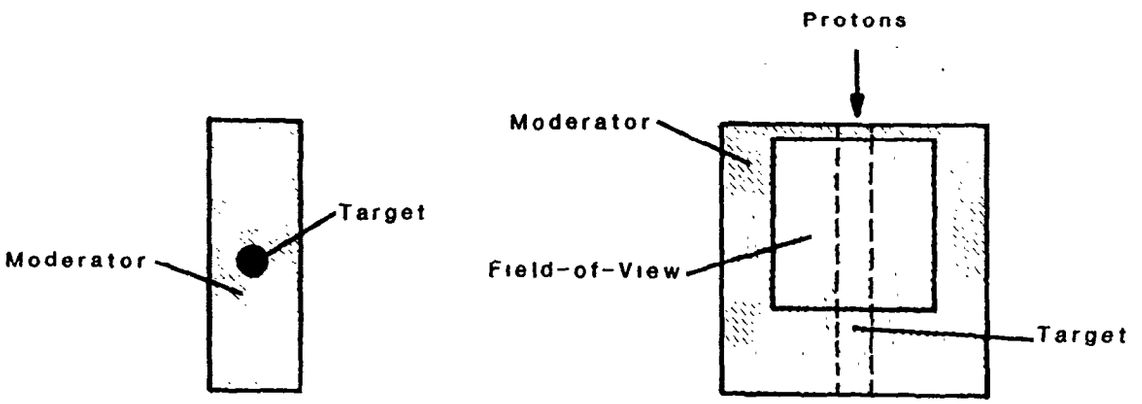

Bare Hybrid

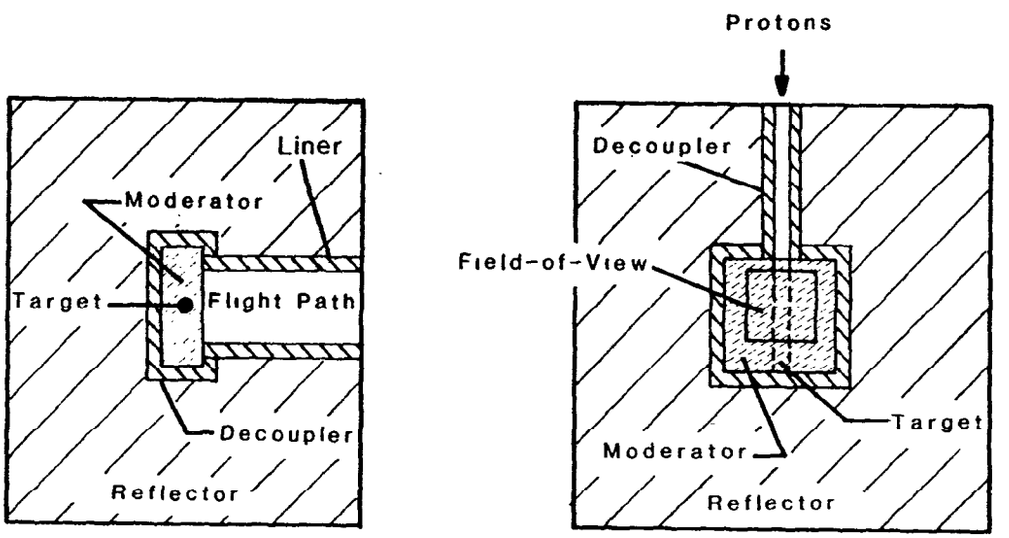

Reflected Hybrid

Fig. 18. Geometries used for calculating reflector efficiencies in a 'slab-type' moderator configuration. The reflected hybrid is a very efficient neutron production scheme; it is only slightly bettered by a reflected slab-target/slab-moderator arrangement.

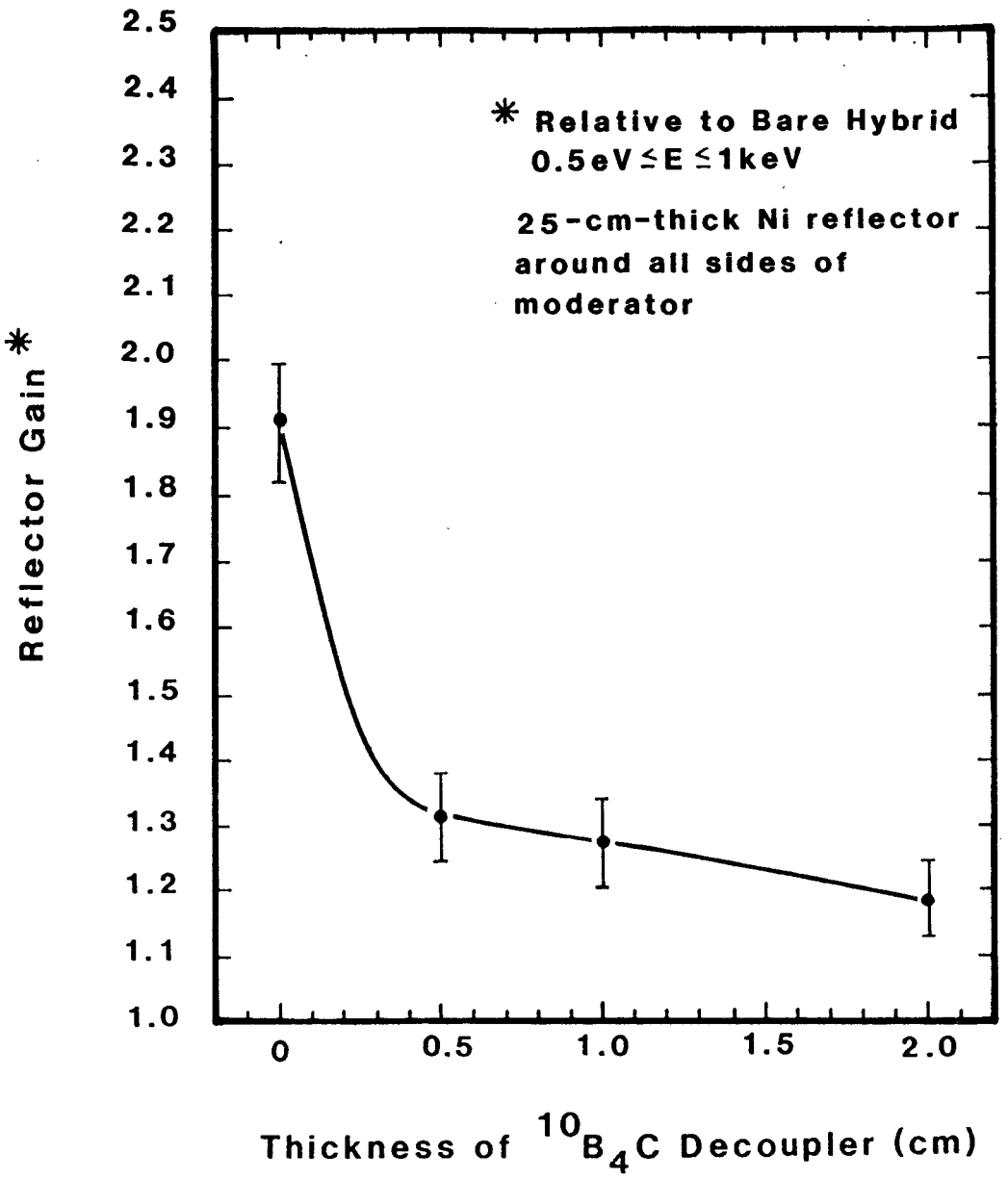

Fig. 19. Effect of decoupler thickness on reflector gain from a reflected hybrid moderator arrangement.

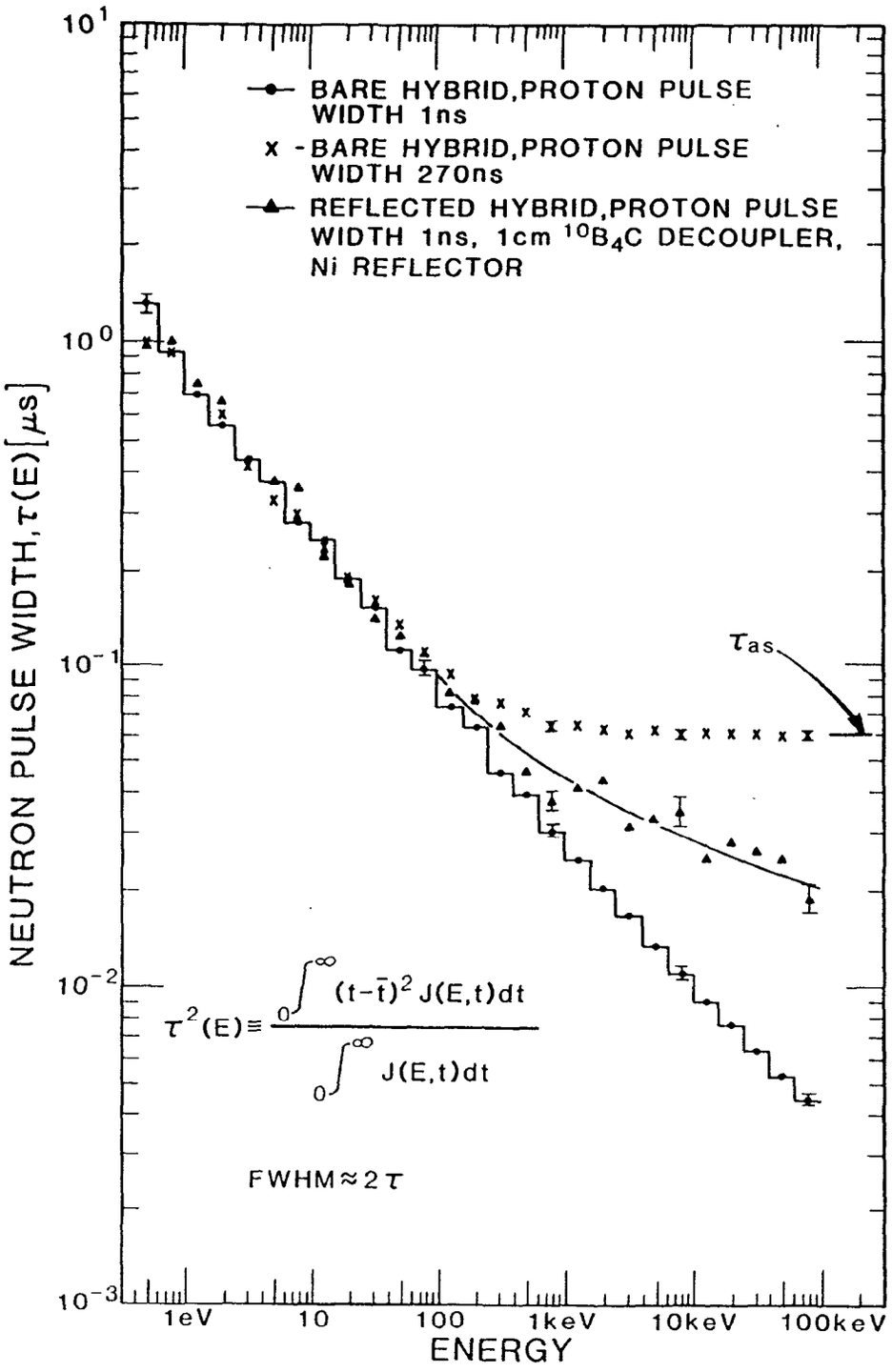

Fig. 20. Pulse width versus energy for various reflector/decoupler configurations.

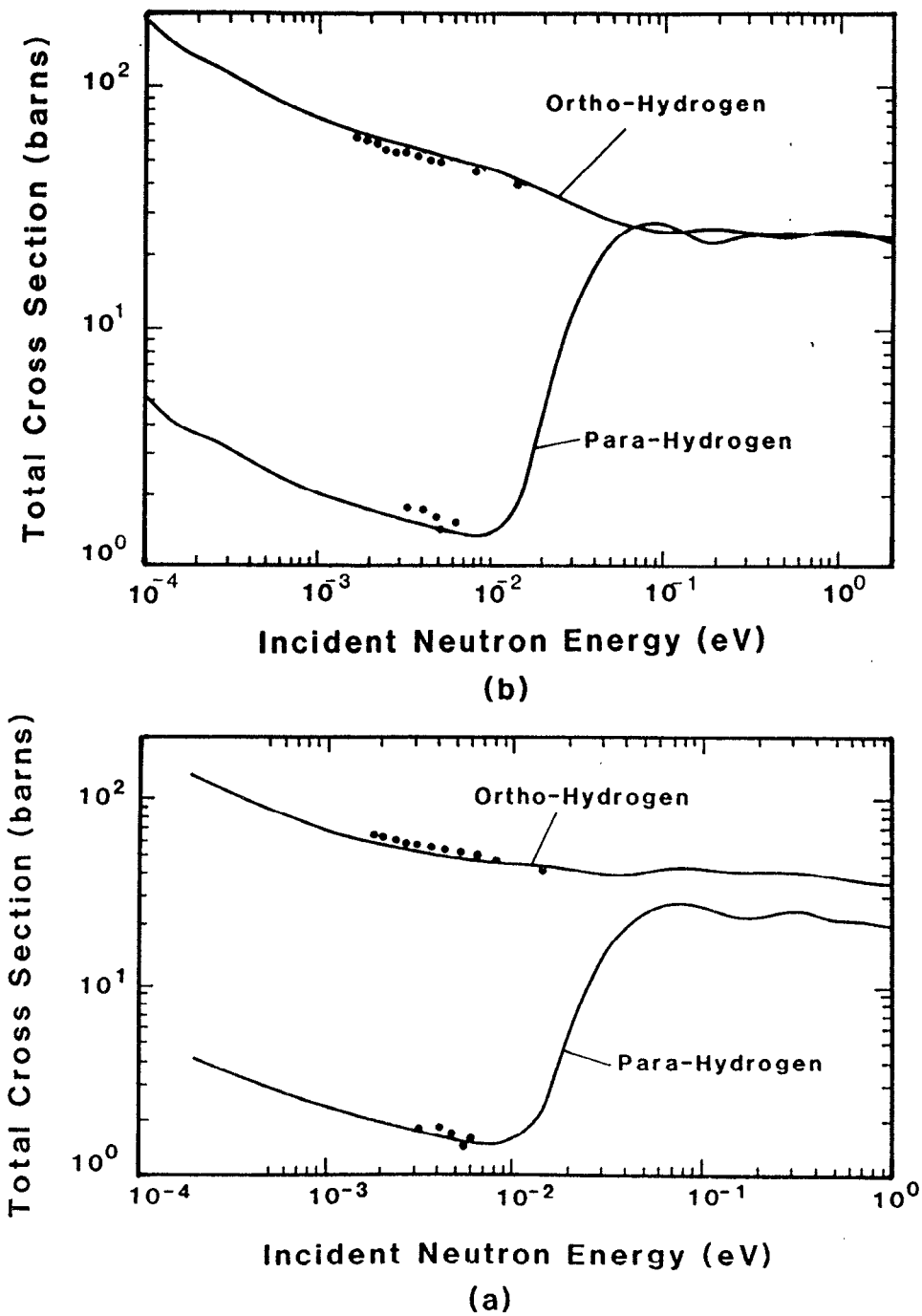

Fig. 21. a) neutron cross sections of para- and ortho-hydrogen as computed by Young and Koppel using their complete formalism, and b) cross sections calculated at Los Alamos using Young and Koppels' approximate formalism.

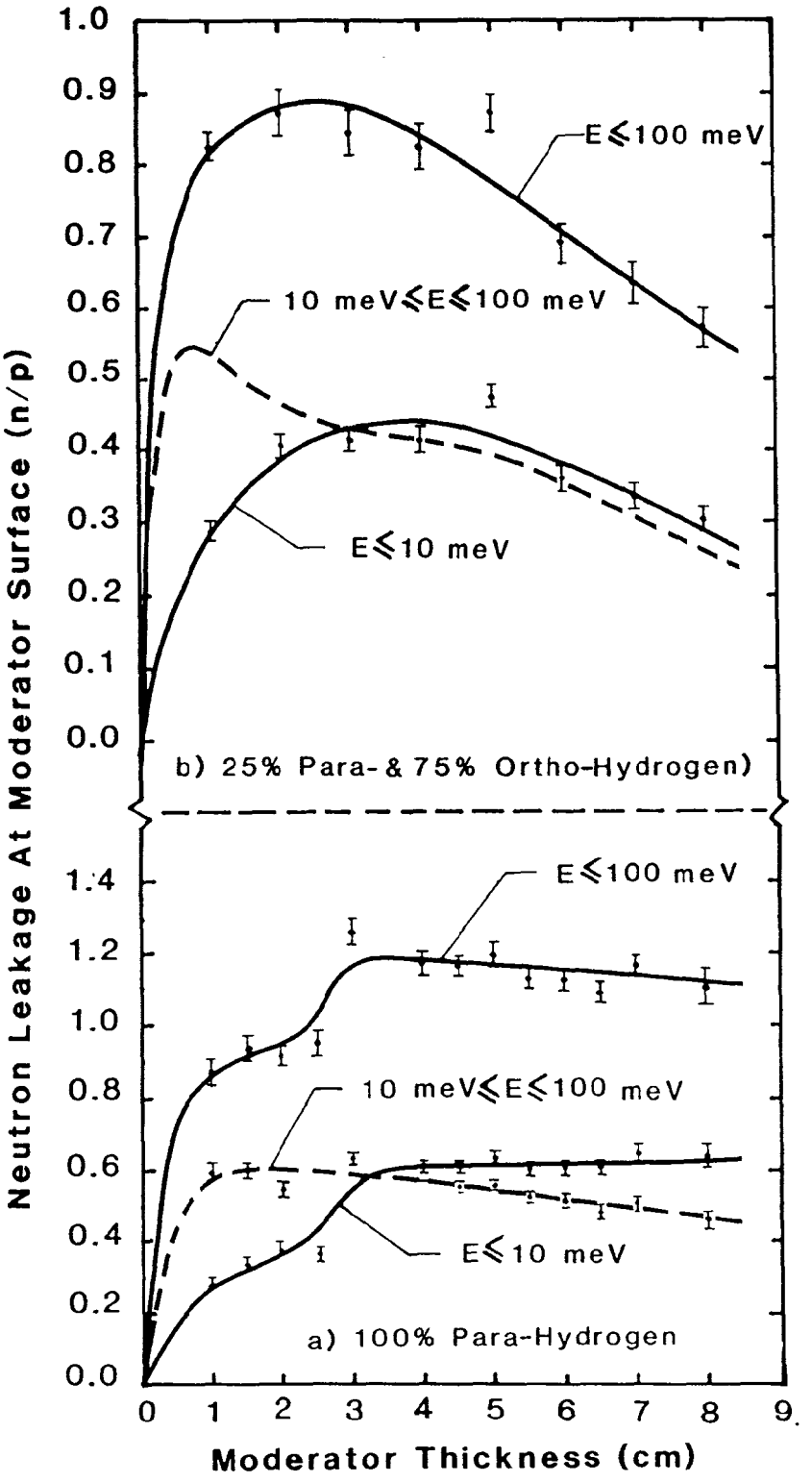

Fig. 22. Calculated cold moderator output versus moderator thickness for a coupled moderator in flux-trap geometry.

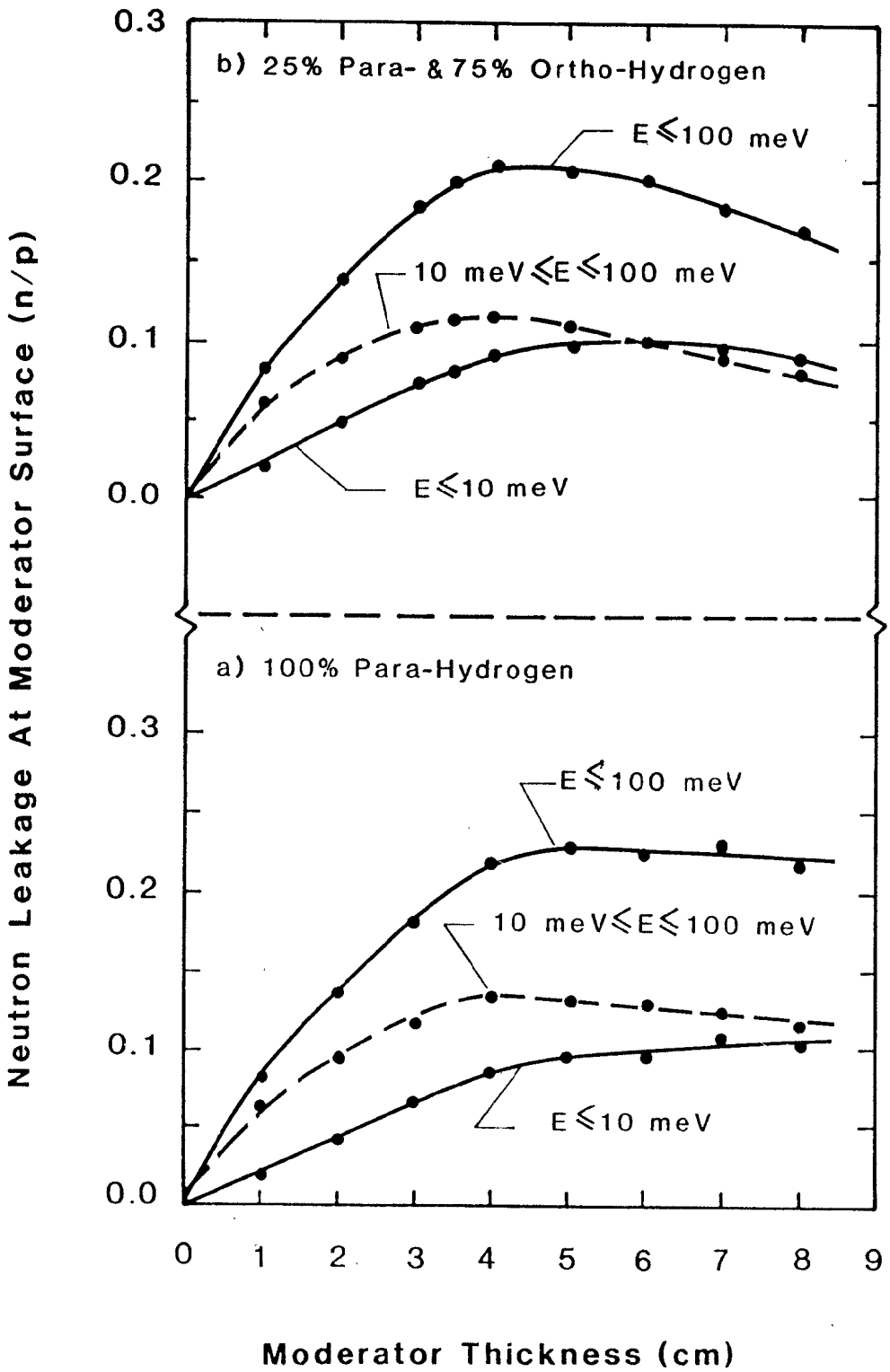

Fig. 23. Calculated cold moderator output versus moderator thickness for a moderator in flux-trap geometry decoupled from the reflector with gadolinium.

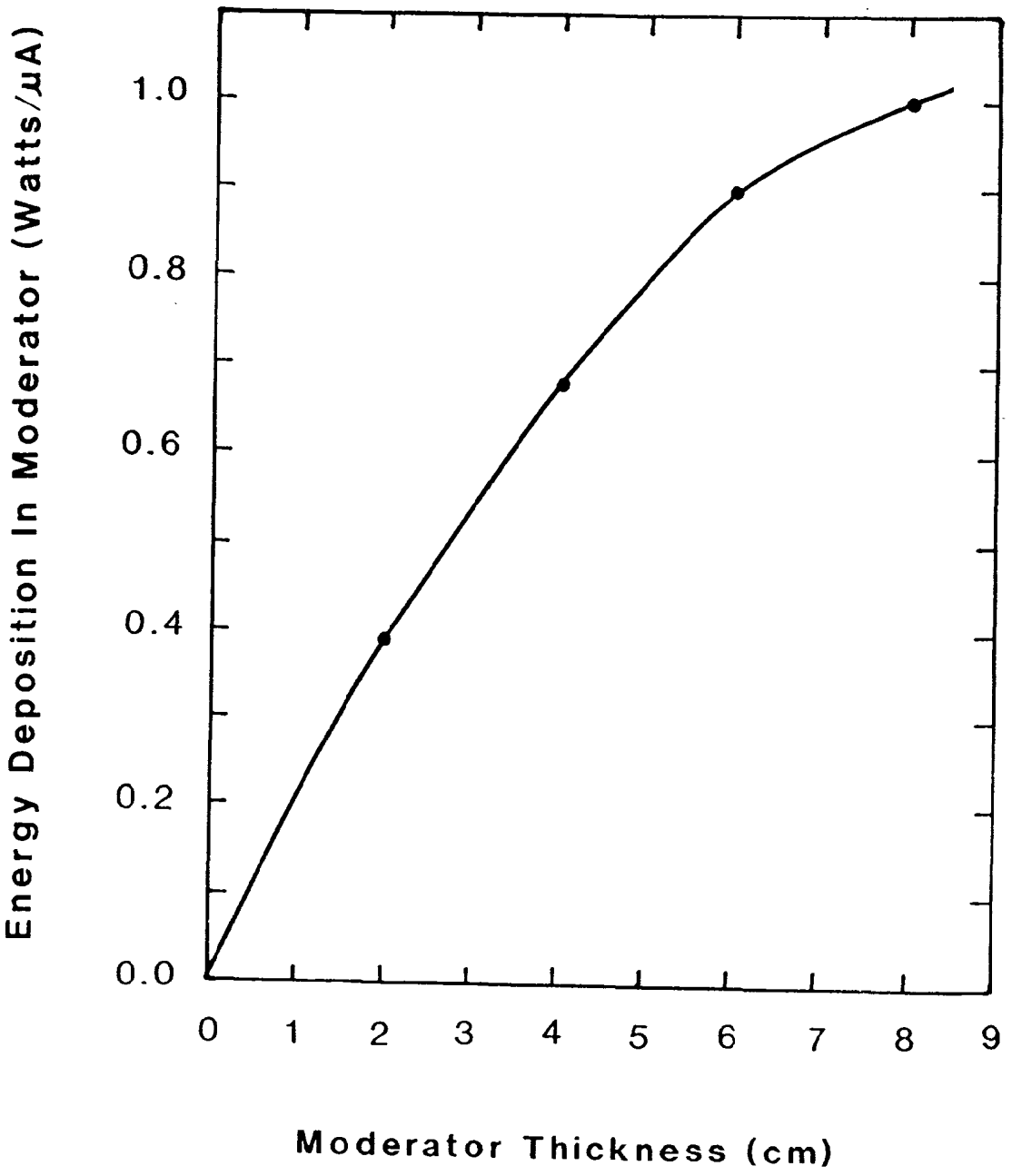

Fig. 24. Calculated energy deposition in a coupled cold hydrogen moderator in flux-trap geometry.

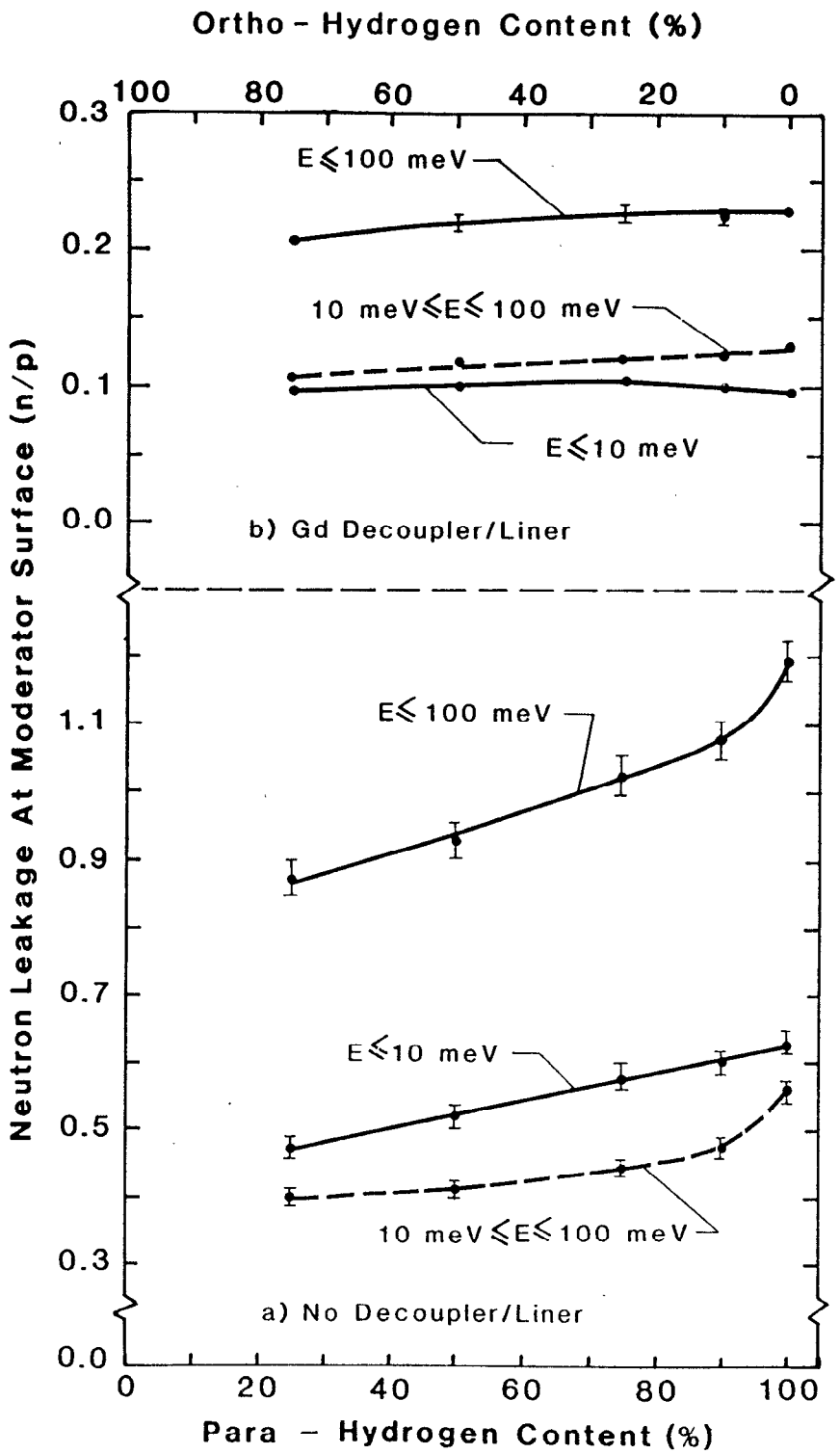

Fig. 25. Effect of para-hydrogen content on cold moderator output. The moderator was a 5 by 13 by 13 cm slab in flux-trap geometry.

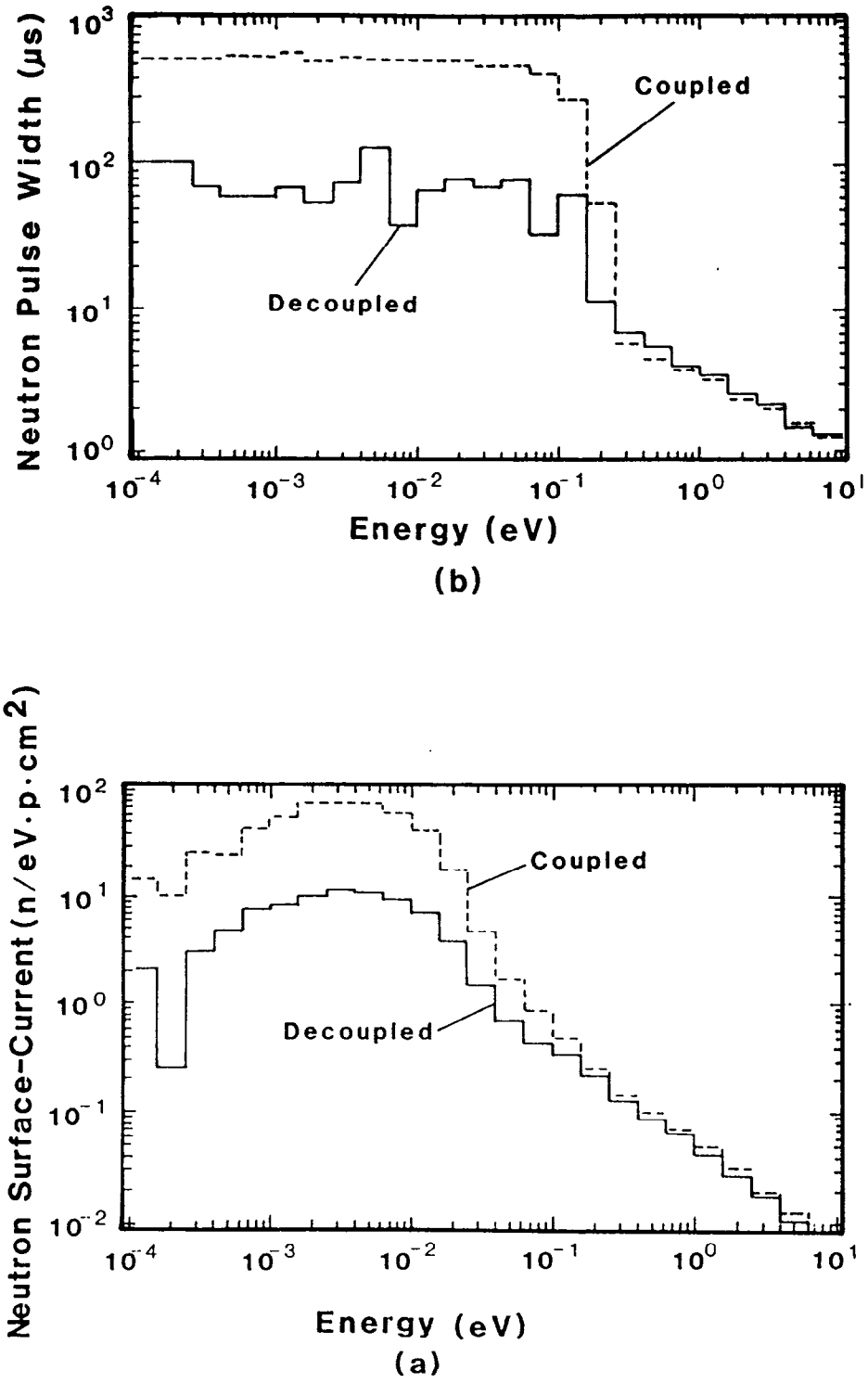

Fig. 26. Calculated neutron intensities and pulse widths for a 100% para-hydrogen cold source. The 5 by 13 by 13 cm slab moderator was in flux-trap geometry.

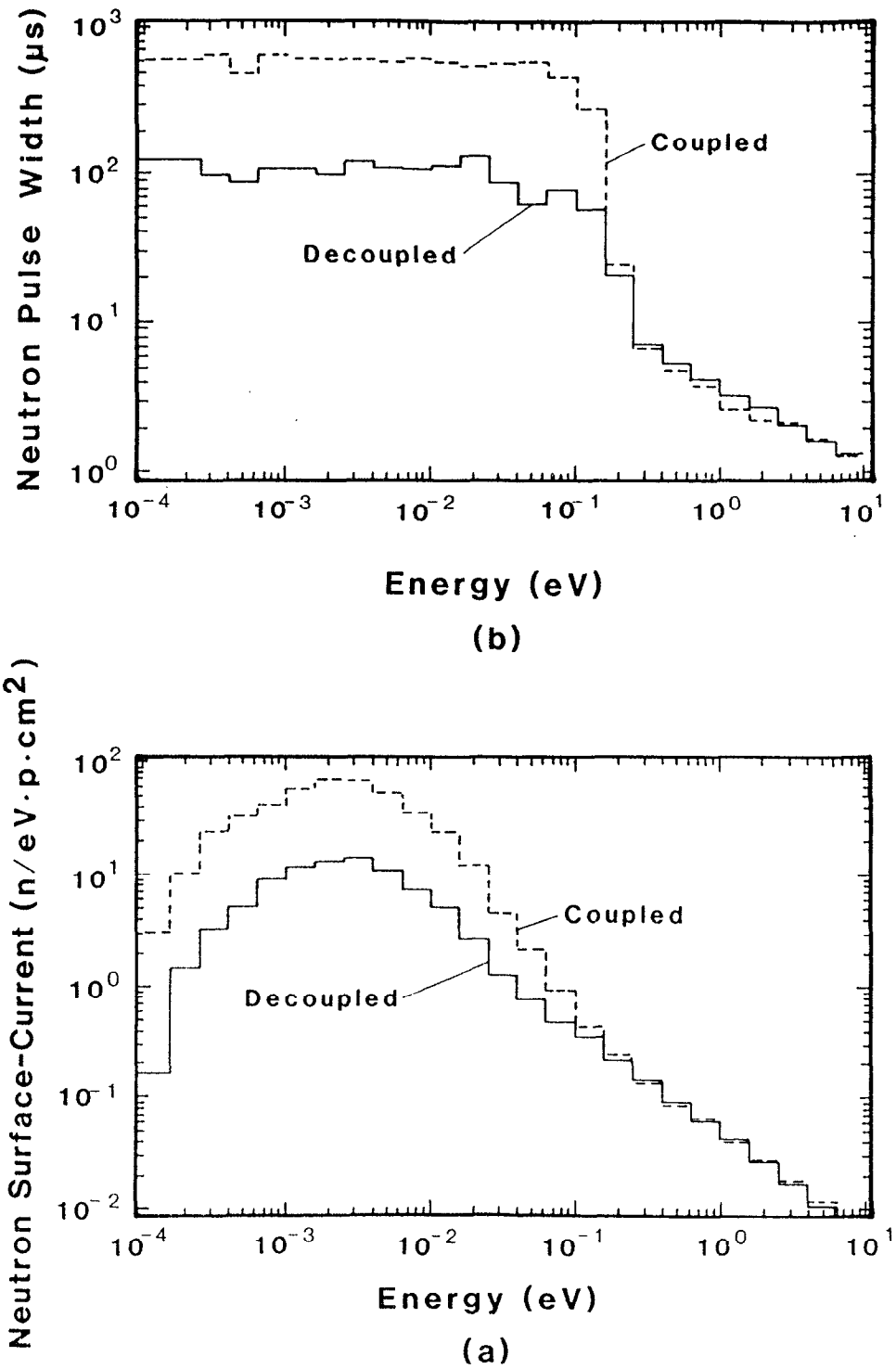

Fig. 27. Calculated neutron intensities and pulse widths for a 25% para- and 75% ortho-hydrogen cold source. The 5 by 13 by 13 cm slab moderator was in flux-trap geometry.

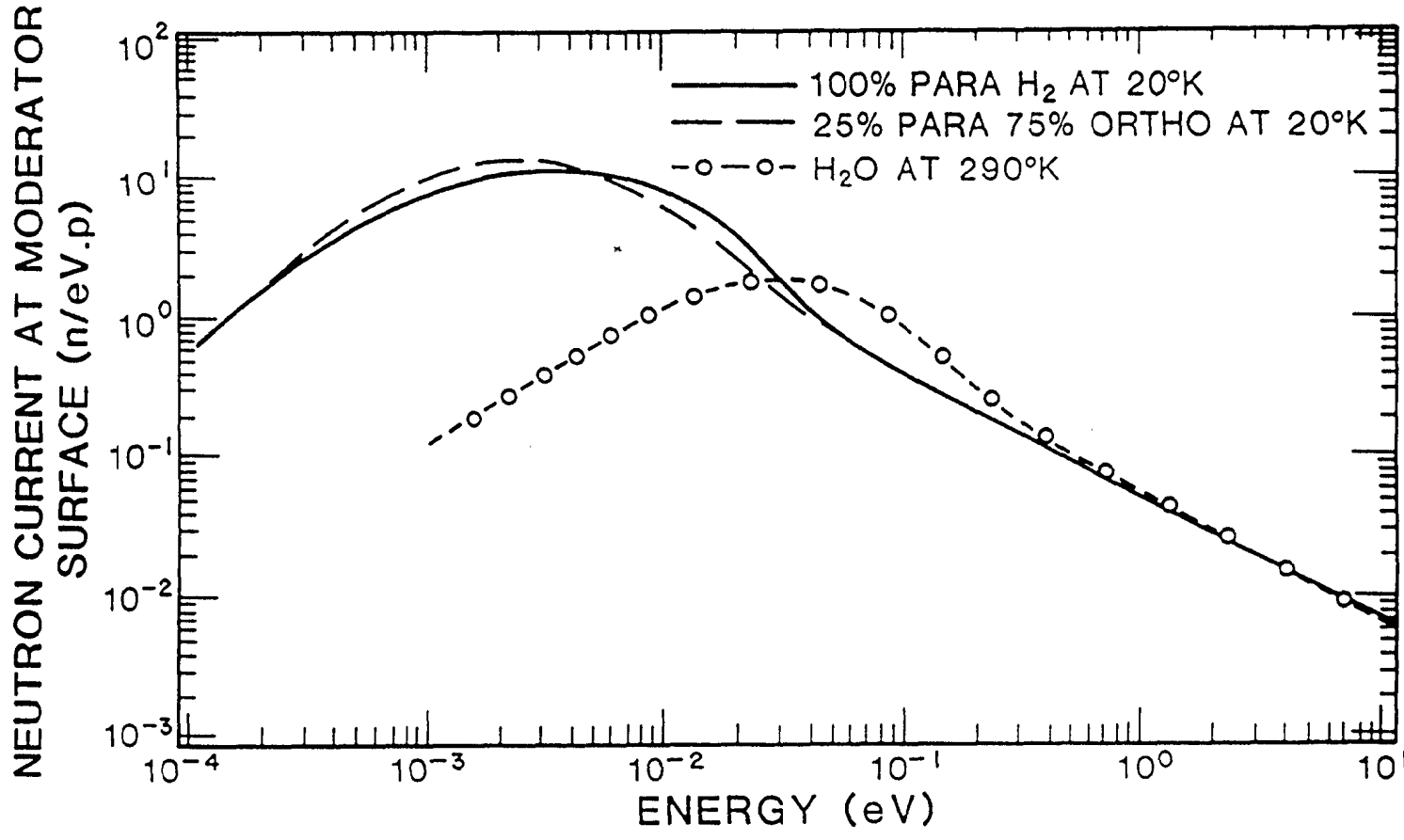

Fig. 28. Calculated LANSCE neutron energy spectrum from ambient and cold moderators.

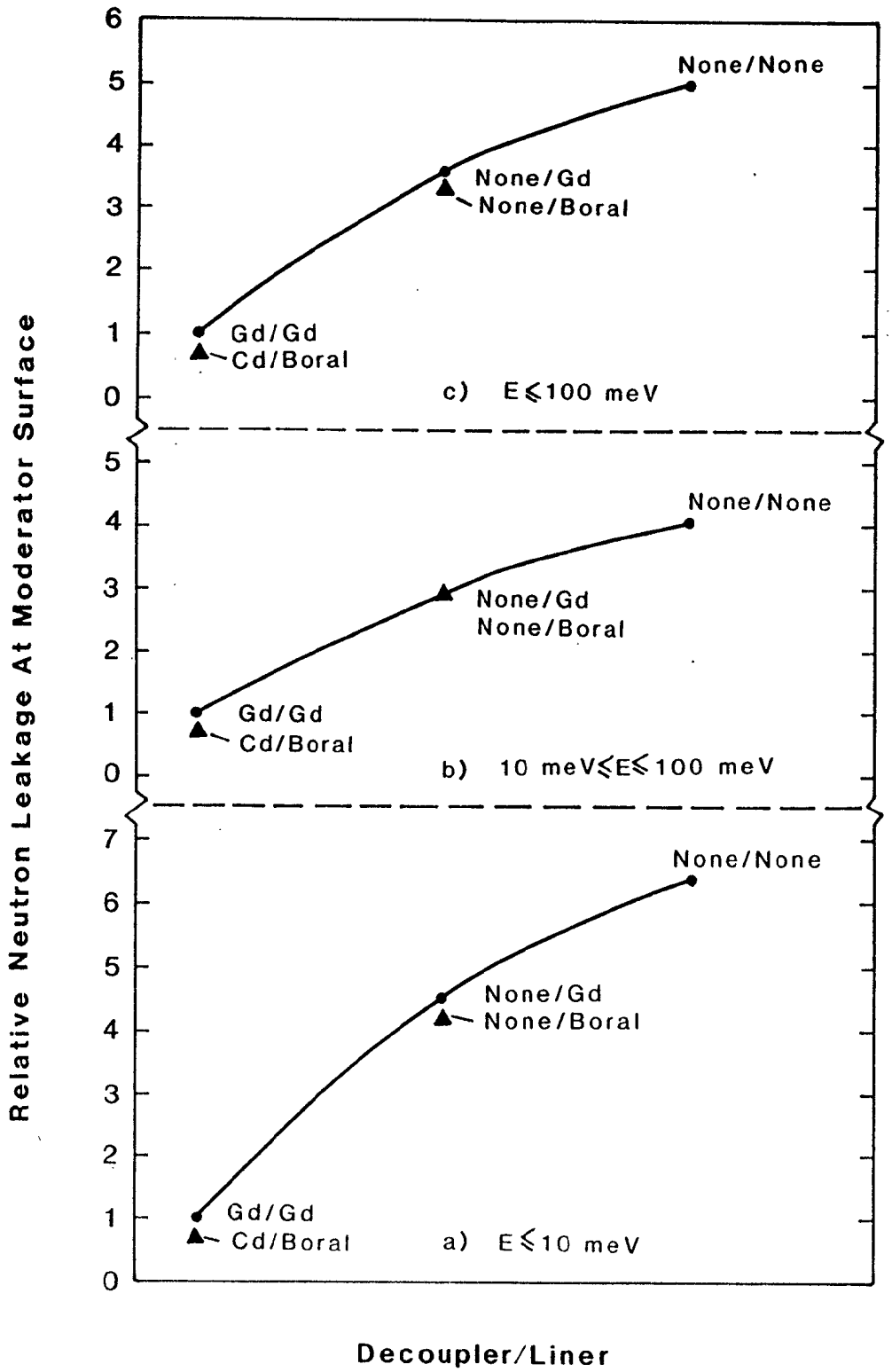

Fig. 29. Calculated neutron performance from a 100% para-hydrogen moderator for a variety of decoupler/liner combinations. The 6 by 13 by 13 cm moderator was in flux-trap geometry.

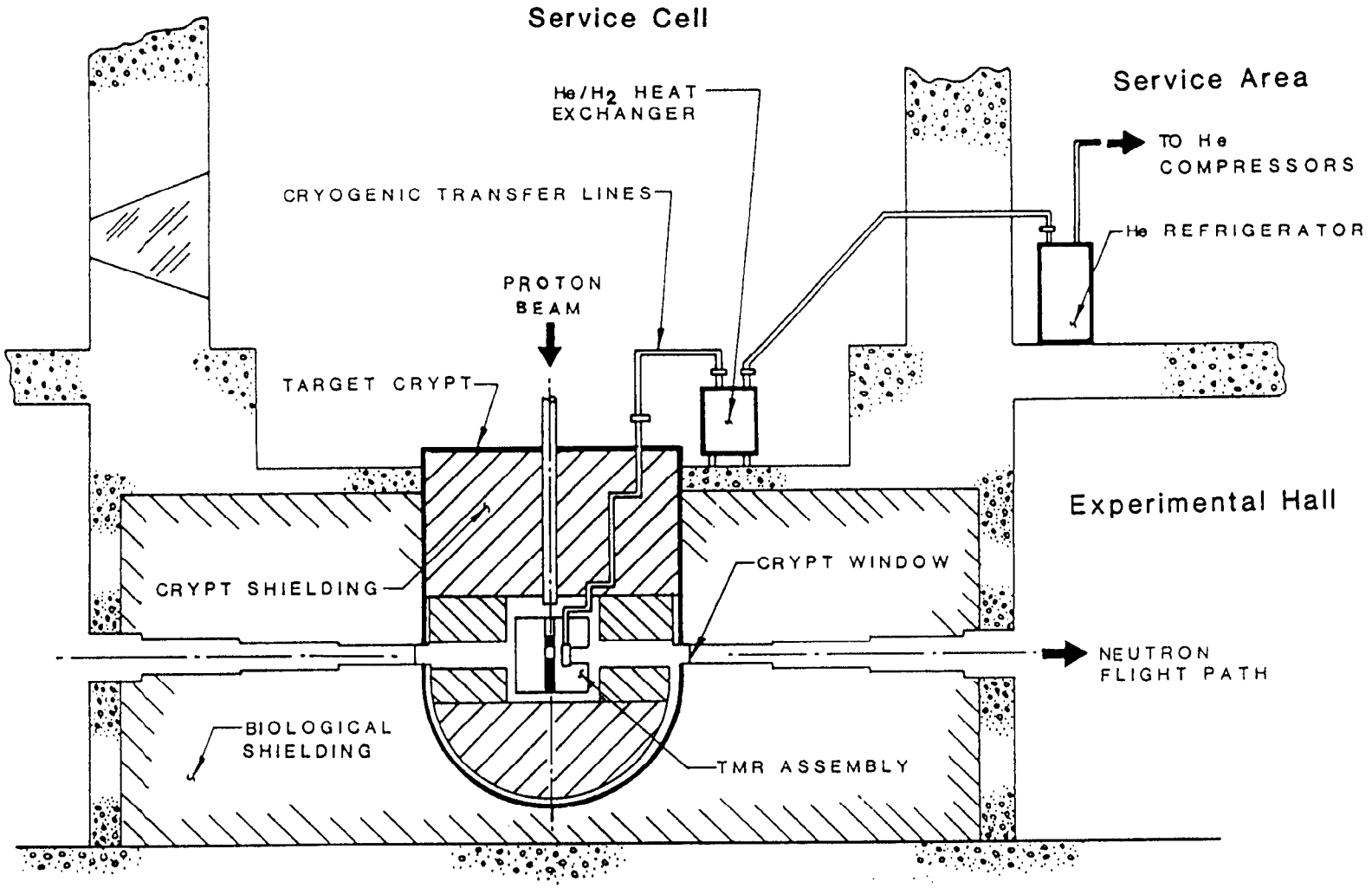

Fig. 30. Equipment layout for the LANSCE liquid hydrogen moderator system.

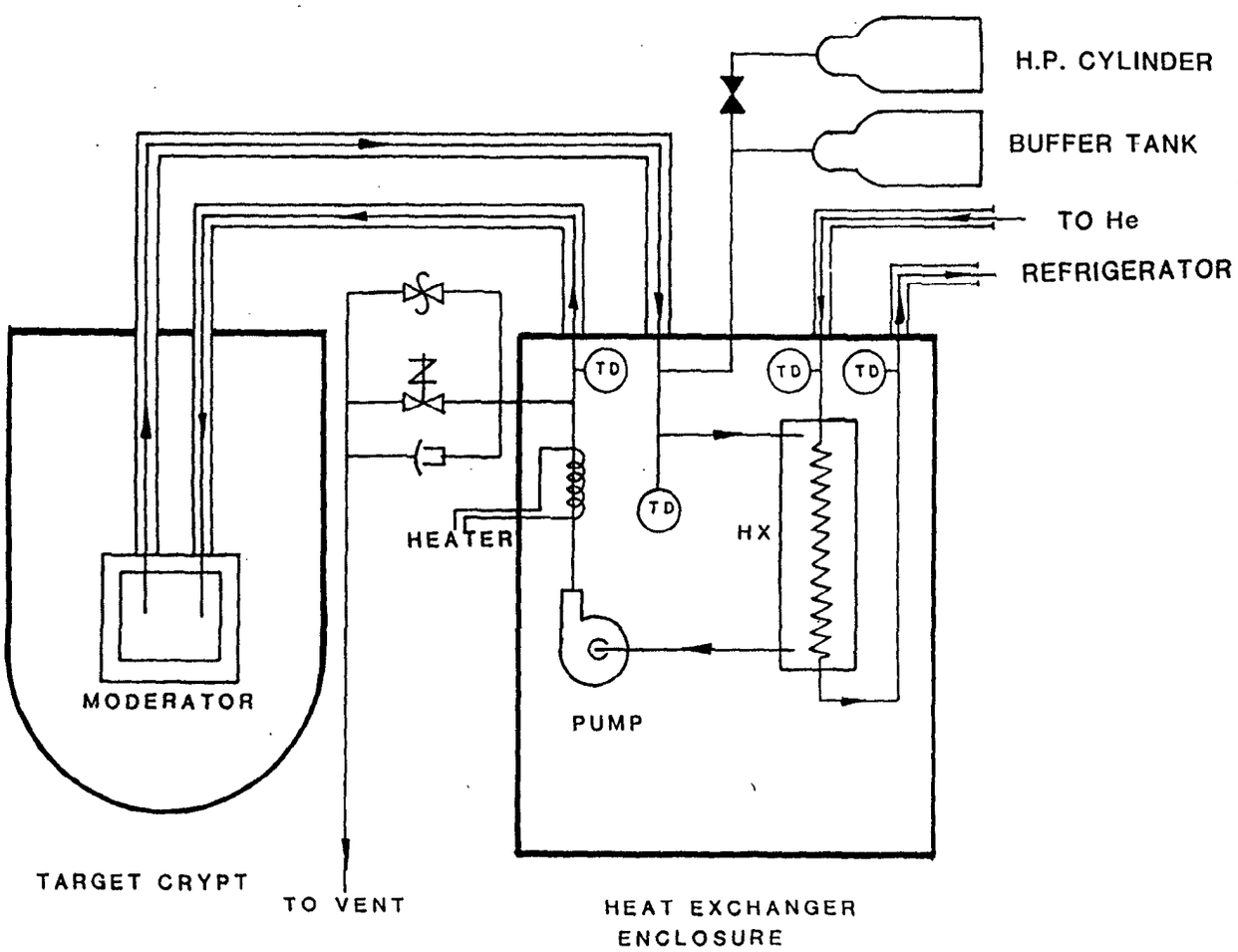

Fig. 31. Simplified schematic diagram for LANSCE liquid hydrogen moderator system.

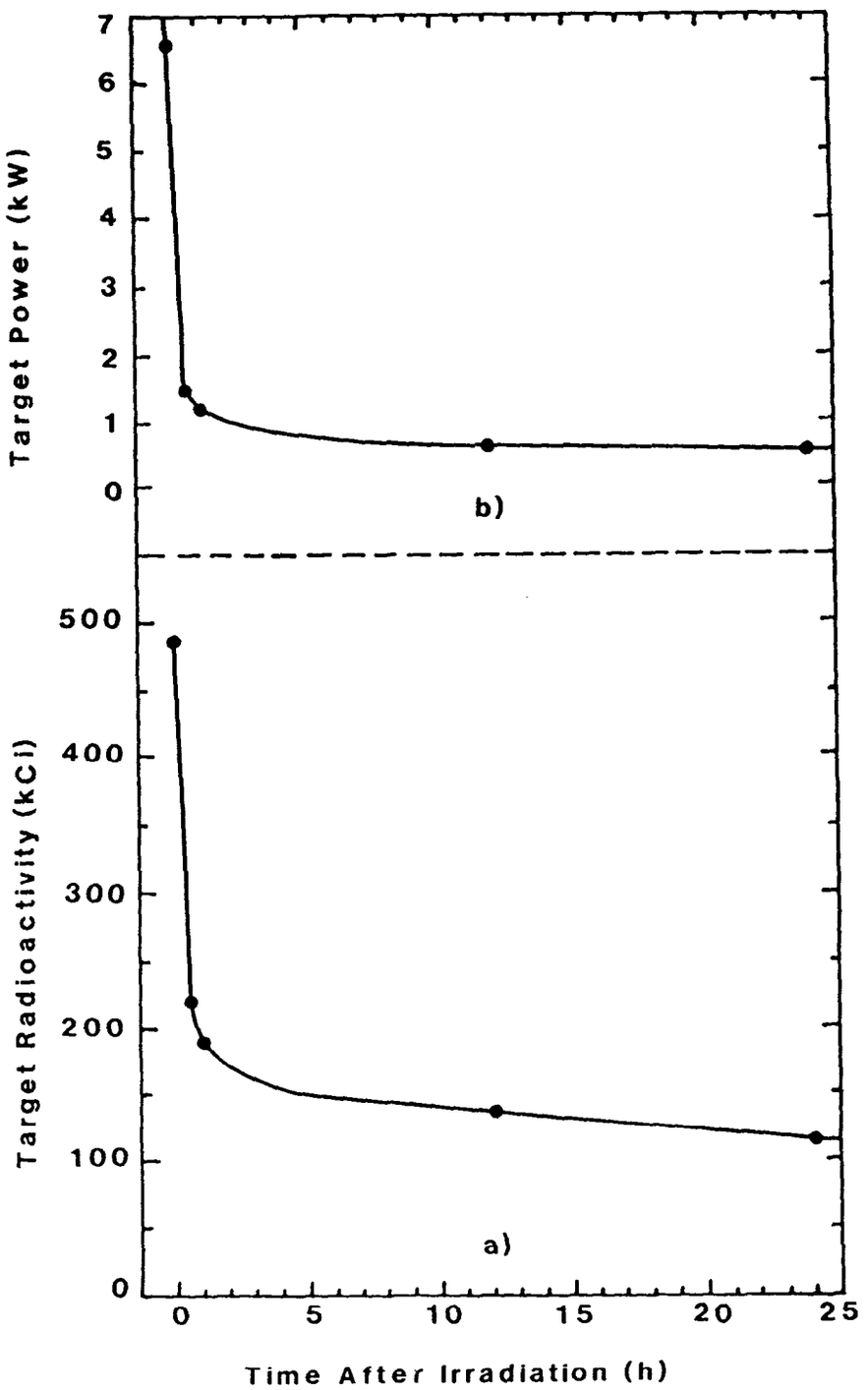

Fig. 32. Time dependent radioactivity and power of a LANSCE depleted uranium target. The target was assumed to be irradiated continuously for one year with 100 μA of 800-MeV protons.

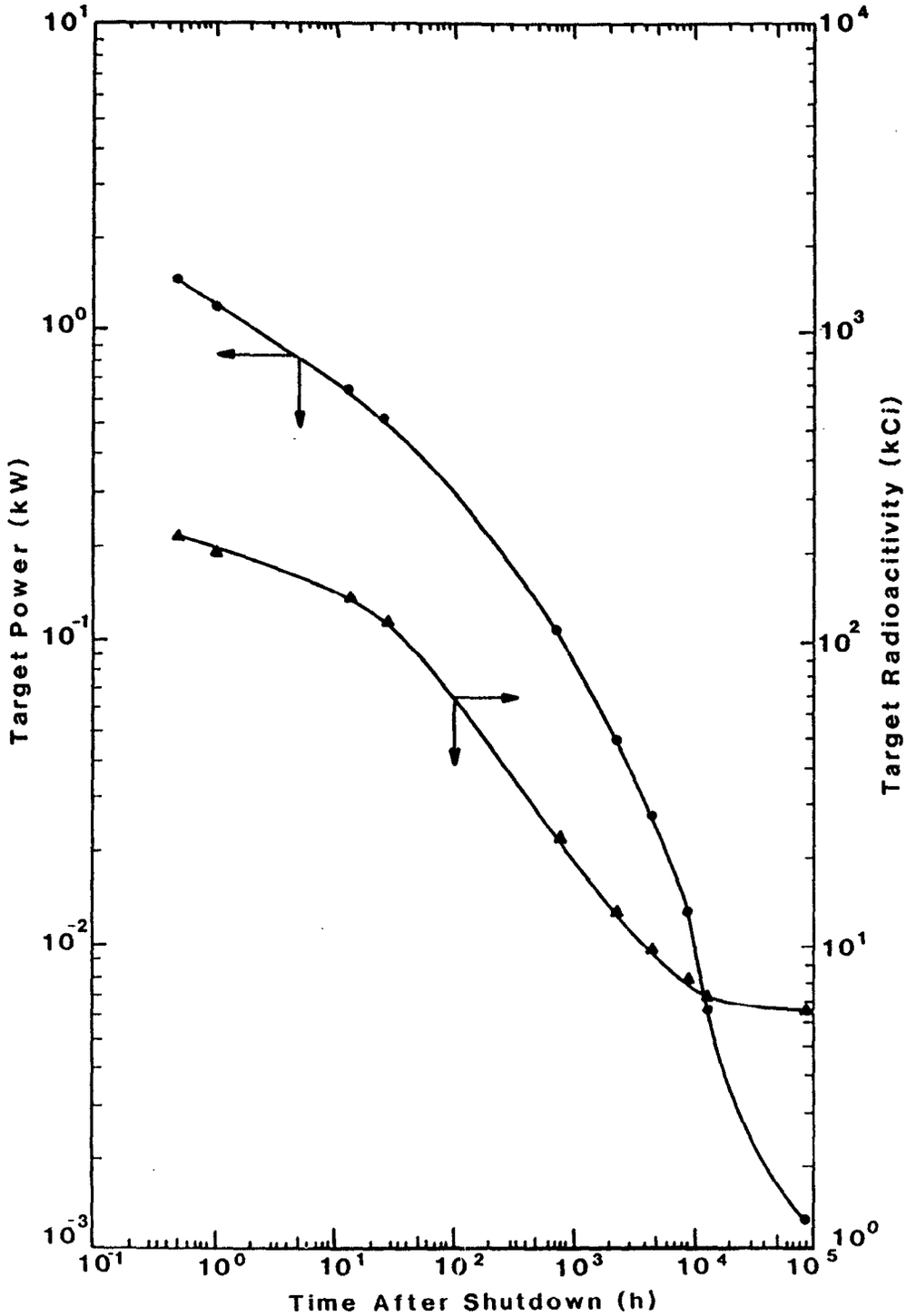

Fig. 33. Time dependent radioactivity and power of a LANSCE depleted uranium target. The target was assumed to be irradiated continuously for one year with 100 μA of 800-MeV protons.

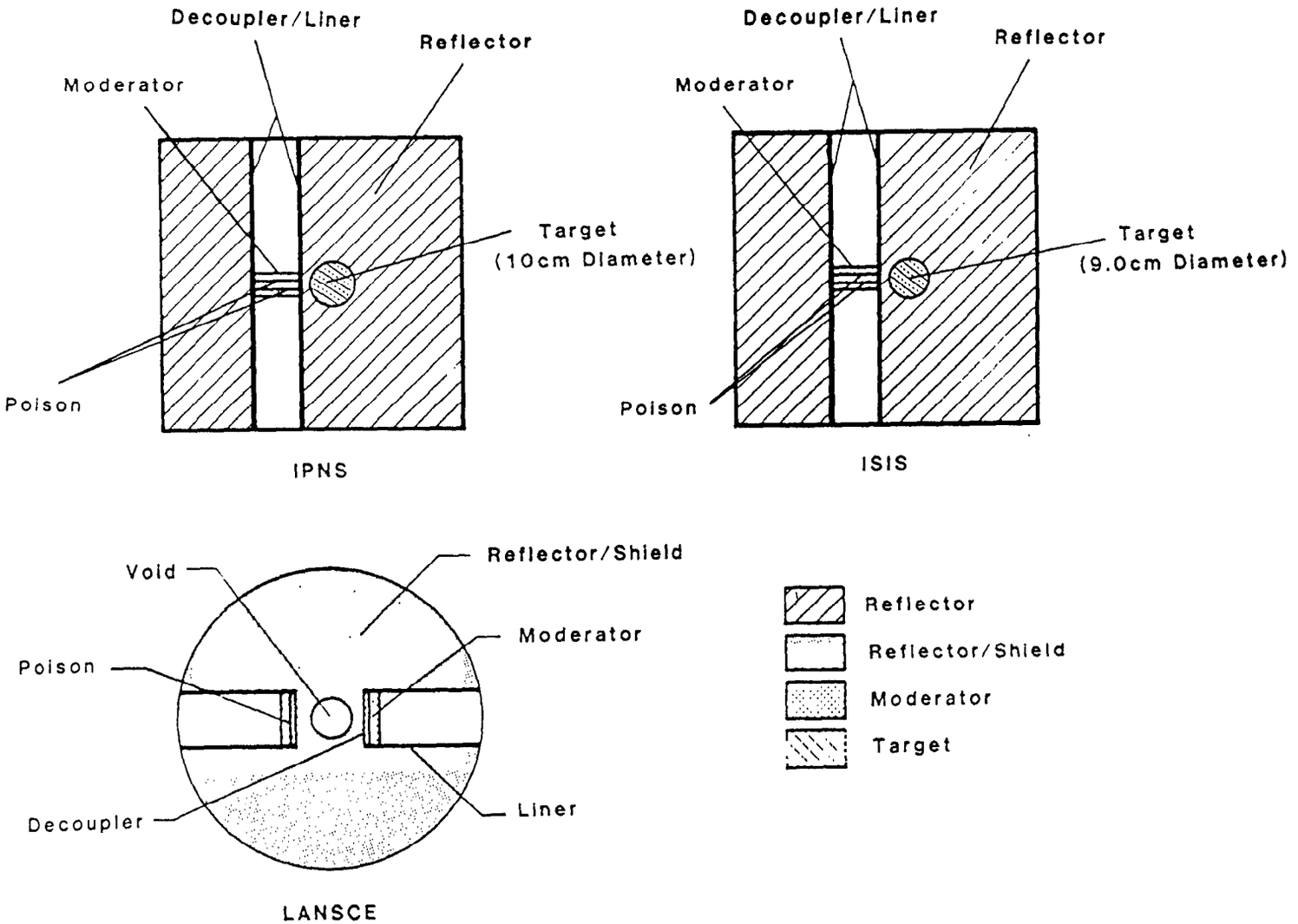

Fig. 34. Target/moderator/reflector geometries used to intercompare wing- and flux-trap moderator configurations.

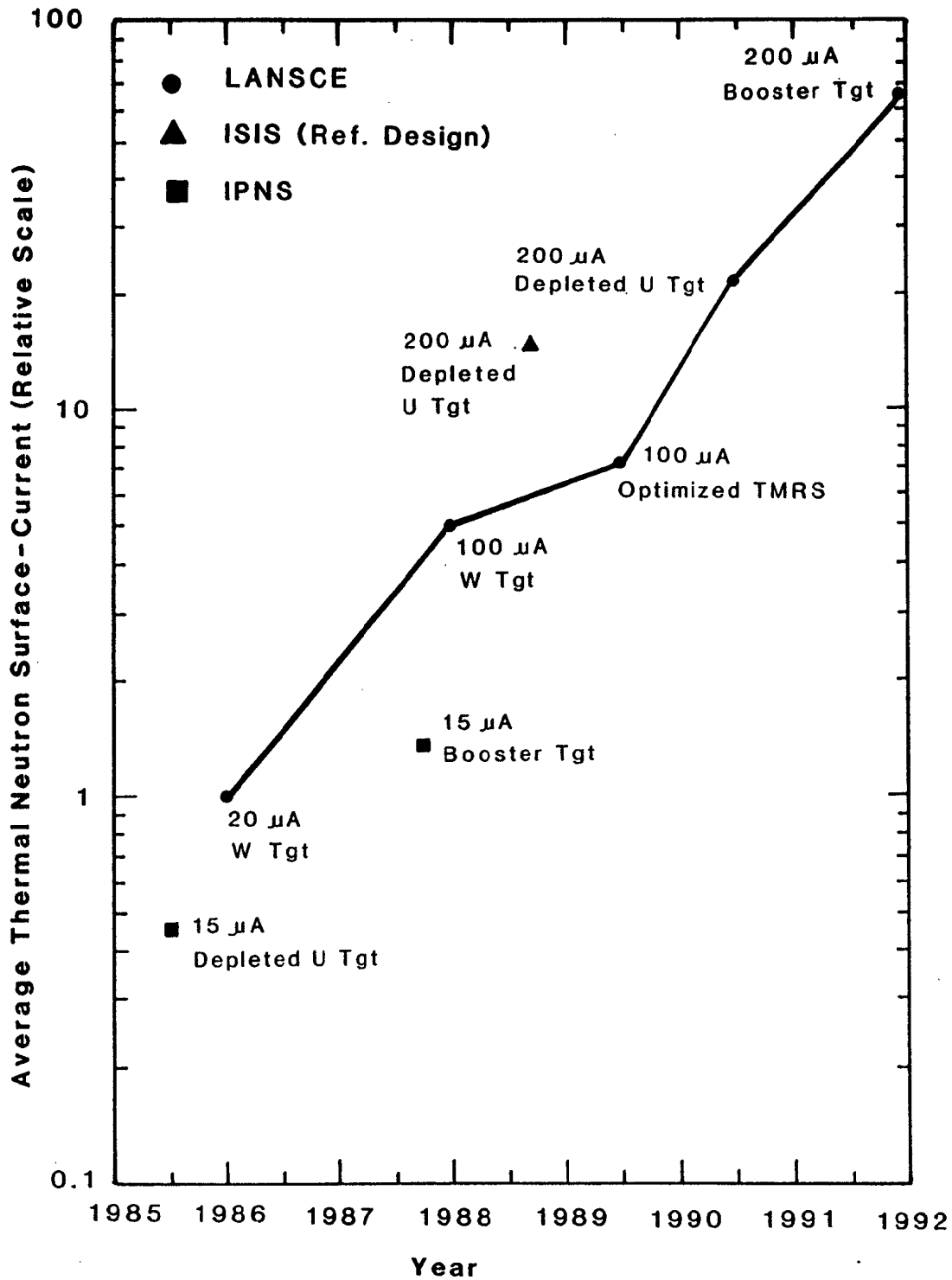

Fig. 35. **Relative** comparison of LANSCE performance (based on **average** neutron production) with other spallation neutron sources. Also indicated is one possible scenario for LANSCE development.

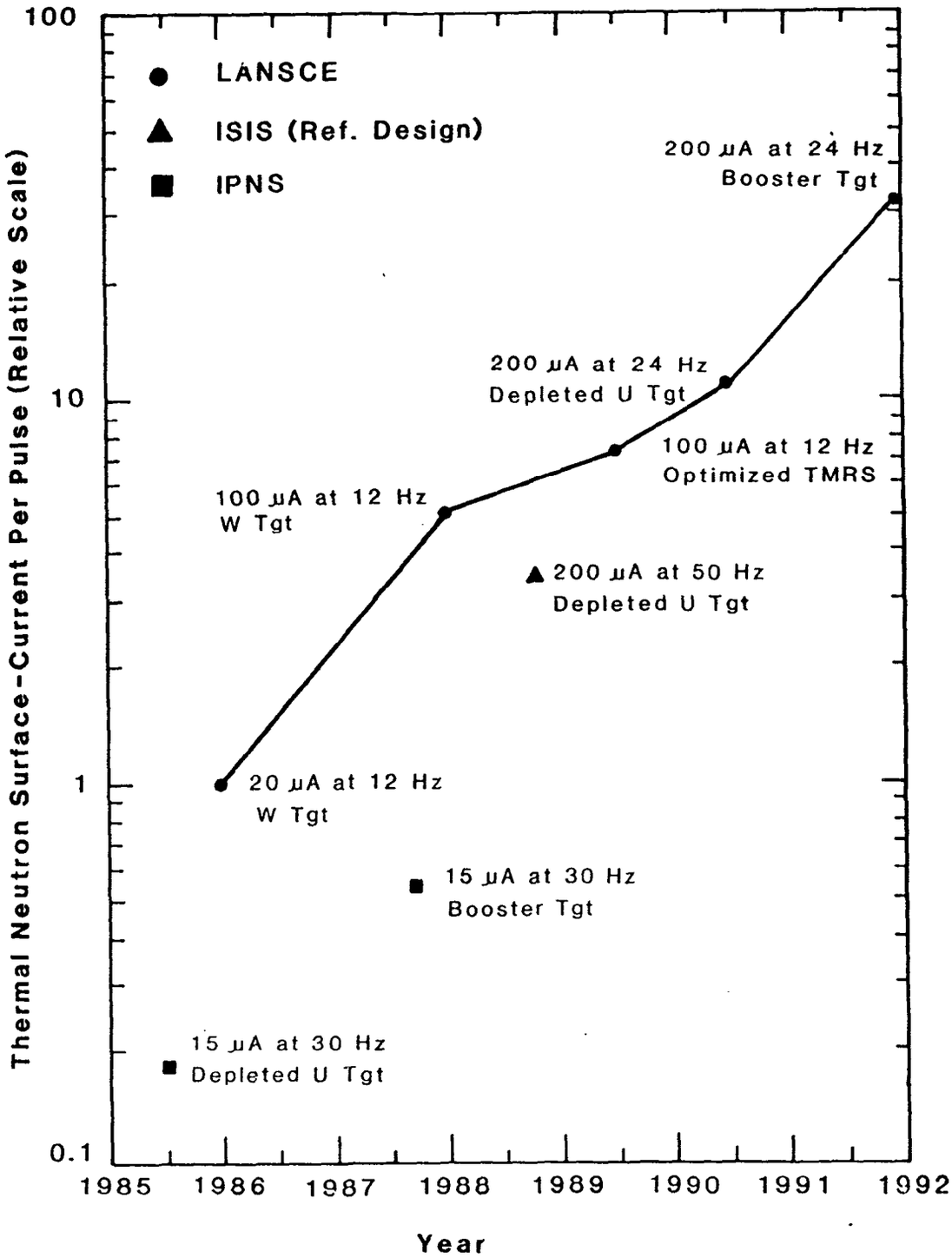

Fig. 36. **Relative** comparison of LANSCE performance (based on **peak** neutron production) with other spallation neutron sources. Also indicated is one possible scenario for LANSCE development.

ICANS IX

INTERNATIONAL COLLABORATION ON ADVANCED NEUTRON SOURCES

22-26 September, 1986

ACTIVATION OF THE HEAVY WATER COOLANT OF THE ISIS TARGET

G H Eaton, T A Broome and M J Bly
Rutherford Appleton Laboratory

1. Introduction

During operation the D_2O coolant of the target becomes highly active. The production rates of radionuclides from interactions in the water have been calculated by Atchison [1] using the HETC Monte Carlo package [2]. These production rates have been used to calculate the buildup and decay of activity, and associated radiation levels using a simple model of the water circuit.

Measurements of the short lived components have been made with a high resolution gamma detector and the results are compared with the predictions.

2. Activation Calculation

The production rates of the radionuclides from [1], together with mean lifetimes and decay modes, are shown in Table 1.

The specific activity, α_T, of an individual nuclide in the target cooling water is given by

$$\alpha_T = \alpha_o \frac{(1 - e^{-t_i/\lambda})\, e^{-t_c/\lambda}\, (1 - e^{-T/\lambda})}{V\,(1 - e^{-T_c/\lambda})}$$

where α_o is the production rate

V is the volume of water in the target

t_i is the time for volume V of water to pass through the target

λ is the mean lifetime

T is the time from startup of the proton beam

T_c is the circulation time for the water around the circuit

These quantities are illustrated on the schematic diagram of the water circuit in Figure 1.

The specific activities in the target coolant for various irradiation and decay times are shown in Table 2.

3. Radiation Levels Around the Cooling Plant

The water cooling system comprising pipes, pumps, filters, heat exchanges etc, are mounted on one of the trolleys in the Target Station services area (see Figures 2 and 4).

To estimate the radiation levels in this area from the active target, moderator and reflector water circuits the pipes were treated as line gamma sources and the dose rate at 1 m from each pipe was calculated.

For a 200 μA beam of 800 MeV protons this procedure predicts a dose rate of 1 Sv/h on the trolley.

The main contribution to the dose is from the β^+ emitters which are relatively short lived. The decay of the dose rate is shown in Figure 3 and after about 3 hours the level becomes fairly constant and is dominated by ^{7}Be. Ion exchange columns in the circuit collect all the ^{7}Be and on this basis it was predicted that entry to the services area for work on the water plant would be possible after about 3 hours when the dose rate would be less than 100 μSv/h. At the present ~ 10% intensity a cooldown period of about 30 min has been found to be necessary before entry. This is somewhat shorter than calculated and the faster fall off of the dose rate is probably a result of the ion exchange columns collecting some of the shorter lived activity in addition to the ^{7}Be.

The high radiation levels around the plant require substantial shielding, 1 m of concrete, and the 6 MeV gammas from ^{16}N dominate this requirement.

4. Measurements of Water Activation

A Lithium drifted Germanium detector is installed outside the Services Area viewing a delay reservoir on a bleed line in the target cooling circuit through a hole in the shielding. The position of this detector is shown in Figure 4 and schematic detail in Figure 5.

The primary purpose of this device is to act as an on-line fission product monitor to detect any failure of the zircalloy cladding on the uranium target discs. The principle of the method is to detect gammas from fission products, for example ^{95}Nb, ^{97}Nb, ^{132}I, ^{124}Sb, which have energies in a region of relatively low background from the normal activity of the water. Calculations [3] indicate that a failure of the cladding will be detected within a few minutes.

Much work needs to be done in commissioning and evaluating this equipment. The water activity measurements described below whilst interesting in their own right are a crucial step in establishing the background counting rate environment in which fission product activity needs to be detected.

4.1 Long lived activity in the ion exchange resin

Samples of the ion exchange resin from the target cooling circuit after 2 months decay time were placed 20 cm from the shielded GeLi detector and the gamma spectra measured. The dominant nuclide present was ^{7}Be and small concentrations (relative to ^{7}Be) of other nuclides were identified which are listed below together with the likely production mechanism.

Nuclide	Half life	Probable target nucleus
Na 22	2.6 y	Many possibilities
Sc 46	84 d	Stainless Steel
Mn 54	312 d	Stainless Steel
Co 56	79 d	Stainless Steel
Co 58	71 d	Stainless Steel
Co 60	5.3 y	Stainless Steel

Nuclide	Half life	Probable target nucleus	
Zn 65	244 d		
Se 75	120 d		
Rb 83	86 d		
Sr 85	65 d		Zircalloy Cladding
Y 88	107 d		
Zr 88	85 d		
Zr 99	66 d		
Nb 95	35 d		
Ag 110M	233 d	Ag	Silver plated seals

Note that the presence of ^{95}Nb as a spallation product makes the use of this nuclide problematic for the fission product monitor.

The nuclides detected are much as expected and provide very useful information for the backgrounds to be expected for fission product detection.

4.2 Short lived activity in the cooling water

The decay of the intensity of the 511 keV annihilation gammas from the β^+ emitters was measured as a function of time after beam turn off. The decay curve is shown in Figure 6.

The relative contributions of ^{15}O, ^{13}N and ^{14}O were calculated by fitting the decay curve with three exponential functions. Figure 5 shows the relative contribution together with the theoretical prediction. Bearing in mind the detail being required of the Monte Carlo program the agreement in relative contributions is excellent. ^{11}C was predicted at a rate of 13% of ^{15}O. This was not evident in the measurements and the discrepancy may well be due to a partial or complete removal of ^{11}C by the ion exchange column.

5. Conclusion

The detection system has performed well and initial operating experience gives confidence that it will provide the required rapid detection of cladding failure in the target.

The agreement between detailed Monte Carlo calculations of activity and measurements is good.

References

[1] F Atchison — A Theoretical Study of a Target REflector and Monderator Assembly for SNS - RL-81-006.

[2] HETC — RSIC computer code collection No CCC-178.

[3] G H Eaton — Proposal for an on-line clad failure detector system for the SNS target station using high-resolution γ-ray spectroscopy - SNS/TS/N10/82.

Nuclide	Mean Life	Production Rate nuclei/proton	Decay Mode (branching ratio)*	Gamma Energy Mev (Branching Ratio)
^{18}F	158.29m	1.06×10^{-5}	β^+	
^{17}N	6.02s	5.00×10^{-5}	β^-(0.05) β^-n(0.95)	0.87 (0.03)
^{16}N	10.29s	1.60×10^{-3}	β^-	6.13 (0.69)
^{15}O	176.15s	1.00×10^{-2}	β^+	
^{15}C	3.53s	7.70×10^{-5}	β^-	5.30 (0.68)
^{14}O	101.84s	3.20×10^{-4}	β^+	2.31 (0.99)
^{14}C	8267y	1.20×10^{-3}	β^-	
^{13}N	14.37m	2.60×10^{-3}	β^+	
^{11}C	29.40m	1.10×10^{-3}	β^+	
^{11}Be	19.92s	1.10×10^{-4}	β^-(0.97) $\beta^-\alpha$(0.03)	2.13 (0.33) 4.67 (0.02 5.85 (0.02) 6.79 (0.04) 7.97 (0.02)
^{10}C	27.63s	2.20×10^{-4}	β^+	0.718 (0.99)
^{10}Be	2.31×10^6y	1.00×10^{-4}	β^-	
^{7}Be	76.88d	1.70×10^{-3}	EC	0.478 (0.1035)
^{3}H	17.51y	1.00×10^{-2}	β^-	

(* Branching ration 1.0 unless shown in brackets).

Table 1. Production rates and decay modes of radionuclides produced in the Target Coolant.

	Irradiation times					
	1s	60s	1h	1d	7d	∞
18F	7.46E+06	4.46E+08	2.23E+10	7.08E+10	7.08E+10	7.08E+10
17N	3.75E+09	2.45E+10	2.45E+10	2.45E+10	2.45E+10	2.45E+10
16N	2.46E+11	2.65E+12	2.65E+12	2.65E+12	2.65E+12	2.65E+12
15O	3.54E+11	1.80E+13	6.25E+13	6.25E+13	6.25E+13	6.25E+13
15C	9.04E+08	3.66E+09	3.66E+09	3.66E+09	3.66E+09	3.66E+09
14O	1.86E+10	8.45E+11	1.90E+12	1.90E+12	1.90E+12	1.90E+12
14C	3.08E+01	1.85E+03	1.11E+05	2.66E+06	1.86E+07	8.03E+12
13N	1.99E+10	1.15E+12	1.69E+13	1.72E+13	1.72E+13	1.72E+13
11C	4.14E+09	2.44E+11	6.36E+12	7.31E+12	7.31E+12	7.31E+12
11Be	1.85E+10	3.60E+11	3.78E+11	3.78E+11	3.78E+11	3.78E+11
10C	3.28E+10	8.17E+11	9.23E+11	9.23E+11	9.23E+11	9.23E+11
10Be	9.18D-03	5.51E-01	3.31E+01	7.94E+02	5.56E+03	6.69E+11
7Be	1.71E+06	1.03E+08	6.17E+09	1.47E+11	9.91E+11	1.14E+13
3H	1.19E+05	7.14E+06	4.29E+08	1.03E+10	7.20E+10	6.69E+13
Totals	6.98E+11	2.41E+13	9.16E+13	9.30E+13	9.39E+13	1.80E+14

Table 2a. Build-up of specific activity of target plate coolant Bq m^{-3}.

The decay of activity, from its saturation value, after beam has been switched off, is shown below.

	Cooling times					
	1m	5m	1h	8h	1d	7d
18F	7.04E+10	6.86E+10	4.85E+10	3.41E+09	7.93E+06	0.0
17N	1.15E+06	0.0	0.0	0.0	0.0	0.0
16N	7.79E+09	5.78E-01	0.0	0.0	0.0	0.0
15O	4.44E+13	1.14E+13	8.31E+04	0.0	0.0	0.0
15C	1.52E+02	0.0	0.0	0.0	0.0	0.0
14O	1.05E+12	9.98E+10	8.44E-04	0.0	0.0	0.0
14C	8.03E+12	8.03E+12	8.03E+12	8.03E+12	8.03E+12	8.03E+12
13N	1.60E+13	1.21E+13	2.64E+11	5.34E-02	0.0	0.0
11C	7.07E+12	6.17E+12	9.50E+11	5.93E+05	0.0	0.0
11Be	1.86E+10	1.09E+05	0.0	0.0	0.0	0.0
10C	1.05E+11	1.78E+07	0.0	0.0	0.0	0.0
10Be	6.69E+11	6.69E+11	6.69E+11	6.69E+11	6.69E+11	6.69E+11
7Be	1.14E+13	1.14E+13	1.14E+13	1.13E+13	1.12E+13	1.04E+13
3H	6.69E+13	6.69E+13	6.69E+13	6.69E+13	6.69E+13	6.68E+13
Totals	1.56E+14	1.17E+14	8.82E+13	8.69E+13	8.68E+13	8.59E+13

Table 2b. Decay of specific activity target plate coolant Bq m^{-3}.

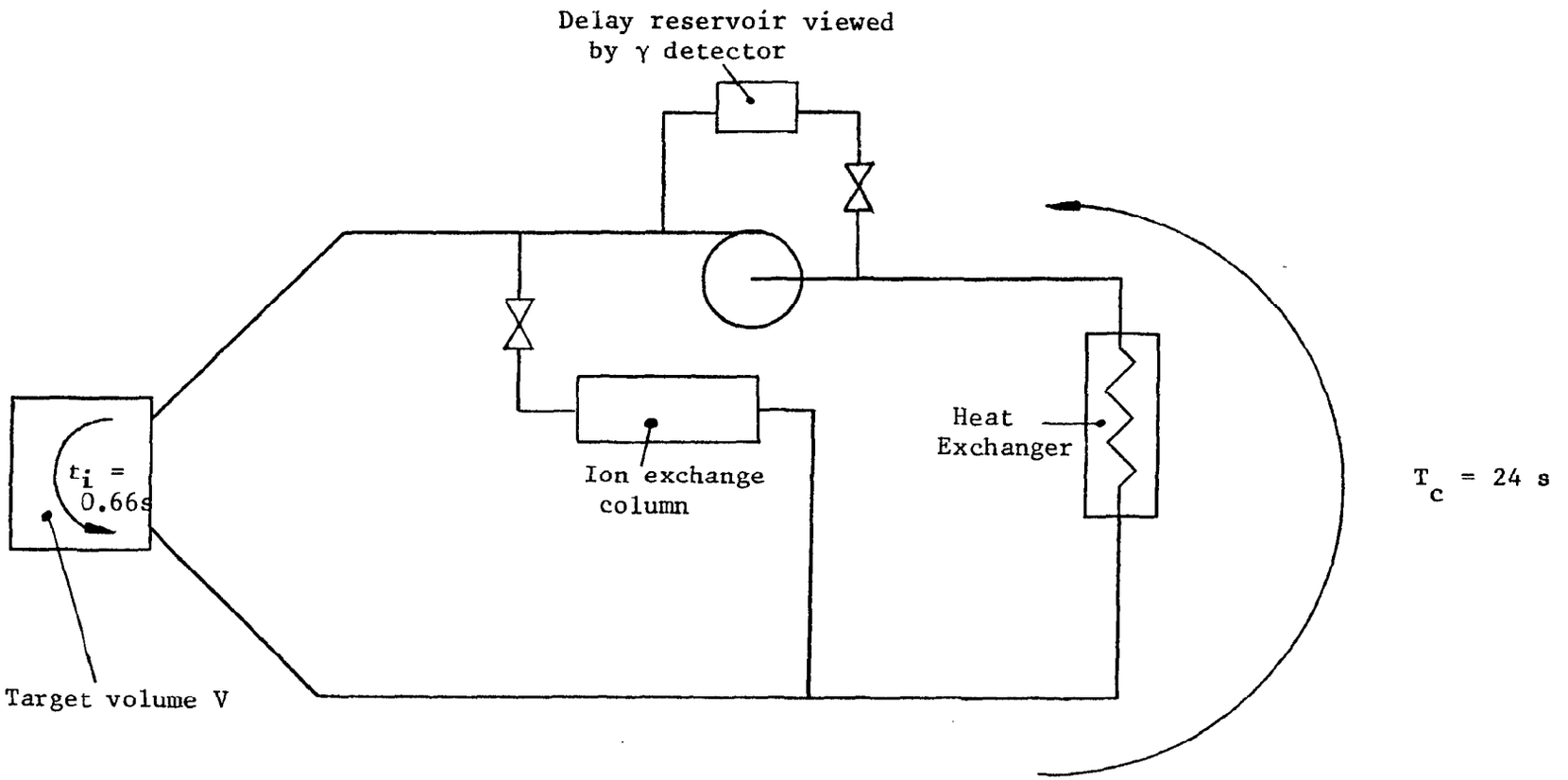

Figure 1. Schematic diagram of the target cooling circuit.

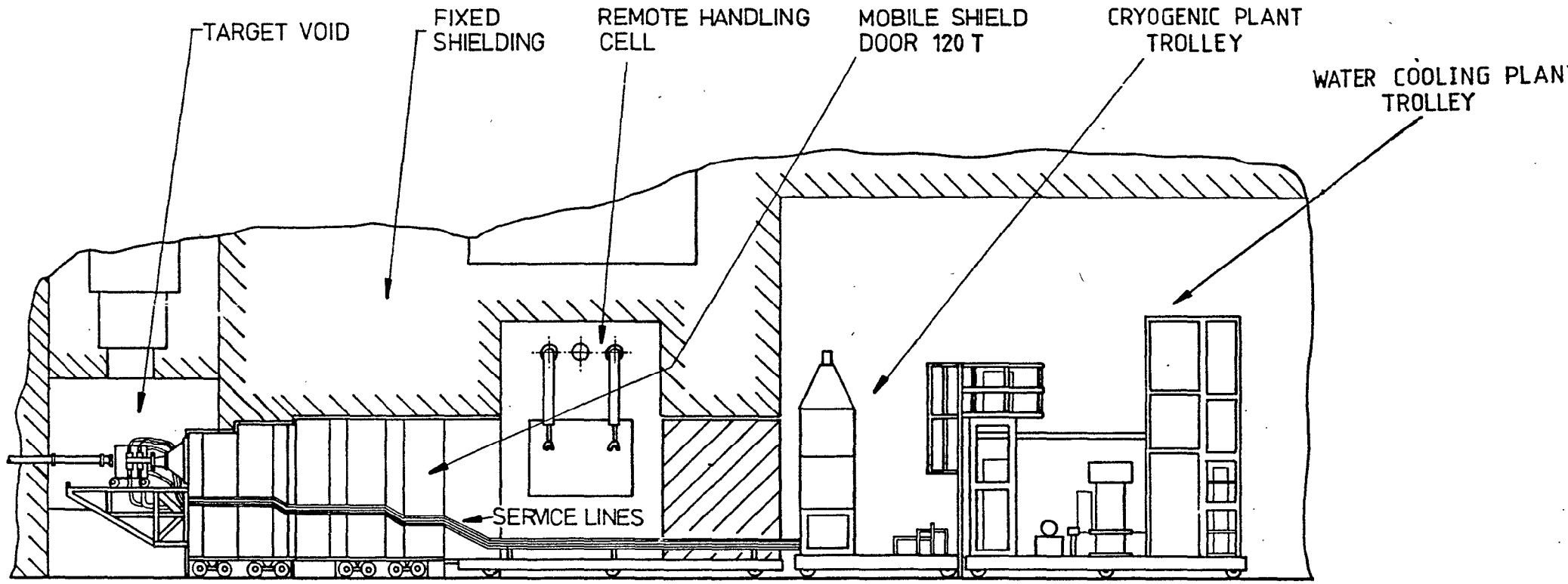

Figure 2. Target station and services area trolleys.

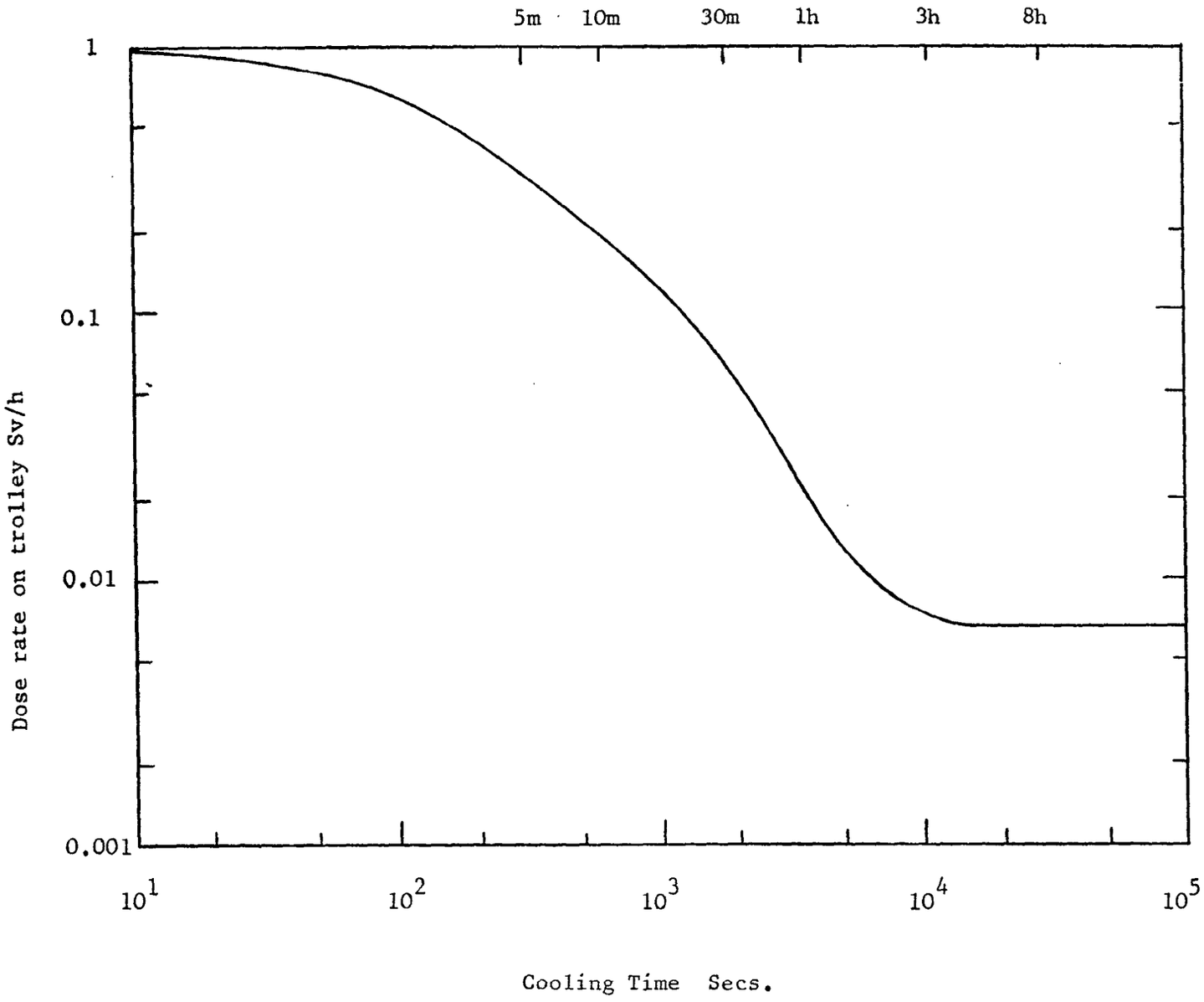

Figure 3. Calculated decay of radiation level on the water services trolley when proton beam is turned off.

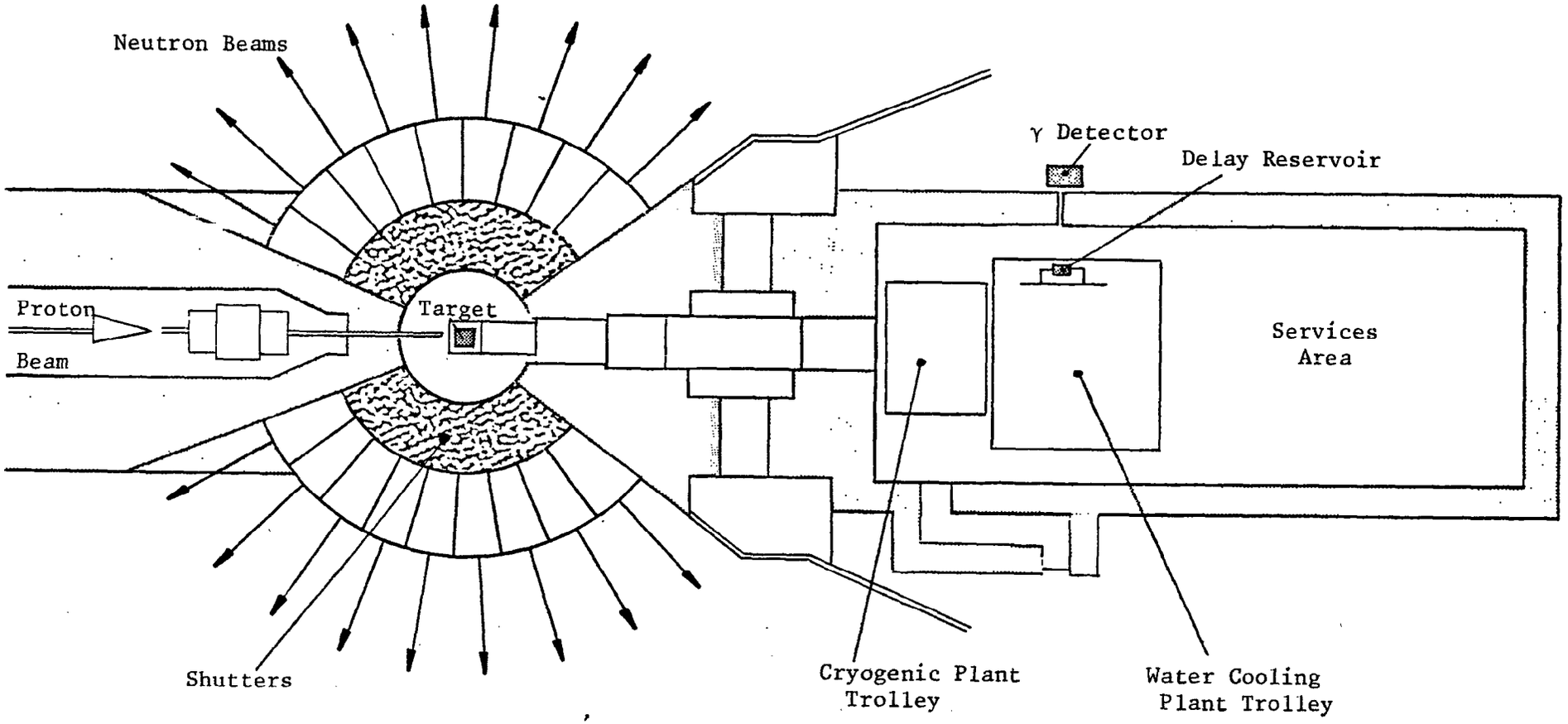

Figure 4. Overall Layout of Target Station.

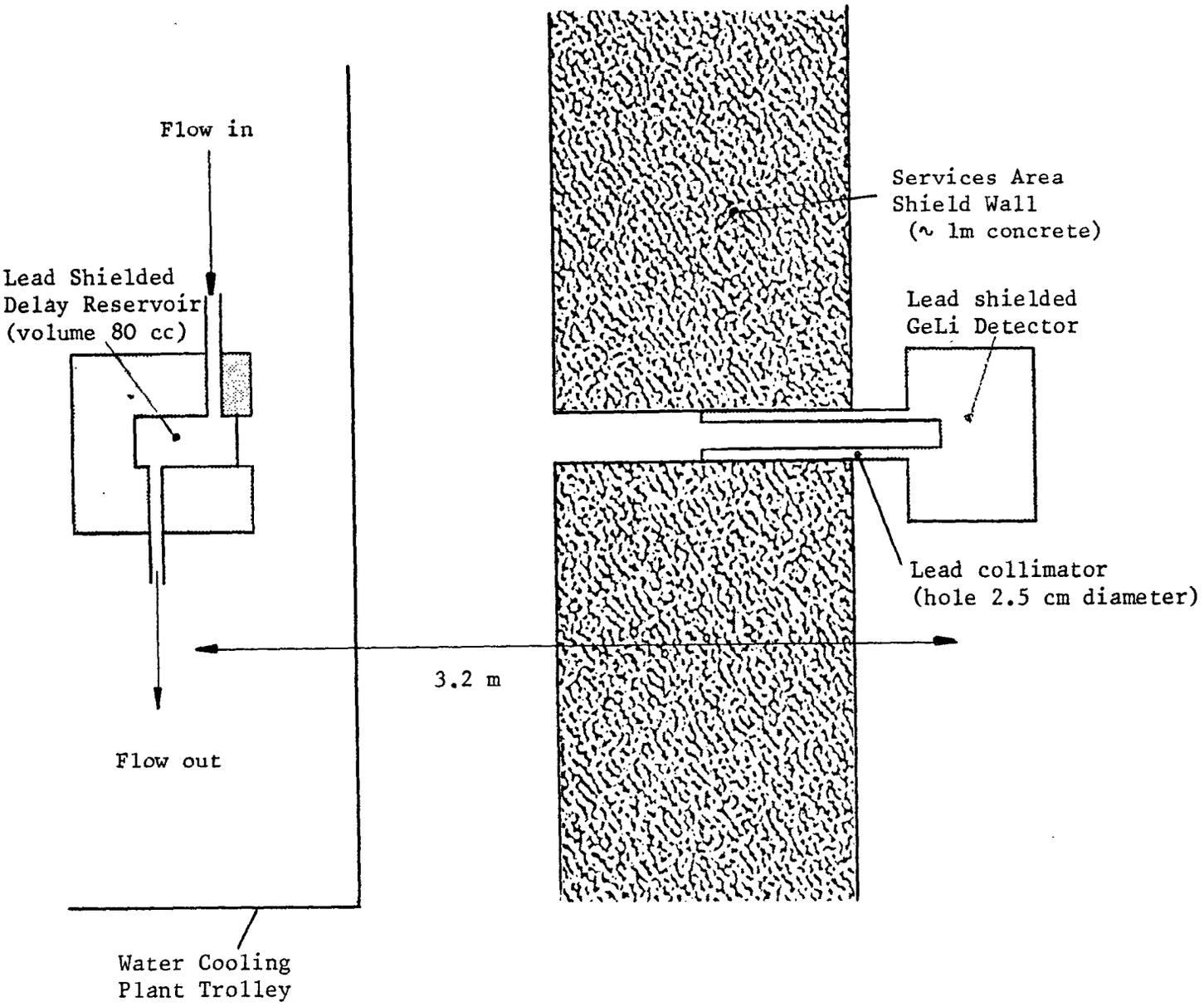

Figure 5. Schematic detail of the arrangement of the delay reservoir and GeLi detector.

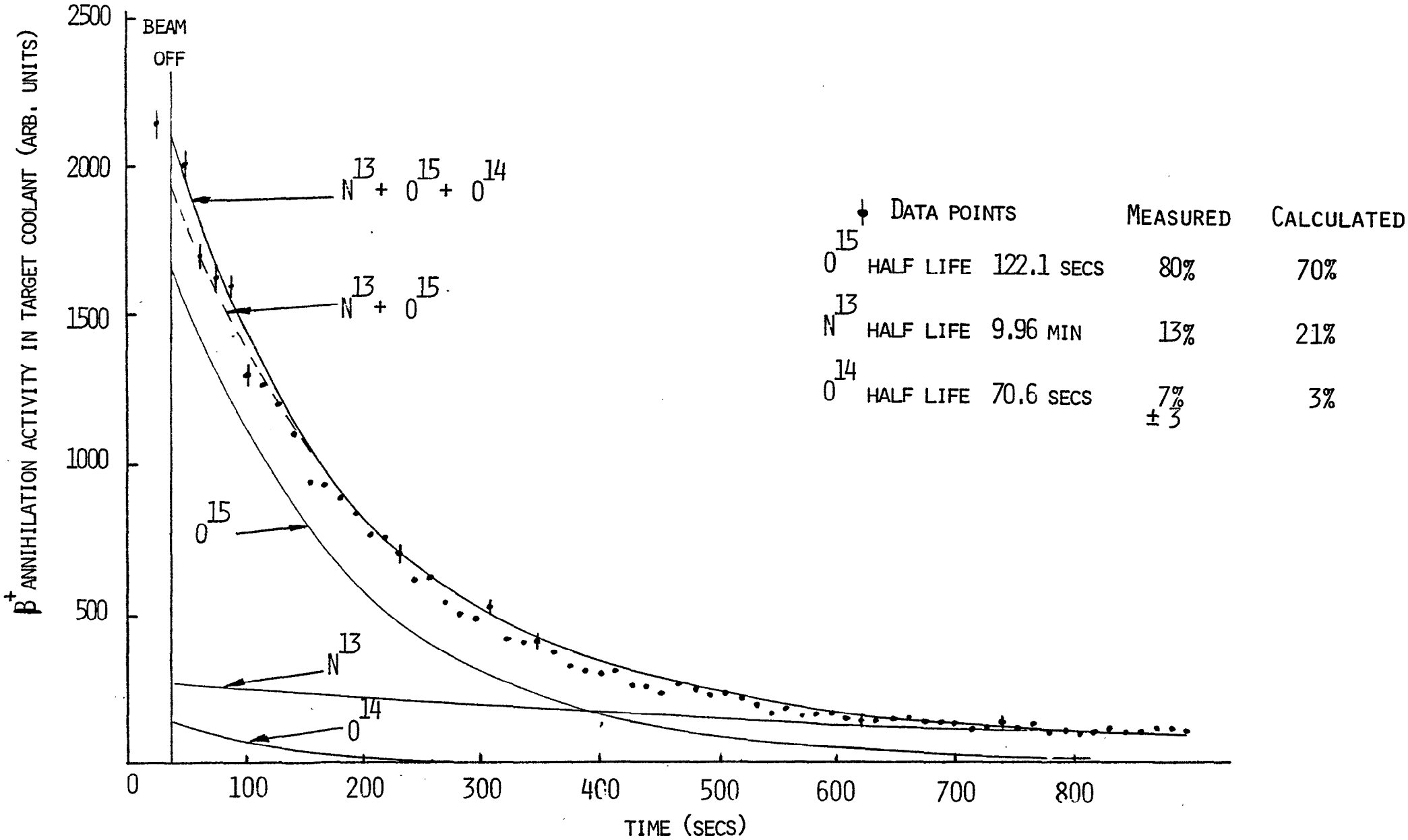

Figure 6. Decay of β^+ annihilation gammas in the target coolant.

ICANS IX

INTERNATIONAL COLLABORATION ON ADVANCED NEUTRON SOURCES

22-26 September, 1986

THERMOFLUID DYNAMICS OF THE SINQ TARGET

- A Natural Circulation Loop as a Target -

Y.Takeda

Swiss Institute for Nuclear Research

5234 Villigen Switzerland

1. Introduction

The target of the spallation neutron source at SIN (SINQ) is a liquid lead bismuth eutectic (LBE) in a vertical cylindrical container with the proton beam entering from below. The thermofluid behaviour of the liquid LBE was investigated based on the natural convection in an enclosure. It has been shown that the natural convection mechanism is effective for transporting energy deposited at the bottom to the heat exchanger located at the top of the target [1].

However, simulation experiments with water showed some instabilities in the total flow. The corresponding bifurcation and axial asymmetry lead to a swaying motion of the rising flow. These would result in difficulties of monitoring the thermofluid behaviour and reduce the controlability of the target.

Therefore, the system was modified by introducing a guide tube, which is a simple coaxial tube, into the container. This new concept leads to advantages, described in the following points;

1) The flow configuration is converted from pure natural convection in a simple enclosure to a natural circulation loop. This simplifies the prediction of overall behaviour of the system.
2) A higher flow rate of the target liquid can be expected. Hence the maximum temperature will be lower and the transient shortened. Furthermore, the effect of local flow disturbances might become smaller.
3) Since the cooled liquid is guided right down to the bottom of the target, increased cooling of the window by target liquid will result.

In this paper are presented the results of the analysis on the thermofluid characteristics of the target system with guide tube, based on the one dimensional natural circulation loop [2]. This analysis is compared with the NACOSPANS experiments.

2. Analytical

2.1 Analytical method

The calculational model is illustrated in Fig.1. The loop consists of two long vertical legs of the same diameter as the guide tube and of the height of the target. One leg corresponds to the inner flow channel of the guide tube and the other to the outer. An internally heated region is located at the bottom of one leg and the heat exchanger at the top of the other. The heat exchanger is simulated by a volumetric heat sink. By assuming a constant flow area over the loop and by neglecting the effects arising from turns at the both ends, the problem becomes one dimensional. Details of the derivation of the equations and solutions are described in [3].

The governing equations in nondimensional form are ;

(1) $$\partial\Theta/\partial\tau + w(\partial\Theta/\partial Z) = \alpha/(2DL^2)\partial^2\Theta/\partial Z^2 + q'$$

where
$$q' = \begin{cases} 1 & : 0 < Z < \delta \\ 0 & : \delta < Z < 1/2 \\ -\Theta & : 1/2 < Z < 1/2+\gamma \\ 0 & : 1/2+\gamma < Z < 1 \end{cases}$$

(2) $$dw/d\tau = -\lambda L w^2/d + Qg\beta/2D^3L \int_0^1 \Theta \, dZ$$

In the above equations, the Bousinesque approximation has been used. The momentum equation has been integrated over the loop to eliminate the static pressure.

The normalized variables are as follows :

(3)
$$\Theta = (T-Ts)D/Q$$
$$\tau = tVs/2L$$
$$w = v/Vs$$
$$Z = z/2L$$
$$\delta = h/2L$$
$$\gamma = l/2L$$

where Vs (= 2DL) is the characteristic velocity.

λ is the friction coefficient in a smooth tube and given by :

(4)
$$\lambda = 64/Re \quad : Re<2000 \text{ (Laminar)}$$
$$\lambda = 0.3164/Re^{1/4} \quad : Re>2000 \text{ (Turbulent)}$$

A closed form solution for the steady state can be obtained when axial heat conduction in Eq.(1) is neglected. They are :

(5) $\Theta = Z/w + C1 = Z/w + \delta\exp(-\gamma/w)/w[1-\exp(-\gamma/w)]$

$: 0 < Z < \delta$

$C2 = \delta/w[1-\exp(-\gamma/w)]$ $: \delta < Z < 1/2$

$C3\exp(-Z/w) = \delta\exp(-Z/w)/w\exp(-1/2w)[1-\exp(-\gamma/w)]$

$: 1/2 < Z < 1/2+\gamma$

$C4 = \delta\exp(-\gamma/w)/w[1-\exp(-\gamma/w)]$ $: 1/2+\gamma < Z < 1$

Fig.2 illustrates the temperature distribution given by (5).

Substituting these temperature results into Eq.(2), one obtains

(6) $-\lambda Lw^2/d =$
$Qg\beta/2D^3L\{\delta(1-\delta)/2w - \delta + \delta\gamma\exp(-\gamma/w)/w[1-\exp(-\gamma/w)]\}$

A steady state velocity value can be obtained by solving this nonlinear equation.

2.2 Analytical Results

Extreme examples can be examined. If $\gamma/w<1$, the following relationship is obtained for the steady state velocity ;

(7) $w^3 \dashrightarrow Qg\beta\delta(1-\gamma)/4D^3L$; $v \dashrightarrow Q^{1/3}$

Therefore, the steady state velocity is proportional to the cube root of beam power. The maximum temperature is

(8) $\Theta max = C2 \dashrightarrow \delta/\gamma$; $Tmax \dashrightarrow Qh/DL$

It is linearly proportional to the input power but inversely to D and L.
The temperature difference is

(9) $\Delta\Theta max = C2 - C4 \dashrightarrow Q^{-1/3}$; $\Delta Tmax \dashrightarrow Q^{2/3}$

This agrees with the results in [4].

A volumetric heat sink rate is obtained from the heat exchanger characteristics based on the total amount of heat transfer.

(10) $UST/\rho CpV = DT$

where U is an average overall heat transfer coefficient, S the total heat transfer area, ρ the density of LBE, Cp the specific heat of LBE, V the volume of the shell of the heat exchanger. Then, D can be estimated from

(11) $D = 2Urn/\rho CpRb^2$

where r is the radius of the heat exchanger tube, n the number of tubes, Rb the radius of the loop.

For the representative numerical values of the real target, U=0.1 W/cm^2K, r=1.5 cm, Rb=5.5 cm, n=30, ρ=10.5 g/cm^3, Cp=0.15 Wsec/gK,

$$D = 0.19 \text{ /sec.}$$

The solution of Eq.(6) is shown in Fig.3 with dimensions of L=350 cm, h=30 cm, l=200 cm. The maximum temperature was calculated like C2 (Eq.5) with the corresponding velocity values (Fig.3). It shows the 1/3 power law for velocity variation as Eq.(7) and a linear proportionality for the maximum temperature as Eqs.(7) and (8) with respect to the input power.

2.3 Numerical Calculations

2.3.1 Simple tube loop

Equations (1) and (2) were solved numerically in order to study the time dependent behaviour of the loop and the effect of axial heat conduction. Details of the numerical methods and most of the results on the time dependent temperature distributions are given in [3].

The effect of input power on the maximum temperature and velocity is shown in Fig.4. The maximum temperature depends roughly linearly on the input power and the velocity shows approximately cubic root of the input power. This agrees with the simplified prediction. However, the velocity value is smaller by factor 2. This is due to the effect of the axial heat conduction.

Fig.5 shows the effect of the volumetric heat sink rate D on the maximum temperature and velocity. The velocity is only slightly affected by D. However, Tmax decreases inversely with increasing D, which also agrees with Formula (8).

2.3.2 The effect of pressure loss at the bottom turn

One might expect that the pressure drop from the U turn bend at the bottom of the target will have a large effect on the flow. In order to investigate this, the governing equation (2) was slightly modified as :

$$(12) \qquad dw/d\tau = -(K+2\lambda L/d)w^2/2 + 2Qg\beta/D^3L \int_0^1 \Theta \, dZ$$

where K is an empirical coefficient of the pressure loss produced by geometry variations such as sudden enlargement, contraction, bends and turning bend [5]. For the present case, it is taken as 2.86. This value is a few times larger than that for the smooth tube pressure loss (the second term in the parentheses) for the

dimensions of real target.
Similar behaviour of the time variation of the maximum temperature and velocity was obtained [3]. However, the stationary value of the velocity is lower, which results in a higher maximum temperature at the steady state. For the case of a representative SINQ-target at 1MW power input and compared with the results without turning loss, the velocity is reduced by about 44 cm/sec and the temperature increased by about 11 ^{0}C.

3 Water Experiments (NACOSPANS)

NACOSPANS is a test rig for water flow experiments in a 2m high cylinder. The apparatus is described in [6]. Flow visualization was made by using ink as a tracer. Movie films were taken for two different input powers of 500 and 800 W. By analysing those films, stationary velocity values were obtained which are plotted in Fig.6. A good agreement is obtained, although those values are slightly lower than predictions.

4. Conclusion

The thermal and fluid dynamic characteristics of the SINQ-target have been investigated analytically and numerically. The Model used is based on a natural circulation loop with uniform heat deposition at the bottom and a volumetric heat sink for the heat exchanger at the top. The analytical method is supported by the water experiments. The following conclusions are drawn.

1) The steady state velocity is proportional to cubic root of the beam power, and the maximum temperature is linearly proportional to the input power. Both analytical and numerical calculations show the same behaviour.
2) The effect of the axial heat conduction on the steady state velocity is large. For a representative SINQ-target a factor of 2 reduction is obtained.
3) The flow is well established with higher velocity level. For a representative SINQ-target it is approximately 160 cm/sec.
4) The maximum temperature increase at the steady state is about 206 ^{0}C. Hence the maximum temperatures will be below 400 ^{0}C and therefore below a level where fast corrosion effects might occur.
5) The effect of the pressure loss due to the U turn bend at the bottom of the loop shows a large effect.

Acknowldegement

The author is thankful to Mr.E.Hofer and Mr.T.Noethiger of EIR for carrying out the flow visualization.

References

[1] Y.Takeda, Nucl. Instr. Methods A237 (1985) 455
[2] A.Mertol, R.Greif, Natural Convection, p.699 Ed. S.Kakac, Hemisphere (1985)
[3] Y.Takeda, SINQ Memo, Thermofluid Behaviour of SINQ Target with Guide Tube - One Dimensional Calculation of Natural Circulation Loop March 1986
[4] Ch.Tschalaer, Proc. ICANS-V, Juelich (1981)
[5] E.N.Pearson, H.Moore, Sodium-Nak Engineering Handbook, Volume II, O.J.Fouster, Ed., Gordon & Beach
[6] Y.Takeda, Proc. ICANS-VII Chalk River, AECL-8488 (1984)

Nomenclature

D	:	Volumetric heat sink rate
g	:	Gravity
h	:	Height of the heated region
l	:	Length of the heat exchanger
L	:	Target height
p	:	Pressure
q,Q	:	Uniform Volumetric heat deposition
Re	:	Reynolds number
t	:	Time
T	:	Temperature
Ts	:	Initial temperature
v,V	:	Velocity
Vs	:	Characteristic velocity
w	:	Dimensionless velocity
z,Z	:	Space coordinate
α	:	Thermal diffusivity
β	:	Thermal expansion coefficient
λ	:	Pressure loss friction coefficient
ν	:	Dynamic viscosity
ρ	:	Density
τ	:	Dimensionless time
θ	:	Dimensionless temperature

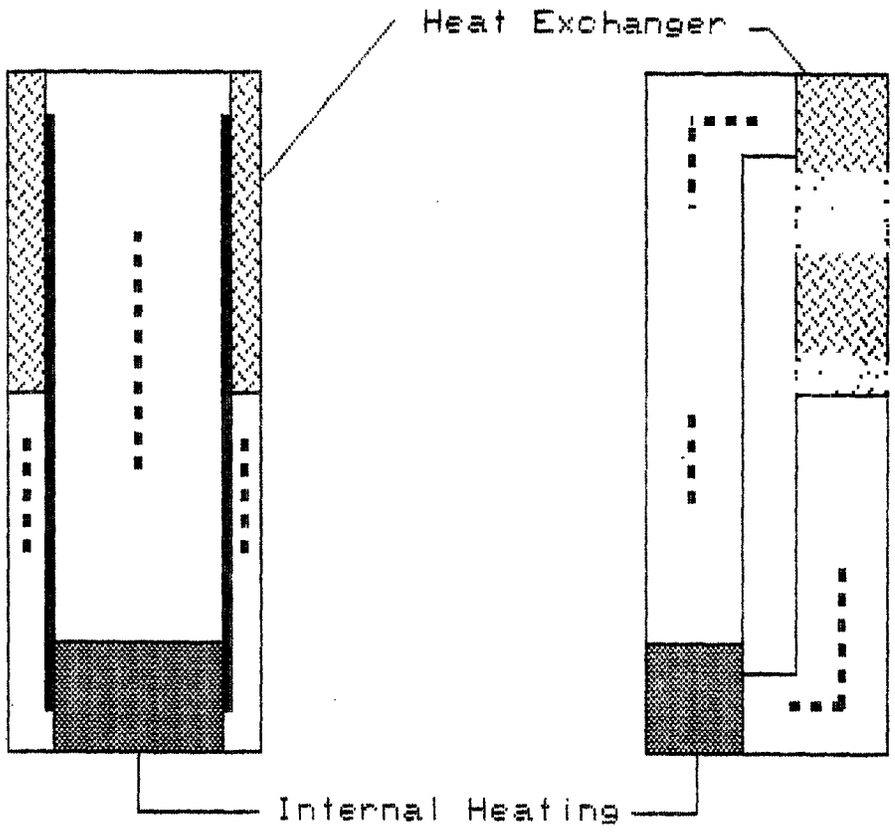

Fig.1 SINQ Target and Calculational Model

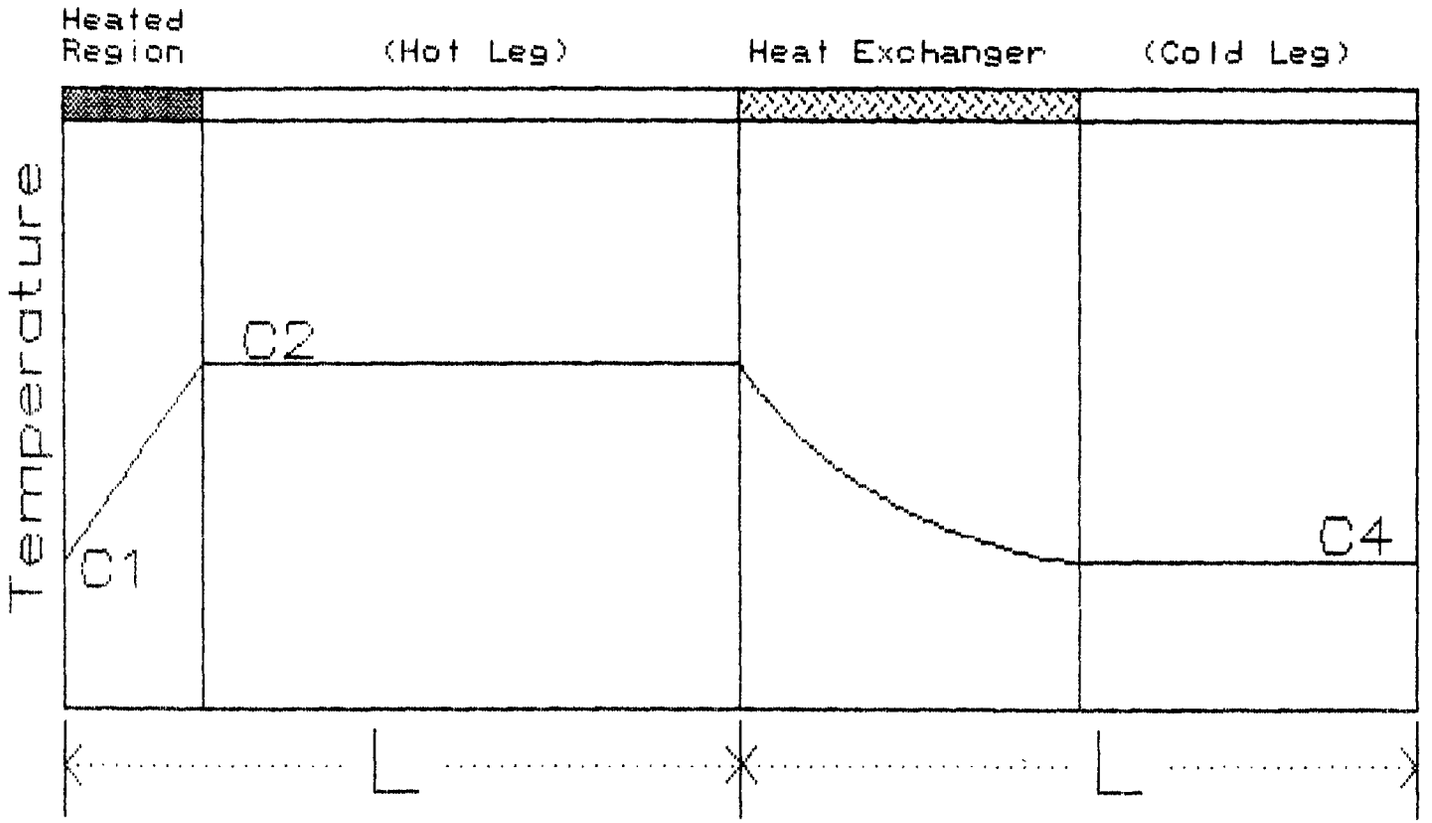

Fig.2 Schematic Temperature Distribution for Steady State without Heat Conduction

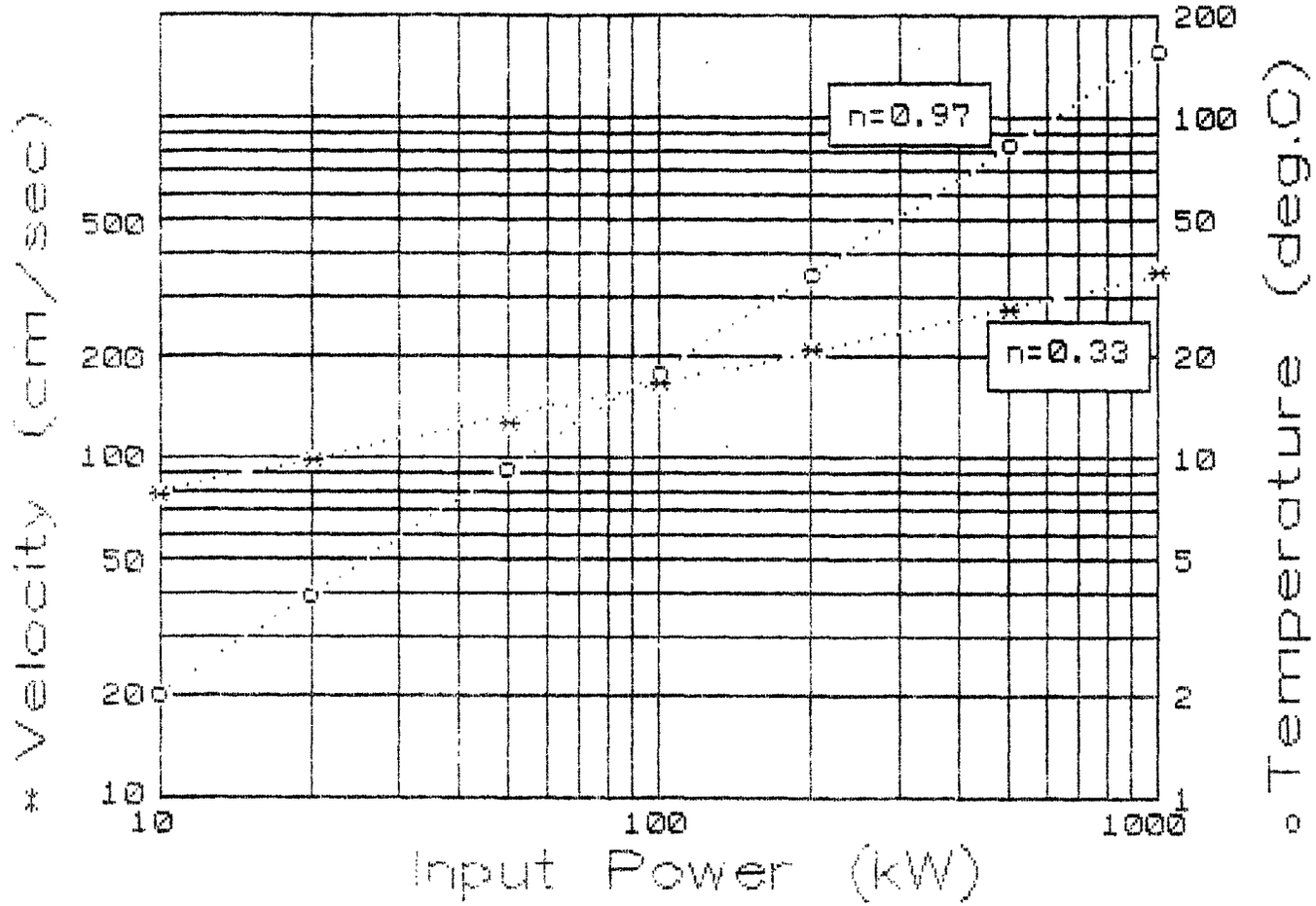

Fig.3 Analytical Results for Steady State Velocity and the Maximum Temperature

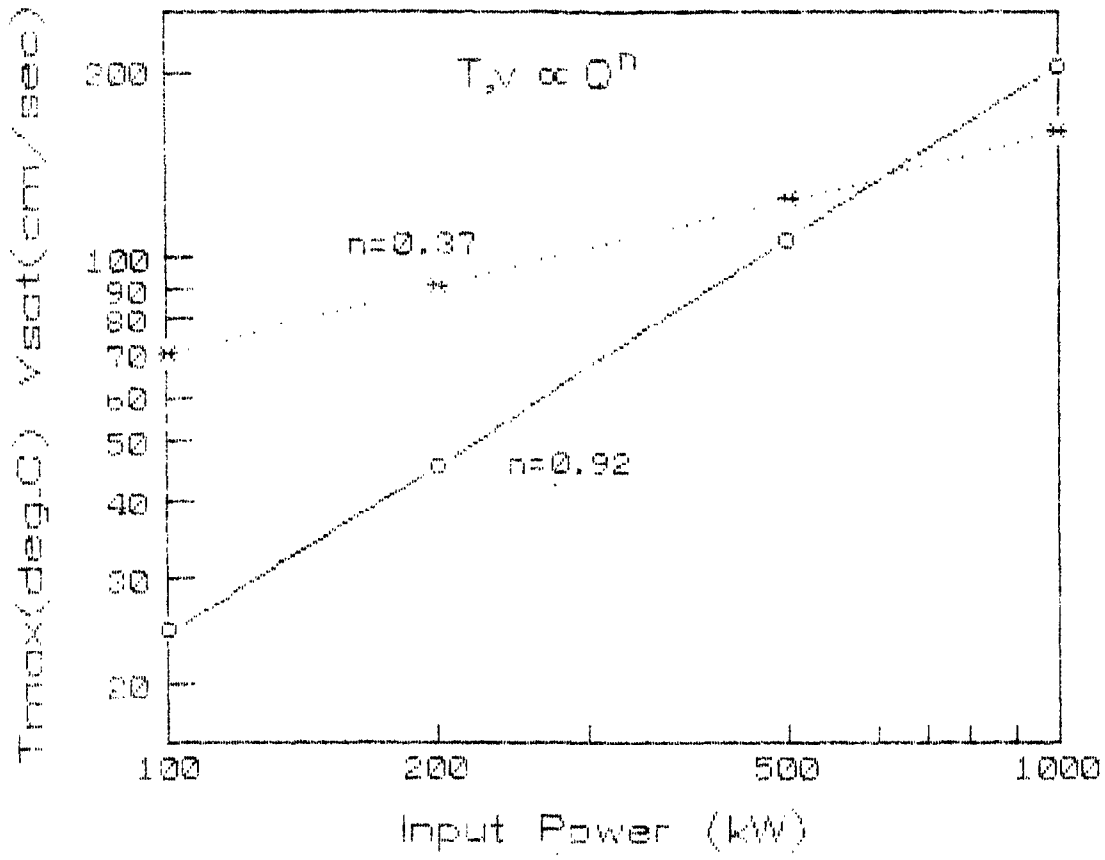

Fig.4 Dependence of the Steady State Maximum Temperature and Velocity on Input Power

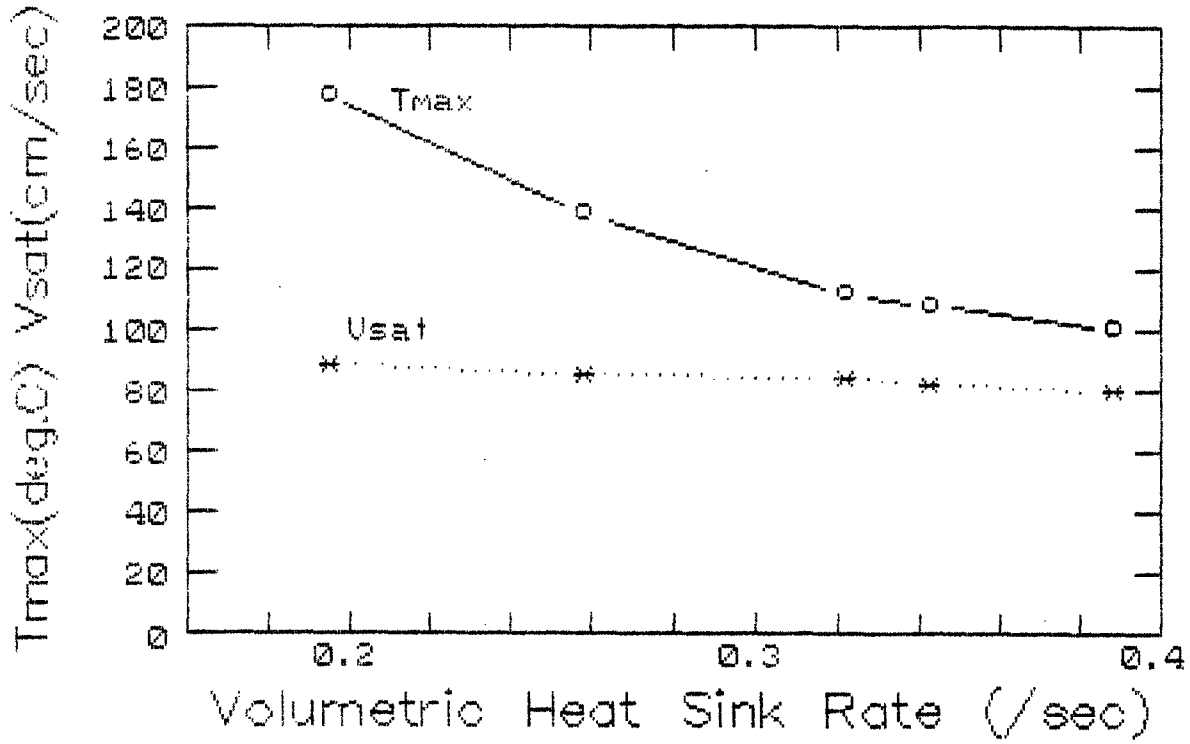

Fig.5 Dependence of the Steady State Maximum Temperature and Velocity on Volumetric Heat Sink

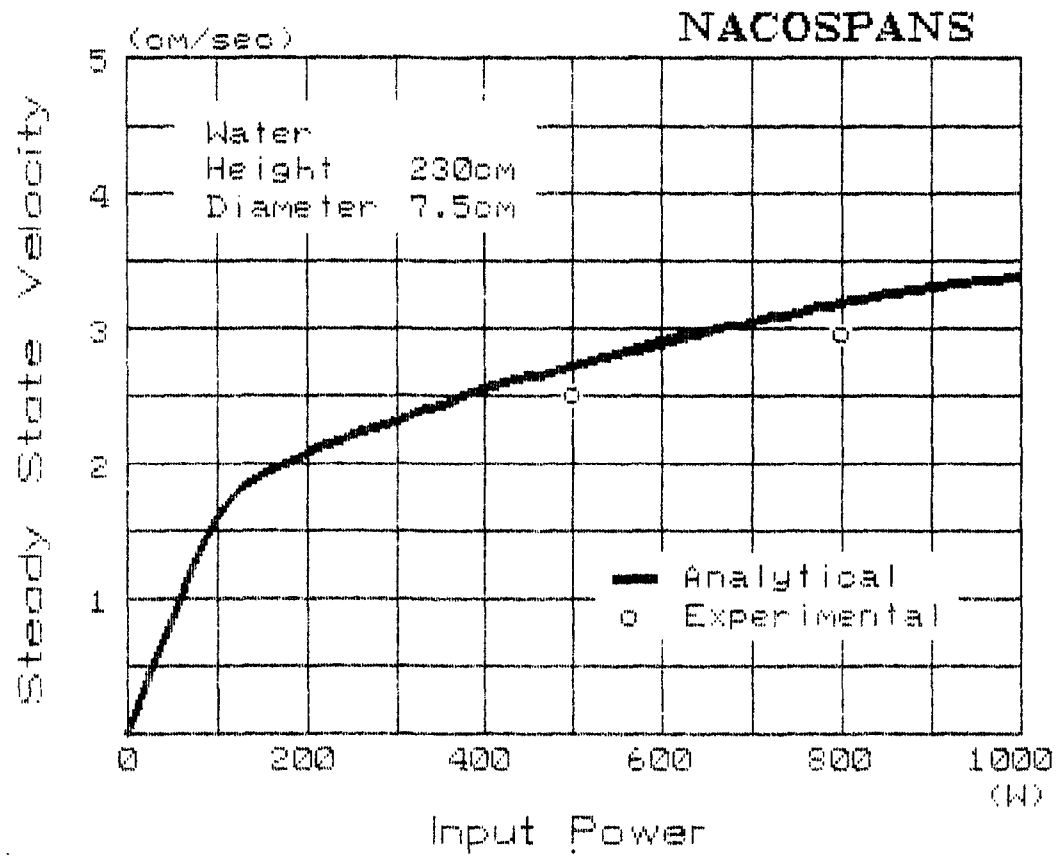

Fig.6 Comparison of Analytical and Experimental Steady State Velocity

ICANS IX

INTERNATIONAL COLLABORATION ON ADVANCED NEUTRON SOURCES

22-26 September, 1986

SUMMARY OF SESSION ON MODERATORS.

J.M. CARPENTER & G.J. RUSSELL

The afternoon of Tuesday was devoted to reports and discussion about moderators. We had five reports: one concerning the "Burping" of cold solid methane; another report on the operation of the LANSCE liquid hydrogen moderator system; another report on the operation of the ISIS cryogenic moderators; another concerning the way moderators deteriorate in performance under irradiation and another report in general about the LANSCE moderators.

Everyone seems to have troubles starting up these systems: we build them; we evacuate them; they are warm and we try to cool them off and fill them up with whatever liquid. Well, there's trouble. The general question that needs to be resolved is that of the stability of these (flowing) liquid methane and liquid hydrogen moderator systems. We need better understanding of how to control these systems, especially during the filling stage which requires of the order of 4 to 8 hours. It sometimes requires an experienced driver to coax the system from where it begins to where we want it to go.

Other questions, which we didn't discuss too much, are: how stable is the temperature of these moderators? How can we control the temperature of these moderators? Maybe we don't need to do anything. Some of the instrument people on the neutron beams say, "I want the moderator temperature to be held within 0.1K", just so they don't have to worry about it! No one that I'm aware of, keeps the moderator temperatures within 0.1K!

The following principal points were made in a discussion on the question of moderator temperature stability:

- *The change of temperature causes a shift of the Maxwellian and hence changes the spectrum shape.*
- *Spectrum shifts between fills of the methane moderator have been observed at ISIS, even though they go back to the same nominal temperature. This effect is not yet understood. It is not certain if this effect occurs also with hydrogen moderators, because only the type of instruments that look at methane moderators seem sensitive to the effect.*
- *The procedures to deal with these spectral shifts are believed to be straightforward; normalise everything to the monitor spectrum before you process the data, although it is not quite as straightforward as first appears because the monitor is not at the same position as the detector (rescale according to wavelength to make these corrections). There are also other problems (to match up resolution broadened Bragg edges, etc). Apart from being an extra thing to do, it also makes it substantially more complicated to do a 1% experiment.*
- *If the spectral temperature becomes unstable, it is possible to recover data. In the case of liquid hydrogen there is a much more severe thing that can happen; the pulse shape (distribution in time of neutrons of a given energy) may well change significantly if the ortho- to para-hydrogen ratio changes. There would seem to be no way of directly monitoring the ortho to para ratio, hence it is difficult to see how to have any ratio other than the stable value at a given temperature. The pulse shape change causes the resolution to change (probably at the "factor of two" level). One could probably monitor it with a crystal analyser and even though in principle one could recover the data, probably experimenters would just say, the source is no longer stable and wait until it's fixed.*

In these respects, I suppose, we are simply not serving the instrument people according to what they would like, but then they are probably making excessive requests - just now we are ignoring them! They (the users) more or less get along. Eventually we are going to have to accommodate them and provide some control.

There is the question of the temperature instability of solid methane that takes place upon intense irradiation at low temperatures (similar questions probably arise in cold D_2O ice systems). Although we are coming to understand these phenomena, there is a great deal more to learn. Certainly an unresolved issue.

We have several liquid methane systems operating but these are all more or less low power; so as ISIS comes up, we will be watching to see what happens to the liquid methane systems when they have to withstand higher dose-rates and higher power densities. Just now, the systems at IPNS and ISIS behave rather acceptably, but it remains to be seen how things behave at higher power densities.

There were several issues resolved in our discussions. We found out how room temperature polyethylene and solid methane deteriorates under irradiation. Probably a result of all that is that in higher power sources we won't use polyethylene ever again, just water. Solid methane is so attractive, that we will continue to use it; from what we know about how rapidly it deteriorates, we can determine a schedule for replacing it. The "Burping" phenomenon is approximately understood, although the thing is not quantified, worked out and controlled. We have operating liquid methane and hydrogen systems, so that we know that these are satisfactory at the present low powers. So we can count as a resolved issue, whether or not we can build and successfully operate these at low powers.

A wild idea surfaced: if we cannot use solid methane at 20K and if hydrogen has such a squirrely scattering kernel that you get a funny spectrum and you would like to do better than that, then how about combining these two in some fashion like circulating a slurry of solid methane suspended (although it doesn't float) in liquid hydrogen. I'm afraid that I must take the blame for this wild suggestion!

Gary Russell has agreed to talk a little bit about the next issue, so I'll just treat this very briefly. There's a body of data on spectra and pulse-widths as functions of temperature and poisoning etc. for polyethylene

and (liquid) water. The same is true for liquid methane. Furthermore, we have reasonably good scattering kernels and calculational methods which are now bench-marked for water/polyethylene and liquid methane. Liquid hydrogen is the apparent inheritor of the role as coldest moderator in high-power systems and yet we don't yet have a body of data describing liquid hydrogen, and we need it if we are going to design good moderators. So one of the important issues that arose in our discussion was the need for a better understanding and a design basis for liquid hydrogen systems (this includes para- and ortho-hydrogen and their mixtures). We need scattering kernels, benchmark calculations and experiments.

> *What's actually needed for these hydrogen kernels to do a good job on thermalisation, is an energy transfer range down to a fraction of an meV and up to several hundreds or thousands of meV (where the kernel becomes independent of the chemical state).*

Gary Russell: Basically, there are three ways of doing neutronic design calculations for complex spallation neutron source systems: a) deterministic transport methods, b) Monte Carlo techniques and c) Walter Fischer's handmade physics. A simplistic view of these different approaches is as follows:

- Deterministic transport methods generally provide "exact solutions" to approximations of the Boltzmann transport equation. Computing errors are systematic, and, aside from uncertainities in the cross section data, arise not only from the discretization of the time-space-angle-energy phase space for numerical computations but also from the fact that, with rare exceptions, full representations of three-dimensional configurations cannot be done. One might paraphrase the deterministic transport approach as potentially giving the right answer to the wrong problem.

- Monte Carlo techniques are used to solve the Boltzmann equation directly. With this method, one can study very complex three-dimensional configurations, and the continuous treatment of energy, space, and angle makes discretization errors in Monte Carlo calculations take the

form of stochastic uncertainties; however, one has to careful that all relevant parts of phase space have been properly sampled and that the problem has converged. In Monte Carlo, two approaches are generally utilized: a) non-analog Monte Carlo, where variance reduction techniques are employed to reduce running time and variance in the problem answer, and b) analog Monte Carlo, which involves a direct computer simulation of physical laws. One may loosely describe the Monte Carlo technique as possibly giving the wrong answer to the right problem.

- Walter Fischer's handmade physics employs one's gut feelings and uses simplified approaches to elicit answers to problems. This strategy is perhaps the most gratifying of all. However, it has been my experience for complex spallation neutron source designs, that intuition can only carry you so far. A good example of this is the LANSCE split-target, flux-trap-moderator target system.

In all cases, the bottom line is that neutronic calculations for complex spallation neutron source design are intricate, and care needs to be taken to assure the answers are believable.

As mentioned above, using the Monte Carlo approach, one can mock-up complex geometries quite well, but the physics must also be right. The physics comes in via the cross sections used; a weak link at low energies is the availability and adequacy of scattering kernels. This is particularly true for liquid hydrogen where more work most certainly is required. Hydrogen is further complicated by the necessity of proper accounting of ortho- and para-hydrogen effects.

The issue of liquid hydrogen scattering kernels came up in the target and moderator session when I was going through some details as to how the LANSCE moderator sizes were chosen. In the LANSCE cold moderator studies, I used a hydrogen kernel gotten from our Jülich collaborators, who, in turn, obtained the kernel from A. Robert of ILL. I cannot comment in detail on the physics of the kernel except for the following general remarks: a) the Young and Koppel formalism for molecular hydrogen gas is used, and b) the kernel should be applicable to liquid hydrogen for neutron energies above 7 meV. This latter restriction is not too comforting, but the severity of the implication depends on how important "liquid effects" are below

7 meV in a practical application. Nevertheless, that is all I had available, and I used it in the LANSCE liquid hydrogen moderator design.

To checkout my calculational procedure for the LANSCE target system, I did a sequence of computations where I varied the thickness of the liquid hydrogen moderator, and another series were I changed the moderator ortho/para composition. My results agreed qualitatively with similar calculations performed by Ralph Neef of Jülich. These latter were done to optimize a liquid hydrogen moderator for the DIDO reactor in Jülich; the same hydrogen kernel was used in both calculations. Since the two computations were done for radically different geometries, the qualitative agreement gave me confidence in my calculational approach. My conclusions were similar to theirs, and we chose the LANSCE hydrogen moderator thickness to be 5 cm. Without regard to neutron pulse width questions, my choice of moderator thickness was based on the following: a) do not sacrifice the integrated (E <10 meV) cold neutron intensity, b) keep energy deposition in the moderator as low as possible, c) more-or-less minimize the effects of differing para-hydrogen concentrations on the integrated cold neutron intensity.

A more stringent test of the adequacy of the hydrogen kernel comes about when comparing measured neutron leakage spectra from a moderator with calculated predictions. Spectra from liquid hydrogen moderators have been measured at ISIS and LANSCE. The ISIS result was obtained during a commissioning run in December of 1984. Phil Seeger recently measured a spectrum at LANSCE, and showed the results at this meeting. A common characteristic of these two spectra is a conspicuous "bump" showing a rise in the neutron intensity in the 10-20 meV energy range. This effect is generally attributed to the rise in the para-hydrogen cross section which also occurs in that general energy realm. In the target and moderator session, Andrew Taylor noted that at the RAL they were unsuccessful in calculating the details of the observed spectrum, and knew of no scattering kernel which reproduced the observed "bump". It was a general consensus that the state-of-affairs of kernels for liquid hydrogen was precarious.

Last evening, I did an "eyeball" comparison between my preliminary calculation of the neutron spectrum leaking from the LANSCE liquid hydrogen moderator and Phil Seeger's measurement. I get agreement of order 25% for integrals of the data from 10-50 meV and below 10 meV. I also plotted

my calculated spectrum on the figure Günter Bauer showed when reporting ISIS moderator performance. My calculated spectrum differs significantly from the spectrum in Günter's figure, and qualitatively has features similar to the ISIS measurement. We must and will be more definitive in these comparisons, and should also concern ourselves with the effects of ortho and para concentrations on neutron pulse widths.

Liquid hydrogen moderators could prove to be very important in high-power spallation neutron source applications. We need reliable "tools" to design these moderators. I would ask those individuals who are working on an improved kernel formalism or those who are contemplating doing so to forge ahead. We need these new tools and better benchmark measurements (with which to compare) if we are to push spallation neutron source performance to the limit.

ICANS IX

INTERNATIONAL COLLABORATION ON ADVANCED NEUTRON SOURCES

22-26 September, 1986

ANALYSIS OF THE BURPING BEHAVIOR OF THE COLD SOLID METHANE MODERATOR AT IPNS*

J.M. Carpenter
Intense Pulsed Neutron Source,

U. Walter
Intense Pulsed Neutron Source and
Materials Science Division,

Argonne National Laboratory,
Argonne, Illinois 60439 USA

and

D.F.R. Mildner
Research Reactor Facility and Department of Physics,
University of Missouri, Columbia, Missouri 65211 USA

ABSTRACT

We report the results of analyses of the "burping" behavior of the cold solid methane moderator at the Intense Pulsed Neutron Source. This work follows one year's successful and productive experience with the "Model I" moderator, which exhibited periodic "burps" (spontaneous rises of the methane temperature following irradiation) and developed a small but liveable methane leak. An earlier report[1] described the design of this moderator and summarized experience with it up to that time. The similarly-designed "Model II" moderator ran at a slightly lower temperature and burped only once, colossally, bursting to open a leak between the moderator container and the vacuum space. This occurred 2-3/4 hours after shutdown following two weeks of operation with a proton current of ~14 μA. The also-similar "Model III" moderator installed in May, 1986, has also developed a leak like that of Model I, despite pursuit of a program of purposely-induced burps. Examination of Model II revealed that a circumferential weld failed due to high internal pressure, such as would be caused by thermal expansion of solid methane or the release of Hydrogen gas upon spontaneous heating. This weld

*Work supported by the U.S. Department of Energy

is the main object of our current attention, as we design a replacement. The present paper deals with the processes which lead to the burping behavior and outlines the analysis of some of the consequences. Our purpose is to determine conditions under which we can operate the system at the lowest possible temperature, avoiding the problems we have experienced to date.

Previously we envisioned a great variety of prospective burp-causing processes that so confused the issue as to prevent the understanding of any one of them. Now it seems clear that some mechanism of radiation-damage energy accumulation and its release is the cause of the burps. We outline a simple theory purporting to describe the phenomenon, which is similar in form to that describing the well-known Wigner energy release in irradiated graphite.

The moderators operated at different temperatures (14K for Model I, 9K for Model II, 12 K for Model III). These provide the lowest measured spectral temperatures of all cold neutron sources of which we are aware, thus producing higher fluxes of long wavelength neutrons and extending the epithermal range to lower energies. It now appears, however, that these low temperatures can put the moderators into an unstable regime of operation. On the other hand KENS has operated a similar solid methane cold moderator, which has exhibited no burps. The KENS system runs at a somewhat higher temperature (~ 20 K) than that at IPNS, and at lower (~x 1/10 - 1/2) dose rates. We show that higher temperatures allow moderators to be operated in a permanently stable regime. We suggest measurements that should be undertaken to quantify and test the results of the theory.

Burp Data

Figure 1 is the record of a typical burp of Model III, which was induced by changing the cooling conditions. The figure shows the temperature registered by the internal thermocouple and the refrigerator backpressure, an indirect measure of the heat load on the system. We interpret the irregular behavior of the temperature, and especially of the backpressure, to be indications of Hydrogen leakage into the insulating vacuum space (we have found Hydrogen to be the major component of a gas sample taken from the insulating space after a burp) which spoils the insulation and induces complex transients in the refrigerator. During the induced burp operation, there is first an initial slight decrease in temperature caused by expansion of the coolant already in the system when the coolant valve is throttled down, followed by an increase in temperature caused by the reduced coolant

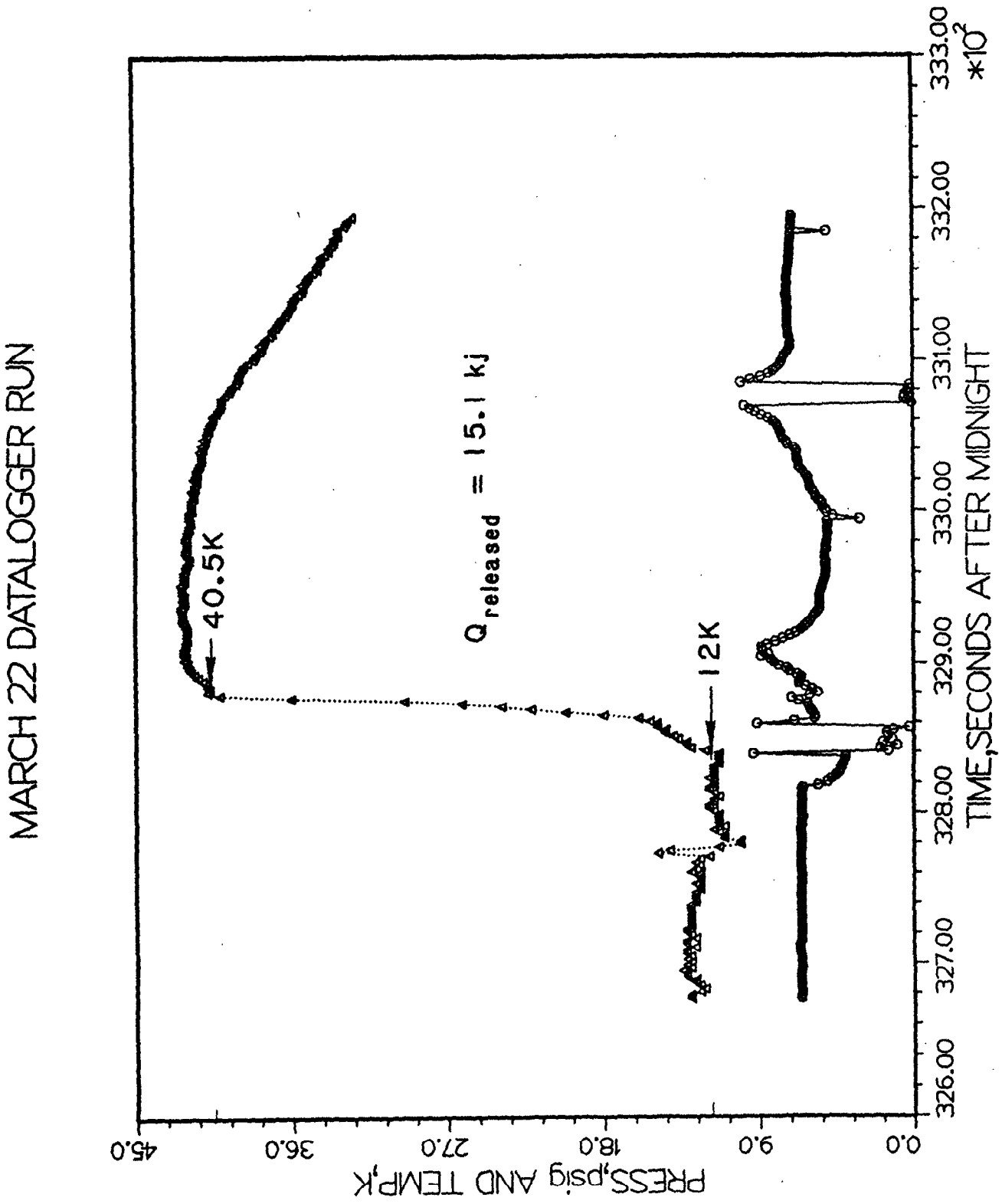

1. A record of a typical burp of the IPNS "Model III" moderator. The upper line gives the temperature of the moderator, and the lower line records the helium backpressure in the refrigerator.

flow. However of greatest interest here is the sudden rise of temperature, which we interpret to be due to the release of stored energy. We relate this temperature rise to the released energy using the thermodynamic data below.

Thermodynamic Data

Figure 2 shows the total heat content Q(T) of the box as a function of temperature T, calculated from literature values of the specific heats and phase transition energies, assuming a uniform temperature throughout the moderator. The masses of aluminum and methane in the Model I moderator box are M_{Al} = 692. gm. and M_{CH4} = 314. gm. (We also account for the presence of the 6% dense aluminum foam [1] in the box).

Burp Data Analysis

We have analyzed a series of burp data for Models I and III, noting the time intervals between each burp and the previous detected burp, and the maximum temperature reached by the internal thermocouple during the burp. Temperatures have been converted to energies using the thermodynamic data. Figure 3 shows the total energy $Q_{released}$ released, calculated from the starting temperature and the maximum temperature of each burp and plotted versus the time between burps, for Model I. Two sets of curves are drawn on Figure 3, each with the assumption that damage energy accumulates in proportion to the time since the last burp, an appropriate assumption on the basis of the simulations described later. The grand average of the $Q_{released}$ data gives a rate of damage energy accumulation of $dQ_{released}/dt$ = 0.4 kjoules per hour. The steepest line that can be drawn through the data of Figure 3 (and two others which seem to be offset by multiples of about 24 hours) has a slope indicating $dQ_{released}/dt$ = 0.7 kjoule per hour; these values bracket the possible values of the rate of accumulation of damage energy,

$$0.4 \text{ kj/hr } (0.11 \text{ w}) < dQ_{released}/dt < 0.7 \text{ kjoule/hour } (0.19 \text{ watts}).$$

These limits pertain to the proton current during those times, about 12 μA. Some of the scatter in the data would probably be eliminated if the abscissa were the total number of delivered protons rather than the irradation times; there may have been undetected burps between the recognized ones.

We have one more burp datum, namely that for the disastrous burp of model II, which took place after two weeks operation at a proton current of about 14 μA. Taking $dQ_{released}/dt$ = 0.5 kjoule per hour for this period gives $Q_{released}$ = 168. kjoules. According to Figure 2, this amount of energy

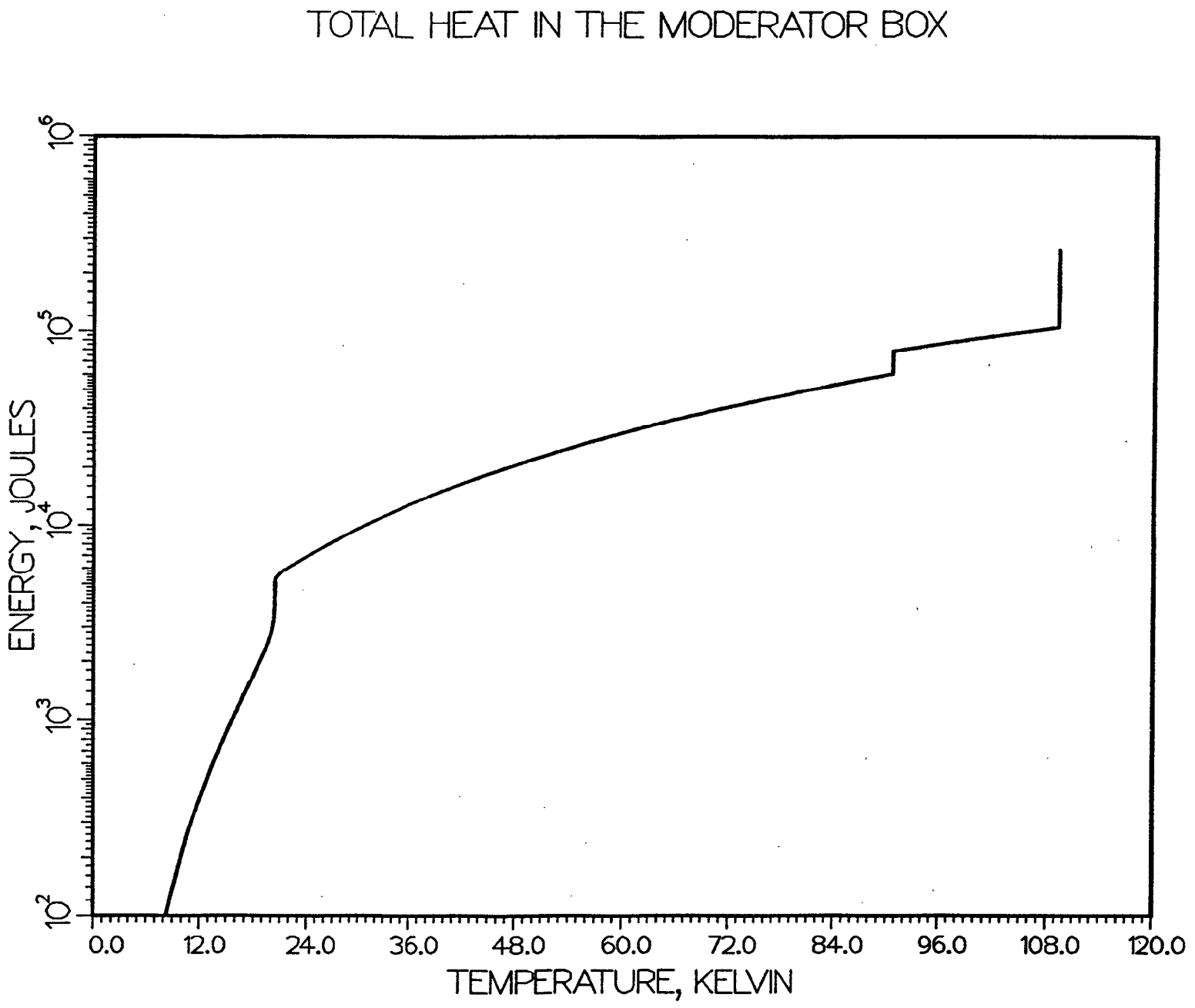

2. The total heat content of the methane-filled moderator box, containing 692 gm of aluminum and 314 gm of methane.

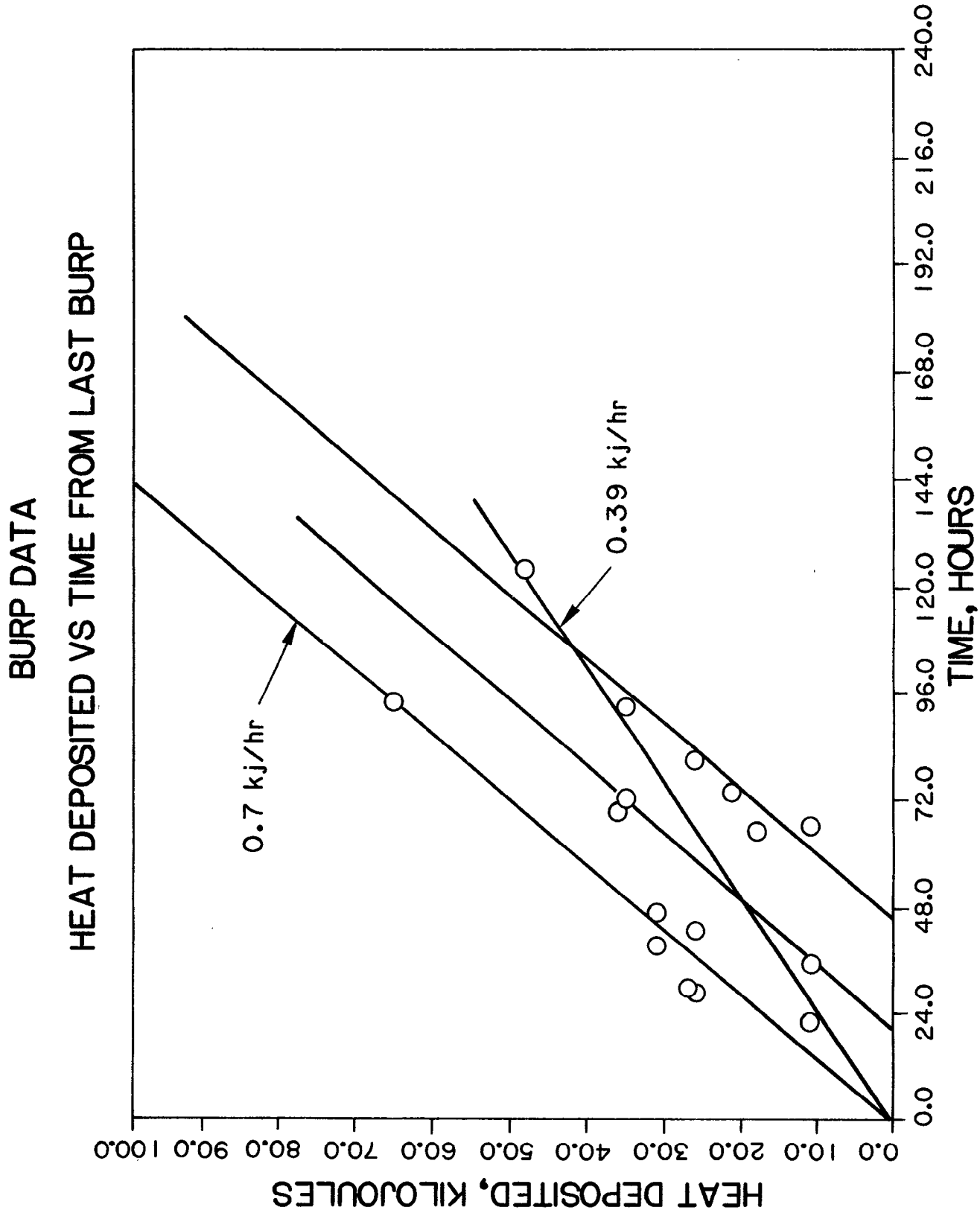

3. The total energy deposited in the moderator box before the burp plotted against the time since the previous burp for the model I moderator. The maximum energy accumulation rate is about 0.7 kjoules/hour, and a minimum of 0.4 kjoules/hr, though other curves may be drawn assuming 24 and 48 hour offsets caused by burps that took place but were not recorded.

would melt the methane and vaporize some, with results that are consistent with what we observed.

Damage Energy and Storage Mechanisms

Radiation damage in aluminum and methane in the moderators of IPNS is presumably due mostly to fast neutrons. There has been considerable study of radiation damage in aluminum at low temperatures, partly as the object of the studies, and partly since aluminum is a common material for construction of irradiation cryostats. There, damage accumulates in the form of Frenkel pairs. For example, an aluminum cryostat irradiated at 6. K at Lawrence-Livermore Laboratory exhibited burps at an accumulated fast (14 MeV) neutron fluence of 2. $\times 10^{18}$ n/cm^2 [2]. At IPNS the fast flux is about 5. $\times 10^{12}$ n/cm^2-sec, so that we would reach this fluence in about 5 days.

Aluminum

About 22. joules/gm of damage energy accumulates in pure aluminum irradiated to saturation at 4. K, and the release of this energy would raise the temperature of aluminum to over 100 K [3]. If, on the other hand, this energy were distributed between the metal and the methane of the moderator, (the cooling time of the moderator, and therefore the time available for this distribution, is about 15. sec), then the total energy would be about 15. kjoules. According to Figure 2 this would raise the temperature to about 36. K. This is somewhat smaller than the temperature reached in the observed burps of the Model I moderator, and much less than what is needed to explain the disastrous burp of Model II. However the damage energy of 22. joule/gm pertains to pure aluminum, while our moderator box is constructed of 6101 alloy, in which the pinning of defects by impurities is expected to lead to the accumulation of a somewhat higher density of defects.

To investigate the effect of damage energy accumulation in Aluminum, we irradiated the empty moderator container to a dose corresponding to 7. $\times 10^{18}$ protons on target (about one day). Figure 4 shows the record of the subsequently induced temperature transient. Taking the temperature change from 21.4 to 43.2 K to represent a rise in the average temperature, this represents about 1.1 j/gm, roughly consistent with expectations.

We conclude that radiation damage energy accumulation and release in aluminum may be one mechanism responsible for the burps, but only may and only one, since the rate of energy accumulation is somewhat too small to explain what we have observed in the small burps of Models I and III and the

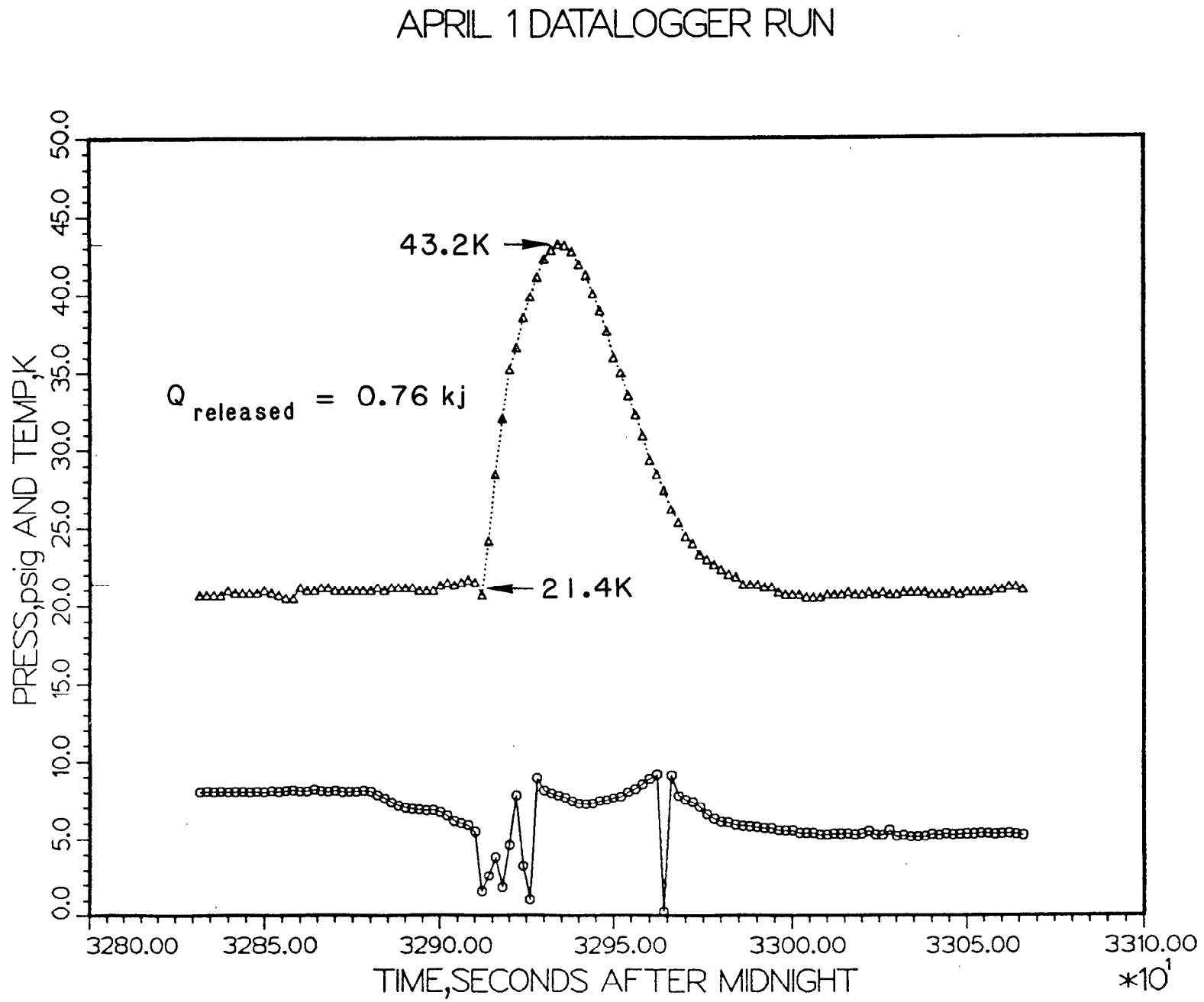

4. The record of the temperature transient induced following irradiation by $7. \times 10^{18}$ protons on target, of the empty Model III moderator box (Aluminum only).

titanic Model II burp in the methane-filled box. Although radiation damage in aluminum is only one of several possible mechanisms for energy storage in our moderators, it may be the triggering mechanism for release of the stored energy.

Methane

We know a great deal less about the details of radiation damage in methane than we know about radiation damage in aluminum, and this relates mostly to the chemical effects. However it is certain that the primary effect is the knocking off of protons from methane molecules, with the consequent formation of a diffuse damage cascade leaving behind protons, CH_3^+ or other fragments, and lattice deformation defects in the methane crystal lattice, each of which represents some stored energy. From chemical analyses of the products collected after several periods of irradiation of the solid methane moderator [1], we know that the long-term rate of conversion of methane to H_2 is about 5.4 mole % H_2 per week relative to CH_4. (Since the mobilities of various species in the solid are expected to be significantly different from those in the liquid, radiation damage data for the liquid should not be considered to be relevant to the problems in solid methane). Even though there may be several relevant species involved, we compute the rate of accumulation of damage energy from neutral hydrogen $H^{(0)}$ only.

The energy released in the reaction $H^{(0)} + H^{(0)} \rightarrow H_2$ is 4.5 eV [4]. According to the long-term rate of production of H_2 in gases analyzed after warmup ($H^{(0)}$ can be produced and stored at a higher rate during cold irradiation, and recombine to produce species other than H_2 upon warmup, so that the relevant rates could be even higher than this estimate), we estimate the rate of accumulation of damage energy as $H^{(0)}$ to be

$$dQ^{(H_2)}/dt = 2.74 \text{ kjoules/hr } (0.76 \text{ watts}).$$

This rate is substantially greater than the rate $dQ_{release}/dt \simeq 0.7$ kjoules/hr, and does not include the energy stored as other species (CH_3^+, etc) which would increase it. On the other hand, this figure is based on the assumption that all the H_2 evolved after warmup is stored as $H^{(0)}$ between burps--this is certainly not true, in view of the inhomogeneity of the damage cascade, and the consequent initially-rapid annihilation of defects. Lacking further information, we assume that we have identified mechanisms adequate to explain the burping behavior on the basis of energy stored as radiation damage induced defects in aluminum and methane, which is released by thermally-activated mechanisms.

Theory

Guided by the idea that energy is produced and stored in some form (Frenkel pairs, interstitial $H^{(0)}$, ...), released by some thermally-activated mechanism, we propose a simple, non-specific, lumped-parameter model of the system, based on the production and thermally-activated diffusion-controlled self-annihilation of a single type of defect, with Newtonian external cooling. There is nothing particularly novel in this approach, since it has been applied to other systems which store energy by various mechanisms while undergoing irradiation. (The best-known example is the study of the thermal annealing kinetics during the release of the stored (Wigner) energy in the form of lattice defects caused by neutron irradiation of graphite [5-10]. There various types of defects, each with different activation energies for migration and different mobilities as a function of temperature, are averaged into one species [5].)

The rate of change of the concentration N(t) of defects at time t is given by the volume rate of production R(t) of defects and by the rate of self-annihilation $K(T)N^2(t)$ of defects; viz.,

$$dN/dt = R(t) - K(T)N^2(t) \ . \qquad (1)$$

(This simple model has been used to describe the release of stored Wigner energy in irradiated graphite [6], though Cottrell et al. [5] have considered a more generalized form of the defect recombination term.) The factor K(T) is a temperature-dependent recombination rate coefficient having a thermal activation factor which is assumed to be of Arrhenius form,

$$K(T) \propto e^{(-\Delta E/k_B T)} \ . \qquad (2)$$

This is arguably proportional to the diffusion coefficient describing the motion of defects. ΔE is the activation energy of the defect, which releases an energy E per defect upon annihilation, and k_B is the Boltzmann constant. (This is what Dickson et al. [7] call a constant activation energy model, though it could be generalized by a more complicated variable activation energy model which depends on the concentration of defects.)

The net sensible heating power deposited in the moderator is the summation of 1) the instantaneous nuclear heating power P(t) deposited in the moderator, 2) the power $EVK(T)N^2(t)$ developed from the self-annihilation of defects, and 3) the rate of heat removal $H(T,t)A(T - T_c(t))$ by the cooling system. The factor H(T,t) is the "film coefficient" describing the transport of heat across an area A from the system to the coolant. The temperature of the moderator system at time t is T(t) and the temperature of the coolant is $T_c(t)$. We note that changes in the cooling conditions may alter H as well as

T_c, so designate both as externally-controlled, explicit functions of time. Hence

$$\rho C(T)dT/dt = P(t)/V + EK(T)N^2(t) - (H(T,t)A/V)(T(t) - T_c(t)) , \qquad (3)$$

where C(T) is the specific heat of the moderator, ρ is the density of the material, and V its volume. When reduced to minimal form, these equations have only a few unknown parameters; however, they are highly non-linear and can exhibit very irregular behavior. Drastic changes in the time behavior can be produced by relatively modest changes in the parameters. (Similar equations have been used to describe the migration and annihilation of point defects in solids, for example in the contexts of creep and radiation-induced growth [11].)

We define the following temperature and time dependent quantities in terms of dimensionless parameters relative to their values at some arbitrary reference temperature T_o :

the defect recombination rate coefficient,

$$K(T) = K_o k(T); \quad \text{so that } k(T) = e^{(-(\Delta E/k_B)(1/T-1/T_o))} ,$$

the specific heat,

$$C(T) = C_o c(T); \quad \text{so that } C_o = C(T_o) ,$$

the film coefficient, whose explicit time variation we subsequently ignore,

$$H(T,t) = H(T) = H_o h(T); \quad \text{so that } H_o = H(T_o) ,$$

the defect concentration,

$$N(t) = N_o n(t) ,$$

the defect production rate,

$$R(t) = R_o r(t) ,$$

and the nuclear heating power,

$$P(t) = P_o p(t) . \qquad (4)$$

Hence equations (1) and (3) can now be put into a reduced form.

We further define the following constants in terms of quantities at the reference temperature T_o:

the equilibrium concentration N_o of defects at the reference temperature T_o,

$$N_o = \sqrt{(R_o/K_o)} ,$$

the time constant τ_N (at the reference temperature T_o) for relaxation of the defect density N(t) to its equilibrium value N_o,

$$\tau_N = 1/\sqrt{(R_o K_o)} ,$$

the time constant τ_T (at the reference temperature T_o) for cooling of the system to its equilibrium temperature (this relaxation time is determined by the ratio of the specific heat to the film coefficient for the system),

$$\tau_T = V\rho C_o/H_o A ,$$

the incremental temperature T_p by which the moderator temperature T would rise above the coolant temperature T_c due to a constant external power P_o,

$$T_p = P_o \tau_T / V \rho C_o ,$$

the incremental temperature T_N by which the moderator temperature T would rise above the coolant temperature T_c due to the equilibrium rate of annihilation $R_o = K_o N_o^2$ of defects,

$$T_N = E R_o \tau_T / \rho C_o . \tag{5}$$

Hence the defect concentration equation (1) and the moderator temperature equation (3) become

$$\begin{cases} \tau_N dn/dt = r(t) - k(T)n^2 \\ \tau_T c(T) dT/dt = T_p p(t) + T_N k(T) n^2 - h(T)(T - T_c). \end{cases} \tag{6}$$

The n (defect concentration) equation is a generalized Ricatti equation. When the defect production rate is constant, $R(t) = R_o$ ($r(t) = 1$, constant), and the temperature of the moderator is constant, $T(t) = T_o$, and thus the recombination rate is constant, $K(T) = K_o$ ($k(T) = 1$, constant), it has a simple solution,

$$n(t) = \frac{n(0) + \tanh(t/\tau_N)}{1 + n(0)\tanh(t/\tau_N)} . \tag{7}$$

Under these conditions, the defect concentration n(t) relaxes smoothly and monotonically from n(0) to 1. When n(0) = 0,

$$n(t) = \tanh(t/\tau_N). \tag{8}$$

(This result has been given by Newgard for defects in irradiated graphite [6]). For small times, $t \ll \tau_N$,

$$n(t) \simeq n(0) + (1 - n^2(0))(t/\tau_N); \tag{9}$$

for long times, $t \gg \tau_N$,

$$n(t) \to 1.$$

When the nuclear heating rate, p(t), the defect concentration, n(t), and the coolant temperature, $T_c(t)$, are all constant, and $c(T) = k(T) = h(T) = 1$, independent of T, the T (moderator temperature) equation (6) has the simple solution

$$T(t) = T_p p + T_N n^2 + T_c + [T(0) - (T_p p + T_N n^2 + T_c)]e^{-t/\tau_T} . \tag{10}$$

Under these conditions, T(t) relaxes smoothly and monotonically from T(0) to a value $T_p p + T_N n^2 + T_c$.

To avoid linearizing approximations, we have coded these simultaneous first-order differential equations in reduced form for solution by Runga-Kutta methods. A few preliminary calculations with guessed parameters and constant coefficients provide some results which relax smoothly and

monotonically to stable conditions, and some which show an oscillating behavior, similar to the regular burping that we have observed. (Similar curves have been produced by Dickson et al. for describing the release of stored energy in irradiated graphite [7].) Figure 5 shows results for a stable case, for which there is a steady rise in the defect concentration N(t) and the moderator temperature T to their constant equilibrium values as a function of time. Figures 6a and 6b show results for an unstable situation, where there is an initial steady rise in the defect concentration N(t) until the occurence of a precipitous release of energy (burp), with a simultaneous sudden increase in the moderator temperature, after which the moderator quickly relaxes to its earlier values. (As in the case of irradiated graphite, the onset of energy release from the moderator is very critically dependent on variations in the initial parameters, and can be initiated suddenly when some local fluctuation sufficiently raises the moderator temperature.) When the volume defect production rate, R(t), and the nuclear heating power, P(t), are constant, these calculations show an increase in the defect density, N(t), which is nearly proportional to time up to the time of the burp. At this point there occurs a very rapid decrease of the defect density with a concurrent increase in the moderator temperature T. The calculations also show that a burp releases nearly all the energy stored in the defects. The crucial factors required for burping behavior are to have a high activation energy ΔE and a low irradiation temperature T, a high defect energy deposition rate ER_o and a long cooling time τ_T.

We have also derived a number of simple and useful results from the fundamental equations in terms of measurable quantities, as guides to the understanding of the system. Fundamental to all of them is the condition that the system becomes unstable when the defect concentration N(t) is so large that (neglecting dC(T)/dT, etc.)

$$EN^2 dK(T)/dT = EN^2 K(T)\Delta E/(k_B T^2) > d/dT(H(T)A/V)(T-Tc) \simeq H(T)A/V,$$

and $$n^2 T_N(\Delta E/k_B T^2)k(T) > h(T) \simeq 1; \qquad (11)$$

that is, when an increase of the moderator temperature causes an increase in the rate of release of stored damage energy which is greater than the increase in the rate of heat removal by the cooling system.

This treatment may be generalized to a defect recombination law that depends on powers of the defect density other than its square, as has been performed for irradiated graphite [5]. We present below some of the results for the expected case that the recombination takes place at a rate

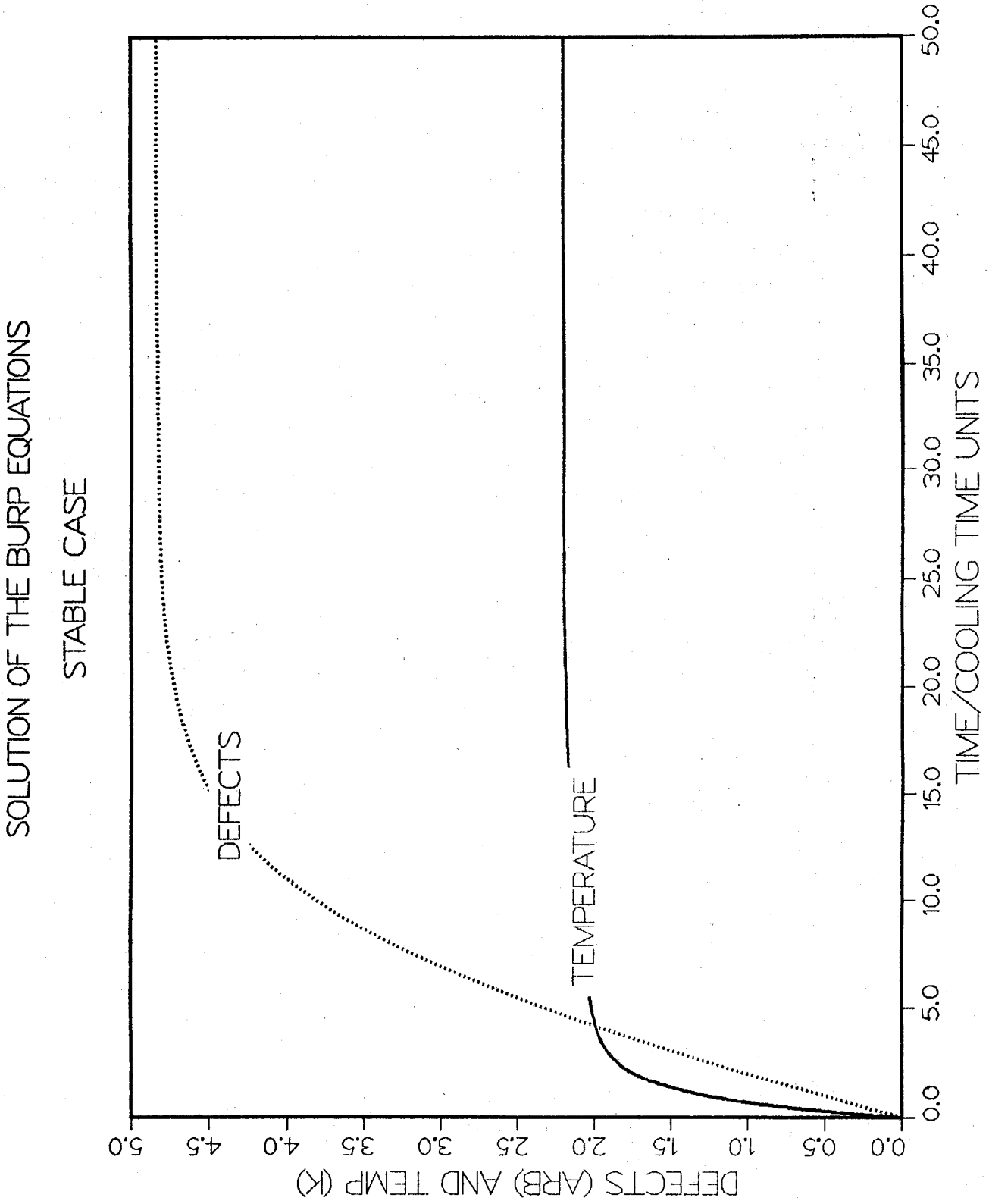

5. The solution of the burp equations for the stable case, showing the steady rise in the defect concentration and the moderator temperature to constant equilibrium values as a function of time.

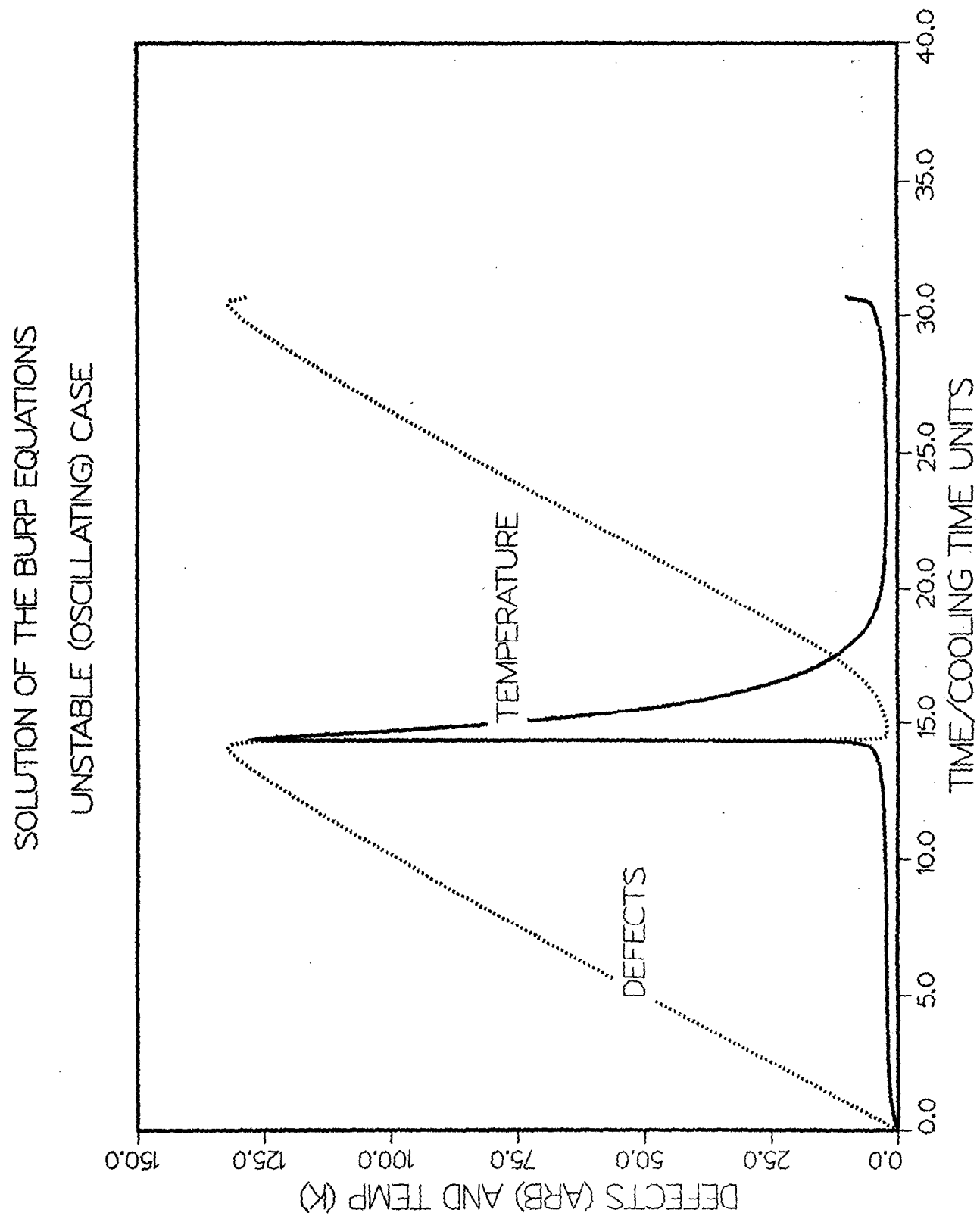

6a. The solution of the burp equations for the unstable (oscillating) case, showing the steady rise in the defect concentration until the occurence of the burp, at which time the defects disappear catastrophically with the simultaneous sudden increase in the moderator temperature.

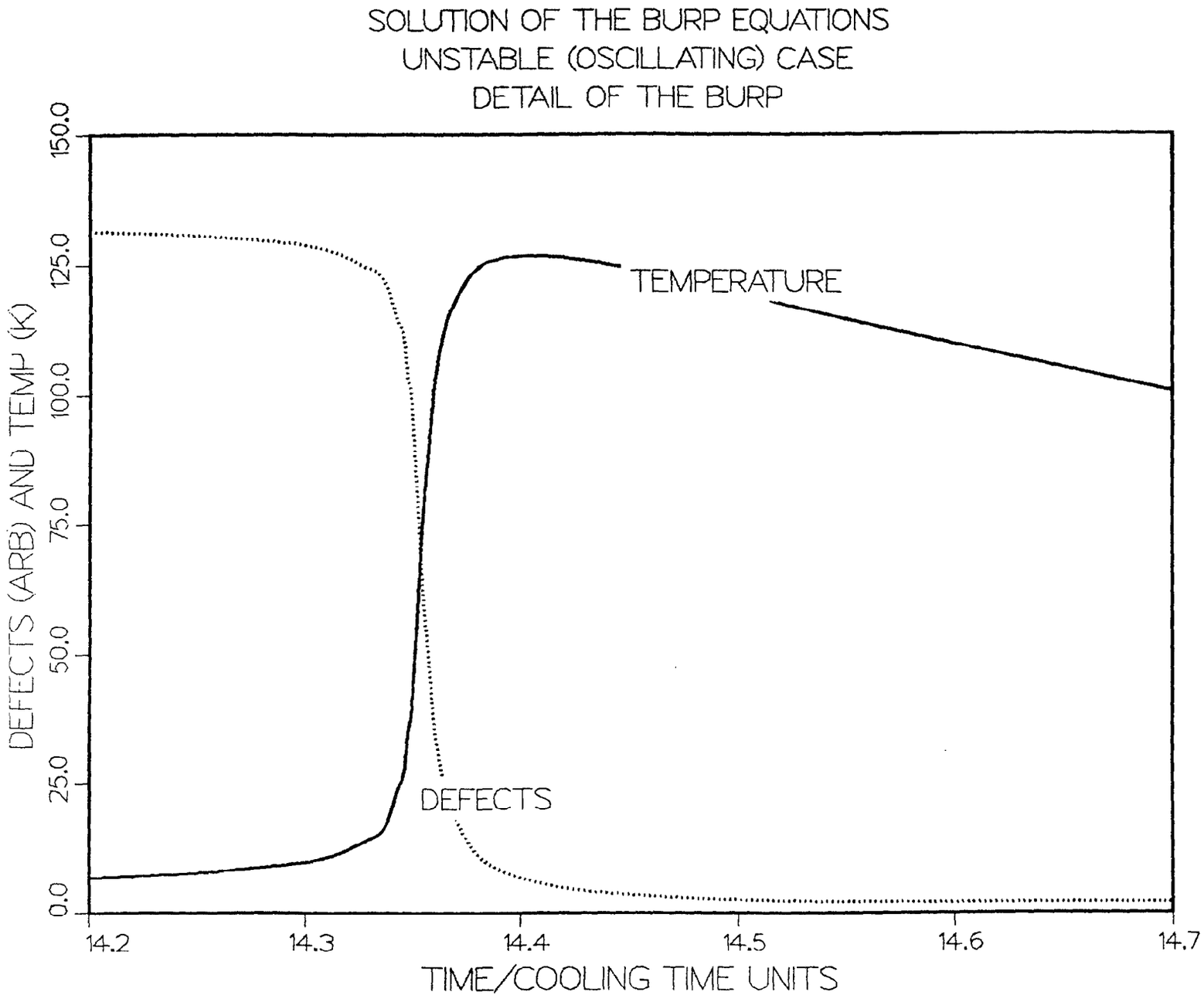

6b. The details of the burp behavior shown in Figure 6a, around the time at which a burp occurs.

proportional to the square of the density of a single species, and for constant coefficients.

Instability Time t_s and Temperature T_s

We express the results in terms of quantities which are independent of the temperature and those which depend explicitly on the temperature. We also assume that the initial defect concentration is zero, n(0) = 0, and that the defect production rate and cooling system conditions (namely H(T,t), thus T_N) are constant. The time t_s and temperature T_s at which the moderator system becomes unstable are related by

$$\tanh^2(t_s/\tau_N)\ T_N k(T_s)(\Delta E/k_B T_s^2) = 1,$$

$$\text{or } t_s = \tau_N \tanh^{-1}\sqrt{(k_B T_s^2/\Delta E T_N k(T_s))}. \tag{12}$$

When $k_B T^2/\Delta E T_N k(T) > 1$, eq (12) has no real solution and this is the condition for permanent stability of the system; presumably the KENS moderator operates in this regime. The stored energy accumulates more slowly at a higher temperature, and saturates at a level at which it appears steadily and stably as heat.

When $\sqrt{(k_B T_s^2/\Delta E T_N k(T_s))} \ll 1$, the instability time t_s is proportional to the argument of the inverse hyperbolic tangent function, corresponding to the proportional regime found in the calculations; that is,

$$t_s \simeq \tau_N \sqrt{(k_B T_s^2/\Delta E T_N k(T_s))}. \tag{13}$$

We can estimate an activation energy ΔE through this equation. The burps of Model I took place at time intervals t_{s1} = 24 hrs at a temperature T_{s1} = 14 K, while the gigantic burp of Model II took place after a time t_{s2} = 336 hrs and at a temperature T_{s2} = 9 K. Hence we can estimate

$$(t_{s1}/t_{s2}) = (T_{s1}/T_{s2})e^{((\Delta E/2k_B)(1/T_{s1} - 1/T_{s2}))},$$

$$\Delta E/k_B = 2\ln\left[\left(\frac{ts1}{ts2}\right)\left(\frac{Ts2}{Ts1}\right)\right]/(1/T_{s1}-1/T_{s2}) , \tag{14}$$

$$= 155.\ K.$$

This result is based on numbers which are not very accurate, and, moreover, the proportionality assumption itself may not be very accurate, since we have only two data points. More accurate measurements of the instability times t_s as a function of the instability temperatures T_s would provide more useful insight into the activation energy ΔE, and therefore into what mechanism is responsible for the burps. The procedure would be to operate for various times t_s, then raise the moderator temperature until a burp occurs--this is T_s. Hence an Arrhenius plot ($\ln(t_s/T_s)$ vs $1/T_s$) would provide $\Delta E/2k_B$ from

the gradient, and the prefactor in the relationship for t_s, (parameters essential to make the theory into a model) and would lend credence to the theory if it were successful. Unfortunately the scatter in the data is so poor as to make this analysis not useful. (Measurements have been performed on irradiated graphite [10] showing a threshold effect in which a slight temperature rise over a short period causes a rapid temperature increase; an extremely slow warm-up avoids this rapid release of energy. In addition, samples irradiated at lower temperatures have much higher and quicker energy releases [5])

More generally, in case the proportionality assumption does not apply, one could instead fit the data to the relationship

$$\tanh(at_s) = bT_s e^{(c/T_s)}, \tag{15}$$

where $a = 1/\tau_N$, $b = e^{(-\Delta E/2k_B T_o)}\sqrt{(k_B/T_N \Delta E)}$, and $c = \Delta E/2k_B$. In this case we also obtain τ_N, the time constant for relaxation of the defect density to its equilibrium value at the reference temperature T_o. There may well be conditions where this analysis is possible.

Burp energy

On the basis of the proportionality assumption, the energy released during a burp is equal to the energy stored as defects; that is,

$$\begin{aligned} Q_{released} &= ER_o t_s \\ &= ER_o[(k_B/\Delta E)(V/ER_o^2 H_o A)(T^2/K_o)e^{(\Delta E/k_B T)}]^{1/2} \\ &= \sqrt{[(k_B/\Delta E)(VE/H_o A K_o)]}Te^{(\Delta E/2k_B T)}. \end{aligned} \tag{16}$$

The energy released increases very rapidly as operating temperature is decreased, as we have observed. The assertion that $Q_{released}$ is proportional to the time t_s elapsed before the burp is the basis for Figure 3. More-refined measurements of induced burps, for which the maximum temperature T_{max} reached is recorded as well as the time t_s elapsed before the burp and the temperature T_s at which it begins, can refine the determination of the rate of damage energy accumulation, which is $ER_o = T_N(\rho C_o/\tau_T)$ in the theory.

More generally, the energy released in a burp is

$$Q_{released} = \int_{burp} dtV\rho C_o c(T)dT^{(N)}(t)/dt, \tag{17}$$

where $dT^{(N)}(t)/dt$ is the rate of change of the defect density, in the absence of nuclear heating power, heat transferred to the cooling system, and the production of defects. Thus more precisely than in the linear approximation,

$$
\begin{aligned}
Q_{released} &= V\rho C_o \int_{burp} dt\ (\tau_N/\tau_T) dn/dt \\
&= V\rho C_o (\tau_N/\tau_T)(n_{before\ burp} - n_{after\ burp}) \\
&\simeq V\rho C_o (\tau_N/\tau_T) n_{before\ burp} \\
&= V\rho C_o (\tau_N/\tau_T) \tanh(t_s/\tau_N). \qquad (18)
\end{aligned}
$$

In general this relationship should be used rather than the linear one which was invoked to interpret the data in Figure 3.

Temperature Rise During Operation and the Cooling Response Time, τ_T

The first-order effect of nuclear heating of the moderator is to raise the temperature of the system. An equilibrium condition is reached for which the moderator temperature is such that the instantaneous nuclear heating power P_o flows steadily to the cooling system. This contribution to the temperature rise is T_P. Source-shutdown transient measurements made shortly after starting up Model I, indicate that T_P is about 1. K for 12. μA, 450. MeV operation.

Those same measurements also indicate that the thermal response time τ_T is about 60. seconds at about 14. K. The estimated instantaneous nuclear heating power based on scaling from measurements on ZING-P′ moderators, is $P_o \simeq$ 10-20 watts. Since $T_P = P_o \tau_T / V\rho C_o$, we would expect (identifying $V\rho C_o$ = dQ/dT = 148. joules/K at 12 K from Table 1), T_P = (10.w)(60.sec)/(148.j/K) = 4.1 K. This is significantly larger than the observed value $T_P \simeq$ 1. K, inaccurate as it is, even though we have used the lower limiting estimate of the nuclear heating power. The cause of this inconsistency is probably the domination of the thermocouple response time in the transient measurement of τ_T. In view of the relationship between T_P and τ_T, we estimate τ_T, which is of critical importance in the theory, to be within the range $8. < \tau_T < 15.$ seconds. There is some evidence that the temperature relaxes faster than that indicated by the installed thermocouple, although this does not serve to refine the estimate of τ_T.

Hence we need better measurements of the nuclear heating power P_o, the temperature rise T_P and the time constant τ_T. This could be accomplished by using a faster thermocouple and more accurate and more frequent recordings of thermocouple emf and coolant backpressure in burp and shutdown transient measurements.

The theory and calculations show a gradual increase of the temperature of the system during steady irradiation. This is caused by the increasing

power appearing in the system due to the increasing defect density and consequently increasing defect annihilation rate. If an equilibrium is reached, this contribution to the temperature rise is $T_N k(T) n^2(t)$. In a stable system and even in an unstable system except near the time of a burp, at least a quasiequilibrium exists, in which the temperature rises by this amount. Figures 6a and 6b show this subtle effect, which was observed during operation of Model II. (The temperature rose from about 7. K to about 9. K during the two-week period of operation.)

This quasi-equilibrium, $dT/dt \simeq 0$, operation of the moderator implies that the moderator temperature is given by

$$T(t) \simeq T_p p(t) + T_N k(T) n^2(t) + h(T) T_o \ . \tag{19}$$

When the nuclear heating power $p(t)$ is constant and the heat removal rate $h(T)$ is constant, there is an increase in the defect concentration $n(t)$, so that the moderator temperature is given by

$$T(t) \simeq (1/h(T))[T_p p(t) + T_N k(T) \tanh^2(t/\tau_n)] + T_o \ . \tag{20}$$

If measurements are made at consistent relative power, $p(t)$, as a function of time in the absence of burps, then with the assumption that $h(T) = 1$, we could determine $(T_p + T_c)$ and $T_N k(T)/\tau_N^2$ in the proportionality regime, or $(T_p + T_c)$, $T_N k(T)$ and τ_N in cases for which $n(t)$ saturates.

Stresses Due to Thermal Expansion of Methane

When the methane warms up as in a burp, it expands. Figure 7 shows the lattice parameter (and hence the density or specific volume) of solid methane as a function of temperature [12]. As an example, we consider a burp which raises the temperature of the moderator from, say, 10 K to 50 K. The lattice parameter of methane changes from a = 5.865 Å to a = 5.925 Å, so the relative expansion is

$$\varepsilon = \Delta a/a = (5.925 - 5.865)/5.865 = 0.0102 \ . \tag{21}$$

As an indicative exercise, we consider the box to be a thin spherical shell of aluminum with a radius R and thickness t, and the methane moderator to be incompressible. The strain in the aluminum shell is equal to the relative expansion of the methane, and the stress is given by

$$\sigma_{Al} = E_{Al}\varepsilon = (10. \times 10^6 \text{ psi}) \times 0.0102 = 102{,}000 \text{ psi} \ , \tag{22}$$

where E_{Al} is Young's modulus for aluminum. We calculate an effective radius for the moderator to be

$$R = (3V/4\pi)^{1/3} = (3.\times 752.\text{cm}^3/4\pi)^{1/3} = 5.64 \text{ cm} \tag{23}$$

where V is the volume of the moderator box. Taking the moderator thickness t to be 0.32 cm, the internal pressure is given by

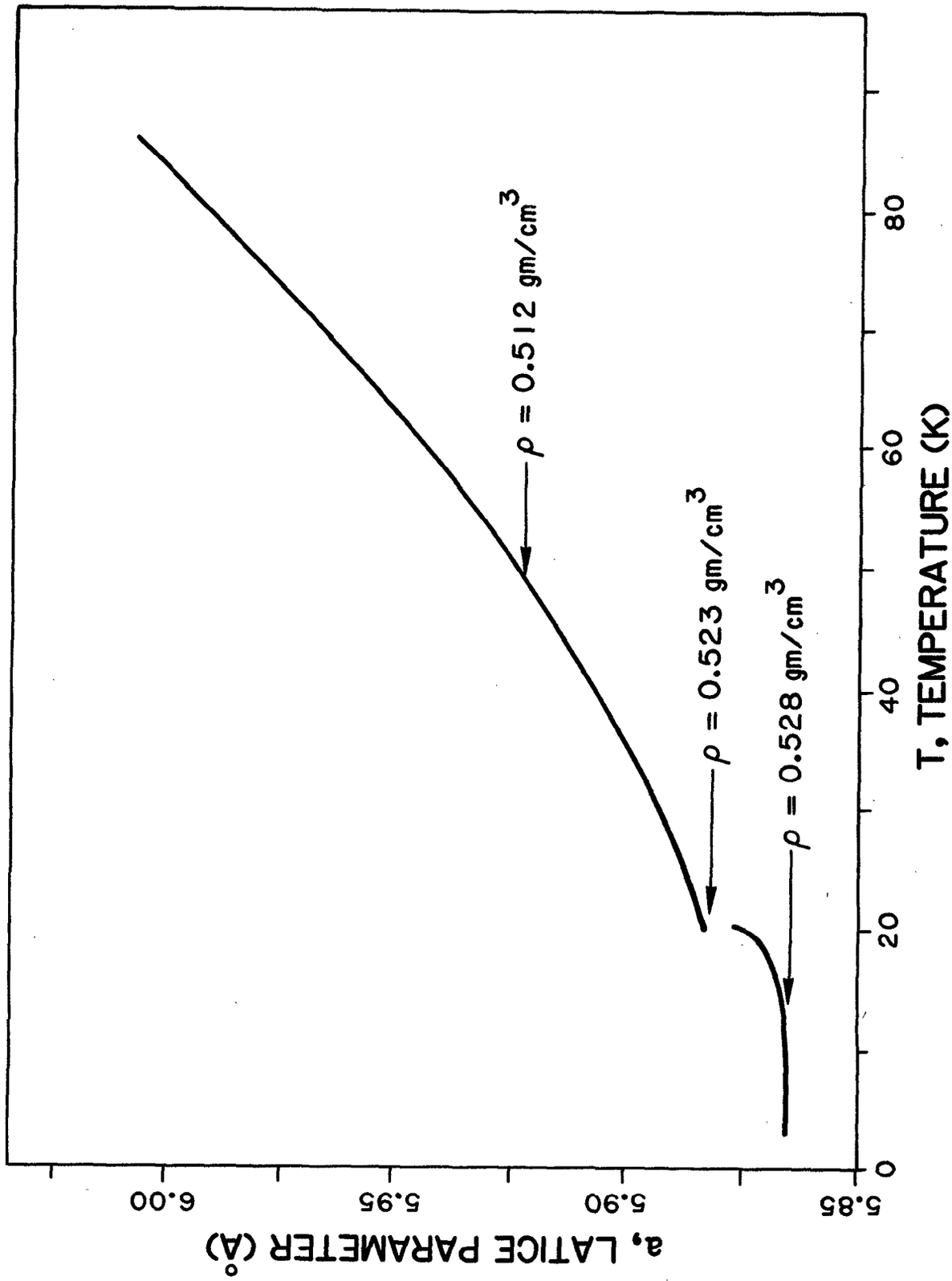

7. The lattice parameter of solid methane as a function temperature, taken from the thesis of Aadsen (Univ. of Illinois, 1975).

$$p = 2\sigma(t/R) = 2. \times (102{,}000.) \times (0.32/5.64) = 11{,}574.\ \text{psi} . \tag{24}$$

With such an internal pressure, the compressibility of the methane reduces the stress, to give a statically indeterminate problem, as the stress analysts call it.

Accounting for the thermal expansion of aluminum, the relative change in the volume of the box is

$$\Delta V_{Box}/V_{Box} = 3\alpha_{Al}\Delta T + (1/V_{Box})(dV_{Box}/dp)p , \tag{25}$$

where α_{Al} is the thermal expansion coefficient of aluminum, ΔT is the change in temperature, dV_{Box}/dp is the rate of change of the volume of the box with respect to internal pressure p. The relative change in the volume of the methane is

$$\Delta V_{CH4}/V_{CH4} = 3\Delta a/a - p/B_{CH4} , \tag{26}$$

where $\Delta a/a(\Delta T)$ is the relative change of lattice constant for temperature change ΔT, and B_{CH4} is the bulk modulus of CH_4. Thus the pressure p is given by

$$p = \frac{3(\Delta a/a - \alpha_{Al}\Delta T)}{(1/V_{Box}dV_{Box}/dp + 1/B_{CH4})} . \tag{27}$$

The relative thermal expansion $\alpha_{Al}\Delta T$ of aluminum at low temperature is 0.010 % between 4. K and 60. K. We take the relative expansion of the methane to be $\Delta a/a = 0.0102$ from equation (21) above, and the factor

$$1/V_{Box}dV_{Box}/dp = (3/R)dR/dp = (3/E_{Al})d\sigma/dp = (3/E_{Al})(R/2t)$$
$$= 2.64 \times 10^{-6}\ \text{psi}^{-1}, \tag{28}$$

as for a spherical box. Measurements of the pressure-temperature isochores in solid methane [13] give

$$(\partial p/\partial T|_V) = (14.7\ \text{psi/bar}) \times (21.7\ \text{bar/K}) = 319.\ \text{psi/K} , \tag{29}$$

and the lattice parameter measurements of solid methane [12] at 50 K (see Figure 7) give

$$(1/V\partial V/\partial T|_p) = (3/a)da/dT = 0.00095\ K^{-1} . \tag{30}$$

This allows an estimate of the bulk modulus of methane from the thermodynamic relationship

$$B_{CH4} = (\partial p/\partial T|_V)/(1/V\partial V/\partial T|_p) ,$$
$$= 319./0.00095 = 3.37 \times 10^5\ \text{psi} . \tag{31}$$

Thus finally we obtain the pressure in the moderator box

$$p = (3.)(0.0102 - 0.0001)/(2.64 \times 10^{-6} + 1./3.37 \times 10^5)$$
$$= 5.40 \times 10^3\ \text{psi} , \tag{32}$$

and the corresponding stress on the box is

$$\sigma = (R/2t)p = 5.64/(2.\times 0.32)\times(5.40 \times 10^3) = 47{,}600.\ \text{psi}\ . \qquad (33)$$

This is substantially lower than the estimate for incompressible methane, and the difference may possibly be significant in a more accurate treatment of the volume change and the stresses in the moderator box.

Stresses Due to Released Hydrogen

When the moderator warms up and burps, it releases hydrogen into a small volume which causes further stresses on the moderator system. Calculating the volume of hydrogen released during a burp from the amount found after warming up the system, namely (0.054 mole H_2)/(mole CH_4)/week[1], after one day there would be

$$H_{2released} = 0.0077 \text{ mole } H_2/(\text{mole } CH_4) \times 314./16. = 0.15 \text{ mole } H_2$$

If we assume for example that 0.2 moles H_2 (0.01 mole H_2/(mole CH_4)) expands into a fixed volume of $V = 30.\ cm^3$ at a temperature of 50 K, then according to the thermodynamic data on H_2, we find that the pressure in the moderator system due to the release of hydrogen gas is

$$p = 24.6 \text{ atm.}$$

Already this is sufficient to stress the box seriously, and to explain the appearance of H_2 in the vacuum insulation space around the moderator. This calculation does not account for the entrainment or solution of H_2 in CH_4, nor the expansion of the box due to pressure. Until dV_{Box}/dp and $d\sigma/dp$ are known, and the simultaneous efects of solid CH_4 expansion and H_2 solubility are incorporated into the calculation, we cannot realistically estimate the stresses that the box must endure.

Summary

We have suggested a model for the cold methane moderator system which seems capable of explaining the observed burping behavior. Measurements suggest approximate values for the parameters in the model, although not very accurately. A number of measurements are suggested which will refine the parameters of the model, and enable a calculation of the behavior of the moderator and determine a safe operating program. In practice, the current program is to heat up the system on a daily schedule, inducing a small burp to prevent the long-term buildup of stored energy. In principle such annealing cycles require only a few minutes to complete, but in practice secondary effects that follow the release of hydrogen into the insulating space sometimes require several hours to overcome.

The purposeful periodic induction of small burps is a macroscopic fix for the burping problem, though severe stresses may be introduced into the moderator. These might be reduced by a strictly controlled operation in which a slow increase in temperature might lead to a controlled release of energy. A microscopic fix might be to introduce as an impurity, some species which would scavenge the responsible energy-storing defects at the operating temperature, and so reduce the buildup of stored energy. The theory outlined above could be modified to include this scavenging. Another microscopic fix might be to arrange that the methane does not expand so severely upon warming, thus reducing the stresses. For example, it is reported [14] that about 10 mole % nitrogen in solid methane causes a decrease in the molar volume with increasing temperature in the range 50 - 60. K.

Further measurements may show up inadequacies in the model insofar as it assumes the dominance of a single defect species. The model could be elaborated to include several species with different production rates, diffusion coefficients, activation energies, production rates and annihilation energies, and spatial variations in the stored energy (as has been done for irradiated graphite [5,7]).

It would also be useful to determine the maximum temperature of a burp that can be safely tolerated, using the maximum stress in the moderator box as the criterion for judging what is tolerable, and therefore the maximum acceptable temperature, and the number of stress cycles that can be expected during the lifetime of the box. Such an analysis needs to be more refined than the above calculations. What is required is a determination of the stress in the box given the maximum temperature (therefore the volume change) reached during the burps, and the compressibility of solid methane as a function of temperature, which plays off against the thermal expansion.

A longer version of this report[15] contains more extensive tables and figures.

Acknowledgements

Many people have helped in this work either directly or by supplying data and ideas. We thank R. C. Birtcher, B. S. Brown, S. S. Cudrnak, R. K. Crawford, T. L. Scott, A. W. Schulke and D. G. Wozniak.

REFERENCES

1. J. M. Carpenter, A. W. Schulke, T. W. Scott, D. G. Wozniak, B. E. Benson and B. D. Leyda, Proc. ICANS VIII, Oxford July 1985, RAL Report RAL-85-110, volume I, 311-318 (1985).

2. B. S. Brown and M. Guinan, private communication.

3. R. C. Birtcher, private communication.

4. Handbook of Chemistry and Physics, The Chemical Rubber Company. Bond Strengths of Diatomic Molecules. H_2: 104.18 Kcal/mole H_2 = 4.5 eV/H_2.

5. A. H. Cottrell, J. C. Bell, G. B. Greenough, W. M. Lomer and J. H. W. Simmons, "Theory of Annealing Kinetics Applied to the Release of Stored Energy from Irradiated Graphite in Air-cooled Reactors", Proc. Second U.N. Intern. Conf. Peaceful Uses Atomic Energy, Geneva 1958, 7, 315-327,United Nations, New York (1959).

6. J. J. Newgard, "Simple Semiempirical Model for Neutron Induced Stored Energy in Graphite", J. Appl. Phys., 30, 1449-1451 (1959).

7. J. L. Dickson, G. H. Kinchin, R. F. Jackson, W. M. Lomer and J. H. W. Simmons, "BEPO Wigner Energy Release", Proc. Second U.N. Intern. Conf. Peaceful Uses Atomic Energy, Geneva 1958, 7, 250-281, United Nations, New York (1959).

8. R. E. Nightingale, J. M. Davidson and W. A. Snyder, "Damage to Graphite Irradiated up to 1000°C", Proc. Second U.N. Intern. Conf. Peaceful Uses Atomic Energy, Geneva 1958, 7, 295-300, United Nations, New York (1959).

9. C. Dalmasso and G.F. Nardelli, "The Wigner Release in Graphite Moderated Reactors", Energia Nucleare (Milan), 6, 307-321 (1959); English translation in USAEC report AEC-tr-4545 (May 1961).

10. E. E. Jones, R. H. McDaniel and J. A. DeMastry, "Stored Energy Release in Irradiated Graphite", A.N.S. Transactions, 15, 208 (1972).

11. See for example S. R. MacEwen and G. J. C. Carpenter, J Nucl Mat 90 (1980) 108, or H. Wiedersich and S. R. MacEwen, ibid 157, for related treatments of creep in irradiated materials.

12. D. R. Aadsen, "Lattice Parameter and Thermal Expansion in Solid Methane", Ph.D. thesis, Univ. of Illinois, 1975.

13. W. F. Lewis, R. K. Crawford, and W. B. Daniels, J. Phys. Chem. Solids, 1974, 35, 1201-1204.

14. K. A. Yakimovich, Proceedings of the Ninth European Conference on Thermophysical Properties, p 353 High Temperatures-High Pressures, 17, (1985) 359.

15. J. M. Carpenter, U. Walter and D. F. R. Mildner, Argonne internal report IPNS Note 38 (1986).

ICANS IX

INTERNATIONAL COLLABORATION ON ADVANCED NEUTRON SOURCES

22-26 September, 1986

THE LANSCE HYDROGEN MODERATOR SYSTEM

H. Robinson and G.J. Russell

Los Alamos National Laboratory
P.O. Box 1663
Los Alamos, New Mexico 87545, U.S.A.

ABSTRACT

At the Los Alamos Neutron Scattering Centre (LANSCE), we have four moderators servicing twelve flight paths. Three of the moderators are light-water; the fourth moderator is liquid Hydrogen at 20K. We flow the liquid hydrogen to and from the moderator canister. The liquid hydrogen moderator system was installed in the summer of 1985, and has operated quite satisfactorily for 2500 hours at average proton beam currents up to 35 μA. We believe liquid hydrogen has potential as a true high-power, high-intensity cold moderator for spallation neutron sources operating with average proton current greater than 100 μA.

We describe the LANSCE liquid hydrogen moderator and planned improvements in our ICANS-IX paper "THE LANSCE TARGET SYSTEM", which may be found on page 177 of these proceedings.

ICANS IX

INTERNATIONAL COLLABORATION ON ADVANCED NEUTRON SOURCES

22-26 September, 1986

Operational Experience with the ISIS Cryogenic Moderators

A T Lucas
Rutherford Appleton Laboratory

1. Introduction

The basic design specifications have been reported at previous conferences together with initial operating experience. By way of a reminder, the fundamental parameters were as follows:-

H_2 System

Supercritical hydrogen at 15 bar pressure and 20 - 25 K with the following estimated heat inputs:-

1.	Nuclear heating in H_2	454 W
2.	Nuclear heating in aluminium vessel	30 W
3.	Heat inleakage	35 W
4.	Transfer losses	6 W
5.	Circulator heat input	60 W
	Total	585 W

Against this, the refrigerator provided by Sulzer Bros (UK) was specified at 600 W at 20 K.

CH_4 System

Liquid methane at 4 bar pressure and sub-cooled to 95 - 100 K with the following estimated heat inputs

1.	Nuclear heating in CH_4	625 W
2.	Nuclear heating in aluminium vessel	13 W
3.	Heat inleakage	26 W
4.	Transfer losses	60 W
5.	Circulator heat input	60 W
	Total	784 W

Against this, the single stage Stirling cycle cryogenerator manufactured by Philips and supplied in standard form, is rated at 1 kW at 100 K.

2. Circuit Description (H_2)

The basic circuit diagram is shown in Fig 1. The two circulators each with remotely operable isolation valves are located in the return leg of the circuit in order to minimise the temperature rise between the controlling sensor and the moderator. An ortho/para catalytic converter of iron oxide compacted into pellets and contained in a wire gauze basket is also located in the flow line of the circuit.

Either circulator can be isolated from the main circuit, pumped out and filled with helium to allow replacement without affecting the main circuit.

3. Circuit Description (CH_4)

The circuit diagram is shown in Fig 2. The circulators were located in the moderator feed line on account of the high density difference between gas and liquid. The cryogenerator is positioned at the highest level, in an attempt to prime the circulator during initial liquifaction.

A pair of remotely valved filters is located in the remote leg.

Both circulators and filters are described in greater detail later.

4. Cooldown Performance

Typical cooldown curves are shown in Figs 3 and 4. The liquifaction phase of the methane system proved the most difficult and tedious part of the operation. This was because of difficulty in keeping the circulators primed with liquid, resulting in vapour locks bringing fluid flow to a standstill. To overcome this, a short circuit bypass valve was added. When the loop had filled with liquid, which was relatively easy on account of the much reduced circuit pressure drop, the bypass valve could be shut and the remainder of the circuit filled and sub-cooled without difficulty.

5. Methane Polymerisation

In the absence of general data on the chemistry of methane in radiation, a relatively large cylindrical filter element with an outside surface area of 385 cm^2 was designed. Flow direction was outside to inside and remotely operated isolation valves afforded replacement without shutting down the system.

The initial filter bore size was 10μ, but because of rapid blocking this was increased to 45μ. It was subsequently noted that periods of rapid blocking coincided with a vertically mis-steered beam when it is possible that the moderators were receiving high energy protons with a correspondingly high level of methane degradation.

6. Recent Modifications

i. CH_4 Filters

It was observed that filters became initially blocked, with with soluble materials which could be readily removed by warming and evacuating the isolated filter unit.

It is unknown at this stage how many times this can be repeated before blockage of a more permanent nature occurs, but it was obviously desireable to enable the regeneration cycle to be carried out remotely. To this end, a pneumatically operated valve panel was installed to enable either filter to be vented, evacuated and purged with inert gas. Heaters and temperature sensors were also fitted to the body of each filter containment. It is intended to regenerate a filter during normal operation of the system.

ii. Methane and Hydrogen Circulators

The basic circulator units were supplied by Philips as modified standard units. In order to meet the RAL safety requirements for flammable gases, the unit was enclosed enclosed in a low pressure inert gas containment.

In order to ease circulator replacement, the main vessel was re-designed as shown in Fig 5. This obviates the need for a separate secondary containment by separating the gas from electrical connections which are in an integral inert gas chamber at the top. The inert gas surrounds the cables and feeds the chamber. Two of the original three rubber 'O' rings which occasionally became chilled and subsequently leaked were eliminated in the new design. The circulator vessels were designed to ASME VIII pressure vessel code, and are regarded as the first step in a circulator development programme.

The thermal break between cryogenic fluid and the nominally room temperature circulator vessel, is effected by an overhung shaft. This suffered problems of instability particularly during its run up to the operating speed of 18,000 RPM, which was overcome by an increase in the shaft diameter at the cost of an increased heat input to the cryogenic fluid. It was also found necessary to provide a step in the shaft with a matching step in the bore of the resin block through which the shaft passes. This acts as an effective block to convective currents greatly reducing transfer into the fluid.

To enable circulators to be warmed up for removal, heaters and temperature sensors were added to the diffusers together with remotely operated pumping and purging facilities.

iii. Circuit Modification

In addition to the above modifications three additional remotely operated cryogenic valves were recently added in order to afford the system improved flexibility.

The problem of liquid filling of the methane system is not fully solved, but plans are in hand to automate the complete cooldown operations using a programmable controller.

Conclusions

The two systems are operating with a fairly high degree of reliability. Circulators continue to be the greatest single cause of breakdowns, although the average life of a unit is probably longer than was at first expected. There is however room for considerable improvement, and at least three full cycles of four weeks running without servicing is considered a reasonable goal for a single unit with the second unit being regarded only as a spare. Whilst existing units have survived such periods and longer, others have suffered premature bearing and other mechanical breakdowns.

One of the problems of the Stirling cycle cryogenerator is that of the control of its output. Unless checked, methane can easily be frozen in the heat exchanger when a vapour block occurs. At the present time, this is avoided by switching off the drive motor, but an electrical heater on the main heat exchanger is to be commissioned in the near future which it is hoped will give much improved control of refrigerative output. Once filled with liquid, a remotely positioned heater now controls the temperature of the system, but this cannot be used during the gas and liquifaction stages on account of the low heat transfer properties of the fluid.

The levels of heat applied by the heater in the two systems, are 450 watts for the methane, and 800 watts for the hydrogen. Because of some heat cycling it is impossible at this stage to ascertain with any degree of accuracy, the heat contribution of the neutrons at running levels so far encountered.

Although designed for pressures of 15 bar at which hydrogen at 20 K is supercritical, the present level of beam current precludes the possibility of boiling if the hydrogen is in a liquid state which was the original purpose of using supercritical hydrogen. The system is therefore run at about 10 bar to give a greater safety margin. This corresponds to a liquid sub-cooled by about 16 K.

A T Lucas
RAL

FIG 1

SCHEMATIC DIAGRAM OF HYDROGEN MODERATOR CIRCUIT

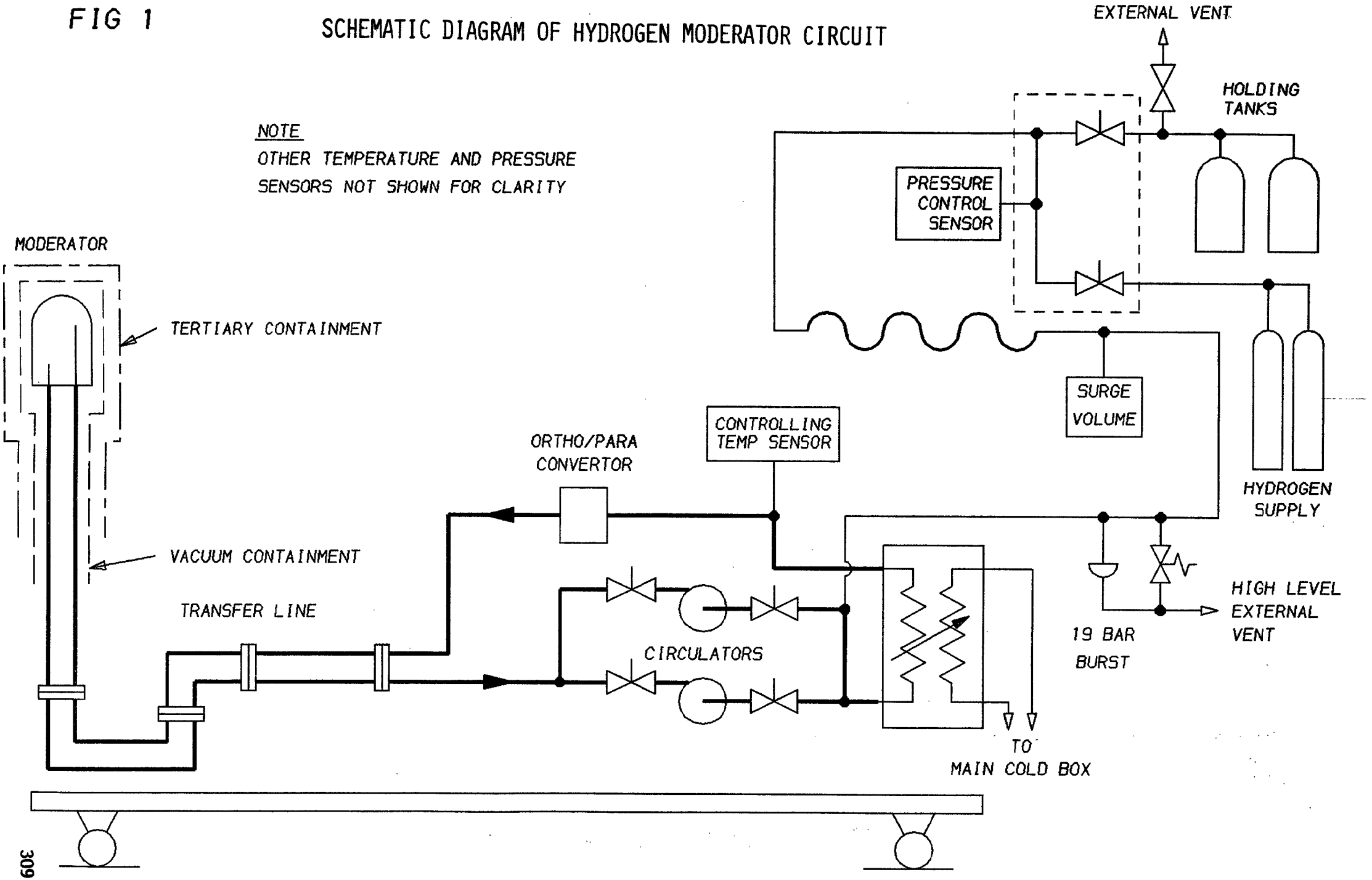

FIG 2

SCHEMATIC DIAGRAM OF METHANE MODERATOR CIRCUIT

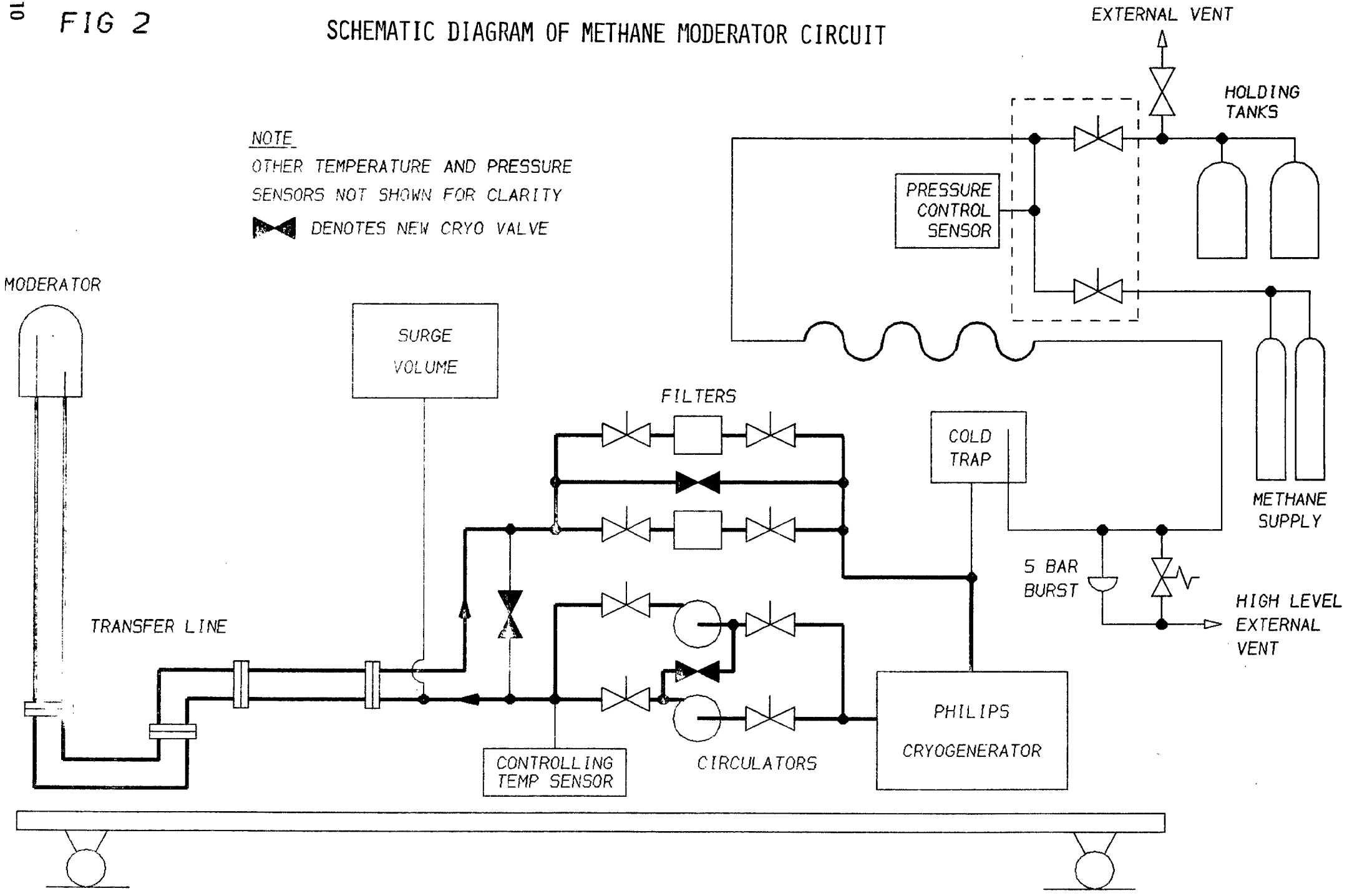

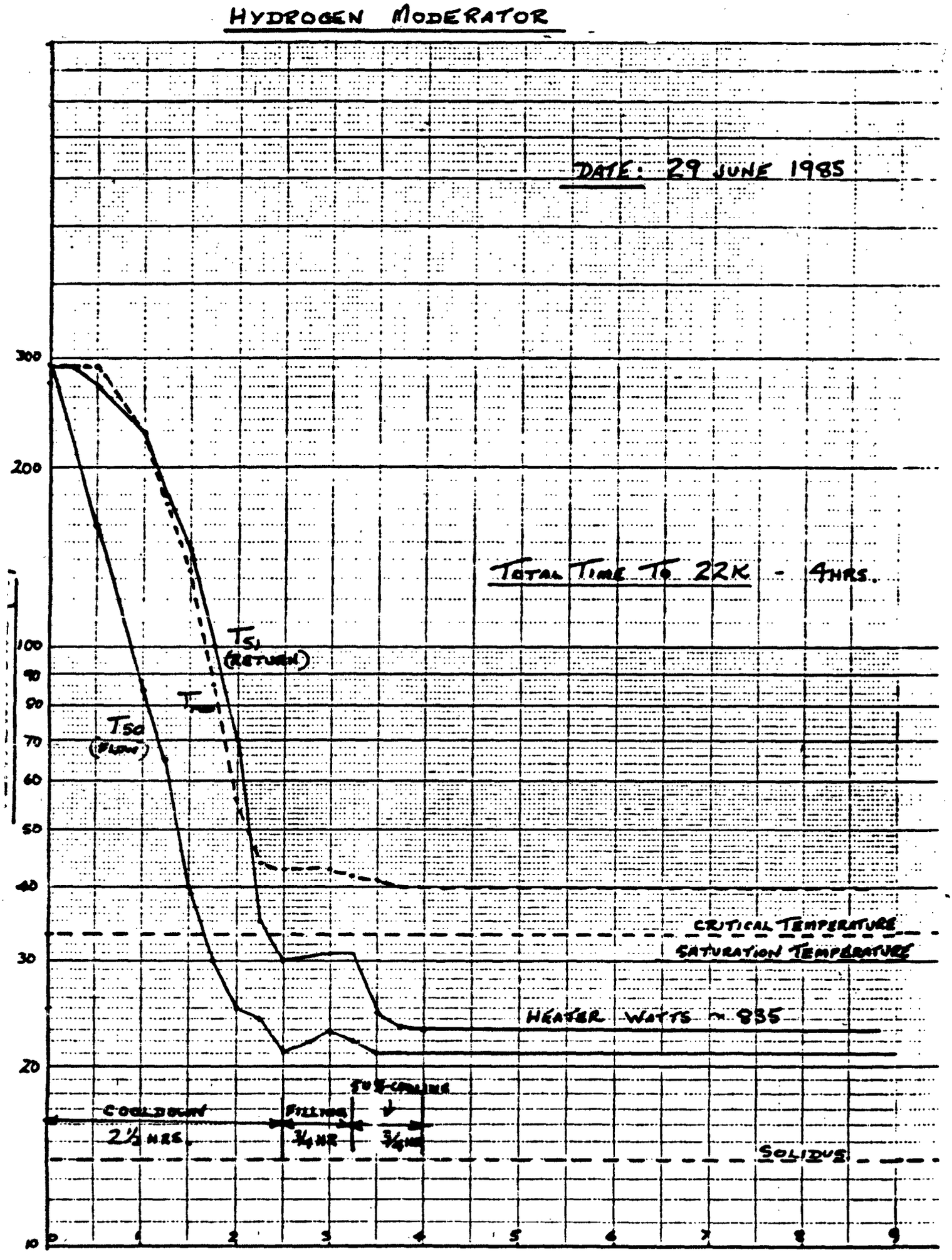
HYDROGEN MODERATOR
DATE: 29 JUNE 1985
TOTAL TIME TO 22K - 4HRS.
Ts1 (RETURN)
Ts0 (FLOW)
CRITICAL TEMPERATURE
SATURATION TEMPERATURE
HEATER WATTS ~ 835
COOLDOWN 2½ HRS.
FILLING ¾ HR
SUB-COOLING ¾ HR
SOLIDUS
300
200
100
90
80
70
60
50
40
30
20
10
0
1
2
3
4
5
6
7
8
9

Figure 3

Figure 4

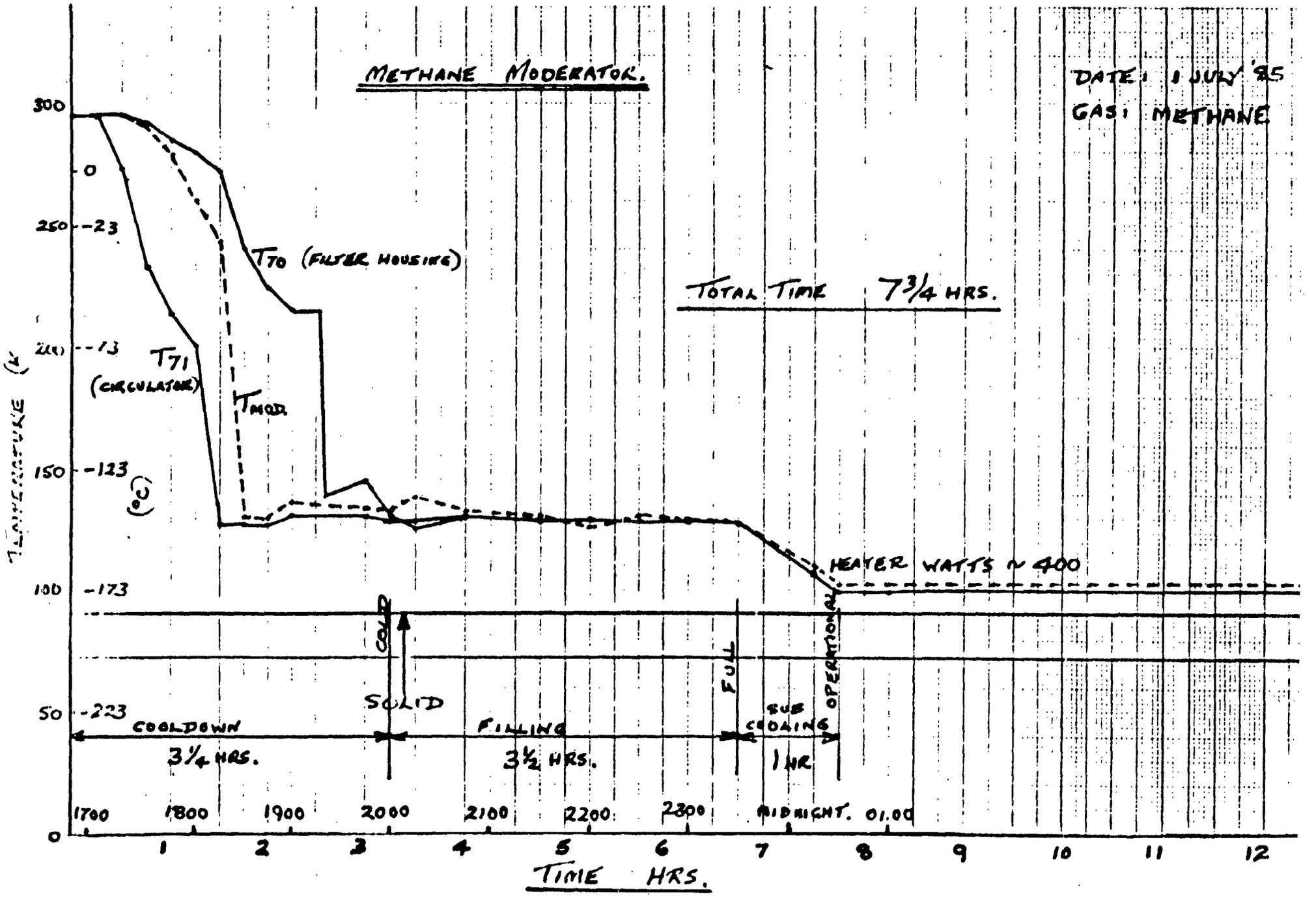
METHANE MODERATOR.
DATE: 1 JULY '85
GAS: METHANE
TOTAL TIME 7¾ HRS.
T_{70} (FILTER HOUSING)
T_{71} (CIRCULATOR)
$T_{MOD.}$
HEATER WATTS ~ 400
COLD
SOLID
FULL
SUB COOLING
OPERATIONAL
COOLDOWN
3¼ HRS.
FILLING
3½ HRS.
1 HR
1700
1800
1900
2000
2100
2200
2300
MIDNIGHT.
01.00
TIME HRS.
TEMPERATURE (K)
(°C)
300
250
200
150
100
50
0
0
-23
-73
-123
-173
-223
1
2
3
4
5
6
7
8
9
10
11
12

FIG 5 MAIN CIRCULATOR VESSEL

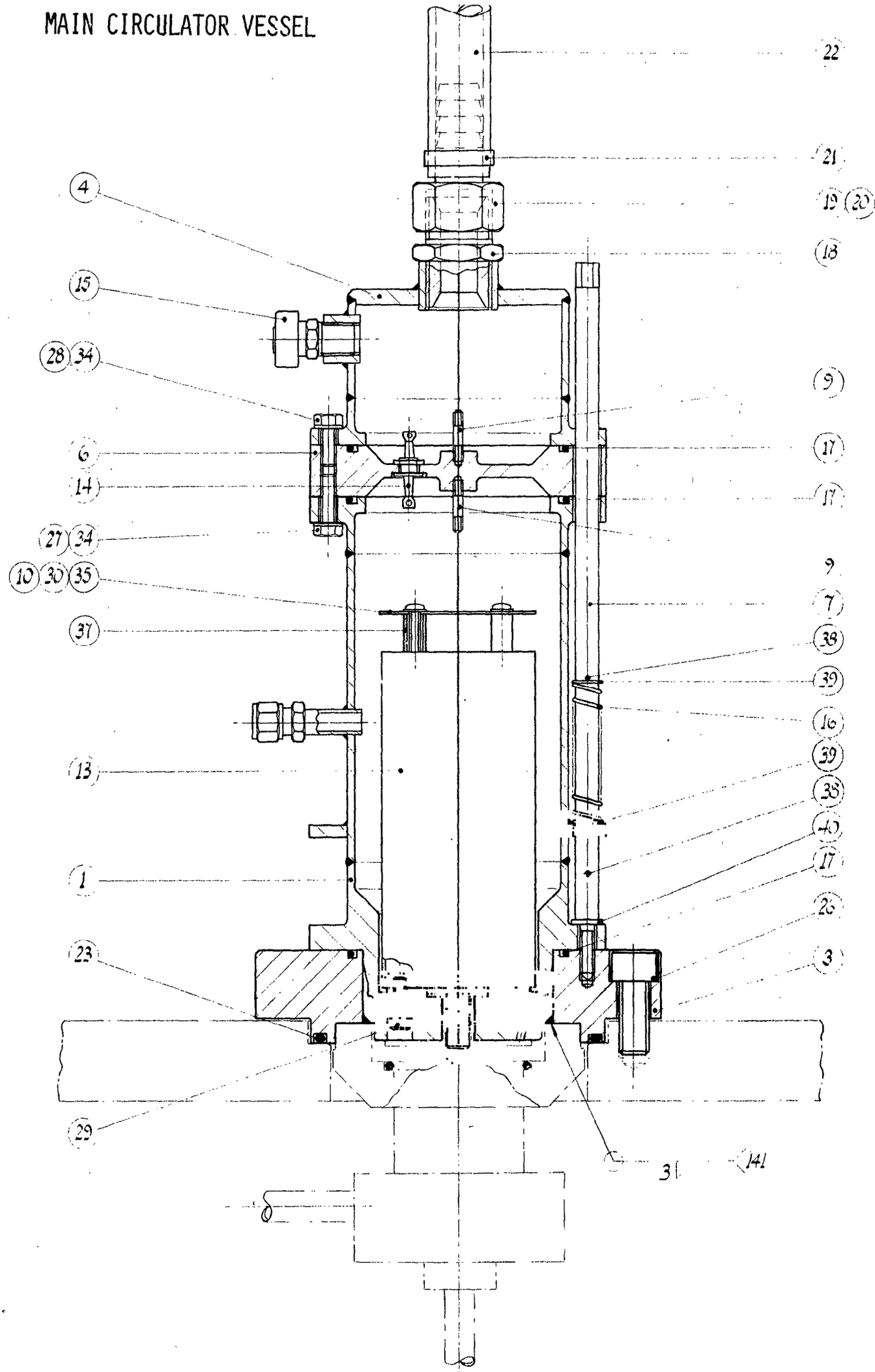

ICANS IX

INTERNATIONAL COLLABORATION ON ADVANCED NEUTRON SOURCES

22-26 September, 1986

Deterioration of Performance of Neutron Moderators Under Intense Irradiation*

John M. Carpenter,

Scott S. Cudrnak[a]

and

Casimer M. DeCusatis[b]

Intense Pulsed Neutron Source Program
Argonne National Laboratory
Argonne, Illinois 60439 U.S.A.

ABSTRACT

In pulsed neutron sources, fixed moderators such as polyethylene and solid methane slow down fast (MeV) neutrons from the primary source to energies of use for spectroscopy ($\lesssim$ 10 eV). Radiation-induced changes in their composition alter their spectral and pulse characteristics. We report the results of fitting time-average spectra from polyethylene and solid methane moderators in Argonne's Intense Pulsed Neutron Source as a function of total fast-neutron radiation dose. The thermal-to-epithermal flux ratio varies most significantly, while the Maxwellian energy and the parameters describing the epithermal component change only slightly. We have used modified forms of Westcott's joining function for this purpose. We provide an integral of the spectrum that is useful for determining the delayed neutron background.

Introduction

In pulsed neutron sources, fixed moderators such as polyethylene and solid methane slow down fast (MeV) neutrons from the primary source to energies of use for spectroscopy ($\lesssim$ 10 eV). Radiation-induced changes in

Work Supported by U.S. Department of Energy

a) Present address: Department of Civil Engineering, Mechanics, and Metallurgy, University of Illinois at Chicago, Chicago, IL

b) Present address: Department of Engineering Science and Mechanics, Pennsylvania State University, University Park, PA

their composition alter the spectral and pulse characteristics of moderators. The purpose of this work is to quantify the changes in the parameters describing the time-average spectrum of neutrons from the moderators of Argonne's Intense Pulsed Neutron Source[1] (IPNS) by fitting empirical functions to observed time-of-flight spectra. The results relate to other pulsed sources which use polyethylene or solid methane moderators. It is particularly significant that simple functions of the same mathematical form, but differing for polyethylene and methane, fit the spectra equally well at all stages of their irradiation.

We find that in polyethylene suffering about $5 \times 10^{18} n/cm^2$ fast neutron fluence, both the thermal-to-epithermal neutron flux ratio and the ratio of epithermal flux to the proton current, both decrease by a factor of about .75. These changes are important, but not unique to pulsed sources, since fluxes and spectra also change by comparable factors from beginning to end of the fuel cycle in some reactors, due to fuel burnup and the changing positions of shim rods. Similarly, we find that the thermal-to-epithermal flux ratio in methane decreases by a factor of about .80 upon irradiation by $8 \times 10^{17} n/cm^2$, while the ratio of epithermal flux to proton current decreases by only .95.

Description of the Moderators and the Measurements

Figure 1 shows the arrangement of the primary source, moderators and reflector of the IPNS. The source (proton target) is of depleted Uranium, irradiated by 450 MeV protons from the Rapid Cycling Synchrotron (RCS). During the period we investigated, the accelerator delivered time-average currents of about 12 μA in pulses 100 nsec in duration at 30 Hz. Figures 2 and 3 show the moderators, which are respectively of polyethylene and solid methane. The moderators are decoupled from the surrounding graphite reflector by 0.5 mm-thick Cadmium. The physical temperature of the polyethylene moderators is about 50 C, and of the methane about 12 K during operation. Our measurements were of the "F" moderator, overall $5.1 \times 10.1 \times 10.1\ cm^3$ in size, heterogeneously poisoned with 0.5 mm-thick Cadmium 2.2 cm below the viewed surface, and of the grooved, solid methane "C" moderator.

The polyethylene moderator was initially of high density material, $\rho = 0.966\ gm/cm^3$, with H/C ratio 2.00. After approximately one year's irradiation, corresponding to $8. \times 10^{20}$ protons on target and a fast-neutron fluence approximately $5 \times 10^{18} n/cm^2$, the polyethylene moderator was removed and its composition examined. Table 1 summarizes the results of analysis of material from "F" moderator before and after irradiation.

IPNS-I *NEUTRON SCATTERING EXPERIMENTAL ASSEMBLY*

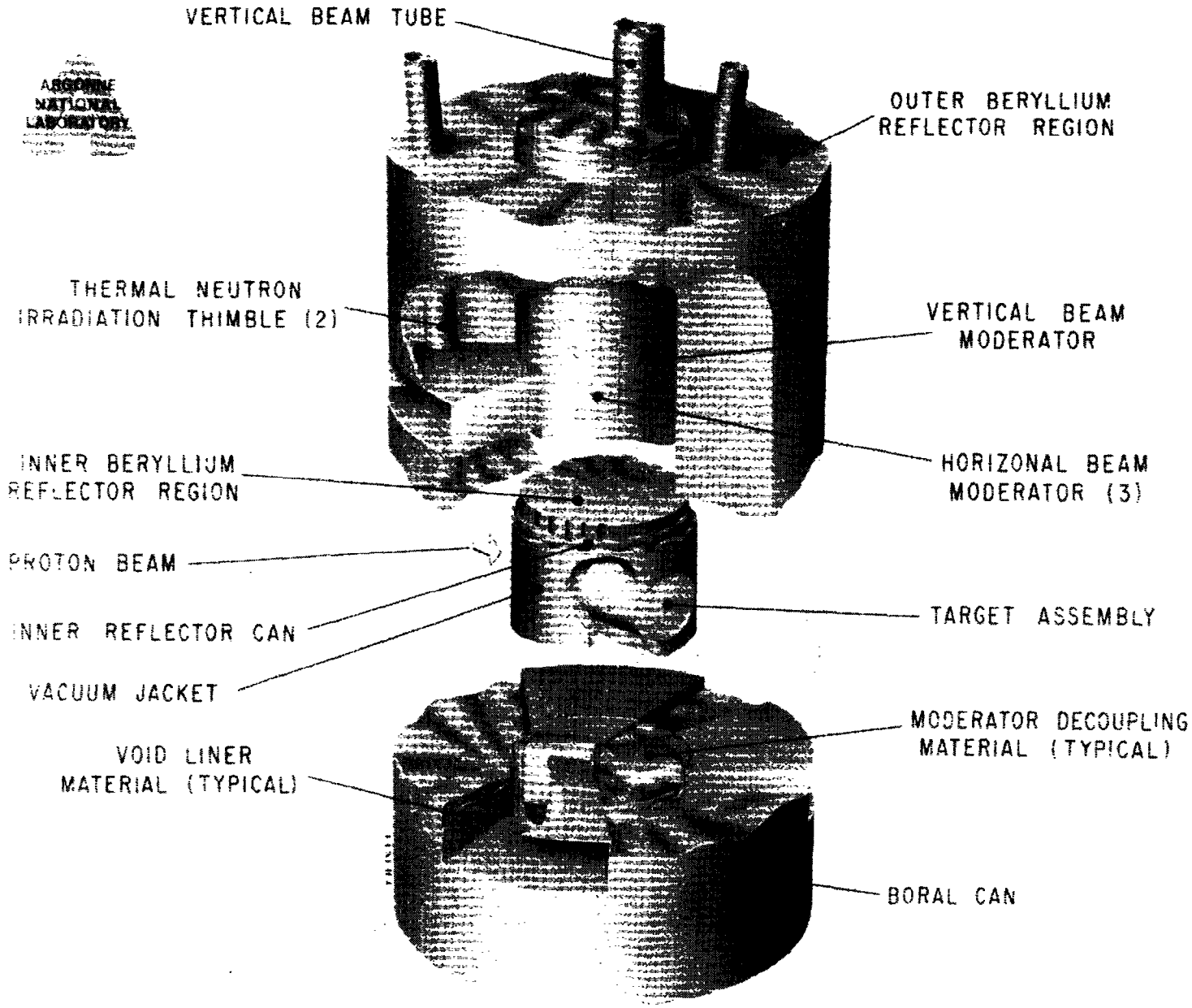

1. The IPNS Target Moderator Reflector system.

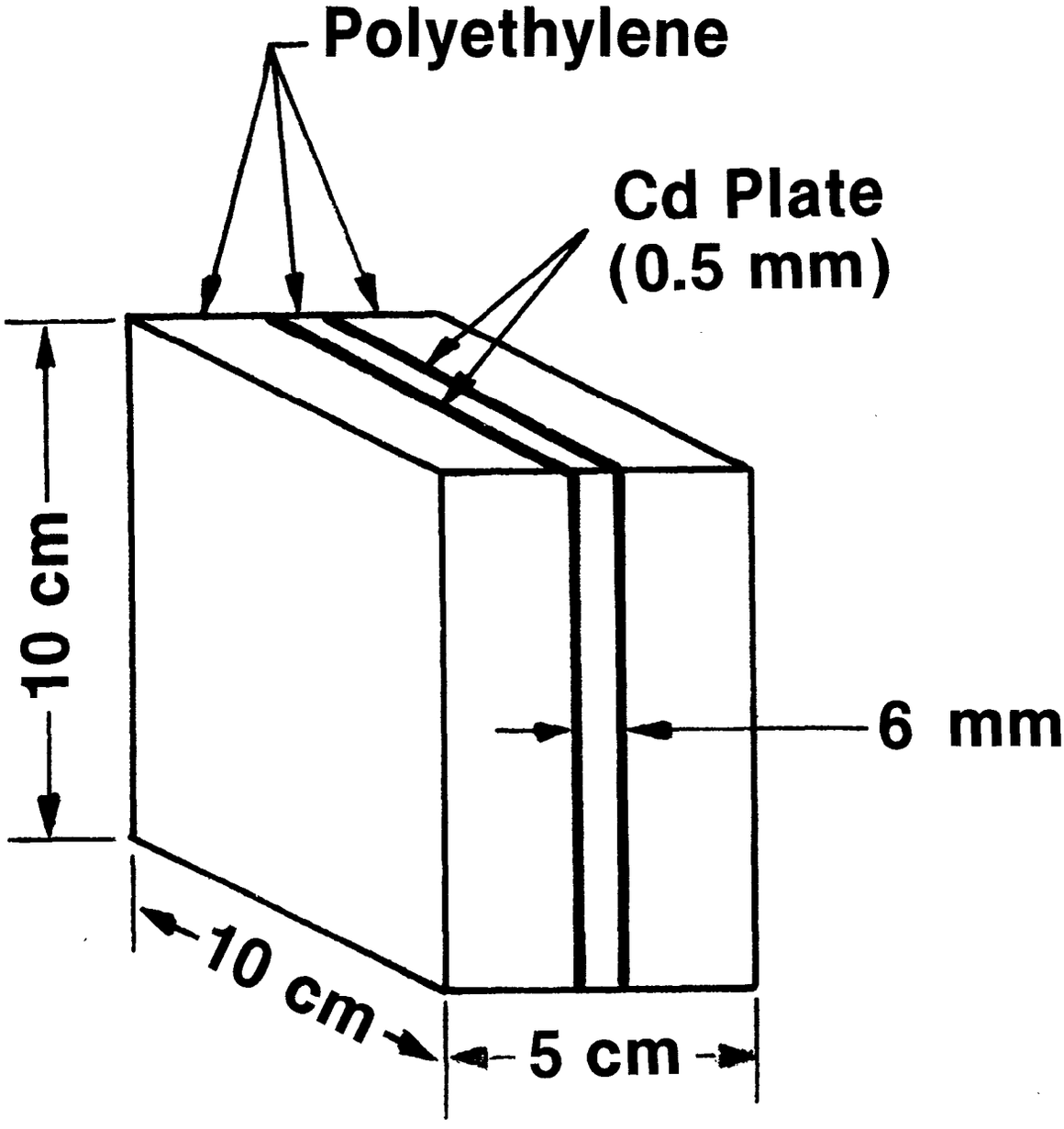

2. The IPNS ambient temperature polyethylene "F" moderator.

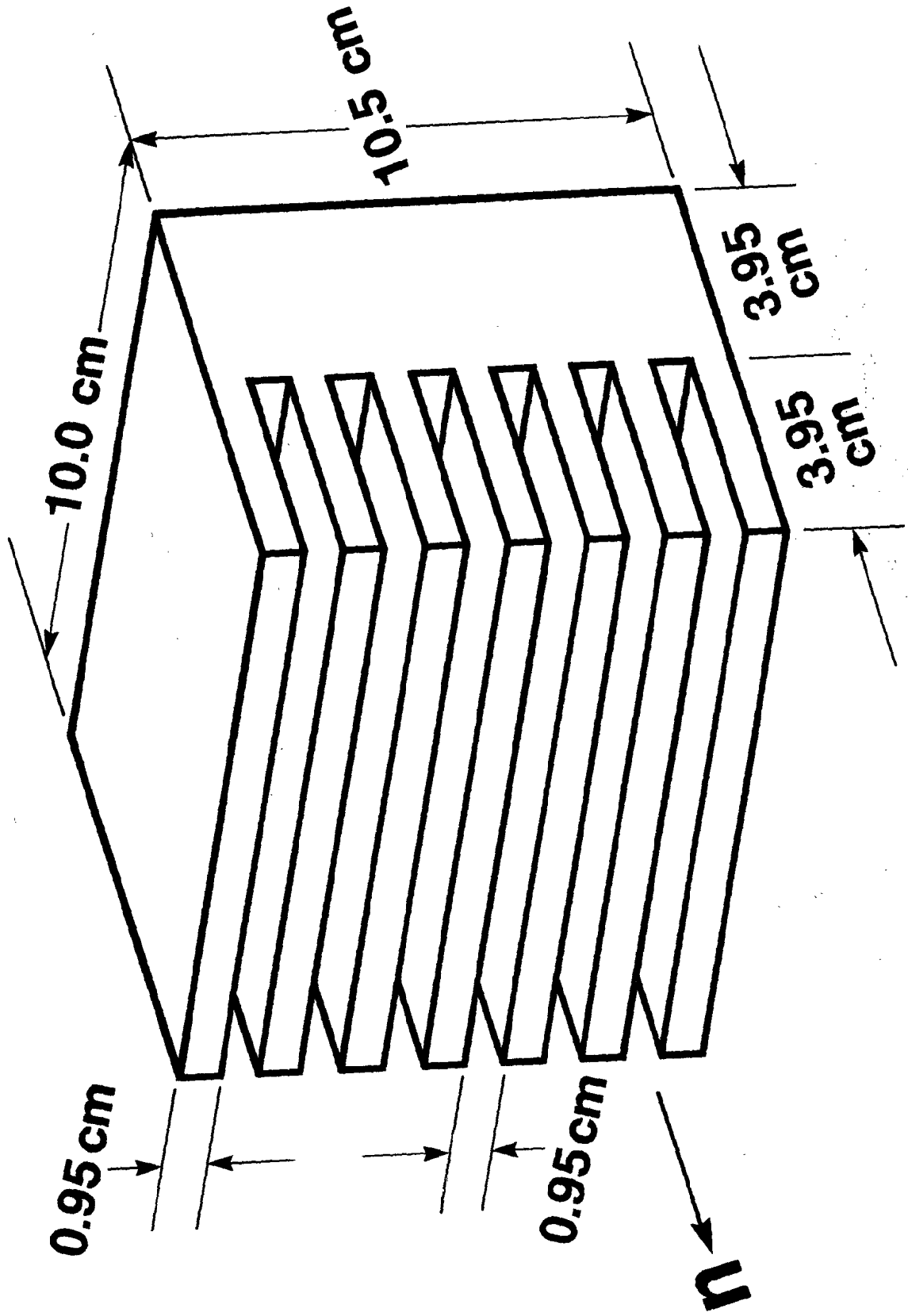

3. The IPNS grooved solid methane moderator.

Table 1

Analysis of Polyethylene Before and After Irradiation

	Before	After 8.1×10^{20} protons on target
Density	0.966	0.990 gm/cm^3
H/C ratio	2.0	1.56

The methane moderator consisted of initially pure (> 0.999) methane gas condensed into the methane container, which for heat transfer purposes contains a 6101 Aluminum alloy foam filling 6% of the volume. (The density of pure solid methane at 12 K is 0.528 gm/cm^3.) The system is described in greater detail elsewhere[2]. Following two periods of irradiation, one 15 days long and the other 55 days long, during which the RCS delivered 6.5×10^{19} and 3.3×10^{20} protons to the target, corresponding respectively to approximately $4. \times 10^{17} n/cm^2$ and $2 \times 10^{18} n/cm^2$ fast neutron fluence in the methane, we collected and analyzed the volatile products, with the results shown in Table 2.

Table 2

Analysis of Volatile Products of Radiolysis of Methane from the IPNS Solid Methane Moderator

Product	Mole fraction* of product, %	
protons on target	6.5×10^{19}	3.3×10^{20}
H_2	5.38	10.6
CH_4	91.37	75.2
H_2O	<0.04	-
C_2H_4	0.20	1.4
C_2H_6	2.30	8.5
N_2	not determined--used as mixing gas	
O_2	0.17	1.4
Ar	0.04	0.1
C_3H_8	0.42	-
hydrocarbons C_3, C_4 & c	-	2.8

*exclusive of N_2.

These analyses indicate substantial deterioration of both CH_2 and CH_4 resulting from irradiation, which is reflected in the measured spectra described below.

Our estimates of the fast neutron fluence F are admittedly crude, and are based on treating the target as a point source of fast neutrons;

$$F = YN_p/(4\pi r^2), \tag{1}$$

where $Y \simeq 17$ neutrons per proton is the neutron yield, $r \simeq 15$ cm is the distance to the center of the moderator, and N_p is the number of protons delivered to the target.

Assuming the average neutron energy to be $E \simeq 1.$ MeV, and the proton cross section to be $\sigma \simeq 4$ barns/proton, with 1/2 the energy given to the proton in each collision, and taking $n = 8.3 \times 10^{22}$ protons/cm^3 to be the density of protons in the polyethylene, we arrive at an estimate of the neutron dose for 8×10^{20} protons on target,

$$D = \sigma Fn(E/2) = 2.3 \times 10^{12} \text{ erg/cm}^3 = 2.4 \times 10^{10} \text{ Rad.} \tag{2}$$

Similar crude estimates of the gamma ray dose lead to estimates about two orders of magnitude smaller than the neutron dose. Protons which might be present in the wings of the proton beam would contribute significantly to the dose, but we can only assert on the basis of measurements on the second target of IPNS, that this component is about two orders of magnitude smaller than the neutron dose.

Beam monitor detectors in two instruments, the Special Environment Powder Diffractometer (SEPD) viewing the ambient-temperature polyethylene moderator through beam port F5, and the Small Angle Diffractometer (SAD) viewing the solid methane moderator through beam port C1, provided the time-of-flight data which are the basis of our results. The detectors were both "thin" $^{10}BF_3$ detectors, whose efficiency is proportional to the neutron wavelength over the entire range of wavelengths (energies) measured. Figure 4 schematically shows the arrangement of the measurements. The flight path lengths were 13.51 m and 6.38 m for the SEPD and SAD beam monitor detectors, respectively. We have included a small correction to the flight path lengths to account approximately for the emission time delay.

The Fitting Functions

The time-average counting rate per unit time-of-flight in a pulsed-source beam monitor spectrum measurement is

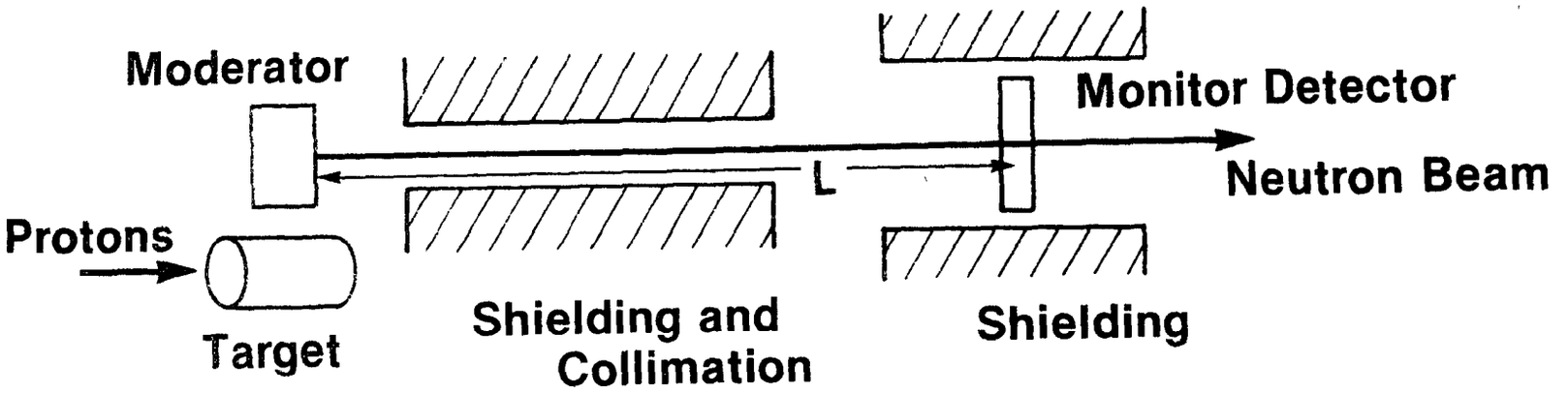

4. Schematic arrangement of the beam monitor detectors used in measuring the spectra.

$$C(t) = \int_0^\infty \eta(E')\Phi(E')\delta(t - L/v')dE' + B = A\eta(E)\Phi(E)(2E/t) + B \qquad (3)$$

where A is the area and $\eta(E)$ is the efficiency of the detector, and $\Phi(E)$ is the time-average flux per unit energy at the detector position. $v = L/t$ is the neutron speed and $E = \frac{1}{2}mv^2$ is the neutron energy corresponding to time t; the related wavelength is $\lambda = h/mv$. The time-average counting rate in a time-of-flight channel of width Δt centered at time t is $C(t)\Delta t$.

We represent $\Phi(E)$ by a Maxwellian function at longer wavelengths, joined smoothly to a 1/E "slowing-down" spectrum at shorter wavelengths,[3]

$$\Phi(E) = \Phi_{MB}(E) + \Phi_{SD}(E) \qquad (4)$$

where $$\Phi_{MB}(E) = \Phi_{Th}(E/E_T^{\,2})\exp(-E/E_T) \qquad (5)$$

represents the Maxwellian part of the spectrum. $E_T = k_B T_{eff}$ is the mean thermal energy, related to the effective temperature T_{eff}, which is usually somewhat greater than the physical temperature of the moderator medium. Φ_{Th} is the integrated Maxwellian flux,

$$\Phi_{Th} = \int_0^\infty \Phi_{MB}(E)dE, \qquad (6)$$

since $\int_0^\infty (E/E_T^{\,2})\exp(-E/E_T)\, dE = 1$.

Polyethylene

The slowing-down part representing the room-temperature polyethylene spectrum is

$$\Phi_{SD}(E) = \Phi_{epi}(1/E)\Delta(E)(E/E_{ref})^{\alpha}. \qquad (7)$$

where the last factor represents the effect of leakage from the medium, and α is called the "leakage exponent". We take E_{ref} = 1000. meV for our purposes. The factor $\Delta(E)$ is the "joining function". Different authors have used several different forms; we used a generalized form of Westcott's[4] joining function,

$$\Delta(E) = [1 + (E_{co}/E)^s]^{-1} \qquad (8)$$

where the cutoff energy E_{co} is ordinarily about

$$E_{co} \simeq 5E_T, \tag{9}$$

and we designate the exponent s the "cutoff exponent". Westcott found the value s = 7 for the spectra he treated. Φ_{epi} is the epithermal neutron flux; assuming $\Phi_{Th}(E_{ref}) = 0.$ and $\Delta(E_{ref}) = 1.$,

$$\Phi_{epi} = [E\Phi(E)]\Big|_{Eref} \tag{10}$$

The detector efficiency was taken to be of the form

$$\eta(E) = K/\sqrt{E}, \tag{11}$$

where K is an unknown constant.

The parameter B represents the delayed neutron background, assumed constant over the time interval between pulses T = 1/f. If δ is the fraction of all neutrons which appear delayed then B represents the counting rate due to a steady source with a spectrum effectively identical to that characterizing the prompt pulse,

$$B = \delta/T \int_0^{Emax} \eta(E)\Phi(E)dE = \Phi_{epi}(\delta/T)F(\Phi_{Th}/\Phi_{epi}, E_T, s, E_{co}, \alpha, E_{max}), \tag{12}$$

so that

$$B/\Phi_{epi} = (\delta/T)F(\Phi_{Th}/\Phi_{epi},\ E_T\ s,\ E_{co},\ \alpha,\ E_{max}). \tag{13}$$

The ratio of the delayed neutron background to the epithermal flux is completely determined if the shape of the prompt spectrum is known, as in our empirical fitting function. We develop the required integral F in the Appendix.

It is interesting to note that, assuming no frame overlap C(t) = 0 for t > T, (the result is true without this assumption)

$$\int_0^T C(t)dt = \int_0^\infty A\eta(E)\Phi(E)dE + BT, \tag{14}$$

then

$$\int_0^T C(t)dt = BT\ \delta/(1 + \delta), \tag{15}$$

so that B is proportional to the integral of the counting rate over the entire frame

$$B = 1/T\ \delta/(1 + \delta) \int_0^T C(t)dt. \tag{16}$$

Methane

The lower physical temperature of the solid methane moderator places the Maxwellian part of the spectrum roughly 20 times lower than that for the room-temperature polyethylene moderator. This exposes a slight "bump" in the slowing-down part of the spectrum which must be fitted in another way. In this case we described the slowing-down part by,

$$\Phi_{SD}(E) = \Phi_{epi}(1/E)\Delta_1(E)\Delta_2(E) \tag{17}$$

where $\Delta_1(E)$ is the same function used in the fitting of the polyethylene moderated neutron spectrum and $\Delta_2(E)$ is the "bump" function,

$$\Delta_2(E) = 1 + A\exp[-(E^p - E^p_B)^2/2\sigma^2] \tag{18}$$

where E_B is the bump energy, and σ represents the width of the bump. We found that the best fit was obtained with p = -2/3, which value we fixed during the least squares analysis. Both Westcott[4] and Mildner et al[5] have found it necessary to describe "bumps" in certain spectra.

Attenuation Corrections

We made no corrections for attenuation due to the presence of air and of aluminum windows between the source and the detector in the polyethylene spectrum. In the solid methane spectrum, we corrected the original data for the combined attenuation effects of the air and aluminum neutron cross sections. The neutron beam passed through 2.82m of air at atmospheric pressure and 0.5in. of aluminum in the solid methane measurement. To account for the attenuation due to this air, we used functions fitted to "Barn book" data for oxygen and nitrogen:

$$\sigma^{\cancel{N2}\ O2}(E) = 3.77(1 + (15.5/E_{meV})^{1.762})^{0.222} \tag{19a}$$

$$\sigma^{\cancel{O2}\ N2}(E) = 10.95(1 + (22.1/E_{meV})^{1.762})^{0.222} \tag{19b}$$

giving a total macroscopic cross section:

$$\Sigma_{total}(E) = 2N_A(0.78\sigma^N(E)+0.21\sigma^O(E))/V_m \tag{20}$$

where N_A is Avogadro's number and V_m is the STP molar volume.

We represented the aluminum cross section in terms of the sum of elastic (Bragg) scattering for ideal polycrystal, with inelastic scattering at large and small k[6], in the vein of the treatment by Marshall and Lovesey.[7] Attenuation corrections were made in the original data enabling us to fit the data as an unattenuated spectrum, rather than making corrections for the attenuation during each iteration of the fitting function. Channel widths Δt were always 20 μsec, while the time ranges fitted varied having minimum times between 500 μsec and 1500 μsec. We made no corrections for resolution, since these are insignificant in the present measurements.

Table 3 shows the parameters used to quantify the changes in the time-average moderator spectra.

Table 3

Parameters for least-squares fitting of moderator spectra

Parameter		Initial values	
		CH_2	CH_4
ratio of thermal to epithermal flux	Φ_{Th}/Φ_{epi}	2.5	3.5
thermal energy	E_T	40. meV	2.0 meV
epithermal flux	Φ_{epi}	first data point	
leakage exponent	α	0.01	----
cutoff energy	E_{co}	180. meV	10.0 meV
cutoff exponent	s	7.	6.15
background	B	1/2 last data point	
bump function coefficient	A	----	0.44

bump energy	E_B	----	305.0 meV
sigma	σ	----	0.018

The values of the parameters were calculated from the recorded number of counts (not normalized) taken on the SEPD and SAD at IPNS. We developed a FORTRAN code for this purpose, using the CERN library code MINSQ[8,9] to perform the (nonlinear) least squares fitting of the parameters. The function minimized was the sum of squares of the deviations of the fitting function from the data, normalized to the square of the estimated error in the data at each point. Thus the minimized function has the χ^2 distribution with known expected value at minimum; our fits typically provided a value of χ^2 only twice the expected value, which for our data represents approximately 2% rms error. The Table gives initial estimates provided to the minimization calculation, although the user of the code can change any of these estimates at execution time.

Figure 5 shows a representative plot of the fitted spectrum function. Such plots typically produced quite good fits (χ^2 on the order of 3000 for a data set of about 1500 points and with 7 fitting parameters in the case of polyethylene, and slightly better in the solid methane with 10 fitting parameters).

Results

Polyethylene

We tracked the behavior of these parameters over the lifetime of both moderators used in IPNS. The polyethylene moderator, next-to-last installed in IPNS, was in place from October, 1983 until January, 1985, during which the target received 8×10^{20} 450 MeV protons. We examined a total of ten data sets chosen to represent roughly logarithmically-spaced intervals spread over the lifetime of the moderator, using the cumulative proton number N_p as a measure of the age of the moderator.

Among all the parameters the thermal-to-epithermal flux ratio varies most significantly, as shown in Figure 6. The function

$$\phi_{Th}/\Phi_{epi} = A\exp(-BN_p) + C\exp(-DN_p), \tag{21}$$

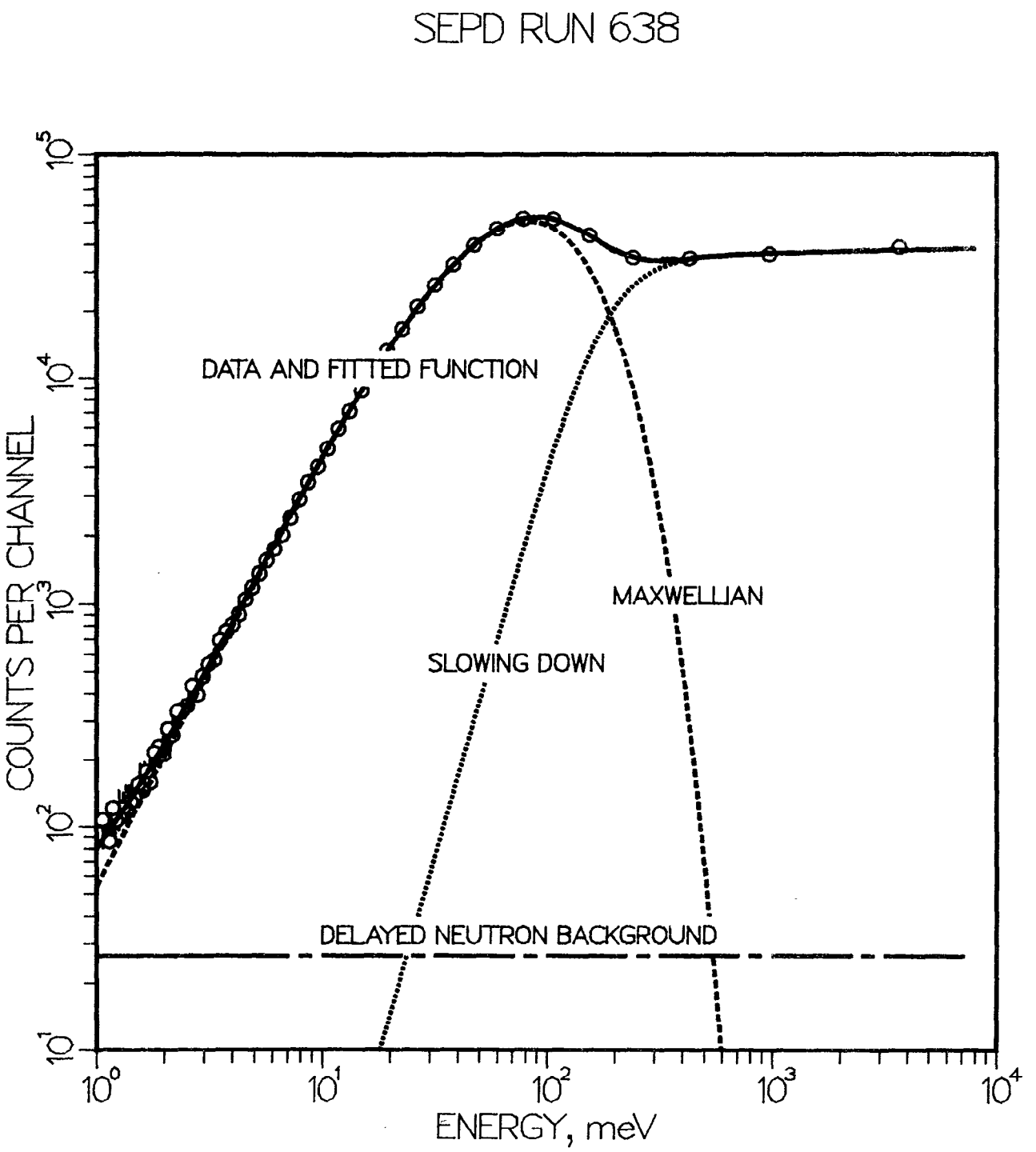

5. The counting rate distribution from the ambient temperature polyethylene moderator after 8.0 × 10^{20} 450 MeV proton irradiation of the IPNS target, as measured in a "1/v" detector. Circles represent every 25th data point. The various lines represent the Maxwellian and the slowing-down components and the time-independent delayed-neutron background.

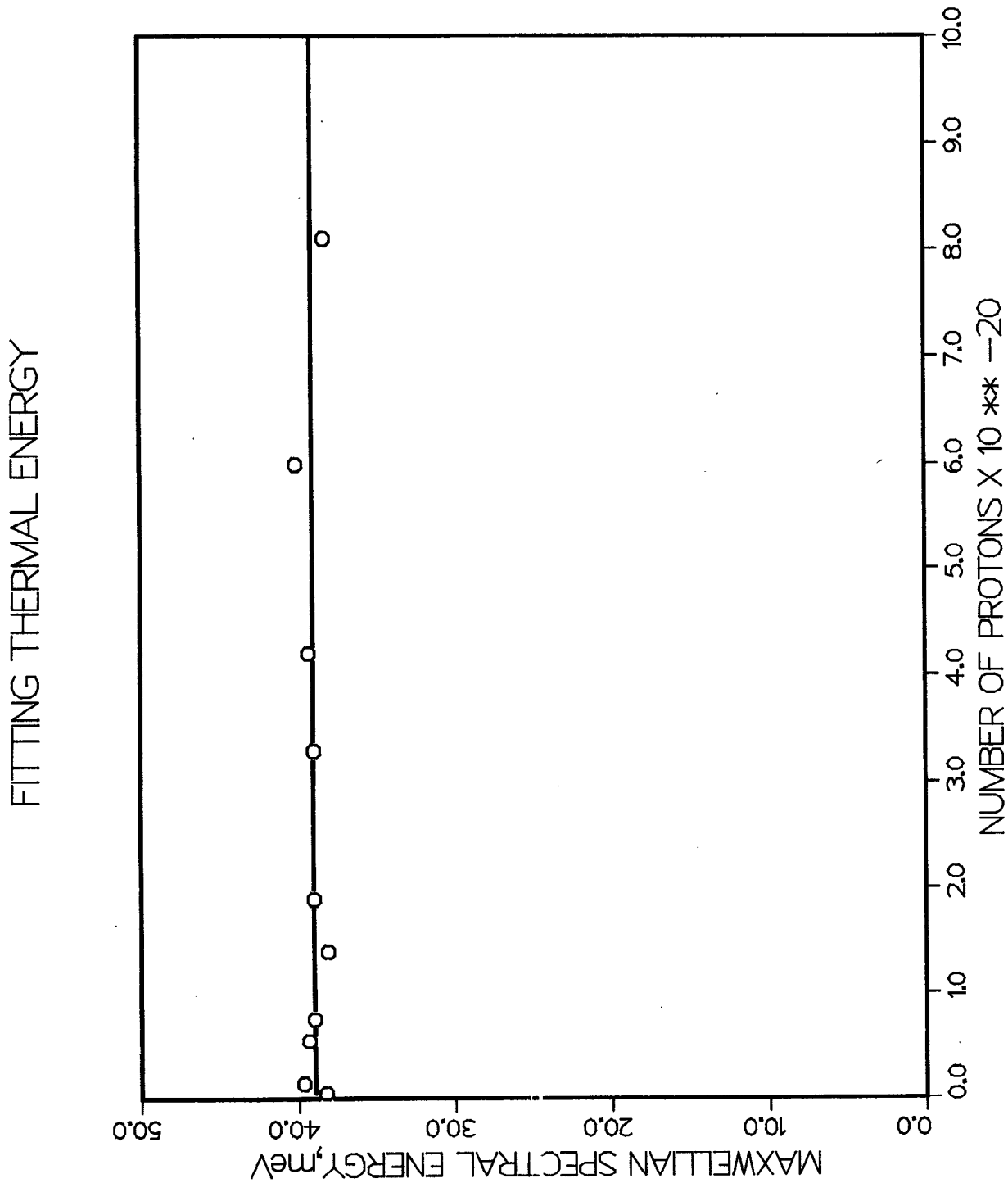

6. The thermal-to epithermal flux ratio ϕ_{Th}/Φ_{epi}, for polyethylene as a function of the number of protons on target.

shown as the solid line in Figure 6, fits the data reasonably well. Similarly, we have fitted the ratio of the epithermal flux to the proton current, Φ_{epi}/I_p to the function

$$\Phi_{epi}/I_p = A'\exp(-B'N_p) + C'\exp(-D'N_p). \tag{22}$$

Figure 7 shows the data and the fitted function. Table 4 summarizes the fitted parameters and estimated errors.

Table 4

Fitted Values of Parameters in ϕ_{Th}/Φ_{epi} and Φ_{epi}/I_p vs N_p

ϕ_{Th}/Φ_{epi}				Φ_{epi}/I_p			
A	0.740	± 0.048	dimensionless	A′	0.584	± 0.060	arbitrary units
B	0.405	± 0.082 × 10^{-20}	protons^{-1}	B′	0.356	± 0.083 ×10^{-20}	protons^{-1}
C	2.49	± 0.078	dimensionless	C′	1.277	± 0.042	arbitrary units
D	0.0072	± 0.004 × 10^{-20}	protons^{-1}	D′	0.0022	± 0.008 ×10^{-20}	protons^{-1}

We assert that D and D′ cannot be 0. in spite of their small values and low significance, since hydrogen still remains to be lost from the moderator (see Table 1.) The similarity of the coefficients B and B′, and D and D′ suggests that the same processes are responsible for the changes in both ϕ_{Th}/Φ_{epi} and Φ_{epi}/I_p. The physical significance of these functions is hidden behind the relationship of the ratios ϕ_{Th}/Φ_{epi} and Φ_{epi}/I_p to the material properties, and of the response of the material properties to irradiation.

The remaining five parameters changed only slightly over the lifetime of the polyethylene moderator; we fitted linear functions to their dependence on proton number:

$$E_T = 38.96(1. + 0.00024 \times 10^{-20} N_p) \tag{23}$$

$$E_{co} = 178.4(1. - 0.0072 \times 10^{-20} N_p) \tag{24}$$

$$s = 3.59(1. - 0.0295 \times 10^{-20} N_p) \tag{25}$$

$$\alpha = 4.5 \times 10^{-6}(1. - 0.049 \times 10^{-20} N_p) \tag{26}$$

The remarkable results are

7. The ratio of the epithermal neutron flux to the time-average proton beam current Φ_{epi}/I_p, for polyethylene as a function of the number of protons on target.

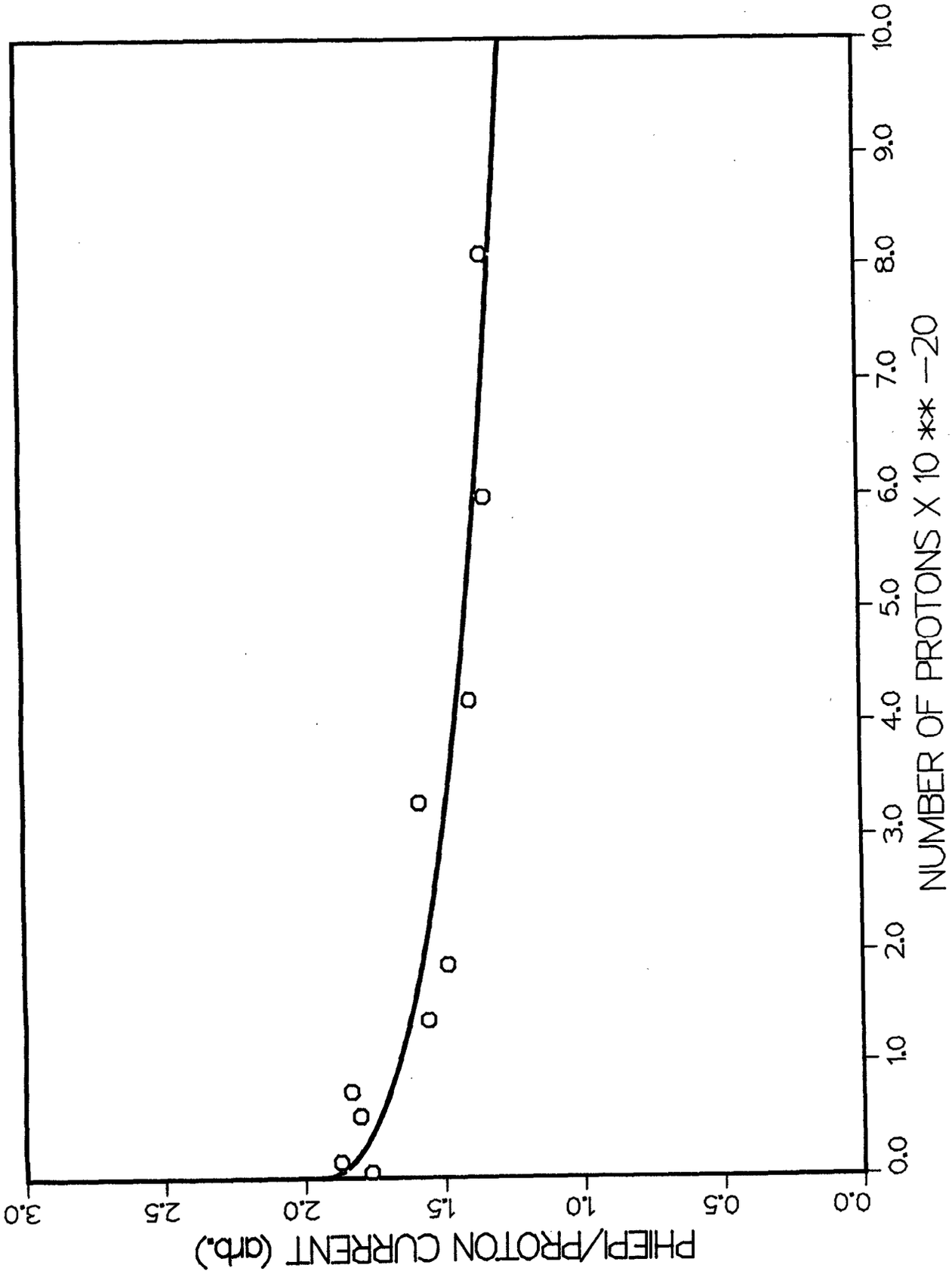

that the value of E_T varies so little, and that the leakage exponent is very small; presumably this is because the data do not extend to sufficiently high energy, so that the cutoff exponent takes up most of the non-1/E behavior.

Figure 8 shows the calculated ratio B/Φ_{epi} as a function of proton number, in which the best fit for the delayed neutron fraction is $\delta = .0024$, which is about 1/2 the value expected based on independent measurements. We attribute this error to the attenuation by materials in the beam path, which is not accounted for in the case of the polyethylene spectra, and to statistical imprecison in the fitted values of B.

Cold Solid Methane

We studied the performance of the solid methane moderator over a period of 21 days during which the target had received 1.23×10^{20} protons. During this period, we collected six spectra for study in order to relate the change in the fitting function parameters to the number of protons on target. Unlike those describing the polyethylene spectra, the parameters describing the solid methane spectra all displayed notable changes as the moderator aged. The ratio ϕ_{Th}/ϕ_{epi} changes significantly, as Figure 9 shows. The difference between the spectral temperture and the physical temperature shows a smooth, gradual increase with respect to the proton number as illustrated in Figure 10. We fitted the parameters of the fitting function either as a decaying exponential function or as a linear function of N_p, according to whether or not there seemed to be significant curvature in the relationship:

$$\Phi_{th}/\Phi_{epi} = 3.168(1 + 0.631 \exp(-5.596 \times 10^{-21} N_p) \quad (27)$$

$$\phi_{epi}/I_p = 9.295(1 + 0.0683 \exp(-1.037 \times 10^{-9} N_p)) \quad (28)$$

$$E_T - k_B T = 1.270(1 - 0.168 \exp(-2.067 \times 10^{-20} N_p)) \quad (29)$$

$$E_{co}/E_T = 4.699(1 - 2.351 \times 10^{-22} N_p) \quad (30)$$

$$s = 6.169(1 - 1.322 \times 10^{-21} N_p) \quad (31)$$

$$A = 0.542(1 - 0.188 \exp(-4.846 \times 10^{-20} N_p)) \quad (32)$$

$$E_B = 306.44(1 + 2.743 \times 10^{-21} N_p) \quad (33)$$

8. The ratio of the constant (delayed neutron) background to the epithermal neutron flux B/Φ_{epi}, for polyethylene as a function of the number of protons on target.

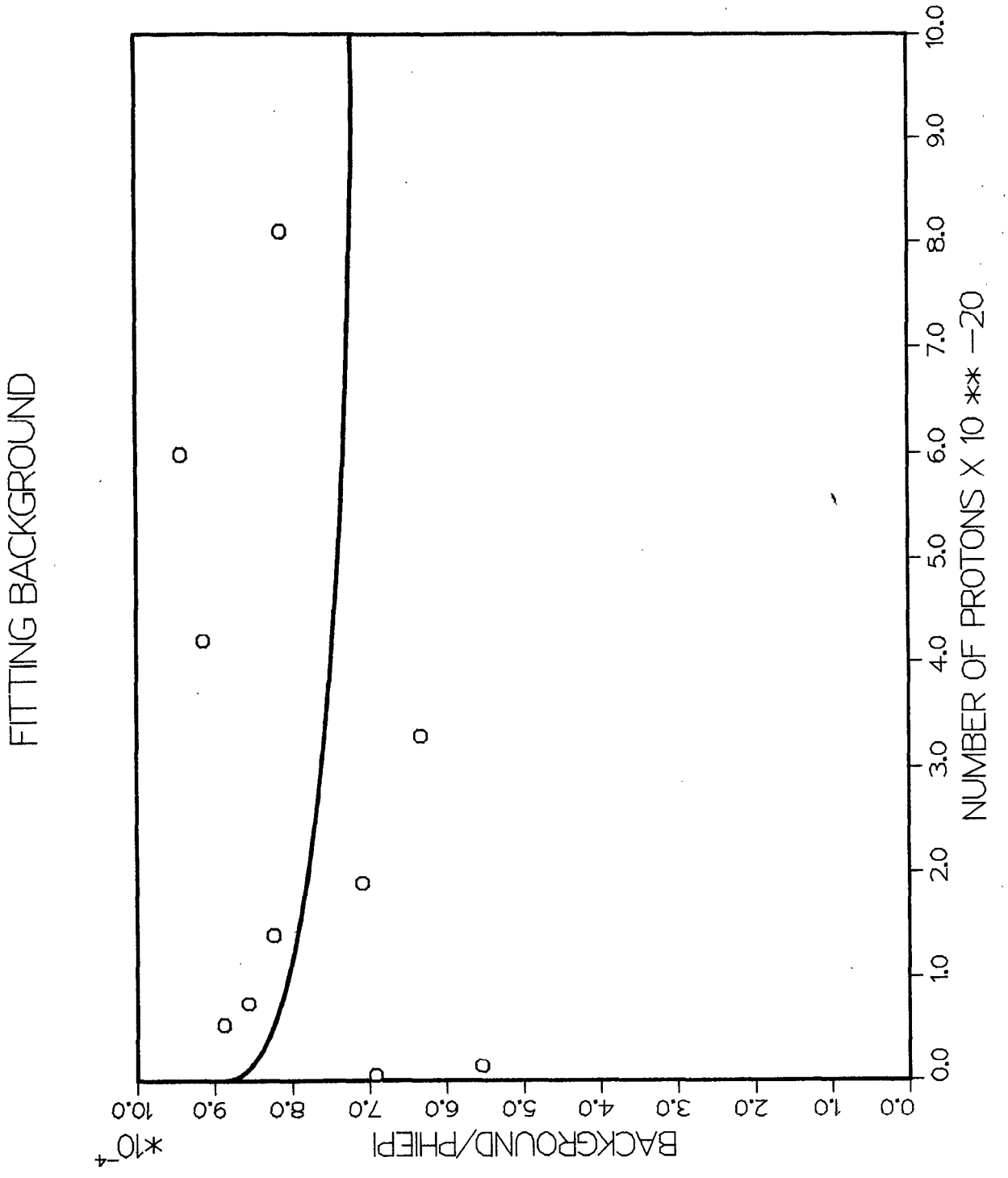

9. The thermal to epithermal flux ratio Φ_{th}/Φ_{epi}, for methane as a function of the number of protons on target.

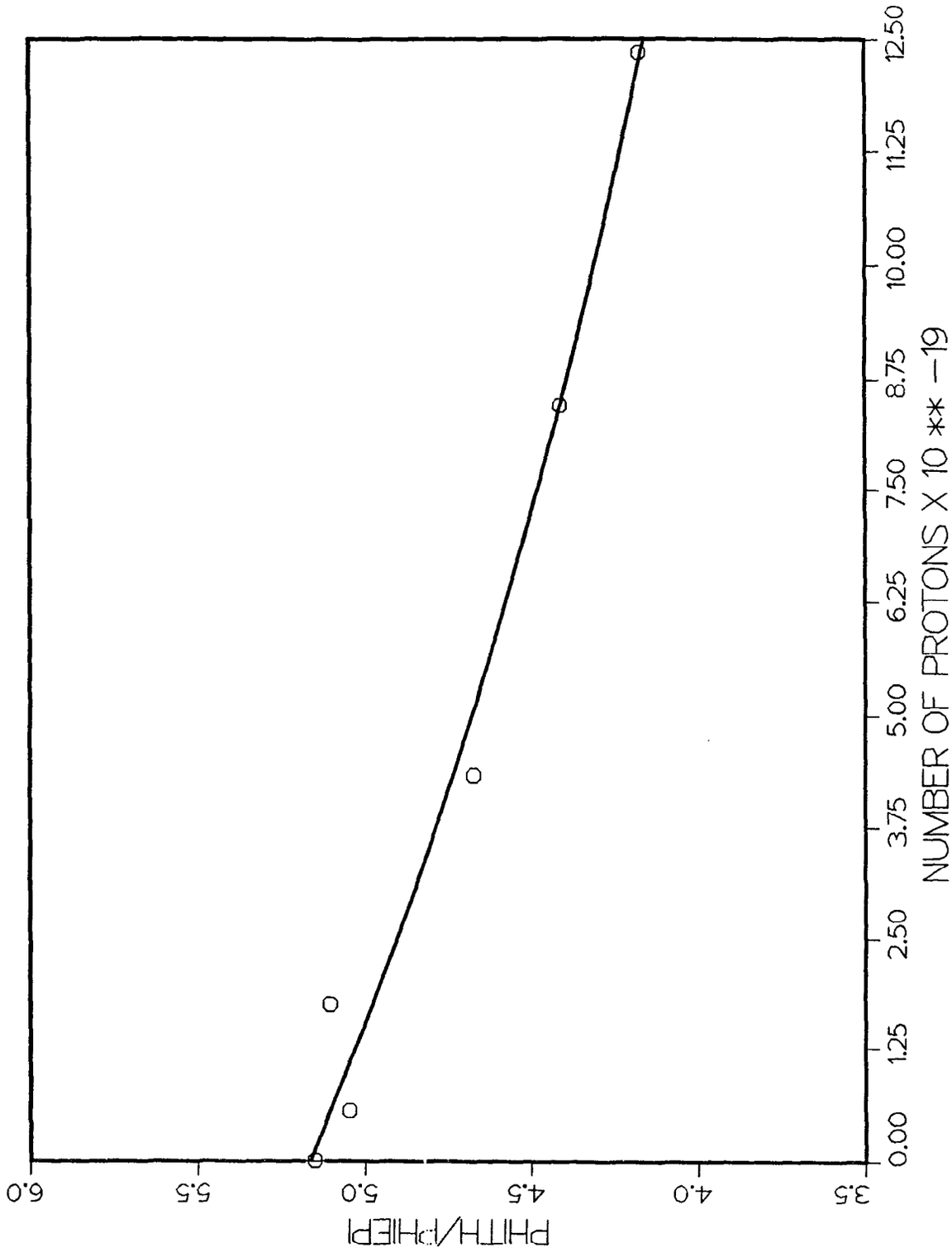

10. The difference between the spectral thermal energy and the physical thermal energy of the moderator $E_T - k_B T$, as a function of the number of protons on target.

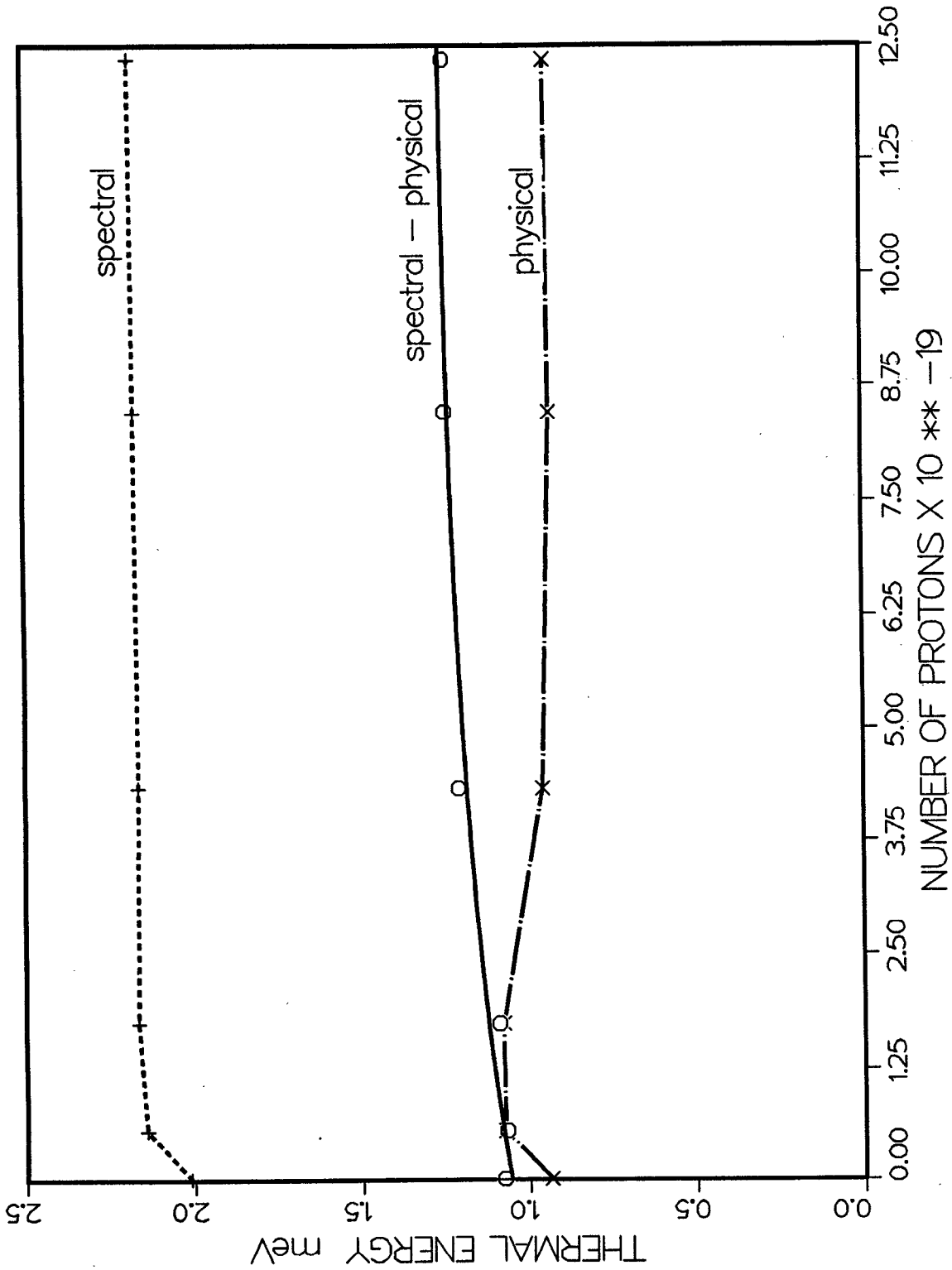

$$\sigma = 2.174(1 - .1805 \exp(-7.206 \times 10^{-21} N_p)) \quad (34)$$

That these changes in moderator performance have not been noted before may seem remarkable. However, IPNS is the first source having sufficient intensity to produce the large changes observed. The most-easily-determined parameter E_T happens to remain almost constant in both CH_2 and CH_4, so that only those instruments which record the spectrum well into the epithermal range and sense a change in the spectral shape could detect the change in the ratio Φ_{Th}/Φ_{epi}. Further, the deterioration seems to be about equally shared between the ratio Φ_{Th}/Φ_{epi} and the ratio Φ_{epi}/I_p (each 10-25 % for the range of doses we examined); the latter represents only a scale shift which can be overlooked in face of short term variations in accelerator current and changes in collimators and monitor detectors, and obscured by gradual improvement in accelerator current. Figures 11 and 12 show the fitted time-average spectra of the polyethylene and solid methane moderator at various stages of change due to irradiation. Although Φ_{epi}/I_p actually decreases with increasing N_p, the curves in Fig. 12 for larger N_p lie above those for smaller N_p due to variation of the shape and location of the bump.

Conclusions

We have quantified the radiation-induced changes in the time-average spectra from polyethylene and solid methane moderators irradiated in Argonne's Intense Pulsed Neutron Source, as a function of accumulated radiation dose. The polyethylene moderated spectra required a seven-parameter fit which describes the Maxwellian component and the slowing-down component of the intensity, and a constant delayed-neutron background. The fitting of the solid methane moderated spectra required a more involved function employing nine parameters. The functions fitted include a general form of Westcott's joining function and, in the case of the methane moderator, a function designed to fit the pronounced bump at roughly 200meV. These provide accurate representations of the spectra at all observed stages of irradiation. We have derived an expression for an integral of the fitted spectral function, which is useful to interpret the delayed-neutron background. The data reveal a significant decrease in the ratio of thermal to epithermal neutron fluxes during irradiation for both of the moderators. The mean thermal energy, and the cutoff energy and the cutoff exponent in the joining function vary only slightly as a function of accumulated dose. The leakage exponent describing the epithermal spectrum for polyethylene has very small values, presumably due to the fact that the data fitted did not extend to sufficiently high energies.

11. The ratio of the flux per unit lethargy to the instantaneous proton current, for the IPNS polyethylene moderator, as a function of neutron energy, at different stages of irradiation, N_p. The scale is arbitrary, but consistent for different values of N_p. From highest to lowest, the curves correspond to N_p = 0., 1., 4., 10., and 20. x 10^{20} protons on target.

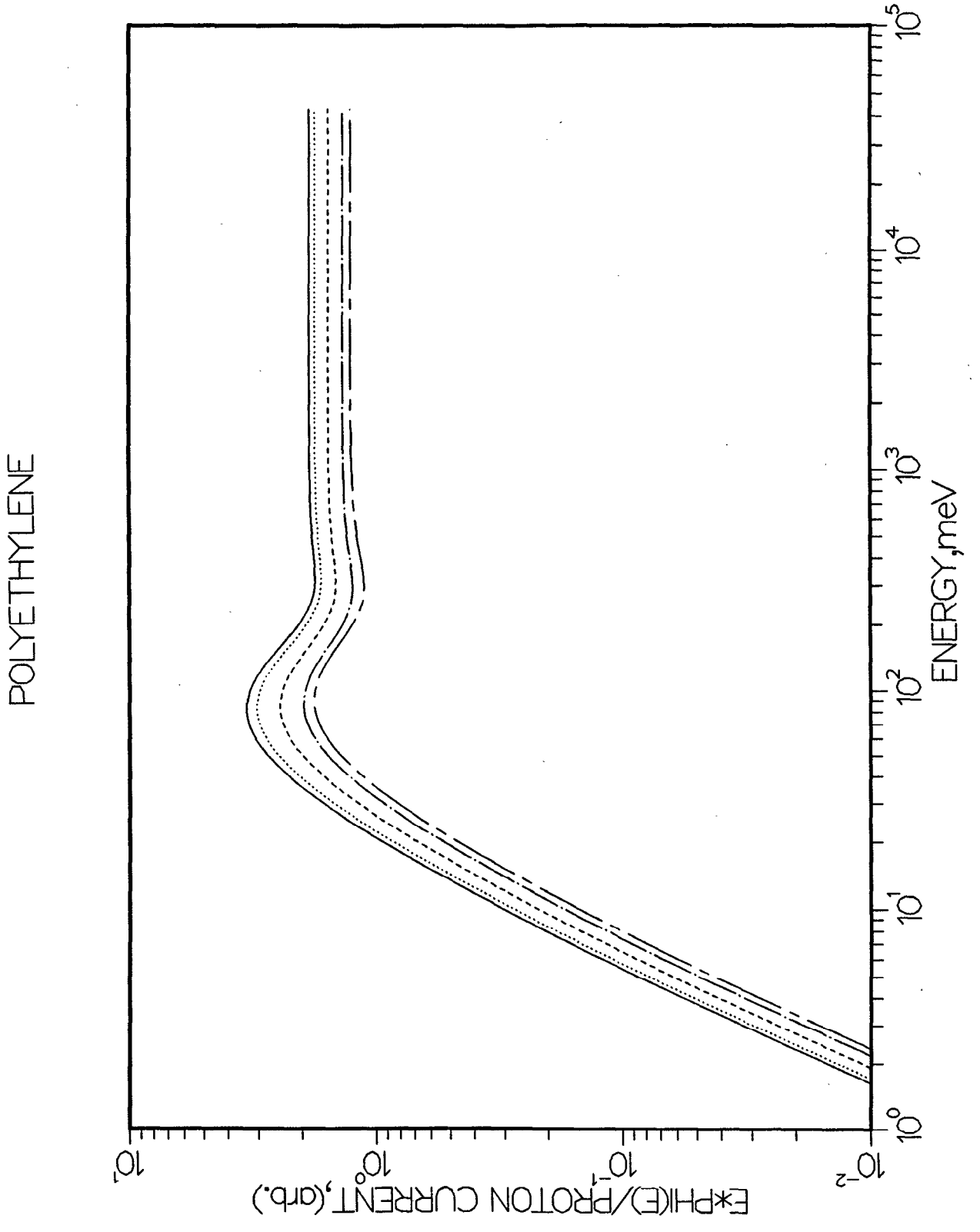

12. The ratio of the flux per unit lethargy to the instantaneous proton current, for the IPNS cold solid methane moderator, as a function of neutron energy, at different stages of irradiation, N_p. The physical temperature is assumed to be 12. K for these curves. The scale is arbitrary, but consistent for different values of N_p, and different from that of Fig. 11. From highest to lowest at low energies, the curves correspond to N_p = 0., 2., 6., 16., and 30. x 10^{19} protons on target.

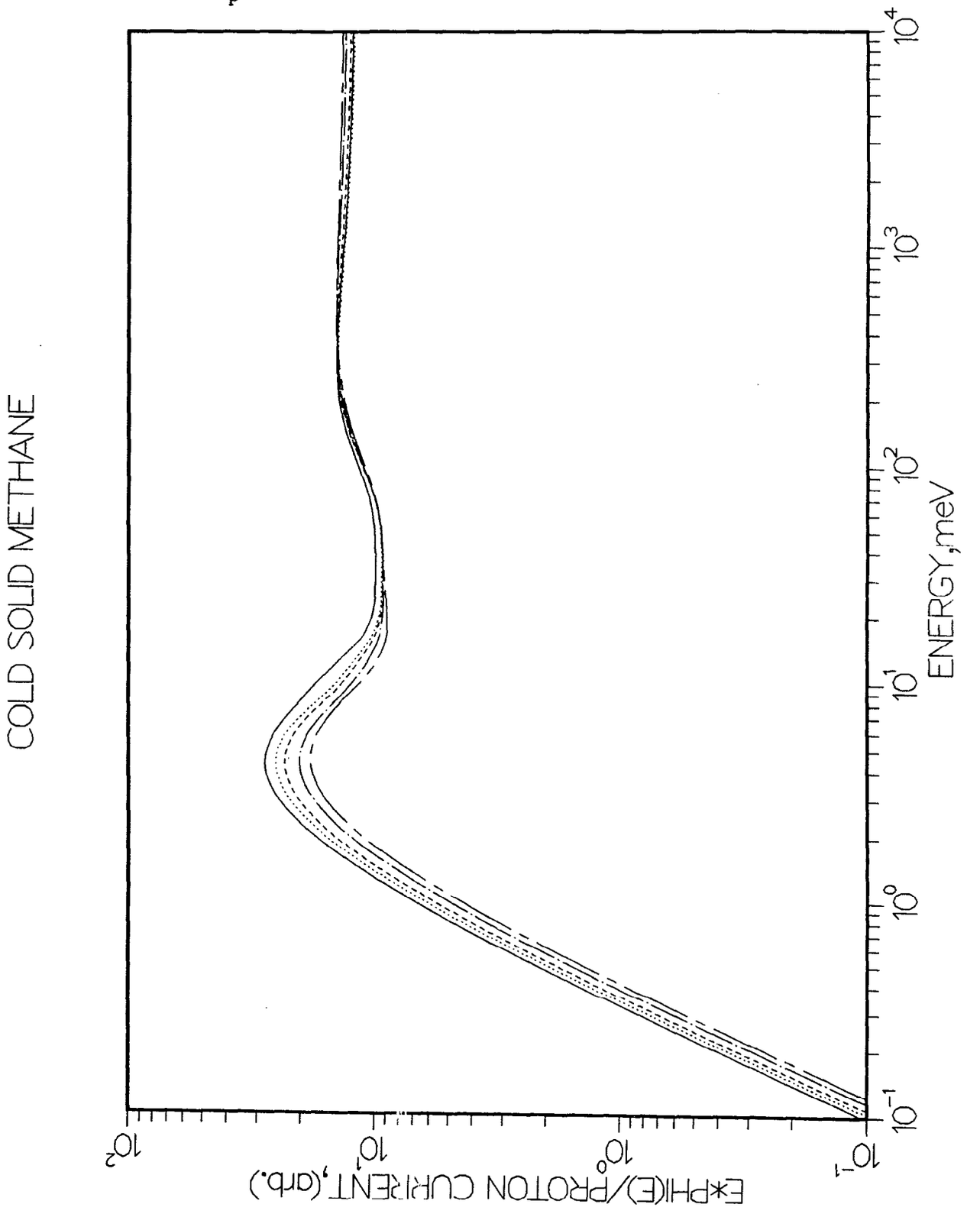

Acknowledgements

We thank F. J. Rotella and T. E. Klippert for their assistance in recovering archived data, and J. E. Epperson and D. L. Worcester for recording spectral data on the SAD. Two of us (SSC & CMD) express their gratitude to the Argonne Division of Educational Programs for support under the Student Research Participation Program.

REFERENCES

1. J. M. Carpenter, G. H. Lander and C. G. Windsor, "Instrumentation at Pulsed Neutron Sources", Rev. Sci. Instrum. 55 (7) 1984 1019.

2. J. M. Carpenter, A. W. Schulke, T. L. Scott, D. G. Wozniak, B. E. Benson and B. D. Leyda, "The IPNS Grooved, Solid Methane Moderator", Proceedings of the VIIIth Meeting of the International Collaboration on Advanced Neutron Sources (ICANS VIII), Oxford, U. K., 1985, to be published as a Rutherford-Appleton Laboratory report.

3. M. M. R. Williams, "The Slowing Down and Thermalization of Neutrons", North-Holland, 1967, p 89 ff. Also, K. H. Beckurts and K. Wirtz, "Neutron Physics", Springer, 1964, p 206.

4. C. H. Westcott, J. Nucl. Energy 2, (1955), 59; "Effective Cross Sections Values for Well-Moderated Thermal Reactor Spectra", Chalk River Report CRRP[A-960 (3^{d} Edition, Corrected), Nov., 1970.

5. D. F. R. Mildner, B. C. Boland, R. N. Sinclair, C. G. Windsor, L. J. Bunce and J. H. Clarke, Nucl. Instrum. Meth. 152 (1978) 437.

6. J. M. Carpenter, "A Simple Formula for the Total Cross Section of a Monatomic Polycrystal" IPNS Note 32, (Argonne internal report) 1986.

7. T. Pomentale, "Minimization of a Sum of Squares of Functions (MINSQ)", CERN Library subroutines.

8. M. J. D. Powell, "A Method for Minimizing a Sum of Squares of Non-Linear Functions Without Calculating Derivatives" Computer Journal 7, (1965), 303-307.

9. W. Marshall and S. W. Lovesey, "Theory of Thermal Neutron Scattering" Oxford, 1971.

Appendix

Calculation of the Delayed Neutron Background

We have fitted the function

$$\Phi(E) = \Phi_{MB}(E) + \Phi_{epi}(E)$$

to the time-average spectrum and wish the delayed neutron background

$$B = \delta/T \int_0^\infty A\eta(E)\Phi(E)dE = \Phi_{epi}\ \delta/T\ F.$$

The purpose of this Appendix is to compute the integral F in the above expression,

$$F = \Phi_{Th}/\Phi_{epi} \int_0^\infty (E^{1/2}/E_T 2)\exp(-E/E_T)dE + \int_0^{Emax} 1/(1 + (E_{co}/E)^S)E^{-3/2}(E/E_{ref})^\alpha dE,$$

where E_{max} is the energy ($\simeq$ 1 MeV) at which we assume the epithermal spectrum to go abruptly to zero, approximately representing the upper limit of the primary source spectrum. The first integral is easily recognized as a gamma function

$$\int_0^\infty (E^{1/2}/E_T 2)\exp(-E/E_T)dE = E_T^{-1/2}\Gamma(3/2) = \sqrt{\pi}/(2\sqrt{E_t}).$$

The second integral can be written

$$\int_0^{Emax} 1/(1 + (E_{co}/E)^S)E^{-3/2}(E/E_{ref})^\alpha dE = \sqrt{E_{co}}(E_{co}/E_{ref})^\alpha\ f,$$

where f is identifiable as an incomplete Beta function. We need not appeal to this relationship, except to note that the integral converges for $\alpha < 1/2$ when E_{max} is finite. It is convenient to express

$$f = \int_0^\infty x^{-1/2-\alpha}/(1 + x^S)dx - \int_0^{xmin} x^{-1/2-\alpha}/(1 + x^S)dx,$$

with $x = E_{co}/E$ and $x_{min} = E_{co}/E_{max}$. This form requires the additional condition $s - \alpha > 1/2$. With the substitution

$$y = x^S$$

the first term is recognizable as a standard integral,

$$1/s\int_0^\infty y^{(1/2-\alpha)/s-1}/(1 + y)dy = (\pi/s)/\sin[\pi(1/2 - \alpha)/s].$$

Since x_{min} in the second term is very small, we approximate the integral to lowest order in x_{min},

$$\int_0^{xmin} x^{-1/2-\alpha}/(1 + x^S)dx \simeq 2x_{min}^{(1/2-\alpha)}/(1 - 2\alpha),$$

so that

$$f \simeq (\pi/s)/\sin[\pi(1/2 - \alpha)/s] - 2x_{min}^{(1/2-\alpha)}/(1 - 2\alpha).$$

It is instructive to note that for small values of $\pi(1/2 - \alpha)/s$,

$$(\pi/s)/\sin[\pi(1/2 - \alpha)/s] \simeq 2/(1 - 2\alpha),$$

which is the result for an abrupt ($s \to \infty$) cutoff at $E = E_{co}$.

Thus finally,

$$F = \Phi_{Th}/\Phi_{epi}\sqrt{\pi}/(2\sqrt{E_T}) + 2/\sqrt{E_{co}}(E_{co}/E_{ref})^{\alpha}f,$$

and

$$B/\Phi_{epi} = (\delta/T)F.$$

These results for $\alpha \neq o$ seem not to have been worked out before, although the present result is similar in content to Westcott's (g+rs) for a "1/v" absorber.

ICANS IX

INTERNATIONAL COLLABORATION ON ADVANCED NEUTRON SOURCES

22-26 September, 1986

SUMMARY OF INSTRUMENT SESSION - PART I

GAVIN WILLIAMS

I am going to share this summary with my co-chairman Kent Crawford. We had the oral sessions on Tuesday and an ad hoc round table discussion yesterday morning. I will summarise the Tuesday morning session which was concerned mainly with what I would call conventional inelastic spectrometers.

We had three direct geometry chopper spectrometers which are all at various stages of development. First was the HET spectrometer, which we have heard a lot about at this meeting. The main components are the Fermi chopper and the large detector which is concentrated in the forward scattering direction. The Fermi chopper can work up to very high incident energies (there is one case where it was used up to 2 eV) and the versatility of the instrument comes from the ease with which you can change the incident energy (just by rephasing the chopper - in fact about three slit packages will cover the incident energy range from about 100 meV to 2 eV). The detector in the scattered flight path is in two main sections: in the forward direction between 3° and 7° there are ^3He detectors and then the high angle detectors, from 9° to 29°, which was a scintillator bank but since the last meeting we have decided to replace this with ^3He detectors. This is simply because the scintillator detector backgrounds were too high for the experiments we are trying to do with this instrument. Another thing that we learnt about is the effect of the Nimonic chopper (also called the background chopper). This is a rotating ultra-fast shutter, which lowers the level of the signal at short times so that it now approaches the detector noise level, and this has been a very important factor in at least two of our experiments. There is a vigorous scientific programme taking place on the instrument and I'd like to mention just three experiments; two are magnetic,

in which we have measured high energy crystal field levels in UO_2, and the J=5/2 to J=7/2 spin orbit excitation in $SmPd_3$; both involved transition energies >100 meV. Currently the high angle (80° – 140°) is being used to measure momentum distributions in He-4.

Now for the ANL correlation spectrometer which is similar in principle to HET, but uses a cross-correlation technique where a "multi-energy" chopper replaces the "single-energy" Fermi chopper in the incident beam. This is a correlation chopper, which is a wheel with a series of open and shut slits and slots in what is called a pseudo random sequence; it is run asynchronously with the source. The advantage of this sort of chopper spectrometer is in the duty cycle. You are actually using simultaneously a whole range of incident energies rather than the single incident energy in the conventional spectrometer. What you actually do is you build up a two dimensional histogram - in one dimension you use the phase of the chopper and in the other the total time of flight; from this information you can actually pick out the spectra you would observe at a whole series of runs at individual energies, and you get all that information at the same time. We discussed the disadvantages of this sort of spectrometer; one is that the resolution varies quite considerably over the (Q,ω) space you are measuring although this is not seen to be a disadvantage in many of the experiments actually carried out. The instrument is probably most useful for measuring $S(Q,\omega)$ in liquids and amorphous solids, and that in fact is what it is being built for. For example, by integrating over all ω you can get a good measure of S(Q) and this does not require the complex inelasticity corrections of normal S(Q) measurements on a liquids diffractometer. There is a result from a very short run with Vanadium, which shows that the technique does in fact work and the spectrum contained just a hint of a very weak inelastic signal. It seems, at least in principle, that the method actually works and we look forward to further developments.

The third chopper spectrometer, the one at NBS, was described by Ian Anderson. Again a Fermi chopper is placed immediately before the sample, but an important feature is the double crystal monochromator which takes the beam out from the main tube, and this will improve considerably the background on this machine. The resolution is determined both by the collimation provided between the two crystal monochromators as well as the chopper open time. Pyrolitic graphite crystals give an excellent perfor-

mance at low energies. The incident energy can be changed continuously between 2 and 20 meV. The elastic resolution is typically 20 μeV for 20′ of arc collimation and they are going to add a PSD at angles somewhere between 0° and 10°. A relevant question for the future is to ascertain whether the beam transmitted through the first crystal can be used by a second spectrometer, since this opens up the possibility of multiplexing beam lines. This will become very important at our sources as the beam tubes get used up. I am very conscious of this already at ISIS and I think the same will be true at other sources, so we should look carefully to see how this spectrometer works out over the next few years.

- *It was pointed out that this would be a very suitable instrument for use at the hydrogen source on SINQ: the double monochromator system would solve at least part of the background problem; and the energy range matches the neutron spectrum expected from the hydrogen source.*

- *This sort of spectrometer could also be useful at a conventional pulsed source. It is an instrument type being considered for ISIS and its actual performance will be of considerable interest.*

Now I come on to the inverted geometry spectrometers, and first ROTAX. Over the last five or six years, perhaps more, there have been a number of crystal-analyser spectrometers built at pulsed sources. They have been used very successfully for incoherent scattering but as yet there isn't a solution to the problem of doing coherent excitation work with single crystals. We have heard over the years about constant-Q spectrometers: the MAX spectrometer in Japan; the constant-Q spectrometer at Los Alamos; we have a spectrometer being built now at ISIS called PRISMA, which is rather similar to MAX; all these spectrometers have the problem of how to get a good constant-Q scan so as to try and compete in some way with the excellent performance you get from the triple-axis machine. We heard about an idea by Tietze and Geick in which if you actually oscillate or rotate the analyser crystals in a carefully phased manner, you can do scans which are at least intermediate between what you get on a constant-Q and a high symmetry spectrometer. It gives you more flexability, is what is claimed, in the $(\omega, \underline{Q})$ scans possible. It's a paper study at this stage and what is now needed is a

development programme to build suitable drive mechanisms to rotate these crystals. Some of the scans require abrupt accelerations and decelerations of the crystal rotation and these may well be difficult to achieve; others require a simple monotonic variation of the analyser Bragg angles. I think we will have to wait a year or so to find out what can actually be done with this method. I think it is interesting and something one should actually pursue as this problem of doing the coherent excitation work with single crystals is still with us. We still haven't found a pulsed source equivalent to the triple-axis spectrometer.

> *At this point there was a short discussion about triple-axis machines which is summarised by saying, the triple-axis will not be replaced. It was also suggested that adequate attention has not yet been given to the focussing properties of time-of-flight instruments.*

Finally the Argonne eV spectrometer presented by Kent Crawford: this again has been with us for many years and is a method of doing eV spectroscopy using nuclear-resonance analysers; the prompt gammas emitted when neutrons are captured at a resonance (they use the 4.28 eV Tantalum resonance and a BGO detector) are measured, so that the energy at that resonance defines the scattered neutron energy. The resolution is determined by the width of the resonance. This spectrometer was designed mainly to measure low-Q processes; this means measuring at very small scattering angles so a major problem is to get good signal to noise conditions. Let me talk about another of the problems first: both the resolution width in the energy transfer and Q may be too large for many experiments and I'm sure that this problem needs to be addressed much more seriously than in the past. Nuclear resonance analyser methods are more easily applicable to momentum distribution work at high angles. The question that people should address more seriously is the suitability of the resonance detector and resonance filter techniques for low-Q spectroscopy. We have to decide at some point whether we are going to achieve the energy transfer- or Q-resolution we need to do interesting physics experiments. Even the possible experiments have not been defined as well as we would like; this, I realise, is partly because we are entering a completely new regime of physics. Progress has been made but it is taking lots of effort in all labs

- at KENS, LANSCE, ANL and ISIS. Kent showed some very nice results where the signal to background has improved as time has gone along, but I think we are still falling far short of the point where we can do actual experiments. Well, that's my view! Kent has also used the technique, developed by Phil Seeger, of using difference measurements with thin and thick resonance foils to improve resolution. The improvement you actually get is still quite modest; you typically reduce the width by about 10 or 20 meV in a line width that is closer to 100 meV (so you are getting a 20% reduction). You do get a much better line shape: it's a nice shape but still 80 meV wide!

There was a long discussion in which the following main points appeared:

- *The present resolution (80 to 100 meV) is possibly sufficient to tackle many physics problems. However, it is also likely that such resolution could be achieved using different spectrometers.*
- *There are ways of improving the resolution (further development of the difference technique, use of "better" resonances, use of cooling techniques etc); taken all together they could allow resolutions of the order of 30 meV to be reached (this caused the comment "That sounds interesting!"). The number of scattered neutron energies would nevertheless be limited. There are still more basic problems which have to be solved first, principally that of signal to background. If one is going to make the effort (and it does take some effort to do it), there is undoubtedly some nice physics to be done.*

ICANS IX

INTERNATIONAL COLLABORATION ON ADVANCED NEUTRON SOURCES

22-26 September, 1986

H E T : THE HIGH ENERGY INELASTIC SPECTROMETER AT ISIS

A D Taylor, B C Boland and Z A Bowden

Rutherford Appleton Laboratory, Chilton, Didcot, Oxfordshire. UK.

INTRODUCTION

The HET spectrometer is a direct geometry chopper spectrometer designed specifically to study systems at high energy transfer ε with low associated momentum transfer Q and good energy transfer resolution $\Delta\varepsilon$. This is achieved by monochromating at high incident energies (100-2000 meV) and scattering at low angles (3°-30°)

Fields of interest include:

- High frequency localised magnetic excitations such as crystal field and spin-orbit transitions in 4f and 5f electron systems, where the electronic form factor severely reduces intensities when Q is greater than 4 $Å^{-1}$.

- Vibrational spectroscopy where the low momentum transfer minimises multiphonon effects and the excellent energy resolution, particularly at high energy transfer allows new features to be distinguished.

- Coherent excitations at high energy transfer in itinerant ferromagnets where again form factor considerations severely limit the available intensity.

In addition a high angle detector array allows measurements to be made at high energy transfer and high associated momentum transfer. Such measurements probe the momentum distribution of particles and is of particular interest for quantum systems such as hydrogenous materials and the helium liquids.

INSTRUMENT

The spectrometer is illustrated in Figure 1 and details are given in Table I. The monochromating chopper, located 10 m from the source, spins on magnetic bearings at frequencies up to 600 Hz and produces a sharp (~1μs) burst of neutrons on the sample. Three different slit packages each made of boron-fibre/aluminium composite are optimised to give peak transmission for 1000 meV, 500 meV and 250 meV neutrons. By rephasing the chopper opening time with respect to the accelerator pulse and by spinning at reduced multiples of the ISIS frequency, monochromatic beams of neutrons ranging from 100 meV to 2000 meV may easily be produced, see Figure 2. Such versatility has been invaluable in optimising the resolution and momentum transfer characteristics of the spectrometer for a given experiment.

The primary flight path and the entire spectrometer are under rough vacuum, and the sample chamber is turbo-pumped to a cryogenic vacuum. Almost all samples are run at low temperature. All internal surfaces of the spectrometer are lined with tiles of a low-hydrogen B_4C mix to minimise the scattering of high energy neutrons, and the same material is used as a shield behind each detector.

Detectors

Scattered neutrons are detected 4 m from the sample in a low angle array (3°-7°) of ^{3}He gas tubes, at 4 m in a movable high angle array (80°-140°) and at 2m in an intermediate angle array (10°-30°). Originally the low angle bank was complete, but only a test octant of 2mm glass scintillators were used at the 2 m position. It was known that the intrinsic background (0.5 n/cm^2/min) in the considerably less expensive scintillator detectors was a factor of 100 worse than achievable with gas detectors, but before operational experience it

was not known whether this intrinsic background would be dominated by all other sources. One result of the quality of spectrometer shielding and the separation by time-of-flight of fast neutron background from signal neutrons was that the major background source for incident energies below 350 meV was the intrinsic noise of the detectors. The difference in intrinsic noise levels may be clearly seen in Figure 3. Signals clearly observed with the gas detectors were not seen in the scintillators. An early decision was taken to use gas detectors throughout the spectrometer. All detectors are now 10 atmosphere ^{3}He tubes 2.54 cm diameter. The majority have 30 cm active lengths, but some 20 cm and 15 cm active length detectors are used in constrained geometries at low angles.

For safety and reliability reasons, the large thin window at 2 m is being replaced in Spring 1987 by an eightfold array of locally thin windows, see Figure 4. This configuration will have 32 detectors mounted immediately behind each window at a distance of 2.5 m from the sample. A total of 256 detectors will be used. The inner four detectors of each group will have a 20 cm active length. The outer 28 will have a 30 cm active length. In the current (October 1986) configuration there are four arrays of 25 large detectors in the horizontal and vertical locations.

Choppers

The chopper control system, whereby the chopper is phased to a master 1MHz oscillator which controls extraction from the accelerator, has proved to be very effective in the majority of cases. An additional veto system has been introduced which rejects data on a frame by frame basis unless an optical monitor of the chopper indicates that the chopper is at the correct time delay with respect to the extracted proton burst. This has eliminated a 10% jitter which occurred under some accelerator operating conditions.

The background suppressing chopper, located upstream of the monochromating chopper, has been recently commissioned. This chopper blocks the beam during the power pulse (see Figure * in reference [1]) with 30 cm of nimonic alloy and prevents fast neutrons from entering the spectrometer. A substantial reduction in background was obtained, allowing experiments to be performed with incident energies up to 2000 meV.

EXPERIMENTAL PROGRAMME

Proposals from the UK neutron scattering community for time on HET have been considered in four categories: Vibrational Spectroscopy; Isotropic Magnetic Scattering; Momentum Distributions and Single Crystal Excitations. Preliminary experiments have now been performed in all four categories with considerable success.

Vibrational Spectroscopy

The versatility resulting from the ease of energy selection proved to be invaluable in optimising many experiments. This is well illustrated in a study of structure in the harmonics of the librational modes in NH4Cl by Goyal et al [2]. The harmonics occurring around 95 meV and 140 meV are shown in Figure 5(a) where the incident energy is 160 meV. Reducing the incident energy to 120 meV (Figure 5(b)) significantly improves the resolution of structure in the first harmonic, but of course does not allow the second harmonic to be observed. The resolution characteristics of the spectrometer are summarised in Figure 6 as a function of the fractional energy transfer ε/E. In this case the choice of momentum transfer Q is not critical.

Isotropic Magnetic Scattering

In magnetic systems the choice of incident energy is more subtle, since the incident energy controls both the momentum transfer (and hence through the form factor, the intensity) and the resolution. The experiments on crystal field transitions in UO_2 by Osborn et al [3] used 360 meV neutrons to show the magnetic nature of the signal by studying the form factor variation, then sacrificed intensity for resolution and Q range by using 290 meV incident energy neutrons, see Figure 7, to resolve the $\Gamma_5 \rightarrow \Gamma_4$ triplet (7 meV), and finally resolved the $\Gamma_5 \rightarrow \Gamma_3$ doublet (3 meV) on the limit of the form factor intensity with 230 meV neutrons.

The strong epithermal component in the ISIS spectrum was exploited in several experiments. The J-->J+1 spin-orbit transition at 129 meV in Sm3+ ions in metallic SmPd3 was observed for the first time [4] and its form factor dependence measured (see Figure 8). An incident energy of 610 meV was used

exploiting a minimum in the absorption cross-section of natural samarium. Previous neutron studies of samarium compounds have only been possible on isotopically enriched systems.

Momentum Distributions

Using the high angle bank and neutrons with incident energies in the range 800 meV to 2000 meV, preliminary studies were made of high momentum transfer scattering from polycrystalline lithium [5], again without the need for isotopic enrichment, and liquid helium, both in the superfluid and normal phase.

Excellent data [6] were obtained on normal helium at high resolution and free from background from the cryostat. These data are shown in the Figure 9. The mean kinetic energy determined from a fit of the impulse approximation lineshape is significantly lower than previous measurements and is closer to the value from Green Function Monte Carlo calculations. Deviations from the impulse lineshape due to final state effects are being investigated. The error analysis is still in progress, but conservative estimates give <KE> = 13.2 +/- 0.5 K.

Single crystal Excitations

Preliminary test measurements were carried out on a single crystal of Pd_3Fe by Mitchell et al [7] to study methods of crystal alignment for future coherent excitations experiments. The crystal was easily aligned on a room temperature goniometer using white beam techniques (chopper removed) and then checked with monochromatic neutrons. Inelastic scans gave encouraging results and several points on the magnon dispersion curve previously measured by a triple-axis spectrometer [8] were observed. For example, Figure 10 shows a magnon at 66 meV along the 111 direction . Unlike their isotropic counterparts, such experiments use only a few in-plane detectors and hence require significantly greater neutron intensity.

CONCLUSIONS

In addition to commissioning the spectrometer, an excellent start to the scientific programme has been achieved. In the field of vibrational spectroscopy, measurements have been made on the metal hydride systems $ZrNiH_x$ and VH_2, on molecular species such as KH_2PO_4 and solid and liquid formic acid, in addition to the NH_4Cl data described above. The suitability of the spectrometer to study high energy magnetic excitations has been well established by the work on $SmPd_3$ and UO_2. Work on momentum distributions and coherent excitations has only just begun but the low intensity tests are very encouraging.

ACKNOWLEDGEMENTS

We would like to thank T J L Jones, J Parker and M Fisher for their work on the chopper systems, T Mott and R T Lawrence for electronic assistance, H E T Users for their patience during commissioning, D Abbley for technical help and J R J Bennett and the Sample Environment Group for their assistance. A special thanks is due to the engineers, physicists and operations crews of ISIS for their hard work and dedication.

REFERENCES

[1] T J L Jones et al These Proceedings

[2] P S Goyal, ISIS Internal Experimental Report, HET/IER/P7/86

[3] R Osborn, ISIS Internal Experimental Report, HET/IER/P6/86

[4] S Culverhouse, ISIS Internal Experimental Report, HET/IER/P8/86

[5] M Hewitt, ISIS Internal Experimental Report, HET/IER/P20/86

[6] P E Sokol, ISIS Internal Experimental Report, HET/IER/P17/86

[7] P W Mitchell, ISIS Internal Experimental Report, HET/IER/P21/86

[8] A J Smith, W G Stirling and T M Holden, J Phys F7, 2411 (1977)

[9] E Balcar and S W Lovsey, J Phys C19, 4605 (1986)

TABLE I

Specification	
Incident energy	100-2000 meV
Energy transfer	20-500 meV
Momentum transfer	Depends on incident energy, energy transfer, and angle of scatter, eg 2.5 $Å^{-1}$ at 200 meV transfer; 40 $Å^{-1}$ (maximum) using high angle detector
Resolution	$\Delta E_0/E_0 = 0.7\%$

Instrument	
Beam	N9
Moderator	316K H_2O poisoned at 1.5 cm
Background Chopper	8 m from moderator, closed at t = 0.
Chopper	10.0m from moderator, 600 Hz phased to ISIS pulse $\pm$ 1/2 μs
Sample position	11.8m from moderator
Beam size	50 x 50 mm^2 max
Detectors	3°-7° 4m counter bank: 50 10 atm ^3He 10°-30° 2m counter bank: 100 10 atm ^3He 80°-140° 4m movable bank: 10 10 atm ^3He
Intensity at sample	4.4×10^3 n cm^{-2} s^{-1} at E_o = 1 eV (full ISIS intensity)
Sample environment	Accepts standard sample environment equipment
Data acquisition	VAX11/730

HET Spectrometer

Figure 1 The layout of the HET spectrometer at ISIS, showing the background reducing chopper, the fast monochromating chopper and the various detector arrays.

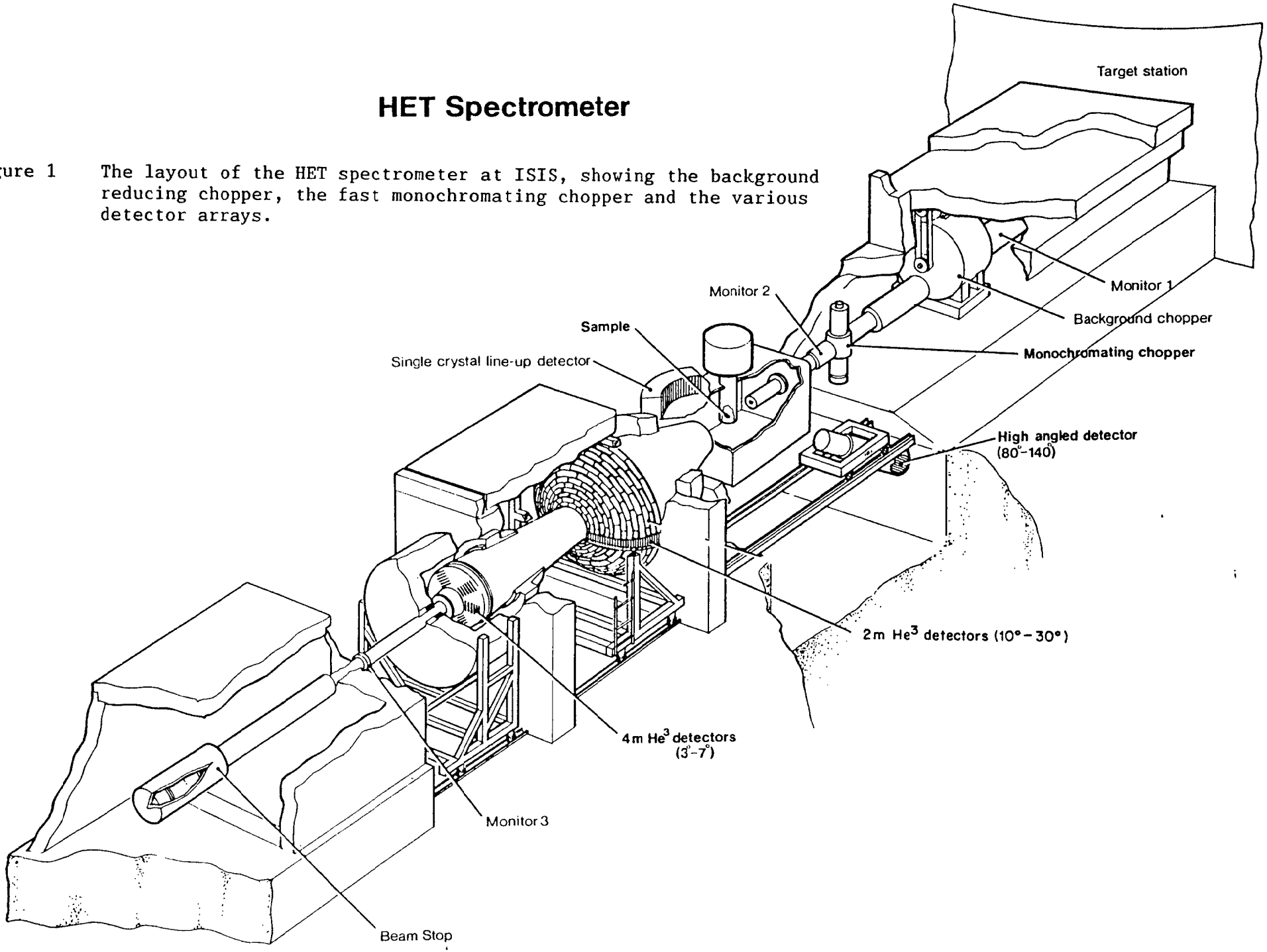

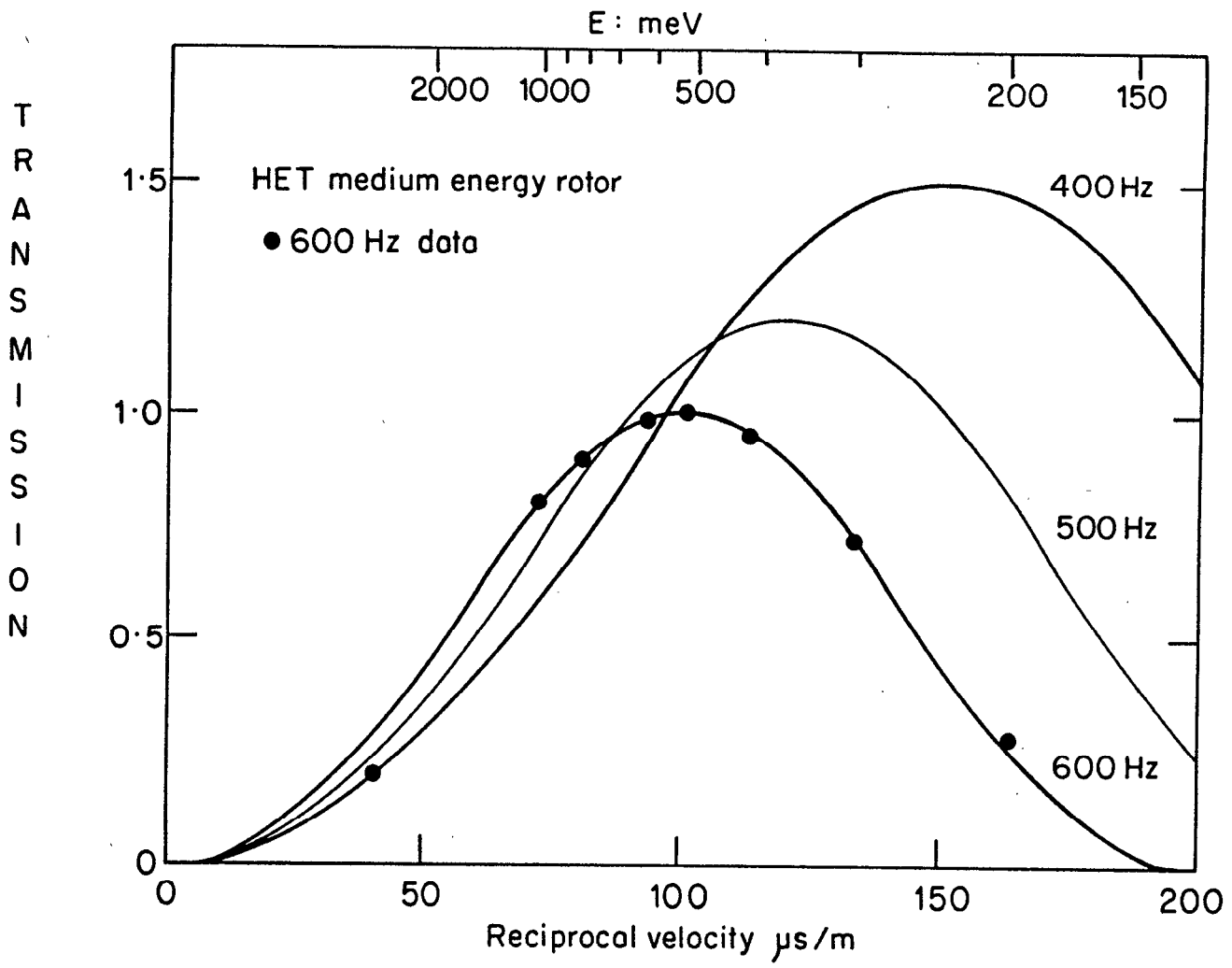

Figure 2 The calculated transmission characteristics of the medium energy HET chopper. It has an effective slit width of 0.89 mm and a radius of curvature of 1.32 m, which give it a peak transmission of 515 meV when spinning at 600 Hz. The data points are an experimental determination of the 600 Hz performance. By reducing the frequency to a lower multiple of the ISIS frequency, the peak transmission may be shifted to lower energies. (Eg: 10*ISIS = 500 Hz is optimised for 360 meV and 8*ISIS = 400 Hz gives 228 meV neutrons.)

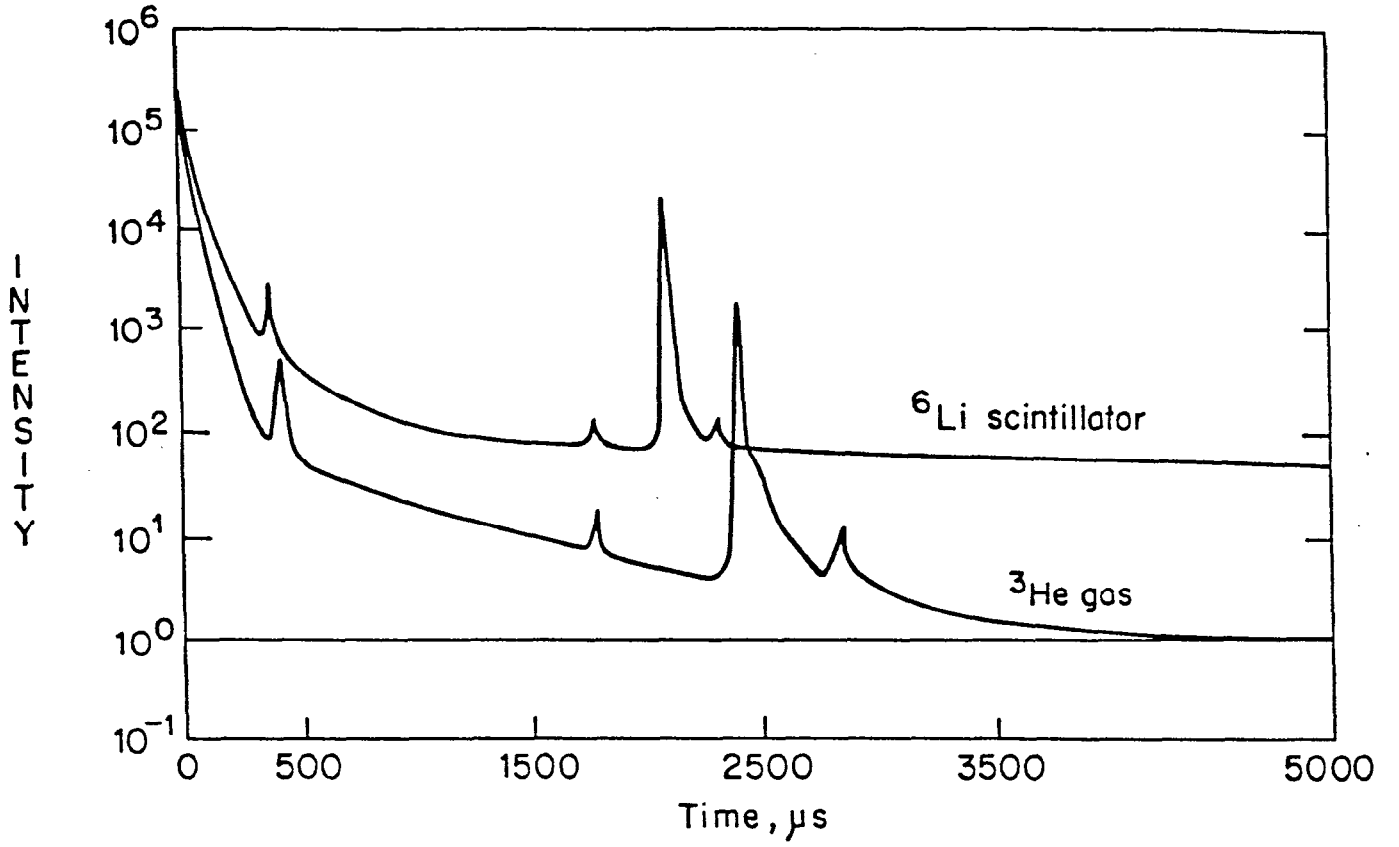

Figure 3 A comparison of the time-of-flight response of the ^{3}He gas detectors and the ^{6}Li glass scintillators. The difference in intrinsic background which dominates at long times is obvious. These data have been corrected for differences in solid angle.

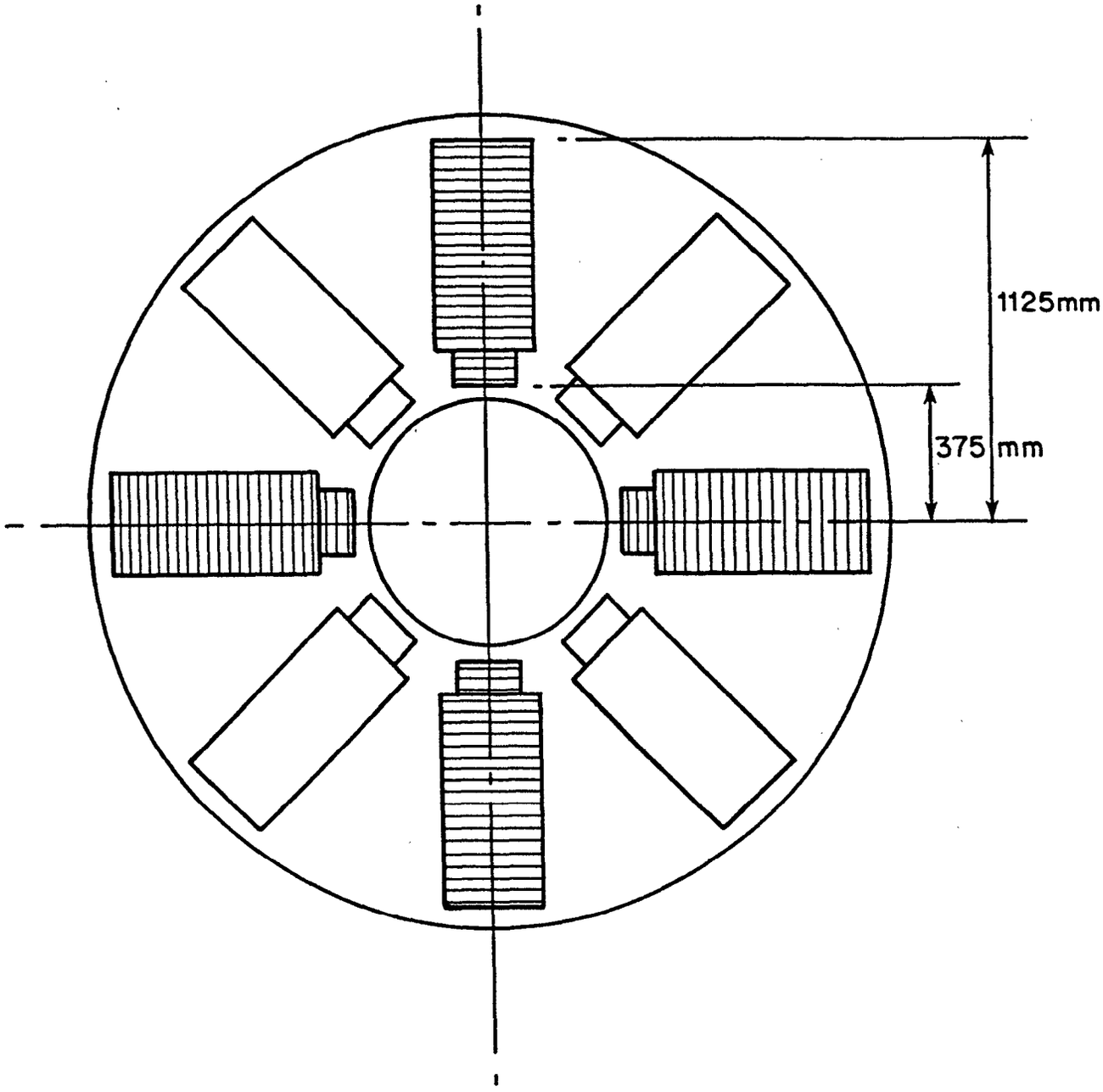

Figure 4 The eight-fold array of thin window and detectors which will provide continuous angular coverage at 2.5 m between 10° and 30°.

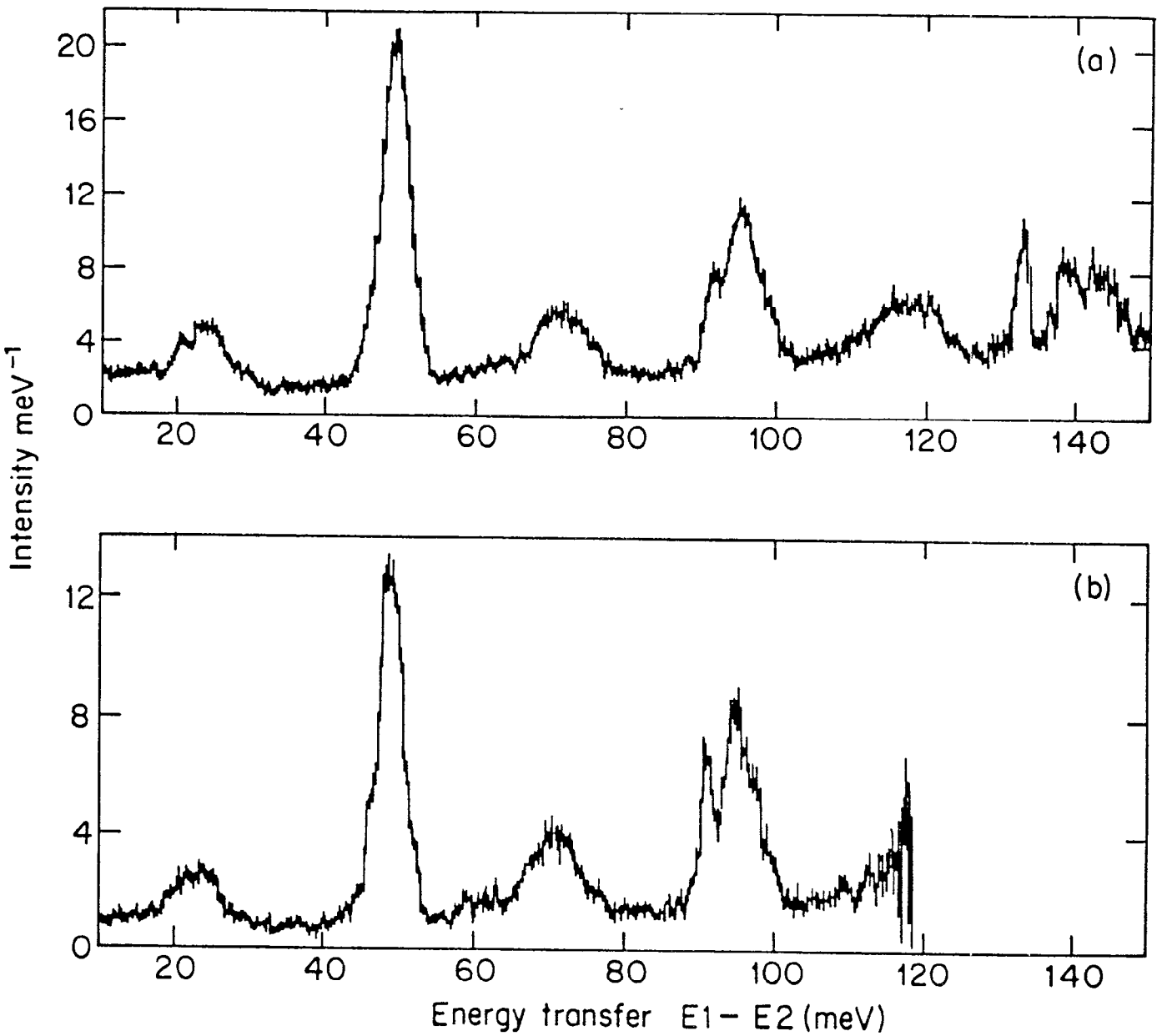

Figure 5 These data show inelastic scattering from the librational modes of NH_4^+ in NH_4Cl at two different values of incident energy. The data from the 4 m low angle array required 140 μA-hr of protons with an incident neutron energy of 160 meV, figure 5(a) and 50 μA-hr at an incident neutron energy of 120 meV, figure 5(b).The fractional energy transfer at 98 meV is 0.61 and 0.82 respectively. The improvement in resolution is in agreement with the calculation of Figure 6.

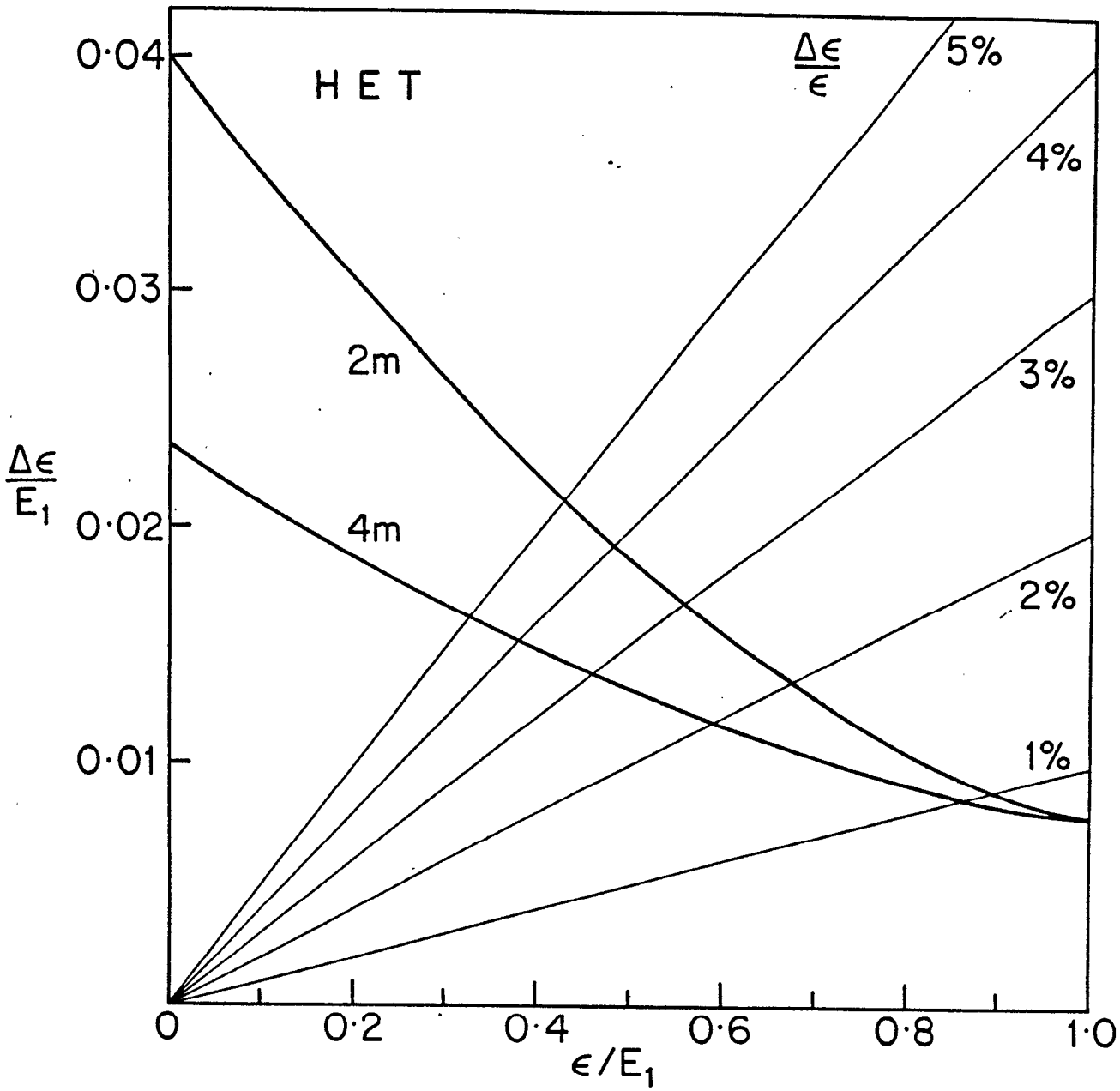

Figure 6 The calculated resolution of the 2 m and 4 m detector arrays on HET as a function of the fractional energy transfer ε/E.

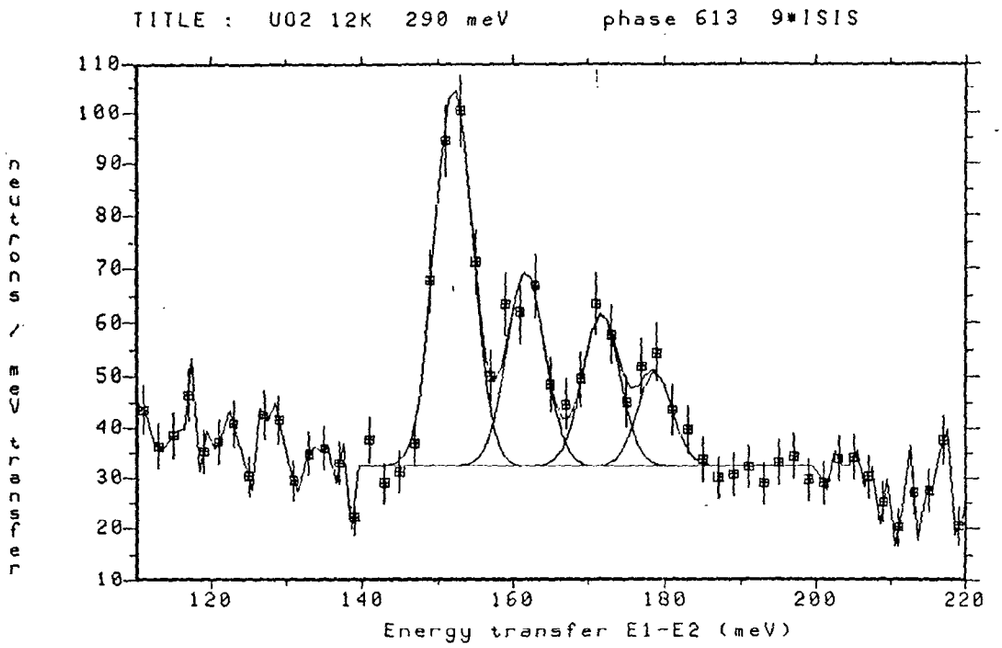

Figure 7a The spectrum of crystal field excitations in UO_2 at 12K measured in the 4 m low angle array ($\phi = 5^0$) at an incident energy of 290 meV. These data were recorded in 512 μA-hr using 80 g of sample. Previous measurements on HET at 360 meV had established the form factor dependence of this signal, but with insufficient resolution to identify details of the transitions involved. A subsequent measurement at 220 meV was able further to resolve the signal, but only at the limits of signal to noise.

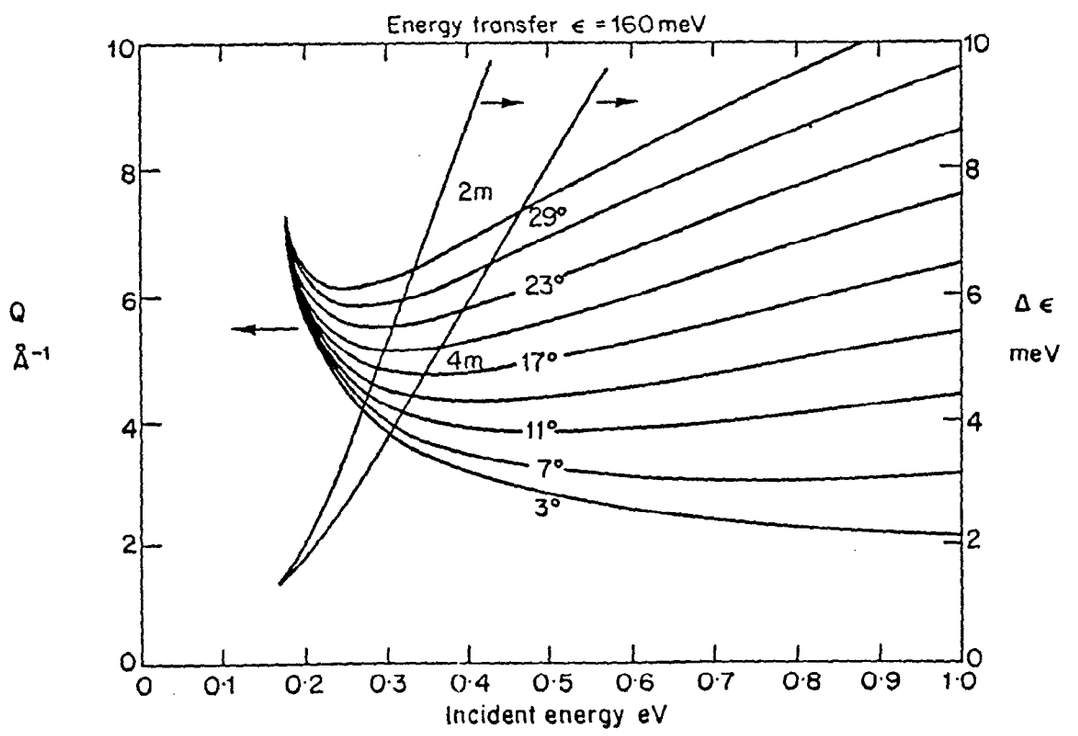

Figure 7b The resolution and momentum transfer characteristics of HET calculated for the 160 meV UO_2 excitations as a function of incident energy. These data allow the experimentalist to optimise the choice of incident energy by balancing resolution against Q (and hence, because of the form factor associated with magnetic scattering, intensity).

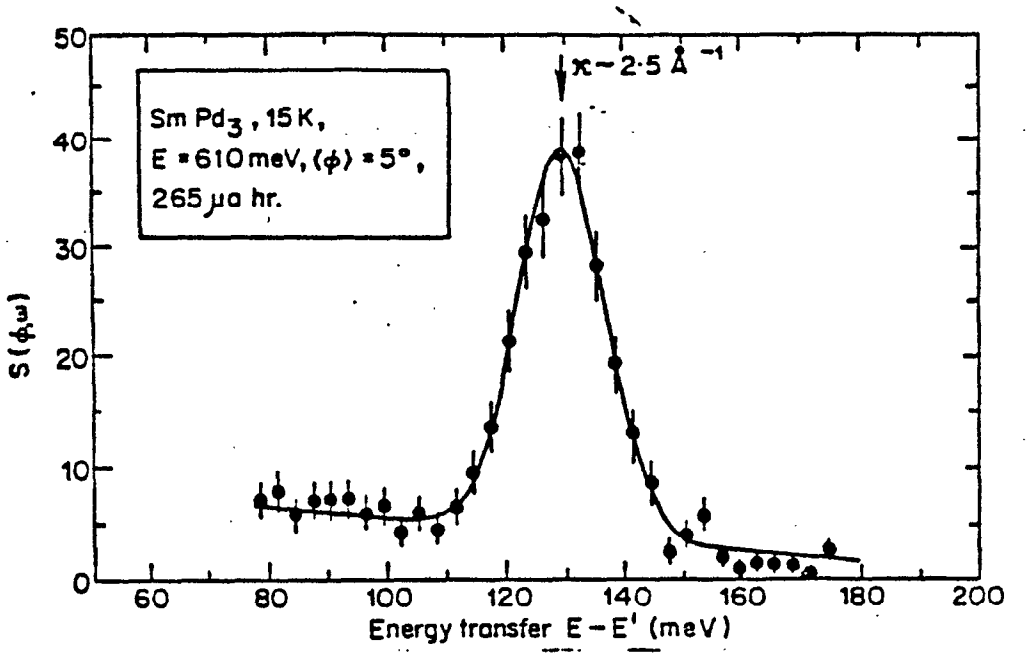

Figure 8a The spin-orbit transition in Sm^{3+} measured in 265 μA-hr at an incident energy of 611 meV. These data correspond to scattering at angles between 3.4° and 7°.

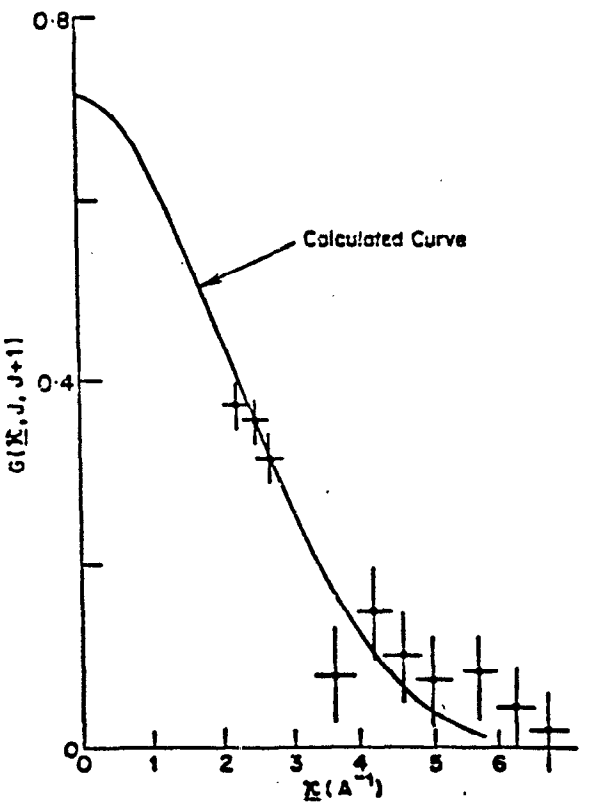

Figure 8b The observed form factor of the above spin-orbit transition in Sm^{3+} compared with the calculations of Balcar and Lovesey [9].

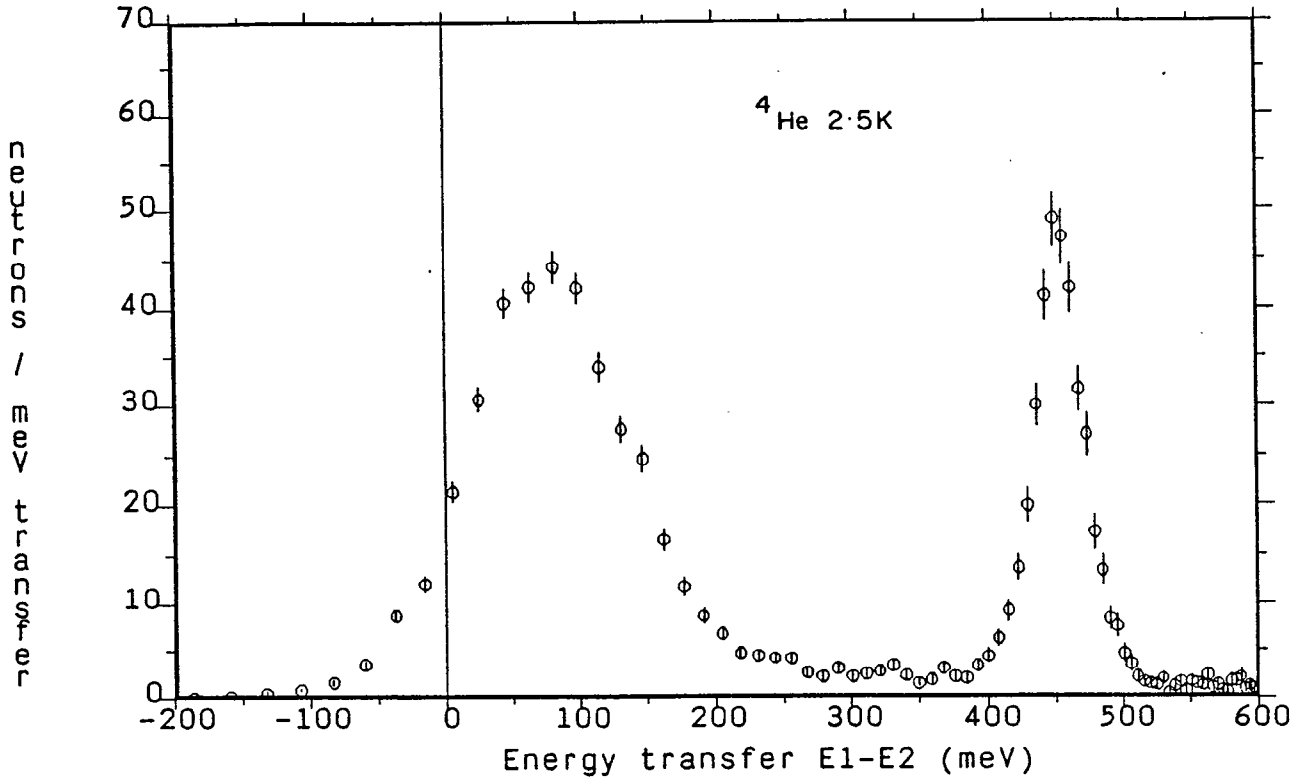

Figure 9 Recoil scattering at 450 meV from liquid helium at 2.5 K measured at an angle of 124°. The incident energy was 828 meV giving a momentum transfer at the recoil energy of 30 Å^{-1}. These data were collected in 1100 μA-hr and the background from the cryostat in 250 μA-hr.

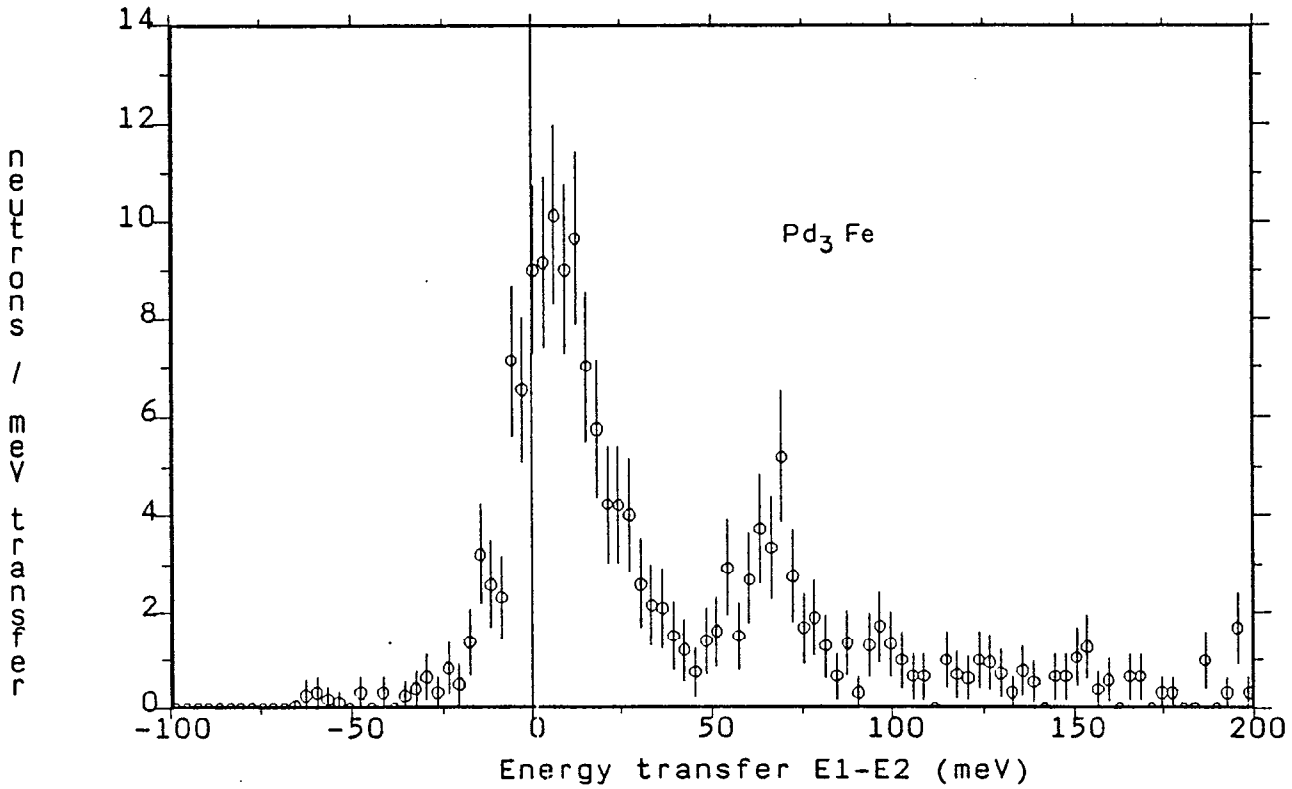

Figure 10 The excitation at 66 meV is a magnon in the 111 direction of Pd_3Fe measured in 300 μA-hr with an incident energy of 230 meV. These data are in agreement with the dispersion curves of reference [8].

ICANS IX

INTERNATIONAL COLLABORATION ON ADVANCED NEUTRON SOURCES

22-26 September, 1986

TEST OF A CORRELATION CHOPPER AT A PULSED SPALLATION NEUTRON SOURCE*

R. K. Crawford,** J. R. Haumann,+ G. E. Ostrowski,**
D. L. Price,++ and K. Sköld†
Argonne National Laboratory
Argonne, Illinois 60439

1. Introduction

The use of correlation time-of-flight techniques at steady-state neutron sources is well established,[1] and has proved to be highly effective in certain extreme situations, for example, highly absorbing samples such as liquid helium-3.[2] In a typical use of this method, a conventional chopper with one pulse per revolution is replaced by a chopper or other device providing a pseudo-random sequence of pulses. Used either with a white beam (for diffraction), or with a beam monochromated with a crystal analyzer (for inelastic scattering), the conditions of the experiment are essentially unchanged, except that the duty cycle is increased by a factor of order N, where N is the number of pulses produced over the period T of the conventional chopper. Because the different data points in the experimental spectrum after analysis have

*Work supported by the U. S. Department of Energy, BES-Materials Sciences, under Contract W-31-109-Eng-38.

**IPNS Division.
+Electronics Division.
++Materials Science Division.
†Visiting Scientist from Studsvik Science Research Laboratory, Sweden.

The submitted manuscript has been authored by a contractor of the U. S. Government under contract No. W-31-109-ENG-38. Accordingly, the U. S. Government retains a nonexclusive, royalty-free license to publish or reproduce the published form of this contribution, or allow others to do so, for U. S. Government purposes.

correlated errors, the statistical gain is in general less than N but may still be appreciable in certain circumstances.[1]

With a pulsed source, the conventional chopper has the primary function of monochromating the beam rather than pulsing it (although it may also have the function of sharpening the pulse in time). In this case, the replacement of the conventional chopper by a pseudo-random pulsing device has the effect of providing a sequence of measurements at different incident velocities, i.e., different incident energies. The statistical comparison in this case becomes less straightforward because the resolution of each measurement is different. An estimate of the gain factor therefore involves an assessment of the range of incident energies over which the data remains useful, and of the relative value of redundant data taken with different resolution and statistical accuracy at different incident energies. Nevertheless, it appears that the method should be favorable in certain cases,[3] similar to the situations (low signal/background, high peak-signal/average-signal) where correlation techniques are favorable in the steady-state situation. At least one demonstration of a statistical chopper in a pulsed beam has been carried out, in this case at a pulsed reactor.[4]

In addition to providing an efficient measurement of the inelastic scattering function S(Q,E), this technique could be valuable in measurements of the elastic structure factor S(Q,0) of amorphous or disordered crystalline solids, by providing an energy analysis which selects the elastic scattering out of the total structure factor S(Q).[5]

In view of these considerations, it seemed worthwhile to carry out a feasibility test of the technique at IPNS. Due to the restricted beam time available for this measurement, shortened further by an unforeseen accelerator breakdown, the data obtained during this test are very limited. Nevertheless, some spectra were obtained and analyzed

successfully, establishing the feasibility of the technique and providing some indication of its usefulness and limitations at a pulsed spallation source.

2. Principle of the Method

The method is already discussed at length in the literature[3-5] and only a brief outline will be given here. A schematic illustration is given in Fig. 1. We consider a chopper with N elements which may be open or closed [F(j) = +1 or -1, respectively]. The transmission of the chopper for a neutron arriving at time j is then

$$F'(j) = \frac{1}{2}\,[F(j) + 1]. \tag{1}$$

where the time is expressed in integral multiples of δ, the pulse width of a single element in the correlation sequence. Suppose that the chopper is phased so that the start of the correlation sequence (j=0) occurs at a time ℓ after the source pulse. Then the intensity recorded in a detector at time k relative to the source pulse is

$$J(\ell,k) = \sum_{i = i_{min}}^{i_{min} + N} F'(i-\ell)S(i,k-i) + B_k \tag{2}$$

where S(i,j) is the signal recorded with a conventional chopper for incident and scattered flight times i and j, and B_k is the background at time k uncorrelated with the chopper.

We define

$$S(i,j) \equiv 0,\ i < 1 \text{ and/or } j < 1, \tag{3}$$

and assume that, for any k, only i values within the range $(i_{min}, i_{min} + N)$ for some i_{min} contribute. (The generalization to cases where this is not true is analogous to the frame-overlap situation with a conventional chopper.)

We now consider a measurement such that all values of $\ell = 1,2.....N$ are encountered with equal probability, and perform a cross-correlation on the data obtained:

$$K(i', k-i') = \frac{1}{N} \sum_{\ell=1}^{N} F(i' - \ell)\, J(\ell,k)$$

$$= \frac{1}{N} \sum_{i=i_{min}}^{i=i_{min}+N} \sum_{\ell=1}^{N} F(i'-\ell)F'(i-\ell)S(i, k-i) + \frac{1}{N} \sum_{\ell=1}^{N} F(i'-\ell)B_k . \tag{4}$$

Let us choose a particular sequence F(j) obeying these conditions:

$$\sum_{J=1}^{N} F(j) = 1$$

$$\sum_{j=1}^{N} F(j)\, F(k) = (N+1)\delta_{jk} - 1 . \tag{5}$$

Then Eq. (4) reduces to

$$K(i', k-i') = \left(\frac{N+1}{2N}\right) S(i', k-i') + \frac{1}{N} B_k . \tag{6}$$

[The restrictions of the range of i in Eq. (2) are needed because the Kronecker delta in Eq. (5) is defined modulo N.] It is seen that K(i', k-i') reproduces the single-pulse scattering function but with a duty cycle $(N+1)/2N \sim 1/2$ compared with $1/N$ in the single-pulse case. The uncorrelated background only contributes with the duty-cycle $1/N$.

It can be shown the statistical gain with the correlation technique compared with the conventional technique is

$$g(i,k) \equiv \frac{[\text{rel. var. } S(i,\ k-i)]_{conv}}{[\text{rel. var. } S(i,\ k-i)]_{corr}}$$

$$= \frac{S(i,k-i) + B_k}{2 \sum_i S(i,\ k-i)} \times M \ , \qquad (7)$$

where M is the number of conventional measurements with the same run time that would be needed to give the required information. For example, for elastic scattering when the Debye-Waller factor is not too far from unity, we may expect $S(i,k-i) \sim \sum_i S(i,k-i) \gg B_k$ and so $g \sim M/2 \sim N/4$ if about one-half of the number of different chopper phases give useful information.

3. Experimental Configuration

The experiments were carried out at the LRMECS spectrometer with the usual Fermi chopper replaced by a correlation disk chopper of the type used in Ref. 2. [For the present measurements, however, the pattern satisfied $\sum F(j) = +1$, Eq. (5), instead of -1 as for the chopper used in Ref. 2]. The sequence of N = 251 elements (226 open, 225 closed) was defined by a pattern cut into a Gd_2O_3-epoxy coating on one surface of the disk over the radius interval where the disk is illuminated by the beam; the thickness of Gd was estimated as 0.21×10^{-3} atom/cm^2. The transmission was measured in a separate experiment to be <10% up to about 150 meV, after which it rose rapidly to 50% at about 230 meV. In order to attenuate the fast neutron component in the beam, a single crystal of

silicon, 15 cm long x 12.5 cm diameter, was placed in the incident beam directly in front of the chopper window.

The chopper was run at a period $N\delta$ = 5020 μsec, giving δ = 20 μsec, which was also chosen as the channel width for the collection of time-of-flight data and the recording of the chopper phase, i.e., the indices k and ℓ in $J(\ell,k)$, Eq. (2). The conditions of having all values of ℓ occur with equal probability was satisfied simply by running the chopper asynchronously with the source. Data were recorded for total flight times corresponding to k = 50.....306, and eight detector groups corresponding to upstream and downstream beam monitors and scattering angles of -5.7°, 14.1°, 29.7°, 63.3°, 91.5°, and 116.7°.

The LRMECS data acquisition system, with some modifications, was used for this test. This system has been previously described,[6] so only the modifications made for this test are described here. The ordinary IPNS discriminator modules produce a 24-bit data word for each neutron event. Within this word, 20 bits contain time-of-flight information, 3 bits identify the detector input within the module, and one bit is used for status information. For the correlation chopper test, four such discriminator modules were modified so that the 20 bits which were previously used for time-of-flight information are now divided into the least significant 8 bits, which are used to represent the chopper phase relative to the accelerator t_o pulse, and the more significant 12 bits, which are used for time-of-flight information (see Fig. 2a).

A magnetic pickup placed on the chopper generates one pulse per chopper revolution. This pulse and the accelerator t_o pulse are fed into a CAMAC module which was built especially for the correlation chopper operation. This module digitizes the time between the last chopper pickup pulse before the accelerator t_o pulse and the t_o pulse itself (see Fig. 2b). This chopper phase information is digitized to 8 bits, allowing

chopper phase values from 1 to 256. This slightly exceeds the actual range of 1 to 251 used for this test. Each chopper phase value covers a span of 20 μsec, which is determined by a scaler counting the 8-MHz time-of-flight clock signal. This 8-bit phase value is latched for use throughout the time until the next t_0 pulse, and is made available on the back of the CAMAC module.

The modified discriminator modules have connectors installed on the back so they can all be connected by ribbon cable to the 8-bit digitized phase information. The internal connections on these modules were modified to prescale the 8-MHz clock signal to provide a basic time-of-flight clock period of 2 μsec for these modules, to shift the resulting digitized time-of-flight information to the more significant 12 bits of the 20 bits previously used for time-of-flight, and to put the 8-bit phase information appropriate to this t_0 pulse period into the least significant 8 bits in this 20-bit region (see Fig. 2a). As before, three of the remaining four bits in the 24-bit data word contains the detector address for the event and one bit contains buffer status information.

The normal IPNS histogramming software on the Z8001 microprocessor was modified to separate the 12 bits of time-of-flight and the 8 bits of chopper phase information. It then calculates the histogramming time-channel from the time-of-flight in the normal way. A maximum of 256 time-channels are allowed, and the width of these time-channels and the starting time of the first channel can be varied subject to the constraint that there is only 12-bit information available (4096 possible time-of-flight values, spanning a range of flight times from 0 to 8192 μsec). For this particular test, all detector groups use 20-μsec time channels. Finally, the actual channel to be incremented is calculated as

$$\text{channel} = 256 \times \text{phase} + \text{time-channel}.$$

This channel constitutes an offset within the phase-time spectrum for the detector producing the event. Events from different detectors can be grouped together, and for each such group of detectors this phase/time spectrum starts at a different location in the histogramming memory. Each such spectrum is preceded by two channels used to store the sum over the spectrum, and this sum is incremented whenever an event is histogrammed in the corresponding spectrum. With this histogramming scheme, (256 x 256 + 2) 16-bit channels are allocated in memory for each detector group. Since only 251 chopper phase values are actually possible with the chopper used in this test, some of these memory channels were never used. However, this inefficiency in the use of memory is justified by the resulting simplification in the software and in the increase in histogramming speed.

Each event is histogrammed only once, and on-the-fly time-focussing is not permitted. Aside from these minor differences and the differences in histogramming noted above, which are necessitated by the inclusion of the chopper phase as a variable, the Z8001 software is unchanged from that used by the standard IPNS systems. The run-setup software on the PDP 11-34 computer was modified to account for the allocation of channels to each detector group as noted above, and to incorporate the fact that the basic clock period used for time-of-flight in this system is 2 μsec rather than the 0.125 μsec used in the standard systems. Otherwise, the run-setup software is essentially the same as for normal IPNS runs. No other PDP software was changed for this test.

A run was carried out on a standard vanadium sample, 1.08 mm thick, placed at an angle of 45° to the beam in transmission geometry. Data were collected for 4.5 h before an accelerator breakdown occurred (the only major breakdown in five years of IPNS operation!) necessitating an

extended shutdown during which the correlation chopper setup had to be dismantled to make way for scheduled LRMECS experiments. It was thus not possible to carry out the planned program of an extended vanadium run followed by a background run and measurements on a series of glass and liquid samples. Nevertheless, the vanadium data obtained provide a demonstration of the feasibility of the technique.

4. Results

The vanadium data were analyzed with the usual set of programs for chopper spectrometer data analysis,[7] modified to carry out the deconvolution of Eq. (4). As a result, data were obtained for essentially 251 different time-of-flight measurements, each corresponding to the different possible phases i' in Eqs. (4) or (6). A typical set of data, for the upstream beam monitor and the 91° detector group at i' = 201, is shown in Figs. 3-4. The cross-correlation procedure clearly gives the correct results for the peak positions and background.

Compared with usual results with the Fermi chopper, the peaks in both monitors and detectors appear symmetric, and the latter are centered at the calculated E = 0 position. Presumably this is because the chopper opening time for a single slit (20 μsec) is symmetric and long compared with the width of the (asymmetric) source pulses at the energies used. For the 91° detector, the elastic peak from the vanadium is clearly distinguished, but there is only a hint of the much weaker inelastic scattering in the region E = 5-20 meV.

Figure 5 shows a plot of peak positions in the time-of-flight spectra for some of the phases analyzed. The data fall on straight lines for each monitor and the detector. The t=0 intercept falls at a phase i' = - 73.4, -73.2, and -73.4, respectively, for Monitor 1, Monitor 2, and the 91° detector, which implies that, within the accuracy of the

measurement, the pulse of neutrons leaves the source at t=0 for all the neutrons measured. Taking the previously measured Monitor 1-Monitor 2 and Monitor 1-sample distances of 4.755 m and 0.462 m, these values imply a source-sample distance of 6.90 m, compared with the nominal value of 6.84 m, and an effective sample-detector distance of 2.52 m compared with the expected value of 2.50 m.

The energy resolutions measured for the elastic peaks in the 91° detector were 1.5, 3.2, and 16.2 meV FWHM for E_0 = 17.5, 25, 98 meV respectively. This gives $\Delta E/E_0$ = 9, 13, and 17% for the three energies, compared with the typical value of 8% with the Fermi choppers. This could be improved, of course, with the use of a shorter time element on the chopper. For a mechanical disk chopper, this requires a narrower slit defining the beam which considerably lowers intensities, or a higher speed of rotation. Other methods, for example, based on white-beam polarizers and spin flippers,[8] could in principle be used also. However, even with a negligible burst time at the chopper, the resolution will at best be constant in $\Delta E/E_0$, so that ΔE will increase linearly with E. This is a serious deficiency of the method if it is used for determining the elastic structure factor in glasses, as proposed in Ref. 5.

Another possible use of the correlation technique to study the structure of fluids and disordered solids is to derive the structure factor S(Q) from the area of S(Q,E) at constant Q. A correlation chopper spectrometer operating on a pulsed polychromatic beam covers a substantial range of the (Q,E) plane--in fact, with considerable redundancy--and thus in principle allows the determination of S(Q) in this way. This procedure, for which resolution is not as critical as for the measurement of S(Q,0), avoids the kinematic corrections (the so-called Placzak corrections) which are necessary for data obtained in conventional total scattering measurements at both pulsed and steady-state sources. The

statistical efficiency of this approach has still to be evaluated, however.

In conclusion, the correlation technique at a pulsed spallation source using a mechanical pseudo-random chopper is found to be technically feasible and can be accomplished with relatively minor changes to a conventional chopper spectrometer. The strong variation of resolution with incident energy is a serious disadvantage for some applications. There may be specific instances in which the method is advantageous to the conventional chopper at such a source, but these remain to be identified.

Acknowledgment

We should like to acknowledge helpful discussions with Drs. J. M. Carpenter, C.-K. Loong, and R. Scherm, and also the assistance of D. Bohringer, T. C. Erickson, R. Kleb, and the operations crew at IPNS for setting up the chopper.

References

1. K. Sköld, Nucl. Instr. and Methods 63, 114 (1968); D. L. Price and K. Sköld, Nucl. Instr. and Methods 82, 208 (1970), and references therein.
2. K. Sköld, C. A. Pelizzari, R. Kleb, and G. E. Ostrowksi, Phys. Rev. Lett. 37, 842 (1976).
3. P. Pellionicz, Nucl. Instr. & Methods 92, 125 (1971); W. Matthes, in Neutron Inelastic Scattering (I.A.E.A., Vienna, 1972), p. 773; R. Amadori and F. Hossfeld, ibid, p. 747.
4. N. Kroó, P. Pellionicz, I. Vizi, G. Zsigmond, G. Zhukov, and G. Nagy, in Neutron Inelastic Scattering (I.A.E.A., Vienna, 1972), p. 763.
5. D. F. R. Mildner and A. C. Wright, J. Non-Cryst. Solids 42, 97 (1980).
6. R. K. Crawford, R. T. Daly, J. R. Haumann, R. L. Hitterman, C. B. Morgan, G. E. Ostrowski, and T. G. Worlton. IEEE Trans. Nucl. Sci. NS-28, 3692 (1981); J. R. Haumann, R. T. Daly, T. G. Worlton, and R. K. Crawford. IEEE Trans. Nucl. Sci. NS-29, 62 (1982).
7. C.-K. Loong and D. L. Price, ANL private communication (June 1985).
8. R. Cywinski, "Polarisation Modulated Crosscorrelation Spectrometry on a Pulsed Neutron Source," Rutherford Appleton Laboratory Report NDR/P2/83 (1983), p. 36.

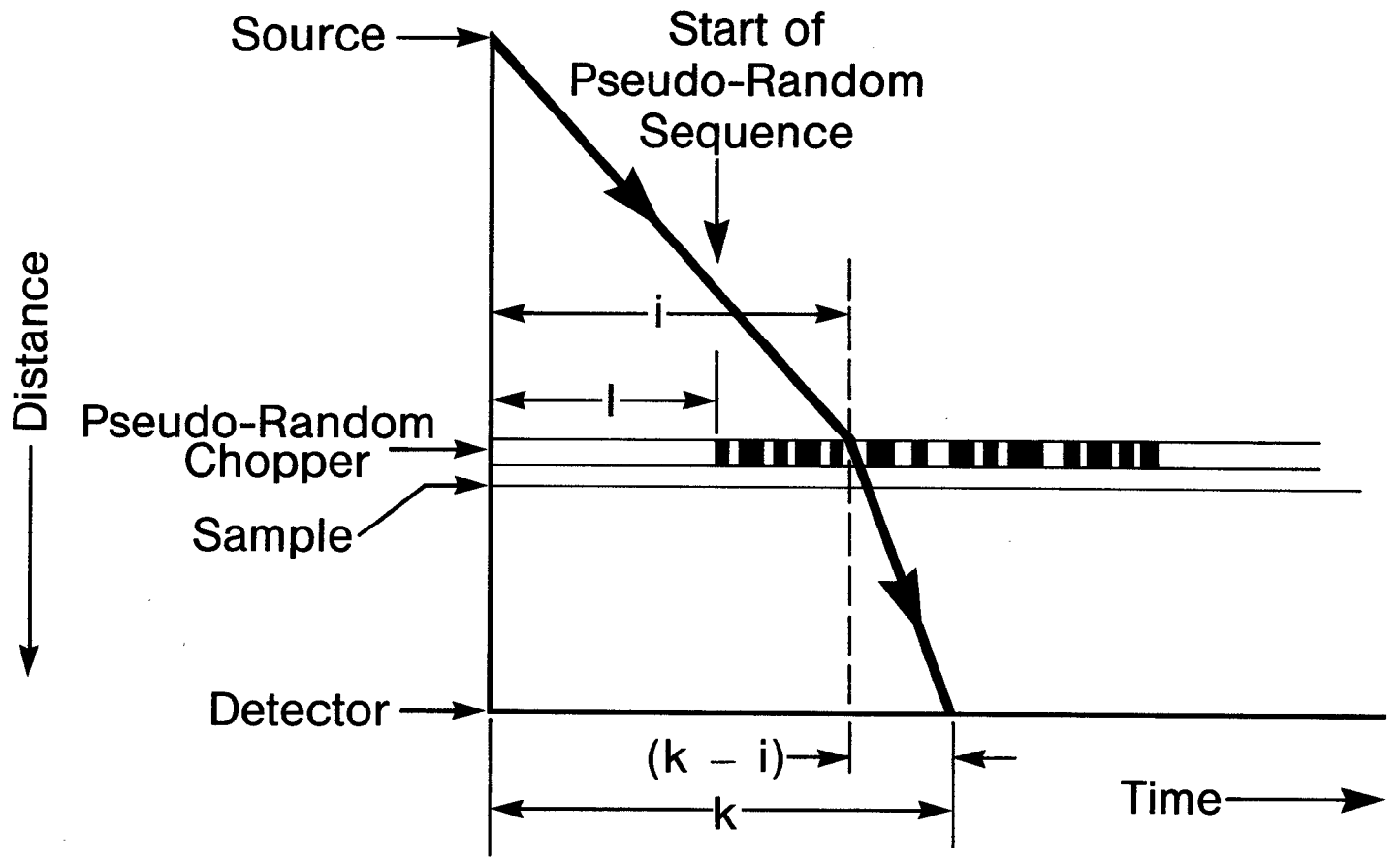

Fig. 1. Schematic diagram of the correlation technique at a pulsed source.

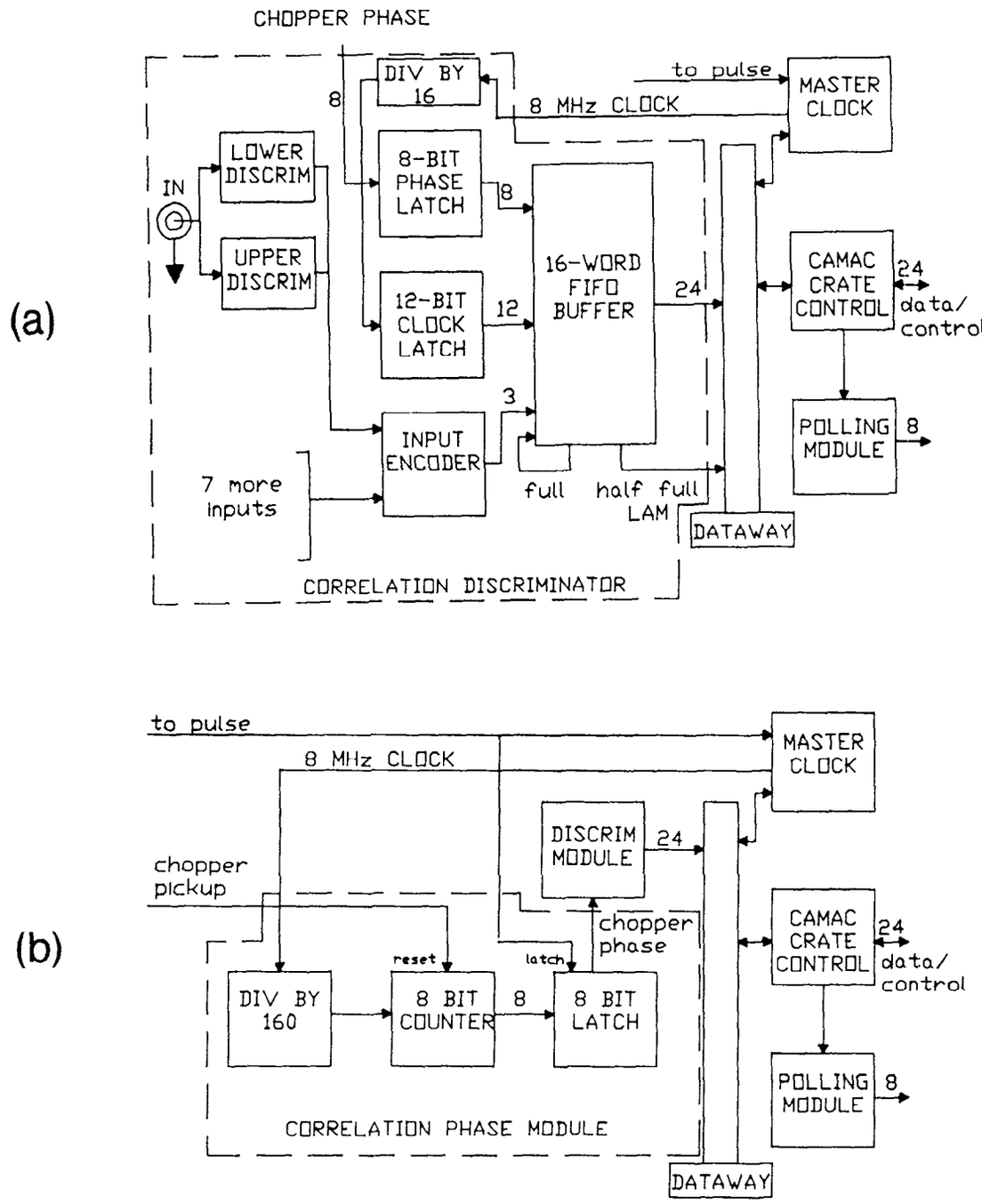

Fig. 2. Schematic diagram of the modifications to the data acquisition electronics for the correlation chopper test. (a) Modified discriminator module; (b) new module for phase encoding.

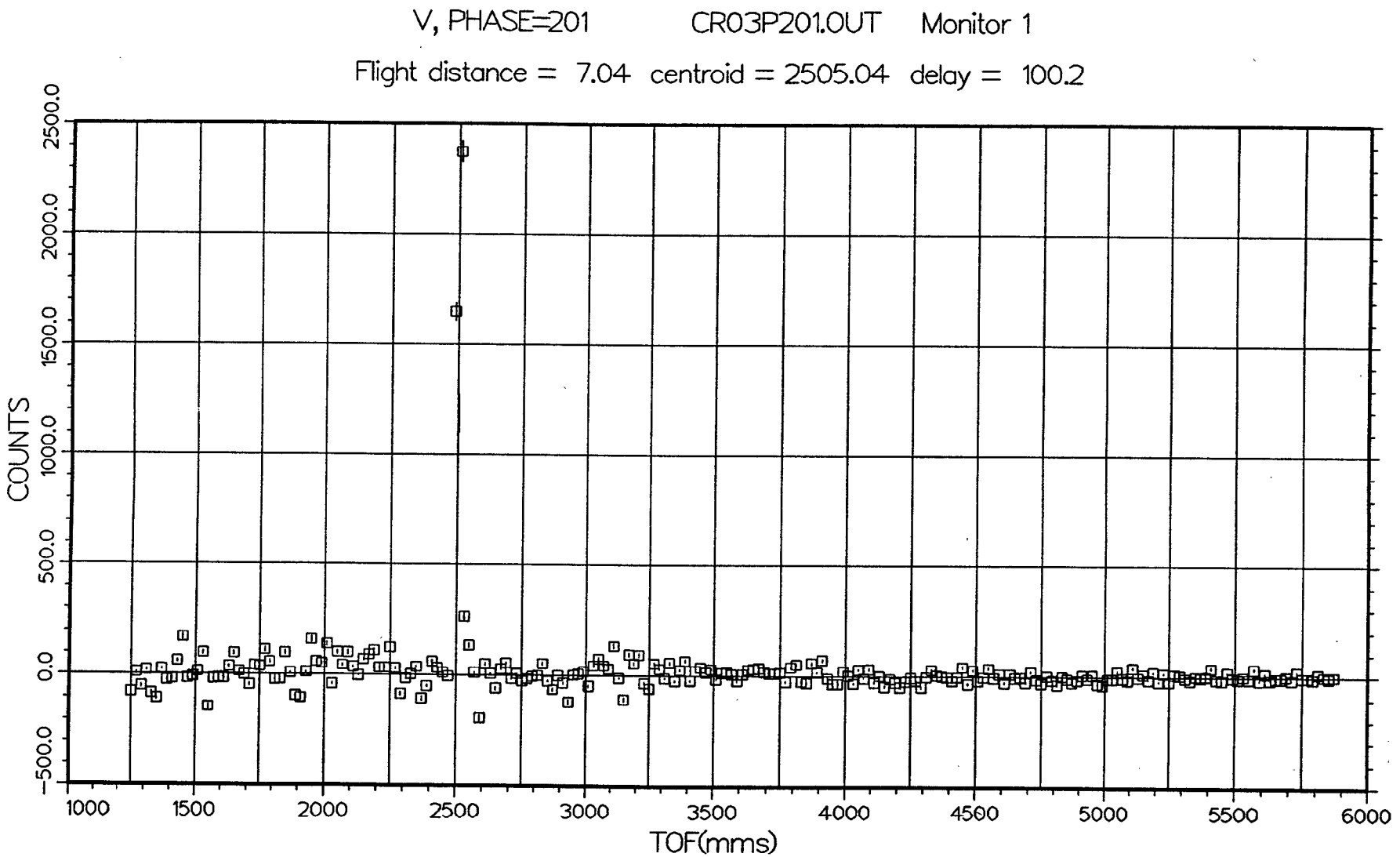

Fig. 3. Example of time-of-flight spectrum for Monitor 1 (upstream of sample), with phase i′ = 201.

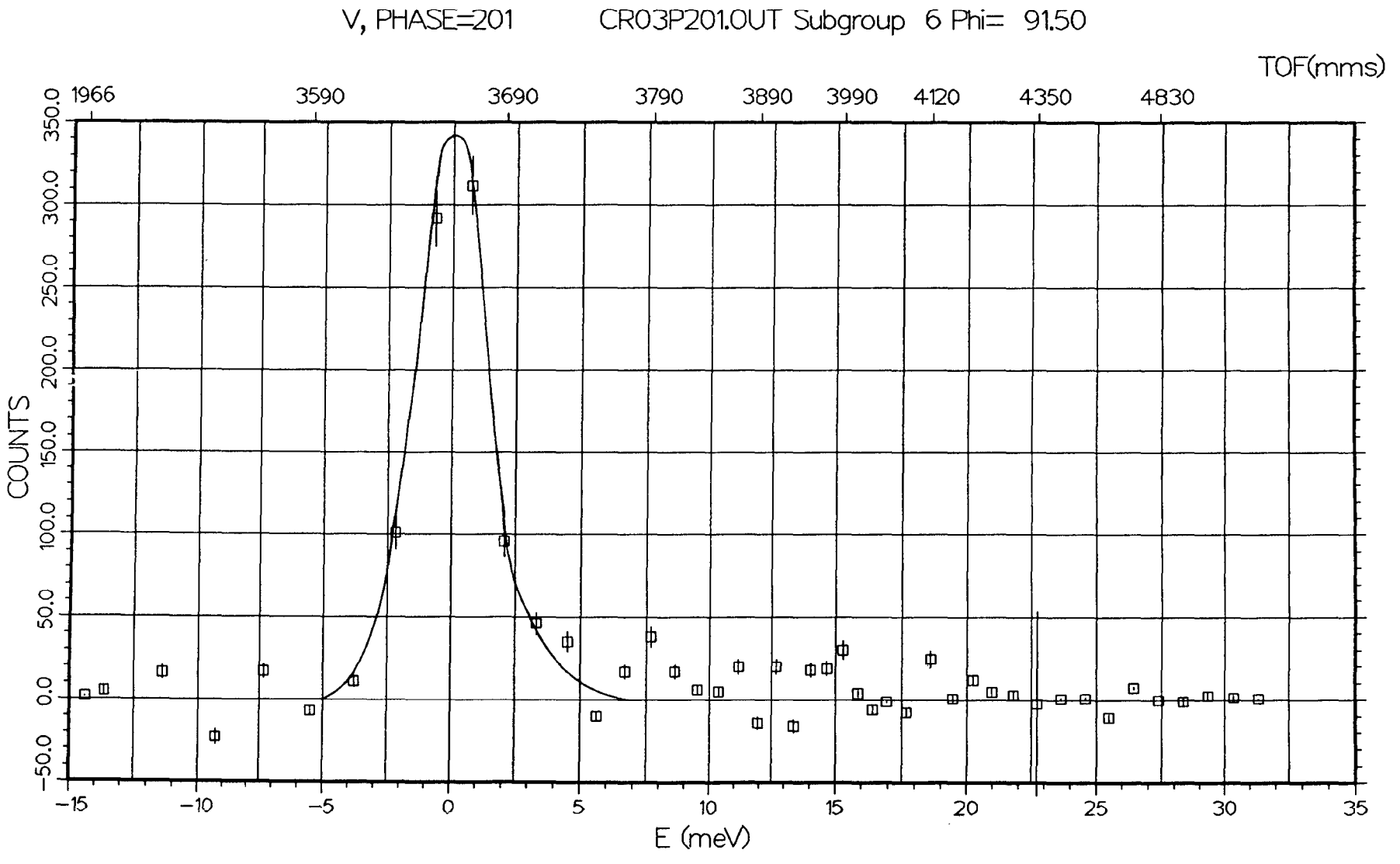

Fig. 4. Same as Fig. 3 for ^{3}He detector at ϕ = 91.5° (vanadium sample). The solid curve is a guide to the eye.

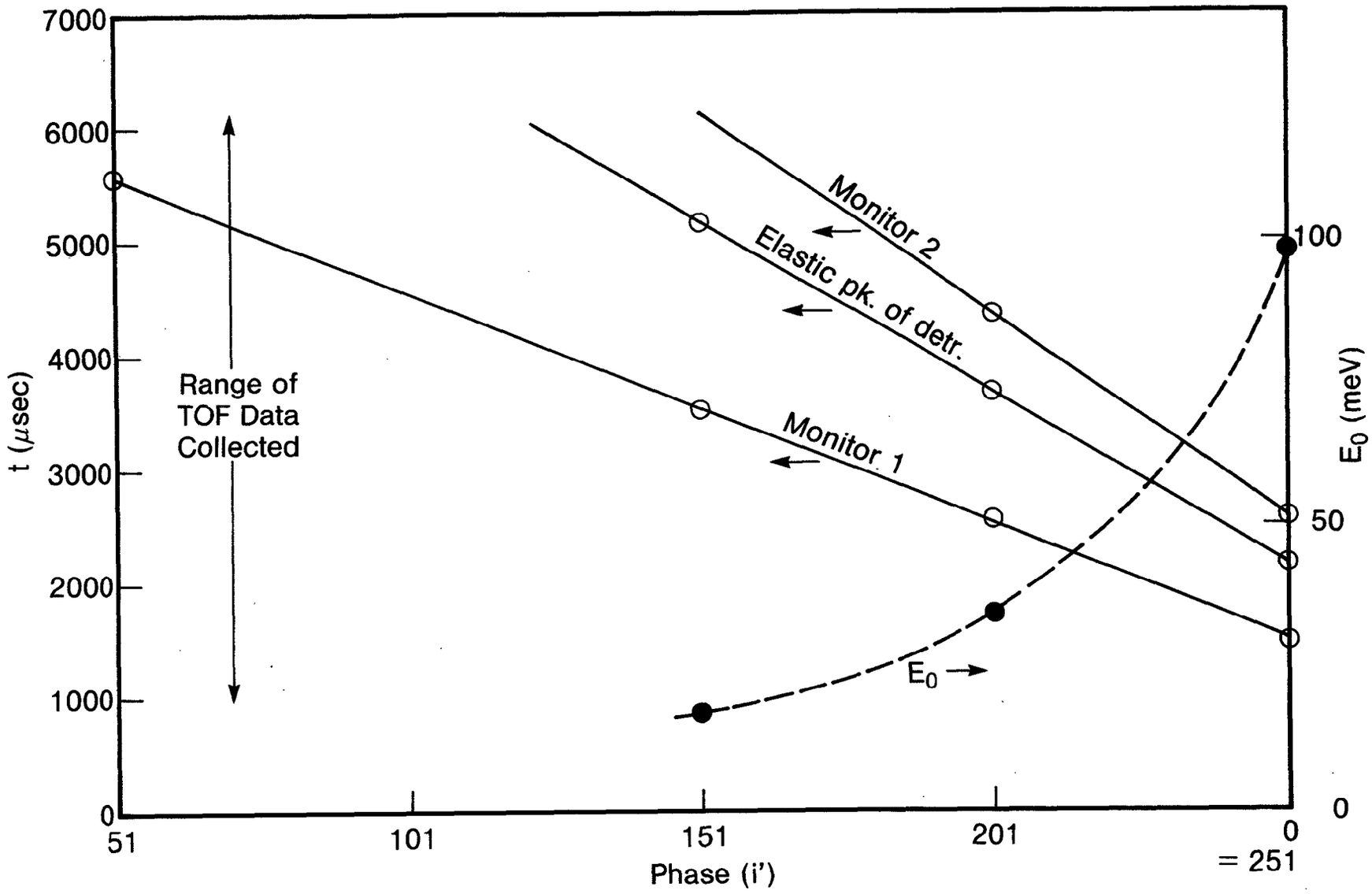

Fig. 5. Plot of some peak positions used in the cross-correlations for the monitors and detector. The lines are eyeball fits through the data: they converge to t = 0 at i' = 73.4. The dashed curve (with scale on right) shows the values of E_o calculated from the monitor peaks.

ICANS IX

INTERNATIONAL COLLABORATION ON ADVANCED NEUTRON SOURCES

22-26 September, 1986

THE NBS NEUTRON TIME OF FLIGHT SPECTROMETER

I.S. ANDERSON[1,2], T.J. UDOVIC[1], J.M. ROWE[1], J.J. RUSH[1] and J. LaROCK[1]

[1] National Bureau of Standards, Gaithersburgh MD 20899, U.S.A.

[2] Swiss Institute for Nuclear Research, CH-5234 Villigen

Introduction

A schematic outline of the new high resolution time-of-flight spectrometer which is designed for quasielastic or near elastic studies is shown in Fig. 1. This spectrometer which is presently undergoing commissioning tests is situated at a 15 cm diameter beam port at the NBS research reactor and will view the new D_2O ice cold source when installed (1). The spectrometer uses a double monochromator system followed by a simple Fermi chopper to pulse the resultant monochromatic beam. This decoupling of the monochromating and pulsing functions allows greater flexibility in optimizing the parameters of each independently. Since the instrument comprises a large detection area close to the reactor face, particular attention has been paid to proper design of the shielding of all parts of the spectrometer in order to reduce detected background. Initial optimization of the shielding allowed this background to be reduced to less than one count per minute per detector.

Monochromator

The double monochromator was chosen for several reasons:

a) the secondary monochromatic beam is removed from the primary beam thus facilitating the task of shielding against a significant fast neutron background,
b) the incoming energy may be readily selected from a continuous range without having to displace large components,
c) in cases where floor space is a constraint such as at beam positions close to a reactor face or moderator, then it is convenient to have the secondary beam parallel to the incident beam.

The effects of the second crystal on the monochromatic beam are threefold: the intensity is reduced by the peak reflectivity of the crystal; furthermore the effective mosaic spread of the system is reduced by a factor of $\sqrt{2}$ in the case of similar crystals and finally the beam divergences before the first

crystal and after the second crystal in such a system are identical for similar crystals. The reduction in the effective mosaic can be allowed for by suitable choice of crystals while the correlation of the incident and exit beam divergences precludes the need for an in-pile collimator which would be difficult to access due to radiation problems since an easily accessible exit collimator is sufficient. However the use of a collimator between the two crystals is essential to reduce multiple reflections and allow complete flexibility in the choice of the incident energy resolution. Thus for two identical collimators of full width, a, before and after the second crystal, the effective beam divergence is given by $a/\sqrt{2}$ which is independent of the crystal mosaics. Thus the resolution in energy may be chosen at will within the constraints of intensity.

At present pyrolitic graphite crystals are used with individual mosaic spreads of 40°. These are mounted on rotary tables which in turn may be translated parallel to the incident beam direction. A rotating shielding drum containing a collimator is situated between the two crystals. In normal operation the rotation of this drum is coupled to the translational movement of the crystals thereby assuring the automatic alignment of the collimator, however the drum may be turned independently to allow the collimator to be removed via a removeable plug in the monochromator shielding. The rotations of the two crystals and the collimator drum are directly coupled to vector resolvers as absolute encoders and in case of failure of these encoders a back-up system using optical switches is installed.

The incoming wavelength may be selected from a continuous range between 2.2 Å and 6.6 Å using this system. For wavelengths above 4 Å a cooled Be filter may lowered into the beam to remove neutrons from higher order reflections.

Chopper

This device is a multiple slit Fermi chopper which effectively decouples the neutron burst time from the beam parameters. The rotor consists of a hollow aluminium cylinder 7.6 cm in diameter and 12.7 cm high spinning about a vertical axis. Two slit packages are available which have slit widths of 0.0635 cm and whose curvature and lengths are optimized for 1.5 Å and 4 Å neutrons respectively. The chopper is driven by a two phase hysteresis motor at speeds ranging from 10000 to 18000 rpm depending on wavelength and frame overlap conditions. A security system monitors:

a) the current in the chopper,
b) synchronous rotation of the chopper and drive signal,
c) chopper vibration,
d) the temperature of the chopper bearings.

If an abnormal condition is sensed for any of these functions the chopper may be tripped and the data aquisition halted automatically.

Primary flight path

The chopper, second collimator and various other beam definition devices are mounted on an optical bench which allows for easy interchange of components without need for lengthy realignment. In particular the collimators may be exchanged or the positions of the collimator and chopper interchanged. Thus under normal conditions the chopper is situated as close as possible to the sample to reduce the time spread of the incident beam in which case a coarse small angle collimator positioned just inside the sample drum is used to reduce scattering from the chopper. However in cases where good beam definition is required for low angles the secondary collimator may be placed after the chopper with a resulting worsening of the energy resolution.

Sample chamber

The sample chamber which is still in the final stages of construction comprises many essential features. It consists of a cadmium lined aluminium drum with thin aluminium entrance and exit windows. The drum is designed to support a secondary vacuum such that it may be used as the outer wall of a sample cryostat thus reducing the amount of extraneous scattering material in the beam. Samples may be inserted into the drum from above by means of a removable flange mounted on a rotating high vacuum seal. This flange is coupled to a stepping motor and encoder such that the sample orientation can be easily adjusted under computer control. Thus the spectrometer can be readily used for elastic diffuse studies in single crystals. The whole drum may be also moved up and down relative to the beam in order to facilitate sample alignment.

An oscillating radial collimator whose function is to shadow the detectors from neutrons which do not originate from scattering in the immediate vicinity of the sample is placed between the sample container and the socondary flight path.

The primary flight path, sample drum and radial collimator are completely surrounded by shielding consisting of 10 cm of wax followed by 2.5 cm of boron carbide.

Secondary flight path and detection system

The secondary flight path consists of a steel vacuum chamber surrounded by shielding of 15 cm of wax followed by 2.5 cm of boron carbide on the outside and lined with 1 mm cadmium sheeting on the inside. The aluminium entrance window is bolted to the front of the flight path which in turn buts up against the sample chamber shielding. The total distance from the sample to the detectors is 2.28 m.

The detection system consists of 71, 46 cm active length, 2.5 cm diameter detectors filled with 4 atmospheres of ^3He covering the range of scattering angles between 25 degrees and 120 degrees. Similar detectors of 23 cm active lengts cover the angular range from 10 degrees to 25 degrees. The shorter de-

tectors are necessary to reduce the detector height contribution to the momentum transfer resolution at low angles. At a later stage a small angle detection system will be implemented consisting of an array of 1.2 cm diameter, 46 cm active length position sensitive detectors allowing the Debye Scherrer rings to be mapped out directly under software control.

Electronics and data acquisition system

The spectrometer is controlled by a microVax II computer directly interfaced to a Camac system. The time of flight data is accumulated in a histogramming memory system residing in the Camac and may be transferred to the computer when required by DMA transfer. The memory/Time of flight interface includes functions which allow the data to be accumulated in different memory regions a feature which is useful for real time experiments.

Summary and future developments

A summary of relevant instrumental parameters is given in Table 1. The spectrometer is in the commissioning stage and as yet no experimental data is available though some additional features are being studied. Firstly if the standard collimators are replaced by reflecting sollers it may be possible to double the intensity for a given energy resolution. Furthermore the introduction of a vertically curved graphite deflector as the second monochromator crystal can significantly increase the effective flux for small samples.

Acknowledgements

The authors wish to acknowledge the support of the technical staff at the NBS reactor.

References

1. R.S. Carter and P.A. Kopetka, NBS Technical Note 1217 (1985) 64.

Table 1: Instrument Details

Beam Size	10 cm x 1 cm
Incident Wavelength	$2.2 < \lambda$ (Å) < 6
Incident Energy	$16.9 >$ E (meV) > 2.27
Collimation	10', 20', 40'

Elastic Energy Resolution (μeV)

Wavelength Å	Collimation (min.) 40	20	10
4	140	80	50
6	30	20	18

Range of Scattering Angles	$1^\circ < 2\theta < 120^\circ$
Elastic Momentum Transfer	$0.01 < Q$ (Å^{-1}) < 4.9
Q Resolution	$\frac{\Delta Q}{Q} < 3\%$

Detectors

$120^\circ > 2\theta > 20^\circ$	4 atmospheres ^{3}He- 2.5cm diameter, 46cm active length
$25^\circ > 2\theta > 10^\circ$	4 atmospheres ^{3}He- 2.5cm diameter, 23cm active length
$10^\circ > 2\theta > 1^\circ$	1.2 cm diameter linear position sensitive 46 cm. active length

Typical Applications:

The instrument is most suited to quasielastic and low energy inelastic studies, such as -

dynamics of hydrogen in metals
diffusion in superionic conductors
spectroscopy and diffusion of adsorbed and adsorbed molecular species
dynamics of polymers and biological molecules
intercalation compounds
hydrogen bonding studies
liquid crystals
tunnelling spectroscopy
elastic diffuse scattering.

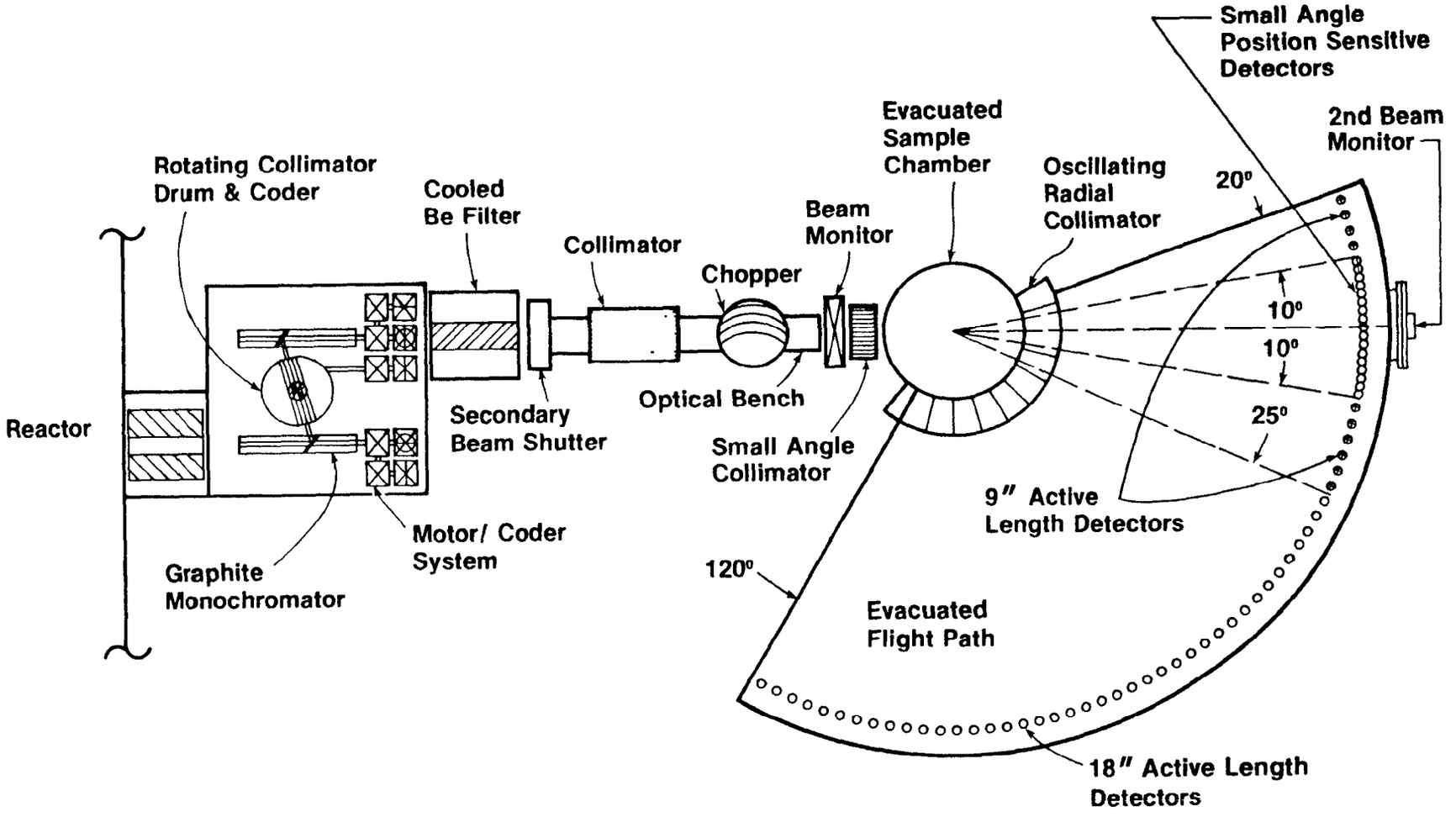

The NBS Neutron Time of Flight Spectrometer

ICANS IX

INTERNATIONAL COLLABORATION ON ADVANCED NEUTRON SOURCES

22-26 September, 1986

THE ROTATING ANALYSER CRYSTAL SPECTROMETER ROTAX

Holger Tietze and Reinhart Geick

University of Würzburg, Röntgenring 8, D-8700 Würzburg, West-Germany

Abstract

The rotating analyser crystal spectrometer (ROTAX) is an improved version of an inverted geometry TOF-X spectrometer, where the user has got the choice of different types of scans. By means of a non-uniformly rotating analyser, a flexibility of the spectrometer will be achieved which is intermediate between the crystal analyser time-of-flight spectrometers like MAX and Constant-Q and the triple axis spectrometer (TAS). In this paper we discuss the possibility of a proper constant-$\vec{Q}$ scan with ROTAX, in addition to constant-$\hbar\omega$ and constant-$\vec{Q}/|Q|$ scans.

Introduction

The instrument most commonly used for studying collective excitations in solids like phonons, magnons etc. is the triple axis spectrometer (TAS)[1-4], especially at continuous neutron sources. However, for pulsed spallation neutron sources the question arises how a spectrometer can be constructed which is adapted to the time structure of the neutron pulses and still has the same flexibility and versality as the TAS. Two different types of spectrometers have been developed so far for coherent inelastic scattering at pulsed sources, namely the multi-analyser crystal spectrometer (MAX in Japan[5] and PRISMA in UK[6] and the Constant-Q spectrometer in UK[7] and in USA[8]).

In a previous paper[9] we have outlined the basic ideas of our proposal for a new type of instrument for coherent elastic and inelastic scattering from single crystals at pulsed neutron sources. While the TAS employs two Bragg reflections, one at the monochromator and the other at the analyser, the instruments at pulsed sources considered here are time-of-flight crystal analyser spectrometers with inverted geometry. For our proposed spectrometer, we have shown[9] that its flexibility and versality is intermediate between the TAS, on one hand, and the MAX and Constant-Q spectrometer, on the other hand. That can be achieved by a non-uniform rotation of the analyser crystal which means an optimum adaption to the pulse structure of the source and a most economic use of the available neutrons (multiplex advantage). The non-uniform rotation of the analyser is, within the limits of feasibility, arbitrarily progammable according to the user's choice, e.g. constant-$\hbar\omega$ or constant-$\vec{Q}/|Q|$ scan. In order to have the same flexibility as with TAS, e.g. the proper constant-$\vec{Q}$ scan, it would be necessary to rotate non-uniformly not only the analyser but also the sample as will be shown in detail below.

Scans with ROTAX

ROTAX can be understood from the basic scattering equations, which govern the scattering triangle. For all instruments with inverted geometry at a pulsed source, the wavevector k_i and energy E_i of the incoming neutrons depend on the incident flight time t_i between moderator and sample (cf. fig. 1). Our basic approach is then to express all other quantities of the scattering process like the wavevector k_f of the scattered neutrons or the analyser Bragg angle θ_A as functions of t_i. k_f and θ_A are connected by Bragg's law

$$k_f(t_i) = \pi / d_A \sin \theta_A(t_i). \tag{1}$$

The flight time between sample and analyser is given by

$$t_a(t_i) = \frac{L_a}{v_f(t_i)} = \frac{m}{\hbar} \frac{L_a}{k_f(t_i)} \tag{2}$$

Equations (1) and (2) have to be solved simultaneously

$$\sin \theta_A(t_i) = \frac{h}{2m\, L_a\, d_A}\, t_a(t_i). \tag{3}$$

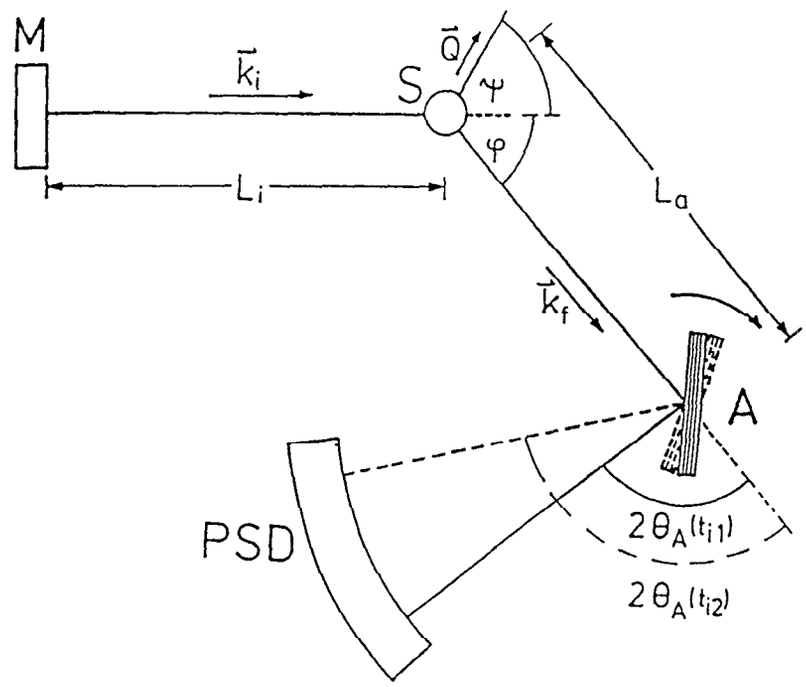

fig. 1
Schematic drawing of the rotating analyser crystal spectrometer (ROTAX); moderator (M), sample (S), analyser (A), detector (PSD).

From our previous study[9] it turned out that, in addition to the scattering angle Φ, one more scattering parameter can be chosen constant, i.e. independent of t_i. Hence, the experimenter can choose between various types of special scans, e.g. const.-$\hbar\omega$ or const.-$\vec{Q}/|Q|$ or const.-$|\vec{Q}|$ scan. In order to perform such a special scan the anaylser angle θ_A (eq. 3) has to be varied according to the appropriate function $t_a(t_i)$ depending on the type of scan. $t_a(t_i)$ can be determined from the scattering triangle, which connects k_i with k_f.

We obtain

$$t_a = L_a \left[\left(\frac{L_i}{t_i}\right)^2 - \frac{2}{m}\hbar\omega \right]^{-1/2} \tag{4a}$$

$$t_a = t_i \frac{L_a}{L_i} \frac{\sin(\psi + \phi)}{\sin\psi} \tag{4b}$$

for the const.-$\hbar\omega$ and const.-ψ scan respectively, where ψ is the sample orientation angle (cf. fig. 1) defining the direction of $\vec{Q}/|Q|$ with respect to the crystal axes of the sample. The resulting curves for the analyser setting are presented in fig. 2, from which the rotation speed can be deduced.

As obvious from eqs. (3) and (4a) the analyser rotation is almost uniform (ν = 19 Hz) for $\hbar\omega = 0$ as long as the $\sin^{-1}$-function is almost linear ($\theta_A < 30°$). For $\hbar\omega > 0$, the curves in fig. 2a exhibit an angular velocity for the analyser increasing from its starting value for t_i = 1 msec. In order to keep the angular velocity within reasonable limits the measurement and the appropriately programmed non-uniform rotation of the analyser should be terminated at about $\theta_A \approx 30°$ or for 2 msec $< t_i <$ 4 msec. For $\hbar\omega < 0$, the curves in fig. 2a show a decreasing angular velocity and the measurement can be extended, in principle, over a wider range. In all cases (const.-$\hbar\omega$ and const.-ψ), the time between the termination of the measurement (rotation of θ_A according to the curves in fig. 2) and the next neutron pulse has to be used to return the analyser back to its original position either by back-rotation or by half or full circle rotation (180° or 360°). Since the derivatives of the curves in fig. 2 correspond mostly to frequencies near to 25 Hz, a total rotation of the analyser by 180° per cycle seems to be preferable at the British spallation source ISIS with a neutron pulse repetition frequency of ν = 50 Hz.

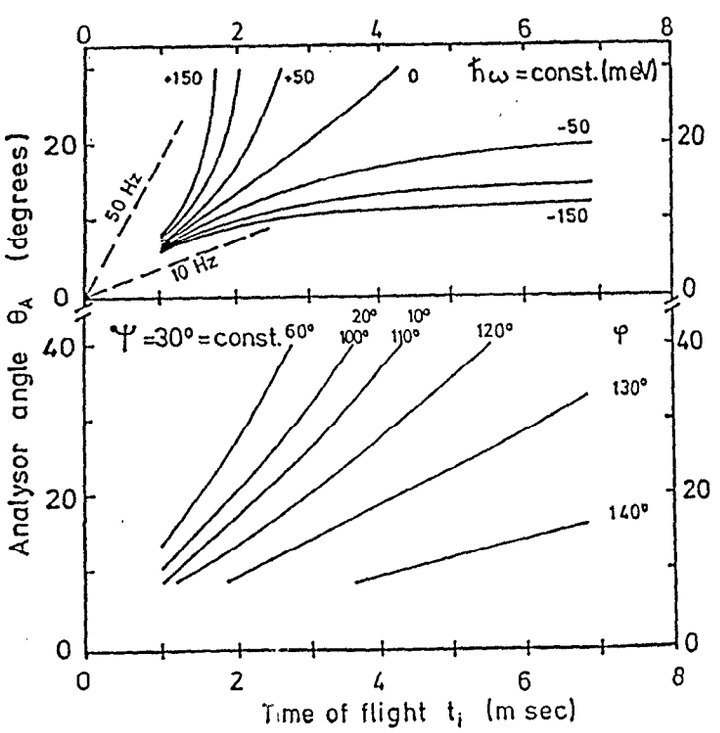

fig. 2
Analyser Bragg angle θ_A as a function of flight time t_i between moderator and sample for ROTAX. (a) const.-$\hbar\omega$ scans for various energy transfers $\hbar\omega$; (b) const.-ψ scans for ψ = 30° and for various scattering angles ϕ.

For a const.-ψ scan eq. (4b) reveals immediately that the non-uniformity of the analyser rotation is smaller in this case as compared to the const.-$\hbar\omega$ scan, where the essential non-linearity originates from the square-root in the denominator of eq. (4a). These properties are clearly demonstrated by the curves of θ_A versus t_i for ψ = const. = 30° and for various scattering angles ϕ in fig. 2b. A further difference to the case $\hbar\omega$ = const. is that θ_A depends in a non-monotonous way on $\sin(\psi+\phi)$. In fact, an angle ϕ_1 and an associated angle $\phi_2 = \pi-2\psi-\phi_1$ generate the same curve $\theta_A(t_i)$. For positive energy transfer $\hbar\omega > 0$ which means $\phi < 120°$ for ψ = 30° the derivatives of the curves in fig. 2b also correspond to frequencies between 10 and 50 Hz. That means again a preferable total rotation of the analyser of 180° per cycle. Due to the smaller non-linearity of the curves, the const.-ψ scans may be extended to analyser Bragg angles up to $\theta_A \leq 45°$ using the neutrons of a pulse arriving between 1 msec $< t_i <$ 4 msec at the sample.

As already mentioned, many other paths for the TOF scan in Q-space may be thought of. But not all of them will be feasible. An example for such a case is a TOF scan where the magnitude of Q is kept constant. For $|\vec{Q}|$=Q=const., we obtain

$$Q^2 = k_i^2 + k_f^2 - 2\, k_i\, k_f \cos\phi \,. \qquad (5)$$

The possible scattering triangles according to eq. (5) are illustrated in fig. 3. It is evident that this type of scan requires $k_i \leq Q/\sin\phi$. In general eq. (5) yields two solutions k_f^+ and k_f^-, but only values $k_f > 0$ are physically meaningful (cf. tab. 1 with the different ranges for energy loss or gain of the neutrons).

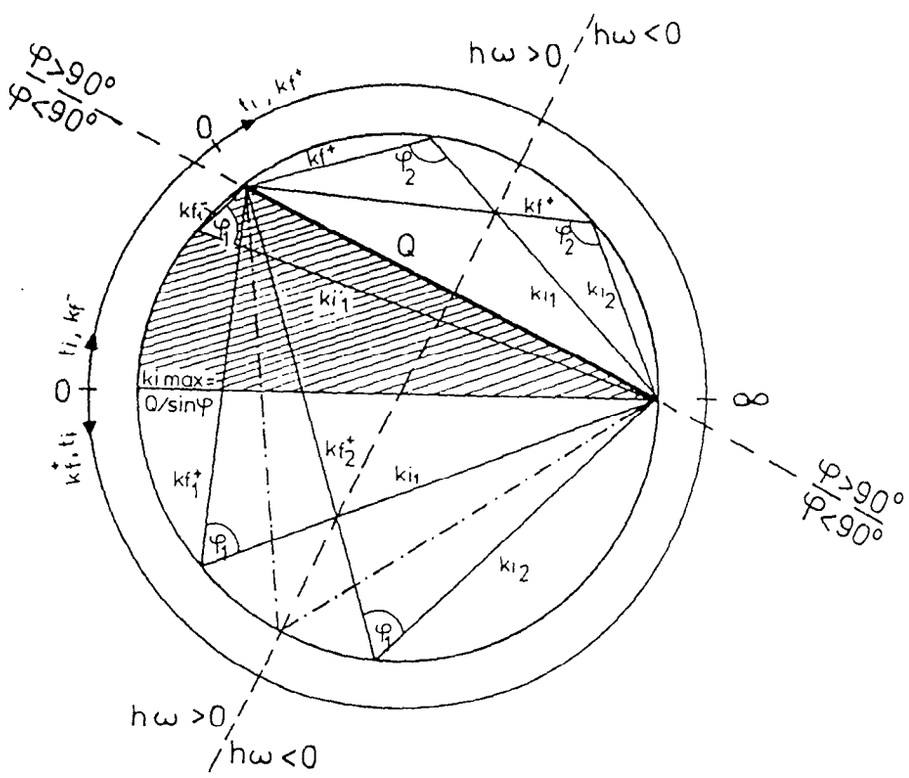

fig. 3
Scattering triangle for const.-$\vec{Q}$ scans with ROTAX. Equivalent solutions for different spectrometer configurations are illustrated for energy gain or loss of the neutrons and for the different types of solutions k_f^- (shaded area) and k_f^+ for the cases discussed in tab. 1.

Tab. 1: Solutions of eq. (5) for k_f^+ and k_f^- yielding energy gain ($\hbar\omega<0$) or energy loss ($\hbar\omega>0$) of the neutrons.

+ Solution: $k_f^+ = k_i \cos\phi + \sqrt{Q^2 - (k_i \sin\phi)^2}$

	$0 \leq \phi \leq 90°$	$90° \leq \phi \leq 180°$
$\hbar\omega \geq 0$	$\frac{Q}{2\sin(\phi/2)} \leq k_i \leq \frac{Q}{\sin\phi}$	$\frac{Q}{2\sin(\phi/2)} \leq k_i \leq Q$
$\hbar\omega \leq 0$	$0 \leq k_i \leq \frac{Q}{2\sin(\phi/2)}$	$0 \leq k_i \leq \frac{Q}{2\sin(\phi/2)}$

− Solution: $k_f^- = k_i \cos\phi - \sqrt{Q^2 - (k_i \sin\phi)^2}$

	$0 \leq \phi \leq 90°$	$90° \leq \phi \leq 180°$
$\hbar\omega \geq 0$	$Q \leq k_i \leq \frac{Q}{\sin\phi}$	———
$\hbar\omega \leq 0$	———	———

The flight time t_a between sample and analyser immediately reads

$$t_a(t_i) = L_a \left[\frac{L_i}{t_i} \cos\phi \pm \sqrt{\left(\frac{\hbar Q}{m}\right)^2 - \left(\frac{L_i \sin\phi}{t_i}\right)^2} \right]^{-1} \qquad (6)$$

and the corresponding values for θ_A are sketched in fig. 4 for $|Q| = 5\ \text{Å}^{-1} = \text{const.}$ The curves for both solutions $\theta_A(k_f^+)$ and $\theta_A(k_f^-)$ start at the common point (+) with infinite rotation speed $d\theta_A/dt_i$. For smaller values of t_i (larger values of k_i) the argument of the square-root in eq. (6) is negative. The curves for $\theta_A(k_f^+)$ show that the analyser has to be accelerated to a rather high rotation frequency and then, starting somewhat away from the common point (+), to be slowed down very rapidly until the line of zero energy transfer (second broken line in fig. 4) is reached. Then, the curves approach an asymptotic value θ_A = const. (MAX spectrometer!) similar to fig. 2a. Solution $\theta_A(k_f^-)$ shows a deceleration from the common point (+) turning to an acceleration then at very high rotation speeds. In general, the non-uniform rotation of the analyser according to this const.-$|Q|$ scan (cf. fig. 4) seems not to be feasible with the drastic deceleration of the rotation to nearly complete stop and then with the subsequent relatively high angular acceleration to complete the cycle. Only for high scattering angles $\phi \geq 120°$ the analyser rotation might be technically feasible.

It is noteworthy to look at the total time-of-flight for this type of const.-$|Q|$ scan. The total time-of-flight t_o is the time of arrival at the detector. It is obvious from eq. (5) that one possible solution is $k_i = Q$ with $k_f = 0$, not depending on ϕ. That would mean a full stop of the neutrons at the sample yielding an infinite total time-of-flight, of course. This is being illustrated in

fig. 5, where the total TOF t_o is plotted versus the incident TOF t_i for various scattering angles ϕ. Again , the common point (+) of both the solutions k_f^+, k_f^- is characterised by the minimum value of t_i. Please remark, that the slope of the curves $t_o(t_i)$ depend on the special kind of the solution k_f^+, k_f^- (cf. tab. 1). Apart from the strange properties of $t_o(t_i)$ for $\phi < 90°$, the curves for $\phi > 90°$ do not reveal an unambigous value of t_o as a function of t_i, i.e. there exist neutrons which overtake previously started neutrons of the same pulse in the secondary part of the spectrometer. For practical use the monotonous ascending branches of $t_o(t_i)$ are applicable only. Hence, the neutrons with higher energies and corresponding flight times $t_i < t_{i,min}$ have to be suppressed physically with an auxiliary chopper between moderator and sample.

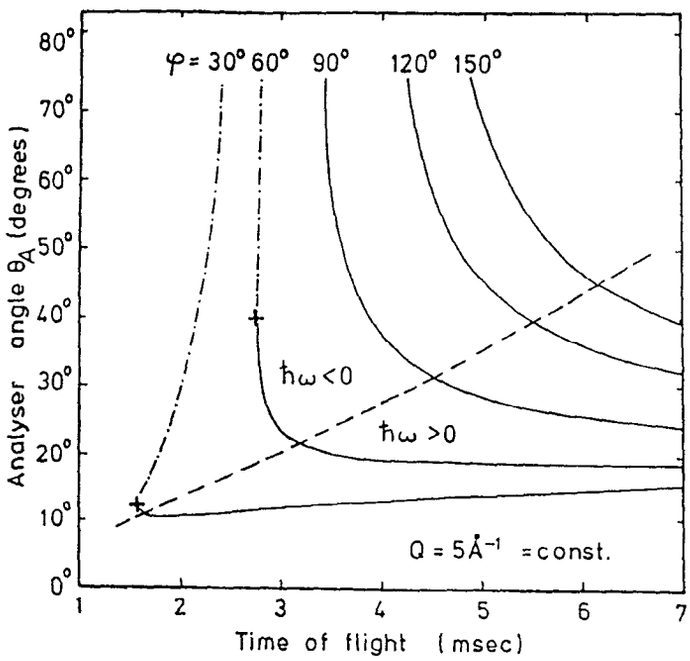

fig. 4
Analyser Bragg angle θ_A versus flight time t_i for a const.-$|Q|$ scan at various scattering angles ϕ. Both solutions for k_f^- (dash-point) and k_f^+ (solid lines) starting at their common points (+) are illustrated and the change of energy transfer is indicated (broken line).

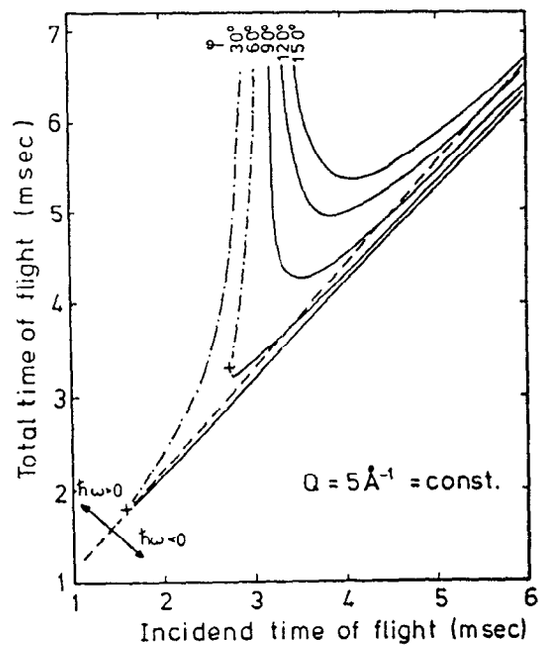

fig. 5
Total time-of-flight t_o between moderator and detector versus incident time-of-flight t_i between moderator and sample. Again dash-points denote solutions of k_f^-, solid curves solutions of k_f^+, (+) common starting points and the brocken line the change of the sign of $\hbar\omega$.

If all these limitations previously discussed are met, the const.-$|Q|$ scan can be performed as a proper const.-$\vec{Q}$ scan if also the sample is non-uniformly rotated, corresponding to

$$\mathrm{tg}\,\psi(t_i) = \frac{k_f \sin\phi}{k_i - k_f\cos\phi} = \frac{k_i \sin\phi \cos\phi \pm \sin\phi \sqrt{Q^2 - (k_i \sin\phi)^2}}{k_i \sin^2\phi \mp \cos\phi \sqrt{Q^2 - (k_i \sin\phi)^2}} . \qquad (7)$$

Eq. (7) is illustrated in fig. 6 and means that $\psi(t_i)$ varies just in such a way that the direction of $\vec{Q}$ remains constant with respect to the crystal axes of the sample during one scan (cf. fig. 3).

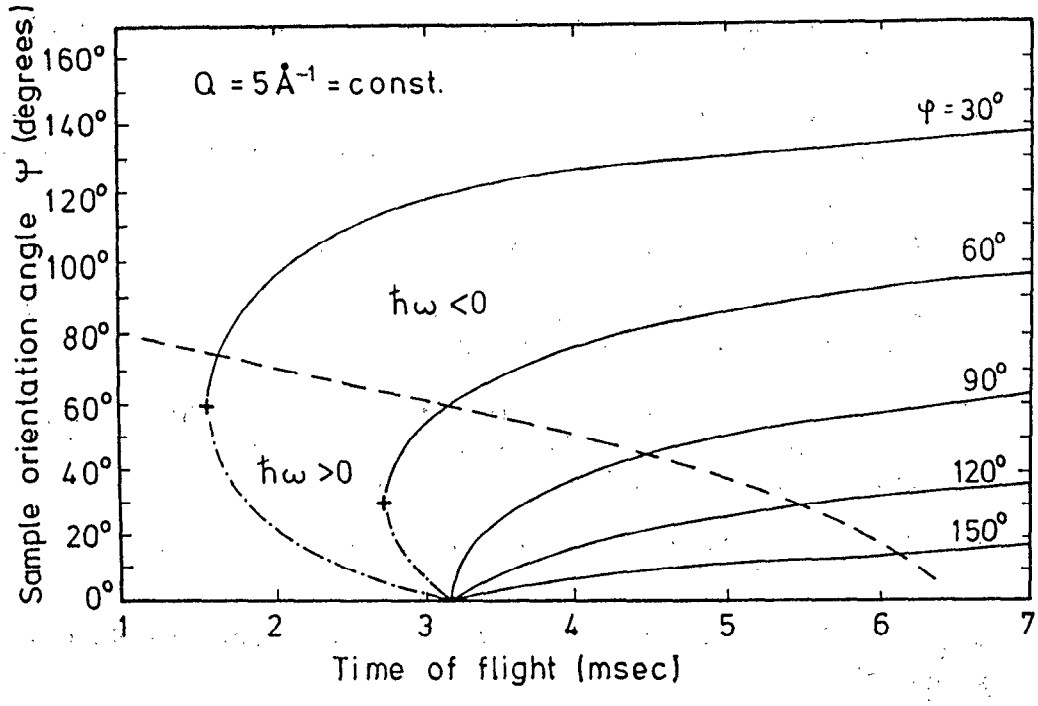

fig. 6
Sample orientation angle ψ versus incident time-of-flight t_i for various scattering angles ϕ and both solutions of k_f^- (dash-points) and k_f^+ (solid).

Conclusions

i) It has been shown, that in principle ROTAX can provide widely variable const.-$\hbar\omega$ and const.-ψ scans, as well as severely limited const.-$\vec{Q}$ scans.

ii) const.-$\hbar\omega$ and const.-ψ scans are rather easy to perform, because $t_o(t_i)$ is a monotonous function and $\theta_A(t_i)$ provides fesible values.

iii) The flexibility of ROTAX ensures that in case of phonon measurements their polarisation can be taken care of.

iv) The limitations for a proper const.-$\vec{Q}$ scan are that the sample has to be rotated non-uniformly and in phase with the pulse structure and the analyser rotation. Further, this mode of operation has to be restricted to scattering angles $\phi \lesssim 120°$, which obviously excludes measurements of magnetic excitations.

Acknowledgements

We would like to thank Dr. J. M. Carpenter (ANL) and Dr. C. G. Windsor (RAL) for valuable discussions. The financial support of the BMFT, Förderkennzeichen 03-Ge 1 Wue-6, is gratefully acknowledged.

References

[1] G. Dolling, in "Dynamical Properties of Solids", ed. by G. K. Horton and A. A. Maradudin (North Holland, Amsterdam, 1974), Vol. 1, p. 541-629.

[2] S. W. Lovesey and T. Springer (eds.): Dynamics of Solids and Liquids by Neutron Scattering, Topics in Current Physics, Vol. 3 (Springer, Berlin-Heidelberg-New York, 1977).

[3] B. Dorner: Coherent Inelastic Neutron Scattering in Lattice Dynamics, Springer Tracts in Modern Physics, Vol. 93 (Springer, Berlin-Heidelberg-New York, 1982).

[4] R. Pynn, Rev. Sci. Instr. 55 (1984) 837.

[5] K. Tajima, Y. Ishikawa, K. Kanai, C. G. Windsor and S. Tomiyoshi, Nucl. Instr. and Meth. 201 (1982) 491

[6] C. Andreani, F. Cilloco, C. Petrillo, F. Sacchetti and C. G. Windsor, Rapporto Interno 1985/4 dell'Instituto di Struttura della Materia del CNR, Frascati (Italia), and priv. commun.

[7] C. G. Windsor, R. K. Heenan, B. Boland and D. Mildner, Nucl. Instr. and Meth. 151 (1978) 477

[8] R. A. Robinson, R. Pynn and J. Eckert, subm. to Nucl. Instr. and Meth. (1985).

[9] R. Geick and H. Tietze, Nucl. Instr. and Meth. A 249 (1986) 325.

ICANS IX

INTERNATIONAL COLLABORATION ON ADVANCED NEUTRON SOURCES

22-26 September, 1986

THE IPNS RESONANCE DETECTOR SPECTROMETER*

R. K. Crawford
Argonne National Laboratory
Argonne Illinois, 60439 USA

1. INTRODUCTION

A pulsed spallation neutron source produces large quantities of neutrons with energies in the range of 1-10 eV. Time-of-flight measurements based on the pulsed nature of the source provide the basis for one energy analysis involving these neutrons, but to do spectroscopy with such neutrons a second energy analysis is required. Traditional methods such as neutron choppers or crystal Bragg reflection do not work well for such high energy neutrons, so new techniques will have to be developed if these neutrons are to be exploited for spectroscopy.

One promising technique is to make use of nuclear resonance absorption of the neutrons. A number of materials have sharp resonances, and these can be used to provide one of the energy analyses required. Resonance absorption in thin foils of absorber material can be used in either of two ways. In the first method (resonance filter method), the foil is placed in the incident or scattered beam and the resulting scattering spectrum from the sample is measured. These measurements are then repeated with the foil removed from the beam, and the results of the first measurement are subtracted from the results of the second measurement to provide a "difference" spectrum which corresponds to having only neutrons of the resonance energy in the beasm in which the foil was placed. In the second method (resonance detector method), the foil is placed in the scattered neutron beam and scattered neutrons having the resonance energy are detected "directly" by detecting the capture gammas resulting from the resonance absorption of the neutrons. The resonance filter technique has been reviewed elsewhere[1], and will not be discussed further here.

*Work supported by the U.S. Department of Energy

A prototype resonance detector spectrometer called the Electron Volt Spectrometer (EVS) has been built and operated at IPNS to gain experience with the technical problems involved in such spectrometry. One of the primary scientific reasons for using such high energy neutrons is to satisfy the kinematic requirements for measurements involving large energy transfers and small momentum transfers, such as are important in the study of magnetic phenomena. In addition to requiring large neutron energies, such measurements also dictate that the scattering angles be small. For this reason the EVS has focussed on scattering at small angles to date. [Some tests have also been made using larger scattering angles (up to 45°) for momentum distribution measurements. These have shown some promise, but are only in a preliminary stage and will not be discussed here.] In the following sections, this instrument will be described, the current understanding of the background in the instrument will be discussed, software developed to simulate the detector efficiency will be described and compared with experimental results, and a test of the use of foil-thickness difference techniques to improve resolution will be presented.

2. DESCRIPTION OF INSTRUMENT

The EVS is a "resonance detector" spectrometer, which operates by detecting promptly-emitted gamma rays resulting from resonant absorption of scattered neutrons in thin absorbers. Closely-coupled gamma ray detectors register the gamma rays, and a computer sorts the resulting pulses according to incident neutron time-of-flight. When a narrow nuclear resonance is used, this resonant capture defines the scattered neutron energy to a fixed value $E_f = E_R$ within the (practical, doppler-broadened) width of the resonance. The time-of-flight t in this spectrometer scans the scattering probability as a function of the incident energy E_i according to

$$\begin{aligned} E_i(t) &= (m/2)\,[L_i/(t - t_f)]^2 \\ E(t) &= E_i(t) - E_R \\ t_f &= L_f(m/2E_R)^{1/2} = \text{constant} \end{aligned} \tag{2.1}$$

where m is the neutron mass and L_i and L_f are the lengths of the incident and scattered neutron flight paths. Several discussions of instruments of this type have appeared in the literature[1-7].

Figure 1 shows the actual configuration of the EVS at IPNS, and Table I gives some of the parameters of this spectrometer. Two different detector geometries for small scattering angles have been used on the EVS, a closely-coupled poorly-shielded geometry (called configuration 1 throughout this paper) and a loosely-coupled well-shielded geometry (called configuration 2 throughout this paper. These are indicated in Table I and are shown respectively in Figs. 2 and 3. The kinematic range of the spectrometer for these small scattering angles is indicated in Fig. 4.

The EVS was designed to detect the gammas from the resonance foil with several separate scintillation detectors, to test the possibility of using gamma coincidence detection techniques to reduce the effects of the inescapable gamma background present. In most tests to date, 8 separate scintillation detectors were used. The data collection system allows the simultaneous collection of events from the individual scintillators ("singles" events), as well as collection of events corresponding to a coincidence (within ~0.5 μsec) between two or more individual scintillator events. A pulse-height analyzer is used to tune the gains on the amplifiers for the individual scintillators and to set the pulse-height discrimination window for each scintillator to correspond to the desired gamma energy window.

3. COLLIMATION AND BACKGROUND

3.1 Collimation

The collimation system for the EVS consists of a series of collimation elements made of lead shot and borax cast in epoxy resin (sufficient resin to fill all voids between the lead shot), alternating with B_4C cast in epoxy resin (minimal resin content). According to Table I, the unscattered neutron beam at the foil position had a penumbra diameter of 3.75 cm and an umbra diameter of 1.84 cm. The inside diameter of the resonance foil was 5.08 cm. With no scattering sample, there was no evidence of a peak at any of the Ta resonances up to 30 eV, which was the extent of the measuring range normally used. Movement of the foil off center indicated a "sharp" beam edge where the resonance peaks suddenly began to be observed. This coincided roughly with the first interception of any part of the foil with a beam penumbra of this calculated diameter. Thus the beam in the EVS has very "clean" edges, indicating that the collimation is quite good, at least at energies up to 30 eV.

3.2 Background - Coincidence Effects

For a random singles background count rate of I_{1B} counts/sec/one-μsec channel, the expected count rate using 2-fold coincidence among 8 scintillators should be reduced to

$$I_{2B} = \left(\frac{N-1}{N}\right) I_{1B}^2 \left(\frac{\tau}{r\ \Delta t}\right) \tag{3.1}$$

where τ is the allowed coincidence time window in sec, r is the pulsed source repetition rate, and Δt is the channel width (1 μsec here). Figure 5 shows "singles" (sum of events from the 8 individual scintillators) and coincidence spectra for a typical run with the detector in configuration 1 and with a polyethylene sample. For this run the singles background count rate (in 8 scintillators) was 9.0×10^{-3} counts/sec/one-μsec channel. Based on this argument (with $\tau = 0.5 \times 10^{-6}$ sec, $\Delta t = 1 \times 10^{-6}$ sec, and r = 30 Hz) the coincidence background should have been reduced to 1.2×10^{-6} counts/sec/one-μsec channel, while the measured coincidence background was 7.5×10^{-5} counts/sec/one-μsec channel. The signal-to-background ratio (signal is taken as peak height minus background level) in this singles spectrum is ~2.5, while in the coincidence spectrum it is ~12. Thus, although the signal-to-background ratio was significantly improved by using the coincidence technique, the improvement was not nearly so much as might have been expected based on an uncorrelated gamma background.

A possible explanation is that there must be one or more sources of correlated (two or more gammas produced essentially simultaneously) gammas fairly near to the detector. To a good approximation for such a source placed some distance from the N detecting scintillators, the probability of single gamma detection is

$$P_{1B} \simeq N\ \nu_B\ \varepsilon_B \tag{3.2}$$

where ε_B is the solid angle subtended at this source by a single scintillator, divided by 4π, and ν_B is the average number of coincident gammas produced by this source. Similarly, the probability of 2-fold coincidence among the N scintillators is approximately

$$P_{2B} \simeq [N(N-1)/2]\ \nu_B\ (\nu_B-1)\ \varepsilon_B^{\ 2} \tag{3.3}$$

(Eqs. 3.2 and 3.3 are simplified versions of Eq. 4.10 below, with ε small and m = k.) Based on this argument the ratio of background counts between the singles and coincidence spectra in Fig. 5 could be accounted for if all

the background were due to a source producing an average of two gammas in coincidence at a distance of about 50 cm from the detector. Of course this is only a rough estimate of the actual distance to the correlated source or sources, since not all of the singles or coincidence backgrounds need necessarily come from such correlated sources.

Likely candidates for such a source are readily apparant in Fig. 1, namely the neutron scattering sample and the collimator just upstream from it, as well as the chamber walls and shielding aperatures around the beam between the sample and detector. All materials have some cross-section for neutron absorption, and some of these absorptions will lead to capture gamma production just as does the resonance absorption in the detector foil. In addition, neutrons scattered in all directions by the sample or collimator may be absorbed in any nearby materials, producing similar results. In this "close-coupling" geometry of configuration 1 (see Fig. 2), the scintillators have a straight "line-of-sight" to the sample, and it is not possible to place any significant gamma absorber in this path without introducing intolerable attenuation of the scattered neutrons we wish to detect. For this reason, the "well-shielded" configuration 2 geometry shown in Fig. 3 was considered. This arrangement makes use of the same resonant foil and the same bismuth germanate (BGO) scintillator crystals used in the first geometry, but moves the scintillators to well-shielded locations around the periphery of the foil. As a consequence, the scintillators subtend smaller solid angles for detecting gamma events in the foil, reducing the overall detection efficiency of the detection system.

Figure 6 shows singles and coincidence spectra from this same polyethylene sample, this time collected with the detector in configuration 2. For this run the singles background count rate was 6.0×10^{-4} counts/sec/one-μsec channel and the coincidence background was 5.0×10^{-6} counts/sec/one-μsec channel. The signal-to-background ratio in this singles spectrum is ~17.5, while in the coincidence spectrum it is ~25. Based on the above analysis, the coincidence background for a random gamma flux in this case should have been 5.3×10^{-9} counts/sec/one-μsec channel. Thus the new configuration significantly reduced the background and improved the signal-to-background ratio, but the remaining background is even more highly correlated than was the background in configuration 1. The sources of this background are discussed further in Section 3.3 below.

Figure 7 shows the singles spectrum for a vanadium sample with the detector in configuration 2. In this case where the sample scattering is much weaker and is not peaked in the forward direction as it is for scattering from hydrogen, and where the sample absorption is strong, the signal-to-background ratio is much worse. The background in the singles spectrum for this sample is 5.3×10^{-4} counts/sec/one-μsec channel, and the singles signal-to-background ratio is ~3.7. Due to the much lower scattering power, it was not possible to get coincidence data for this sample in a reasonable measurement period.

3.3 Background - Filter Measurements

A series of runs were made in configuration 1 and configuration 2 with lead, iron, and beryllium filters in the beam upstream from the sample. These filter materials were chosen to provide transmissions which would discriminate between gammas, high energy neutrons, and low energy neutrons in the incident beam, in an attempt to pinpoint the source of the measured background. For each type of filter material, a "transmission" was calculated based on the measured beam monitor data, according to the expression

$$\text{Transmission} = \frac{\text{Bkgnd with Filter} - \text{Bkgnd with Gate-closed}}{\text{Bkgnd with No-filter} - \text{Bkgnd with Gate-closed}} \qquad (3.4)$$

where data from all runs has been normalized on the same basis (pulses, or pulses combined with beam current). A similar "transmission" was calculated using the measured singles data both with and without a polyethylene sample in the beam for both configurations, and for configuration 2 with a vanadium sample as well. The results of these "transmission" measurements can be accounted for by assuming the background is made up of the following components:

A. A background component due to ~ 4 MeV gammas coming down the beam and interacting with something other than the sample.

B. A background component due to ~ 4 MeV gammas coming down the beam and interacting with the sample.

C. A background component due to ~ 100 keV neutrons coming down the beam and interacting with something other than the sample.

D. A background component due to ~ 100 keV neutrons coming down the beam and interacting with the sample.

E. A background component due to non-beam sources.

Using this 5-component model to compare the measured "transmission" data with the expected transmissions of these filter materials for neutrons[8] and gammas[9] of various energies, it was possible to calculate the relative magnitudes of each of these components in the background for each detector configuration. These results are shown in Table II. Table II shows a factor of about 20 reduction in most of the background components in going from configuration 1 to configuration 2. Component A was reduced much more, however (at least a factor of 1000). This Table shows that for flight times around 350 μsec the overall reduction in the background was roughly a factor of 20, but that at times around 100 μsec the reduction was much greater. These considerations seem to indicate that while some of component A was present at the longer times, most of component A was concentrated at the shorter times. Thus while Table III shows a "total" background reduction factor of 33 between the two configurations, the background in the region of interest around 300-400 μsec was reduced by only a factor of about 20.

4. CALCULATED AND MEASURED DETECTOR EFFICIENCY

4.1 Calculation of Detector Efficiency

The neutron detection process in a resonance detection system such as that on the EVS has four major components. These are:

1) resonant absorption of the neutron in the resonance foil

2) production of prompt gamma cascades by decay of the compound nucleus formed in step 1)

3) interception of one or more of these gammas by individual scintillators around the resonance foil

4) detection of these gammas by the scintillator detector systems

In order to understand the performance of the various prototype detector geometries well enough to design an improved detector system, software has been developed to simulate each of these independently, as well as to look at the combination of components 2) and 4). Although the four components are not all strictly independent (eg - the number of gammas formed in a cascade is correlated with their energies, leading to a correlation of the number of gammas with their detection probabilities in the scintillators), only the correlations between components 2) and 4) are sufficiently strong to require their simultaneous treatment. When it comes to predicting the

performance of different detector configurations, separate approximate treatment of the effects involved in each process is much more illuminating than would be a more accurate calculation in which all effects are treated together to allow for correlations. Therefore, the software packages for the various processes have been kept separate so far, rather than combining them into a single package. The various processes are discussed below.

4.2 Resonant Absorption of Neutrons

The resonance absorption cross-section σ'_{abs} for neutrons in the center-of-mass system is described by the Breit-Wigner formula[10,11]

$$\sigma'_{abs} = (h^2/8\pi mE')\, g_J \frac{\Gamma_n \Gamma_r}{(E'-E_R)^2 + (\Gamma/2)^2} \tag{4.1}$$

$$\Gamma = \Gamma_n + \Gamma_r \tag{4.2}$$

where h is Planck's constant, Γ_n, Γ_r, and Γ are the neutron width, the radiative capture width, and the total width of the resonance centered at the center-of-mass energy E_R, g_J is a statistical spin factor, and E' is the energy of relative motion of the neutron and target nucleus in the center-of-mass system.

In any real resonant absorber, the cross-section σ_{abs} in the laboratory system depends also on the motion of the resonantly absorbing nuclei, so the cross-section expression given above must be modified to account for this "doppler broadening". It can be shown[11,12] that a reasonably accurate treatment is to take the effective cross-section in the laboratory to be the center-of-mass cross-section given by Eq. 4.1 convoluted with a gaussian of standard deviation $\Delta/\sqrt{2}$, where

$$\Delta = (4mEkT^*/M)^{1/2} \tag{4.3}$$

with E the neutron energy in the laboratory, M the mass of the target nucleus, and

$$kT^* \simeq (3k\theta_D/8)\coth(3\theta_D/8T) \tag{4.4}$$

(The approximation 4.4 is justified only for high temperatures[11], but in fact it is quite a good approximation throughout the temperature range.)

The program FOIL accepts input parameters for one or more resonance foils and for one or more resonances per foil. From these it calculates T^*

using Eq 4.4, Δ using Eq. 4.3, and numerically performs the gaussian convolution with Eq. 4.1 to get σ_{abs}. It also calculates the absorption probability $p_A(E)$ for the foil according to

$$p_A(E) = 1 - e^{-\sigma_{abs}(E)\, d} \tag{4.5}$$

where d is the foil thickness in units of absorbing nuclei per cm^2. Figure 8 shows calculated absorption probabilities for the 4280 meV Ta resonance for three different thicknesses of foil, based on the known resonance parameters[13] and other data for Ta metal at 300 K. In this figure one can clearly see the strong wings due to the intrinsic Lorentzian shape of the resonance line (doppler effects produce significant modifications only near the peak). These wings are significant at energies of several hundred meV away from the resonance peak, and will lead to difficulty in measuring weak inelastic peaks at energy transfers below about 500 meV when the Ta (or any other) resonance is used in a resonance detector spectrometer.

4.3 Production of Gamma Cascades

When a slow neutron is absorbed by a heavy nucleus of mass A, an excited nucleus of mass A+1, sometimes called a compound nucleus, is formed. This nucleus has an energy which is an amount U_o above the ground state, where U_o is the binding energy of the neutron in the compound nucleus. For most heavy nuclei, U_o is about 6-7 MeV. For the nuclei of interest, the dominant method of de-excitation of this excited nucleus is by prompt gamma decay. Depending upon the selection rules for the particular compound nucleus, the initial decay may be directly to the ground state of the nucleus, or to any of a large number of excited states of this nucleus. If the decay is to a lower-energy excited state, this state usually can itself decay via prompt gamma emission. The net result of such a neutron capture is then a cascade of prompt gammas[14], occurring within about 10^{-14} sec, with the total energy of these gammas adding up to the initial excitation energy U_o.

The statistical model of cascade gamma production was first formulated by Blatt and Weisskopf[10], and has been used by a number of authors[15-18] to calculate gamma spectra of heavy nuclei. In this model, the nuclear energy levels are assumed to be distributed continuously according to a "statistical" distribution. The derivations and assumptions involved in the various uses of this model were summarized by Lynn[11], who also reviewed some

of the efforts to fit the experimental spectra using this model. The program GAMMA incorporates a "Monte Carlo" computational scheme based on the statistical model to generate gamma cascades between the energy U_0 and the ground state. Figure 9 shows a cascade gamma spectrum calaulated using this statistical model Monte Carlo approach with the "best" choice of the one adjustable parameter in the model. Also shown is an experimental measurement[19] of the cascade gamma spectrum for Ta. As seen in Fig. 9, the calculated curves reproduce the experimental spectrum quite well for gamma energies above about 0.8 MeV. The calculations start to diverge from the experimental data at lower energies, which is where the statistical theory is expected to break down. For gamma energies above about 0.8 MeV, the statistical model appears to be a fairly good model of the actual cascade process in Ta.

The program GAMMA also calculates the probability f_ν of having a given number ν of gammas with energies within a selected window in a cascade, and this is tabulated in Table III. The quantity f_ν is strongly dependent on the energy window used for gamma selection. However f_ν is not strongly dependent on details of the level densities assumed in the model, so at least for gamma energy windows with lower limits above about 0.8 MeV the program GAMMA should give fairly good values for f_ν. (Note that the average total number of gammas per cascade in Table III comes out to be about 4, also in good agreement with earlier statements[6].)

4.4 Gamma Detection in Scintillator Crystals

The pulse height of the output pulse from the photomultiplier-preamp combination coupled to a scintillator is proportional to the light output by the scintillator (assuming good optical coupling), and this in turn is proportional to the energy deposited in the scintillator. Thus pulse-height discrimination on the output pulses can be used as a means of selecting only those events resulting in energy deposition values within a preselected range. The net undisturbed transmission of gamma rays of energy E through a thickness d of a material is given by[20]

$$I(E) = I_0(E)\, e^{-\mu(E)d} \tag{4.6}$$

where the total linear attenuation coefficient $\mu(E)$ is given by

$$\mu(E) = \sum_i n_i [\sigma_{ph}(E) + \sigma_c(E) + \sigma_{pp}(E)]_i$$

$$= \mu_{ph}(E) + \mu_c(E) + \mu_{pp}(E) \quad (4.7)$$

Here $\sigma_{ph}(E)$, $\sigma_c(E)$, and $\sigma_{pp}(E)$ are the atomic cross-sections for photoelectric absorption, compton scattering, and pair production for gammas of energy E in atoms of type i, and n_i is the number density of atoms of type i in the material.

A Monte Carlo routine SCNTDET has been developed to follow a gamma along its path in a scintillator until it and/or all lower energy gammas produced in the scintillator either deposit all their energy or leave the scintillator. In the process, this program keeps track of the energy deposited. The program contains detailed cross-section information for the various gamma-interaction processes[21], which is used to determine the point and type of interaction of a gamma within the scintillator according to the probability distribution given by Eqs. 4.6 and 4.7. This program has been tested against published pulse-height data[22] for NaI scintillators in specific geometries, with good agreement.

Table IV shows data generated by the program GAMMA, similar to the data in Table III. However, in Table IV, the routine SCNTDET has been used within GAMMA to select only those gammas which would be detected by 2.5 cm diameter by 2.5 cm long BGO scintillators in configurations similar to those encountered in detector configuration 2 (gamma source on cylinder side at midplane, 4.3 cm from cylinder center). Comparison of Tables III and IV shows an enormous difference in the probability distributions f_ν for production and f_ν' for detection (with pulse-height discrimination) of ν gammas. A large number of the gammas are missed by the detector because they deposit less than their full energy in the scintillator. This points out that an obvious improvement in the detector system would be to use larger scintillators to improve the probability of interaction of both the primary gamma from the resonance foil and of the secondary gammas (compton scattering or electron-positron anihilation) produced within the scintillator.

4.5 The Effects of Discrete Gamma Detectors - Coincidence Probabilities

As discussed above, a single neutron capture results in the production of several gammas of varying energies, and for present purposes these can be regarded as being produced simultaneously with no angular correlation among

them. If ν detectable (ie - will be detected if they are directed toward a scintillator) gammas are produced within the detector energy acceptance window in such an event, then the evaluation of $P(\nu,k)$, which is the probability that k or more of these gammas will impinge upon exactly k separate scintillation detectors, is just a counting problem. If ε_i is the fraction of the total solid angle subtended by the ith scintillator at the gamma-producing event, and there are N scintillators, then

$$P(\nu,k) = \sum_{m=k}^{\nu} P_m(\nu,k) \tag{4.8}$$

where $P_m(\nu,k)$ is the probability that exactly m gammas will impinge on exactly k scintillators under these conditions. Evaluation of $P_m(\nu,k)$ gives

$$P_m(\nu,k) = C_m^{\nu} \left(1 - \sum_{j=1}^{N} \varepsilon_j\right)^{\nu-m} \left[\sum_{l_1=0}^{m}{}' \cdots \sum_{l_N=0}^{m}{}' \varepsilon_1^{l_1} \varepsilon_2^{l_2} \cdots \varepsilon_N^{l_N} T_{ml} \right] \tag{4.9}$$

where

$C_m^{\nu} = \dfrac{\nu!}{m!(\nu-m)!}$	is the number of ways m gammas can be selected from ν total
$(1 = \sum_{j=1}^{N} \varepsilon_j)^{\nu-m}$	is the probability that ν-m gammas are not detected
$[\sum_{l_1=0}^{m}{}' \cdots \sum_{l_N=0}^{m}{}' \varepsilon_1^{l_1} \cdots \varepsilon_N^{l_N} T_{ml}]$	is the probability of detecting the remaining m gammas in exactly k scintillators with at least one in each of the k scintillators
$\sum_{l_1=0}^{m}{}' \cdots \sum_{l_N=0}^{m}{}'$	sums are constrained so that $\sum_{i=1}^{N} l_i = m$ and exactly k of the l_i are non-zero
$T_{ml} = \dfrac{m!}{l_1! l_2! \cdots l_N!}$	is the number of ways the m gammas can be arranged in the N scintillators with a particular set of occupation numbers $\{l_i\}$

For a special case, namely all ε_i the same, Eqs. 4.8 and 4.9 reduce to the simplified form given by Muradyan[23]

$$P'(\nu,k) = \sum_{m=k}^{\nu} C_m^{\nu} (1-N\varepsilon)^{\nu-m} \varepsilon^m C_k^N \left[k^m + \sum_{t=1}^{k-1} C_t^k t^m (-1)^{k-t}\right] \tag{4.10}$$

In practice, if ε is small only the term $m = k$ is significant. Although this special case is almost never exactly satisfied, this simplified form is quite useful for estimating the magnitude of effect which will result from changing the detector geometry[6].

The actual probability of detecting a gamma in at least one scintillator ("singles" probability) when a neutron is absorbed in the resonance foil is

$$P_1 = \sum_{\nu=1}^{\nu_{max}} \sum_{k=1}^{\nu} \langle P(\nu,k)\rangle f_\nu' = \sum_{\nu=1}^{\nu_{max}} P_{1\nu} \tag{4.11}$$

where < > means average over all possible event positions within the resonant foil, and f_ν is the fraction of neutron absorptions which result in exactly ν detectable gammas with energies within the acceptance window for the scintillation detectors. Similarly, the probability of detecting gammas in coincidence in two or more scintillators ("2-fold" coincidence probability) is

$$P_2 = \sum_{\nu=2}^{\nu_{max}} \sum_{k=2}^{\nu} \langle P(\nu,k)\rangle f_\nu' = \sum_{\nu=2}^{\nu_{max}} P_{2\nu}$$

$$= P_1 - \sum_{\nu=1}^{\nu_{max}} \langle P(\nu,1)\rangle f_\nu' \tag{4.12}$$

Table V shows values of P_1 and P_2 calculated for the two detector configurations and for different discriminator energy windows. These tabulated values are based on the values for $P(\nu,k)$ obtained from Eqs. 4.8 and 4.9 using the program DETPROB, together with the values for f_ν' from Table IV.

4.6 Experimental Tests of Calculated Detector Efficiency

The calculated detector efficiency can be compared with the measured data rates for the runs shown in Figs. 5-7. For the polyethylene sample, the total number of hydrogens in the beam was $N_H = 5.6\times10^{22}$, and assuming a total cross-section of 20 barns for H the laboratory-frame scattering[24,25] at small angles from this sample can be reasonably estimated as $N_H(d\sigma_H/d\Omega)_{lab} = 0.36$ cm^2/sr. For the vanadium sample, the number of atoms in the beam was roughly $N_V = 1.3\times10^{23}$, giving $N_V(d\sigma_V/d\Omega)_{lab} = 0.050$ cm^2/sr.

The measured flux from a 100 cm^2 polyethylene moderator in the F position at IPNS is[26]

$$EI_p(E) \simeq 3 \times 10^{10} (A_{source}/100) \qquad \text{neut/sr-}\mu\text{A-sec} \qquad (4.13)$$

at E = 1 eV. Since this is the epithermal region, I_p (E) should vary as 1/E. Using a source current J_s = 12 μA, a channel width Δt = 1 μsec, and an elastic scattering energy of E = 4280 meV giving an elastic flight time of t = 384 μsec, with other data from Table I, gives

$$\Phi_s(t)\ \Delta t = [EI_p(E)]_{1\ eV}\ (1/E)\ J_s\ (1/L^2)\ (2E/t)\ \Delta t$$
$$\simeq 470 \qquad \text{neutrons/cm}^2\text{-sec-chan} \qquad (4.14)$$

as the number of neutrons incident on the sample per unit area per unit time per one μsec channel at the detector, for a neutron energy of 4280 meV.

Using the above values and data from Table I, the number of neutrons on the detecting foil with the polyethylene sample should be

$$I_{pf}(t)\ \Delta t = \Phi_s(t)\ \Delta t\ \Delta\Omega \left(N_H \frac{d\sigma}{d\Omega}H\right)_{\phi_{lab}}$$
$$\simeq 1.02 \qquad \text{neutrons/sec-chan} \qquad (4.15)$$

and for a vanadium sample it should be

$$I_{vf}(t)\ \Delta t \simeq 0.143 \qquad \text{neutrons/sec-chan} \qquad (4.16)$$

Table VI shows the measured singles and coincidence data rates (minus background) for the peak channel in the 4280 meV elastic peak in the spectra in Figs. 5-7. Also shown in the table are the corresponding rates calculated using Eqs. 4.15 or 4.16 for the number of neutrons on the detector foil, along with the data in Table V for the detector efficiency per neutron absorbed in the foil, and data from Fig. 8 for the foil absorption probability for a 12.5 micron thick Ta foil (used for configuration 1 measurements) and for a 7.5 micron thisk Ta foil (used for configuration 2 measurements).

As seen in Table VI, the absolute data rates measured in the singles peaks were lower than the calculated values by factors ranging from ~2 (vanadium, configuration 2) to ~4 (polyethylene, configuration 1). However the calculated ratios between singles and coincidence data rates agreed fairly well (within ~25%) with the measured ratios for both configurations.

The discrepancies between the calculated and measured values for absolute data rates can be due to the values used for the incident neutron flux, for the sample scattering probability, for the absorption efficiency of the foil, for the gamma production per foil absorption, or for the gamma detection efficiency of the scintillator-photomultiplier-electronics system (eg - discriminator settings for some of the measured data might have drifted from the values used in the calculation), or a combination of these. The difference between the polyethylene and vanadium results for the same configuration indicates that at least part of the discrepancy between calculated and measured values lies in the estimation of the sample scattering, rather than in the calculations of detector performance. This is consistent with the relatively good agreement for singles-to-coincidence ratios achieved in the calculations, since these ratios do not depend on the amount of sample scattering.

4.7 Discussion of Detector Efficiency

As can be seen in Table V, the efficiency of the detector is quite low in configuration 2, with the calculated detection probability of a 4280 meV neutron incident on a 7.5 micron foil being about 2.7%. This efficiency could be improved in several ways. Increasing the resonance foil thickness would increase the probability of absorption at the peak, and hence increase the detection efficiency. However, for a 7.5 micron thick Ta foil this absorption probability is already ~0.6, so there is not much room for improvement there. Increasing the foil thickness would worsen the resolution (see Section 5 below), so this is not a desirable approach.

A much better approach would be to increase the size and number of scintillators used. Comparison of Tables III and IV shows that for reasonable pulse-height windows about 50% of the gammas produced with energies within this window do not deposit enough of this energy in the scintillators presently used to be detected. Thus a factor of nearly 2 improvement in the detection efficiency of a single scintillator is possible. In addition, the present scintillators subtend only a very small solid angle at the gamma source in the resonance foil (in detector configuration 2 on the average the 8 scintillators cover only 0.075 of the total solid angle for gamma interception) so most of the gammas produced will not hit any scintillator. With careful design it should be possible to

increase this by at least a factor of 5. To a first approximation the singles detection efficiency scales linearly with improvements in the gamma detection efficiency of a single scintillator, and also scales linearly with increases in solid angle for gamma detection, so an improvement of nearly a factor of 10 in the singles detection efficiency over that seen for the prototype detector configuration 2 should be possible. Unfortunately, to a first approximation the measured background should scale in the same manner. However, any such increases in singles detection efficiency will appear roughly squared in the coincidence detection efficiency, so increasing the scintillator size may offer significant improvement in the signal-to-background seen in the coincidence spectra, as well as improving the coincidence detection efficiency to a high enough value to make the use of this technique practical.

The tests reported here show that although there are still some problems, the detector simulation software gives sufficiently reliable results to be a useful design tool. Future efforts with this software will be directed to the study and/or design of a detector system employing large scintillators, in an effort to quantify the assertion made above about the effects of scintillator size and to arrive at an improved detector design.

5. USE OF DIFFERENCE TECHNIQUES TO IMPROVE RESOLUTION

As noted in Section 4.2, the Ta resonance is fairly broad, and has broad Lorentzian wings. However, the detection probability for a neutron is proportional to the absorption probability $P_A(E)$ of the foil, as given by Eq. 4.5, rather than to the absorption cross-section $\sigma_{abs}(E)$ alone. Thus the peak in detection probability given by $p_A(E)$ has a somewhat flatter top than does $\sigma_{abs}(E)$, due to saturation effects in the exponential in Eq. 4.5, and the extent of this saturation depends on the thickness of the absorbing foil. Figure 8 shows clearly the flattening of the peak due to saturation of the absorption as the foil thickness is increased. This latter feature can be used to good advantage to narrow the peak and to remove most of the wings. To do this, spectra are taken with two different thicknesses of foil, normalized to match in the wings, and subtracted. Such a subtraction of the calculated curves for the 7.5 micron and 25 micron Ta foils is also shown in Fig. 8. The potential improvements from this technique are quite

evident in the figures, although this improvement can only be gained with a significant increase in counting time per experiment, and then only if the background can be properly subtracted in each case. Preliminary demonstrations of the feasibility of using such difference techniques to improve resolution have been reported[1,5,6] by other investigators.

Figure 10 shows data for a sample of ZrH_2 on the EVS. The sample was placed at 10.5 m from the source and 0.5 m from the resonance foil. This made the average scattering angle ~ 4.45°, giving Q ~ 3.6 A^{-1}. Data were collected with a ~ 7.5 micron thick Ta foil, a ~ 25 micron foil made of two thicknesses of ~ 12.5 micron Ta, and with no Ta foil. The no-foil "background" run was fit with a quadratic function, and the resulting smooth background was subtracted from the 7.5 micron and 25 micron raw data to produce the curves shown in Fig. 10. Not surprisingly, the fundamental inelastic mode of the hydrogen vibration in ZrH_2 is not resolved. However, by subtracting the 25 micron data, scaled to match the 7.5 micron data in the wings as shown in Fig. 10, from the 7.5 micron data, the results shown in Fig. 11 are obtained. Also shown in Fig. 11 are the calculated results based on the relative amplitudes of the elastic peak and the various inelastic peaks predicted by harmonic oscillator theory[29] for an oscillator frequency of 140 meV (which is approximately the value for ZrH_2). In the calculation, the harmonic oscillator results have been broadened according to the 7.5 micron - 25 micron "difference resolution function" shown in Fig. 8. The overall amplitude of the calculated curve has been scaled to match the elastic peak, but there are no other adjustable parameters. Although statistics are not good enough to get a really good picture of the shape of the inelastic scattering, the elastic peak has clearly been sharpened enough by this difference technique so that the inelastic data can be resolved, and the overall magnitude of the inelastic scattering is in good agreement with the calculated value. The three data sets required a total collection time of ~ 135 hours for a sample of ZrH_2 which put ~ $2x10^{22}$ H atoms in the beam , with the accelerator producing an average current of ~ 12 μA. With a more efficient detector (see Section 4.7) much better statistics could be achieved in this amount of time. Thus this technique does seem to provide a practical approach to the improvement of resolution in such an instrument, at least for some types of problems.

TABLE I - Operating parameters for the EVS at IPNS.

Incident Path L_i	10 m	
Scattered Path L_f	1 m	
Resonant Foil Geometry	annular, centered on beam	
Resonant Foil Size	10.16 cm od, 5.08 cm id	
Resonant Foil Solid Angle at Sample	0.0061 sr	
Scattering Angle	1.5° - 3°	
Resonant Foil Material	Ta	
Resonance Energy E_R	4.28 eV	
Beam Diameter at Moderator - Umbra	5.65 cm	
Beam Diameter at Sample	2.54 cm	
Beam Diameter at Foil - Umbra	1.84 cm	
Penumbra	3.75 cm	
Gamma Detectors	8 BGO* cylinders 2.54 cm dia, 2.54 cm long	
	Configuration 1	Configuration 2
Gamma Detector Configuration	45° apart, centered 4.6 cm from beam center and 2.5 cm from foil	30° apart, centered 8.26 cm from beam center in plane of foil

* BGO stands for a bismuth germanate crystal directly coupled to a Hamamatsu model R268 photomultiplier.

TABLE II - Magnitudes of different contributions to the background with different samples and detector configurations. Values given are the contribution per second.

Background Source	Range(μsec)	Polyethylene Sample Config 1	Polyethylene Sample Config 2	V Sample Config 2	Config 1:2 Ratio
gamma-no sample	100-600	4.9	0.000	0.000	> 1000
gamma-sample	100-600	0.51	0.030	0.033	17
neutron-no sample	100-600	0.81	0.045	0.054	18
neutron-sample	100-600	0.72	0.108	0.195	7
non-beam	100-600	0.72	0.051	0.117	14
Total	100-600	7.6	0.234	0.399	33
Total one channel	100-101	0.098	0.0015	0.0022	65
Total one channel	350-351	0.010	0.00066	0.00051	15

TABLE III - Probabilities for production of different numbers of coincident gammas within selected energy windows, calculated using the statistical model Monte Carlo program GAMMA.

Number of Gammas ν	Probability f_ν no window	Energy Window (MeV) 0.8-5.2	0.8-3.0	1.5-5.2
0	0.000	0.037	0.061	0.039
1	0.003	0.024	0.356	0.287
2	0.064	0.446	0.199	0.612
3	0.283	0.418	0.310	0.061
4	0.387	0.073	0.072	0
5	0.206	0.002	0.002	
6	0.051	0	0	
7	0.006			
8	0.001			
9	0			
$\bar{\nu}$	3.911	2.472	1.983	1.696

$\bar{\nu}$ = Average number produced within energy window per cascade.

TABLE IV - Probabilities for different numbers of coincident detectable gammas using scintillators with pulse-height discrimination, calculated using GAMMA and SCNTDET with gammas incident from the side on a 2.5 cm dia x 2.5 cm long BGO scintillator.

Number of Detected Gammas ν	Probability f_ν'			
		Discriminator Window (MeV)		
	no window	0.8-5.2	0.8-3.0	1.5-5.2
0	0.000	0.481	0.542	0.672
1	0.003	0.399	0.355	0.299
2	0.063	0.109	0.093	0.028
3	0.277	0.010	0.010	0.000
4	0.389	0.001	0.001	0
5	0.209	0	0	
6	0.052			
7	0.006			
8	0.000			
$\bar{\nu}$	3.921	0.651	0.572	0.357

$\bar{\nu}$ = Average number detected within energy window per cascade.

TABLE V - Weighted total singles and 2-fold coincidence detection probabilities for different gamma detection energy windows, calculated using detectable gamma frequency data from Table III and scintillator "hit probabilities" $P(\nu,k)$ given by DETPROB.

Window (MeV)	Detector Configuration 1		Detector Configuration 2	
	P_1	P_2	P_1	P_2
no window	0.567	0.130	0.268	0.0302
0.8 - 5.2	0.125	0.0040	0.051	0.00081
0.8 - 3.0	0.111	0.0036	0.045	0.00072
1.5 - 5.2	0.070	0.0008	0.028	0.00016

TABLE VI - Calculated and measured data rates (minus background) in the peak channel for the 4280 meV elastic peak for the runs shown in Figs. 5-7. The discriminator window for gamma detection was set to 0.8-3.0 MeV for all three runs. Calculated values are based on Eqs. 4.13 or 4.14 together with the appropriate P_1 or P_2 values from Table V and foil absorption probabilities from Fig. 8, and are in units of counts/sec/one-μsec channel.

Config	Sample	Singles		Coincidence		Ratio	
		Calc	Meas	Calc	Meas	Calc	Meas
1	polyethylene	0.091	0.023	0.0029	0.00085	31	27
2	polyethylene	0.028	0.010	0.00044	0.00012	64	83
2	vanadium	0.0039	0.0020				

REFERENCES

1. Newport, R. J., Paoli, M. P., Pugh, V. T., Sinclair, R. N., Taylor, A.D., and Williams, W. G., ICANS VIII - Proceedings of the Eighth Meeting of the International Collaboration on Advanced Neutron Sources, RAL-85-110, Rutherford Appleton Laboratory, 562-576 (1985).

2. Sinclair, R. N., Moxon, M. C., and Carpenter, J. M., Bull. Am. Phys. Soc. 22, 101 (1977).

3. Allen, D. R., Mitchell, E. W. J., and Sinclair, R. N., J. Phys E: Sci Instrum 13, 639-646 (1980).

4. Carpenter, J. M., Watanabe, N., Ikeda, S., Masuda, Y., and Sato, S., Physica 120B, 126-130 (1983).

5. Watanabe, N., Proceedings of the 1984 Workshop on High-Energy Excitations in Condensed Matter, Los Alamos, Feb. 13-15, 1984. LA-10227-C, Vol 1.

6. Allen, D. R., Mitchell, E. W. J., and Sinclair, R. N., "Coincidence Counting Techniques for an Epithermal Neutron Resonance DetectorSpectrometer", preprint.

7. Paoli, M. P., Mitchell, E. W. J., Sinclair, R. N., and Taylor, A. D., ICANS VIII - Proceedings of the Eighth Meeting of the International Collaboration on Advanced Neutron Sources, RAL-85-110, Rutherford Appleton Laboratory, 577-592 (1985).

8. Hughes, D. J. and Schwartz, R. B., Neutron Cross Sections, BNL 325, Second Edition, Brookhaven National Laboratory, 1958.

9. Davisson, C. M., "Gamma-Ray Attenuation Coefficients", Appendix I in Alpha-, Beta-, and Gamma-Ray Spectroscopy, Vol. 1, ed. K. Siegbahn. North-Holland, Amsterdam, 1974.

10. Blatt, J. M., and Weisskopf, V. F., Theoretical Nuclear Physics. Wiley, New York, 1952.

11. Lynn, J. E., The Theory of Neutron Resonance Reactions. Clarendon Press, Oxford, 1968.

12. Fodarero, A., The Elements of Neutron Interaction Theory. MIT Press, 1971.

13. Mughabghab, S. F. and Garber, D. I., Neutron Cross Sections, Volume I, Resonance Parameters, BNL 325, Third Edition, Brookhaven National Laboratory, 1973.

14. Motz, H., and Backstrom, G., "Neutron Capture Radiation Spectroscopy", in Alpha-, Beta-, and Gamma-Ray Spectroscopy, Vol. 1, ed. K. Siegbahn. North-Holland, Amsterdam, 1974.

15. Groshev, L. V., Demidov, A. M., and Pelekhov, V. I., Nuclear Physics 16, 645-656 (1960).

16. Strutinski, V. M., Groshev, L. V., and Akimova, M. K., Nuclear Physics 16, 657-673 (1960).

17. Bergqvist, I., and Starfelt, N., Nuclear Physics 39, 353 (1962).

18. Starfelt, N., Nuclear Physics 53, 397-408 (1964).

19. Groshev, L. V., Demidov, A. M., Pelekhov, V. I., Sokolovskii, L. L., Bartholomew, G. A., Doveika, A., Eastwood, K. M., and Monaro, S., Nuclear Data Tables A5, 243-431 (1969).

20. Davisson, C. M., "Interaction of γ-Radiation with Matter", in Alpha-, Beta-, and Gamma-Ray Spectroscopy, Vol. 1, ed. K. Siegbahn. North-Holland, Amsterdam, 1974.

21. Harshaw Scintillation Phosphors, Third Edition, The Harshaw Chemical Co., Solon OH, 1978.

22. Neiler, J. H., and Bell, P. R., "The Scintillation Method", in Alpha-, Beta-, and Gamma-Ray Spectroscopy, Vol. 1, ed. K. Siegbahn. North-Holland, Amsterdam, 1974.

23. Muradyan, G. V., Schepkin, Yu. G., Adamchuk, Yu. V., and Ustroev, G. I., Kirchatov Institute Report, IAE-2634, 22 (1979).

24. Goldstein, H., Classical Mechanics. Addison-Wesley, Reading, Mass. (1950).

25. Egelstaff, P. A., and Poole, M. J., Experimental Neutron Thermalisation. Pergamon Press, Oxford. (1969).

26. Carpenter, J. M., Potts, C. W., and Lander, G. H., ICANS-VI, Proceedings of the Sixth Meeting of the International Collaboration on Advanced Neutron Sources, ANL-82-80, Argonne National Laboratory, 78-101 (1983).

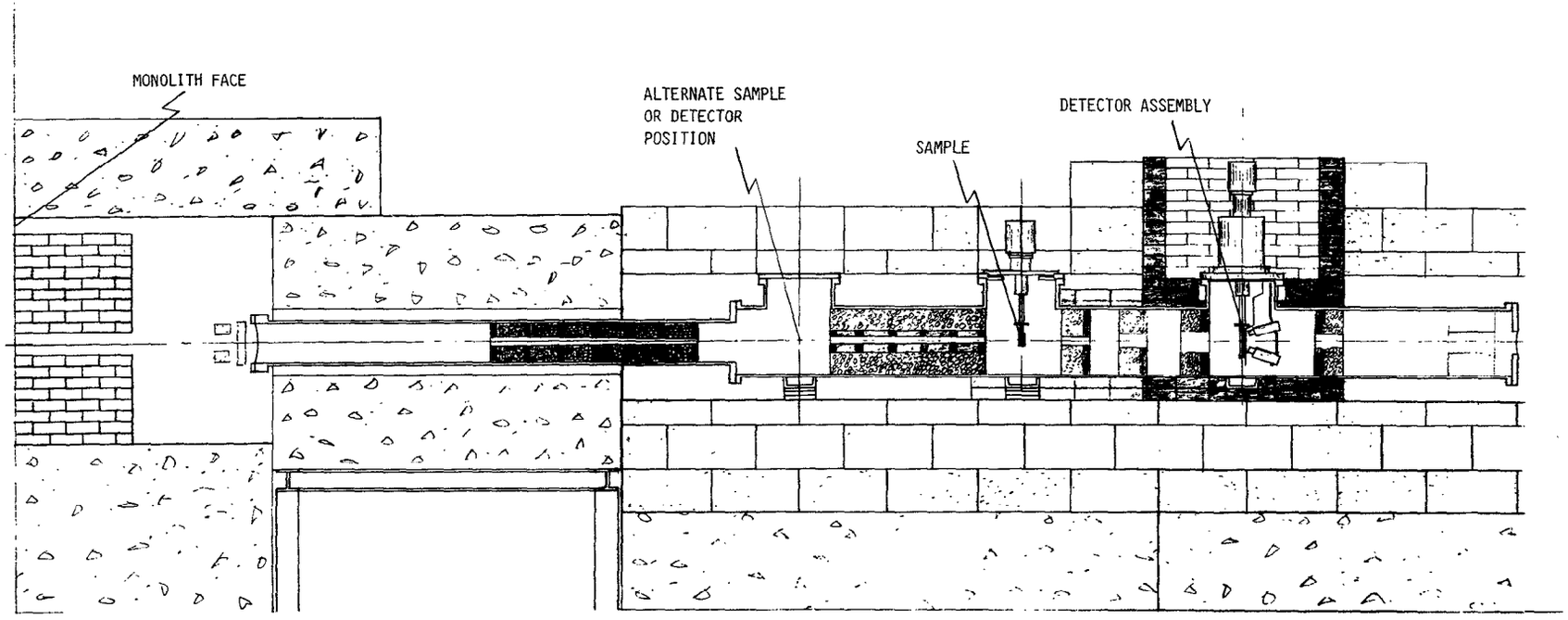

Fig. 1. Side view of the EVS flight path. The neutron beam is incident from the left. The configuration 1 detector assembly is shown. (See Table I and Figs. 2 and 3 for detector configuration specifications.)

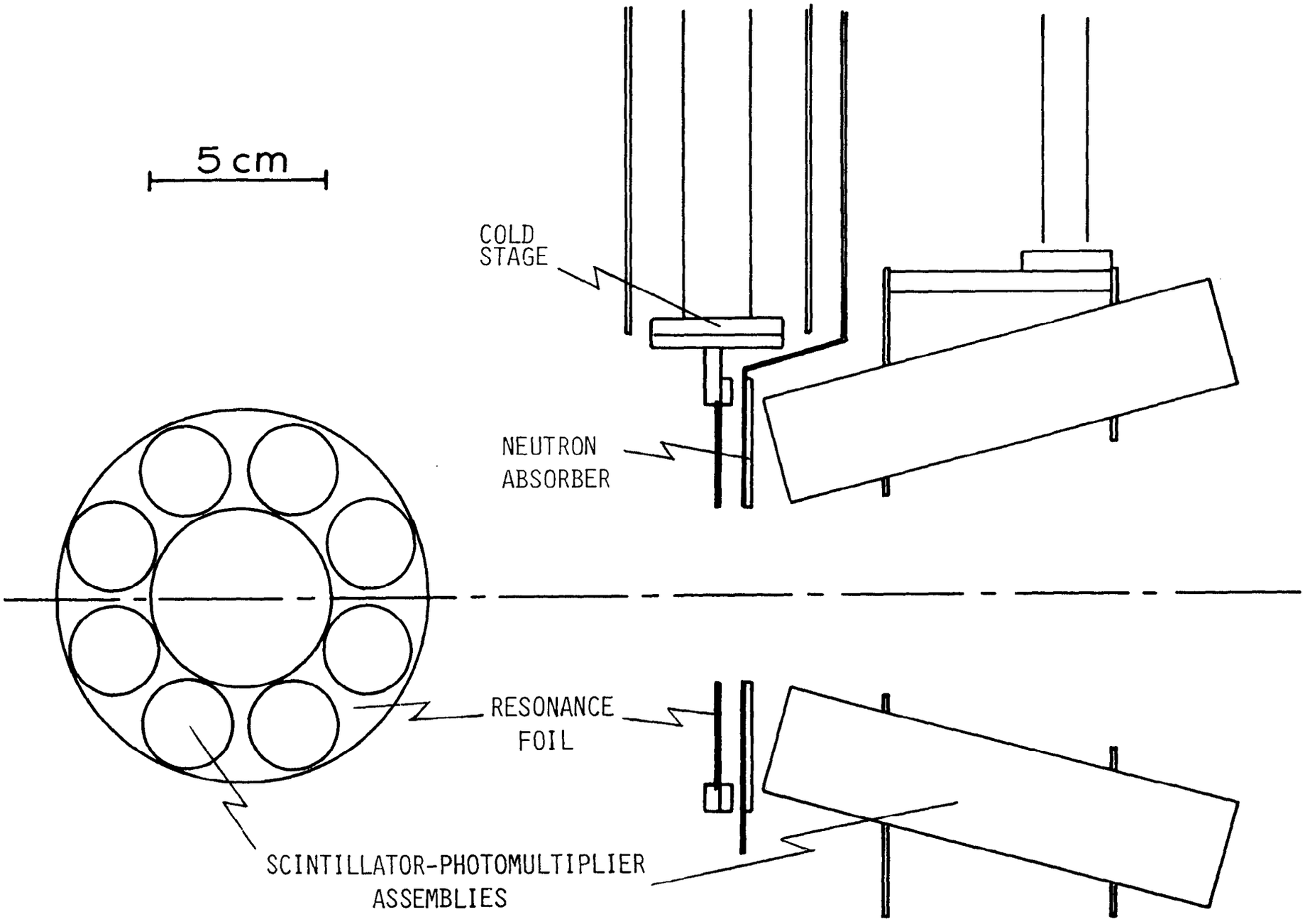

Fig. 2. Detector configuration 1. The beam is incident from the left.

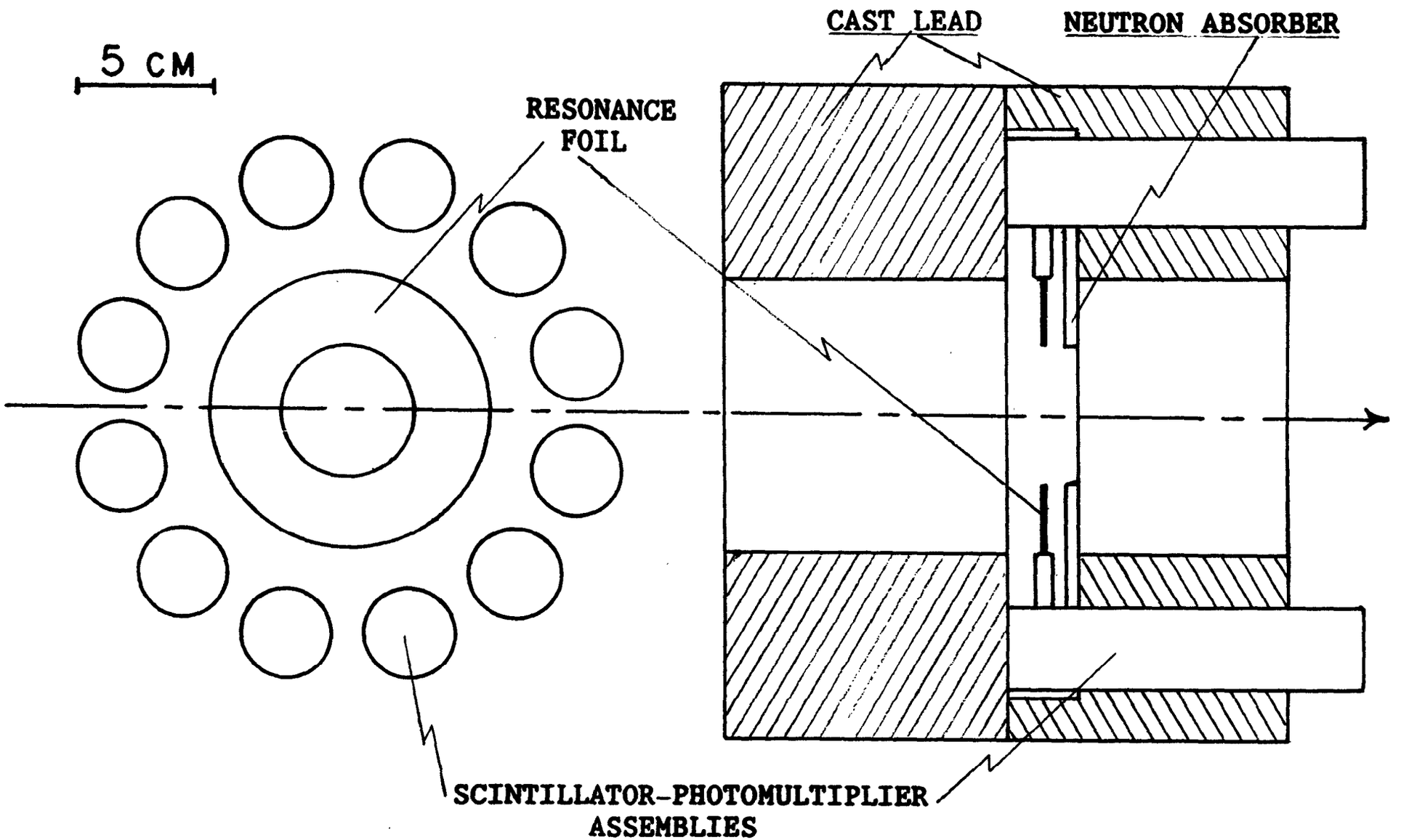

Fig. 3. Detector configuration 2. The beam is incident from the left. Only 8 of the 12 scintillator positions were occupied.

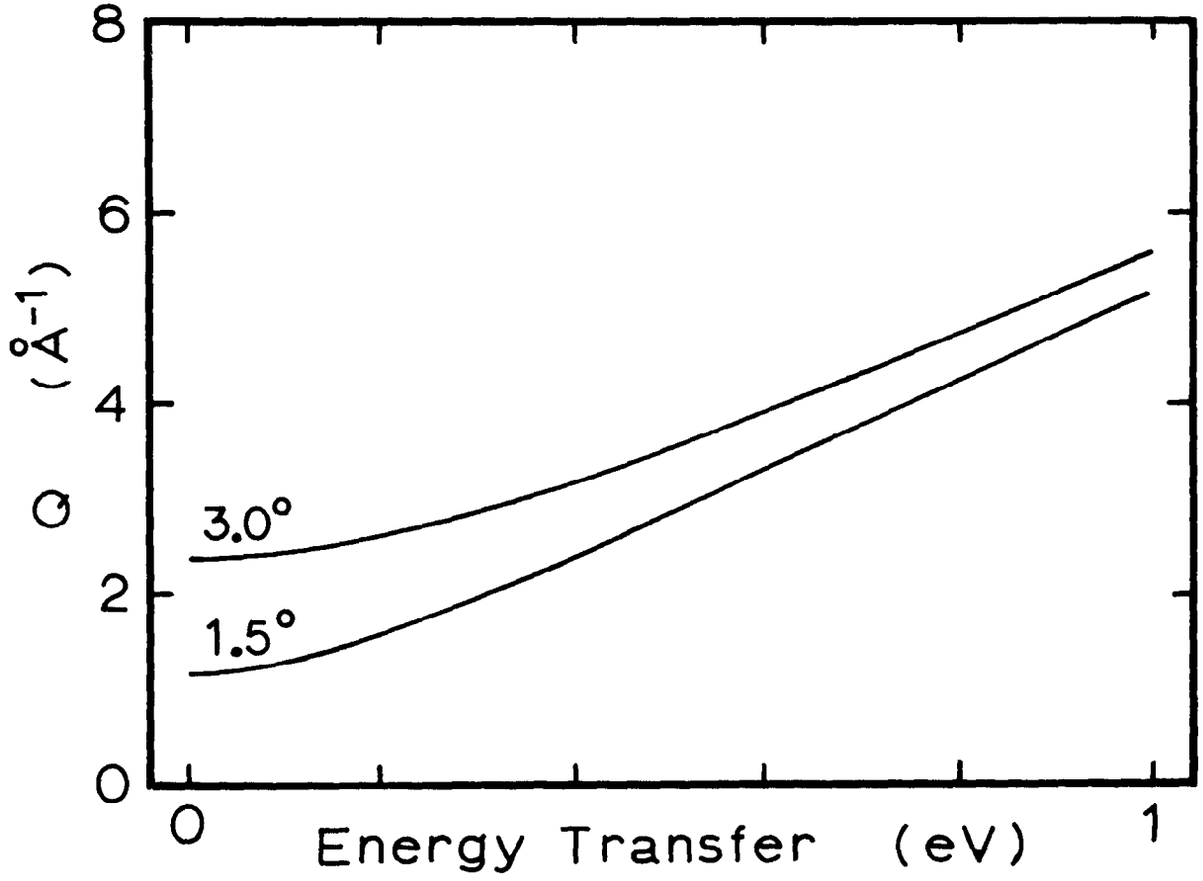

Fig. 4. Kinematic range of the detector for the EVS in configurations 1 and 2.

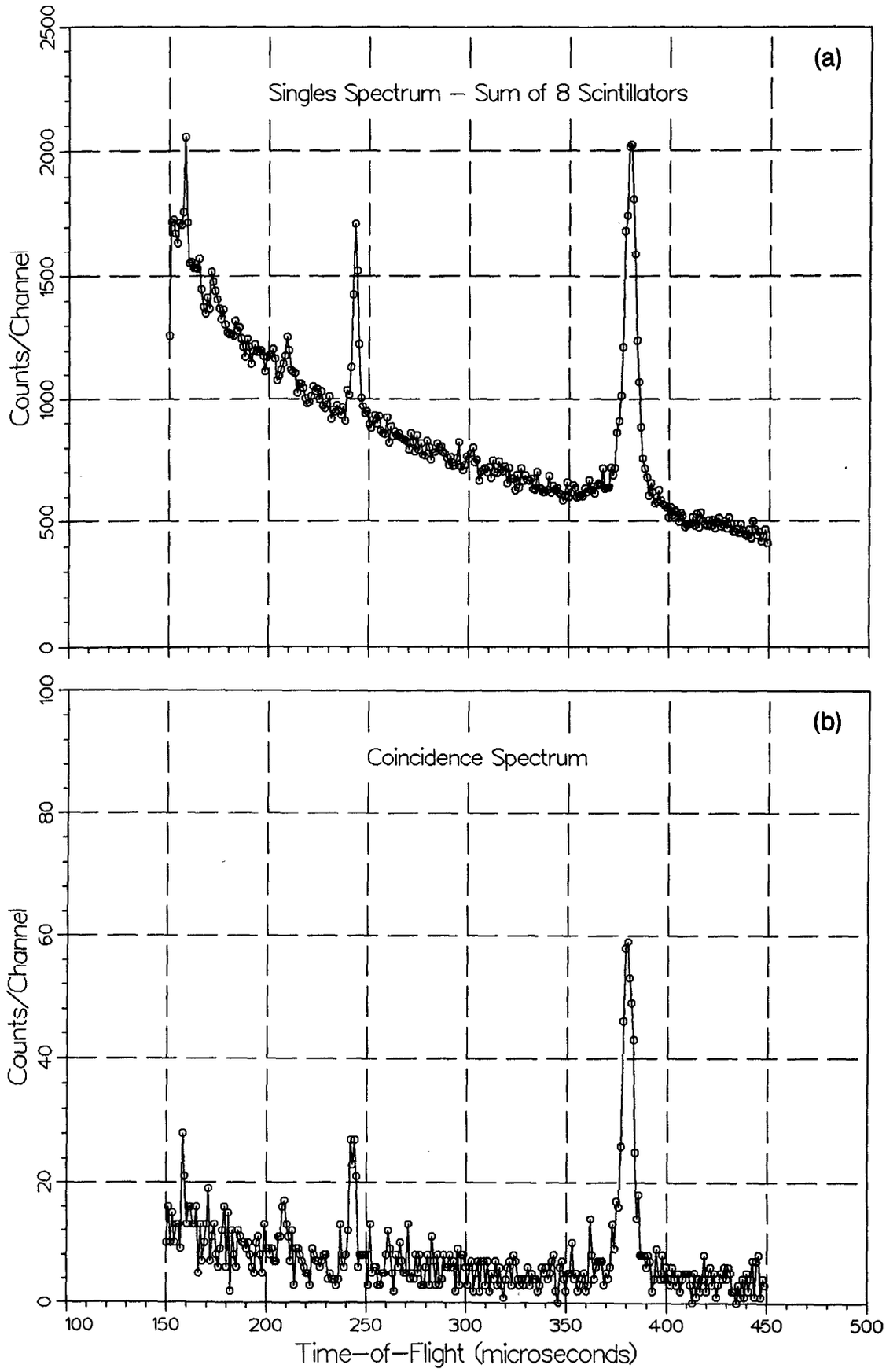

Fig. 5. Typical EVS spectra for detector configuration 1 with a polyethylene sample. (a) "Singles" spectrum sum of 8 scintillators; (b) 2-fold coincidence spectrum.

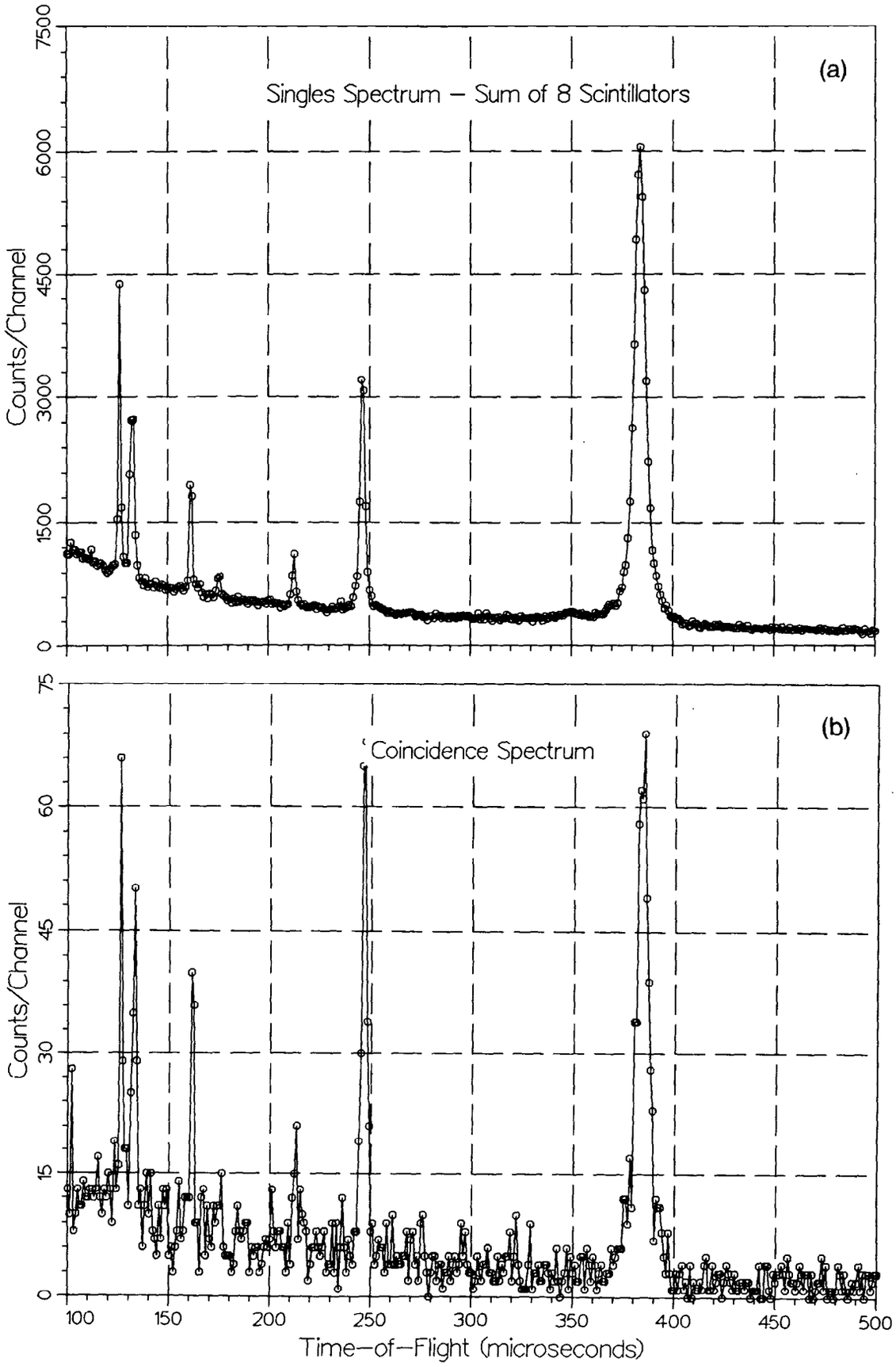

Fig. 6. Typical EVS spectra for detector configuration 2 with a polyethylene sample. (a) "Singles" spectrum sum of 8 scintillators; (b) 2-fold coincidence spectrum.

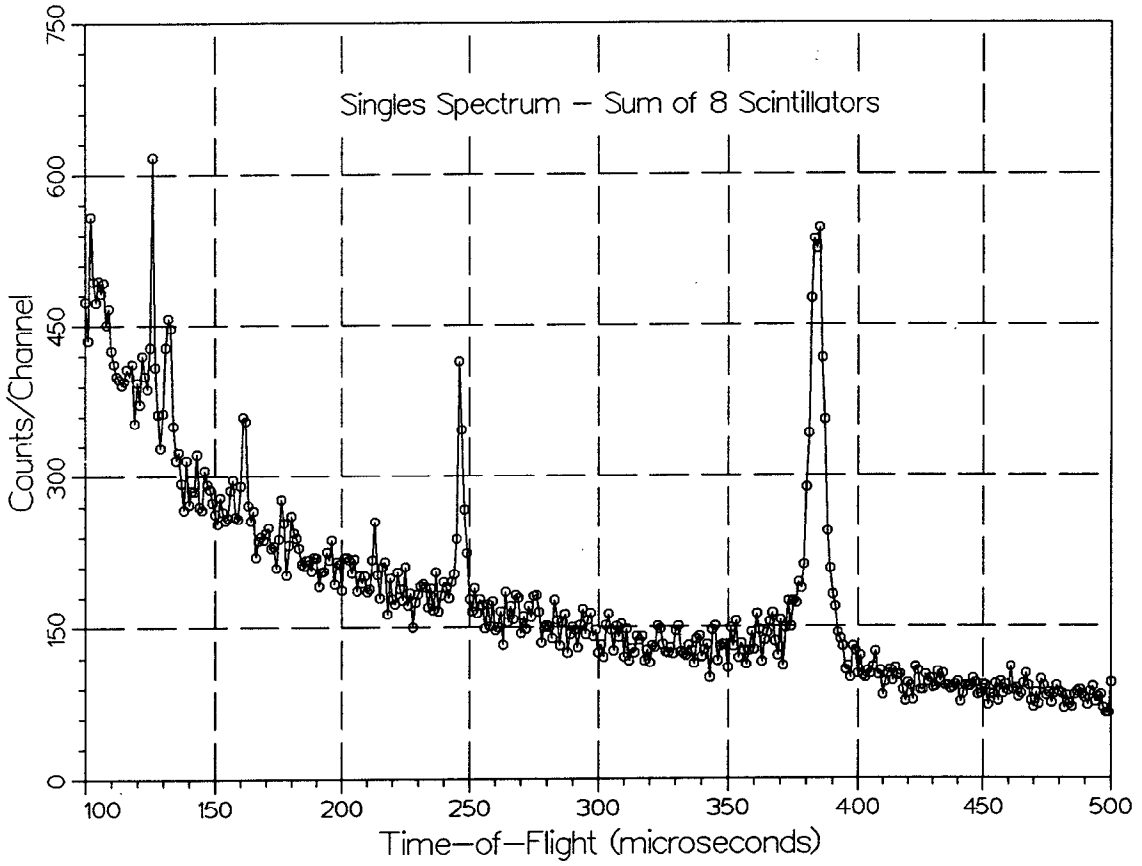

Fig. 7. Typical EVS spectrum for detector configuration 2 with a vanadium sample. "Singles" spectrum sum of 8 scintillators.

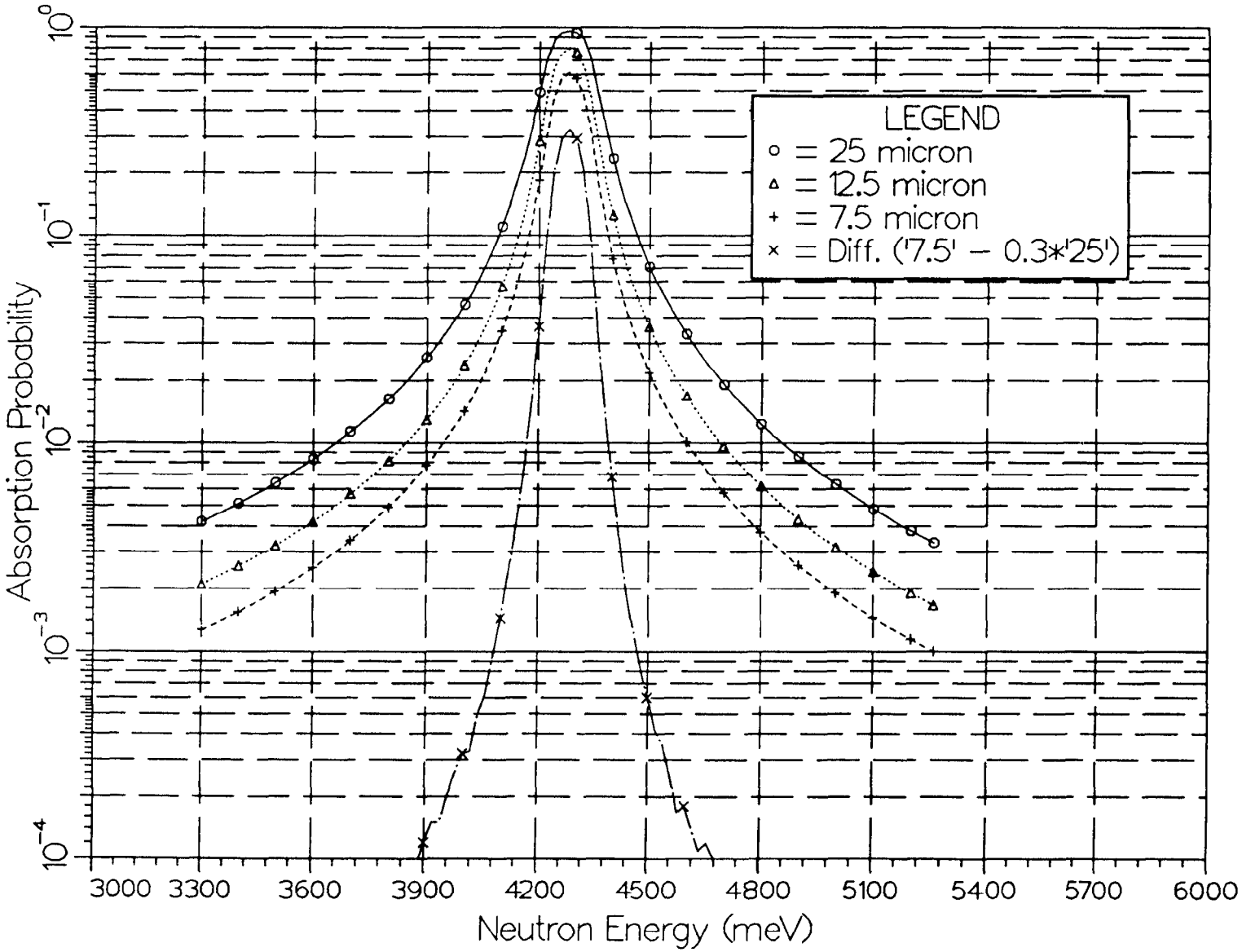

Fig. 8. Resonance absorption in Ta foil, calculated by the program FOIL. Plotted curves are absorption probabilities for 25 micron thick, 12.5 micron thick, and 7.5 micron thick foils. The difference between the 7.5 micron data and 0.3 times the 25 micron data is also plotted.

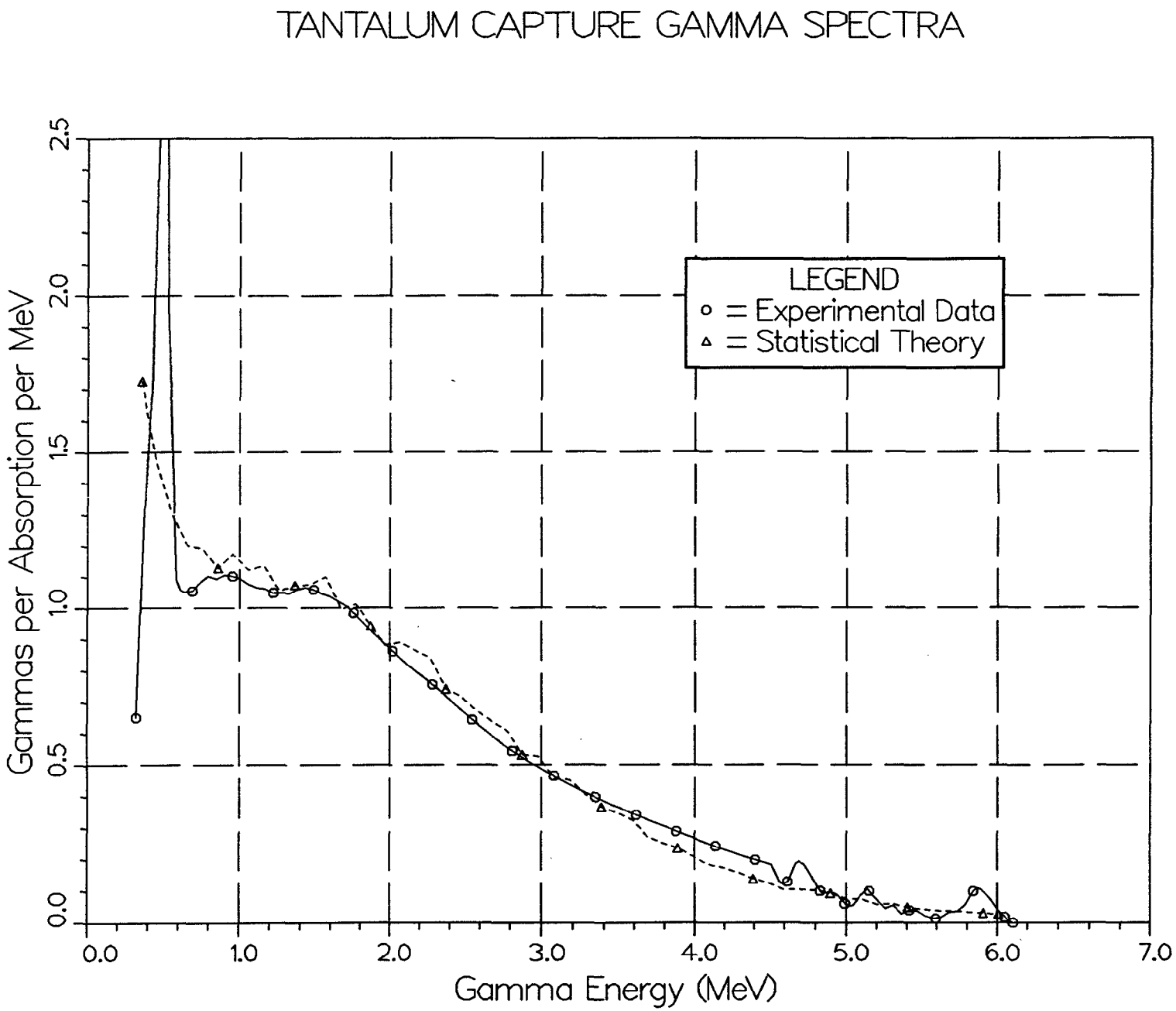

Fig. 9. Experimental (Ref. 19) and calculated capture gamma spectra for thermal neutrons on Ta. No adjustments were made in the horizontal or vertical scales for the experimental or calculated curves (numbers are absolute).

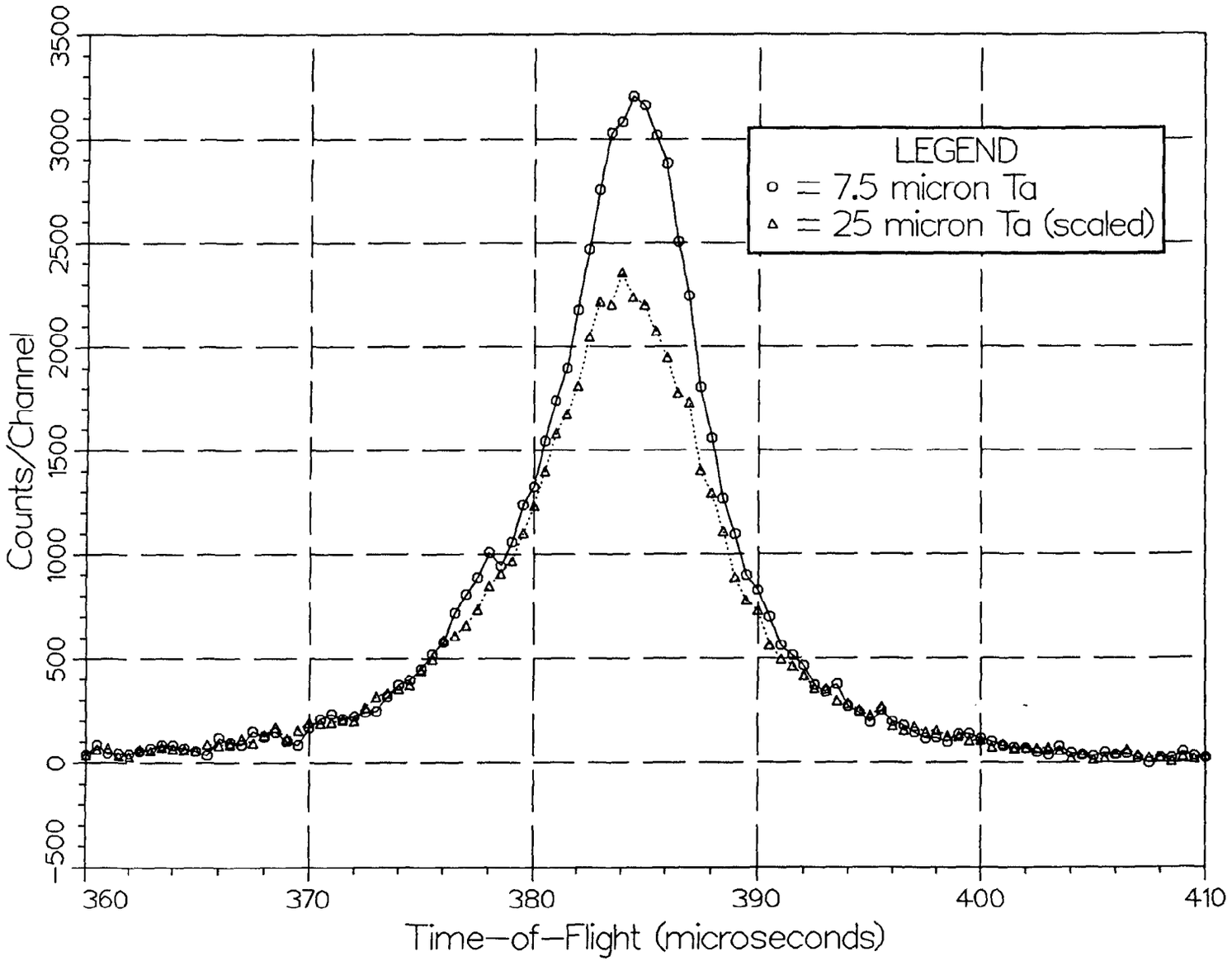

Fig. 10. Data for ZrH_2 sample near the 4280 meV elastic peak. The 7.5 micron values are the actual measured data (minus background), while the 25 micron values are the raw 25 micron data (minus background) scaled to match to match the 7.5 micron data in the wings of the Lorentzian peak.

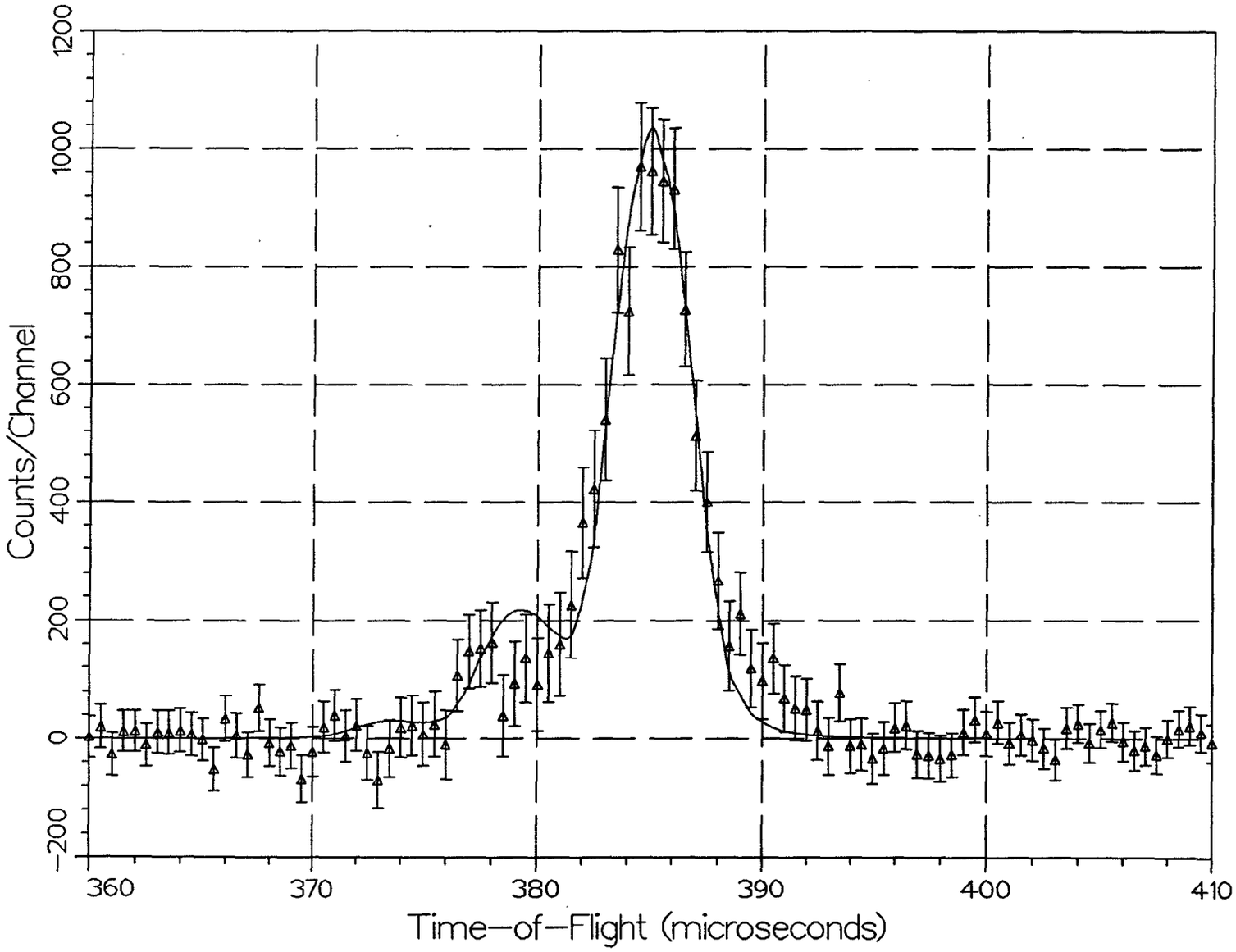

Fig. 11. "Difference" data for ZrH_2. Data points are the difference between the two curves in Fig. 10. The curve is calculated using harmonic oscillator theory with an oscillator energy of 140 meV, along with the calculated difference resolution curve of Fig. 8.

ICANS IX

INTERNATIONAL COLLABORATION ON ADVANCED NEUTRON SOURCES

22-26 September, 1986

SUMMARY OF INSTRUMENT SESSION - PART II

KENT CRAWFORD

Formal presentations on various instruments and techniques continued in the afternoon of Tuesday. There were several things covered there: Phil Seeger gave two talks, one discussing the low-Q spectrometer and the other giving an overview of the status of the rest of the instrumentation at LANSCE. That was followed by a presentation by Mike Johnson of a very innovative idea on the use of computed Tomography to extract inelastic information from total-scattering data. Then Yasuo Endoh discussed the status of the TOP spectrometer as well as talking about the current status of instruments at KENS. Mike Johnson talked about some of the future problems that can be expected for data acquisition systems as instruments become more sophisticated and sources keep improving. Then since that exhausted all the available time on Tuesday, we had a spill-over session in which the more wide-based discussions took place (that was on the Thursday morning); I will go on to that after a brief walk through the instrument presentations.

The low-Q diffractometer that Phil talked about is, I think, going to be a very exciting machine. It has been carefully designed to make good use of the available neutrons and a lot of care has been put into the shielding to avoid various problems which have been anticipated with the detector. Unfortunately they have only just got the machine together (not all the pieces are there yet) and there has only been a very small amount of running time; so the main experimental results Phil had to report on were that he has successfully measured (to one significant figure!) the gravitational constant at Los-Alamos, and that he measured the spectrum from the LANSCE hydrogen moderator. They found that everything that they were able to test did work.

Other instruments that are operational at LANSCE include the filter difference spectrometer which has been running successfully for a number of years. It's a quite high data rate instrument and uses the slightly different Bragg cut-off edges of Be and Be-oxide filters which are placed alternately around the sample. The sample has a large solid angle for scattering. There's very little Q-resolution in this machine but it's designed for a very high data taking rate or alternatively to measure from very small samples. This instrument has been going for some time and has been reported in some detail at earlier ICANS. There's a constant-Q spectrometer which has also been reported at earlier meetings. I guess it's best to say it's still in a development mode. They have measured phonon dispersion curves and it works more or less as anticipated. There are still various problems associated with this machine. There's a single crystal diffractometer which has been running fairly routinely for several years and that again is a standard sort of instrument. Then there are a couple of powder diffractometers, one of which - the high intensity diffractometer - has been running more or less routinely for quite a while. They have recently moved it to a larger distance, so there will be some work to get it going again.

I am now going to go on to Mike Johnston's approach: what got him thinking about this was the idea of computerised tomography. This has been around for a long time in terms of the various body scanning computerised tomography techniques. The idea in X-Ray computed tomography is to send some beams through a sample from several directions, each of which measures an integral of what is along its path. If you have enough of these different path integrals going across the volume you are interested in, you can deconvolute and end up with what's in each of the elements within the volume. Whereas for computed tomography for medical applications these are paths in physical space, X & Y, there's no reason why you have to restrict yourself to these sorts of paths. If you are looking at any other two-dimensional space, you can do a similar thing. For example, if you have a diffractometer with a number of detectors in it, then each of these detectors is actually measuring a path integral along all the elastic and inelastic scattering on some locus in $(Q - \omega)$ space. If each of the detectors is located at a different angle it is measuring along a different locus in $(Q - \omega)$ space, and if you move to sufficiently different angles you can get some of these loci crossing one another and build up a pattern of

what's really happening in the elastic and inelastic scattering processes. In the region where you have enough of these crossings, you can figure out what's going on in individual elements of $(Q - \omega)$ space. He's done some (at this stage limited) simulations of this technique, starting out with some arbitrary inelastic contour patterns in $(Q - \omega)$ space. After grinding away for several hours on the VAX he came out with a reconstruction of the original patterns. There are a lot of things which still have to be looked at in terms of this technique. It was pointed out that possibly combining this with the correlation technique (this will provide a different sort of path integral and somewhat more information) might be the most efficient way to go. But that is something which has the capacity of eating up many hours of the VAX before it's clear how useful it may be.

The next paper was on the TOP spectrometer at KENS; this is a time-of-flight spectrometer for low energy polarised neutrons. They use a curved mirror to do the polarising and have the appropriate flippers and other polarisation handling and analysing devices; part of the paper was concerned with the development of some of these. The paper was primarily devoted to talking about the new data-acquisition system for this instrument. This system is based on using personal computers, so it's quite inexpensive and has turned out to be very successful for tackling the task. They have done quite a bit of software development on the system, so it has the flexability to present the data in a variety of ways and to control the various aspects of the experiment. Several different scientific measurements that have been made on this instrument were also reported.

The final formal presentation was on problems of data acquisition with future sources or future developments of current sources. Now, the most sophisticated and refined data acquisition system is that of ISIS. They have done a pretty careful optimisation, to build a system that can handle the size of data arrays that were anticipated along with the expected data rates. The problem comes when you have to go beyond this, because one of the first limits you find is that if you make data arrays significantly bigger than the present ones, you are going to start to involve hours to move them through the physical links in the system. If you can measure a spectrum in half an hour and it takes you two hours to get it out of the system and into the computer, you are not really in a good situation. So there has to be thought given as to how you can compress the data; how much you can

compress on the fly; how much you can compress immediately after you get the data. This is a question which is far from being resolved.

That leads on to the spill-over section, where we had several topics; we started out talking about background and monitors and spent some more time talking about the state of the data treatment problem and got back to backgrounds. Let's talk about these separate topics.

Contrary to what has been said earlier, there is a fairly universal concensus that **NOT** every neutron is a good neutron. In fact, the only ones that are any good are the ones that have gone through the process you are intending to measure, and any one that reaches your detector by any other route is a bad neutron. In fact, most of what goes on in instrumentation is figuring out how to get rid of bad neutrons. Measuring the good ones is relatively easy; handling of the bad ones is the difficult problem. There was some general discussion of various background problems that people have encountered but there wasn't anything terribly unique. I think that as far as instrumentation was concerned, the message that came through was that you have to do everything right, in some sense, and pay attention to everything you should, use the right materials, worry over your shielding process. If the target and moderator people have made life difficult for you, then you have to do something for the beam before it gets out, such as using a chopper or a rotating collimator or sticking filters in the beam.

One of the things which is showing up is that, it seems fairly certain that - even when using He-3 detectors - in some situations you do have to worry about gammas, so you had better be careful about the shielding, the collimation, etc. from the gamma point of view as well as from the neutron point of view. People who have been working with scintillation detectors have recognised from the beginning they are going to have to worry about this problem. Depending on where your detector is this can mean direct target beam gammas or those from (n, γ) capture. In the low-Q instruments at ANL or LANSCE, some (gas detectors) are placed in the incident beam, and the direct γ's produce a measurable (significant) pulse. Probably a reasonable fraction of the overloading of the detector with the primary pulse comes from the gammas; cross-sections are similar to, if not higher than, those for fast neutrons for these detectors. We have found gas position-sensitive detectors are quite gamma-sensitive - calculations show that as well. You can do some electronic discrimination to help you out.

but it depends on how sophisticated it is just how far you can improve things, and even then you can only go so far.

There was a short discussion of technical details of gas detectors.

Moving onto the question of beam monitors. One problem found to be common to both Los Alamos and Argonne concerned using BF_3 for the low efficiency detectors to be used as beam monitors. It has, so far, been impossible to get commercial detectors with a specified efficiency. The monitors that are used at ISIS use a different technique: these have, I think, been reported before and involve using tiny beads of scintillator. These seem to work quite well.

One of the things that came out of the meeting was, that a monitor need which we are not sure is really being addressed, is that for small-angle instruments. You would like a beam monitor which sits downstream from the sample and can be operated at the same time as you are measuring on, and without interfering with the information from, your area detector (which means presumably you mount it just in front of the beam stop or somewhere like that). What comes out (neutrons and gammas) from the beam stop is a restriction, but this type of monitor would provide the capability of making transmission measurements concurrently with the actual scattering measurement, which would be very useful for small angle instruments.

- *It was pointed out from the audience that ISIS does in fact have a detector like that in place now; these monitors consist of a (normal size rather than beads) scintillator element array embedded in Boron Carbide, so the monitor is a beam stop, but the perfomance has not yet been evaluated. Some advantage may come because they use a beam bender for the instrument and operate this detector system outside the main beam.*

- *A LiF coated surface barrier detector was tried at Argonne that sort of worked until what was assumed to be fast neutron radiation damage wiped it out!*

Finally, on the data treatment problem there are really two problems caused by increasing data set size. If you expand much beyond what you

have planned for in designing the system, transfers take longer than is reasonable. There is not only a problem for transfer but also of what-do-you-do with the data after you get it. The other thing is that for an instrument to be very useable, you have got to be able to see whether you are doing things right and to do this in a reasonable time (a reasonable time is thought to be about 5 mins). Some of the instruments produce their data in a very intelligible form, so that you can see what it is you are measuring. With a lot of others, this is not the case (for example many time-of-flight instruments) and you have to do some combining or other type of manipulation on the data in order to get anything which remotely resembles what it is you are trying to measure. When this process takes too long a time (as it will with very large data sets) it becomes much less satisfactory. This is a problem not so much for now, but certainly for the future.

At the moment, the data acquisition systems at ISIS and IPNS are at the opposite extremes. These are dictated by the planned level of intensity of the two facilities; ISIS was forced to go for high speed and so they don't do much operation on the data on-line. I think they do about as much as they can, but it does limit the flexibility of what they can do, for example, for data compression. IPNS, on the other hand, knew from the beginning it was not going to be a super-intense source and so were able to go for the opposite approach and do everything in software. Hence they have quite a flexible system and do quite a lot of data compression on-line, and their data-sets are not nearly so large. Some time in the future there has to be a marriage of these two approaches to keep data sets from growing. There remain the questions of: at what stage should one put in data compression? how much can be done on the fly? how much has to wait until everything is collected? One of the problems is that some of the corrections may be, for instance, wavelength dependent and you may have to collect all data before you can do any compression.

ICANS IX

INTERNATIONAL COLLABORATION ON ADVANCED NEUTRON SOURCES

22-26 September, 1986

THE LOW-Q DIFFRACTOMETER AT THE LOS ALAMOS NEUTRON SCATTERING CENTER

P. A. Seeger, A. Williams, and J. Trewhella

Los Alamos National Laboratory, Los Alamos, NM 87545, USA

Abstract

Instrument criteria are presented for the Low-Q Diffractometer (LQD) at the Los Alamos Neutron Scattering Center (LANSCE), and a design is shown to meet these criteria. The collimator consists of multiple-aperture pinhole plates, and incorporates "dynamic gravity focusing" to center all wavelengths on the detector. Preliminary test results, making use of the Proton Storage Ring, a liquid hydrogen moderator, and two different position-sensitive detectors are shown.

1. Introduction

Since our report at the preceding ICANS meeting[1], considerable progress has been made in the implementation of the Low-Q Diffractometer (LQD) and its position-sensitive detectors. A prototype instrument was operated in December, 1985, using the liquid hydrogen moderator[2] and an Anger camera[3]. First tests of the almost-completed instrument were made in September, 1986, using a two-dimensional ^{3}He proportional counter. The LQD is being installed on flight path 10 (the northeast corner) in the existing experimental hall. With the Proton Storage Ring (PSR) operating at 24 Hz, the flight path of 12.65 m allows use of neutron wavelengths out to 13 Å before frame overlap, without the need for choppers or filters. An elevation view of the instrument is shown in fig. 1.

This flight path views a liquid hydrogen moderator which produces a neutron spectrum peaked at a wavelength of 2.4 Å but with usable flux from 0.3 to 15 Å. For design purposes when estimating the low-Q limit of the instrument we have chosen λ = 8 Å to represent the maximum wavelength for obtaining statistically significant results.

The detector resolution and efficiency are assumed to be good enough not to affect optimization. For instance, the proposed larger Anger camera has an rms resolution better than 1.5 mm, and it will be digitized in bins 2.3 mm square. This will not contribute significantly to the resolution if the sample-to-detector distance is greater than 3 m. The ^{3}He detector, however, has an rms resolution of nearly 4 mm, and also somewhat lower

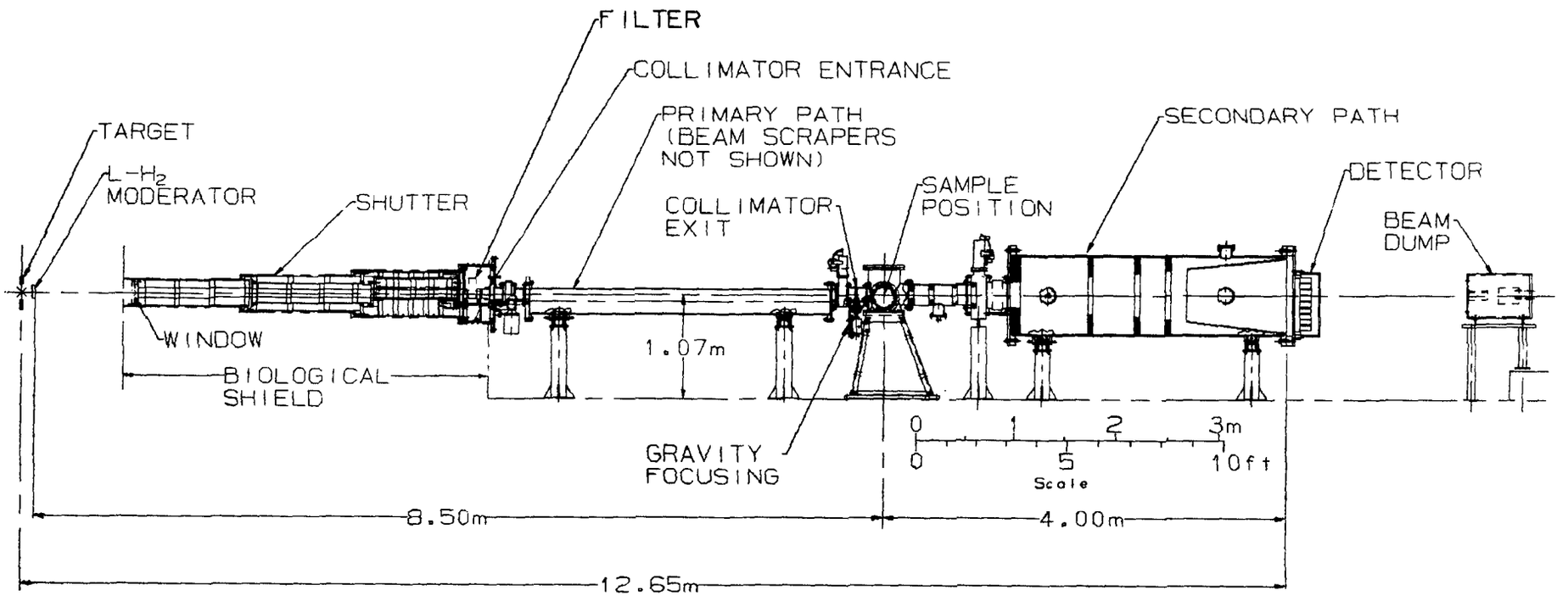

Fig. 1. Elevation view of the Low-Q Diffractometer.

efficiency than the Anger camera; we expect to use this detector only until the new and larger Anger camera is built.

2. Design Criteria

The parameter of interest in a small-angle experiment is the momentum transfer, $\hbar Q$, which is inversely proportional to the wavelength and approximately proportional to the scattering angle. The primary requirement of the instrument is to be able to take statistically significant data at a minimum value of Q of the order $Q_{min} = 0.003$ Å^{-1}. With $\lambda_{max} = 8$ Å, the minimum scattering angle is

$$\theta_{min} = \frac{\lambda_{max} Q_{min}}{2\pi} = 3.8 \text{ mrad}$$

We also require an rms resolution at least as good as 30% at Q_{min}, so that the standard deviation of θ must be

$$\sigma_\theta < 1.15 \text{ mrad.}$$

These angular criteria establish the relative sizes of the collimator apertures.

An obvious design goal is to maximize the counting rate of an experiment. Once the angular parameters are determined, however, there is very little which can be done to affect the flux on sample[4]; for instance, if the instrument is shortened to gain flux by the $1/R^2$ increase of solid angle, then the area of moderator seen at any point on the sample must be decreased by exactly the same factor to maintain resolution. For a given moderator surface brightness (n/cm^2/ster/s), the only way to increase intensity is by increasing the sample size, up to the limit that the full moderator surface is being used. Since frame overlap (as well as the available space in the experimental hall) limits the scale factor by which the design can be multiplied, the only way to increase sample size is through use of multiple-aperture collimators.

The third criterion is to allow an extended dynamic range in Q, up to at least 1.0 Å^{-1}. This is readily accomplished by utilizing a wide band of the pulsed source wavelength spectrum, and by using an area detector covering a reasonably large angular range. We will be able to record all wavelengths longer than 0.3 Å, relying on time of flight to eliminate the power pulse. We have also allowed for the possibility of including a filter to eliminate the high-energy neutrons to reduce backgrounds for experiments using only long wavelengths.

3. Collimator Aperture Sizes

Optimization of the variance of the scattering angle due to moderator and sample collimation requires that[5)]

$$\overline{r_1^2} / \overline{r_2^2} = \left(\frac{L_1 + L_2}{L_2} \right)^2 ,$$

or that the root-mean-square radii of the moderator and sample are proportional to their respective distances from the detector, where L_1 is the incident flight path length and L_2 is the sample-to-detector distance. We choose path lengths based on practical considerations, and hunt for aperture sizes which satisfy the above criteria. If the result is unsatisfactory, we can modify the path lengths and repeat the procedure. Since the geometry is additionally complicated by the separation of the defining apertures from the source and sample, a Monte-Carlo code was run to evaluate and optimize the variance. A typical result (for L_1 = 8.75 m and L_2 = 3.75 m) is

$$R_1 = 5.47 \text{ mm}, \quad R_2 = 3.03 \text{ mm},$$

producing penumbra radii at the moderator and sample of

$$R_M = 16.2 \text{ mm}, \quad R_S = 3.6 \text{ mm} .$$

4. Multiple Apertures

These moderator and sample sizes do not take full advantage of the available source area. Multiple aperture sets, all converging to the same point at the detector, increase the intensity without affecting the resolution. Figure 2 illustrates a set of 7 holes to match the size of the moderator (120 mm x 120 mm) and to illuminate a sample 36 mm in diameter. Intermediate beam scraping baffles are required to prevent neutrons crossing from one imaginary tube to another in the multiaperture system. The "Primary Path" pipe in fig. 1 will contain a rotating assembly to allow three different collimators, probably with one, seven, and nineteen holes, respectively.

5. Dynamic Gravity Focusing

At 24 Hz, neutrons recorded at the end of the frame will have fallen 8.5 mm under the influence of gravity. Rather than increasing the size of the beam stop, we want to select the neutrons whose parabolic trajectories strike the detector at its center; the "Gravity Focusing" device indicated in fig. 1 does this by pushing the collimator exit aperture plate upward during each beam pulse. The maximum excursion (for 13 Å neutrons) is

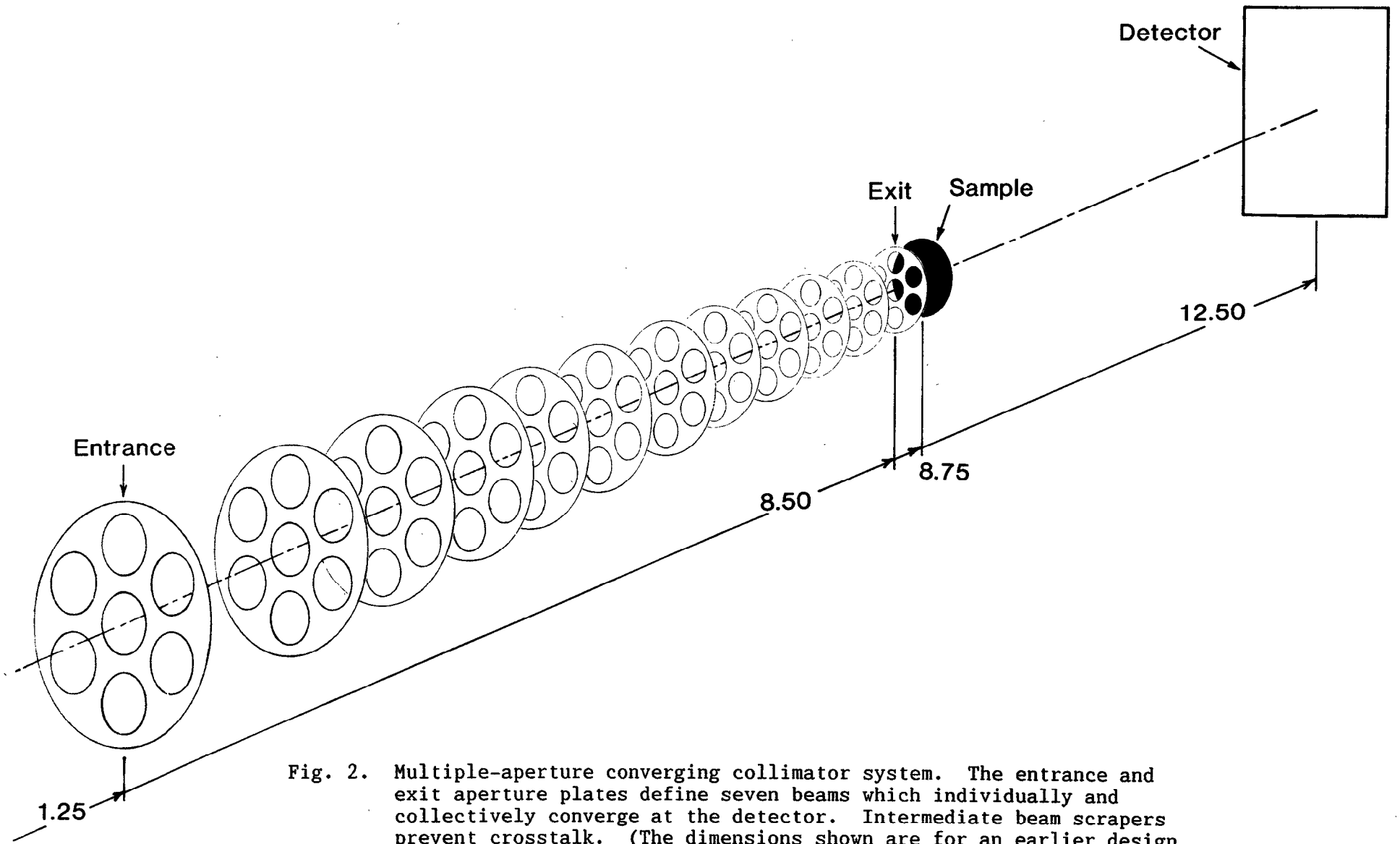

Fig. 2. Multiple-aperture converging collimator system. The entrance and exit aperture plates define seven beams which individually and collectively converge at the detector. Intermediate beam scrapers prevent crosstalk. (The dimensions shown are for an earlier design than fig. 1.)

0.82 mm. Without correction, the droop at the detector would be 4 mm. Also note that the beam-scraper apertures must be enlarged to include all the trajectories to be used.

The hydraulic servoamplifier system for the gravity focusing has been ordered, and we hope to have it working in early 1987.

6. Sample Chamber

The vacuum chamber at the sample position is 300 mm in diameter and 450 mm high. There are access flanges on the top, bottom, and both sides. A remotely controlled sample changer will be provided, as well as controlled humidity and temperature environments.

For experiments requiring larger or highly specialized environments, the sample chamber and the pipe spool attached to it may be removed, providing an open length of 1 m.

7. Detector

The detector represented in fig. 1 is an Anger camera. The 50-mm thick optical glass disperser plate is used as the vacuum window, so that there are no windows in front of the scintillator. The detector area (300 mm x 450 mm) is off-center to increase the dynamic range. A 9 x 7 array of photomultipliers detects about 700 photons from each neutron capture in the ^{6}Li-loaded glass scintillator, and linear combinations of the signals identify the location of each individual event. Using our optimized encoding scheme[6)], the time per event has been reduced (from the value of several μs in the standard Anger camera) to only 0.4 μs. This is very significant because of the high instantaneous data rates expected at LANSCE. Furthermore, the encoding in different parts of the detector may be done in parallel, so that simultaneous events may be recorded.

The Anger camera is expected to meet our design requirements, but is still under development. As a temporary alternative detector, we have purchased a ^{3}He position-sensitive proportional counter from the Risø National Laboratory in Denmark[7)].

8. Test with Anger Camera.

In December, 1985, the LQD was assembled using a previously used shutter and collimator[8)] in order to test the liquid hydrogen moderator and also the behavior of the Anger camera when placed in the direct neutron beam. The new and old parts of the instrument were not well aligned with each other, however, and there was not enough memory to record the whole detector in two dimensions. Coupled with the (expected) early-time

saturation of the detector electronics, this made it impossible for us to measure the beam position or the detector resolution. The saturation has subsequently been improved by decreasing time constants in the photomultiplier preamplifiers. The detector did "survive" in the direct neutron beam (at 10 μA proton current), and at times later than 2 ms gave a measurement of the flux from the liquid hydrogen moderator (fig. 3). This spectrum shows the peak of intensity at 14 meV (below which para hydrogen is transparent to neutrons), Bragg absorption edges in the aluminum vessel of the moderator, and a long-wavelength distribution which is similar to a Maxwellian.

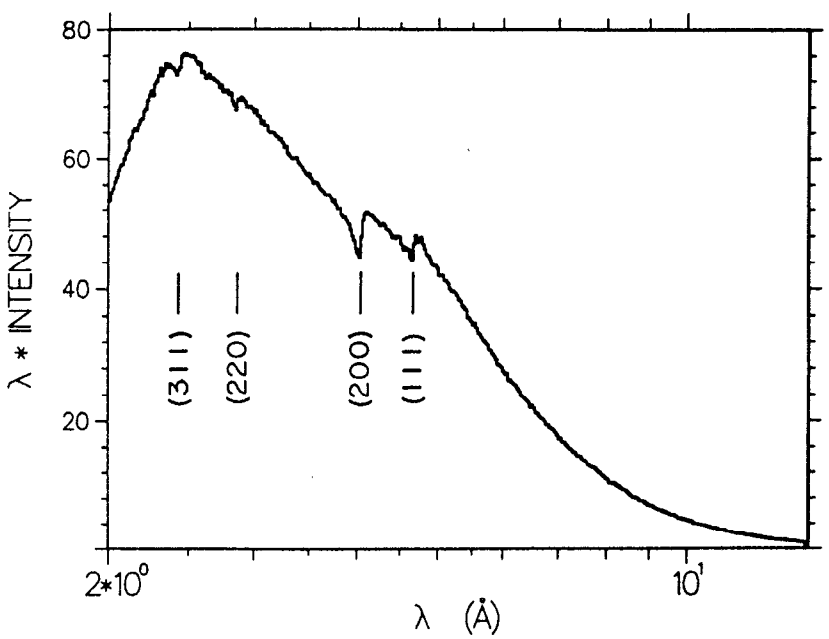

Fig. 3. Long-wavelength spectrum from the liquid hydrogen moderator. No corrections have been made for detector efficiency, or for absorption in the aluminum vessel. There is a quasi-Maxwellian tail corresponding to about 30 K, but the dominant feature is the peak at 14 meV resulting from transparency of para hydrogen.

9. Test with the ^{3}He Detector.

The instrument was reassembled in nearly its final form and another test run was made in September, 1986. The detector in this case was the newly acquired ^{3}He detector from Risø. A beam stop of pressed ^{6}LiF, 25-mm diameter by 30 mm long, was attached to the front of the detector. However we did not yet have the entrance aperture of the collimator installed, so the neutron beam was much larger and only 1/3 to 1/2 of the beam was intercepted by the beam stop. We placed about 10 cm of Pb at the sample position to attenuate the beam and to scatter neutrons into the full detector area.

The preamplifiers on the vertical dimension of the detector, purchased from Ordela, Inc., which were designed for use on position-sensitive

detectors, showed no signs of saturation at the time of the proton pulse. Unfortunately we had damaged the horizontal preamps, and an attempt to replace them with "standard" preamps failed because they saturated and remained dead for longer than the 38.6 ms counting frame. Thus although the data acquisition system was capable of recording a full 2-Mword histogram (283 time channels × 86 X-bins × 86 Y-bins), we were unable to encode the X position. Each value of Y represents a strip across the circular detector face. Figure 4 shows observed time spectra at several vertical positions for 8 hours of beam at 22 μA. At Y = 50 there is a large contribution from the direct beam since it was larger than the stop. The first four Bragg edges of Pb are marked. At short wavelengths, the transmission of the Pb is 8%, and the other 92% of the beam is multiply scattered into 4π ster. Figure 5 is a summation of the wavelength band from 1.2 to 2.8 Å, plotted vs. vertical position. A Gaussian has been drawn through the direct beam profile. At wavelengths longer than 5.7 Å we observe the full beam with only small-angle scattering, as illustrated in fig. 6 for a wavelength of 12 Å. Note that the beam center is considerably lower on the detector, due to gravity.

10. Future Schedule.

The single-aperture collimator will be completed and a variety of calibration samples will be run in December, 1986. Guided by the results of those tests and the tests already performed, the instrument will be completed during the following six-month shutdown of LANSCE. The gravity focusing mechanism and the multiple-aperture collimators will be installed, a small scintillator monitor detector will be mounted at the center of the beam stop in front of the main detector, the new Anger camera will be built, and a filter will be designed to be placed before the collimator entrance aperture. New permanent shielding will be installed around the detector and around the collimator apertures. We will also be developing and adapting software to analyze the 1986 data and to be prepared for the 1987 run cycle. The instrument should be fully operational and ready for outside experimenters by the end of 1987.

Acknowledgments

The LQD would not be as well along as it is today without the help which has been received from colleagues at the IPNS and at ISIS, in the true spirit of ICANS. This work is supported by the U. S. Department of Energy.

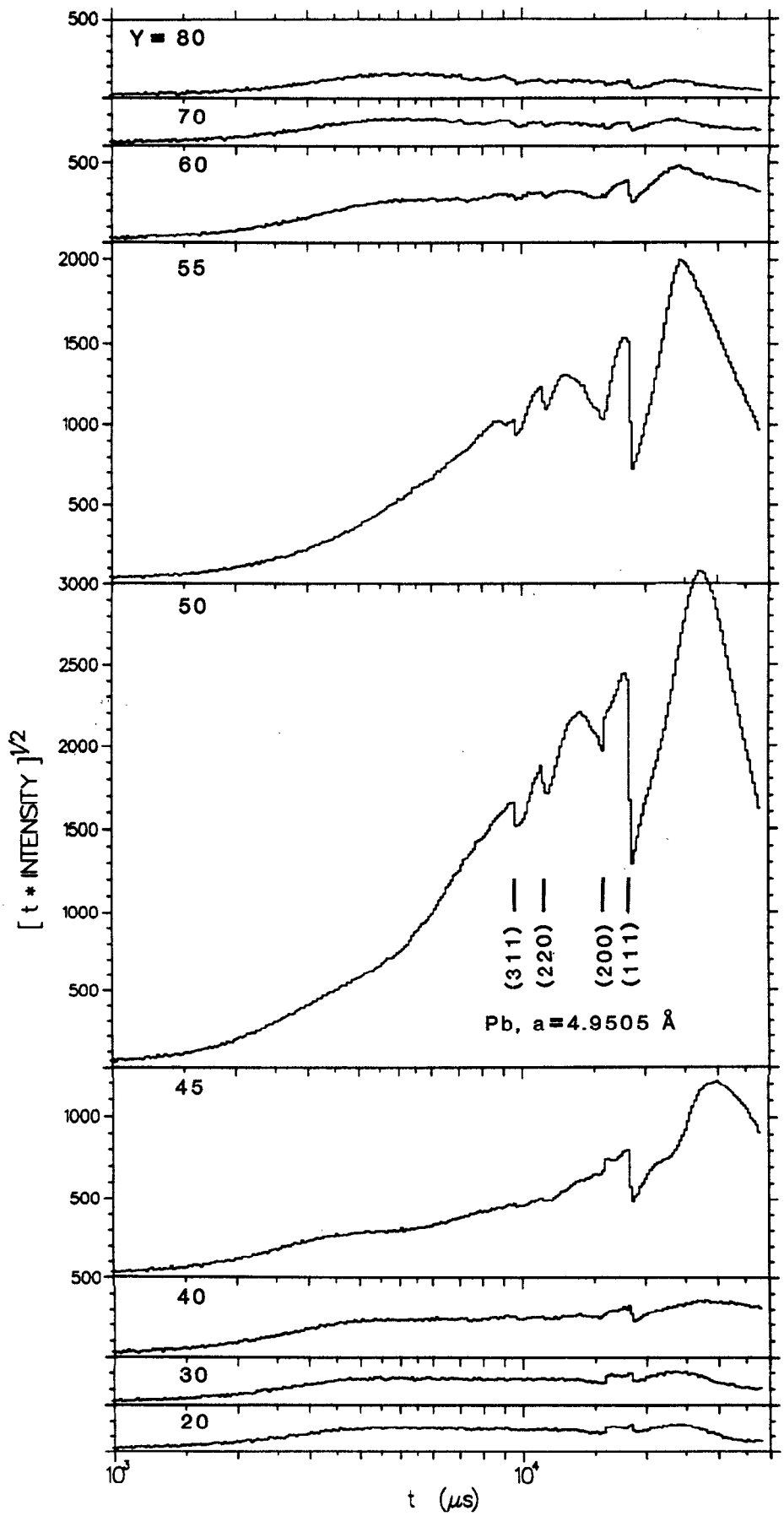

Fig. 4. Time-of-flight spectra at various vertical positions, summed across the horizontal extent of the detector. Each unit in Y is about 9 mm. There was 10 cm of Pb in the beam, leading to both large- and small-angle scattering, and to strong Bragg effects.

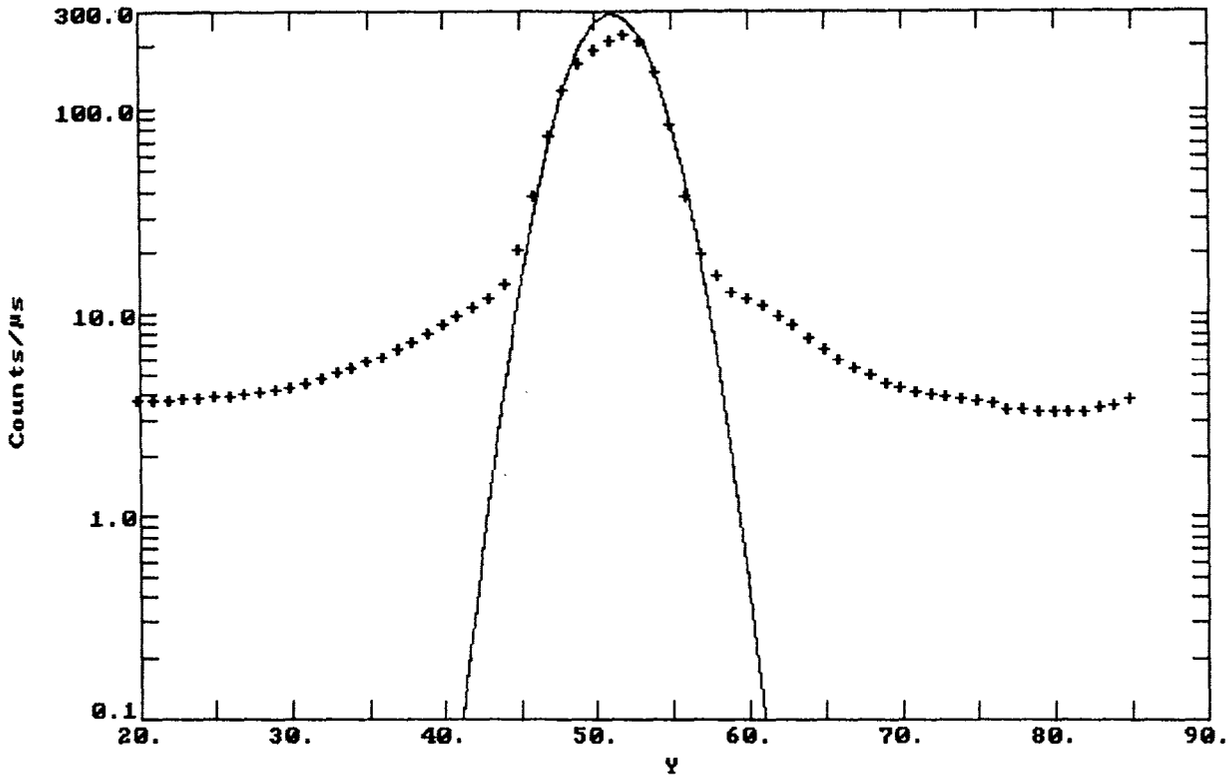

Fig. 5. Count rate as a function of vertical position, in the wavelength range 1.2 to 2.8 Å. The direct beam profile is estimated by the Gaussian; it is larger than and somewhat higher than the beam stop. In this range the scattering should be relatively isotropic.

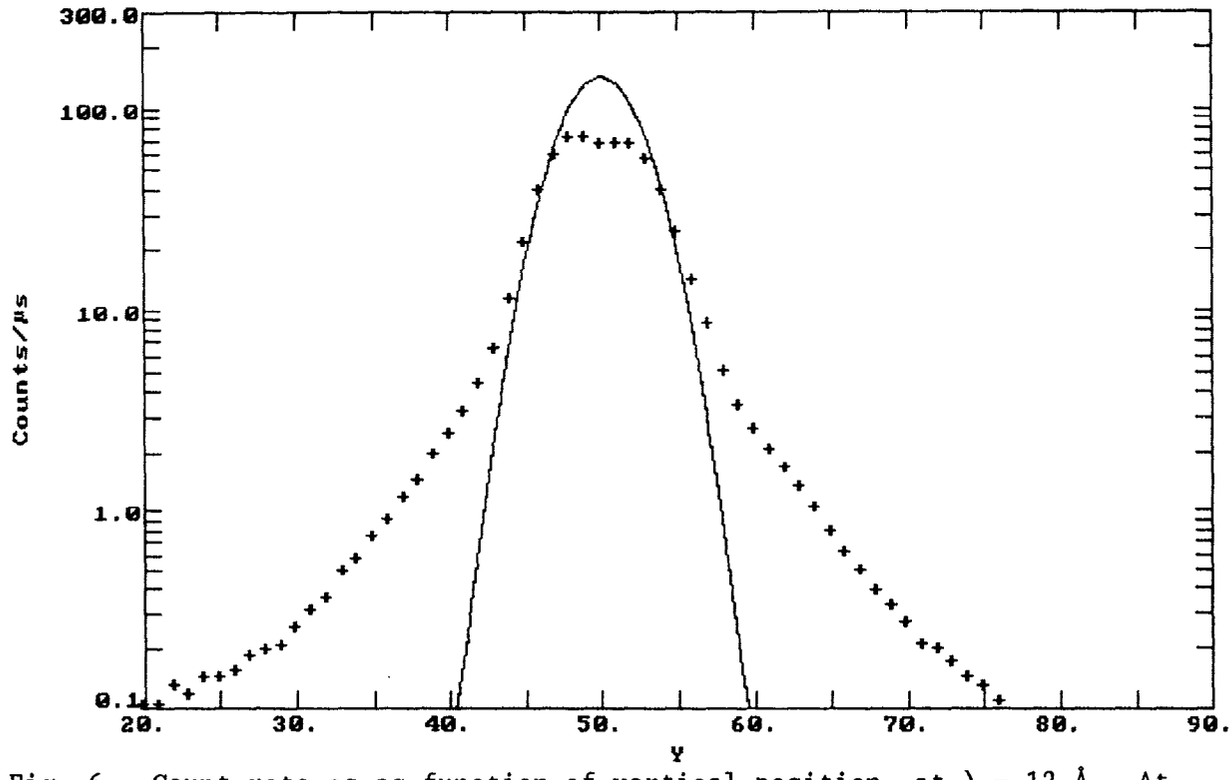

Fig. 6. Count rate as as function of vertical position, at λ = 12 Å. At this time the beam has fallen far enough to be centered on the beam stop. Small-angle scattering from the 10-cm Pb sample is apparent.

References

1. P. A. Seeger, A. Williams, and J. Trewhella, Proceedings of the Eighth Meeting of the International Collaboration on Advanced Neutron Sources, report RAL-85-110, vol. 2, p. 441 (1985).

2. H. Robinson, G. J. Russell, K. D. Williamson Jr., and F. J. Edeskuty, AIChE Symposium Series **82** (1986) 172.

3. P. A. Seeger and M. J. Nutter, Proceedings of the Eighth Meeting of the International Collaboration on Advanced Neutron Sources, report RAL-85-110, vol. 3, p. 717 (1985).

4. P. A. Seeger, Physica **136B** (1986) 106.

5. P. A. Seeger, Nucl. Instr. and Meth. **178** (1980) 157.

6. P. A. Seeger, IEEE Trans. Nucl. Sci. **NS-31** (1984) 274.

7. J. K. Kjems, R. Bauer, B. Breiting, and A. Thuesen, in "Neutron Scattering in the 'Nineties", IAEA-CN-46 (1985) 489.

8. C. G. Windsor, "Pulsed Neutron Scattering" (Taylor & Francis, London, 1981) p. 261.

ICANS IX

INTERNATIONAL COLLABORATION ON ADVANCED NEUTRON SOURCES

22-26 September, 1986

The Determination of the Complete Neutron Scattering Law $S(\kappa,\omega)$ from Total Scattering Experiments using Computed Tomography.

M W JOHNSON

Rutherford Appleton Laboratory
Chilton,Oxon,OX11 OQX

ABSTRACT

This paper describes how the considerable body of knowledge on image reconstruction from path integrals (computed tomography) may be applied to total, time-of-flight neutron scattering experiments (ie those involving no experimental energy analysis) to obtain the neutron scattering law $s(\kappa,\omega)$. It is possible that such reconstruction techniques may have wide application in the fields of neutron powder diffraction, amorphous scattering, liquids scattering and quasi-elastic incoherent scattering. The technique was first described by the author in reference [1] .

1 INTRODUCTION

In a time-of-flight neutron scattering experiment in which no energy analysis is performed the recorded intensity in a particular detector and time channel is related to a curved path integral over the κ,ω plane. Adjacent time channels from the same detector provide an integral over a neighbouring, parallel, curved path. Typical paths for a detector at a scattering angle (2Θ) of 10° are shown in Fig.1a. Detectors at different scattering angles have different paths and those for 30° and 60° are shown in Fig.1b and 1c.

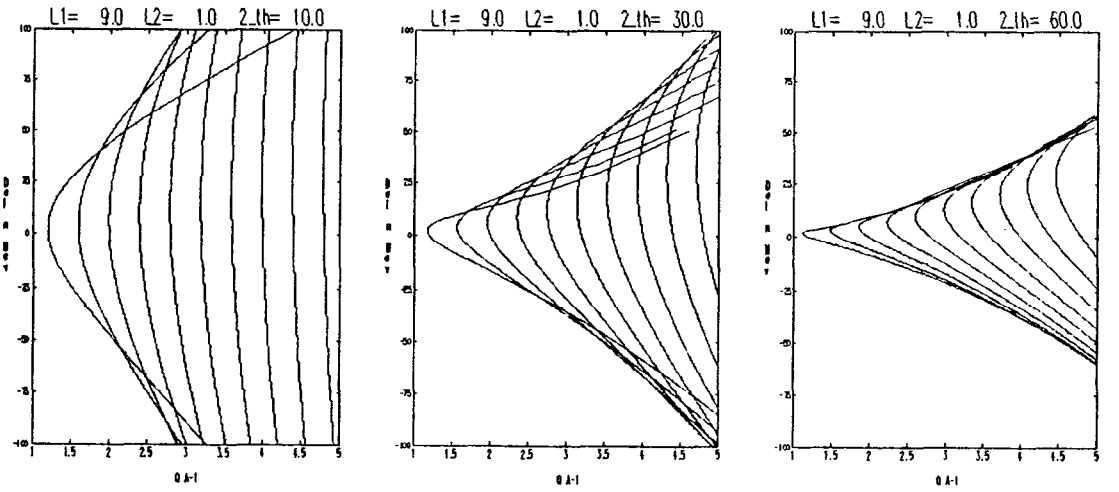

Fig 1

If the path integral can be written down in terms of a scattering law which is path-independant the problem may be mapped to the image reconstruction problem solved in real-space tomography.

In §2 we show how a total-scattering time-of-flight experiment may be expressed in a form suitable for reconstruction, and an example of a reconstruction is given in §3.

2 TOTAL NEUTRON SCATTERING

We consider an idealised time-of-flight neutron scattering experiment in which a pulsed, white beam of neutrons is incident on a sample (S) and detected (D) at a scattering angle of 2Θ, Fig 2. All neutrons are assumed to leave the moderator (M) at time t=0 .

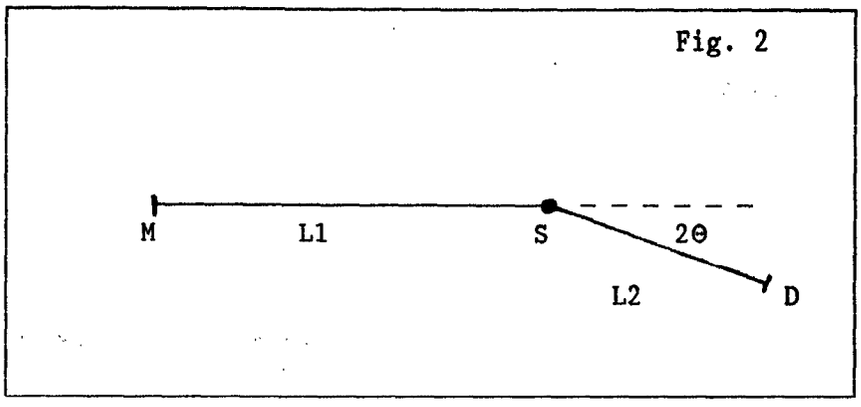

Neutrons arriving at a time t at the detector may have been elastically or inelastically scattered , but their overall flight time determines a relationship between their primary and secondary energies E1 and E2.

We have

$$t = t1 + t2 = \frac{m}{\hbar}\left(\frac{L_1}{k_1} + \frac{L_2}{k_2}\right) = \sqrt{\frac{m}{2}}\left(\frac{L_1}{\sqrt{E_1}} + \frac{L_2}{\sqrt{E_2}}\right) \qquad - 2.1$$

Thus neutrons arriving at a particular time must have scattered from a point on a locus in the (E1,E2) plane defined by eq. 2.1.

More usefully we may describe this locus in the (κ,ω) plane where

$$h\omega = E_1 - E_2 \qquad - 2.2$$

$$\underline{\kappa} = \underline{k}_1 - \underline{k}_2 \qquad - 2.3$$

$$\kappa^2 = k_1^2 + k_2^2 - 2k_1k_2\cos(2\Theta) \qquad - 2.4$$

For any value of E_2 ,E_1 is defined (eq.2.1) and from these values hω and κ may readily be determined (eqs. 2.2,2.4). The loci in the (κ,ω) plane are illustrated in Figs.1a-1c.

The point of selecting the (κ,ω) plane is that, as a consequence of the first Born approximation to the cross section [2], all neutron scattering cross sections may be described in the form

$$\frac{d^2\sigma}{d\Omega dE_2} = \frac{k_2}{k_1} F(\kappa,\omega) \qquad - 2.5$$

where $F(\kappa,\omega)$ is a function only of κ,ω and not k_1 or k_2 .

For example a monatomic liquid has:

$$F(\kappa,\omega) = \frac{N\sigma_c}{4\pi} S(\kappa,\omega) \qquad - 2.6$$

Thus $F(\kappa,\omega)$ may be regarded as an 'image' in the κ,ω plane, which remains fixed when 'viewed' from differing angles. The different angles are provided by the varying loci corresponding to different t,L1,L2 combinations. The 'view' is obtained from the fact that the number of neutrons recorded in a particular time channel are related to an integral over a locus in the κ,ω plane.

The number of neutrons arriving per unit time n(t) between times t and $t+\delta t$ in the idealised experiment shown above is given by:

$$n(t) = \int_{(\kappa,w)\ \text{locus}} d\omega \frac{d^2\sigma}{d\Omega dE_2}\phi(E_1)\eta(E_2)\left(\frac{\partial E_1}{\partial t}\right)_\omega \qquad - 2.7$$

$$= \int_{(\kappa,w)\ \text{locus}} d\omega \frac{k_2 N\sigma_c}{k_1 4\pi} S(\kappa,\omega)\phi(E_1)\eta(E_2)\left(\frac{\partial E_1}{\partial t}\right)_\omega \qquad - 2.8$$

a path integral over the (κ,ω) plane. Writing eq.2.8 in a discrete form we have

$$n_p = \sum_{i=1}^{n} \sum_{j=-m}^{+m} w_{ijp} S_{ij} \qquad - 2.9$$

where Sij is the value of $S(\kappa,\omega)$ in cell $\kappa_i \omega_j$ in the κ,ω plane and w_{ijp} is a weight for that cell for path p. Note that we have chosen n κ cells (i=1,n) and 2m+1 ω cells (j=-m,..,0,..+m) corresponding to the integral from $-\omega_{lim}$ to $+\omega_{lim}$

In the example of a monatomic liquid the weight would be:

$$w_{ijp} = \int_{(\kappa_i, w_j)\ \text{cell}} d\omega \, \frac{k_2 N \sigma_c}{k_1 4\pi} \phi(E_1) \eta(E_2) \left(\frac{\partial E_1}{\partial t}\right)_\omega \qquad - 2.10$$

We may further use the fact that the two halves of the κ,ω plane ($\omega<0$ and $\omega\geq 0$) are related by the 'detailed balance' condition [2] :

$$S(\kappa,\omega) = \exp\{\hbar\omega/k_B T\} S(\kappa,-\omega) \qquad - 2.11$$

Separating the equation 2.9 into two we may write:

$$n(t) = \sum_i \sum_{j=-m}^{j=-1} w_{ijp} S_{ij} + \sum_i \sum_{j=0}^{j=m} w_{ijp} S_{ij} \qquad - 2.12$$

$$n(t) = \sum_{i} \sum_{j=0}^{j=m} (w_{ijp} + w_{i-jp}\exp\{-\hbar\omega_j/k_BT\})S_{ij} \qquad - 2.13$$

$$n(t) = \sum_{i} \sum_{j=0}^{j=m} w'_{ijp}S_{ij} \qquad - 2.14$$

The inversion of the problem posed by eq.2.14 is completely analogous to the image reconstruction problem. A method of solution and references to similar problems is given in [1].

3 AN EXAMPLE

To illustrate the possibilities of this method the following steps were followed.

A discrete scattering law S_{ij} for an ideal gas was set up using a rectangular cell array on the κ,ω plane. Six ω cells spanned the region 0.0 to 50.0 meV, and 18 κ cells the range 1.0 to 5.0 Á-1. S_{ij} was calculated for the centre of each cell from the expression:

$$S(\kappa,\omega) = \frac{1}{\sqrt{4\pi\varepsilon k_BT}} \exp\left\{-\frac{(\varepsilon-\omega)^2}{4\varepsilon k_BT}\right\}$$

where $\varepsilon = \hbar^2\kappa^2/2M$

A table of the values of S_{ij} thus produced is shown in Table a. Eighteen time of flight values were chosen for each of ten scattering

angles and their corresponding loci in (κ,ω) space computed (see Fig.1). The t-values at each scattering angle were chosen to cross the near centre of each elastic channel. The scattering angles were $10,20,30,40,50,60,70,80,90,100^{o}$.

w_{ijp} were calculated for each path and the 180 path integrals computed from eqs. 2.10,2.13 with the assumption that the incident neutron spectrum, $\phi(E_1)$, followed that for an ambient moderator on the ISIS source [3]. The path integrals were then given random errors corresponding to fractional errors of ~ 0.5%.

The reconstruction algorithm was then applied, using only the knowledge of the path integrals and their loci on the κ,ω plane.

Table 1b gives the values of the reconstructed S_{ij} values after 500,000 cycles (~30m cup for VAX8600). This shows remarkable agreement over the entire κ,ω plane and produces good estimates of the width (in ω) of the central peak feature and identifies the shift in its centre of gravity.

0.00	0.00	0.00	0.00	0.00	0.00	0.01	0.02	0.06	0.13	0.22	0.34	0.48	0.63	0.78	0.92	1.06	1.17
0.00	0.00	0.00	0.00	0.01	0.03	0.09	0.19	0.33	0.50	0.69	0.88	1.06	1.22	1.35	1.45	1.52	1.57
0.00	0.00	0.01	0.06	0.18	0.36	0.60	0.86	1.12	1.35	1.54	1.68	1.78	1.85	1.87	1.86	1.83	1.78
0.03	0.18	0.49	0.91	1.34	1.72	2.01	2.21	2.33	2.39	2.39	2.34	2.27	2.18	2.07	1.95	1.83	1.71
2.40	3.23	3.66	3.81	3.78	3.65	3.46	3.25	3.03	2.81	2.59	2.38	2.19	2.01	1.84	1.68	1.53	1.39
7.62	6.26	5.28	4.53	3.94	3.46	3.06	2.73	2.44	2.19	1.97	1.77	1.60	1.44	1.30	1.18	1.06	0.96

Table 1a

0.01	0.01	0.01	0.01	0.01	0.02	0.01	0.05	0.07	0.13	0.24	0.32	0.49	0.61	0.78	0.92	1.12	1.15
0.01	0.01	0.01	0.03	0.02	0.01	0.08	0.18	0.31	0.48	0.69	0.88	1.08	1.23	1.35	1.47	1.47	1.56
0.01	0.02	0.09	0.00	0.17	0.39	0.60	0.89	1.13	1.36	1.55	1.68	1.78	1.84	1.87	1.86	1.83	1.80
0.02	0.06	0.41	0.93	1.31	1.70	2.01	2.19	2.31	2.39	2.38	2.34	2.26	2.18	2.07	1.94	1.83	1.71
2.42	3.24	3.67	3.81	3.79	3.65	3.46	3.25	3.05	2.81	2.59	2.41	2.19	2.03	1.85	1.69	1.53	1.40
7.61	6.27	5.28	4.53	3.95	3.46	3.06	2.72	2.45	2.17	1.94	1.77	1.58	1.43	1.29	1.16	1.05	0.95

Table 1b

4 CONCLUSIONS

It is possible that the method described above may be of considerable use in separating elastic from quasi-elastic or inelastic scattering in neutron powder diffraction. If the K-range accessible to many detectors is sufficiently large the technique may be extended to liquids and amorphous problems and possibly the mapping of quasi-elastic incoherent cross sections.

REFERENCES

1. M.W.Johnson "The Determination of the Complete Neutron Scattering Law S(Q,ω) from Total Scattering Experiments using Computed Tomography." Rutherford Appleton Laboratory Report, RAL-86-041.

2. S.W.Lovesey "Theory of Neutron Scattering from Condensed Matter" Oxford University Press, Oxford ,1984.

3. A.D.Taylor "SNS Moderator Performance Predictions" Rutherford Appleton Laboratory Report, RAL-84-120.

INTERNATIONAL COLLABORATION ON ADVANCED NEUTRON SOURCES

22-26 September, 1986

NEW DEVELOPMENT OF TOP SPECTROMETER

Y.Endoh, S.Itoh and S.Mitsuda*
Department of physics, Tohoku university
Sendai 980 Japan

*Permanent Adress:
Institute for Solid State Physics University of Tokyo,Ropponngi Tokyo 106 Japan

ABSTRACT

We report on the research development of the instrumentation of the TOP installed at the C-3 guide tube looking at the cold neutron moderator at KEK. This paper mainly deals with the newly installed data acquisition system using the PC9801 computer system combined with the time analyser which was also developed at KEK. A new multi dimensional time analyzer system with the position sensitive detectors will be installed near future.

1 INTRODUCTION

We published technical report on the instrumentation using spallation pulsed polarized neutrons, namely the TOP spectrometer installed at the C-3 quide tube looking at the solid methane moderator cooled at about 20K[1-3]. The TOP spectrometer , we believe,was completed as the first instrument which produces polarized neutron pulses with continuous wavelengths, although the wavelength region is longer than 0.3nm . Since then it has continuously been improved and also has been used for numbers of studies on solid state physics. This report is mainly described on the data handling system consisting of 4) the personal computer PC9801, several CAMAC and GPIB modules. Although the cost for this system is relatively low compared with the similar

system using the LSI-11 microcomputer, the performance is satisfactory for our purpose of the data acquisition, analysis and the control of several environmental devices.

In the next section we present the new data handling system together with some examples of data out put. The third section will be devoted to the description of a new time analayzer system for small angle scattering using polarized neutrons, which is now under construction.

2 TOP DATA ACQUISTION SYSTEM

As we described in the previous paper[3] (here after we call paper 1), the TOP instrument is capable to polarize cold pulesed neutrons with a magnetic Soller mirror polarizer[1] and it has been used for various diffraction studies as well as the polarization analysis[5]. Figure 1 depicts a schematic structure of this instrument which is duplicated from the paper 1.

The TOP data acquistion system is aimed to be used for data taking and analyzing and additionally, it is used as the controller of the TOP instrument. The data handling room is located in the building separated from the experimental hall and therefore a terminal was equipped for the sake of remote control as well as communication to the computer in the experimental hall.

The host computer of PC 9801E with ancillary processores, 8 inches disks (20M Byte) and hard disk is able to operate the GPIB and CAMAC modules via GPIB interface board and CAMAC crate controller respectively. Either raw data or their analyzed data are immediately displayed on the color CRT screen and also they are edited on screen. These pictures also turn to the hard copys

immediately. Besides the standard roles as mentioned above an extra role was added that slave computer which is assigned by users can be used as the local station communicating with the big laboratory computer , for instance. Note that the role of master or slave computer is always altered by users convenience.

The data which should be handled are listed below:

1 Digital counts distributed in multichannels of the time analyzers and signals to show the status of the time analyzers.
2 Digital out puts from the multimeters to show the environmental conditions such as temperature.
3 Several warning signals and those from limit switches.

Main controlling items are also listed:

1 The gate of each channnel and switches distributing the digital counts in time analyzers to desired channels.
2 Pulse motor drivers of various goniometers at polarizer, sample and analyzer positions.
3 Power supplies for the magnets for the polarization analyzer, in particular the vector analyzer.

Since the system is oblized to operate in the way of multitask , it was necessary for us to develop an operation system software due to the fact that the real time sharing multi operation system for this particular computer is not available yet. We have introduced a software adaptor of VMX86 with which we could modify the personal computer system to the multitask operating system. The following two figures illustrate the hardware configuration of the TOP data acquisition system and

the conceptual drawing of our multitask system. Concerning the latter figure, we explain more in detail.The real time task of TCFEE always monitors the digital out puts detecting environmental conditions such as temperature and warning signals . The back ground tasks function the way of time slice and they are commanded by users.

Although users are able to access their own made users programs, we have prepared general programs for the purpose of data acquisition , primary data handling, data analysis and data transfer, besides several controlling softwares. The following chart illustrates how the TOP data flow with these prepared softwares. Finally we presesnt here several examples of data displays which are actually colored pictures on the CRT screen. We can obtain the data either by choosing any prepared format or by making user's own format. We can also edit these dataon screen. Users usually transfer the data into the floppy disks and bring them to their own institution with them.

3 TOP MULTI DIMENSIONAL TIME ANALYZER SYSTEM

Although a detector bank for small angle diffraction is equipped now, the TOP spectrometer can not always produce satisfactory data with high resolution. In particulary the small Q data are not taken yet.Therefore we aim to replace it to a position sensitive detector (PSD) system. For that purpose, we must develop the TOP multi demensional time analyzer system (MDTA) which are now under construction. The following schematic drawing illustrates the block diagram for it.

At this moment we will use three linear PSD.Digital signals from each detector are added into the 64 positional channels

times 32 timing channels. The typical resolution in Q/Q is considered to be 0.1 corresponding to the mesh of 1cm in position times 1 msec in time. Since our measurements are dependent on neutron polarization, the additional coincidence with the spin flipper must be taken and the special circuit must be prepared distirubuting the data to at least two different (neutron spin up and down) channels. We aim to have 16 channels in total.

We hope to complete this system before the end of this year and to start the experiment by using this new system at early stage of next year.

To conclude we succeeded to develop the data acquisition system with a personal computer PC 9801. We feel that the cost performance for our system is very good. If we require much higher grade than the present performance we will face the limited capability of personal computer.But we hope that the present TOP data acquisition system can handle the complicated data of polarized neutron small angle scattering measured with a new TOP PSD system.

REFERENCES

1) Y.Endoh,J.Mizuki,Y.Sasaki and H.Ono,P609 Proc,Icans IV KEK, Tsuknba, October 1980

2) Y.Endoh,Y.Sasaki,J.Ono,S.Mitsuda and S.Ikeda, Physica 120B(1983) 45

3) Y.Endoh,S.Ikeda,S.Mitsuda, and H.Fujimoto,Nucl.Instr.Meth.A240 (1985)115

4) S.Mitsuda,Y.Endoh and S.Itoh,KEK Internal 85-13,January 1986 (in Japanese)

5) For instance, Y.Endoh and Y.Ishikawa, Physica 136B(1986) 64,references are there in.

FIGURE CAPTIONS

Fig.1 Schematic drawings of the TOP spectrometer duplicated from paper 1.

Fig.2 Hardware configuration of the TOP data acquistition system. Master or save computer is assigned by users. (See taxt)

Fig.3 Conceptual drawings of developed multitask operation system of the TOP data acquisition system.

Fig.4 Present data flow through our general softwares for the TOP data acquisition system.

Fig.5 Typical examples of the graphic displays of the data taken with the TOP data acquisition system. (a) Real time display of TA data, (b) display of the information of the data area. (c) The display of data analyzed to the polarization representation.

Fig.6 Schematic drawings of the multi dimensional time analyzer system for the linear position sensitive detector.

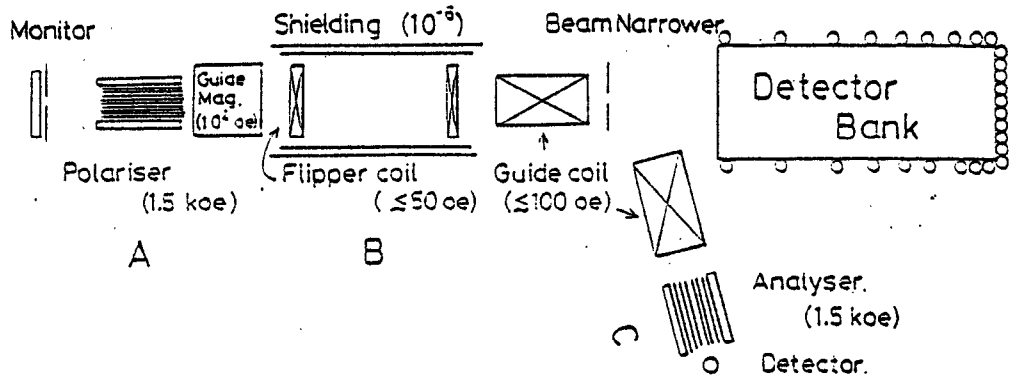
Monitor
Shielding (10^{-6})
Beam Narrower
Guide Mag. (10^{-2} oe)
Detector Bank
Polariser (1.5 koe)
Flipper coil (≤50 oe)
Guide coil (≤100 oe)
A
B
Analyser. (1.5 koe)
Detector.

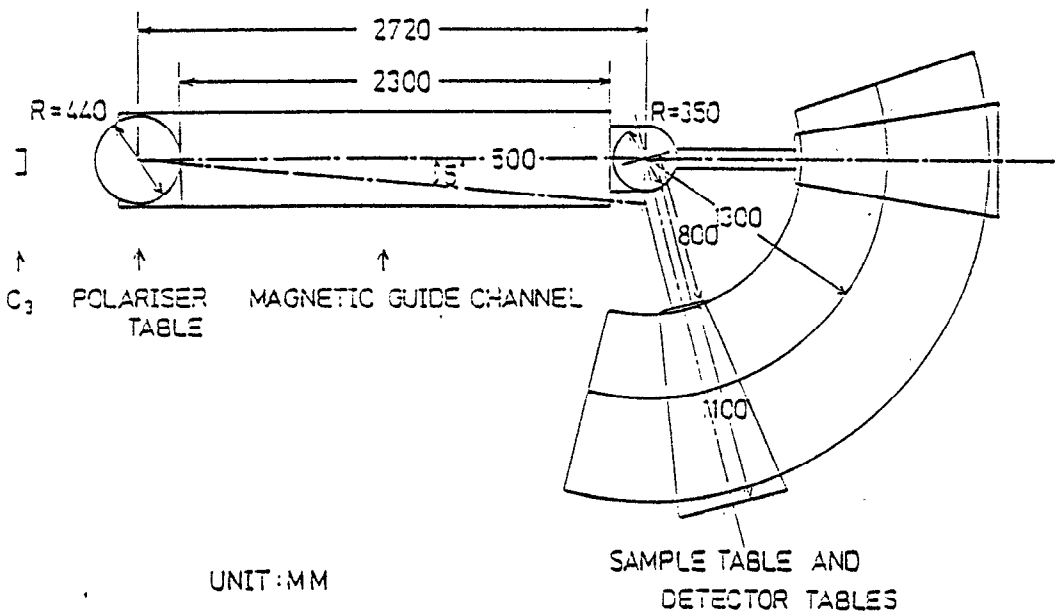
2720
2300
R=440
R=350
500
15°
300
800
100
C_3
POLARISER TABLE
MAGNETIC GUIDE CHANNEL
SAMPLE TABLE AND DETECTOR TABLES
UNIT : MM

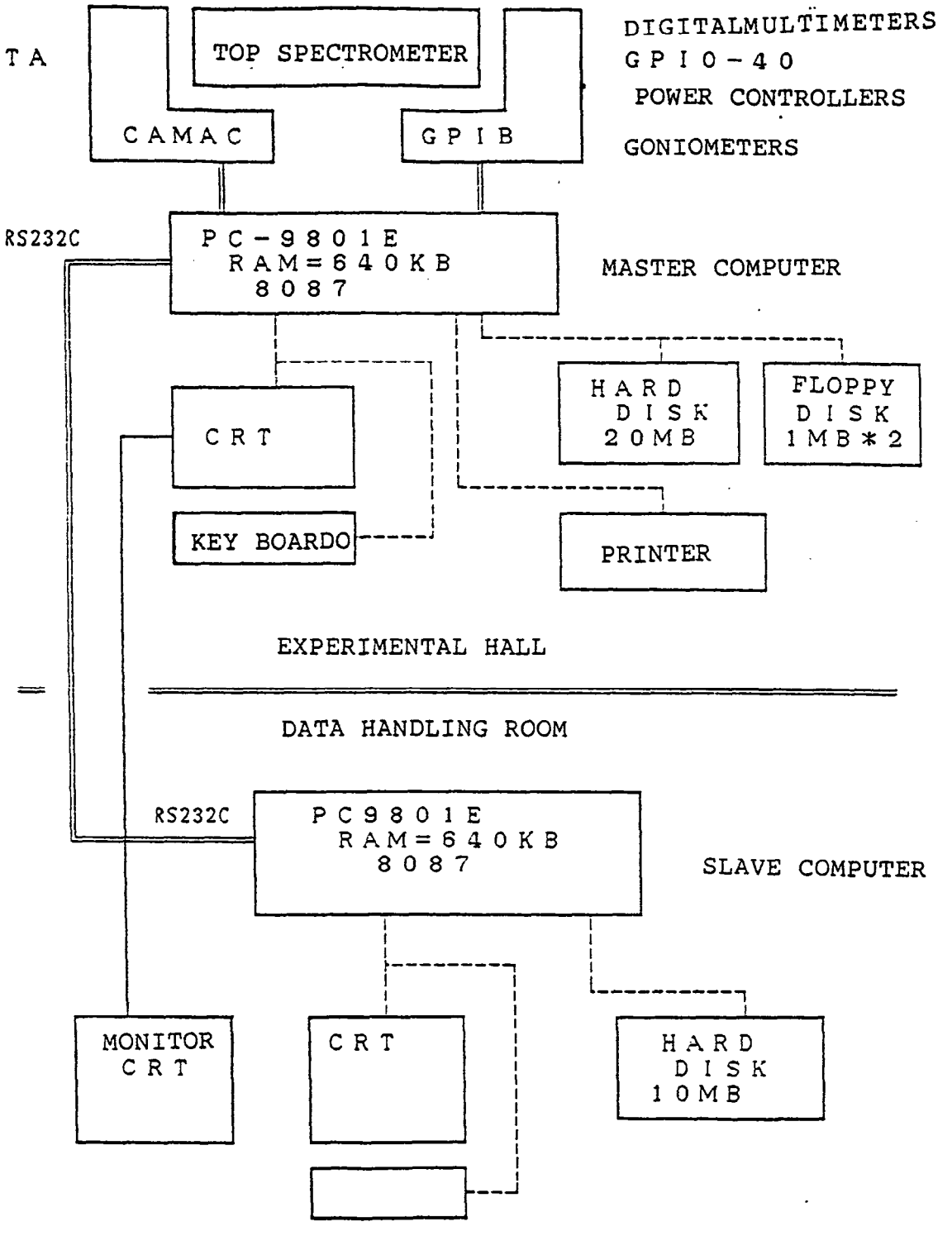
TA
TOP SPECTROMETER
CAMAC
GPIB
DIGITALMULTIMETERS
GPIO-40
POWER CONTROLLERS
GONIOMETERS
RS232C
PC-9801E
RAM=640KB
8087
MASTER COMPUTER
CRT
HARD DISK 20MB
FLOPPY DISK 1MB*2
KEY BOARDO
PRINTER
EXPERIMENTAL HALL
DATA HANDLING ROOM
RS232C
PC9801E
RAM=640KB
8087
SLAVE COMPUTER
MONITOR CRT
CRT
HARD DISK 10MB

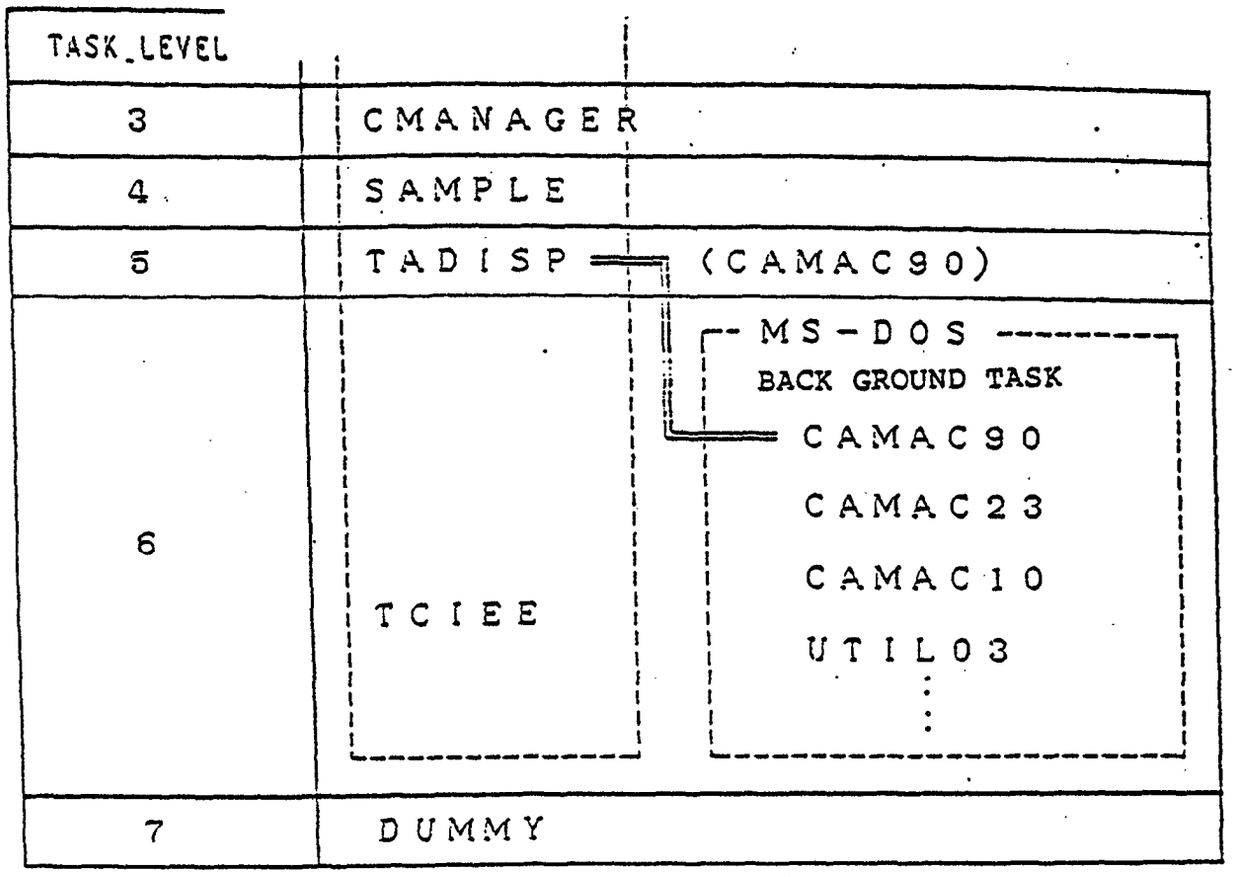
TASK_LEVEL
3
CMANAGER
4
SAMPLE
5
TADISP
(CAMAC90)
6
TCIEE
MS-DOS
BACK GROUND TASK
CAMAC90
CAMAC23
CAMAC10
UTIL03
7
DUMMY

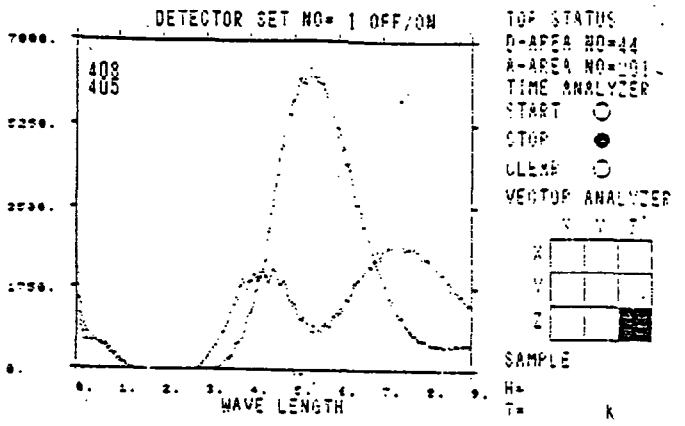

BACK UP FILE

[illegible]	[illegible]	[illegible]	COMMENT	[illegible]
1	T-350719-01 2350 2400	1985-7 -19 2 -11-30 1985-7 -19 12-30-57	[illegible] coil #1.1 [illegible] counter=2,3,4,5,6	[illegible] 273.9 .00
2	T-350706-15 2800 2751	1985-7 -7 11-31-9 1985-7 -8 12-31-47	coil #1.1 HEX=2.5 K OE	[illegible] 273.9 .00
3	T-350620-02 172 171	1985-6 -20 7 -2 -9 1985-6 -20 7 -23-2	P(NO=3)+P(NO=1) SCAN 10*10 MASKED	[illegible] 273.9 .00
4	T-350620-02 172 171	1985-6 -20 7 -2 -9 1985-6 -20 7 -23-2	P(NO=3)+P(NO=1) SCAN 10*10 MASKED	[illegible] 273.9 .00
5	T-350719-03 148 146	1985-7 -19 16-30-16 1985-7 -19 17-16-2	TEST OF U.METAL DEPOL	[illegible] 273.9 .00
6	T-350719-03 381 380	1985-7 -19 17-17-21 1985-7 -19 18-11-15	TEST U-METAL H=6 Oe depol	[illegible] 274.9 .00
7	T-350719-05 78 75	1985-7 -19 18-20-23 1985-7 -19 18-37-59	TEST OF R.COIL FOR L.P	[illegible] 274.9 .00
8	T-350719-05 197 197	1985-7 -19 18-39-9 1985-7 -19 18-59-36	TEST OF COIL H=2 -	[illegible] 273.9 .00
9	T-350719-07 85 85	1985-7 -19 19-10-9 1985-7 -19 19-21-32	TEST OF COIL H=3 A	[illegible] 274.9 .00
10	T-350719-08 159 157	1985-7 -19 19-25-39 1985-7 -19 19-47-42	BASE DATA FOR COIL R UN	[illegible] 273.9 .00

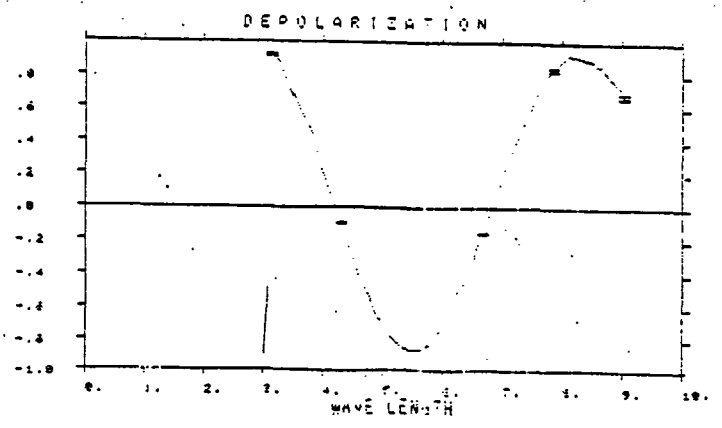

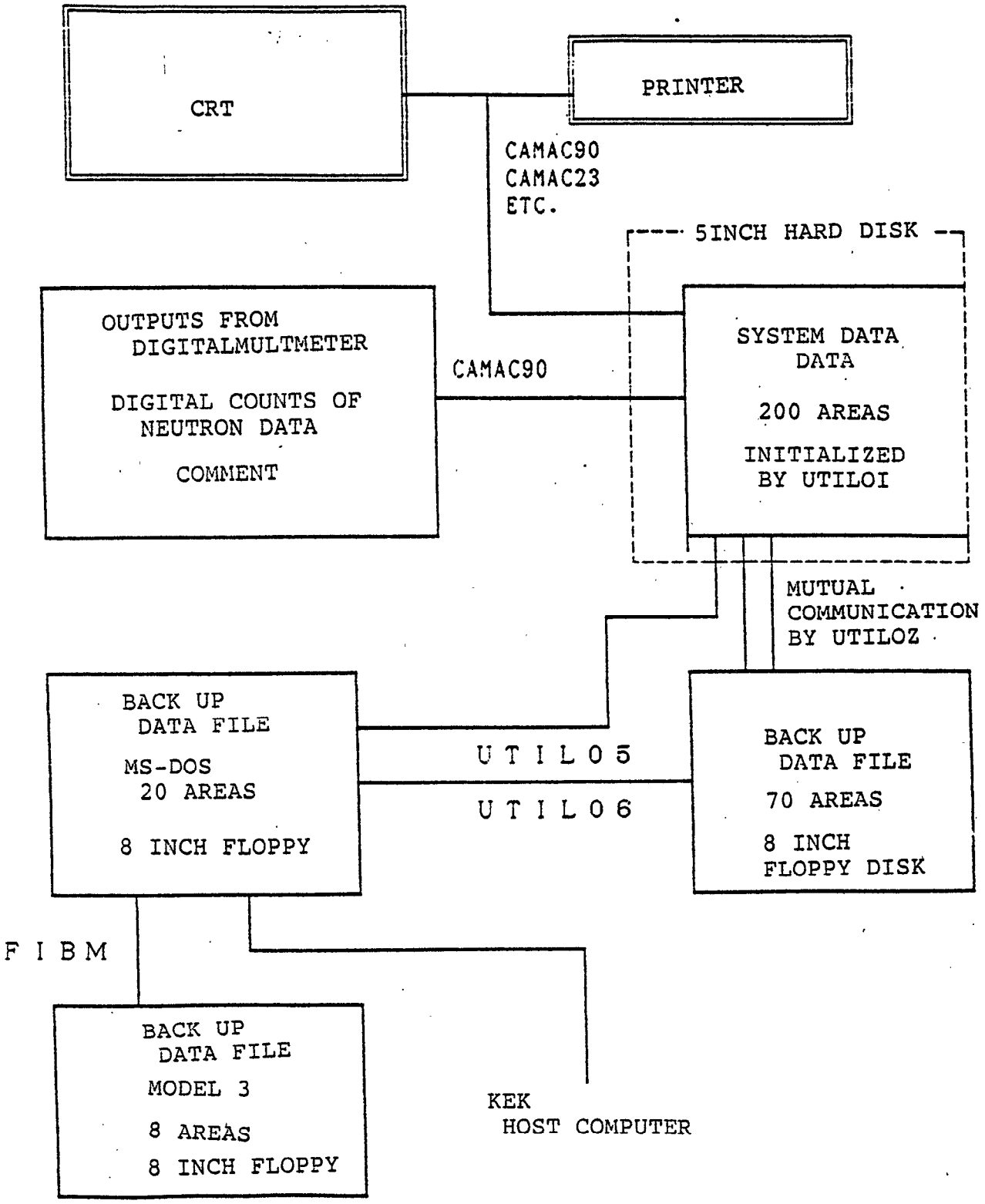
CRT
PRINTER
CAMAC90
CAMAC23
ETC.
5INCH HARD DISK
OUTPUTS FROM
DIGITALMULTMETER
DIGITAL COUNTS OF
NEUTRON DATA
COMMENT
CAMAC90
SYSTEM DATA
DATA
200 AREAS
INITIALIZED
BY UTILOI
MUTUAL
COMMUNICATION
BY UTILOZ
BACK UP
DATA FILE
MS-DOS
20 AREAS
8 INCH FLOPPY
UTIL05
UTIL06
BACK UP
DATA FILE
70 AREAS
8 INCH
FLOPPY DISK
FIBM
BACK UP
DATA FILE
MODEL 3
8 AREAS
8 INCH FLOPPY
KEK
HOST COMPUTER

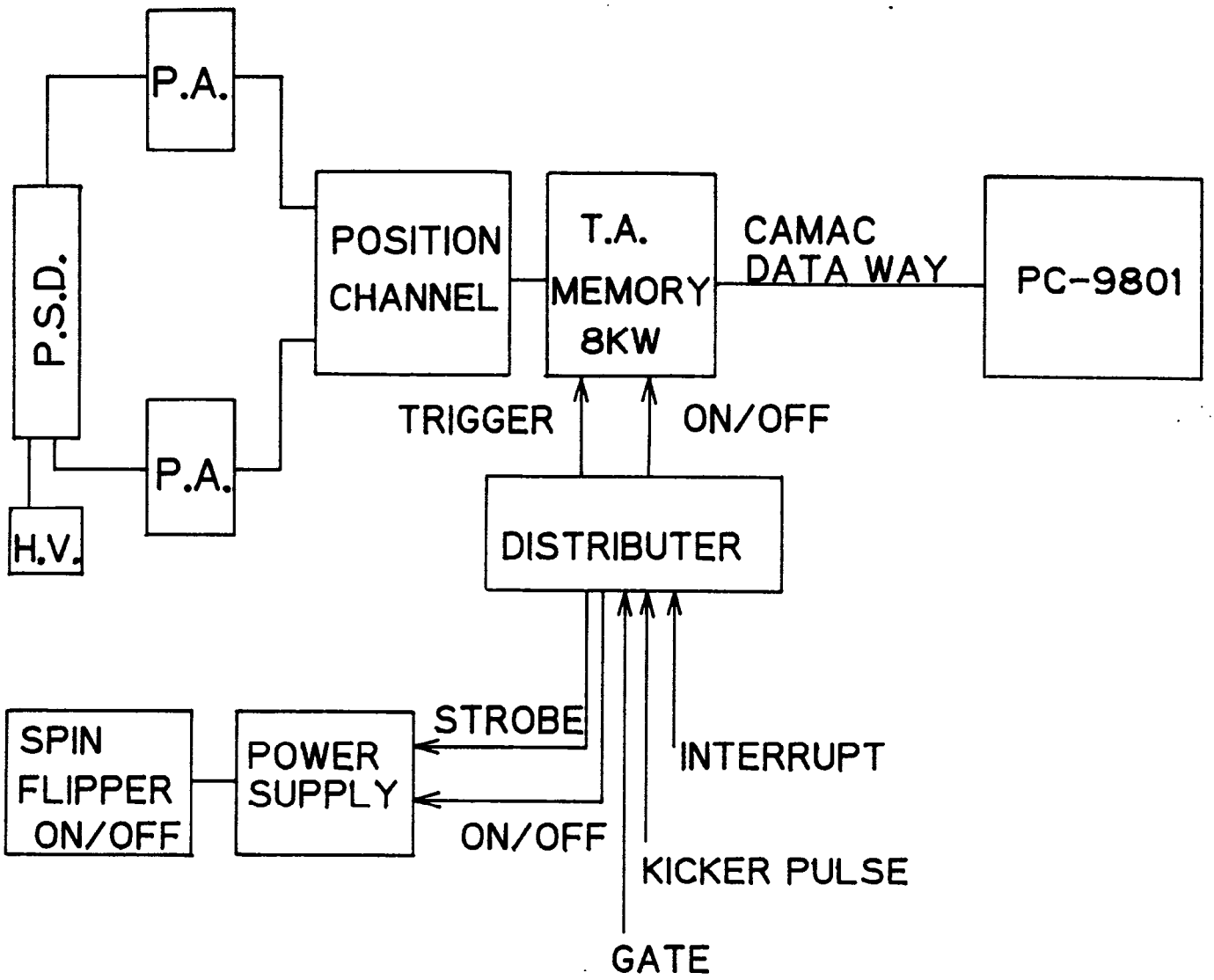
P.A.
P.S.D.
H.V.
P.A.
POSITION CHANNEL
T.A. MEMORY 8KW
CAMAC DATA WAY
PC-9801
TRIGGER
ON/OFF
DISTRIBUTER
SPIN FLIPPER ON/OFF
POWER SUPPLY
STROBE
ON/OFF
INTERRUPT
KICKER PULSE
GATE

ICANS IX

INTERNATIONAL COLLABORATION ON ADVANCED NEUTRON SOURCES

22-26 September, 1986

DATA ACQUISITION AND ANALYSIS : A FORWARD LOOK

M W Johnson,W C A Pulford,S P H Quinton

Rutherford Appleton Laboratory
Chilton,Didcot,Oxon,UK

1 INTRODUCTION

Improved neutron detector technology now enables neutron scattering instruments with many thousands, or even tens of thousands, of detectors to be built. This increase in detector numbers will have significant effects on the associated data acquisition systems for time-of-flight instruments and in this paper we attempt to identify some of the problems that are likely to arise over the next two to five years. Having posed the problem we will look at one or two solutions.

Over the next few years anger cameras will enter service with around 16,000 detector elements per camera. Single crystal instruments can quite sensibly employ 3 such cameras per instrument making a total of 48,000 detector elements on a single instrument. Using 700 time channels implies a total of 33 million time/position channels.

Similarly, new powder instruments with up to 10,000 individual scintillator tiles may be built which, when combined with the need to employ 4,000 time channels requires a total of 40 million channels storage.

Even instruments with more modest storage requirements, can quickly multiply them by the need to store time-dependant data.

2 THE EXISTING ISIS DATA ACQUISITION SYSTEM

To see how these developments will affect data acquisition systems we will examine the particular case of the ISIS PUNCH system. This is shown in figure 1.

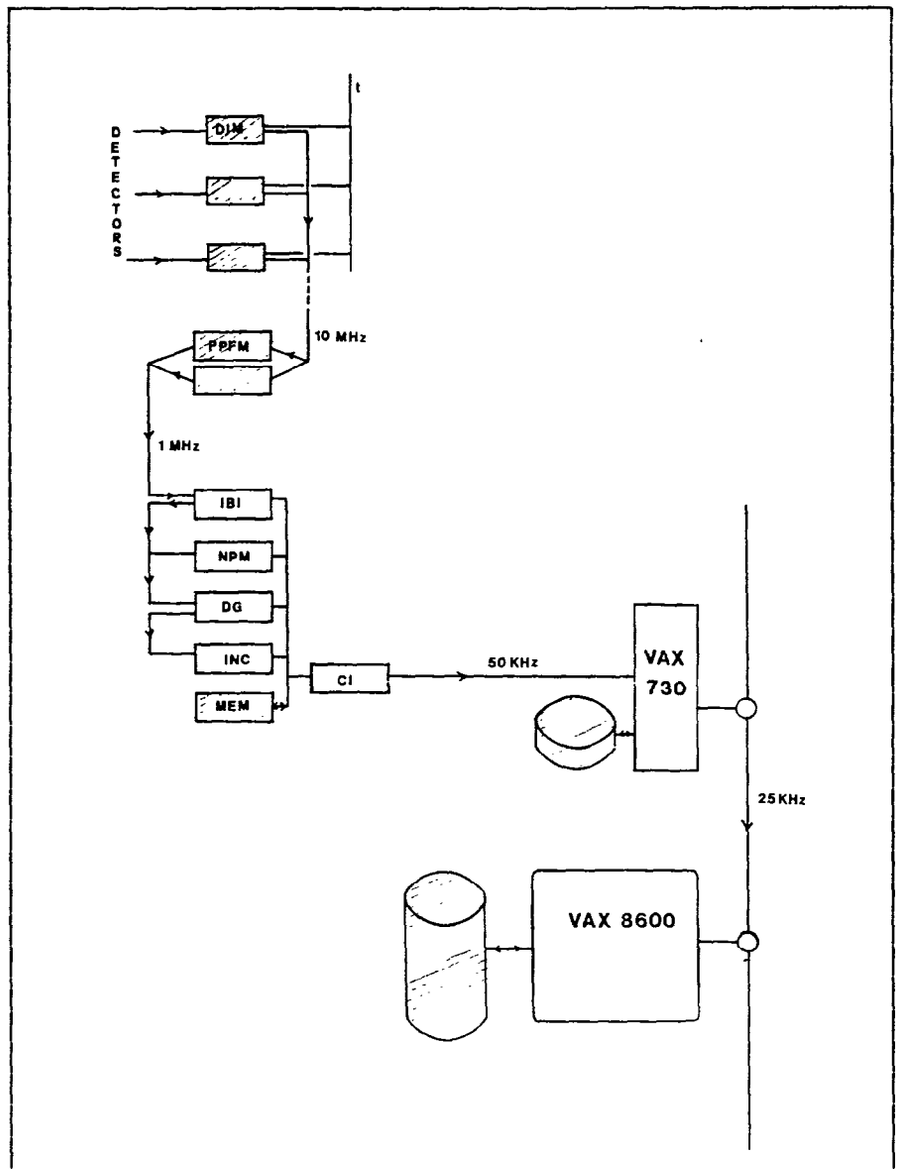

Fig. 1

The shaded components indicate the points at which data is stored. In the DATA INPUT MODULES (DIM) the neutron event is time stamped and the time descriptor stored for up to 5μs before being read out on the 10 MHz

instrument crate bus. It is then stored for one frame (20ms) in the PING PONG FRAME MEMORY (PPFM). This is to ensure that the data is not corrupted by any incorrectly taken data during the frame. Following compaction from 40 to 24 bits in the DESCRIPTOR GENERATOR (DG) the event descriptor is finally recorded by incrementing the appropriate word in the BULK STORE memory (MEM) , where it effectively remains for one run. The histogram of events is then copied to the FRONT END MINI COMPUTER disk, where it may reside for one or two days, and on to HUB computer where it may last for some tens of days for further analysis. Notice that data is stored for increasing lengths of time at subsequent locations and each pathway between storage points must be fast enough to remove all the data in the storage time of the 'up-stream' location. The transition rates within the existing ISIS PUNCH system are shown in FIG.1. In particular the transfer between the DAE memory (MEM) and the Front End Minicomputer (VAX 730) is at an effective rate of 50 Kbytes/s, and the transfer rate over the Cambridge Ring is 25kbytes/s. Thus a run using a total of $0.5\ 10^6$ time-of-flight channels that requires 2 Mbytes of memory storage in the bulk store can be transferred to the FEM computer in a total elapsed time of 40 seconds. Since most runs have a duration well in excess of 40s, no major problems arises from this combination of run size and transition speed.

3 THE PROBLEM

For the data sets described in §1 the memory storage requirement is obviously a lot higher. An experiment using 40.10^6 time-of-flight channels will require 80 or even 160 Mbytes of memory depending whether two or four bytes of memory are used for each channel. Figure 2 shows a simple modification to the existing data acquisition electronics which shows the MEM module converted to a memory controller and large numbers of new memory cards introduced in a separate crate. This overcomes the present limit of 16Mbytes on the capacity of the bulk store, and with memory prices as low as £200/Mbyte a total memory configuration of 100 Mbytes is entirely feasible.

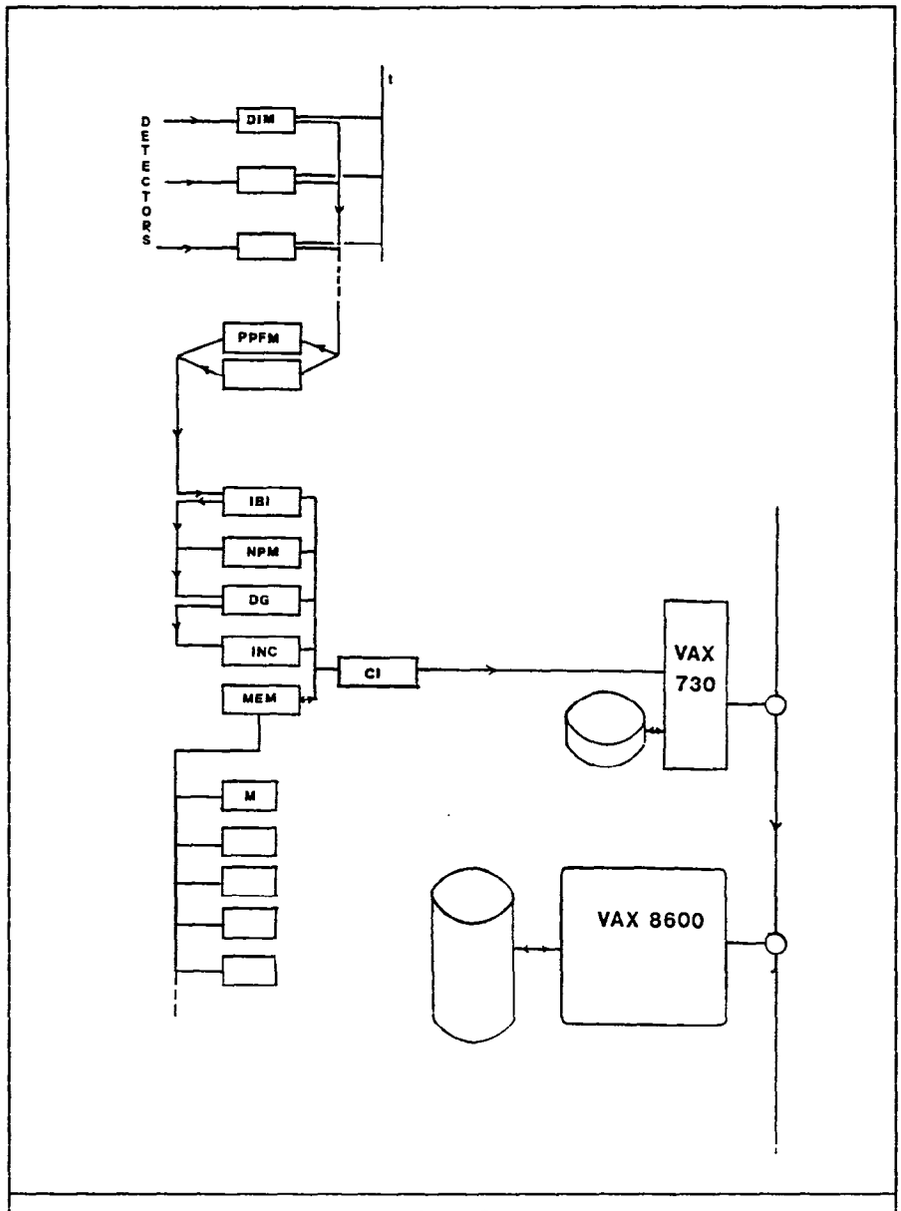

Fig. 2

However, with data sets of 80 Mbytes, the existing transfer speeds imply a transfer time of ~30m to the FEM computer and ~60m to the HUB computer. Clearly runs may last less than 1 hour and hence the transfer time will become a serious problem. This could, in principle, be solved by improved transfer speeds between the DAE-FEM and FEM-HUB , although many of the limits to these transfer rates are determined by VAX system software and may prove difficult , in practice, to change by orders of magnitude.

More than the transfer time, there is also the problem of the shear bulk

of data to be stored and the problem in displaying the entire data in some useful form. The elegant solution therefore resides in some form of data compression that may be applied either before, or at the histogramming memory stage.

4 POSSIBLE SOLUTIONS

So far two types of data compression have been identified. The first applies to single crystal instruments where the data is sparse and consists of regions of intensity in a 3-d histogram. The data may be compressed by factors of 1000 or more by extracting the integrated peak intensities and positions of the discrete Bragg reflections. The second technique applies to powder and LOQ instruments where the data compression takes the form of a transformation of the time coordinates before the spectra from different detectors may be added together. The data may also have to be corrected for wavelength dependent effects before the transformation.

4.1 Incrementer Solution

In the case of single crystal data it is conceivable that an 'intelligent incrementer' (INC figure 2), provided with knowledge about the sites of high intensity in the single crystal data, could be used to assign short words to background and long words to the high intensity regions. This has two disadvantages. It is inflexible, in that you have to know the structure and orientation of the crystal beforehand, and there is the danger of missing weak reflections. Alternatively, short words could be assigned to all regions and overflows stored as a list in a separate area of the bulk store. However, in either case, the methods would only save a factor 2 or 3 in the data storage requirement.

4.2 Descriptor Generator Solution

In the case of powder diffraction it is conceivable to shift this

intelligence to the descriptor generator (DG in Fig.2) and by providing the information necessary to shift the x coordinate on the fly a large number of individual detector elements could be summed together before the descriptors reach the memory components. For an intelligent descriptor generator to run at speeds required of a powder instrument (i.e. around 1 MHz) special signal processing chips would have to be used whose logic was essentially hard wired. This again has the disadvantage that it is inflexible. If 32 bit processor chips were used in their place this would give complete flexibility in the transformation of the descriptor on the fly but would reduce the data acquisition rate to around 10 KHz. A drawback for both DG solutions is the fact that subsequent wavelength dependent corrections would have to be performed on averaged data, with the possible erroneous assignment of weights to the correction factor.

4.3 Intelligent Memory Solution

A third possible solution is shown in figure 3. In this solution the large memory array is segmented into a number of individual memory boards each equipped with its own processor, shown as p1, p2, p3 etc. in figure 3. Programs would be down loaded via the CI interface into program storage areas (P). By a suitable choice of processor/memory board size, the data could be processed in between 10 and 100s to compress the data from the large area of memory (M - Fig.3) to the compressed area (C). This would be especially suitable for peak intensity determination in SXD type machines and the same architecture could be employed in powder machines and low Q machines. The use of the incident spectrum in the data analysis process would present no inherent difficulties since the incident spectrum would be available in part of the memory at the time of analysis. It is further possible that the compressed areas of memory could be directly connected to display systems in order to provide fast real time displays for the experimenter who is trying to determine the course of the run. Clearly in the case of powder analysis if processor p1 wishes to access memory allotted to processor p4 there is considerable advantage is the processors could be linked and it is in this way that the transputer with its inter-processor link could provide an additional advantage.

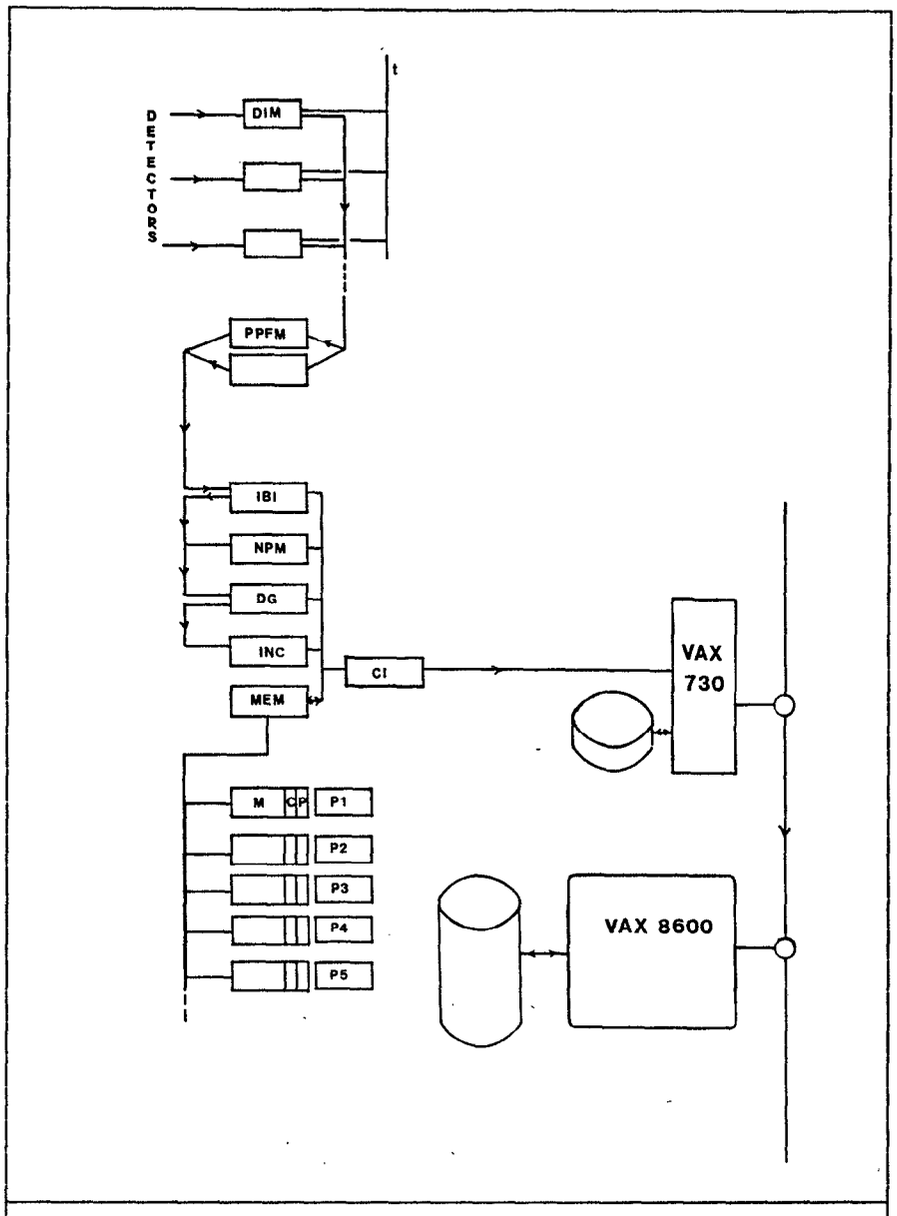
t
DETECTORS
DIM
PPFM
IBI
NPM
DG
INC
MEM
CI
VAX
730
M
CP
P1
P2
P3
P4
P5
VAX 8600

Fig. 3

ICANS IX

INTERNATIONAL COLLABORATION ON ADVANCED NEUTRON SOURCES

22-26 September, 1986

POLARISING FILTER DEVELOPMENTS AT ISIS

J Mayers[+], R Cywinski*, I R Harris[x], M Hixon[x], W G Williams[+]

[+] Rutherford Appleton Laboratory, Chilton, Didcot, Oxon, OX11 0QX

* Department of Physics, Reading University, Reading, RG6 2AF

[x] Department of Materials Science, Birmingham University, P O Box 363, Birmingham B15 2TT

As part of the development program for the polarised neutron instrument POLARIS on the ISIS spallation neutron source, tests have been performed on prototype neutron polarising filters for pulsed neutrons. The principle of operation is to align samarium nuclei at millikelvin temperatures. There is then preferential absorption of one of the two neutron spin states near the 96 meV nuclear resonance absorption in samarium. The best results obtained so far have been with a filter of sintered $SmCo_5$ cooled to 0.014K in a dilution refrigerator. The measured polarising efficiency of this filter is between 98% and 67% with corresponding total transmittances of 10% and 33% within the energy range 10 meV to 150 meV. The average value of P^2T over this range is greater than 70% of the theoretical optimum obtainable by this method.

1. INTRODUCTION

The POLARIS instrument on the ISIS spallation neutron source is at present devoted to developing polarised neutron techniques on pulsed neutron sources. The measurements described here, performed on the POLARIS beamline, are part of the program for developing efficient neutron polarisers for such sources. We wish to develop devices which will polarise both over a broad energy band in the cold and thermal neutron ranges and at epithermal neutron energies. The first requirement is necessary so that time of flight techniques can be used on a 'white' beam. The second because at present the only practical devices for polarising neutrons at high energies utilise Bragg reflections from magnetic single crystals such as the Heusler alloy Cu_2MnAl or iron-cobalt. The resulting monochromation of the neutron beam is very wasteful on a pulsed neutron source where time of flight techniques can be used to define the neutron energy. It is possible to produce low energy 'white' polarised neutron beams by using supermirrors. In principle, supermirror guides could also be constructed to operate at epithermal energies but so far their useful range of operation is limited to energies below 30 meV. Polarising filters have advantages over supermirror guides even if these could be made to operate at epithermal energies. Probably the most important advantage is that a filter will accept all beam divergences whereas the divergence of the beam transmitted by a guide is limited. However the polarising filters are more difficult to operate.

The theory of operation of resonance absorption neutron filters has been fully described previously (1,2,3), so we give only a brief description here. The filters operate by preferentially absorbing one of the two neutron spin states at energies close to neutron resonance absorption energies in aligned rare earth nuclei (4). The method depends upon producing a high atomic moment alignment in the filter either by using a ferromagnetic material or by applying a magnetic field (> 0.1 Tesla) to a paramagnetic material. At sufficiently low temperatures the nuclear moments will then align, parallel to the atomic moments, in the hyperfine

field produced by the orbital motion of the 4f electrons - the Rose-Gorter effect (5).

The Sm^{149} isotope has a nuclear polarisation of ~ 90% at 15 mK and there is a Breit-Wigner resonance centred at ~ 96 meV and with a width of ~ 67 meV (6,7). The wings of the resonance extend sufficiently far to make this isotope a useful neutron polariser at all energies between 0 and 200 meV. There is also a higher energy resonance at ~ 870 meV, which could be used to polarise neutrons at energies between 750 and 950 meV. The capture cross-sections in Sm^{149} for the two neutron spin states are

$$\sigma_{\pm} = \sigma(1 \pm \rho P_N) \qquad (1)$$

where $\rho = \frac{I}{I+1}$ is a nuclear spin weighting factor. Sm^{149} has a nuclear spin of 7/2 so that the two spin state capture cross-sections are in the ratio 8:1 at $P_N = 1$. In this paper we describe measurements on prototype filter materials containing polarised samarium nuclei.

We have concentrated on developing metallic filter materials as these have better thermal conductivity. At the high neutron intensities on ISIS it is anticipated that the extraction of the heat produced within the filter by the neutron capture process is likely to be problematical. A metallic material will allow heat to be easily conducted from within the filter to its surface. Probably more importantly a good metal to metal contact between the filter and the dilution refrigerator, used to attain the necessary millikelvin temperatures, will eliminate problems associated with the Kaptitza thermal resistance at the filter surface.

In principle a paramagnetic material will give a better performance than a ferromagnetic material unless a filter consisting of a single ferromagnetic domain can be produced. This is because of the presence of depolarisation effects in ferromagnets, which limit both the ultimate polarisation of the beam and reduce the transmitted intensity. However, so far we have been unable to find a metallic material containing samarium which behaves paramagnetically at ~ 15 mK, the temperature necessary to generate a high nuclear polarisation. At such low temperatures even small interactions will tend to cause magnetic ordering.

In the following section we describe measurements made on a 5% solid solution of samarium in palladium, which we hoped would behave paramagnetically, but which showed evidence of magnetic interactions between the samarium atoms. We also describe the results of measurements on a filter consisting of the ferromagnet $SmCo_5$. This material has produced by far the best polarising performance of any polarising filter so far developed.

2. MEASUREMENTS ON $Pd_{0.95}Sm_{0.05}$

The samarium and palladium used in the preparation of the filter were supplied by Rare Earth Products and Johnson Matthey Chemicals Ltd. The purity of the samarium was 99.99% and the palladium was 'specpure'. The alloy was prepared in the Department of Materials Science and Metallurgy at the University of Birmingham. Appropriate amounts of the two metals were argon arc-melted several times on a water cooled copper hearth and the resulting button was homogenised for two weeks at 1200°C in an argon atmosphere. The homogeneous alloy was cold rolled to a thickness of 0.84 mm and then annealed for a further six hours at 800°C to relieve internal strains. Energy dispersive X-ray analysis gave a composition of 5 at % Sm. The filter was soldered to a copper plate which was attached by screws to the bottom of the dilution unit of a dilution refrigerator supplied by Oxford Instruments Ltd.

In the first measurement, the transmittance of the filter was measured at a temperature of 1.2K. The transmittance of the filter is essentially

$$T_h = \exp(-\,Nt\,\sigma) \tag{2}$$

where Nt is the number of samarium atoms/cm^2 and σ is the absorption cross-section of samarium. All other absorption and scattering processes within the filter are negligible compared to the samarium absorption. The samarium absorption cross-section as a function of energy E can be written as

$$\sigma(E) = \left(\frac{A_1}{E}\right)^{\frac{1}{2}} \frac{A_3}{1 + \left[\frac{2(E-A_1)}{A_2}\right]^2} + \frac{A_4}{E^{\frac{1}{2}}} + \left(\frac{A_5}{E}\right)^{\frac{1}{2}} \frac{A_7}{1 + \left[\frac{2(E-A_5)}{A_6}\right]^2} \tag{3}$$

The first and third terms are Breit-Wigner forms for the nuclear resonances nominally at 96 meV and 872 meV (6,7). The second term is a negative energy resonance which becomes significant only at low energies and gives a capture cross-section which is inversely proportional to the neutron velocity. The neutron energy is related to its time of flight, t, by $E = 5.2276 \times 10^6 L^2/t^2$ where L, the moderator to detector distance is in metres, t is in μsec and E in meV. [The moderator-detector distance, 10.55 m was calculated by fitting the transmitted time-of-flight spectra from uranium and iridium for which the resonance energies are known accurately.]

Figure 1 shows the measured PdSm transmittance and a fit to the data using the functional form given by equations 2 and 3.

We obtained the values

A_1 = 96.3 (± 0.1) meV
A_2 = 62.7 (± 0.3) meV
A_3 = 5.17 (± 0.03)
A_4 = 0.34 (± 0.01)
A_5 = 878.0 (± 1.0) meV
A_6 = 68.1 (± 0.1) meV
A_7 = 0.774 (± 0.001)

The quoted errors are estimates obtained by observing the variation in the final fitted parameters as the input values to the fitting routine were varied. The energy values are in good agreement with resonance parameters given by Marshak et al (6) and Asami (7). The number density Nt was calculated from A_3 and A_4 using a value for σ (98 meV) of 18200 barns and for σ (870) of 2760 barns; this gave the value $Nt = 2.84 \times 10^{20}$ Sm atoms/cm^2. This number density is slightly greater than the optimum value for a samarium filter (8).

In order to characterise the filter performance it is also necessary to find the ratio of the neutron transmittance at operating temperature (T_c) to that at 1.2K (T_H). At 1.2K the nuclear polarisation, P_N, is insignificant. It can easily be shown (1,2) by using equation (1) to calculate the transmittances of the two neutron spin states, that

$$\frac{T_c}{T_H} = \cosh\ (\rho P_N\ Nt\sigma) \qquad (4)$$

The measured transmittance ratio for $Pd_{0.95}\ Sm_{0.05}$ is shown in Figure 2 together with the fit to equation (4). Using the value of $Nt\sigma$ calculated from the transmittance at 1.2K, the nuclear polarisation, P_N, was found to be 0.336. The measurements were performed at a temperature of 25 mK (measured by Co^{60} nuclear orientation thermometry) and in a field of 2.5 tesla. Under these conditions the expected nuclear polarisation for Sm is ~ 0.78.

The most probable explanation for the low nuclear polarisation is that there are magnetic interactions between the Sm atoms. This hypothesis is supported by the observation that when the magnetic field was reduced to zero, some nuclear polarisation was retained. Figure 3 shows the measured and fitted transmittance ratio at zero field. The fit gave a residual polarisation $P_N = 0.18$, confirming that the filter is not behaving as an ideal paramagnet.

The transmittance, T, and the polarising efficiency, P, of the filter are given by

$$T = \exp(-\ Nt\sigma)\ \cosh(\rho P_N\ Nt\sigma) \qquad (5)$$

$$P = \tanh\ (\rho P_N\ Nt\sigma) \qquad (6)$$

P and T, calculated using the fitted values of $Nt\sigma$ and P_N, are shown in figure 4 as a function of wavelength. Both P and T are significantly lower than the values achievable in a fully aligned Sm filter.

3. MEASUREMENTS ON SINTERED $SmCo_5$

$SmCo_5$ is widely used as a commercial ferromagnet with high coercivity and magnetic inductance. The filter used for the neutron measurements was also prepared and characterised at the Department of Physical Metallurgy, University of Birmingham. Slices of dimensions 4 cm x 1 cm x 0.1 cm were cut from a parent block of sintered $SmCo_5$ using a low speed 'isomet'

diamond cutting wheel. These slices had their magnetic C-axis in the plane of the slice and along the 1 cm edge. Each slice was subsequently spark planed to a thickness of 0.024 cm to give the required Sm atomic thickness.

A small sample of the material was analysed on a Sucksmith type magnetic balance to find the degree of magnetic alignment. The remanence both parallel ($Br_{\parallel}$) and perpendicular ($Br_{\perp}$) to the alignment direction was measured. The mean value $\langle\cos\theta\rangle$ where θ is the angle between the crystallographic c axis of the individual particle and the alignment direction of the filter was determined using an empirical model and found to be 0.91.

A filter of dimensions 3 x 4 cm was constructed by laying the slices side by side. This was contained inside a hollow aluminium filter holder and the measurements were performed with the filter immersed in the He^3-He^4 mixture of the dilution refrigerator. Good thermal contact between the material and the mixture was expected because of the large surface area/volume ratio of the sintered material, where the measured particle diameter was ~ 1 micron. The procedure used to characterise the filter performance was identical to that described in section 2. The neutron beam was collimated to a 1 x 2 cm size to ensure that all detected neutrons had passed through the filter. The values of the ^{149}Sm nuclear resonance parameters obtained from the fit to the filter transmittance at 4.2K were

A_1 = 96.1 (± 0.1) meV
A_2 = 67.3 (± 0.1) meV
A_3 = 4.15 (± 0.04)
A_4 = 0.235 (± 0.01)
A_5 = 870.2 (± 0.1) meV
A_6 = 75.2 (± 0.1) meV
A_7 = 0.61 (± 0.01)

These are also in good agreement with previously published values of these resonance widths and positions. In figure 5 we show the measured transmittance ratio for $SmCo_5$ together with a fit to the data. The temperature of the dilution unit measured by Co^{60} nuclear orientation

thermometry was 14 mK. The solid line is a fit to the function (1,2)

$$\frac{T_c}{T_H} = \exp(-Dt)\ [\cosh(Kt) + \nu\sinh(Kt)]\ \exp(C_4/\sqrt{E}) \tag{5}$$

where $Kt = [(Nt\,\sigma\rho C_1)^2 + D^2]^{\frac{1}{2}}$ (5a)

$Dt = C_2(1-C_3{}^2)/E$ (5b)

$\nu = Dt/Kt$

This expression is more complicated than that of equation 4 because of the inclusion of depolarisation effects within the ferromagnetic material. In the model used to calculate depolarisation (1,2) the fitting parameter C_2 is related to the mean particle size and C_3 is the particle alignment factor, $\langle\cos\theta\rangle$. The parameter C_4 must be included to account for the different concentration of He^3 in the mixture surrounding the filter at 1.2K and 14 mK (9). Finally, parameter C_1 is equal to the product of the particle alignment $\langle\cos\theta\rangle$ and the local nuclear polarisation with respect to the particle c axis. This product is the apparent nuclear polarisation experienced by neutrons passing through the filter. We obtain the values

$C_1 = 0.81\ (\pm\ 0.01)$

$C_2 = 5.0\ (\pm\ 3.0)$ meV

$C_3 = 0.9\ (\pm\ 0.2)$

$C_4 = 1.05\ (\pm\ 0.05)\ (\text{meV})^{\frac{1}{2}}$

It can be seen from the quoted errors that the fit is very sensitive to the value of C_1 ($= P_N \langle\cos\theta\rangle$) but relatively insensitive to C_2 and C_3. This is not unexpected when there is good alignment. In the limit of perfect alignment, equations 5 reduce to equation 4 and there is no dependence on C_2 and C_3. A more accurate value for C_3 can be obtained by using the value $P_N = 0.91$ calculated for Sm at the measured temperature of 14 mK. The alignment factor is then

$$\langle\cos\theta\rangle = \frac{C_1}{P_N} = 0.89$$

This is in excellent agreement with the value determined from the measurements of remanent magnetisation. The value of the mean particle diameter derived from C_2 is again in excellent agreement with that found during the filter characterisation.

The parameter C_4 can also be checked independently. The attenuation of the He^3 in the mixture at 1.2K was measured by taking the ratio of the transmittance at 1.2K with the mixture condensed around the filter to that at 4.2K with the mixture extracted. This transmittance was fitted to the function

$$T_{He} = \exp(-C/E^{\frac{1}{2}}) \tag{6}$$

and gave $C = 2.31\ meV^{\frac{1}{2}}$. At 14 mK the mixture contains 6% He^3 (10) so the proportion of He^3 in the mixture at 1.2K can be calculated from C and C_4.

$$\text{Proportion of } He^3 \text{ in mixture at } 1.2K = 6\% \times \frac{2.31}{1.05} = 13.2\%$$

This is in very satisfacatory agreement with the nominal value of 15%.

It can be seen that excellent fits to the data were obtained and that there is good agreement with other measurements where comparison is possible. The parameters can therefore be used with some confidence to determine the performance of the filter at different neutron energies. The polarising efficiency is (1,2).

$$P = \frac{\tau \tanh(Kt)}{1 + \nu \tanh(Kt)} \tag{7}$$

$$\text{where } \tau = \frac{Nt\,\sigma\rho C_1}{Kt} \tag{7a}$$

and the transmittance is

$$T = \exp(-Dt - Nt\,\sigma)\ [\cosh(Kt) + \nu \sinh(Kt] \tag{8}$$

The values of P and T obtained from the fitted parameters for the $SmCo_5$

filter are shown in Figure 6. In Figure 7 P and T for an 'ideal' filter with the same value of σNt but with $\langle \cos\theta \rangle = 1$ are shown for comparison. It can be seen that the performance of the filter is close to the best obtainable. It can be shown that the effective intensity of the polarised beam produced by a filter is proportional to the product P^2T for a wide range of sample properties (8). Figure 8 shows P^2T as a function of neutron wavelength for the measured and ideal filters. The prototype filter gives between 70 and 80% of the effective neutron intensity of the ideal filter.

DISCUSSION

The performance of the $SmCo_5$ filter described in this paper is as to our knowledge the best measured so far of any neutron polarising filter. It could be used as a component of a polarised neutron instrument on a pulsed source. We now plan to measure the filter performance at higher neutron intensities so as to examine whether there is any onset of beam heating effects. The measurements described here were performed at 2% of full ISIS intensity on a 1 x 2 cm filter area. This corresponds to $\sim 10^6$ neutron/sec absorbed by the filter. At full intensity and with an incident beam size of 3 x 4 cm the heat load will be increased by a factor of 300. We also intend to measure the filter polarising efficiency directly by scattering the transmitted beam from a Heusler alloy polarising crystal (3).

Although the polarising efficiency of the $SmCo_5$ filter is worse than that expected from a perfect paramagnet (3), the material has a compensating advantage. This is that there is no need to apply a magnetic field to align the atomic moments. This makes the technique for obtaining a polarised beam simpler. More importantly it provides the possibility of constructing a large area filter for analysing scattered neutrons. The feasibility of building a large area $SmCo_5$ filter will be explored in the future.

REFERENCES

1. J Mayers, R Cywinski, T J L Jones and W G Williams, 'Neutron Tests on Samarium Polarising Filters', Rutherford Appleton Laboratory Report RAL-84-118 (1984).

2. J Mayers, R Cywinski, T J L Jones and W G Williams, J Phys D Appl Phys 18, 1843 (1985).

3. F F Freeman and W G Williams, J Phys E Sci Inst 11, 459 (1978).

4. R Cywinski, J Mayers and W G Williams, 'Resonance Absorption Polarising Filters for Epithermal Neutrons', Rutherford Appleton Laboratory Report RL-81-043 (1981).

5. M E Rose, Phys Rev 75, 213 (1949).

6. H M Marshak and V L Sailor, Phys Rev 109, 109 (1958).

7. T Asami, K Okamoto, K Ideno and Y Ohno, J Phys Soc Japan 26, 225 (1969).

8. J Mayers, 'Errors and Optimum Polarising Filter Thicknesses in Polarised Neutron Experiments', Rutherford Appleton Laboratory internal report NDR/P6/84 (1984).

9. O V Lounasmaa, 'Experimental Principles and Methods Below 1K', Academic Press, London p18 (1974).

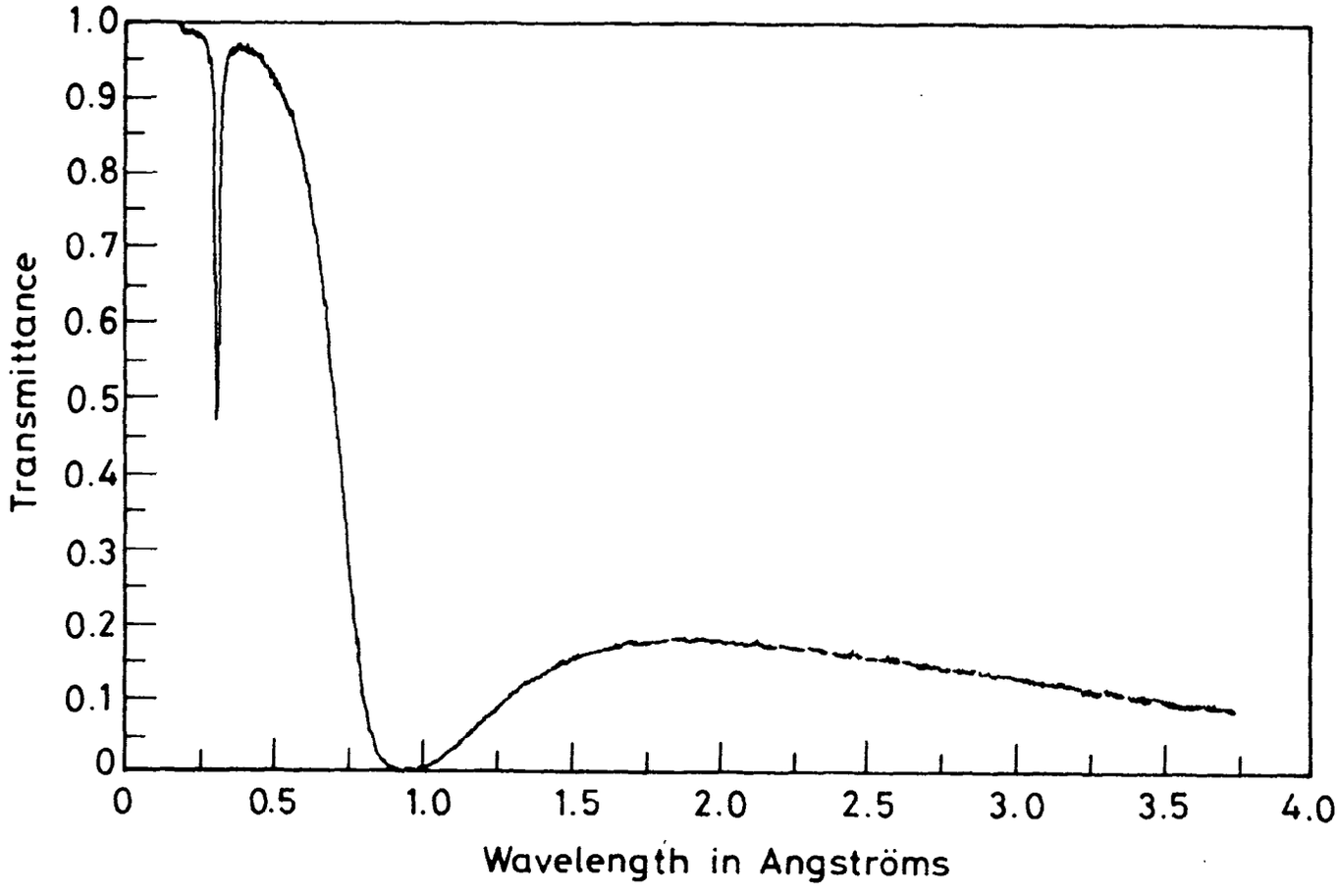

Figure 1. Transmittance of $Pd_{0.95}Sm_{0.05}$ at 1.2K

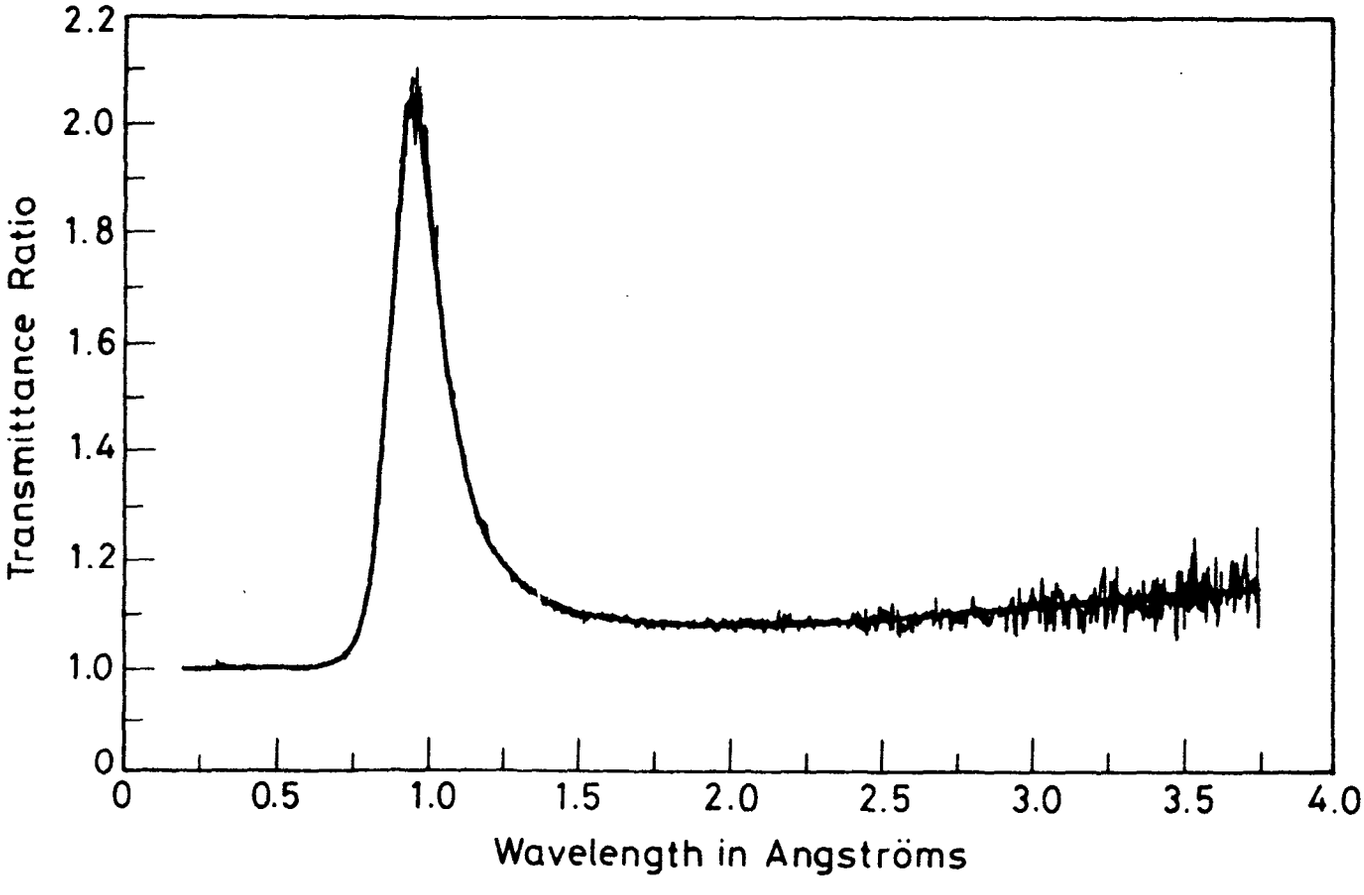

Figure 2. Transmission Ratio for $Pd_{0.95}Sm_{0.05}$, 25mK : 1.2K. Applied field = 2.5 Tesla

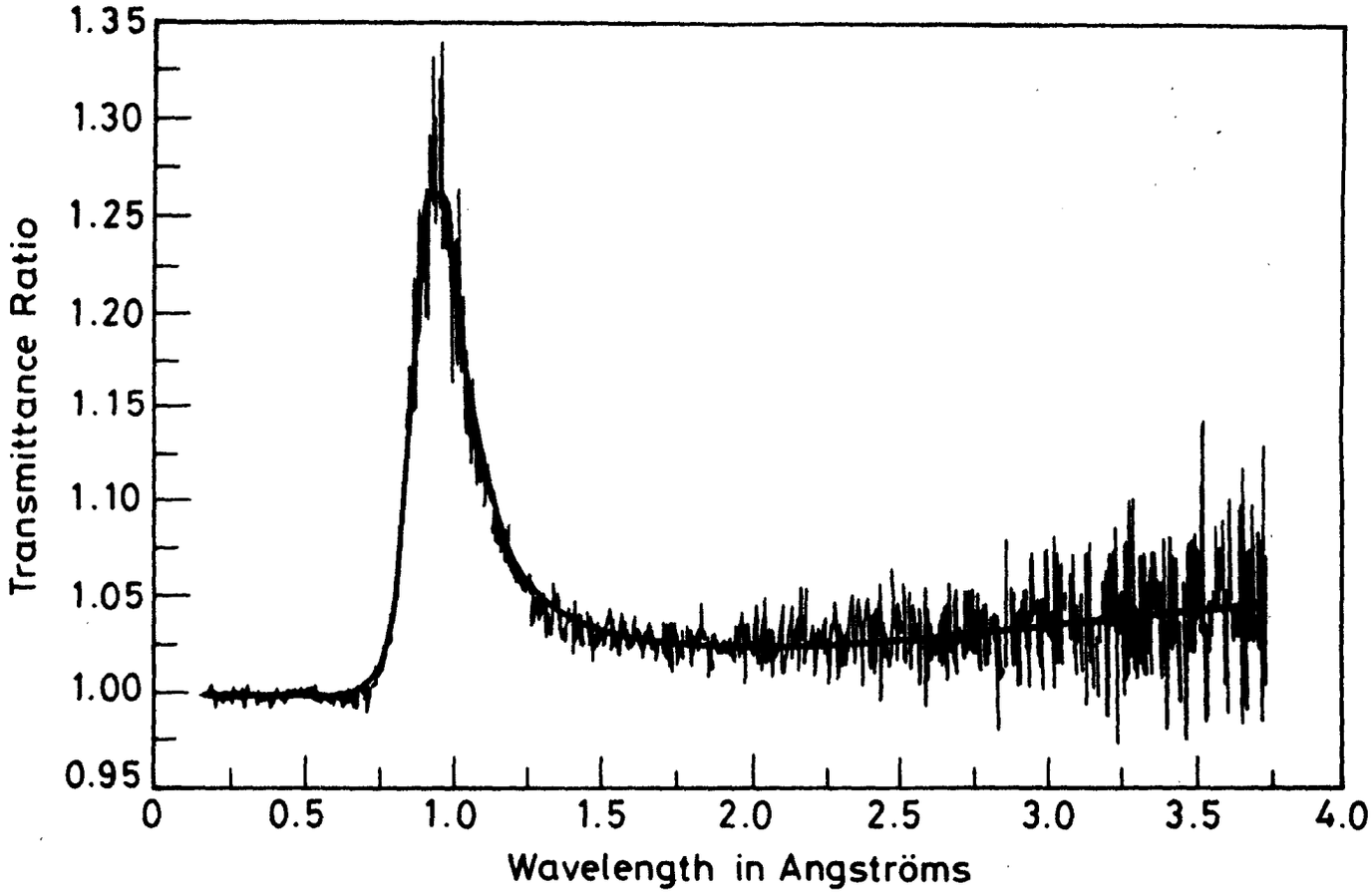

Figure 3. Transmission Ratio for $Pd_{0.95}Sm_{0.05}$, 25mK: 1.2K. Applied field = 0

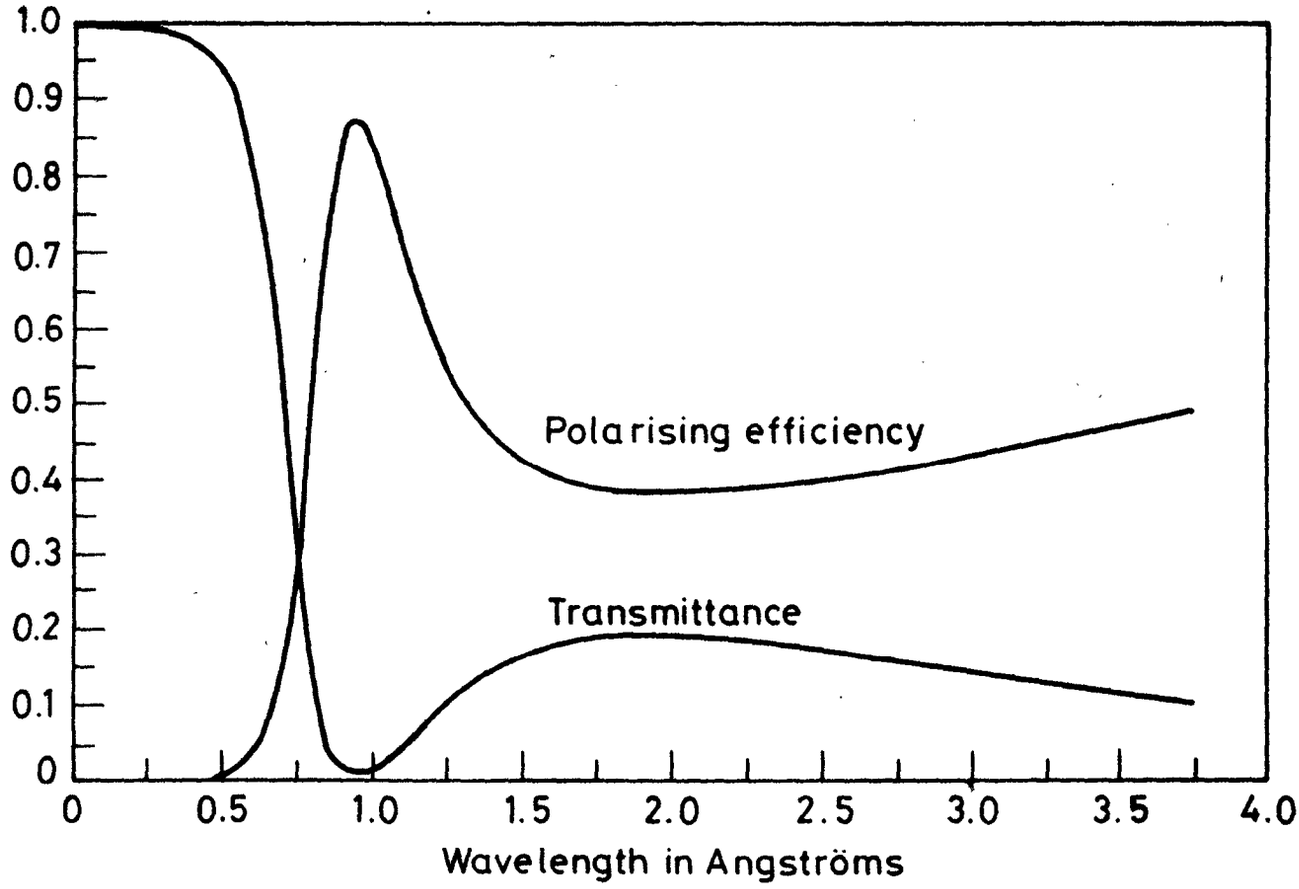

Figure 4. Polarising efficiency and Transmittance of $Pd_{0.95}Sm_{0.05}$. Temperature = 25mK. Applied field = 2.5 Telsa

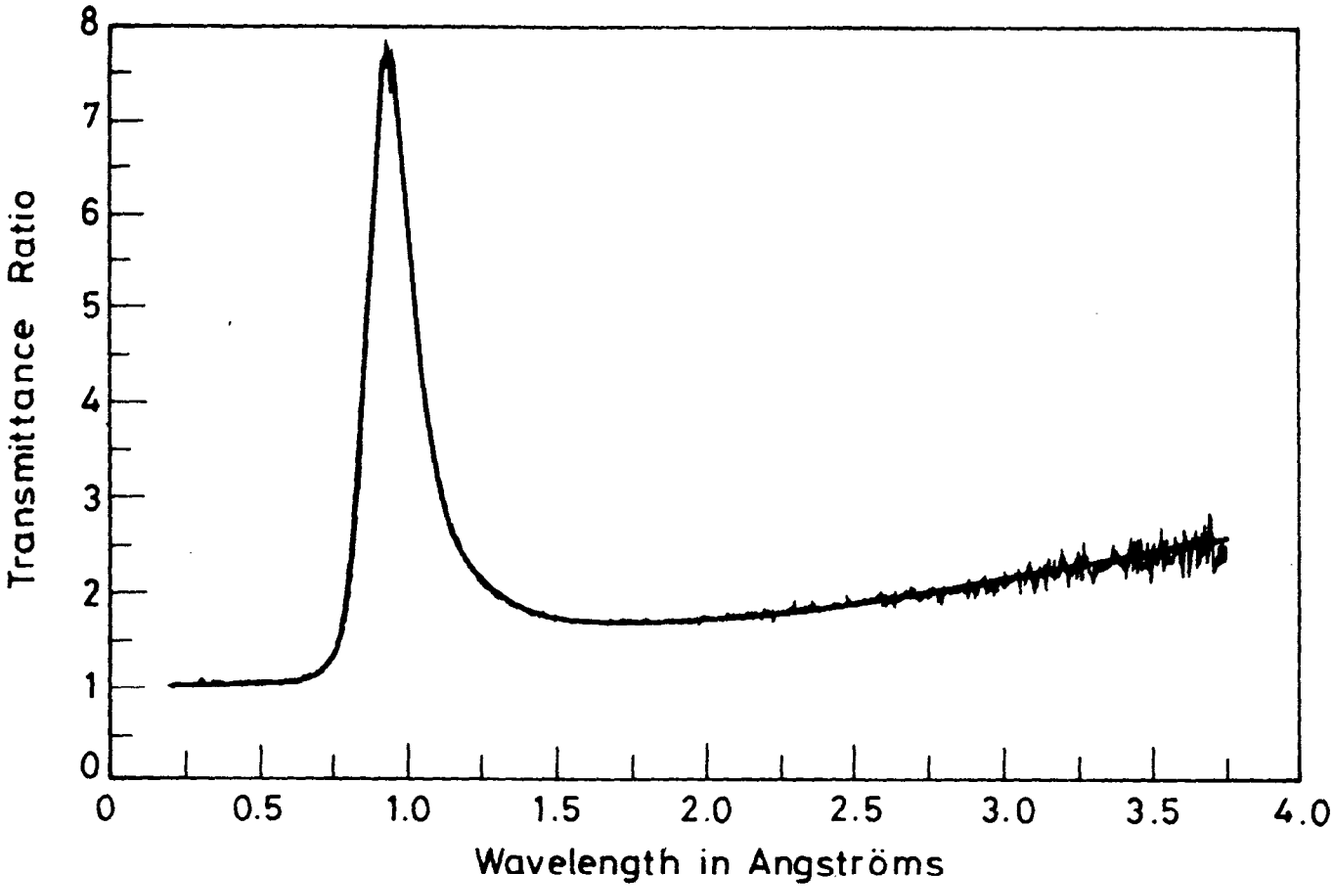

Figure 5. Measured and Fitted Transmittance Ratio for $SmCo_5$ Filter. 14mK: 1.2K

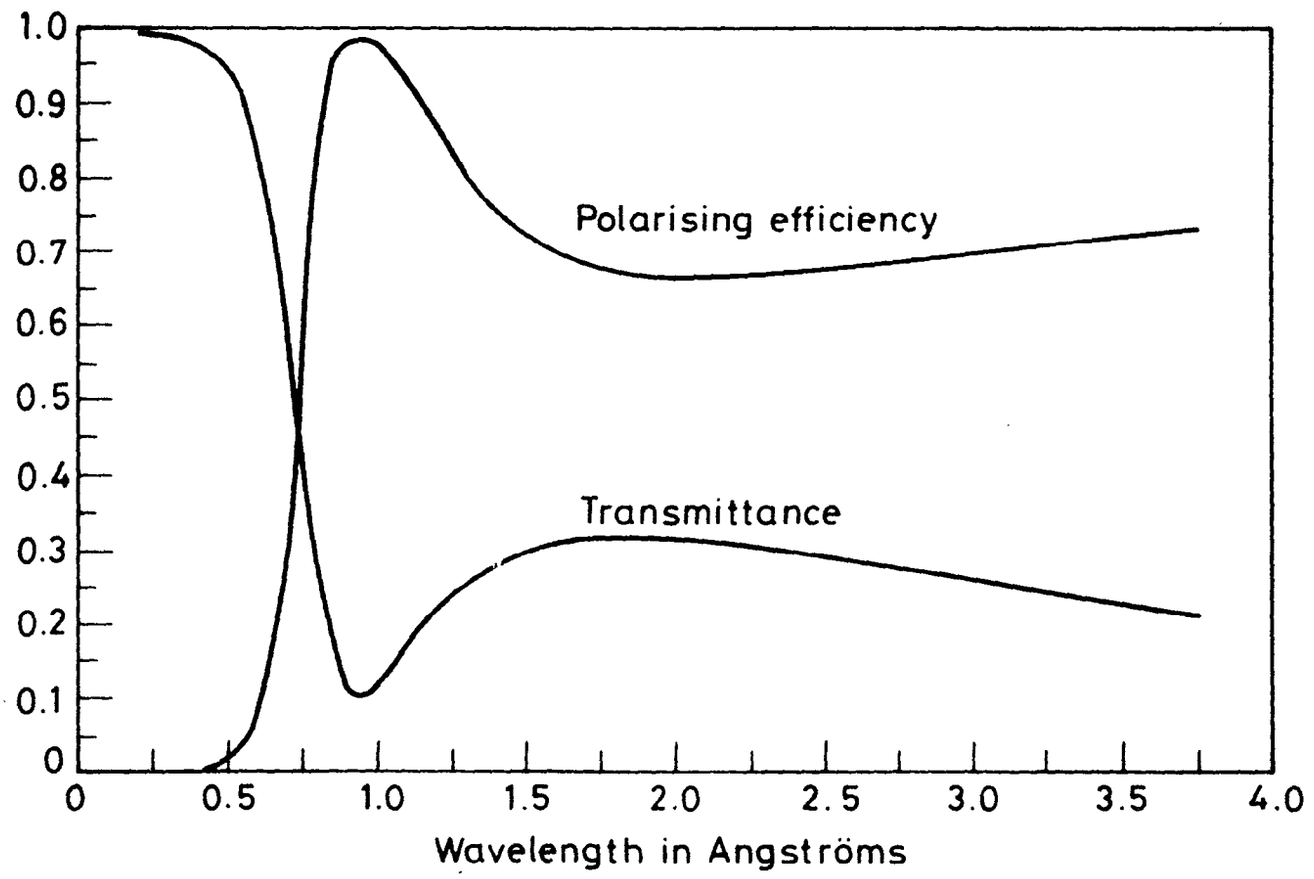

Figure 6. Polarising efficiency and Transmittance of $SmCo_5$ Filter. Calculated from Fitted Parameters

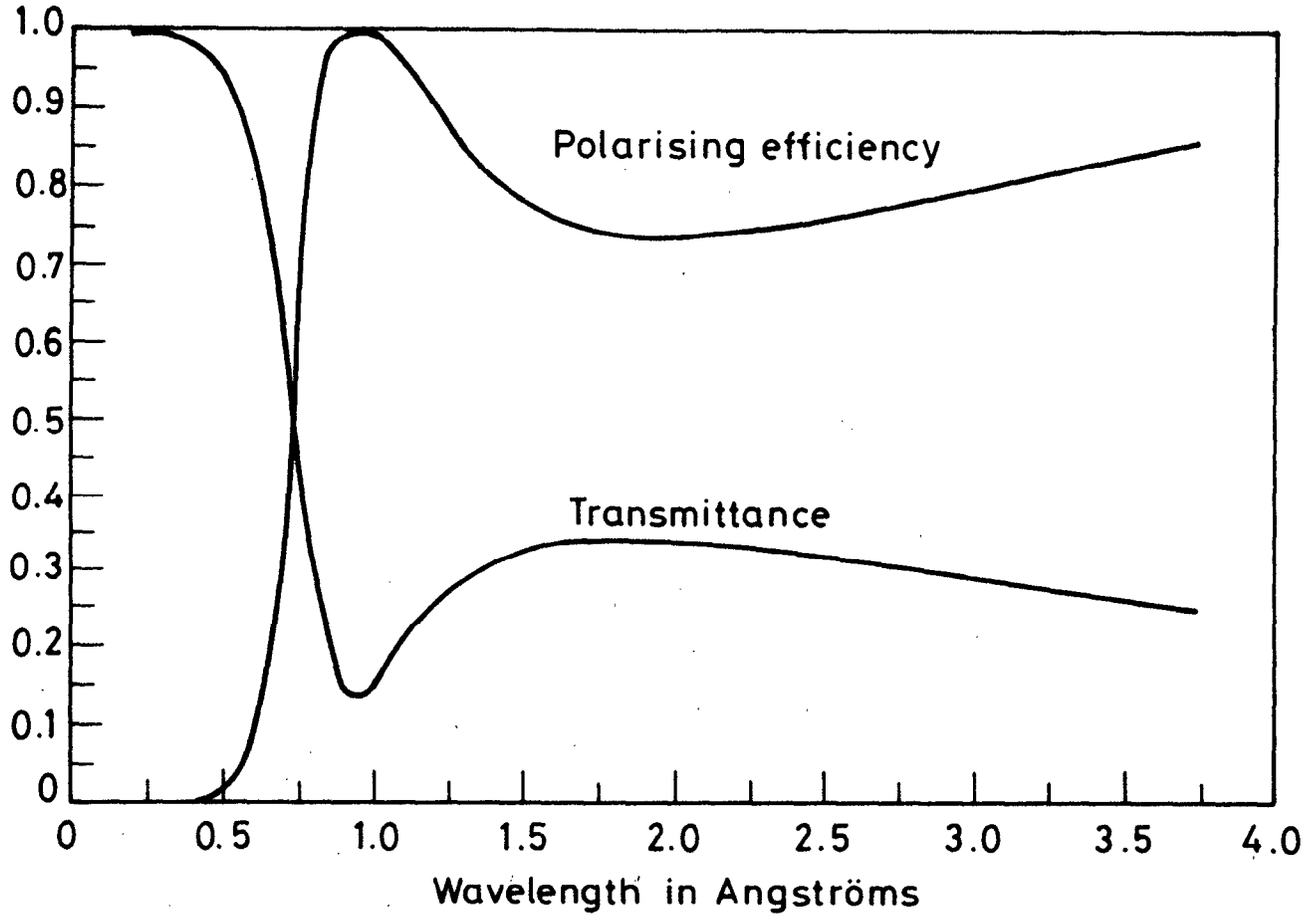

Figure 7. Polarising efficiency and Transmittance of 'Ideal' $Sm\,Co_5$ Filter

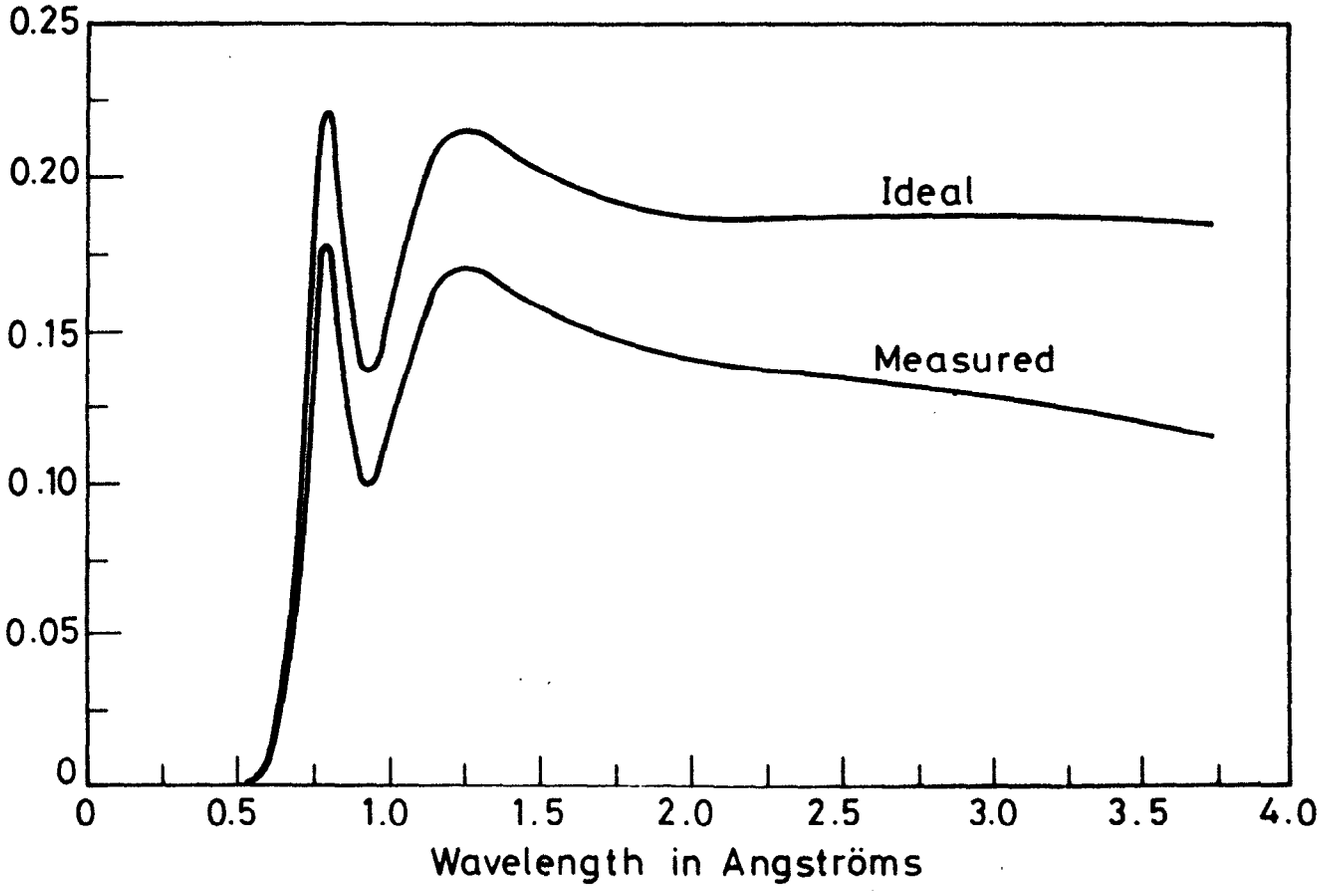

Figure 8. Measured and 'Ideal' values of the Product P^2T

Rigi-Kulm

ICANS IX

INTERNATIONAL COLLABORATION ON ADVANCED NEUTRON SOURCES

22-26 September, 1986

CRISP, A PULSED SOURCE NEUTRON REFLECTOMETER FOR SURFACE STUDIES

J Penfold, R C Ward and W G Williams

Rutherford Appleton Laboratory
Chilton, Didcot
Oxon OX11 0QX

A time-of-flight neutron reflectometer, installed on the spallation neutron source, ISIS, is described (1).

Particular features of the time of flight method: fixed sample geometry and sample illumination, constant resolution in $\sin\theta/\lambda$, and simultaneous measurement over a wide range of $\sin\theta/\lambda$ for approximately constant statistical accuracy, are highlighted.

Examples of its potential use to study problems in surface chemistry and surface magnetism are presented.

Preliminary commissioning results are included.

Introduction

In recent years a number of neutron optical phenomena have been investigated (2). Critical reflection of neutrons has been extensively exploited in neutron scattering measurements and techniques, especially in the applications of neutron guide tubes (3,4), and neutron spin polarisers (5,6).

More recently neutron reflectivity measurements above the critical reflection angle have been applied to investigate interfacial phenomena (7-9) and surface magnetism (10,11).

Traditionally critical reflection measurements using cold neutrons have been made on reactor sources by performing θ-2θ scans with a well monochromated and collimated beam. The wavevector transfer resolution in such measurements is determined by both $\delta\theta$ and $\delta\lambda$. For fixed collimation $\delta\theta$ and monochromatisation $\delta\lambda$ the resolution is a function of the angle of incidence θ through a $\cot\theta\delta\theta$ term. Furthermore the area of the sample illuminated varies with θ necessitating geometric corrections.

More recently time of flight techniques have been exploited by Felcher (10,11) on a pulsed neutron source, and by Farnoux (12) on a reactor source. There are three main advantages in using a white beam time of flight technique on a pulsed neutron source like ISIS:

(i) The reflectivity profile is measured in a fixed geometry. The range of $\sin\theta/\lambda$ measured is determined by a wide band of incident wavelengths, $\Delta\lambda$, at a fixed angle of incidence, θ. The area of sample illuminated is constant.

(ii) There are also consequences for the resolution in $\sin\theta/\lambda$. On ISIS this resolution is determined only by the collimation, $\delta\theta$, as the time of flight resolution contribution from the $\delta\lambda$ term is $\delta t/t \sim 0.5\%$, which is negligible compared with typical values from the divergence ($\cot\theta\delta\theta$) term ($\sim 5\%$). As a result the resolution is essentially constant over the $\sin\theta/\lambda$ range measured.

(iii) Reflectivity and spectral profiles combine to give a slowly varying measured intensity over most of the $\sin\theta/\lambda$ range of the measurement. It is therefore possible to collect data with approximately the same statistical error at all $\sin\theta/\lambda$ values in a fixed measurement time.

Instrument Design and Specification

A general schematic plan of the instrument is shown in Figure 1. The need to investigate liquid surfaces dictates that the incident beam should be inclined to the horizontal at an appropriate reflection angle. The wavelength range needed in the measurements must extend as far as possible into the cold neutron region and the instrument is therefore located on the N4 beamline, viewing the 20K H_2 moderator.

A horizontal slit geometry with an incident beam ~ 50 mm wide and ~ 2 to 4 mm high is used and is collimated at a fixed inclined angle of 1.50° to the horizontal plane. This is the highest inclination angle that can be constructed conveniently in the ISIS shutter apertures; it allows a sufficiently large $\sin\theta/\lambda$ for the liquid surface studies - 0.052 $Å^{-1}$ at λ = 0.5 Å. The sample position is located at 10.25 m from the source and the sample-detector distance is 1.75 m at which single He_3 gas detector is located.

A single disc chopper, located at 6 metres from the moderator is used to define the wavelength band $\Delta\lambda$ and to partially suppress frame overlap contamination. Additional suppression of long wavelength frame overlap neutrons is provided by a series of thin Ni films evaporated onto single crystal silicon mirrors and which are inclined to the incident beam at the critical reflection angle corresponding to the shortest wavelength which can produce frame contamination.

Horizontal slits after the mirrors and before the sample position define the beam collimation and size.

An option to insert a supermirror polariser, magnetic guide fields and a spin flipper between the normal sample position and the frame overlap mirrors has been included to enable polarised neutron experiments to be performed.

A wavelength range, $0.5 \leqslant \lambda \leqslant 26.4Å$ gives a range in $\sin\theta/\lambda$ of $.001 \leqslant \sin\theta/\lambda \leqslant .052Å^{-1}$ at a fixed angle of incidence $\theta = 1.5°$. This represents the maximum $\sin\theta/\lambda$ range available for experiments on liquid surfaces. For solid surfaces this range can be extended to higher and lower values of $\sin\theta/\lambda$ since the angle of incidence can be changed by rotating the sample out of the horizontal plane. Many of the polarised beam experiments on surface magnetism will for example be performed on solid surfaces at much smaller incident angles, typically $\theta \sim 0.5°$.

The resolution in $\sin\theta/\lambda$ has two contributions: a $\cot\theta\delta\theta$ term and $\delta\lambda/\lambda = \delta t/t$ term. $\delta t/t$ is given by a convolution of the moderator pulse width, δt_{mod}, and the time channel width in the time of flight electronics. δt_{mod} is ~ 100 μs for energies ⩽ 10 meV and ~ 20 λ for

energies $\geqslant$ 10 meV, thus $\Delta t/t \sim 5 \times 10^{-3}$ for a 12 m flight path. If the time of flight channel width is ~ 100 μsec then the resultant $\delta t/t$ is ~ 0.7%. The resolution required in $\sin\theta/\lambda$ is ~ 2 to 5% and therefore on the ISIS is determined essentially by the contribution from $\cot\theta\delta\theta$. The collimation angles required to achieve resolutions ~ 2 to 5% in $\sin\theta/\lambda$ are ~ 1 mrad. For solid surface experiments at reflection angles $\theta \leqslant 1.5°$, such resolutions are easily maintained by reducing the slit widths and hence divergence $\delta\theta$.

Science

Critical reflection of neutrons provides information on the scattering density or refractive index variations perpendicular to a surface. We will highlight particularly the application to problems in surface chemistry and surface magnetism.

The use of contrast variation, through deuterium-hydrogen exchange, is particularly important for hydrogenous system, and is therefore relevant to a number of problems in surface chemistry. Calculations for a number of such systems have been made (7), and some measurements are also available (8,9). Typical systems that have been considered include Langmuir-Blodgett multilayers, soap films, density profiles at a liquid-vapour interface, insoluble monolayers at a liquid surface, adsorption of soluble organic materials at a liquid-vapour interface, wetting phenomena, adsorption at the surface of an electrode, and polymer film surfaces and interfaces.

The potential of the technique is illustrated with a calculated example of a polymer film (9a). Figure 2 shows the reflectivity profile for a 200 Å $pmma_{d8}$ film on a P_sh_8 substrate, where the solid and dashed lines correspond to a sharp and diffuse boundary.

Magnetic materials have a spin dependent refractive index, will give rise to two different reflectivity profiles R^+ and R^-. This has been used extensively as the basis for the production of polarised neutrons by critical reflection. Critical reflection of polarised neutrons is a particularly sensitive probe for problems in surface magnetism. Felcher has published (10,11,13) results and calculations of the critical

reflection of polarised neutrons applied to a range of problems in surface magnetism. These include the measurement of the magnetic flux penetration into a superconducting film of niobium (11), calculations of the contribution to the reflectivity profile of the magnetic dead layer on a ferromagnetic surface (10), and of surface critical phenomena in ferromagnets (13).

A particularly fascinating current area of research is that of magnetism at surfaces and interfaces. Freeman et al (14) have reviewed the status of the theoretical modelling of surface magnetism and has drawn attention to several discrepancies between reported results. Although early models showed that the surface layers of a ferromagnetic like Ni were magnetically dead, later calculations by Wang and Freeman (15) and Jepsen et al (16) showed that the Ni(001) surface has a moment similar to that in the bulk. In contrast to these results Wang and Freeman's calculations on Fe(001) (17) showed a large increase in the surface magnetism for a 7 atomic layer calculation; similar results have recently been reported by Victoria et al (18).

For the purposes of illustration we show the flipping ratios (R^+/R^-) calculated for the magnetisation profile published by Victoria et al (18) for Fe(100) in Figure 3; the reflection angle used was $\theta = 1.5°$. Enhanced magnetism effects only become apparent at the shorter wavelengths (~ 5Å) or larger ($\sin\theta/\lambda$), where the reflectivities are $R^+ \sim 10^{-3}$, $R^- \sim 10^{-4}$.

Preliminary Commissioning

Some initial commissioning of the CRISP spectrometer have now been carried out. The initial aim has been to obtain a reflectivity profile and hence optimise the spectrometer geometry and reduce background levels.

Initial operation has been without the frame overlap chopper: as a result the wavelength band is limited to 0.5 to 6Å, and to beam sizes $\leqslant$ 1.5 mm.

Shown in Figure 4 as the solid line is the measured reflectivity profile for a 750Å copper film on a glass substrate; also plotted as the dashed line is the calculated reflectivity.

References

(1) J Penfold and W G Williams, Rutherford Appleton Laboratory report, RAL-85-045 (1985).

(2) A G Klein and S A Werner, Rep Prog Phys, 46, 259 (1982).

(3) B Jacrot, IAEA Vienna (1970) pg 225.

(4) C J Carlile, M W Johnson and W G Williams, Rutherford Appleton Laboratory report, RL-79-084 (1979).

(5) K Abrahams, W Ratynski, F Strecher-Rasmussen and E Waring, Nucl Inst and Meth, 45, 293 (1966).

(6) J B Hayter, J Penfold and W G Williams, J Phys E, 11, 454 (1978).

(7) J B Hayter, R R Highfield, B J Pullman, R K Thomas, A I McMullen and J Penfold, J Chem Soc Faraday Trans 1 (1981) 1437.

(8) R R Highfield, R K Thomas, P G Cummins, D P Gregory, J Mingins, J B Hayter and O Scharpf, Thin Solid Films, 99 (1983) 165.

(9) R R Highfield, R P Humes, R K Thomas, P G Cummins, D P Gregory, J B Hayter, J Mingins and O Scharpf, J Coll and Int Sci, 97 (1984).

(9a) J S Higgins, J Penfold, unpublished work.

(10) G Felcher, Phys Rev B 24 (1981) 1595.

(11) G P Felcher, R T Kampwirth, K E Gray and R Felici, Phys Rev Letters, 52 (1984) 1539.

(12) B Farnoux, IAEA Conference CN-46 (1985).

(13) G P Felcher, R Felici, R T Kampwirth and K E Gray, 30th Conf in Magnetism and Magnetic Materials, San Diego (Nov 1984) to be published in J Appl Phys.

(14) A J Freeman, Journal de Physique, Colloque C7 Supplement No 12, 43 (1982) L67.

(15) C S Wang and A J Freeman, Phys Rev, B21 (1980) 4585.

(16) O Jepsen, J Madsen and O K Andersen, J Magn Magn Mat, 15-18 (1980) 867.

(17) C S Wang and A J Freeman, Phys Rev, B24 (1981) 866.

(18) Victoria, Phys Rev B30 (1984) 3896.

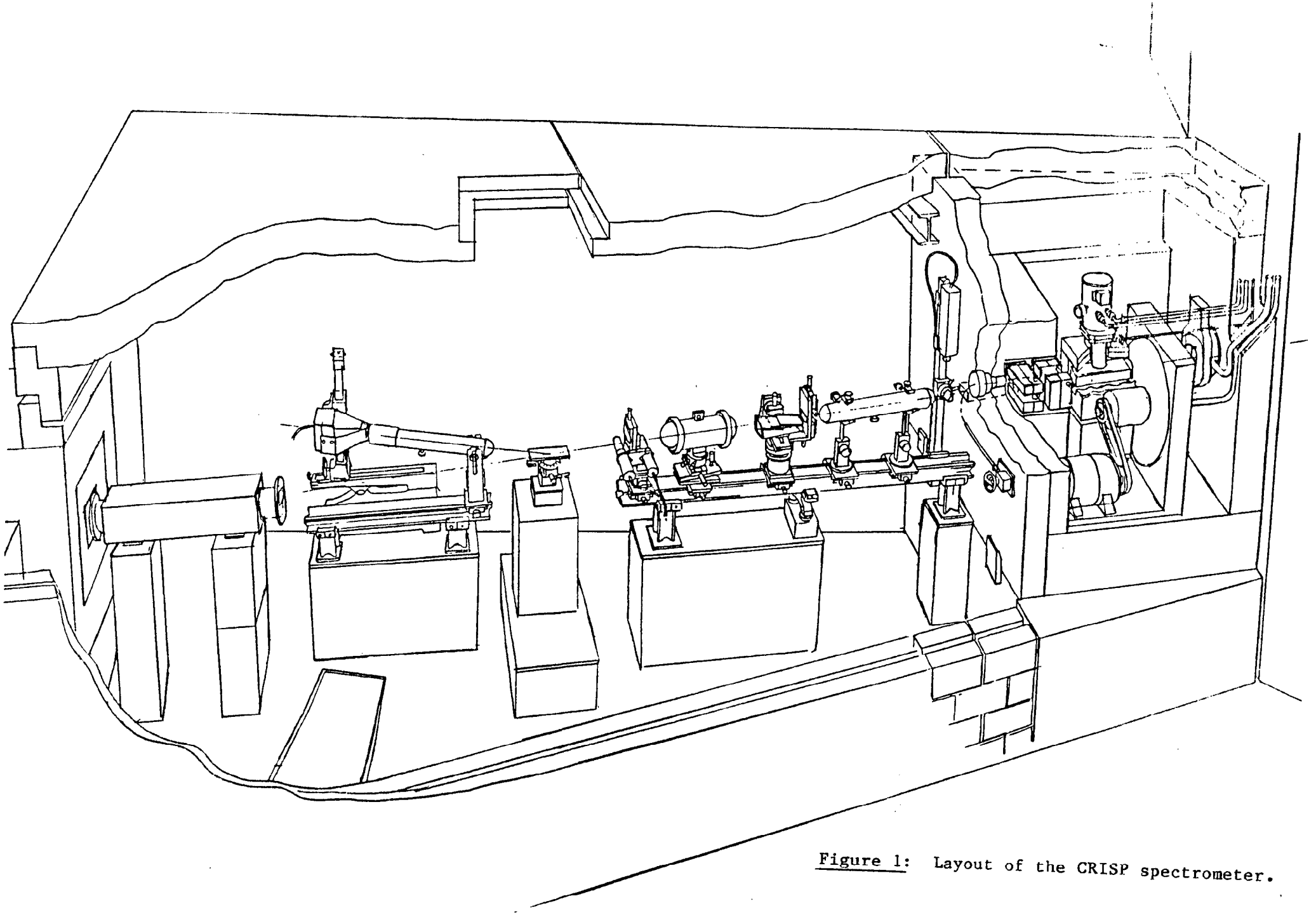

Figure 1: Layout of the CRISP spectrometer.

Figure 2: Calculated reflectivity profile for 200Å $pmma_{d8}$ film on a $P_s h_8$ substrate with (i) —— sharp and (ii) --- diffuse boundary.

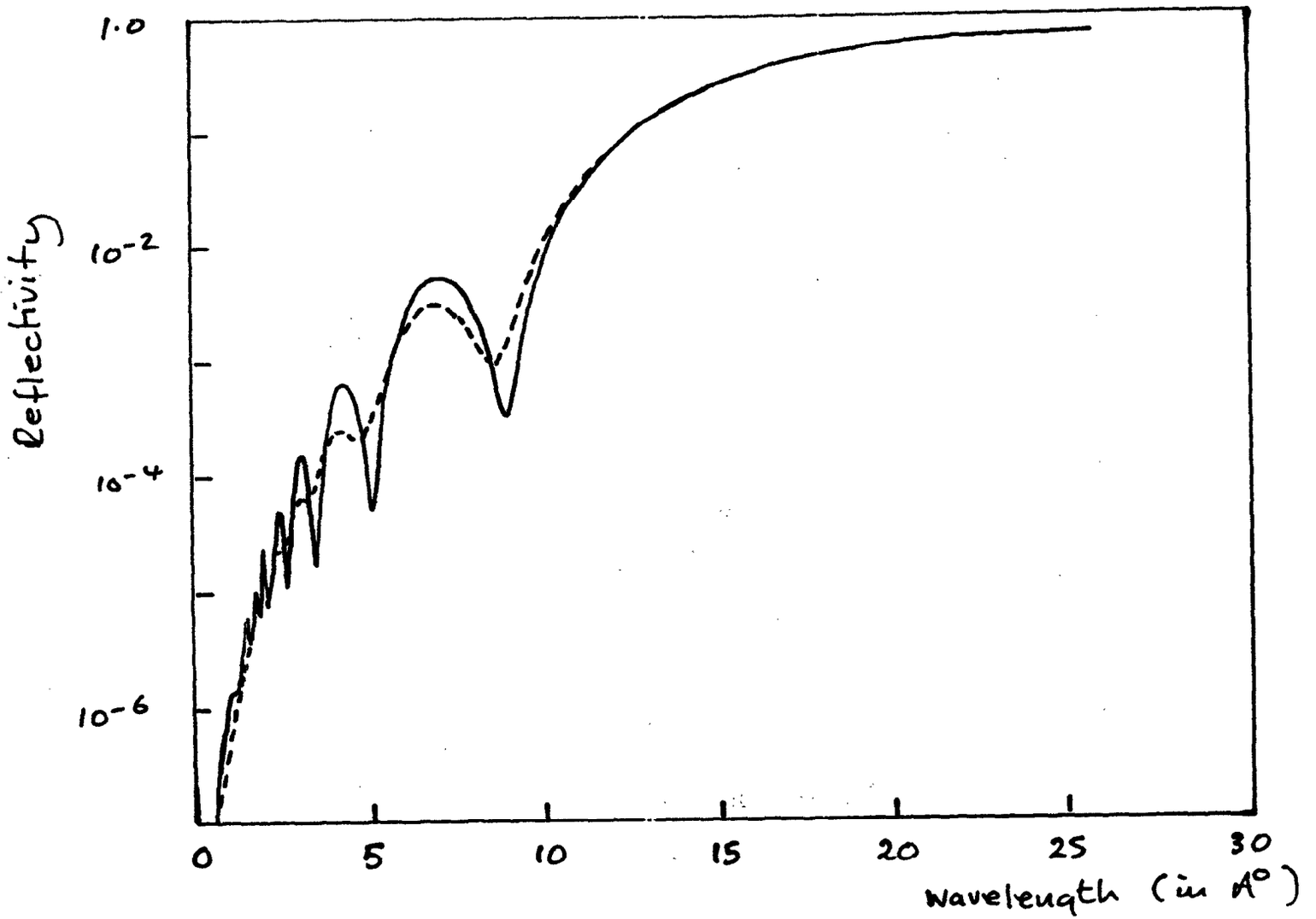

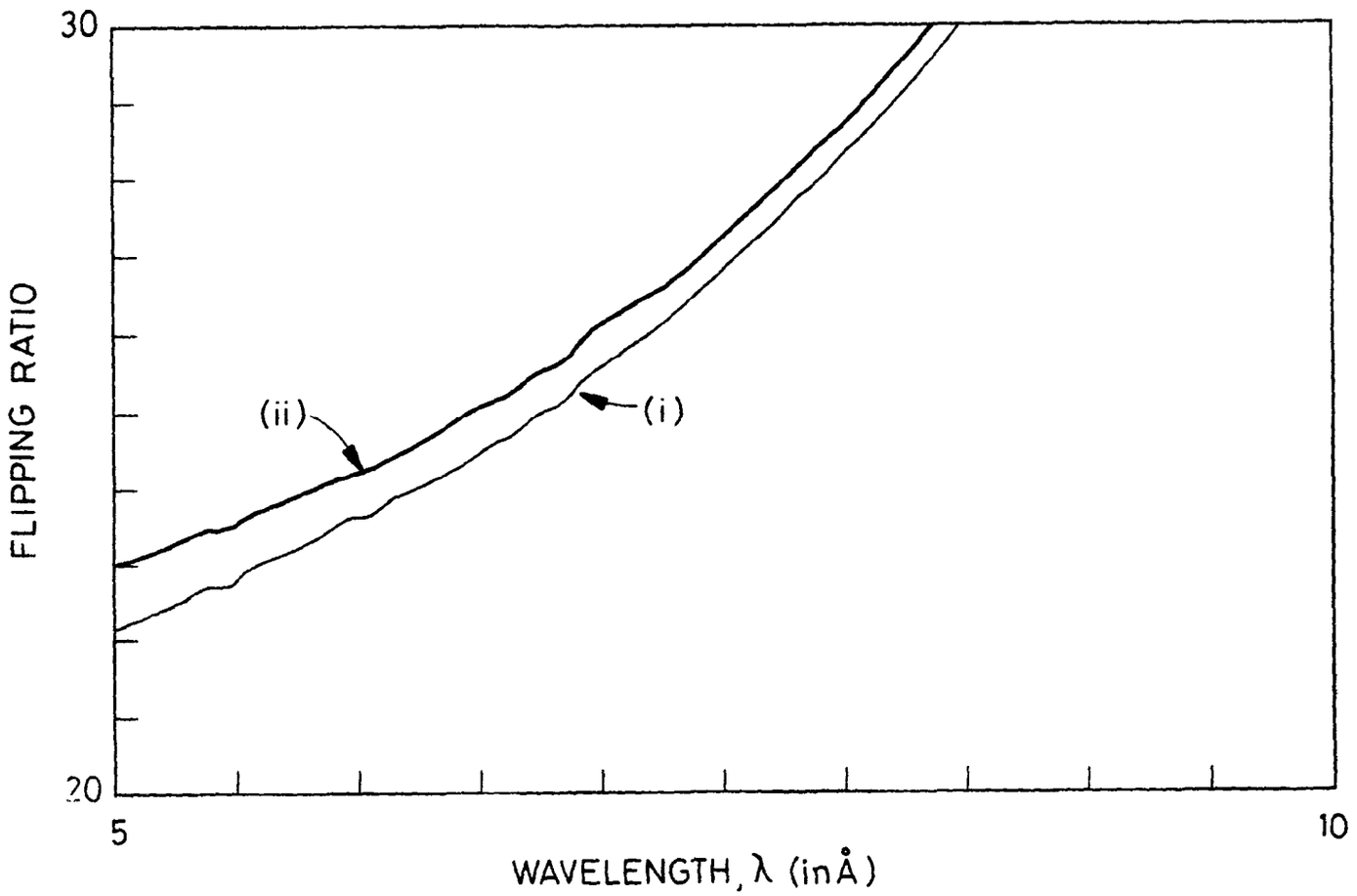

Figure 3: Flipping ratio (R^+/R^-) versus wavelength for (i) bulk iron, (ii) magnetisation profile published by Victoria et al (18) for Fe(100), $\theta = \theta = 1.5°$, $\delta\theta = 0.075°$.

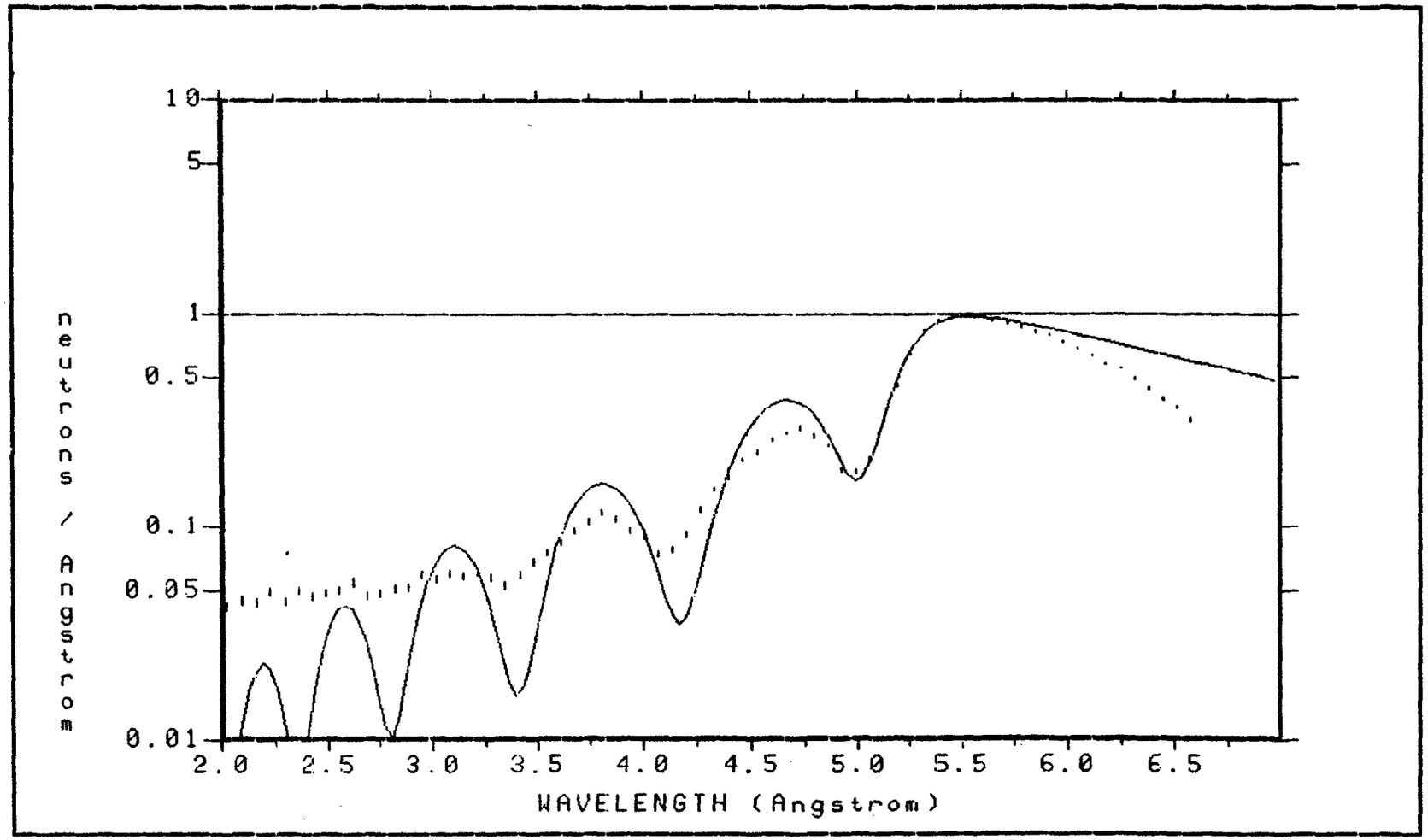

Figure 4: Reflectivity profile for 750Å copper film in glass substrate (i) ——— measured on CRISP, ~ 10 μAhrs, θ = 1.5°, Δθ ~ 5%, and (ii) --- calculated reflectivity profile.

ICANS IX

INTERNATIONAL COLLABORATION ON ADVANCED NEUTRON SOURCES

22-26 September, 1986

HIGH RESOLUTION MOLECULAR SPECTROSCOPY USING TFXA AT ISIS

J Penfold

J Tomkinson

Rutherford Appleton Laboratory

Chilton

Didcot

Oxon OX11 0QX

The design and performance of a time focused crystal analyser spectrometer, TFXA, at the ISIS spallation neutron source is presented.

The combination of time and energy focusing provides good (~ 2 to 3%) energy transfer resolution over a wide range of energy transfers (10 to 500 meV).

The influence of multiple scattering on inelastic neutron scattering spectra of molecular vibrations is illustrated with results in hexamethylenetetramine. The capabilities of the spectrometer are illustrated with recent results from the librational mode splitting, of ammonium bromide.

New developments in data analysis using refinable normal coordinate analysis programs are demonstrated with recent data on 1-4 Benzoquinone.

1. Instrument Design

The time-focused crystal analyser, TFXA, is an indirect geometry time-of-flight inelastic scattering spectrometer, using a time-focused pyrolytic graphite analyser to give good count rates, and good energy transfer resolution over a wide range of energy transfers. The design of the spectrometer is illustrated in Figure 1.

The spectrometer is based on a time-focusing geometry in which the sample and detector arrays are in the same plane, and the analysing crystal is set parallel to this plane. In such a geometry, for an ideal crystal, all detected neutrons have the same flight time after scattering. In addition to the time focusing, (2) the Marx principle is used to provide energy focusing. This reduces the positional uncertainty in the analysing energy, and is a feature not previously exploited in crystal analyser spectrometers. It enables the good energy transfer resolution to be maintained down to energy transfers of a few meV.

As the energy of the detected neutrons is small compared with the incident energy, their scattering vector is practically independent of scattering angle. Thus, there can be little variation in the momentum transfer, Q, independent of energy transfer. This is realtively unimportant in molecular vibrational spectroscopy, where the dispersion of the vibrational mode is small or cannot be easily studied. Further, this particular kinematic arrangement renders spectra less sensitive to multiple scattering effects, and as seen later can be exploited to advantage (3).

The simultaneous measurement of the elastic line and a wide range of energy transfers which includes both the internal and external mode vibrations, with good energy transfer resolution offers new possibilities in vibrational spectroscopy.

2. Instrument Performance

During the early running of ISIS, the performance of the TFXA spectrometer was assessed from the vibrational spectra of zirconium hydride (ZrH_2) and potassium hydrogen maleate (KHM). Good resolution and an excellent signal-to-noise performance were observed. Measured intensities were in good agreement with calculation. All aspects of the instrument performed to expectation.

The calibration of the final energy and secondary flight path length values associated with each detector were obtained from the relative positions of the elastic and known inelastic features. The initial calibration using the 140 meV hydrogen vibration of ZrH_2 has been further

refined using the 46.87 meV transition in hexamethylenetetramine (HMT). The elastic line is located at zero energy transfer to within 0.01 meV, and is described by a Gaussian of FWHM of 0.25 meV, in excellent agreement with the calculated elastic resolution. Errors in calibration of peak positions are estimated to be $< 0.5\%$.

A number of inelastic features, measured so far, have widths close to the instrumental resolution; for example, the 46.87 meV transition in HMT has a width of 1.12 meV (cf. resolution width of 0.82 meV) and the 144.5 meV vibration in bromoform has a width of 4.6 meV (cf. resolution width of 3.1 meV). For such inelastic features, the line shape in not Gaussian but is described by the characteristic time shape of the ambient water moderator on ISIS.

Early samples have provided a stringent test of data reduction procedures, which present data proportional to cross-section or scattering law in relative or absolute units. Good agreeement with simple harmonic oscillator theory is obtained in these examples, and lends confidence to the data reduction procedures.

Signal-to-noise level is in general excellent. At short times the characteristic break in intensity at the infinite energy channel can be seen.

A detailed analysis of the elastic line shows characteristic wings associated with the thermal diffuse scattering from the pyrolytic analysing crystals.

3. The Influence of Multiple Scattering on Inelastic Neutron Scattering Spectra of Molecular Vibrations (3)

Recent calculations of multiple scattering effects in vibrational spectroscopy suggest that the momentum transfers associated with a TFXA measurement give little weight to multiple phonon scattering effects, i.e. elastic/inelastic, inelastic, and elastic/elastic being the dominant multiple scattering terms. This stems principally from the momentum transfer vector Q being insensitive to scattering angle and determined principally by the energy of the mode being studied, provided it is of

significant energy transfer, for spectrometer with low final energy such as TFXA. To confirm these calculations we have carried out a series of measurements on different percentage scatterers of hexamethylenetetramine, HMT: HMT is a particularly suitable test material as it has a series of sharp well defined modes at relatively low energy transfers.

The measurements confirm the calculations; as is demonstrated in Figure 2 where the ratio $(R(\omega)_d)$ of scattering from i) 1.9 mm/ 0.9 mm sample thicknesses and ii) 5.4 mm/0.5 mm sample thickness is plotted.

The bold dots correspond to calculated points. The apparent failure of some of the points to correspond with observation is due to the simplicity of the model; in that the external density of states was included only as a delta function, and phonon wings are not included in the calculation.

Figure 3 demonstrates the effect of scattering strength on the observed width of spectral bands. The intense feature at 47 meV is a good candidate for investigation. This band is assigned to ν_{16}, a deformation mode of the carbon-nitrogen skeleton. The width of the ν_{16} band in HMT is the narrowest reported for an NIIS spectrum, 11.5 cm^{-1} [4]. Our spectra from the samples of different scattering strengths were normalised at their peak heights and overplotted. This is shown in Figure 3. It is seen that there is no dramatic increase in band width. Rather a slight broadening at the base. The subtraction of two normalised spectra (strongest minus weakest) is also shown in Figure 3. Here the differences at the base have been strongly emphasised. We may conclude that to first order the widths of spectral bands are independent of scattering strength.

We may conclude for reflection neutron inelastic spectrometers with low final energy, that

i) samples that scatter only 10% of the incident beam are probably inefficient. Neutrons which have been down scattered once can be scattered again, elastically, and are still well described by the one phonon approximation. Total sample scattering strengths of up to 25% are to be recommended for experiments where the inelastic bands occur

at energy transfers greater than 40 meV and relative band intensities are acceptable, i.e. molecular spectroscopy.

ii) Samples that have high scattering strengths continue to show understandable increases in the detected count. These increases arise from multiple inelastic scattering.

Therefore initial experiments of a survey nature on uncharacterised samples are recommended to have scattering strengths, of ca 50%, thereby dramatically reducing the experimental time (by factors of ca 4 to 5).

iii) Degradation of spectral quality will manifest itself by a loss of structure, by weak high energy features becoming less "visible" and by all bands broadening slightly at their base.

4. Splitting of Higher Harmonics of the NH_4^+ Librational Mode in NH_4Br (5)

The rotational motion of ammonium ions in ammonium halides (6) and in the mixed salts of ammonium and alkali halides (7,8) has been extensively studied using the neutron incoherent inelastic scattering (NIIS) technique. These studies show that the librational frequency, ν_6, of the NH_4^+ ion is smaller when the ion resides in an octahedral environment than in a tetrahedral environment. For a given crystal symmetry, ν_6, decreases going from Cℓ- to I-. The ground librational state of NH_4^+ ions in rock salt alkali halides having symmetry O_h, shows a large (~ 1 meV) tunnel splitting (9) and ν_6 (0-1) gives a broad peak in the scattered neutron spectrum (7,8) indicating that the first excited state also has considerable structure. At appropriately low temperatures, pure ammonium halides have a cubic ordered structure and the NH_4^+ ion resides in a tetrahedral (T_d) environment. In this phase, ν_6 (0-1) gives a sharp peak in neutron experiments. The tunnel splitting of the ground or the higher librational states is expected to be small (10); it is however expected that even in this phase higher librational states may show structure because of the anharmonic effects (11). So far this has not been seen in neutron studies because they were confined to the fundamental ν_6 (0-1) transition. With the availability of high resolution neutron

spectrometers on sources which provide epithermal neutrons, it is now possible to examine the details of the higher excited states. This work reports the first NIIS observation of splitting of the higher overtones of the librational modes of NH_4^+ ions in NH_4Br (Phase IV) (12).

The experiments on polycrystalline ammonium bromide were carried out at a temperature of 6.2 K and the sample scattered 15% of the incident neutrons. The measured scattering law $S(Q,\omega)$ is shown in Figure 4 as a function of energy transfer.

The assignment of various peaks and their comparison with optical data are summarised in Table 1 in particular, the translational optical mode is seen at ~ 20 meV and the fundamental librational mode ν_6 (0-1) at ~ 43 meV. In earlier neutron studies (6) in phase III of NH_4Br, these modes were observed at 20.2 and 41.5 meV respectively. NIIS data on phase IV of NH_4Br have not been previously reported.

Having identified the various peaks, we shall concentrate on ν_6 (0-1) and its harmonics, ν_6 (0-2) and ν_6 (0-3). Expanded plots of the measured spectrum in the region of these modes are shown in Figure 5. We note that both ν_6 (0-2) and ν_6 (0-3) show structure. Thus ν_6 (0-2) consists of two prominent peaks at 81 meV and 86 meV and ν_6 (0-3) consists of two main features at 118 meV and 126 meV. This splitting is not an artifact of acoustic phonon wings. We believe that the splitting of ν_6 (0-2) and ν_6 (0-3) seen in the present experiments is the electrostatic field splitting as predicted by Hüller and Kane (11), and observed for $NH_4C\ell$ in optical experiments (13). We have calcualted the energies of higher librational states for NH_4Br using the formulation developed by Hüller and Kane and the potential suggested by them. The comparison between the calculated and the measured energies is given in Table 1. All the predicted peak positions show excellent agreement with the data. The structure which appears to be present but unresolved in the fundamental region is probably best described in terms of the dispersion of the NH_4^+ librational mode, although the NH_4^+ ion librations in ordered $NH_4C\ell$ showed no dispersion (14).

The integrated relative intensities of the three bands are in very good agreement with the calculations for an oscillator mass of 3.9 neutron

masses, which corresponds to the fact that only hydrogen atoms move during the librational motion and that the NH_4^+ ion has four attached hydrogen atoms.

5. First Observation of the Optically Inactive Modes in Solid 1-4 Benzoquinone (15)

The geometry of 1,4 benzoquinone, shown inset into figure, is though to change markedly on passing from the vapour phase to the solid. Specifically the C=C bond lengths fall from 1.344 Å [16] in the vapour phase to 1.322 Å [17] in the solid. The vibrational spectrum of the molecule should be sensitive to these changes but unfortunately two of the most important vibrations, associated with the C=C deformations, are optically inactive (Au). They have only been observed in the gas phase, and then as weak combinations.

The inelastic incoherent neutron scattering spectrum of 1,4 benzoquinone solid at 20K obtained on TFXA is shown in Figure 6. Also shown is a best fitted valence bond model of the molecular vibrational spectrum. This was achieved using the CLIMAX suite of programs [18]. The same model calculation applied to the gas phase geometry demonstrates that the Au modes are indeed the most sensitive vibrations. However even this sensitivity does not fully explain the large frequency shifts. The most likely explanation is that C-H---O=C contacts, important in crystal formation, are lost on vapourisation.

Acknowledgements

The authors wish to acknowledge the collaboration with P S Goyal on the multiple scattering in HMT, and the splitting of higher harmonics of the NH_4^+ librational mode in NH_4Br.

We wish to thank D K Ross for numerous informative discussions and much useful advice with regard to crystal analyser spectrometers.

We express our gratitude to G J Kearly for making his CLIMAX suite of programs readily available.

References

1. S Ikeda and N Watanabe, Nucl Inst and Meth, 221 (1984) 571.

2. D K Ross, unpublished work.

3. P S Goyal, J Penfold and J Tomkinson, Rutherford Appleton Laboratory report no RAL-86-070.

4. H J Lauter and H Jobic, Chem Phys Lett, 108 (1984) 393.

5. P S Goyal, J Penfold and J Tomkinson, Chem Phys Letters, 127 (1986) 483.

6. G Venkataraman, K Usha Deniz, P K Iyengar, A P Roy and P R Vijayaraghavan, J Phys Chem Solids, 27 (1966) 1103.

7. A B Gardner, T C Waddington and J Tomkinson, J Chem Soc Faraday Trans II, 73 (1977) 1191.

8. P S Goyal and B A Dasannacharya, J Phys, C12 (1979) 219.

9. A Heidemann, J Howard, K J Lushington, J A Morrison, W Press and J Tomkinson, J Phys Soc Japan, 52 (1983) 2401.

10. M Prager, W Press, B Alefeld and A Hüller, J Chem Phys, 67 (1977) 5126.

11. A Hüller and W Kane, J Chem Phys, 61 (1974) 3599.

12. C H Perry and R P Lowndes, J Chem Phys, 51 (1969) 3648.

13. L R Fredrickson and J C Decius, J Chem Phys, 66 (1977) 2297.

14. H C Teh and B N Brockhouse, Phys Rev, 83 (1971) 2733.

15. J Penfold and J Tomkinson, accepted for publication in J Chem Phys.

16. K Hagen and K Hedberg, J Chem Phys, 59 (1973) 158.

17. J Trotter, Acta Cryst, 13 (1960) 86.

18. G J Kearly, J Chem Soc Faraday Trans 2, 82 (1986) 41.

19. N E Schumaker and C G Garland, J Chem Phys, 53 (1970) 392.

Table 1

Summary of the inelastic scattering spectrum of NH_4Br (6K)

This Work (meV)	(10) Theory (meV)	(19) IR Data (meV)	Symmetry Species		
10	--	--		ν_A acoustic branch	translational phonon density
20				ν_o optic branches	of states
43.1	42.4	--	F_2	ν_6 (0→1)	
53	--	49.9		ν_6 (0→1) + ν_A	
62	--	63.2		ν_6 (0→1) + ν_o	
81.0	80.2		A		
84.2	82.95		E	ν_6 (0→2)	
85.7	83.32	83.3	F_2		
118.0	116.4		F_2		
	122.38	122.4	F_2	ν_6 (0→3)	
124.0	122.75		A		
127.0	122.94	125.2	F_2		
145		150.7		ν_6 (0→3) + ν_o	
175	--	173.3	F_2	ν_4 internal NH_4 deformation	

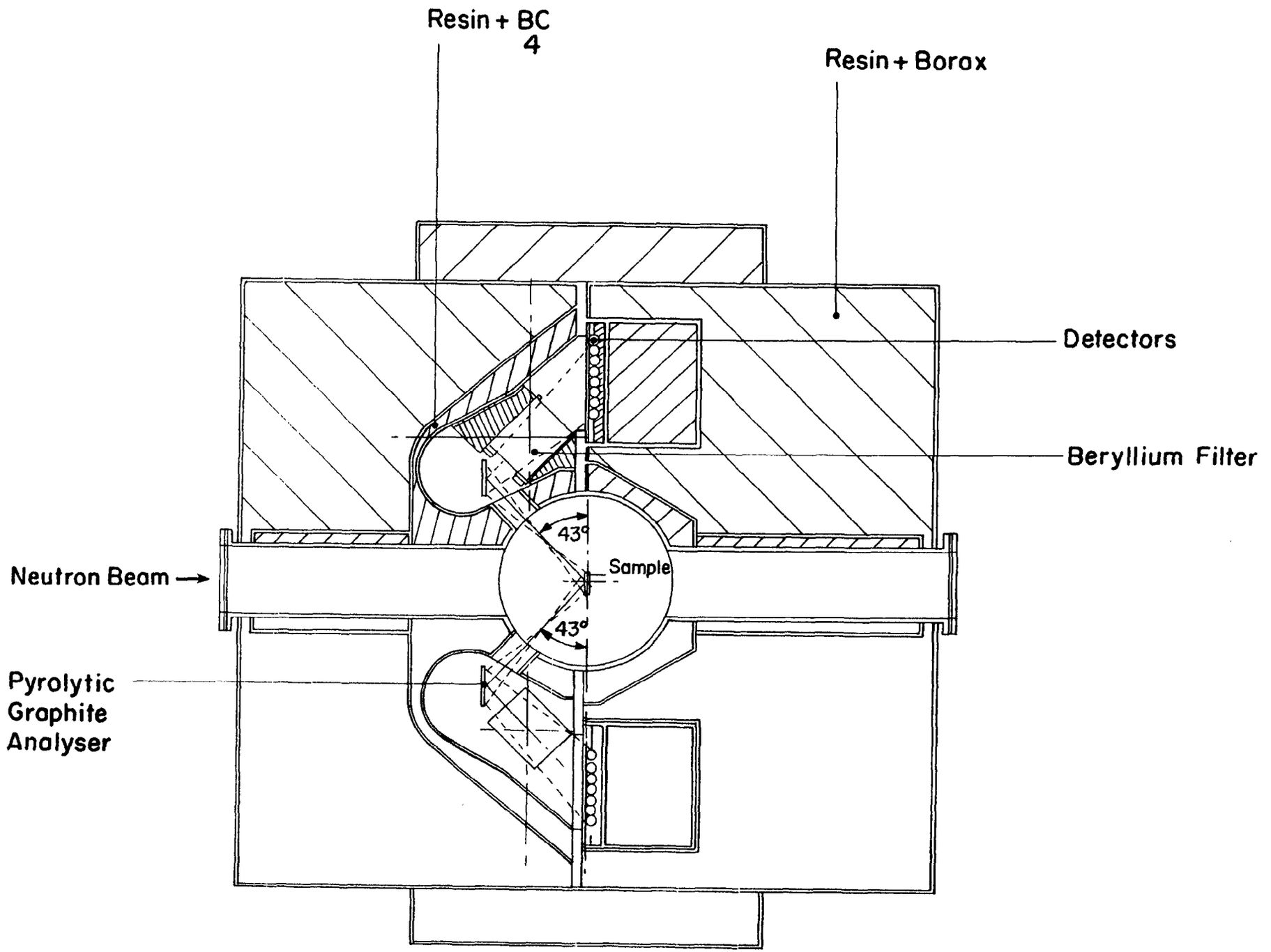

(1) Design of the ISIS time focused crystal analyser TFXA.

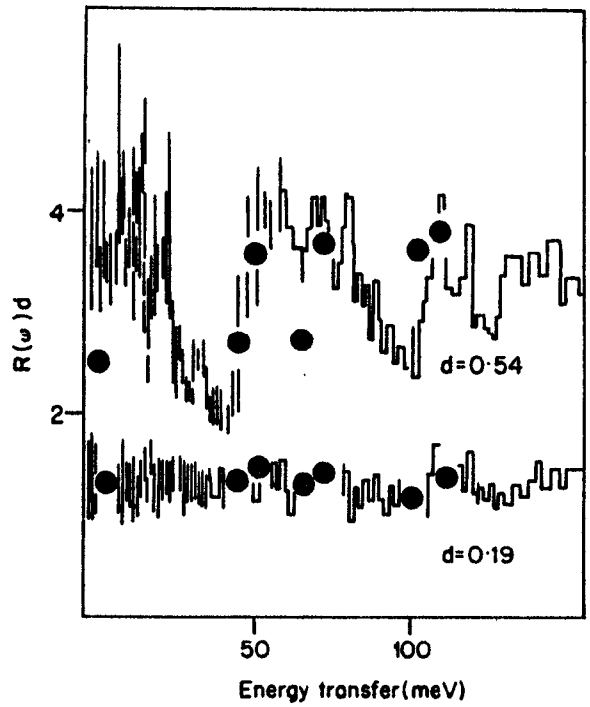

(2) Comparison of the calculated $R(\omega)_d$ values with observation. The calculated points are the bold dots.

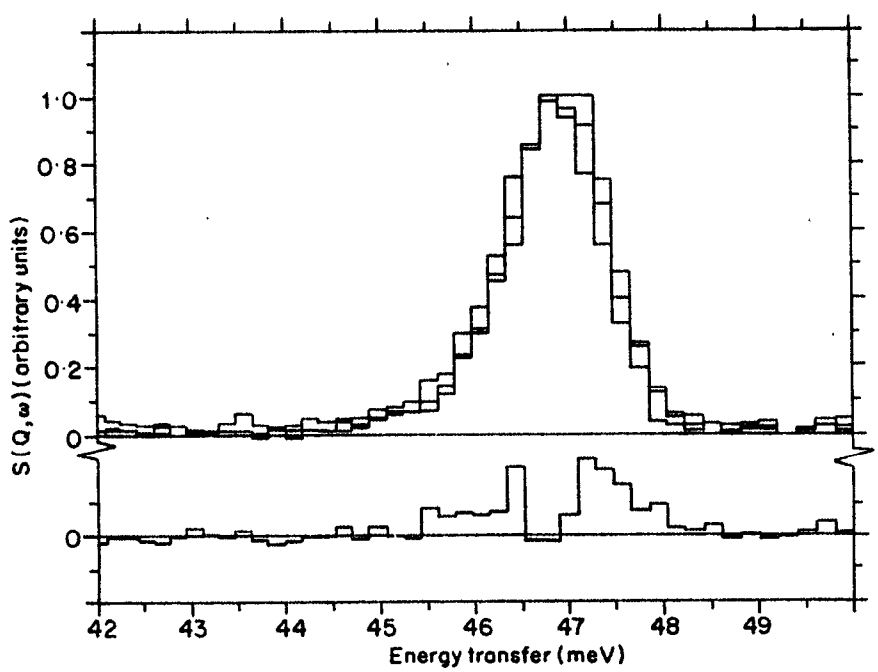

3) Detail of the spectra of HMT around 47 meV neutron energy transfer, showing the normalised observations of ν_{16} mode. Also shown, below, the difference between the normalised results for the thickest and thinnest samples.

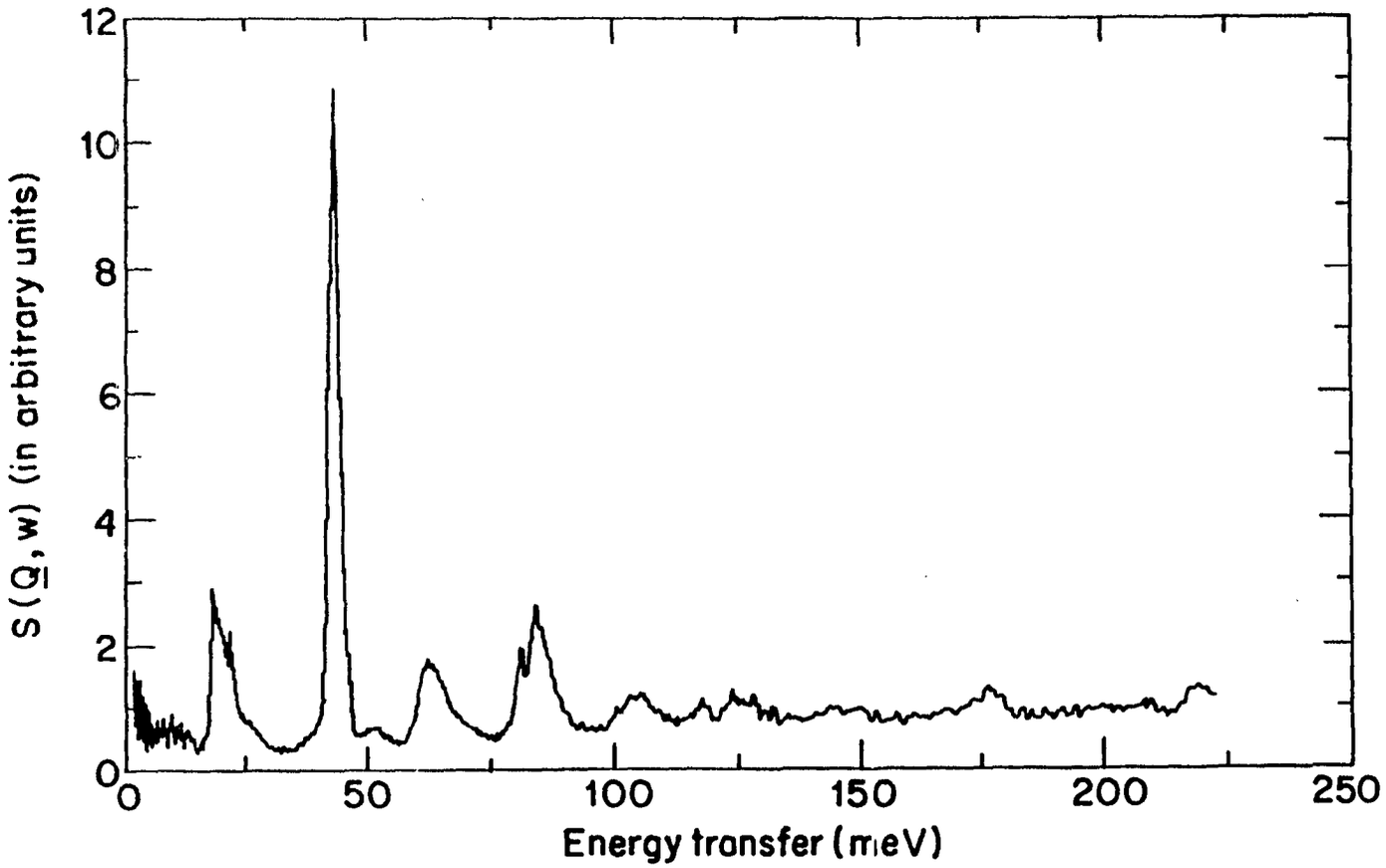

(4) The inelastic incoherent neutron scattering spectrum of NH_4Br at 6K.

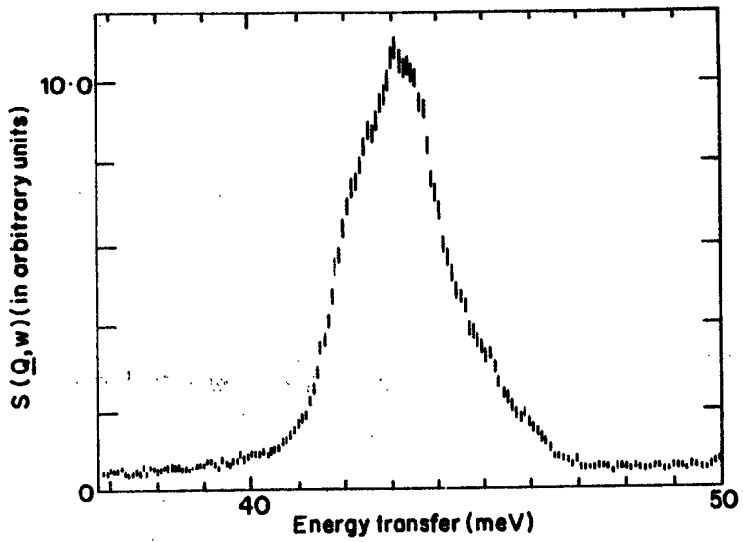

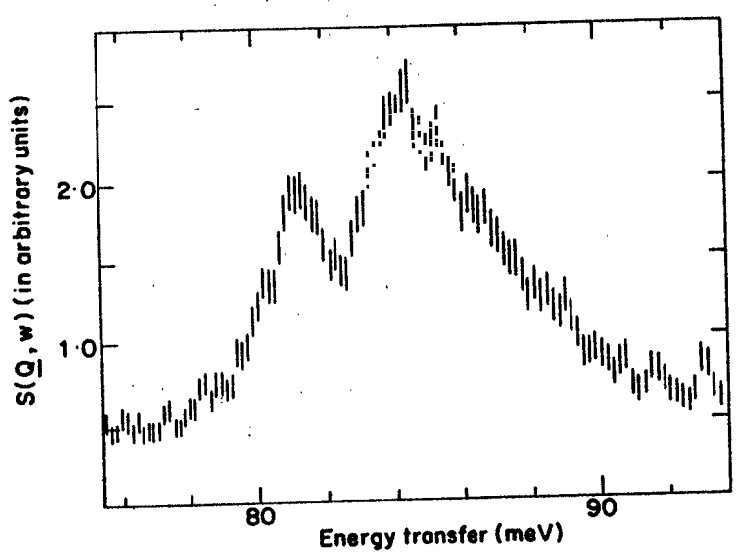

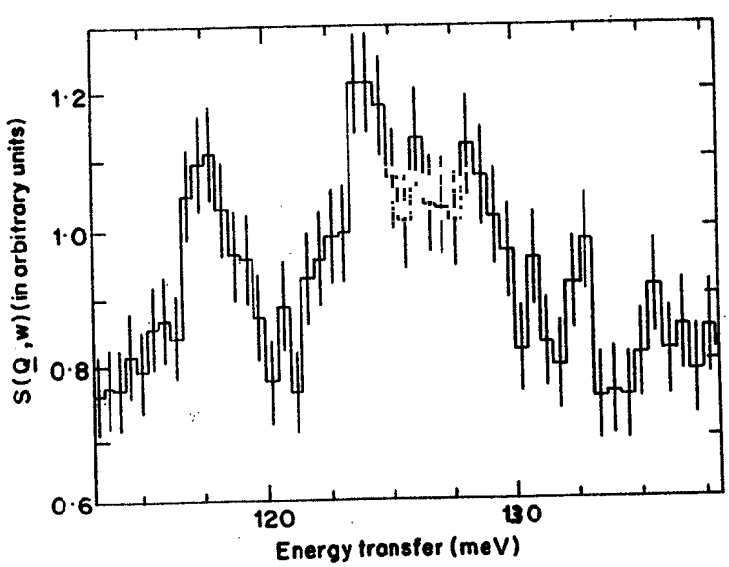

(5) Expanded plots of the NH_4Br spectrum shown in figure covering the 0→1 (a), 0→2 (b) and 0→3 (c) transitions of the librational mode of the ammonium ion.

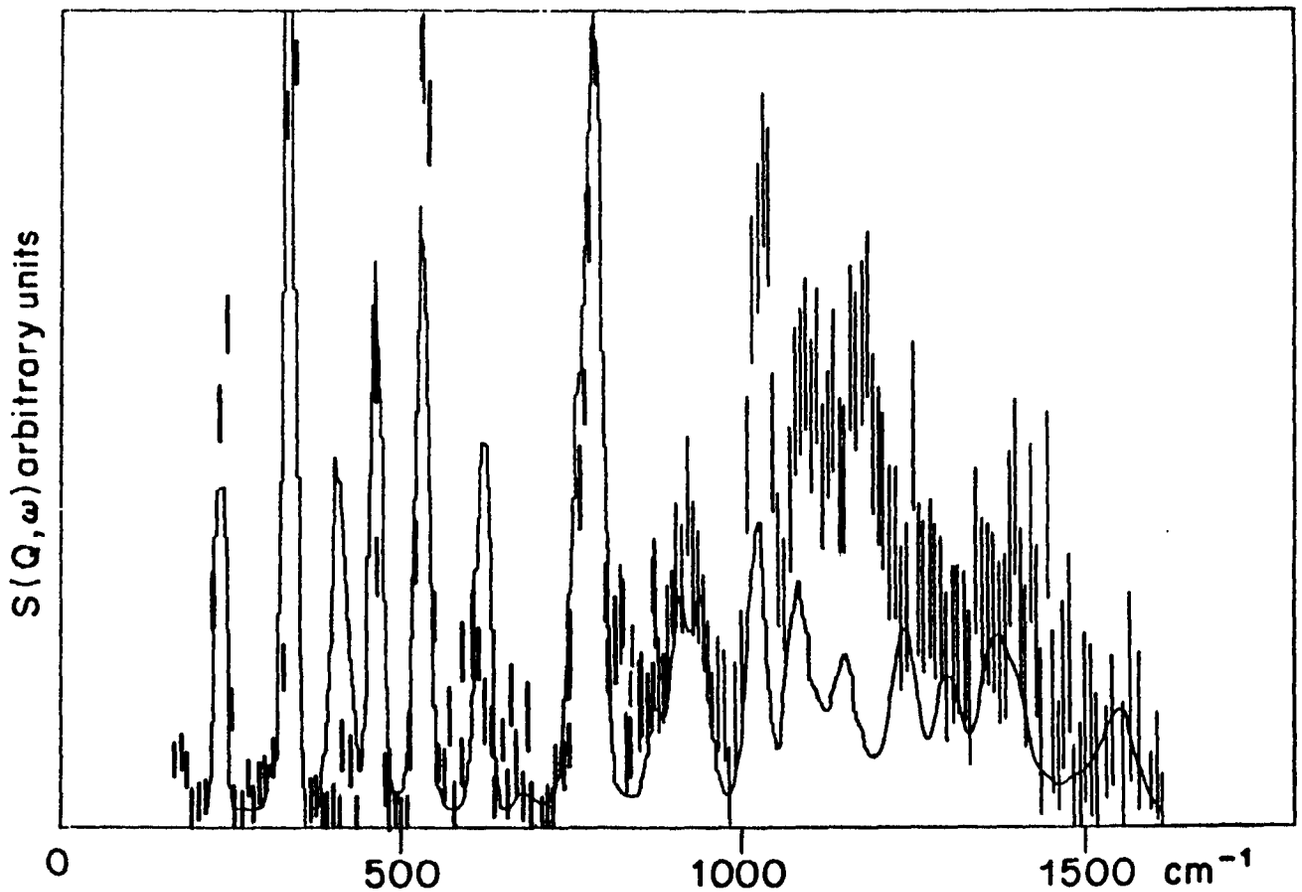

(6) The inelastic incoherent neutron scattering spectrum from 1,4 benzoquinone, at 20K. Only the spectral range from about 200 to 1500 cm^{-1} is shown. The vertical lines represent the data points, with error bars, and the solid line is the best fitted model discussed in the text.

ICANS IX

INTERNATIONAL COLLABORATION ON ADVANCED NEUTRON SOURCES

22-26 September, 1986

NEUTRON BEAM SHIELDING AT ISIS

A D Taylor, T A Broome and D J Picton[+]

Rutherford Appleton Laboratory, Chilton, Didcot, Oxfordshire UK

[+]Physics Department, Birmingham University, Birmingham UK

INTRODUCTION

This paper presents some of the details and rationale behind the neutron beam shielding concepts employed at ISIS. These concepts have now been evaluated at 20 μA operation (1/10 of final design goal) and we are happy to report that no significant (≥10 μS/hr) radiation levels have been experienced in the experimental hall.

BULK SHIELD

The bulk shield has a radius of 5.9 m and is of a conventional design with an iron core and concrete outer shell. The inner void vessel, which contains the target-moderator assembly, has a radius of 1.6 m. The ratio of iron to concrete is 3:1, and the dimensions are dictated by the need to attenuate the hard component (> 100 MeV) of the spectrum, so there is some enhancement of the shield in the forward direction. Figure 1a illustrates the general layout.

Eighteen inserts are provided through the bulk shield, see Figure 1b. Within each insert, neutron beam collimation systems may be constructed which view

any moderator (upper, lower, front, rear). This flexibility will allow the beam configuration to be changed, if required by the scientific programme, without disturbing the general shield. Each of the eighteen beamlines may be independently closed by means of mechanical shutters . The iron and concrete shutters are 2 m thick in the beam direction and a helium atmosphere is provided in the neutron collimator section. The shutters are moved vertically by mechanical jacks to open and close each channel. When closed, the dose rate in the beam at the instrument is < 10 μSv/hr.

COLLIMATION

All ISIS collimation is based on the iris principle proposed by Fluharty. Close to the source in the shutter, the irises are made of scintered B_4C. In the rest of the system, low hydrogen density B_4C rings 5 cm thick are used to define the thermal and epithermal beam. These rings are separated by spacers of slightly greater diameter whose surfaces are either 'bright' (ie can see the source) or 'viewed' (ie can be seen by the detector), but never both. An example is shown in Figure 2. These beam-defining irises are set in a general collimator made of iron shot loaded borated resin, designed to minimise the escape of high energy neutrons and to decouple the beam from its surroundings. Both these components are moulded into rings which are located within a vacuum pipe. Collimator sections are then made up by housing the round vacuum pipes in a 30 cm cross-section rectangular steel box which is filled with iron shot loaded borated wax. This achieves the transition from the round vacuum pipe to a square shape thus facilitating the tight packing of beamline shielding.

NEUTRON BEAMLINE SHIELD AND BEAMSTOPS

Biological shielding of the neutron beamlines is achieved by surrounding the collimation system with steel which is then further enclosed in borated wax. In the absence of sophisticated transport calculations, the following model was adopted to estimate the shielding required transverse to the ISIS beamlines and around the beamstops.

The shielding requirements parallel and perpendicular to the neutron beam are

considered separately. In the former case, shielding is dominated by the need to attenuate any very high energy (> 15 MeV) neutrons in the beam. At these energies all materials are quite transparent with very long mean free paths, eg 17 cm in iron. This problem is not important in the beam line shield, since any neutron emerging at a small angle must penetrate a large thickness of shielding material, but it is significant in the design of the beamstops (see below). The spectrum of neutrons emerging transverse to the beam is much softer, and may be described by an evaporation spectrum with a 1/E slowing down component. Here broad beam mean free paths, determined from one dimensional transport calculations, are substantially shorter (eg 6.25 cm in iron, 9.6 cm for borated wax).

At any given distance along the neutron beam, an equivalent point-source term may be generated by considering the number of neutrons which could be stopped in a given spectral region.

$$S_o = \frac{fI_oA}{L^2} \quad n/s$$

where f is the integral dE/E over the spectral range of interest

$I_o = 7\ 10^{12}$ n/eV.sr.200μA.s

A = area of beam

L = distance from source.

This point source will produce a dose D at a distance R of

$$D = \frac{S_o}{4\pi R^2 Q}$$

where Q is the quality factor converting $n/cm^2.s$ to μSv/hr.

The number of mean free paths λ of shielding material required to reduce this dose to D_o at a distance R is then

$$\lambda = \ln [D/D_o]$$

The 'standard' beamstop design assumed the following parameters:

f = integral over <u>all</u> energies = 18

$I_o = 7\ 10^{12}$ $\qquad$ $Q = 2$

$A = 20$ cm $\qquad$ $D_o = 2.5$ μSv/h

$L = 10$ m $\qquad$ $R = 1$ m

giving

$$\lambda = \ln \left[\frac{fI_oA}{L^2} \cdot \frac{1}{QD_o} \cdot \frac{1}{4\pi R^2}\right]$$

$$= 9.9 + \ln \left[\frac{A}{L^2R^2}\right] \qquad \text{with A in cm}^2 \text{ and L, R in m.}$$

To stop the entire beam, the above parameters indicate that 8.3 mfp of shielding material is required to produce the appropriate reduction in dose. Since typical broad beam mean free paths are 6.25 cm for iron and 9.6 cm for CH_2, this suggests 52 cm thickness of iron. Complete absorption of the thermal neutrons leaking from the iron may then be achieved by a further 30 cm outer layer of boarated wax. This system would therefore be suitable to reduce the dose to acceptable levels 1 m from the source. This calculation may be iterated to give the number of mfp required to produce the appropriate dose reduction at the surface of the shield.

Less conservative parameters would be

f = integral from 0.1 - 10 MeV = 5

$I_o = 7\ 10^{12}$ $\qquad$ $Q = 2$

$A = 15\ \text{cm}^2$ $\qquad$ $D_o = 2.5$ μSv/h

$L = 15$ m $\qquad$ $R = 0.85$ m

giving

$$\lambda = \ln \left[\frac{fI_oA}{L^2} \cdot \frac{1}{QD_o} \cdot \frac{1}{4\pi R^2}\right]$$

$$= 8.63 + \ln \left[\frac{A}{L^2R^2}\right]$$

$$= 6.25$$

ie 39 cm of iron.

Although this calculation could be refined and tailored more closely to individual beam parameters, the effective reduction is small. The practical situation at RAL was that a great deal of spare iron shielding was available, but with minimum thicknesses of 60 cm. The practical arrangement for transverse shielding around a beamline is illustrated in Figure 3.

This approach may also be used to give a crude estimate of transverse beamline shielding by regarding the collimation system as a linear beamstop. In the above calculation the beam area A is replaced by the amount of beam scraped off in the section of interest. Because of the logarithmic dependence on A and the need to shield closer to the source, the thicknesses required are similar.

With beamstops, in addition to concern about the transverse shielding, care must be taken to attenuate any high energy component (> 15 MeV) of the neutron beam. In this region mean free paths in all materials increase by a factor 3 (eg λ^{he}_{Fe} = 17 cm). Calculations with the HET Monte Carlo code using the computed ISIS beam escape spectrum indicate that a significant quantity of longitudinal shield is required. Hence a 1 m length of Fe , decoupled with high density polyethylene, is used as a core for ISIS beamstops. (Longitudinal shielding of a beamline is not a problem). This core is then surrounded by the standard 60 cm of iron and 30 cm of borated wax, see Figure 3. Backscattering into the spectrometer is suppressed by a plug of B_4C powder before the beamestop core. All indications are that we have erred on the side of safety*

[*Note Added in proof: New measurements on a partially constructed beamstop at 30 μA show significant radiation levels (50 μSv/hr) on the Fe surface before the addition of the outer wax shield.]

SPECTROMETER SHIELDING

The function of both the bulk shield and the beamline shield and beamstops is to minimise the biological radiation dose in the experimental hall. The spectrometers themselves have additional shielding whose function is to minimise neutron background in the detectors. In general, all spectrometers are enclosed in steel tanks containing a 30 cm thick layer of borated wax (3 atomic % boron) which neutronically decouples the spectrometers from their

environment. The interior surfaces of most spectrometers are lined with 5 mm B_4C tiles (< 5 % hydrogen) to minimise the effects of spurious scattering and (n,γ) reactions. The low-hydrogen B_4C mixture is also employed behind all ^3He detectors to minimise back-reflected neutrons.

CONCLUSION

The combination of the above shielding concepts and the pulsed nature of the source has produced background levels in the detector systems during ISIS operation which are close to the intrinsic detector limits (eg 0.1 counts/gas tube/minute). No biological radiation problems have been encountered.

ACKNOWLEDGEMENTS

We are indebted to our ICANS colleagues from KENS, LANCE, IPNS and SNQ for discussions and providing data on the performance of their neutron beam shielding.

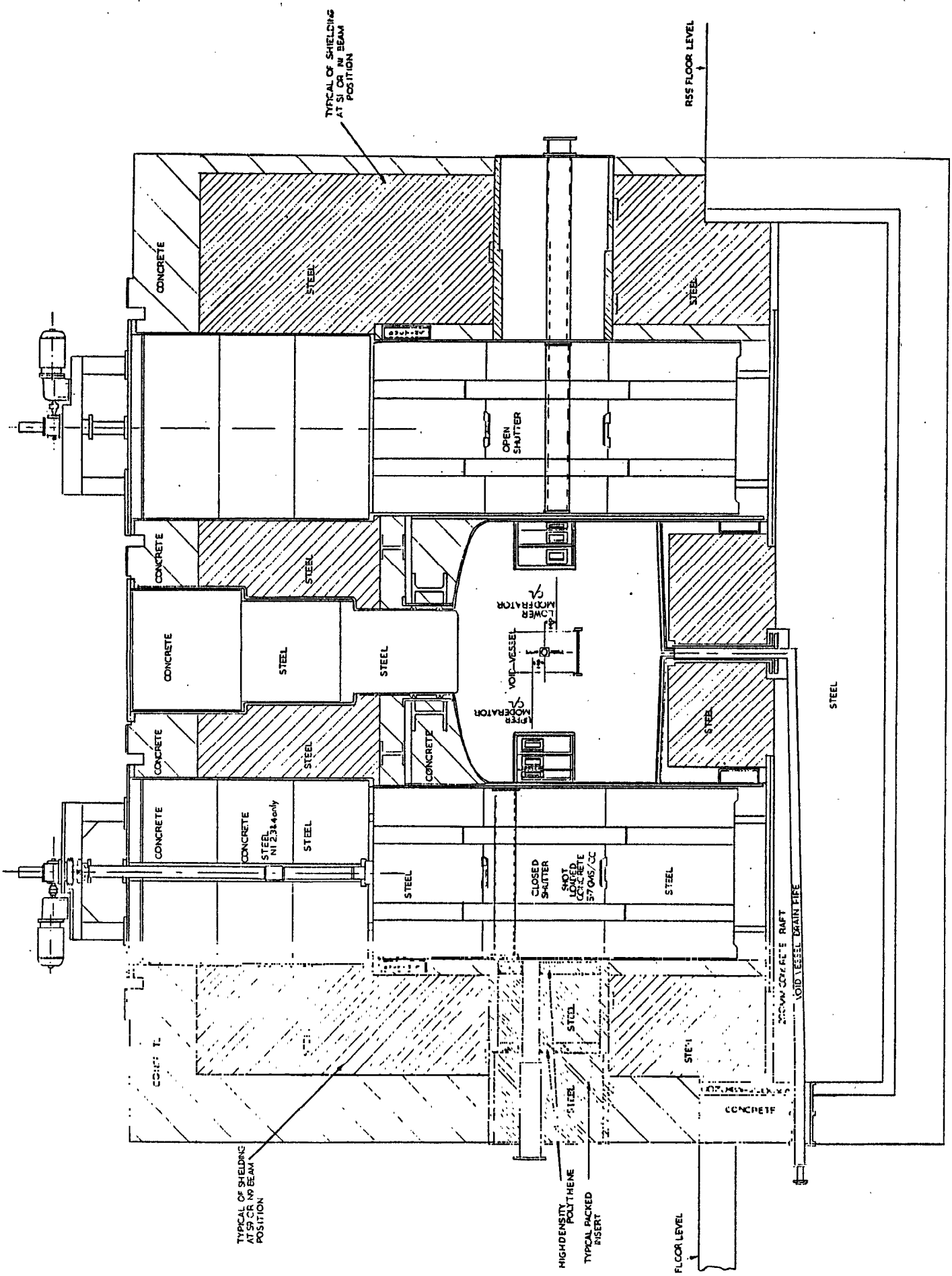

Figure 1a A vertical section through the ISIS bulk shield.

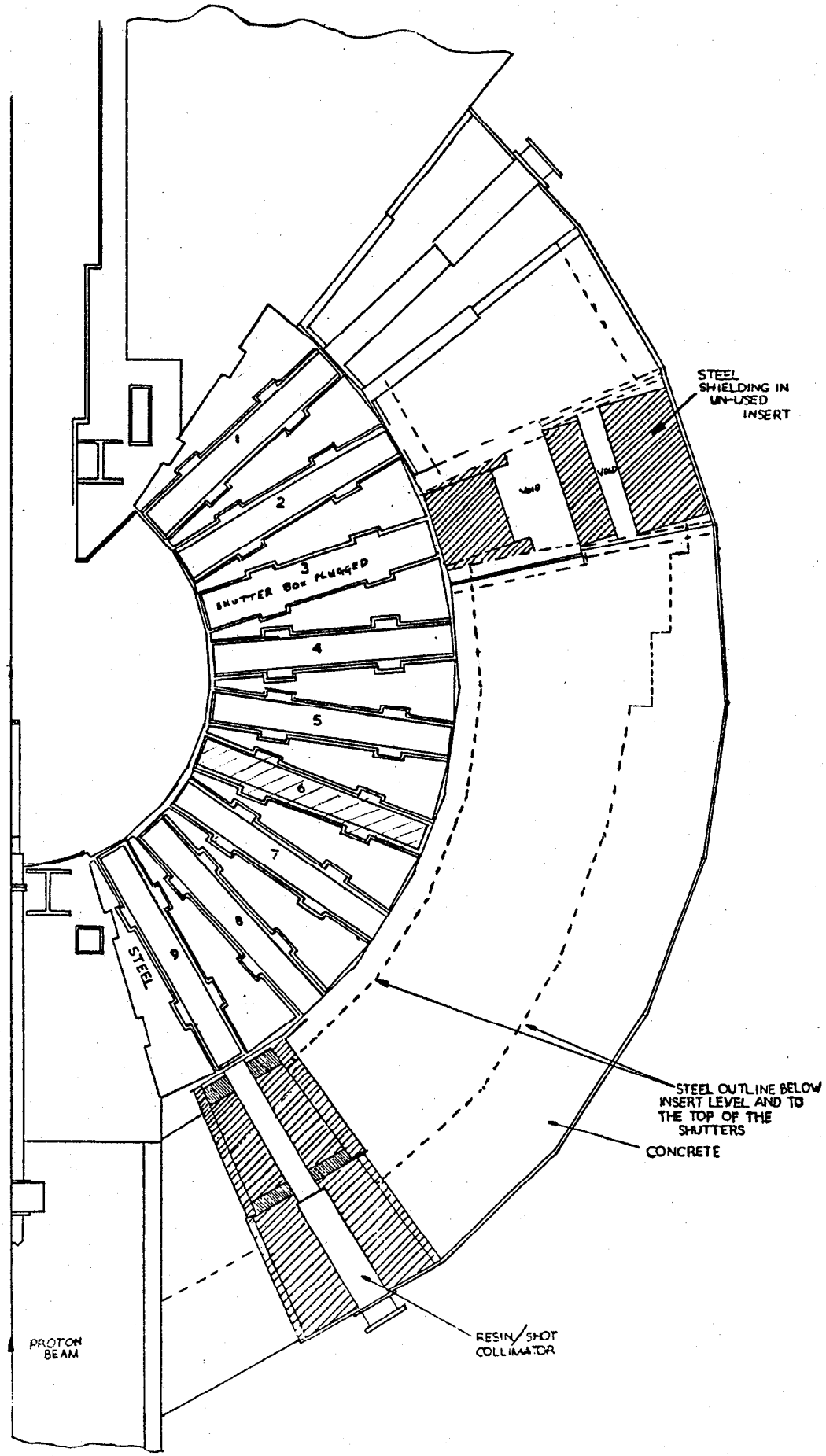

Figure 1b A horizontal section showing the location of nine beam ports in half of the ISIS bulk shield.

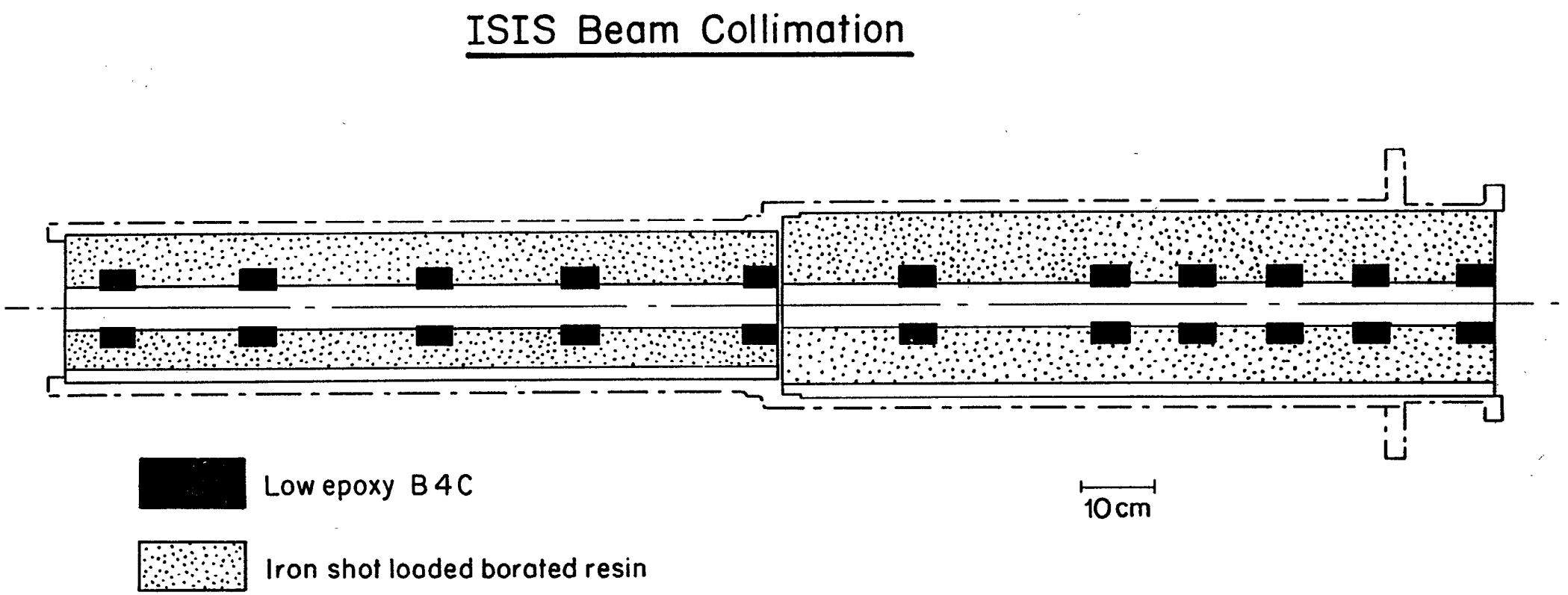

Figure 2 A typical section of ISIS neutron beam collimator showing B_4C beam-defining irises and iron-loaded borated resin spacers.

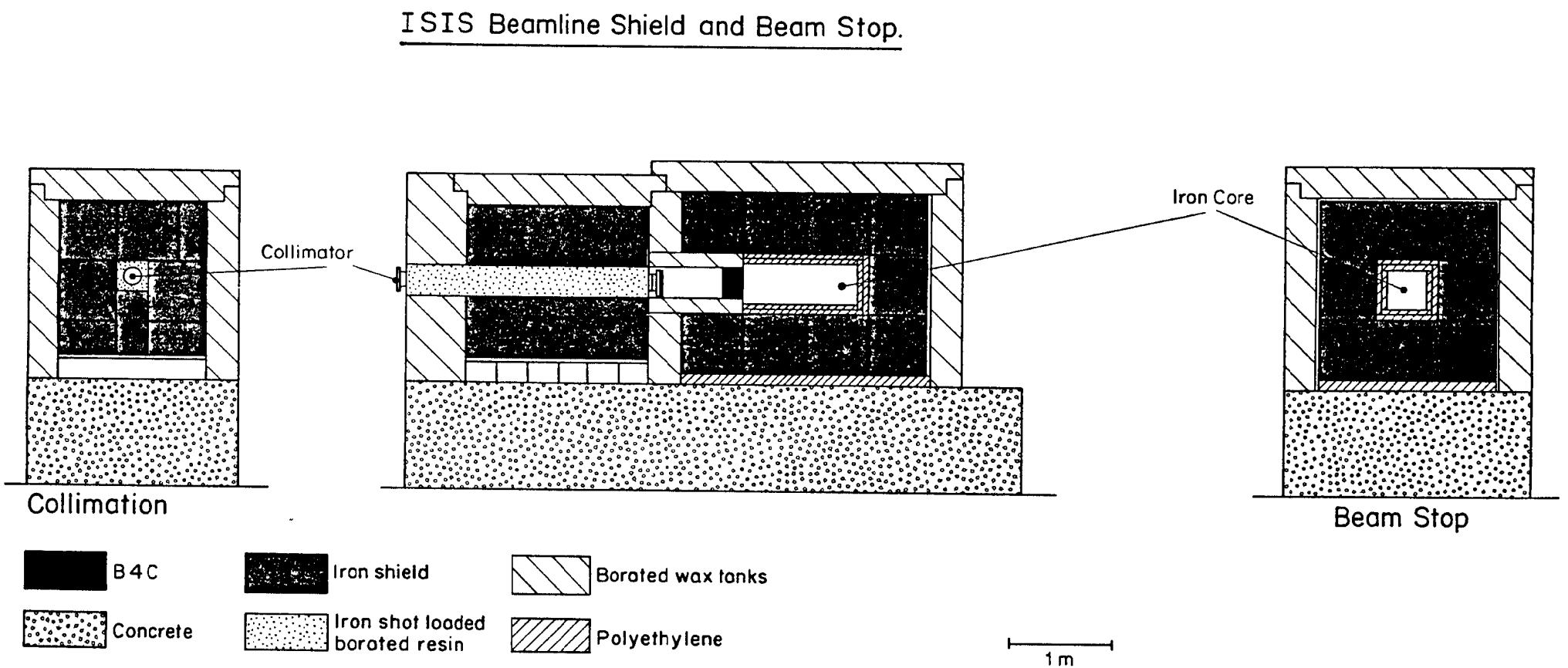

Figure 3 Beamline and beamstop shielding at ISIS.

ICANS IX

INTERNATIONAL COLLABORATION ON ADVANCED NEUTRON SOURCES

22-26 September, 1986

THE H E T BACKGROUND SUPPRESSING CHOPPER

T J L Jones, I Davidson, B C Boland, Z A Bowden and A D Taylor

Rutherford Appleton Laboratory, Chilton, Didcot, Oxfordshire UK

INTRODUCTION

The high speed fast Fermi chopper on HET [1] has proved to be an effective and versatile primary monochromating device for energies ranging from 100 meV to 2000 meV [2]. At energies above 350 meV, however, a source of background, due to very energetic neutrons penetrating the light aluminium body and boron slit package of the fermi chopper and downscattering in the sample to thermal energies, becomes significant. This had been anticipated in the original design, and provision had been included for a background-suppressing chopper to be located upstream of the monochromator. This paper gives details of the design and construction of this device and illustrates its effectiveness in extending the incident energy range of the spectrometer to several eV.

DESIGN

The background chopper is designed to be closed at the beginning of each ISIS pulse to prevent high energy neutrons and gamma rays from entering the spectrometer. It must then be fully open a few hundred microseconds later to allow the required epithermal beam to be monochromated by the Fermi chopper.

To achieve this the device has a rotor in the form of a vane (like a double

bladed paddle wheel), see Figure 1, which rotates on a horizontal axle mounted 250 mm above and parallel to the neutron beamline of the spectrometer. The vane is 300 mm long in the direction of the beam and at each tip there are 60 mm wide by 55 mm high rectangular blocks of nimonic 75 alloy (75% Ni, 19.5% Cr, 4% Fe). Nimonic is chosen for its good high energy neutron cross-section and its high tensile strength. A rotor completely made of this alloy would have excessive mass and inertia, and so the design has the outer nimonic tips linked to the 60 mm diameter central steel axle by a spaced assembly of 14 tapered plates and 2 end discs machined from 12 mm thick aluminium alloy and distanced by 8 mm thick 120 mm diameter spacing rings. The attachment of the nimonic blocks to these plates is by means of two pairs of 25 mm diameter titanium tie rods which are fitted, through the length of the vane, into jig-bored and reamed holes 25 mm in from their outer ends and similar pairs of holes in tabs, machined on the inner surface of the top blocks, which interleave the plates.

The chopper can rotate at 50 Hz or 100 Hz. All operation so far has been at 50 Hz. At these speeds, there is an enormous amount of stored energy in the rotor and seizure of an axle bearing would result in its catastrophic break-up. The Al/alloy plates are therefore not rigidly joined to the axle. Instead at their central point they are keyed onto a cylindrical phosphor bronze bush which sleeves the axle to form a safety bearing. A pair of 4 mm diameter shear pins, which fit into this bush and into a flange on the axle, provide driving force to the vane but in the event of seizure of the axle these break to allow the vane to freewheel on the shaft.

The axle is suspended at each end on dual-row self aligning ball races, carried in housings which bolt to the end plates of the evacuated spinning tank, and is rotated by a toothed pulley and belt system driven from a 30 kW induction motor powered by a phase-controlled inverter system.

The speed and phase control electronics permits the choice of rotational frequencies of either 50 Hz or 100 Hz. The chopper is located 8 m from the source and so at these frequencies it transmits neutrons with energies below 1 eV an 4 eV respectively.

PERFORMANCE

Before the introduction of this chopper on HET, a time-dependent background, originating at the same time as the proton pulse and having an effect decay constant of 1.5 ms, limited the quality of data taken at high incident energies. As a result, prior to the installation of this chopper, the bulk of running had been confined to energies less than 350 meV. Attempts to improve shielding and minimise scatter failed to reduce this background component. Further it had been shown that this background was entirely sample dependent and disappeared when the sample was removed. Careful tests proved that it was due to high energy neutrons penetrating the fast chopper at zero time and being inelastically scattered, sometimes to sub-cadmium energies, in the sample.

The slow nimonic chopper was installed on March 1986 and has proved to be invaluable on HET for performing experiments on weak magnetic systems with high energy neutrons. Figure 2 compares scattering data from vanadium taken with and without the chopper. The background levels before and after the elastic line are close to source off values.

This chopper has contributed greatly to the success of many of the experiments described in reference [2].

REFERENCES

[1] T J L Jones, J H Parker, I Davidson, K Boden and J K Fremery, 'Experience with the KFA/IGV (Julich) Magnetic Bearing System on as SNS Neutron Chopper', in Proceedings of the Eighth Meeting of ICANS, Rutherford Appleton Laboratory Report RAL-85-110 (1985), p707.

[2] A D Taylor, B C Boland and Z A Bowden, ' HET : The High Energy Inelastic Spectrometer at ISIS', these proceedings.

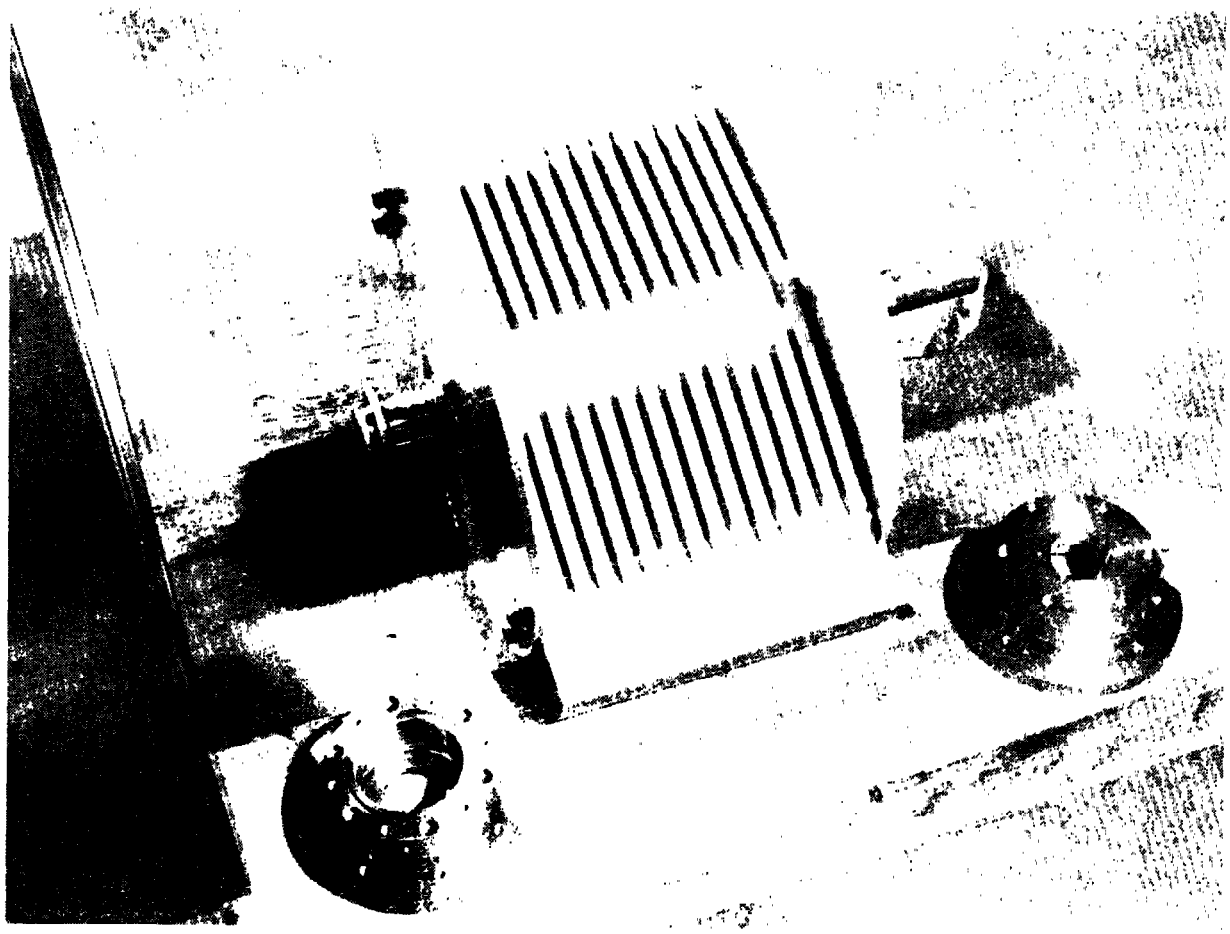

Figure 1 The HET nimonic background-suppressing chopper removed from its housing.

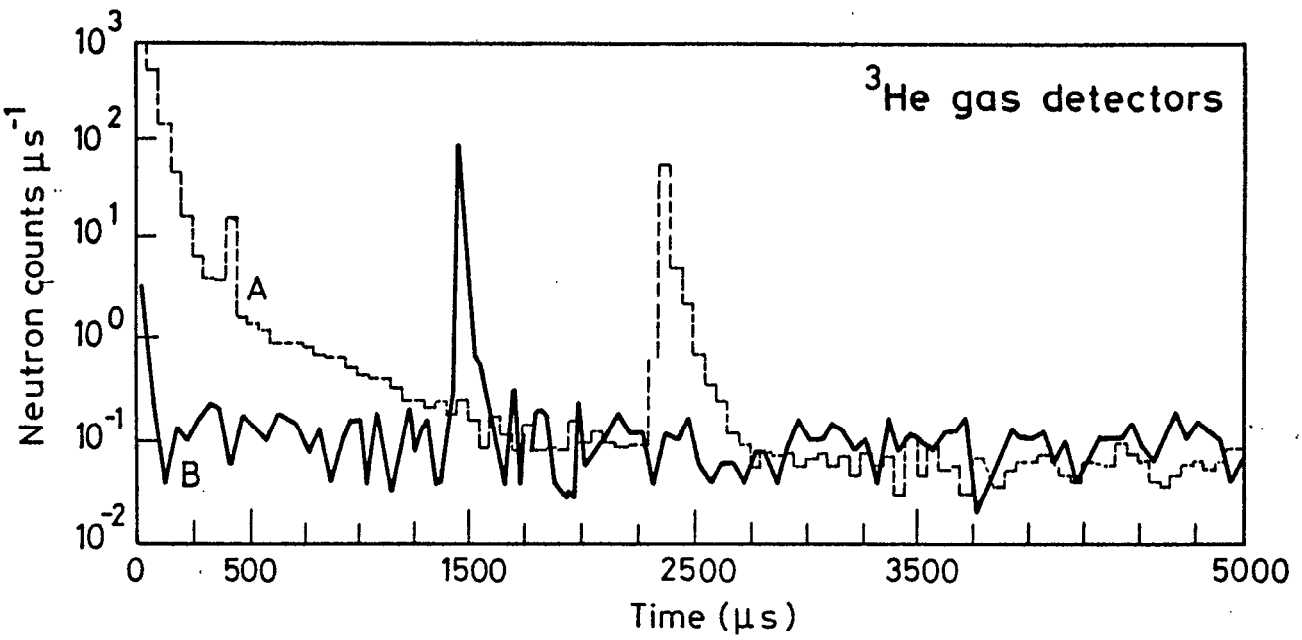

Figure 2 Comparison of time-of-flight scattering data from vanadium taken without (A) the chopper and with (B) the chopper. For clarity two different incident energies (A : 220 meV and B: 600 meV) are shown. The background effect is independent of the choice of fast chopper energy.

ICANS IX

INTERNATIONAL COLLABORATION ON ADVANCED NEUTRON SOURCES

22-26 September, 1986

M A R S -- A Multi-Angle Rotor Spectrometer at the Pulsed Neutron Source ISIS

A D Taylor[x], R C Ward[x], W G Williams[x], Y Endoh[+] and N Watanabe[+]

[x]Rutherford Appleton Laboratory, Chilton, Didcot, UK
[+]KEK, Oho-Machi, Tsukuba-Gun, Ibaraki-Ken, Japan

INTRODUCTION

The design for the Multi-Angle Rotor Spectrometer, MARS, currently being constructed on the ISIS pulsed neutron source is presented. MARS is a direct geometry chopper spectrometer designed for studying inelastic processes with an energy transfer resolution $\Delta\varepsilon/\varepsilon \sim 1\%$. The spectrometer will have an extensive detector bank with a continuous angular coverage from 3° to 135° and a Q resolution $\Delta Q/Q \sim 2\text{-}5\%$ allowing interpolation of $S(\phi,t)$ to $S(Q,\varepsilon)$ and the spectrometer will view the 100K liquid methane moderator giving an effective lower bound for the incident energy of 50meV.

The instrument design parameters have been optimised for experiments in the following four main scientific categories.

(1) Coherent excitations: measurement of the dynamic structure factor $S(Q,\varepsilon)$ in polycrystalline and amorphous solids, liquids and gases.

(2) Magnetism: measurement of the magnetic response of 3d-systems over the whole excitation spectrum; magnetic spectroscopy in f-electron metals and alloys.

(3) Molecular spectroscopy: measurement of a large range of energy transfers (eg. 10meV to 250meV) with good energy resolution ($\Delta E_o/E_o \sim 1\%$) over a large Q range.

(4) Momentum distribution: mesurement of the dynamic structure factor $S(Q,\varepsilon)$ at large Q where the impulse approximation becomes valid.

SPECIFICATION

The instrument will be sited on the S6 beam hole viewing the gadolinium poisoned 100K methane moderator. A Fast Fermi chopper with a variety of interchangeable curved slit-slot packages optimised for several incident energies in the range 50 to 1000 meV will be used as the monochromating chopper. An additional chopper positioned between the moderator and the monochromating chopper will be used for background suppression. The beam line will have the option to accomodate a neutron beam polariser between the monochromating chopper and the sample. The sample position is at 11.7 metres from the moderator and typical beam sizes will be 6 x 6 cm^2.

Due to constraints imposed by neighbouring instruments, the 4 metre evacuated secondary flight path will be in the vertical scattering plane and there will be the potential to have a continuous coverage of 30cm ^{3}He detectors in the angular range of $2\theta = 10^o$ to 135° with a total of 3 detectors on the Debye Scherrer cone at any one angle. In addition there will be a low angle detector bank with 6 linear arrays of detectors positioned around the straight through beam in the angular range of 3° to 10°. The detector tank has been designed such that there will be continuous detector coverage without any shadows from structural supports inside the tank in the angular range 3° to 30°. Between 30° and 135°, the gaps in the detector array due to structural supports will be less than 1.3^o every 15°. The sample and detector tanks will have a common rough vacuum system, but will be separated by a thin aluminium membrane, thus allowing the sample region to be differentially pumped to a cryogenic quality vacuum.

A summary of the full instrument specification is given in Table 1 and a schematic layout of the detector and sample tank, together with the low angle detector array, is given in Figure 1.

Table 1

Instrument specification

Moderator	100K CH_4 poisoned at 2.25cm
Monochromating Chopper	10.0m from moderator, 400-600 Hz phased to ISIS pulse to within 1/2 μs
Sample position	11.7m from moderator
Beam size	6cm x 6cm
Detectors	3°-10° 4m low angle counter bank, 10 atms ^3He 6 azimuthally symmetrical detectors at each angle
	10°-135° 4m high angle counter bank, 10 atms ^3He 3 detectors at each angle
Incident energy	50-1000 meV
Energy resoultion	$\Delta E_o/E_o \sim 1\%$

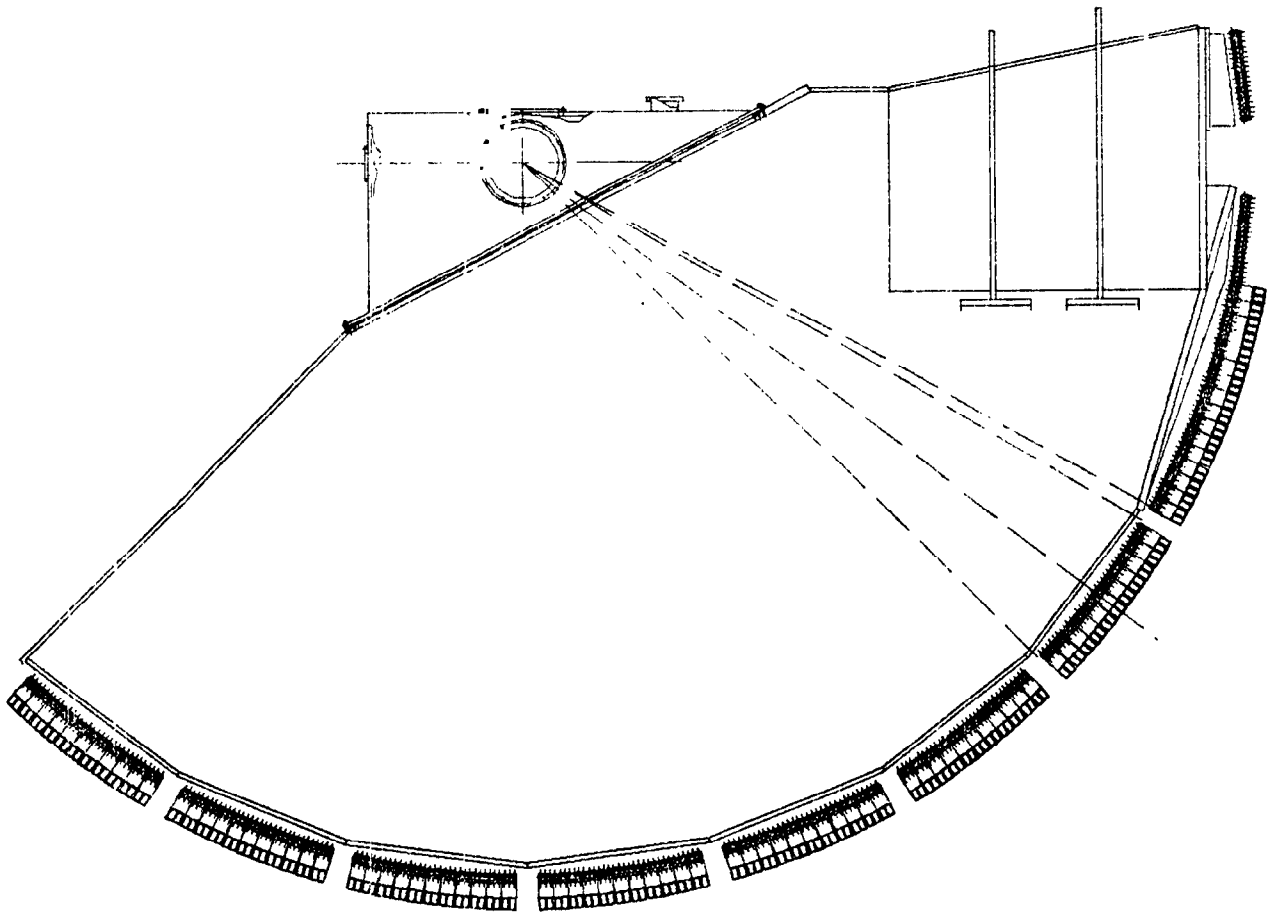

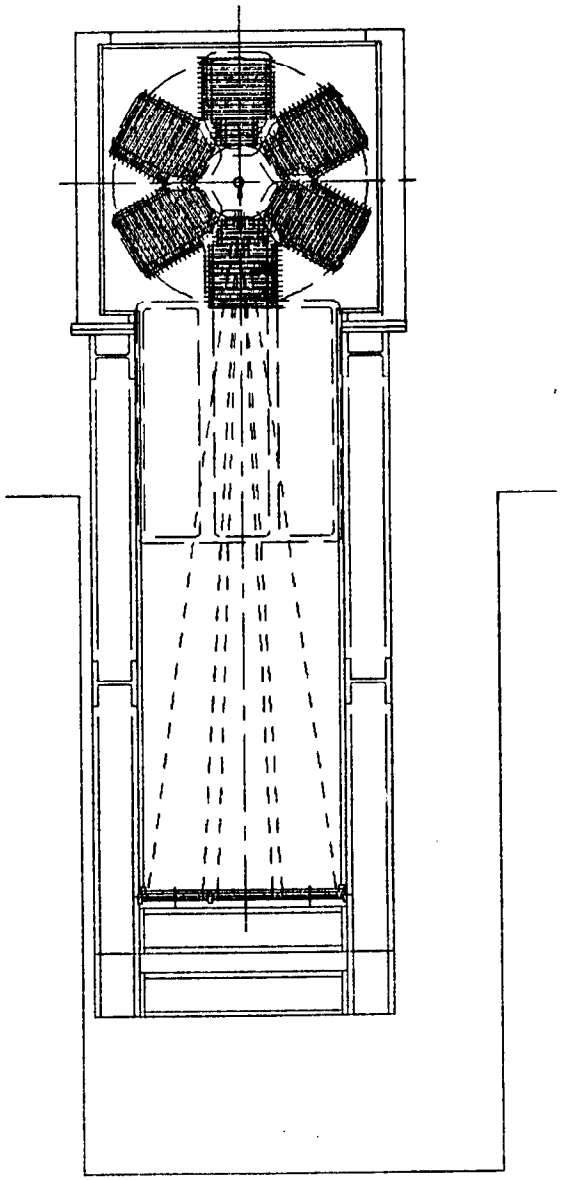

Figure 1 A schematic layout of the sample and detector tank showing the location of the high and low angle detector arrays. The high angle detector bank is in the vertical scattering plane with three detectors at each angle. The low angle detector bank has six-fold symmetry about the straight through beam

ICANS IX

INTERNATIONAL COLLABORATION ON ADVANCED NEUTRON SOURCES

22-26 September, 1986

Liquid and Amorphous Total Scattering Instrument at KENS
- HIT -

M. Misawa, T. Fukunaga*, T. Yamaguchi** and N. Watanabe

National Laboratory for High Energy Physics,
Oho-machi, Tsukuba-gun, Ibaraki-ken, 305, Japan

* Research Institute for Iron, Steel and Other Metals,
Tohoku University, Sendai 980, Japan

** Department of Electronic Chemistry,
Tokyo Institute of Technology,
Nagatuta, Midori-ku, Yokohama 227, Japan

Abstract

Liquid and Amorphous Total Scattering Instrument (HIT) at KENS is in operation since 1980. It was originally designed to measure the S(Q) of liquids and amorphous solids composed of heavy nuclei with high count rate and modest resolution of the momentum transfer Q. Recently proposals which desire to measure the S(Q) of materials composed of light nuclei or with better resolution are increasing in number. The effects of the resolution and the inelastic scattering on observed S(Q) are, therefore, reexamined using machine parameters of the HIT. Current performance of the HIT is briefly reported as well.

1. Introduction

The Liquid and Amorphous Total Scattering Instrument (HIT) at KENS was constructed in 1980. Since then it has been operated for more than 5 years. During this period many users from outside universities performed measurements of S(Q) on various kinds of liquids and amorphous materials. Many scientific results have been obtained using this machine and significant contributions to the structure determination of liquids and amorphous solids have been made.

The HIT machine was originally designed to measure the S(Q) of liquids and amorphous solids with high count rates and modest resolution of momentum transfer Q.[1] The target materials we supposed were those composed of heavy nuclei or those of which inelastic scattering is not significant.

Recently proposals to measure the S(Q) for the materials containing light nuclei or with better resolution are increasing in number at KENS. Therefore we reexamined the effects of the resolution and the inelastic scattering on observed S(Q) using the machine parameters of the HIT. In this report we summarize the current performance of the HIT machine briefly and discuss how the resolution and the inelastic scattering affect the observed S(Q).

2. Outline of the machine

A schematic drawing of the current HIT machine is shown in Fig. 1. The machine views the ambient temperature solid polyethylene moderator. A sample is located 5,053 mm from the moderator. The evacuated sample chamber is 450 mm in diameter so that it has enough room to install a sample changer and sample enviromental equipments such as a high temperature furnace, low temperature refrigerator, magnet and so on. The neutron flux at the sample position is about 5×10^5 n/cm^2/sec/2μA in the range of 0.3 to 0.7 Å which we use mainly for S(Q) measurement.

The neutron detectors used are He-3 gas counters (1/2" in diameter, 12" in active length and 20 atm in filled pressure). In the high angle region (150° and 90°) the detectors are located at geometrical time focusing positions, while in the lower angle region they are located at electrical hardware time focusing positions described later in detail. The scattered flight path length has been determined to give both high

count rates and modest geometrical Q resolution. The scattering angle and the flight path length for each detector now used are listed in Table 1.

The electrical hardware time focusing system which consists of a CAMAC module was newly developed.[2] The block diagram is shown in Fig. 2. The new system is the same in principle as the time focusing one using a computer. The main difference between the two systems is that the former system does not need any computing time so that it can fit measurements with the higher count rate. In this system each detector has own time analyser, of which the time width $\Delta\tau$ is chosen easily by a software to satisfy the following time focusing condition.

$$\Delta\tau = \frac{L \sin\Theta}{L_r \sin\Theta_r} \Delta\tau_r , \qquad (1)$$

where L and 2Θ are the total flight path length and the scattering angle, respectively. Subscript r denotes the reference detector. The all time analysers (sub modules in Fig. 2) involved in a certain detector bank are controlled by one main module. The counts accumurated in a sub module during time interval $\Delta\tau$ are added to the stored counts in the corresponding address in Q-space of the main memory giving a time-focused result. The system is controlled by a personal computer PC 9800 (NEC). Acceptable maximum count rate is expected to be about 6 counts/μs per each time analyser.

3. Geometrical resolution

The resolution in Q space was estimated by a Monte Carlo technique. The geometrical sizes of moderator (100 x 100 mm^2), sample (8 mm in diameter and 40 mm in height as a typical case) and detector (1/2" in diameter and 4 ∿ 12" in length depending on scattering angles) were taken into account. The time structure of the incident neutron pulse was included in an approximate manner as well. The resolution ΔQ was defined as a root mean square deviation of the Q value from the mean value $\bar{Q}$, i.e. $\Delta Q = \langle (Q - \bar{Q})^2 \rangle^{1/2}$. The calculated results are shown in Fig. 3. The broken lines show the case of the poor resolution, while the solid lines do the case of the good resolution. In the latter a limitted detector height was assumed except for 90° detectors, while in the former a slightly off time focusing position was chosen for 90° detector bank.

Usually we utilize the neutrons only in the wavelength range of 0.3 - 0.7 A for the S(Q) measurement, except for the low Q measurement with low angle counter, in order to avoid the serious distortion of S(Q) arising from non-constant Q scan of the instrument. The range between the two dots on each curve in the figure corresponds to this wavelength range. Figure 4 demonstrates the effect of the geometrical resolution on the simulated S(Q) for a model system. The result suggests that the resolution ΔQ must be at least 0.2 A^{-1} or less if one requires the precise measurement of S(Q).

4. Effect of the inelastic scattering

The inelastic scattering is a serious problem in the S(Q) measurement when a sample contains light atoms. In order to know how the inelastic scattering affects observed S(Q) at high Q, we simulated experiment on the HIT using the following simple models of $S(Q,\omega)$'s.

$$S_{self}(Q,\omega) = \left[\frac{M}{2\Pi\hbar^2 Q^2 kT} \right]^{1/2} \exp\left[- \frac{M}{2\hbar^2 Q^2 kT} \left(\hbar\omega - \frac{\hbar^2 Q^2}{2M}\right)^2 \right],$$

$$S_{int}(Q,\omega) = \left[\frac{M^*}{2\Pi\hbar^2 Q^2 kT} \right]^{1/2} \exp\left[- \frac{M^*}{2\hbar^2 Q^2 kT} \left(\hbar\omega - \frac{\hbar^2 Q^2}{2M^*}\right)^2 \right]$$

$$\cdot\ (S(Q)-1) \quad , \qquad (2)$$

where M is the atomic mass and M^* is the effective mass for the coherent scattering just for convenience. This model is enough to examine the effect of the inelastic scattering on S(Q) in high Q region although it is not in low Q. In the simulation an incident neutron spectrum $\Phi(E)$ was approximated by the following analytical form,

$$\Phi(E) = \Phi_o \left[\Phi_{th} \left(\frac{E}{E_T^2} \right) \exp\left(- \frac{E}{E_T}\right) + \Phi_{epi} \frac{\Delta(E)}{E^{0.878}} \right], \qquad (3)$$

where E_T = 35.2 meV, Φ_{th}/Φ_{epi} = 6.89 and $\Delta(E) = 1/[1 + (5E_T/E)^7]$.
The detector efficiency $\eta(\lambda)$ was approximated by the following equation,

$$\eta(\lambda) = 1 - \exp(a + b\lambda + c\lambda^2) \qquad (0.05 < \lambda < 9.6\ A)\ , \tag{4}$$

where a = 0.01839, b = -1.44457 and c = 0.007479. Figure 5 shows the instrumental integration paths calculated for the HIT machine. The integration of $S(Q,\omega)$ with respect to ω is carried out by the HIT along these integration paths with weighted factors of Φ (E) and $\eta(\lambda)$. S(Q)'s simulated for M/m = 100 and M^*/m = 200, where m is a neutron mass, are shown in Fig. 6. The effect of the inelastic scattering on the simulated S(Q) is not serious as expected for samples with heavy mass. On the other hand for samples with light mass such as M/m = 11 and M^*/m = 27 the effect is serious as shown in Fig. 7. The following three effects on the S(Q) due to inelastic scattering may be confirmed :

i) deviation of $S_{self}(Q)$ from the unity,

ii) damping of the oscillation of S(Q), and

iii) phase shift of the oscillation of S(Q).

All of three effects are significant at higher scattering angle. We have often encountered these three effects in actual experiments. Among these three effects, the second and the third are very important for structural investigations.

Powles[3)] proposed a correction method for the inelastic scattering for various molecules, but it seems hard to make precise corrections when a sample contains three or more chemical species. The materials we are interested in are often multi-component systems, such as aqueous solutions. Therefore, we are planning to install a new detector systems at the lower scattering angles (less than 30°) using ^{6}Li glass scintillators. In order to measure the S(Q) in the range of Q over 30 A^{-1} or more with a reasonable resolution, the momentum resolution must be less than 0.2 A^{-1} in the whole Q range. To achieve this required resolution and to still keep good count rate, a coarse converging collimator may be useful, and the glass scintillators will be arranged as many as possible along the Debye-Scherrer cone on a focusing sphere of the converging collimator. Design work to improve the HIT is in progress.

Acknowledgement

The authors would thank Mr. S. Satoh for providing the new time analyser system including computer software. Their thanks are also to all members of the HIT group.

References

1) N. Watanabe, T. Fukunaga, T. Shinohe, K. Yamada and T. Mizoguchi, Proc. of ICANS-IV, KENS Report II (1981), 539.

2) S. Satoh, KEK Internal 85-8 (1985) (in Japanese).

3) J. G. Powles, Molec. Phys. 36 (1978), ibid 37 (1979) 623.

Table 1. Parameters of the HIT machine

(Scattered flight path length at detector center L_2, scattering angle at detector center 2Θ and time width of time analyser $\Delta\tau$)

Detectors	L_2 (mm)	2Θ (degree)	$\Delta\tau$ (μsec)	Note
150° bank				
150 a2	301.6	155.3		
150 a3	327.0	152.5	2.0	geometrical
150 a4	349.9	150.0		time focusing
90° bank				
90 a1	255.5	93.6		
90 a2	330.0	90.2	2.0	geometrical
90 a3	418.3	87.6		time focusing
50° bank				
50 b1	514.1	42.0	4.0	electrical hardware
50 b4	500.5	47.8	4.5	time focusing
30° bank				
Fa 15	586.3	26.2	4.0	electrical hardware
Fa 18	557.0	31.5	4.75	time focusing
20° bank				
Fa 11	631.1	20.0	8.0	electrical hardware
Fa 13	607.17	23.0	9.125	time focusing
13°				
Fa 6	697.6	13.3	8.0	
7°				
Fa 6	779.4	7.4	8.0	

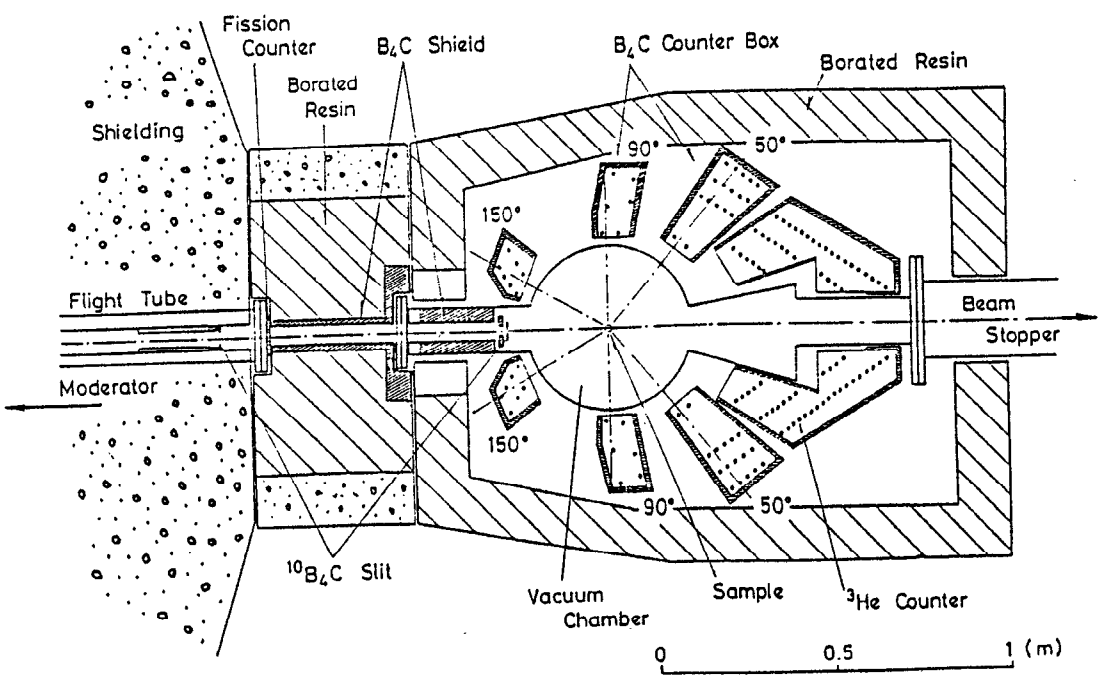

Fig. 1. A schematic drawing of the current HIT machine.

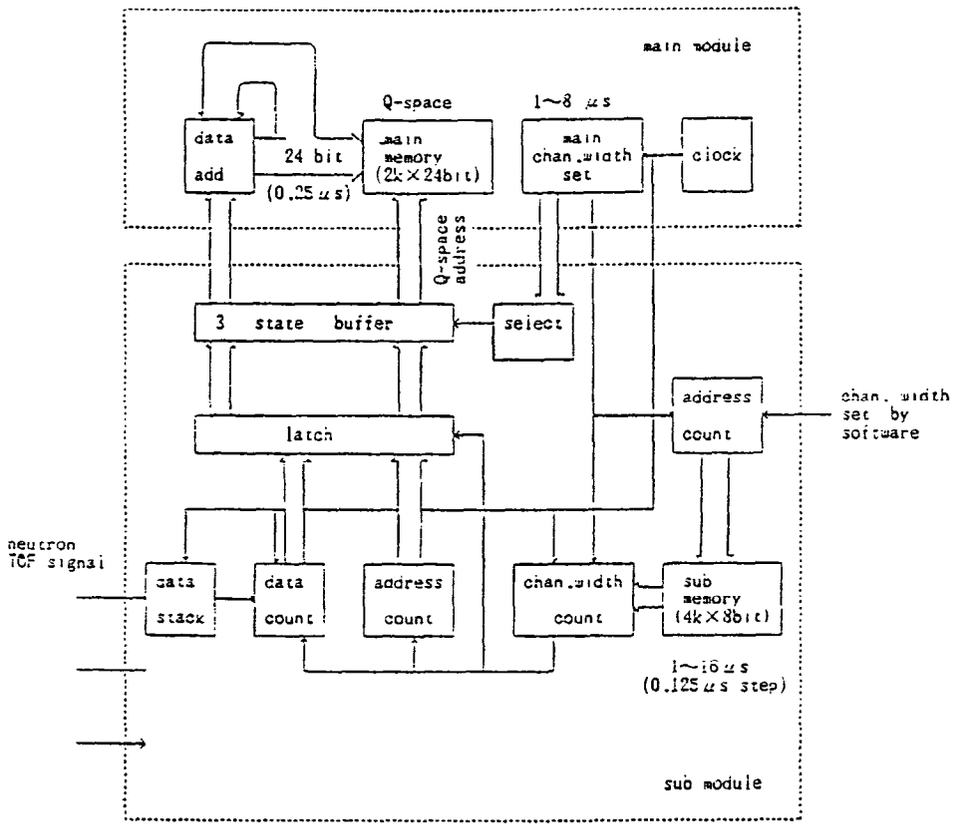

Fig. 2. Block diagram of CAMAC module for hardware time focusing.

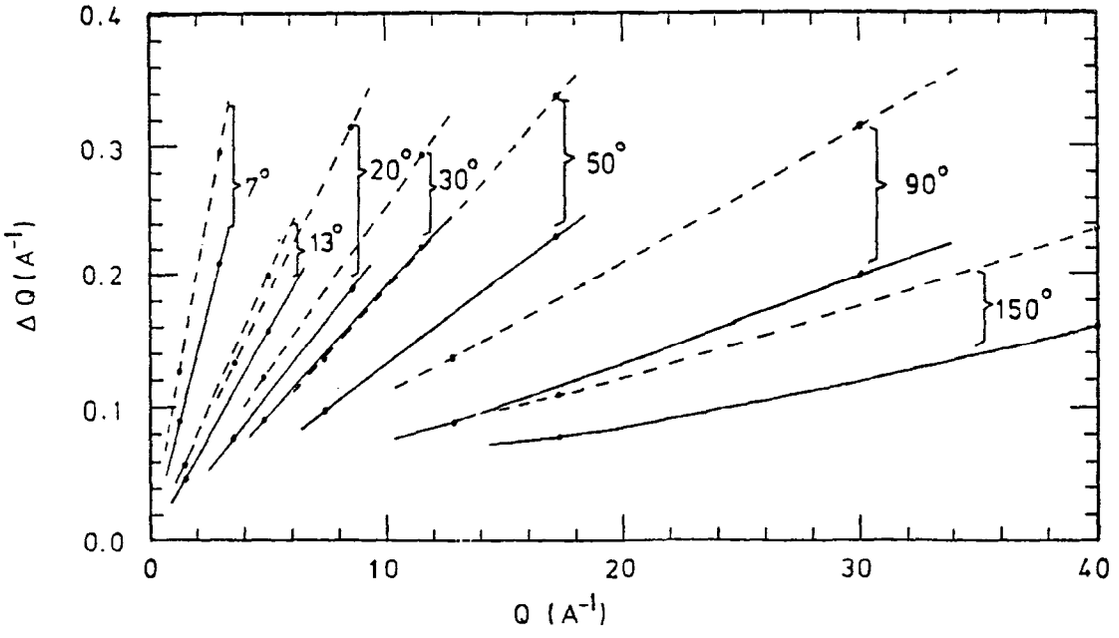

Fig. 3. Geometrical resolution of momentum transfer Q calculated for various detector banks now used in the HIT. Broken lines show poor resolution, while solid lines good resolution. The region between two dots on each line corresponds to the wavelength between 0.3 and 0.7 Å.

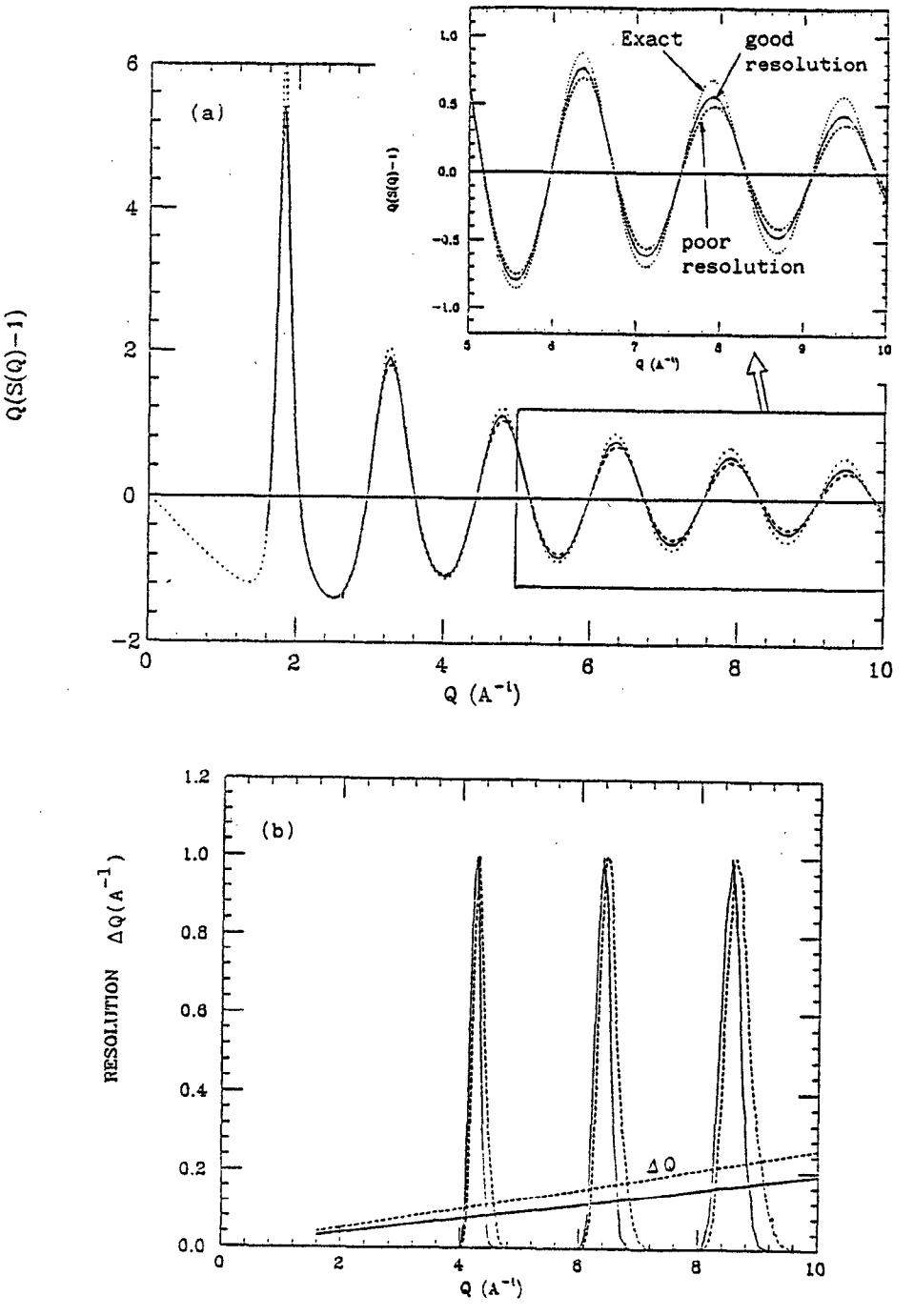

Fig. 4. Effect of the Q resolution on S(Q).
(a) The dotted curve is an exact S(Q) calculated for hard sphere system. Broken and solid curves are the S(Q)'s calculated with the poor and good resolutions shown in the lower figure.
(b) A resolution ΔQ for 2Θ = 30° which is the same as already shown in Fig. 3. Solid line shows good resolution, while broken line poor resolution. Resolution functions at ca. 4.2, 6.4 and 8.5 A^{-1} are shown as well.

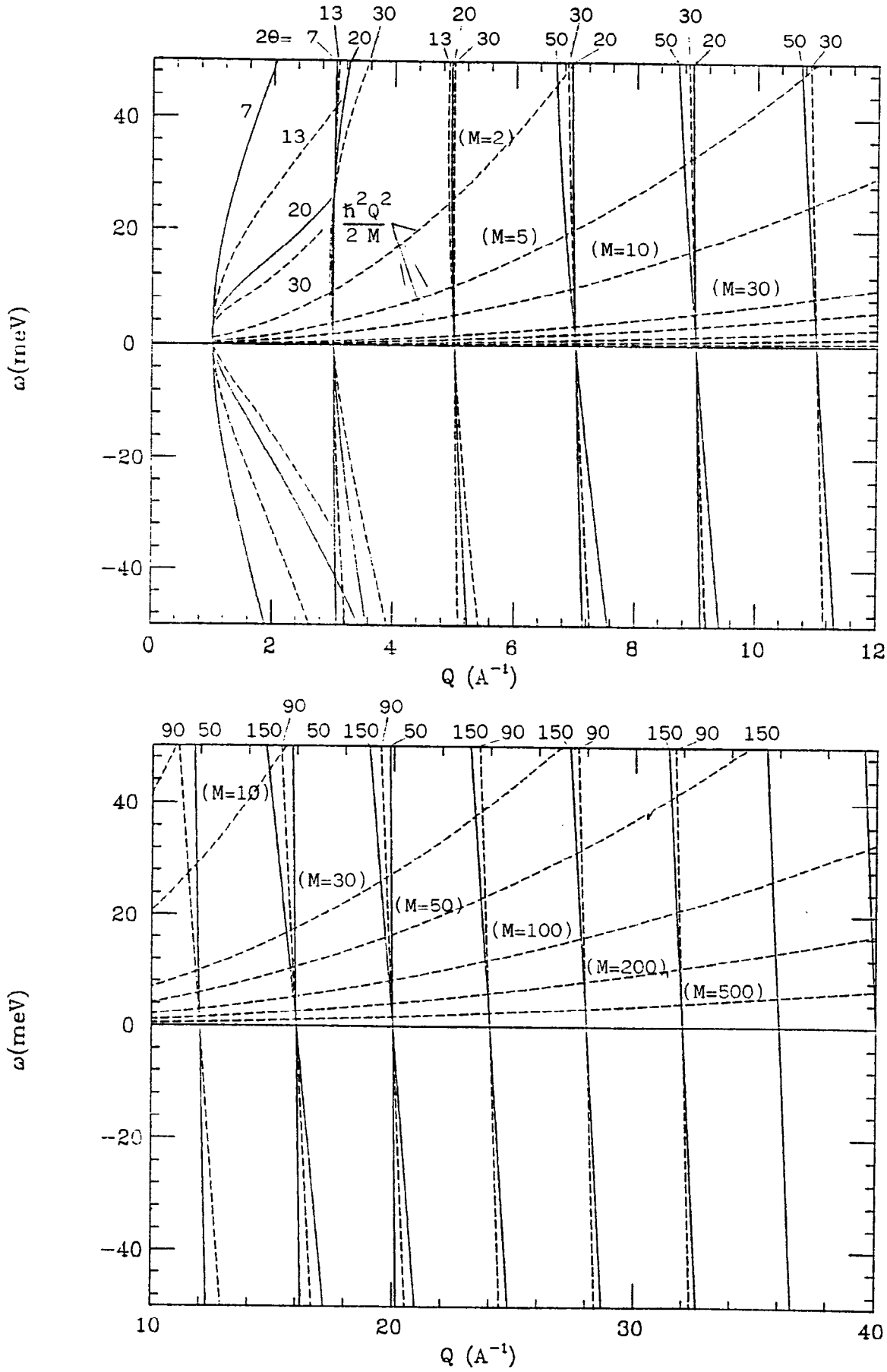

Fig. 5. Instrumental integration paths of the HIT. Curves of recoil energy $\hbar^2Q^2/2M$ for various M's are also shown.

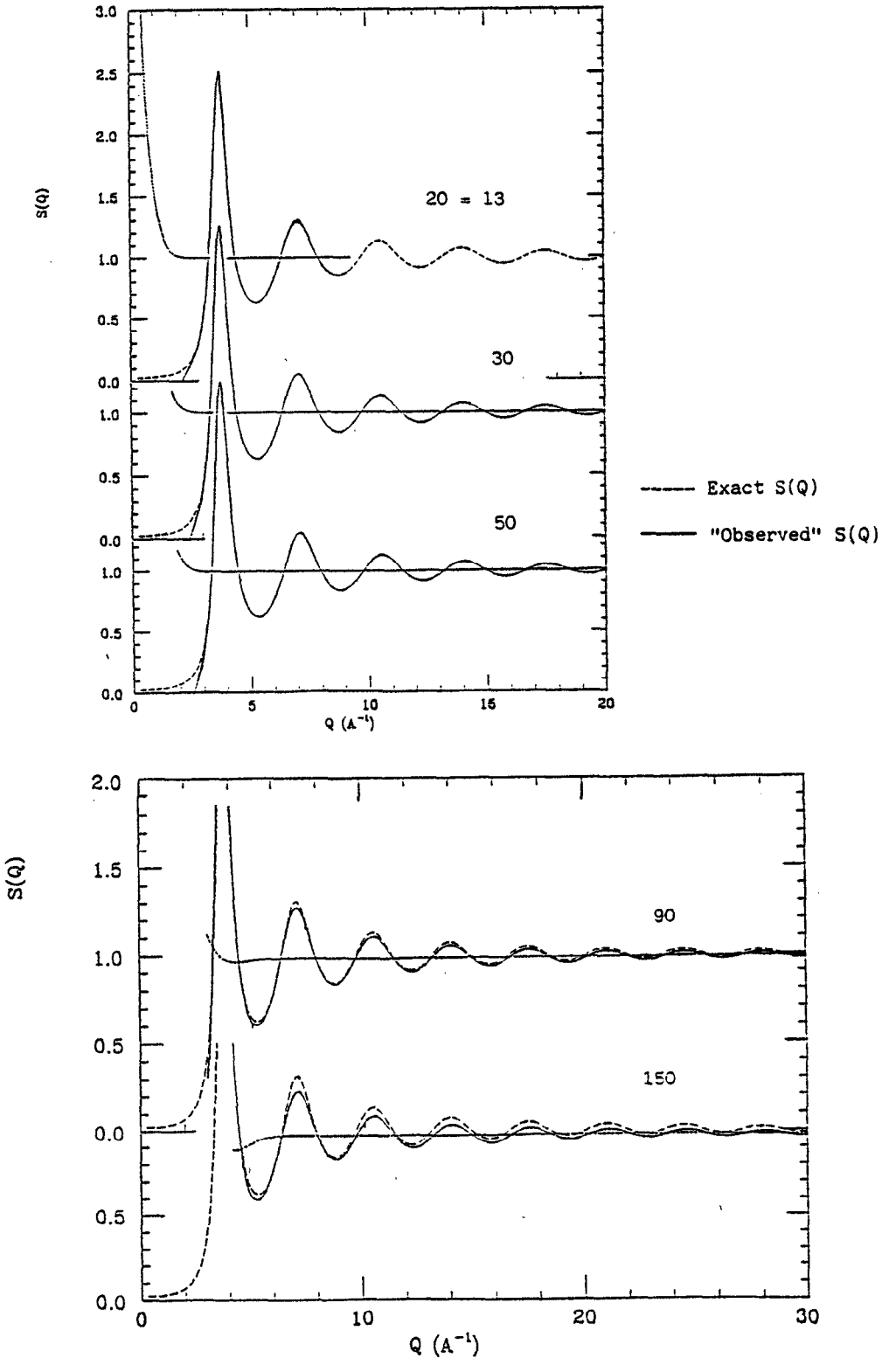

Fig. 6. The comparison of S(Q)'s simulated for heavy nuclei (M/m = 100, M^*/m = 200, solid curves) and exact ones (broken curves).

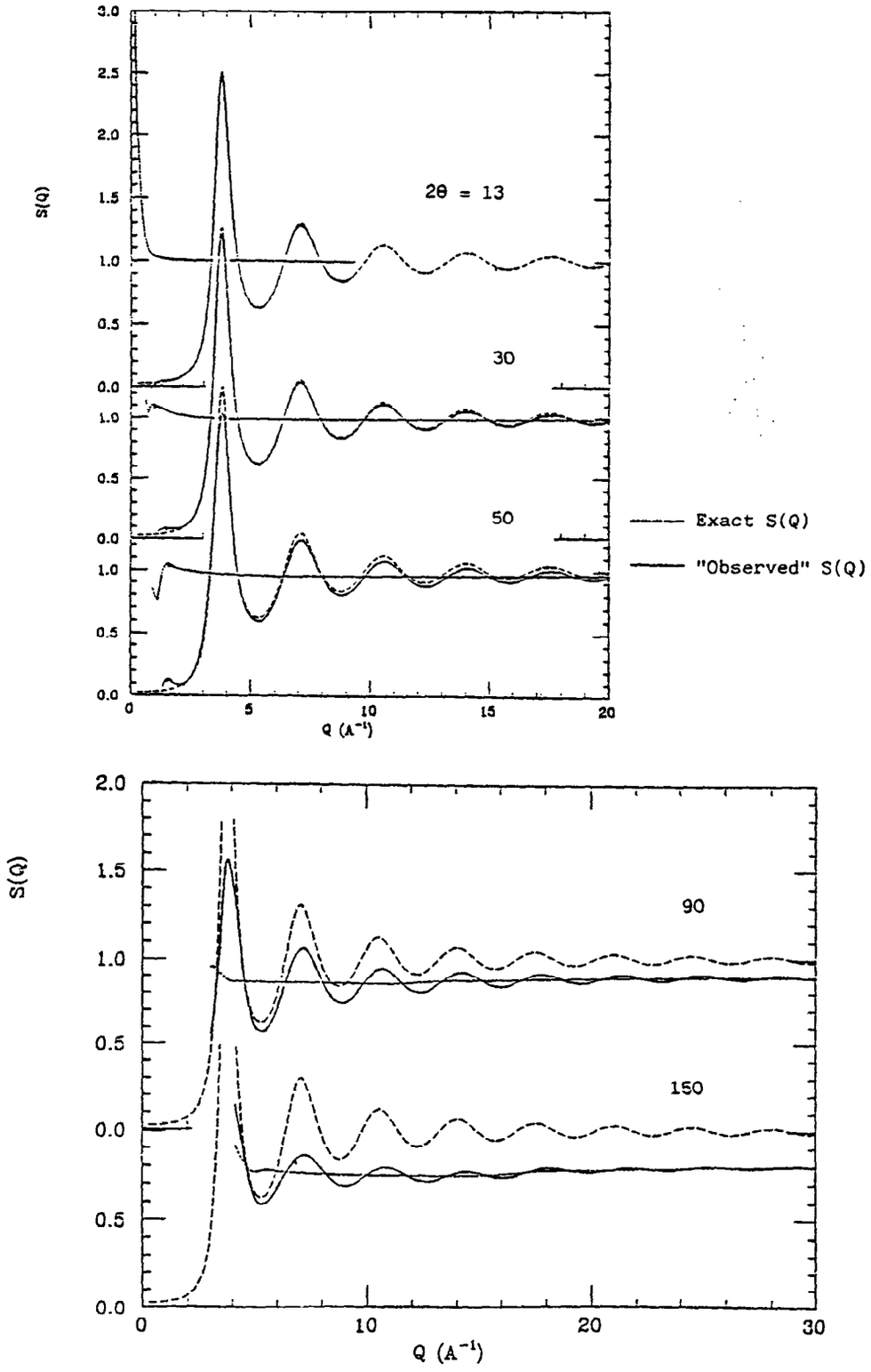

Fig. 7. The comparison of S(Q)'s simulated for light nuclei ($M/m = 11$, $M^*/m = 27$, solid curves) and exact ones (broken curves).

ICANS IX

INTERNATIONAL COLLABORATION ON ADVANCED NEUTRON SOURCES

22-26 September, 1986

SUMMARY OF THE WORKSHOP ON BOOSTERS AND NEW CONCEPTS.

ALAN CARNE

Our session was yesterday morning. We had three contributions on Boosters and New Concepts, and although there were only three contributions, there was plenty of discussion during and after and we easily filled the time available. We had two contributions on boosters, one from Jack Carpenter on the IPNS booster target and one from Dave Picton on the possibilities of enriching Target-I for ISIS, and then some discussion on these two papers. Finally, Walter Fischer presented a description of the ASTOR project.

The first paper was a very comprehensive review of progress on the IPNS enriched uranium booster target. Its basic design requirement was to fit within the existing space and to match the available cooling power of about 100 kW from the cooling system. The reason why they are interested in a booster is because of the limited proton intensity from the IPNS synchrotron (about 20 μA). This limit of a fairly low intensity is an important point in the philosophy of the design of boosters.

The basic operational parameters are: a K_{eff} of 0.8, a power gain of about 7 (which brings the total power to about 90 kW), the neutron production is increased by a factor of about 5 on the existing depleted uranium target and the moderator flux (the thing that really matters) is increased by a factor 3. The water cooling system provides 90 US galls/min and the target centre line temperature is $527°F$ ($275°C$), which is quite modest and a very good number to have. Those characteristics are calculated on the assumption of 500 MeV, 20 μA and a 3 cm FWHM beam spot. It turns out that they have, apparently, about a 30% tolerance on their available cooling capability. That sounds rather low to me, but, in fact, there are built-in tolerances and so it's not too bad. The target itself is uniformly

enriched, with half inch disks at the front increasing to one inch at the back (as the energy deposition falls off). Short pulses are, of course, required and obtained by using a cylindrical decoupler (of boron) with a cut-off energy of about 100 eV; it's obtained by using a very interesting B-Cu composite.

As part of the complete and rather detailed survey of the performance of the target, some thermal-hydraulic stress analyses were done. The second disk from the front is the most highly stressed. Nevertheless, the fatigue life on the cladding (assuming 10 cycles per day) is about 27 years, which is rather comforting. In fact what rather more impressed me was the expectation of only 10 cycles per day of gross temperature changes; that sounds quite a good accelerator!

There was some heat transient analysis shown, where the classic accident scenario - you lose the coolant on the target and you ask yourself what happens - was examined. The target temperature rises to about 980°C after 5400 secs (ie still about two hundred degrees below the melting point of uranium) so basically, the target is safe as far as the outside world is concerned. That is a very important point. Activation was also considered; the worst case releases were still about 2% within the US guidelines, so again it sounds quite good. A number of safety studies were done which considered several possible configurations of the assembly; in all cases K_{eff} did not exceed about 0.93. We are told that K_{eff} about 0.95 is the value where the safety people really become very concerned. So it all sounded very encouraging and things are going quite well.

But we discovered there was a little dark cloud. That is, due to the casting process that was done by ORNL, the uranium shows texture (large grains and an anisotropic distribution). What one would like is small grains in a random orientation, because of the problem of radiation growth. Now, with the grain sizes that were found, predictions were made of target lifetime of somewhere between 1.3 and 2.1 years; the two numbers depend on whether one considers shrinkage in the radial direction, because of the preferred orientation of the grains, or axial growth. ANL would like 5 years. But those are the predicted numbers; there are some things which can be said about them which could be comforting but are not quantitative.

The target is expected to increase the thermal neutron current by about a factor of 3 to the experiments. Clearly because it is a heavily enriched target, there is a problem due to increased background from delayed neu-

trons and the delayed neutron fraction increases to about 3%. We heard from Kent Crawford, in another session, about the experimental steps that can be taken; but on the whole, the folk at Argonne must learn how to handle this increased background and then we will find out how serious it is.

We heard one or two things about the licensing and security; not too many, because, as the paper itself states, "Security" will not tell you too much about security. Jack painted a picture of armed guards, moats and alligators (it would be really quite pretty to have that around the Rutherford lab. as well).

Some other numbers have impressed me, considering the amount of effort which has gone in so far. I think over the last 3 years (when things have been done in earnest) a total of about 30 man-years effort has gone into designing and building the target. And the cost is 1.5M$. *[A comment was made by J Carpenter that the 30 man-years is somewhat an overestimate. He had 10 people working, but only part time, for a period of about 3 years.]* The target should be in by the end of 1986; it depends on how things go with the textured uranium. I think we should all like to say Good Luck to Argonne in this task. We at ISIS and at LANSCE will be watching you and are very concerned to see how well it goes as we have a great deal to learn from you.

The next paper was by Dave Picton, on some of the possibilities of enriching the ISIS Target-I. There are again similar types of constraints as at IPNS. That is, we have to satisfy still the basic shape of the target assembly and the power density (about 0.75 kW/cc). In fact, that limiting power density doesn't give much scope for uniform enrichment, because we are already at this peak value at the front of the target. There are three options: one is axial enrichment only, second to combine that with annular enrichment and third, to turn cicular plates into rectangular ones which could be variably enriched in either direction. The variations with the cylindrical target were all done at 9 cm, which is the present target material diameter. For the slab type target, a 10 by 20 cm^2 slab was considered. In all cases a homogeneous mixture of target material and coolant was used. One of the main aims was to flatten the power distribution, because we are near the acceptable peak power density at the front end of the target already.

We were presented with a large number of graphs, but I will do my best to reduce them to a small number of results. The first case was for an axially enriched target where a "semi-practical" distribution of enrichment in four 7.5 cm long zones was used; zero for the front quarter, second quarter 20%, then 50%, then 90%. The gain was quite small, a little more than unity for the front and a little more than two at the back end. The corresponding slab type target gives a similar gain for about half the enrichment. In some ways that would be a step forward, but in either case they are rather complicated devices, technically difficult to realise.

Another possibility was to vary the enrichment in both directions, axially and radially, and allow the power to go up to the maximum sensible available on the present target system of about 1.5 MW. Again, gains were a little greater than one at the front end and a little more than two at the back. An interesting and rather surprising result shown was that, in this assembly (which was "semi-realistic" and included decoupler, Be-reflector and D_2O coolant), the gain in thermal neutron current from the moderators was almost identical to the gain in fast neutron production. This is because in our case the Be-reflector is a moderating reflector and softens the spectrum of the neutrons reflected into the moderators.

There was a developing theme in the discussion associated with both presentations and which came through strongly during the second, that already even at relatively modest intensities, as for IPNS and the still modest intensity of ISIS, the users are becoming very concerned about backgrounds. Background is dominating discussions, as we have heard in all today's summaries. Put this into target terms: if the beam intensity is very low, then it's worth having a booster (as the Argonne have done) and because the proton beam intensity is low there is plenty of technical scope to do so and actually improve the thermal neutron current. However you do get a penalty of increased background. We heard from ANL, that there are things we might do and things we might do experimentally, but one still has to learn how to handle the increased background. If, however, the proton intensity is high, so already you are using a large fraction of the available technical limit on the target power density and heat flux (within the target itself), then the gains available by enriching the target are small. The gains must be measured against the technical complexity and of course the penalty of increased backgrounds. So it really does divide those things

up and is leading to us to, we hope, clear conclusions about the way ISIS should go.

The last presentation was from Walter Fischer, on ASTOR. This is an accelerator and storage ring, an SIN "update". The reference design is for an energy of 2.2 GeV with a mean current of about 300 μA. It is based on the isochronous cyclotron so that one might well achieve a beam loss of 0.1% (which he called a conservative design but clearly at these energies and intensities is a very necessary design criterion if a difficult thing to achieve). The motivation for this work is essentially particle physics - especially neutrino studies - but clearly it's a potential neutron source (and I was going to say good neutron source but that may not be a properly qualified expression!). It has a high pulse repetition frequency (of about 2 kHz) with a pulse length of 150 to 300 nsec. It is possible to reduce the repetition frequency but the mean current goes down at the same time. Because of this high repetition rate, it is a system that would be good for the high epithermal region, 3 to 10 to 50 eV. There is scope for eV spectroscopy but, one must find good science against competition from synchrotron light sources, for example. Questions were asked about moderators and the possibilities of metal hydrides were recalled, which we at ISIS had looked at in the past but had discarded. Decouplers for high epithermal energies will be a problem, because the intent would be to take out the complete thermal part of the neutron spectrum. There were remarks that the spectrometers will be hard and we got back to the question of background.

We are always back to the problem of background these days!

ICANS IX

INTERNATIONAL COLLABORATION ON ADVANCED NEUTRON SOURCES

22-26 September, 1986

PROGRESS ON THE IPNS ENRICHED URANIUM BOOSTER TARGET*

A. E. Knox, J. M. Carpenter, J. L. Bailey,

R. J. Armani, R. N. Blomquist, B. S. Brown,

D. R. Henley, A. G. Hins, B. A. Loomis,

A. W. Schulke and H. R. Thresh

Argonne National Laboratory
Argonne, Illinois 60439 USA

ABSTRACT

We describe the Enriched Uranium Booster Target designed for use in Argonne's Intense Pulsed Neutron Source. This report contains a general description of the system, and descriptions of the thermal-hydraulic and loss-of-coolant accident analyses, of the neutronic, criticality and power density calculations, of the assessment of radiation and thermal cycling growth, and of the disk fabrication methods. We also describe the calculations of radionuclide buildup and the related hazards analysis and our calculations of the temperature and stress profiles in the disks, and briefly allude to considerations of security and safeguards.

I. Introduction

The purpose of the Enriched Uranium Booster Target (the "Booster") is to increase the intensity of the neutron beams from IPNS. Conceived in 1980, the design project began in earnest three years ago. We took the design-limiting constraints to be the maximum power (about 100. kW) that could be dissipated by the existing cooling system without major modification and with the maximum-envisionable current delivered by the Rapid Cycling Synchrotron, and the space restrictions of the existing moderator, reflector, target-

*Work supported by the U.S. Department of Energy

handling and beam port arrangements, consistent with safety and security requirements. We described our progress up to about a year ago in an earlier report.[1]

The final design consists of a set of Zircaloy-2-clad, 77.5% ^{235}U enriched alloy disks of the same constitution as the present, depleted-Uranium target,[1] cooled by H_2O, and decoupled from the immediate surroundings by a layer of newly-developed ^{10}Boron-Copper composite material to provide a short prompt-neutron generation time and thus preserve a short response time. The value of k_{eff} is .80 for this target in its operating surroundings. The heat to be dissipated is about 83.kW for a 20.μA, 500. MeV beam, the maximum proton beam power envisionable. (With the present target, the thermal power is about 10. kW for a 15 μA, 450 MeV beam.) The expected gain in neutron beam intensity for the same proton beam conditions is a factor of about 3 (not $1/(1 - k_{eff}) = 5.$, because the proton-induced source neutrons are not all distributed in the $k_{eff} = .80$ mode and because the target-moderator coupling differs in the Booster case from the present case; furthermore because the depleted uranium target has a significant gain, $1/(1 - k_{eff}) \simeq 1.1$). We expect that the fraction of neutrons which appear delayed will increase significantly from its present value of about 0.0044, to about 0.03, and are devising both hardware and software measures to cope with this in the instruments in which the increase is found significant. We further expect to have to make some local modifications to the main shielding and that of some of the scattering instruments. We have already installed two flowing liquid CH_4 moderators, operating at about 100.°K, that we believe will be suitable for the higher power target; we are constructing a new grooved, solid CH_4 moderator of improved design, for installation with the Booster.

Because the power density distribution is much broader in the multiplying booster target than in the depleted uranium target, disks need not be much thinner than those in the present target in spite of the much larger total power. We need 1/2-inch thick disks only in the front section of the target; the remainder are 1" thick. 304 stainless steel flow guides maintain 0.060" thick channels between disks for cooling. Eight disks chosen so as to provide the maximum amount of diagnostic information, contain a centered, stainless-steel-clad thermocouple located in a 1/16" diameter, Zircaloy-2 thermowell. The assembly of disks, compressed by concentric Inconel springs, rests in a welded vessel of 304 stainless steel. Flexible, corrugated, steel-braid-sheathed, stainless steel tubes carry cooling water to and from the target.

Alloying, casting, machining and Hot Isostatic Pressure bonding of the target disks has been done under contract at the Oak Ridge Y-12 facility, using processes similar to those developed at Argonne for producing the present depleted Uranium target disks. Differences in the casting processes have led to a somewhat-less-desirable metallurgical state of the Booster uranium, than that of the material of the present target. Figure 1 shows the Booster target located in the moderator/reflector assembly.

The cooling system is essentially the same as has been in use with the present target; we have joined the two identical systems, each of which previously cooled one of the two targets (the Radiation Effects Target, no longer used but still available, and the Neutron Scattering Target), for parallel, simultaneous operation to cool the Booster. To provide for removal of the substantial fission product decay heat in the event of loss of the primary cooling system, we have installed a low-capacity backup cooling system operated from two battery-supplied uninterruptable power sources. Other minor modifications have made it possible to backfit for D_2O cooling if we find it necessary to shorten the Booster response time. As previously, the cooling systems lie in sealed, Helium-filled tanks, vented to the facility exhaust, which is continuously monitored for radiation. Each circuit contains filters, heat exchangers, surge tanks, ion exchangers, flow and gross gamma radiation monitors as earlier. There is one fission product monitor. During operation, we will periodically remove cooling water, demineralizer resin and surge tank gas samples to monitor for abnormal radioactivity. This remains our method for sensing clad integrity and provides a criterion for continued target operation.

We have installed a somewhat upgraded system of instrumentation, controls and interlocks for use with the Booster. Figure 2 schematically shows the Booster Target cooling system.

We do not expect clad failure due to fatigue under cyclic thermal stress to limit the life of the target. Somewhat greater metallurgical texture in the Booster target material than in that of the present target, combined with greater burnup, will lead to somewhat anisotropic dimensional changes in the disks--at the time of writing we are assessing these effects, which we now believe will limit the target service lifetime to about five years.

The total costs (engineering and supporting studies, process development, fabrication and installation) amount to $1.5 M. We have used a computer-based PERT system to plan and control the project. Installation and first operation are expected in Fall of 1986. We have recorded slow neutron beam spectra from the moderators under what we hope will be reproducible

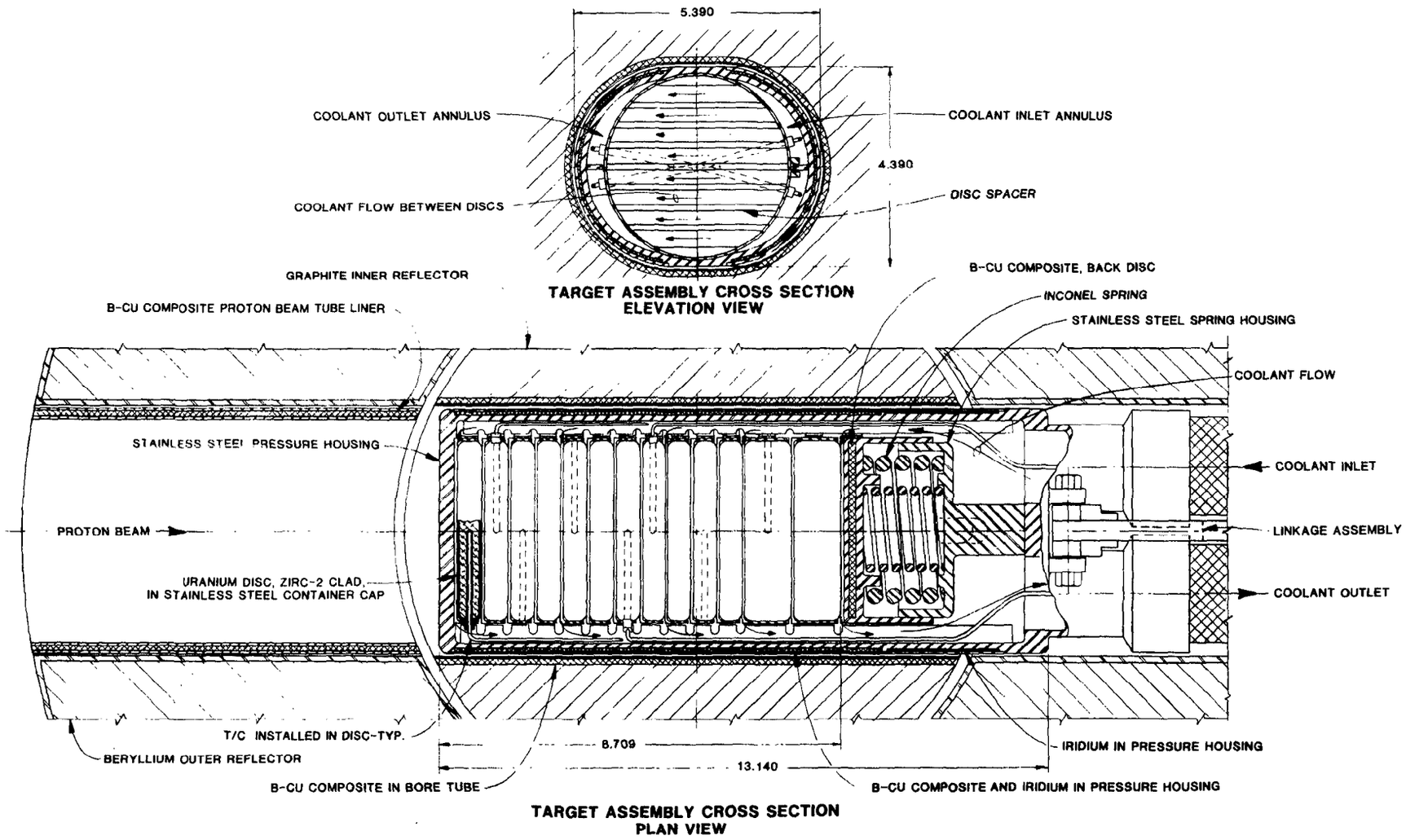

Fig. 1 Booster Target Installed in Moderator/Reflector Assembly

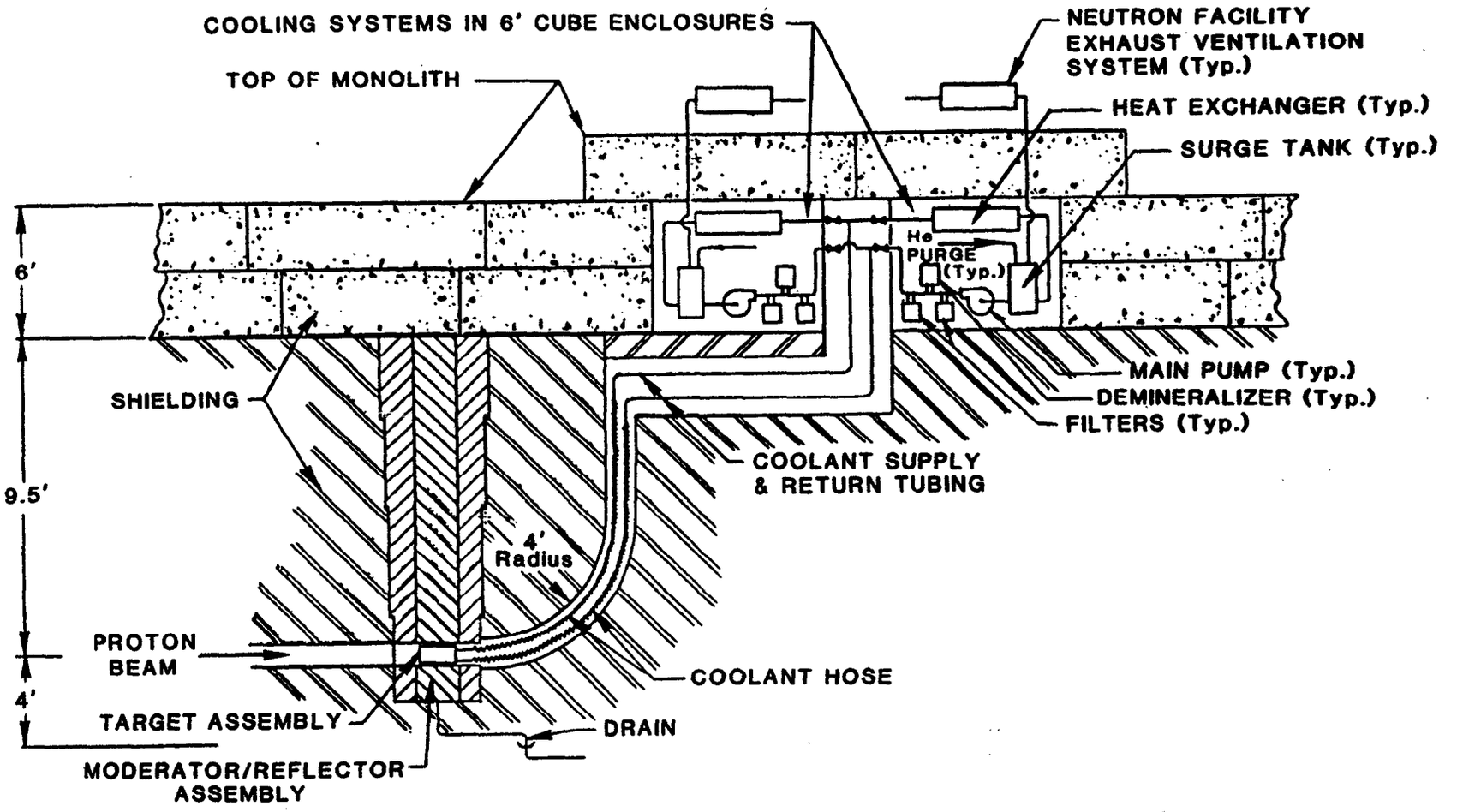

Fig. 2 Cross Section Elevation Through IPNS Facility

conditions prior to the end of operation of the present target, in preparation for relative intensity measurements after Booster installation.

II. Thermal-Hydraulic Analysis

Cooling System

The increased power in the Booster target requires twice the coolant flow of that in the present target; modifying the two existing, independent systems (Neutron Scattering Target and Radiation Effects Target) for parallel operation provides the required coolant flow. On the basis of field tests of a single system, we have developed a computer model[2] of the hydraulic behavior of the cooling system, with which we calculate the relationship between pressure differential and flow rate, the "performance curve", of the combined systems at the tee connections to the Booster target. Figure 3 shows this Cooling System Supply curve, which we have used in the course of hydraulic analysis to describe the interface between the cooling system and the target itself.

Field measurements have also provided the heat removal capacity of the existing heat exchangers; these tests indicate that the two heat exchangers together are adequate for the increased heat load of the Booster target. Table 1 gives the operating parameters of the cooling system.

Table 1

Operating Parameters of the Cooling System

Coolant	H_2O
Minimum coolant flow rate	90. gpm
Maximum coolant supply temperature	120. °F
Temperature Differential	6.5°F
Pressure Differential	18. psi

Booster Target Analysis

Coolant flows to and from the target through pipe connections made at the back (opposite the proton entry) end of the target (see Figure 1). Channeling in the back of the target housing directs flow to the inlet plenum and from the outlet plenum, which constitute the space between the round target disk caps and the elliptical vessel. When the disks and caps are assembled in the housing (they are compressed by coil springs located in the back of the vessel) slots in the face of each cap form parallel flow ducts

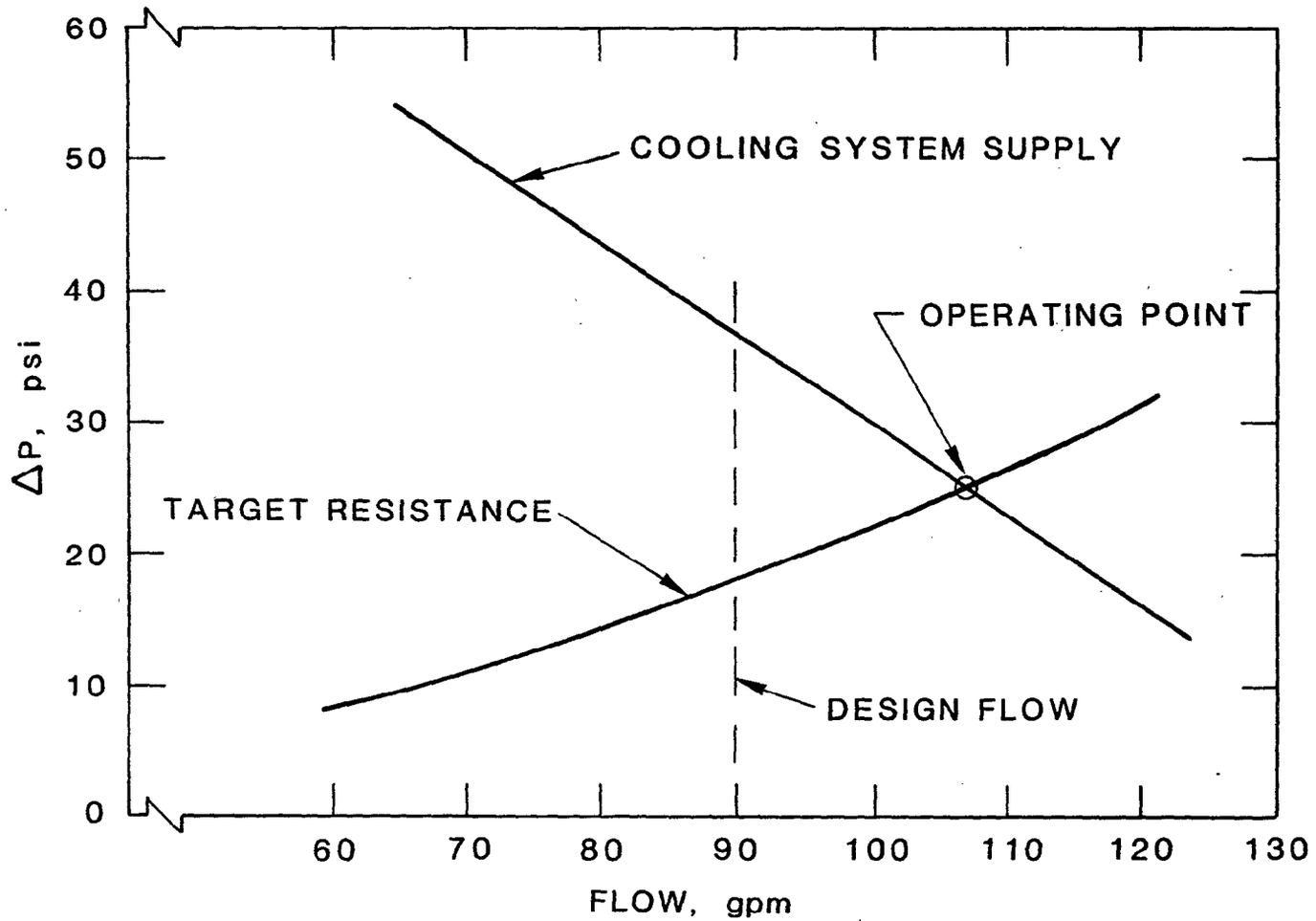

Fig. 3 Hydraulic Performance Curves for the Two Cooling Systems Operating in Parallel

connecting the inlet and outlet plenums. Forced convection in these ducts cools the faces of the disks. An accurate small-clearance fit between the caps and radial arcs machined in the housing walls prevents short circuiting of coolant past the caps.

The assembled target has 13 target disks and 14 flow channels. The front seven channels are full flow channels, and comprise three main slots and two cirumferential leakage paths; the seven channels in the back carry reduced flow on account of the lower local power density, and comprise eight main flow paths and two leakage paths.

A study by the general systems code SALT, using the Darcy equation with Kármán-Nikuradse friction factors and Crane's[3] entrance and exit loss coefficients to calculate pressure drops, has determined the pressure drops and the velocity and pressure profiles in the assembly, its associated hoses and piping up to the tee connections. Figure 4 schematically represents the computer model of the target. Using these results and the performance curve of the cooling system, we have developed a superimposed curve of the supply and resistance pressure differentials vs. flow rate. The performance curves indicate that at 90 gpm total flow rate, the two pumps operating in parallel produce a head well in excess of what is required (approximately 13 psi). A new control valve, located in the target return line, will be used to throttle the flow (see Figure 2). This analysis provides the flow conditions (velocities, Reynolds numbers, pressure drops) for each disk and channel, for the following cases:

a) Two main pumps running (normal operation)
b) Broken springs (abnormal)
c) Total flow rates 5 to 150 gpm (parametric study for developing performance curves).

The notes on Figures 4 and 5 (below) correspond to the flow conditions for the normal operating case.

Flow rates from these calculations, used in conjunction with the Dittus-Boelter correlation, provide convective coefficients which are used in turn as input for the calculation of the temperature profiles in the disks.

III. Disk Temperatures and Stresses

We have modeled disks of both one inch thickness and one-half inch thickness using the finite element computer code ANSYS. The HETC/VIM Monte Carlo code provides internal heat generation rates, which for these purposes we take to be at the upper 3σ limit computed for 500 MeV, 20 μA, 3.0 cm fwhm diameter proton beam conditions (the maximum operating case). A curve

FIGURE 4

HYDRAULIC COMPUTER MODEL FOR THE BOOSTER TARGET

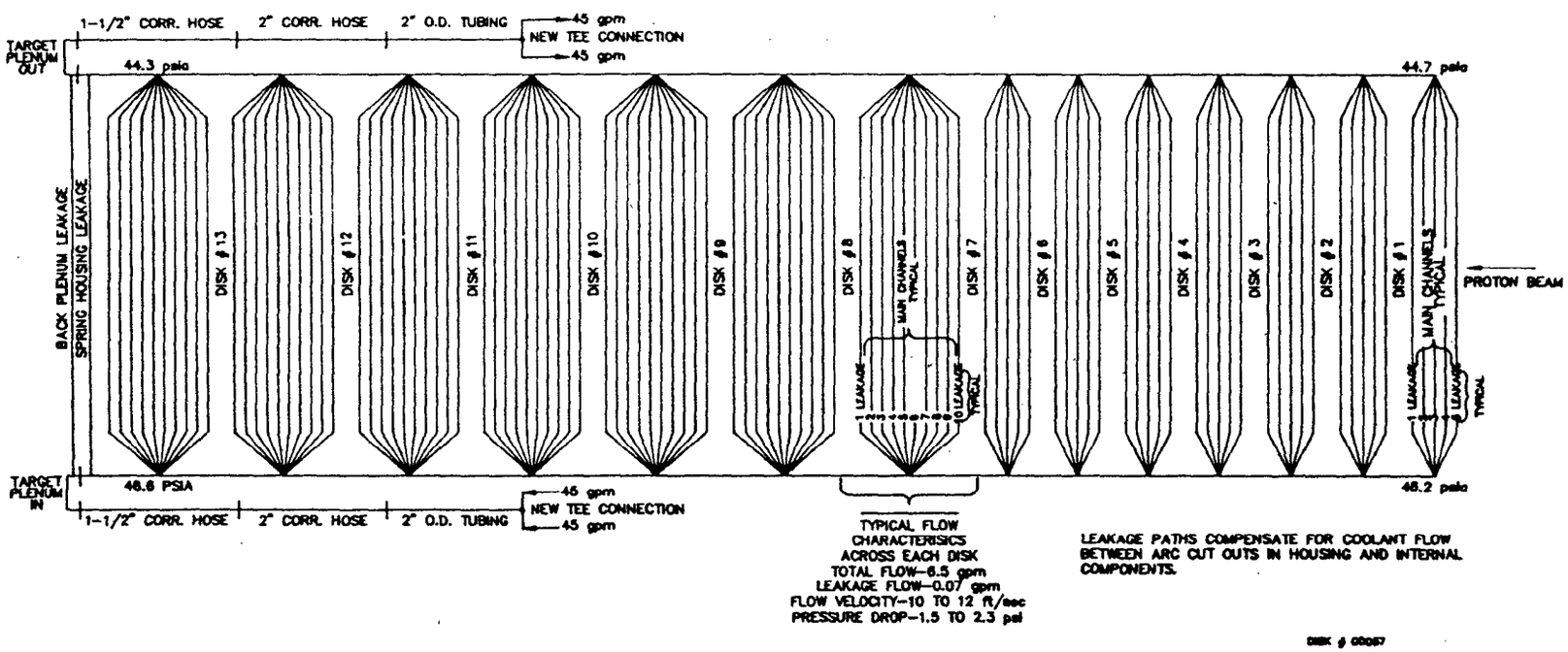

Fig. 4 Hydraulic Model for IPNS Booster Target

fitting routine smoothes the radial power density profile, which we assume has an underlying functional form

$$P(r) = P_o/(1. + ar^2 + br^4),$$

from the Monte Carlo data, binned into four radial bins, and provides data in thirty-eight radial bins for the ANSYS code. We assume the axial power density distribution to be uniform within each one-half inch thick disk, and uniform within each of the two one-half inch regions of each one inch thick disk. The hydraulic analysis provides convective boundary conditions at the disk faces, where we assume for the convective coefficient an area-weighted average over the entire disk face. We assume that the disk circumferences are insulated.

We have calculated the temperatures and stresses in disks #2, #3, #4, #7, #8 and #12 for the maximum operating case. Figure 5 summarizes the results, showing the center temperatures (maximum uranium temperatures) and clad surface centerline temperatures (maximum surface temperature in the flow channels). The highest temperatures both in the uranium (527 °F) and on the surface (248 °F) occur in disk #2; therefore that disk has been used in detailed studies of the off-normal and parametric studies. The hydraulic analysis has determined that the minimum saturation temperature in the flow channels is 267 °F; this provides a heat flux margin of 13% against nucleate surface boiling in the channels. Figure 6 shows the temperature distribution in disk #2. This distribution is the basis for the thermal stress analysis described below.

The thermal analysis for the broken springs case uses the convective coefficients calculated from the hydraulic analysis for that condition. We calculate temperatures for two cases of blocked channels; with the central flow path blocked and with both outer flow paths blocked. Results from these cases indicate that some clad damage may occur under these off-normal conditions, but that no significant safety issues arise.

We have studied the effect of a nonbonded cladding region by calculating temperature distributions for several different sizes of circular insulated areas centered on the face of the disk, and the insulating effect of the spacer by calculating the temperature distribution for an insulated circular region the same width as the spacer strip. Results of these calculations indicate that nonbonds of 1/8 inch diameter and smaller and the 1/8 inch wide spacer strips, have little effect on the temperature distribution in the target disks.

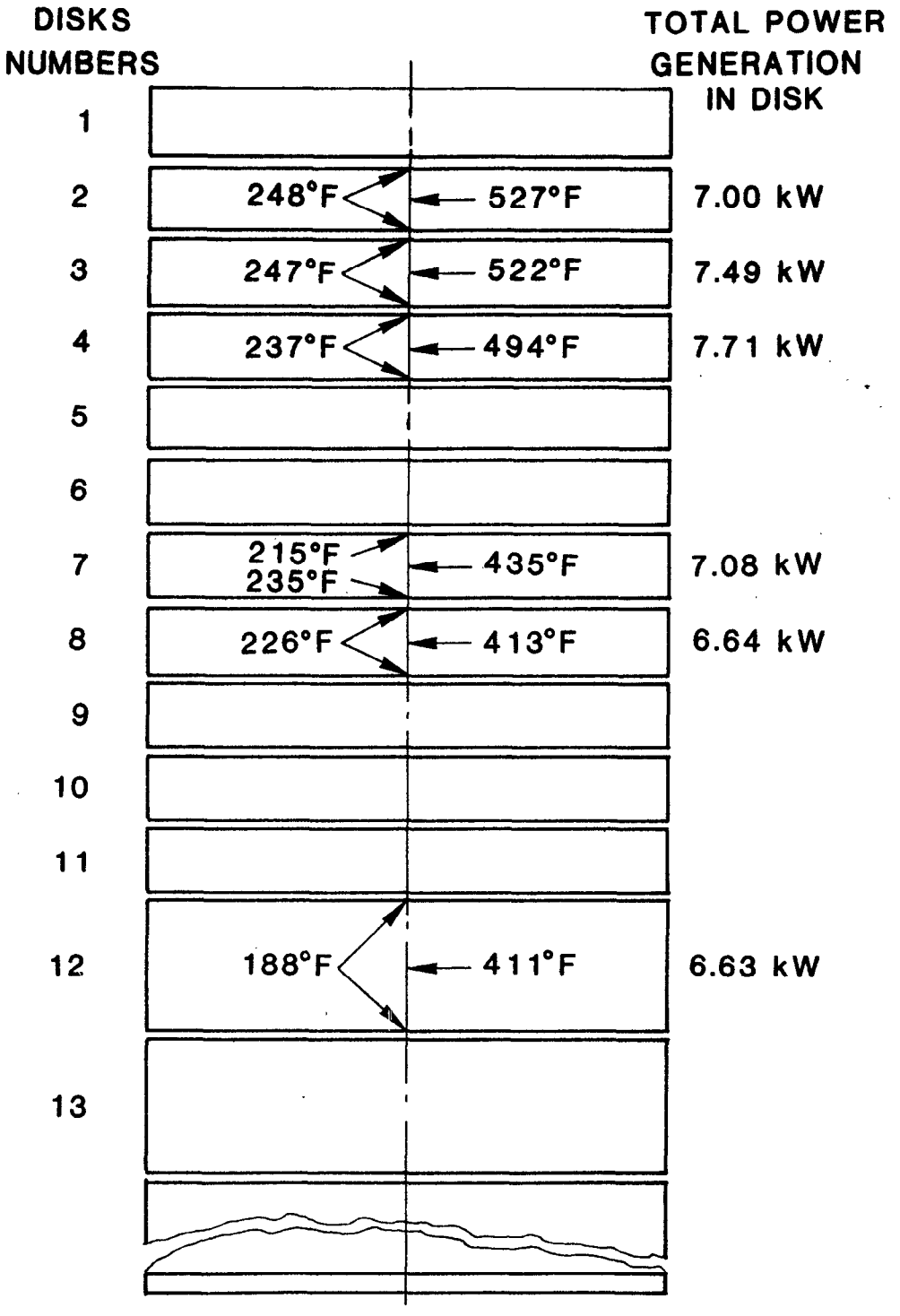

Fig. 5 Maximum Surface and Internal Disk Temperatures at 500 MeV, 20 μA, 3.0 cm fwhm, Operation

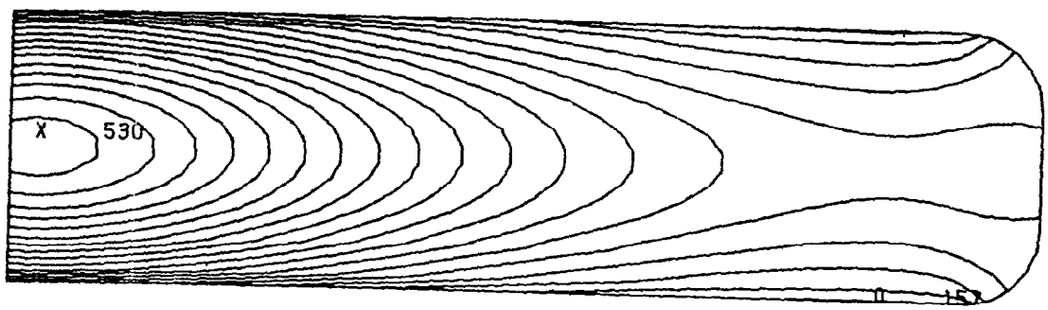

Fig. 6 Temperature Distribution for the #2 Disk at 500 MeV, 20 μA, 3.0 cm fwhm Operation

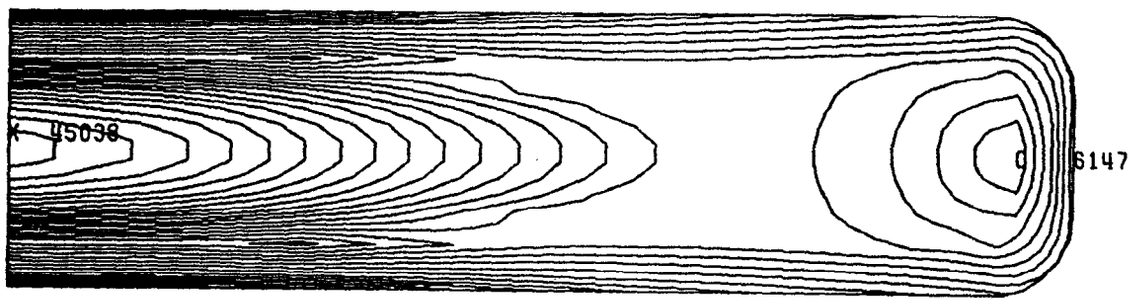

Fig. 7 Stress Intensity Distribution for the #2 Disk at 500 MeV, 20 μA 3.0 cm fwhm Operation

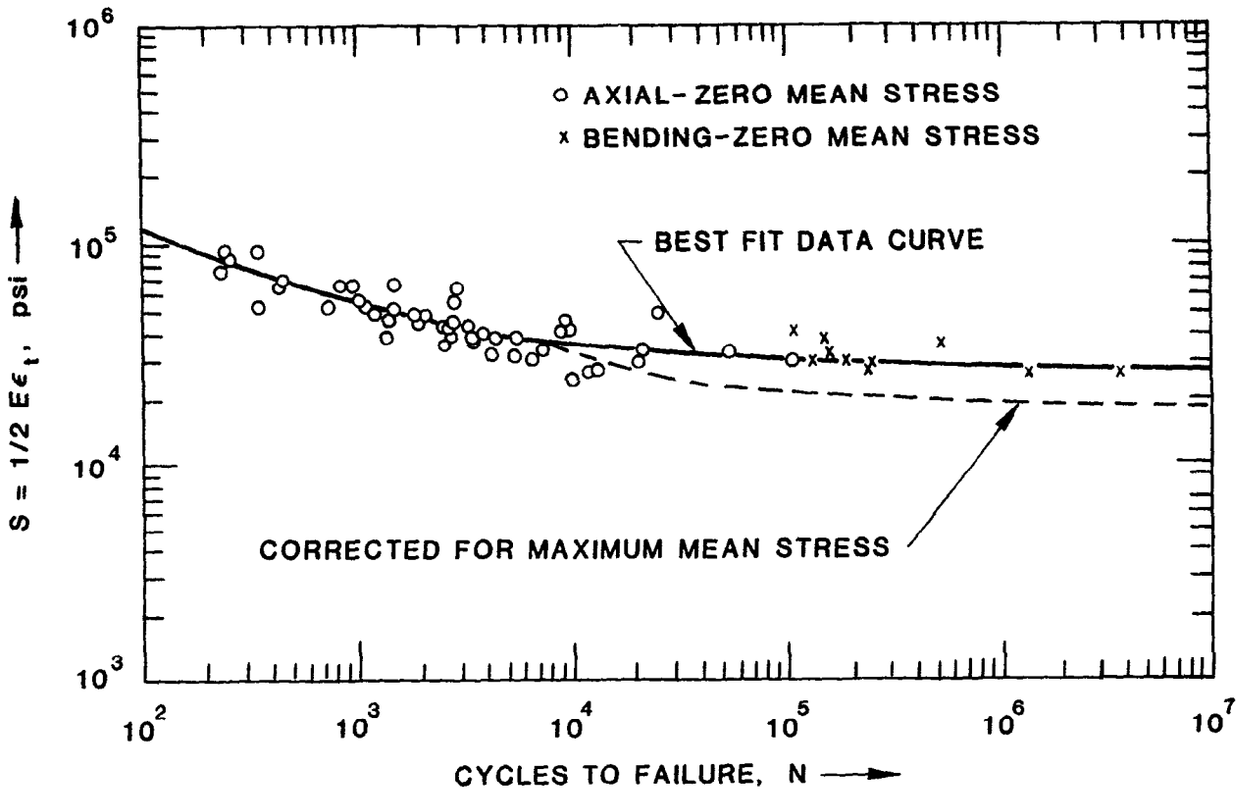

Fig. 8 Irradiated (1.5×10^{21} to 5.5×10^{21} nvt) Zircaloy Fatigue Data Curve - Room Temperature to 600F. Data from reference 8.

We have developed two models to study conditions under normal and off-normal conditions. Figure 9 shows both the 1/4-round and the 1/2-round models. We have studied the following cases:

a) Coolant flow requirements under beam shutdown conditions (used to decide the size of decay heat removal pumps) - normal.
   Result: 2 gpm flow is required to prevent damage to target disks.

b) Decay time required before cooling can be stopped (used to determine requirements for safe removal and storage of the irradiated target) - normal.
   Result: 45 days of cooling are required to prevent damage to target disks.

c) Stoppage of primary flow with proton beam off (used to determine the length of time before cooling must be provided) - off normal.
   Result: A minimum of 11 hours are available until damage occurs to the target disks.

d) Total loss of coolant (used to determine whether autocatalytic ignition of Zircaloy cladding occurs, and that the temperatures remain below the melting temperature of all materials)- off normal.
   Result: Figure 10 shows the temperatures of various materials as a function of time, assuming infinite prior operation. Some oxidation but no autocatalytic ignition of cladding occurs; no materials melt.

e) Stoppage of secondary flow through heat exchanger (used to determine the length of time before remedial measures must be taken) - off normal.
   Result: After 22 hours, the primary coolant temperature reaches 180 °F, at which temperature cavitation begins in the primary pumps.

V. Radiation and Thermal Cycling Growth

During operation, the Booster target disks will undergo anisotropic dimensional changes that could limit the target lifetime by opening bypass coolant flow paths, closing coolant flow paths, straining the target vessel or cracking cladding. Irradiation-induced growth and thermal cycling growth depend on the grain size and the degree of preferred orientation (texture) of the uranium; we are currently quantifying these characteristics of the material by neutron diffraction methods. Figure 11 compares the neutron diffraction patterns of randomly-oriented uranium and the as-cast Booster target material, from a depleted uranium test casting. Measurements were made at the IPNS Special Environment Powder Diffractometer. Further,

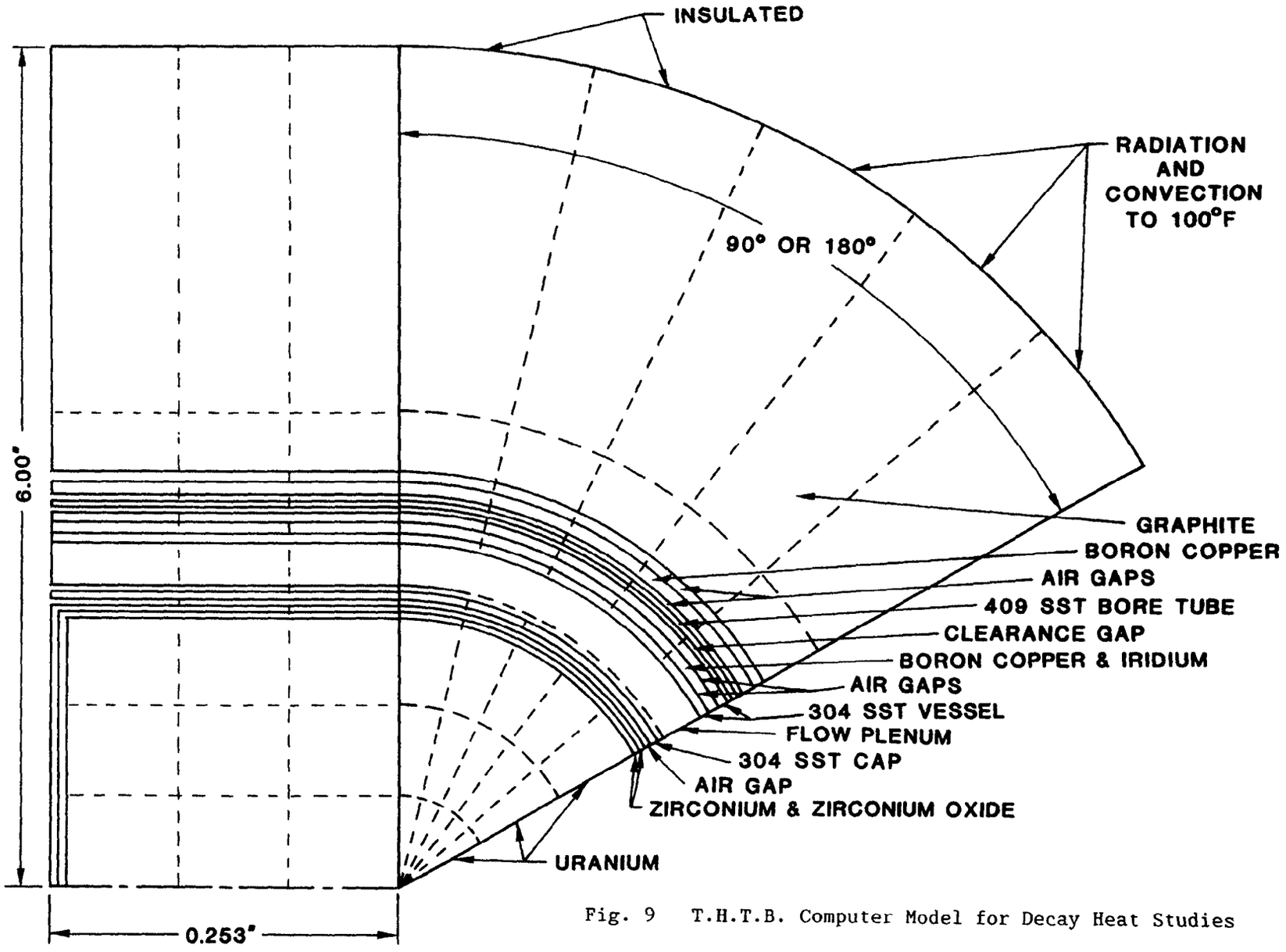

Fig. 9 T.H.T.B. Computer Model for Decay Heat Studies

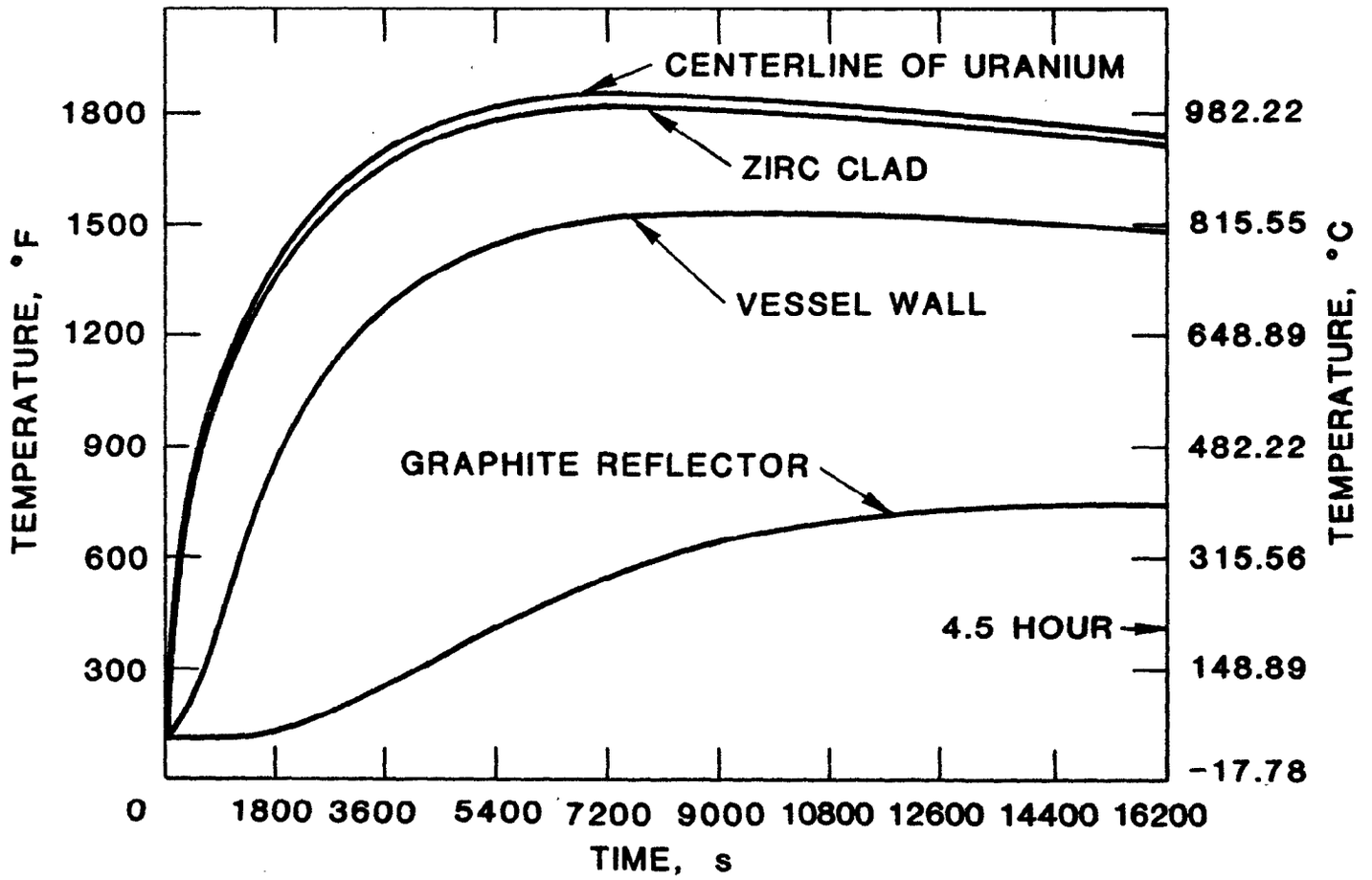

Fig. 10 Thermal Transient for the Loss of Coolant with Decay Heat and Zirconium Oxidation Case

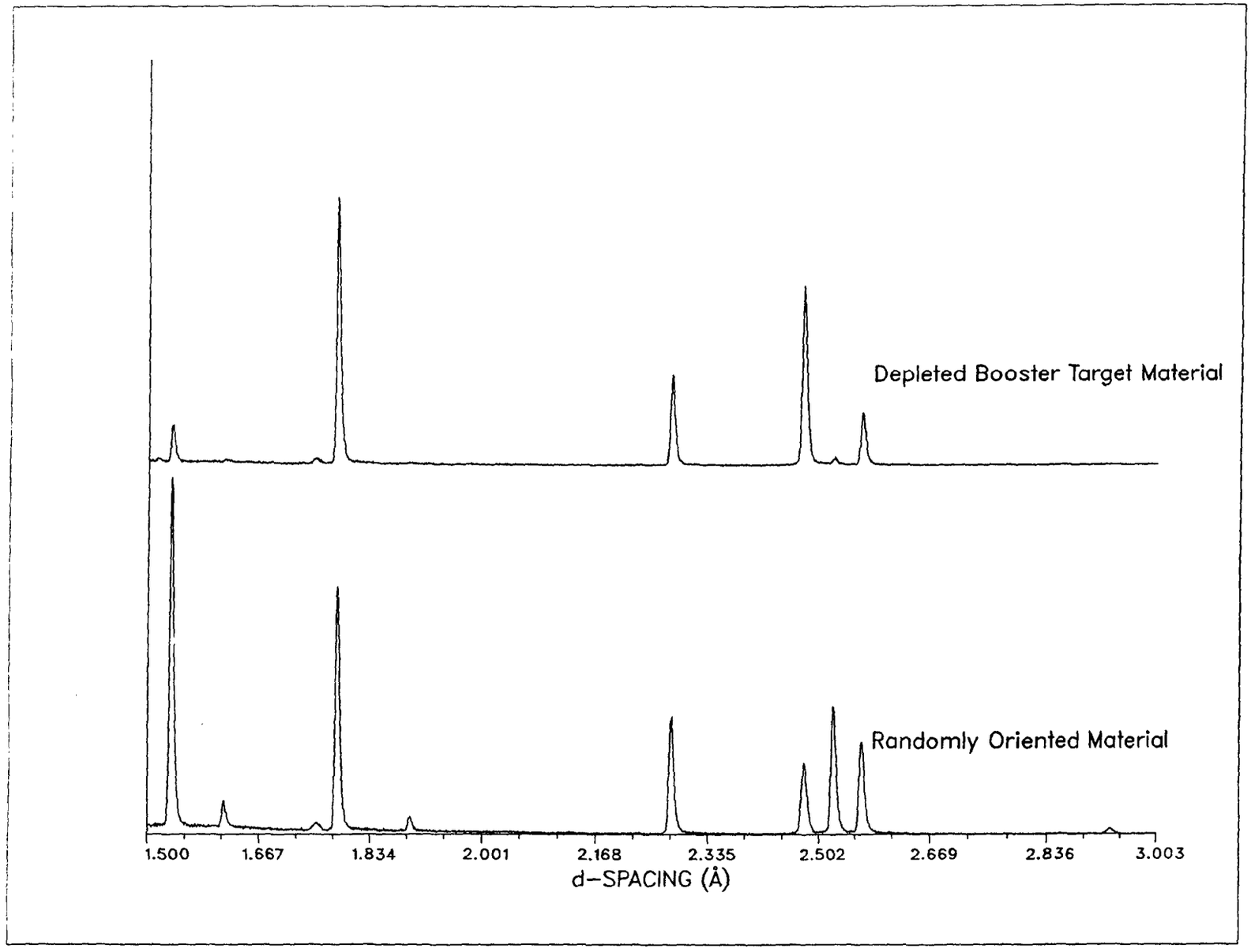

Fig. 11 Neutron powder diffraction patterns of randomly-oriented depleted uranium and of as-cast (depleted) Booster target material.

quantitative texture measurements are being made at the powder diffractometer and the single crystal diffractometer at the Missouri University Research Reactor. Preliminary texture measurements and analyses have shown that irradiated target disks will exhibit a net radial shrinkage and a net axial growth exceeding the volumetric swelling due to solid fission products, gaseous fission products and cavitation.

The volumetric swelling rate is $\Delta V/V = 5.2 \pm 0.06$ %/at% burnup [5,6]; since this swelling is isotropic, the relative length change is $\Delta l/l = 1.7 \pm 0.02$ %/at% burnup. Anisotropic growth takes place without net volume change. For nominal operating conditions, 16 μA, 450 MeV. 3. cm fwhm proton beam diameter, and 26 weeks per year operation, the maximum radially-averaged burnup rate is 0.063 at%/yr, and the maximum central burnup rate is 0.083 at%/yr. The target can accommodate at most 2 % radial shrinkage of the uranium before bypass flows become troublesome, and at most 9 % axial growth before the springs become fully compressed. If anisotropic growth rates were known and included in the calculations of the dimensional changes, the time to exceed these limits can be estimated. For example, if the anisotropic growth rate is $\Delta l/l = 54$%/at.% burnup (current estimate derived from texture measurements[7] on as-cast, HIP treated material, for unalloyed, unrestrained uranium) and the radial shrinkage rate is 27%/at.% burnup, then the lifetime of the target would be about 1.3 years, limited by radial shrinkage. Axial growth limits would be exceeded after 2.1 years. We are considering β-phase heat treatment to reduce the texture of the material and mechanical means to accommodate the growth, meanwhile assessing the accuracy of these predictions. Recall that the estimate of lifetime considering clad fatigue failure for continuous operation and more severe circumstances is about 27 years.

The average target burnup, conservatively assuming five years at the expected operating conditions and duty cycle is 0.225 at% and the concomitant peak burnup is 0.75 at%. The effects on target structural materials other than uranium, due to nuclear radiation associated with these burnup figures, are negligible except in the case of the cladding, which we have taken into account by use of data for irradiated Zircaloy in estimating clad fatigue life.

VI. Disk Fabrication

Assembly Process Description

Oak Ridge Y-12 plant, with technical support of ANL, is fabricating the clad, enriched uranium disks. Casting, machining, bonding, and inspection

procedures are adaptations of the methods developed at ANL for producing the depleted uranium target. Figure 1 above shows the target disk and vessel design. Electron beam welds seal the split cladding cans on the disk circumference. A high temperature and pressure HIP bonding operation creates a diffusion bond between the cladding and the uranium core. Final machining reduces the initially .060 inch thick cladding to .040 inches on the circumference and .020 inches on the faces.

Process Qualification

This phase of the work employed depleted uranium alloy material to establish proven processing, manufacturing and inspection procedures. Y-12 has produced, assembled, bonded, and tested four qualification disks, two of 1/2 inch thickness and two of one-inch thickness. Argonne provided the machined cladding cans. Due to criticality considerations, we substituted the Y-12 process of vacuum induction casting into a rectangular slab mold, for the ANL procedure of consumable arc casting. To provide the required high purity atmosphere during bonding, we installed at Y-12 an upgraded, small HIP bonding unit from ANL. A single cycle does not always produce complete bonds in the corners of the disks. This is due to the mismatch of the volume contraction and stiffness of uranium and zircaloy, which stresses the interface upon cooldown, leaving the clad in compression. Little is known about the strength of the bond, but the extrusion constant is a good measure of the stiffness of the materials: 6000 psi and 16,500 psi for uranium and zircaloy-2 respectively at 820°C and 30,000 psi and 50,000 psi at 650°C. The difference aggravates the problem of clad-core separation during cooldown. A second cycle shows a good probability of bonding disks which have flaws after the first cycle.

We have examined three qualification disks nondestructively and destructively to characterize the materials and verify the adequacy of the design. Measurements included determining chemical additive content, uranium grain size and texture, clad weld penetration, clad-core bond quality and machined final clad thickness. Final review has determined that the established procedures are capable of providing acceptable target disks.

Disk Production

Clad Can Fabrication. ANL has fabricated the Zircaloy-2 cladding cans from a 4-1/2 inch diameter annealed forging. The nominal 4 inch diameter, 1/2 or one inch deep, .060 inch thick cans have closely-held dimensions

chosen to allow convenient assembly and tight fitup at bonding temperature. Drumhead bowing and weld face warpage are persistent problems that we have overcome by reducing the machining cuts to small, closely-controlled steps and using special hold down fixtures, pads and clamps. The inner surfaces of the cans must be free of foreign matter to promote diffusion bonding. Adjustment of machining speed, feed rate and cutting lubricants has produced surfaces of the needed quality.

Thermowell Tube Fabrication. ANL has also produced the thermowell tubes, machined from 1/2" diameter round stock, 2-3/8" long, drilled to provide a hole of final size. Special precautions prevent hole arching. After drilling, the outer diameter is machined concentric with the bore. A gas tungsten arc weld bead seals the end of each finished tube; x-ray inspection verifies the quality of the weld.

Uranium Core Casting. Enriched uranium feed material is melted by a vacuum induction technique in a graphite-coated crucible. Elemental alloying additives, nominally 350 ppm Si, 250 ppm Fe, and 450 ppm C, combine in the melt to produce an composition resistant to thermal cycling growth and irradiation swelling. The melt is held at 1325 °C for 15 minutes, poured into a graphite book mold coated with a mold wash of ZrO_2-$ZrSiO_2$ and air cooled. The size of the castings for one-inch thick disks is 1.3" × 4.5" ×10"; for 1/2" thick disks, 3/4" × 9" × 9". Standard machining practices produce finished cores. Carbide drills introduce holes for the thermowells; overcoming problems of stuck drills and hole runout requires trial and error experience. Core blanks provide samples for chemical analysis and metallography. As-cast uranium grains are approximately of ASTM size 2, with prominent subgraining as shown in Fig. 12.

Disk Assembly and Bonding. Cleaning inspected disk components before assembly and welding is essential. Wire brush cleaning removes surface oxidation from the inside surfaces of the Zircaloy cans. Manual cleaning with a Skotch-Brite pad, followed by a pickling dip in nitric acid, a rinse in a bath of isopropyl alcohol and wire brushing, prepares the uranium adequately. Visual inspection of the uranium surface shows whether or not the surface oxide, as indicated by a mottled, darkened appearance, has been removed. Proper cleaning of the uranium is critical for success in diffusion bonding.

Metal handling tools insert the uranium core into the cladding cans in a dry box atmosphere; a radial 0.005" core-clad gap and 0.003"-0.008" axial gap optimize the fitup during assembly. Next the assembly is placed in the

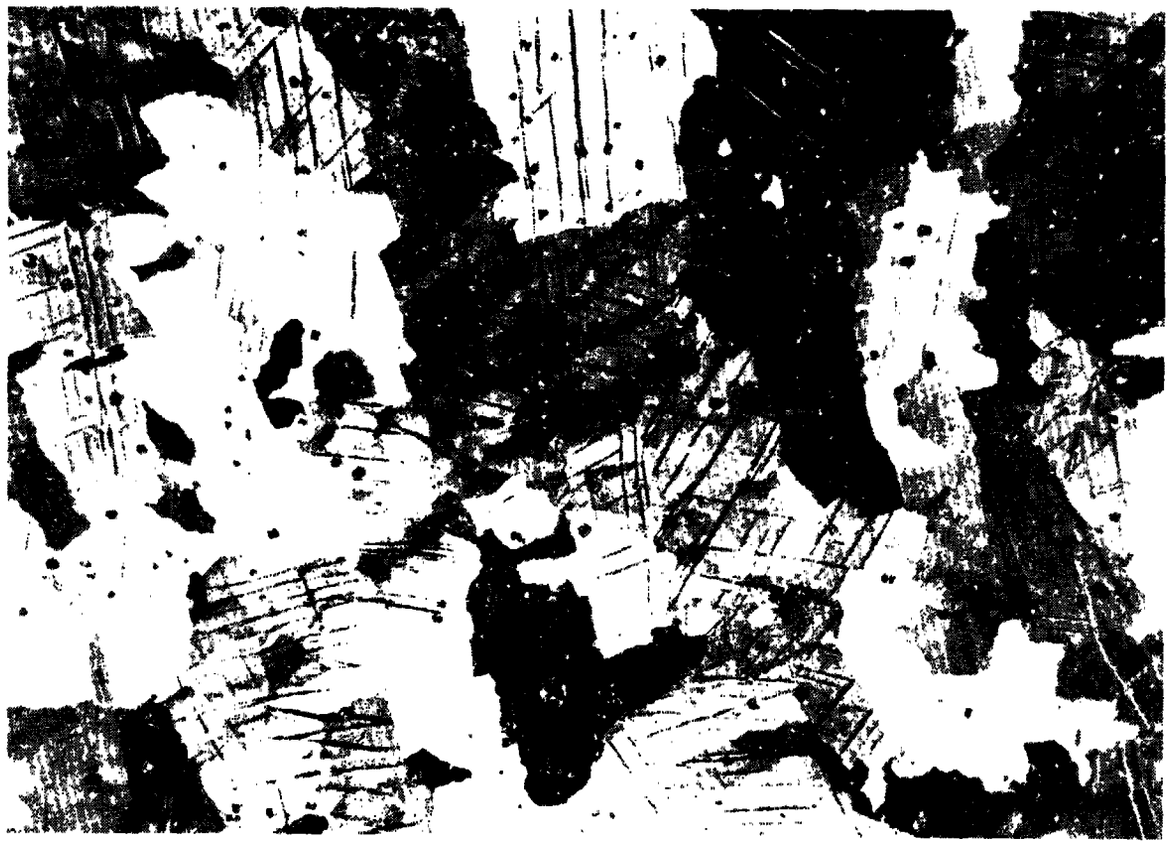

Fig. 12 Typical Cast Uranium Grain Size Distribution. Magnification (approximately x100) is such that the base of the figure represents 1.3 mm. ANL Neg. MS-85-0718-2.

electron beam welding chamber and evacuated. The weld seals the can halves on their circumference as the assembly is rotated. Selected and qualified welding parameters effect the proper penetration, which extends 30-70% into the clad wall. Excessive penetration causes uranium alloying in the weld, and catastrophic cracking. The clad separation beneath the weld joint heals completely during the HIP bonding process. Electron beam welds also seal the thermowell tubes to the cans. Welding must be done in a short time after cleaning and assembling the components, meantime they must be stored in inert containers.

A Hot Isostatic Pressure bonding process produces a metal-to-metal bond between the cladding and the uranium of the sealed disk assemblies. A bed of Zirconium chips accompanies the disks in the bonding unit, as a getter of impurities. Purge cycles of evacuation and introduction of high purity argon gas and the use of the getter chips prevent heavy oxidation of the cladding, which makes it very stiff and seems to lead to debonding during cooldown. Following a one-hour heatup to 840. °C and pressurization to 25,000. psi, the temperature and pressure remain at the maximum for three hours; a controlled, slow cooldown at 1. °C/min follows until the temperature reaches 200. °C. The expected superficial oxidation of the cladding can be removed by emery paper. Figure 13 shows a typical clad-core bond zone.

Final machining produces close tolerances on disk thickness and diameter. HIP bonding produces some undulation of the disk surfaces, so that precise disk surface maps have to be made before alignment in the lathe. Frequent measurements during machining enable the clad face thickness to be held in the range 0.017/0.025".

Inspection. Chemical analysis of the cast uranium core samples give the Si, Fe, and C additive content as well as the content of other metallic impurities. These results along with examinations of grain structure in metallographic sections and crystallographic texture in diffraction samples, provide for the assessment of uranium swelling.

Ultrasonic tests check the entire disk surface, including the rounded corners, for completeness of bonding, and can detect nonbonded areas down to a diameter of 1/16". Y-12 and ANL test methods compare successfully. Calculations indicate the thickness of cladding after final machining, although this approach presents some difficulties. We spot-check the clad thickness with a portable ultrasonic unit calibrated against standards of known thickness.

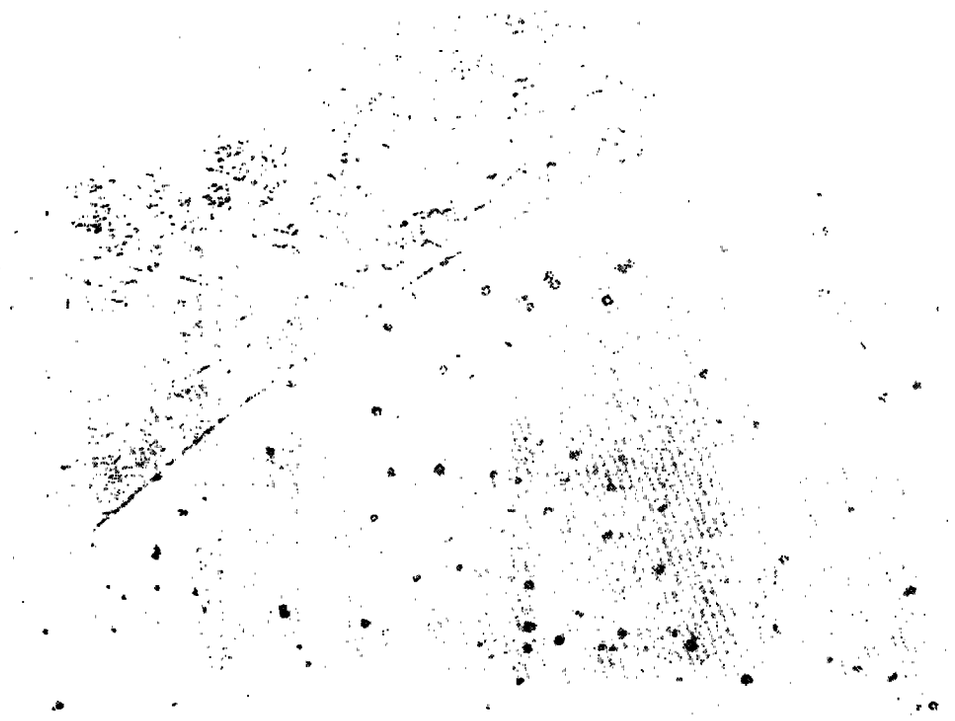

Fig. 13 Typical Clad-Core Bond Interface After HIP Bonding at 840°C for Three Hours

Other inspections which take place throughout processing and prior to shipment include mass spectrometer leak testing, visual inspection, weighing, measurement of thermowell dimensions and checks for surface uranium contamination.

VII. Radiological Hazards

We expect the highest long-term operating conditions to correspond to 16. μA, 450. MeV proton beam current with a beam size between 3. and 4. cm fwhm diameter. These conditions will produce 56. kW total thermal power (49.2 kW fission, 6.8 kW spallation), although we have assumed higher values for purposes of conservative design. Because of this relatively low power and because we expect to operate only about half the time, the radionuclide inventory is not so large as to constitute a significant radiological threat to the public. We have demonstrated this through an analysis based on the most probable mechanism of release of radionuclides to the coolant water, that is a crack in the cladding in the most highly stresed target disk. The analysis further conservatively assumes (1) five years' continuous operation at 18. μA, 500. MeV (total power 74.9 kW), (2) 30 days' continuous operation after a clad crack 1. mm wide develops across the face of a disk (normally, this would be detected in no more than four hours in the course of regular monitoring of gas samples), and (3) a breach of the target cooling system which releases all the cooling water to the atmosphere. We have assessed the consequences both of the water being filtered through the IPNS effluent control system and when it is released unfiltered (as a result of a tornado or earthquake, for example).

The computer code ORIGEN has calculated the fission product buildup, ORIHET computed the spallation product buildup, and DOSER determined the hazard of the release to a receptor at the ANL site boundary[8]. The basis for the case of unfiltered release is that 100% of the noble gases, 50% of the halogens and 0.1% of the solids are released; for the unfiltered case the fractions are 100% of the noble gases, 50% of the halogens and 10% of the solids. Both analyses assume a wind speed of 1. m/sec and Class F wind stability conditions. Table 2 shows the results, expressed as a fraction of the 10CFR100[9] guideline values.

Table 2

Clad Breach Dose Consequences

ORGAN	10CFR100 GUIDELINE DOSE, rem	DOSE IN FILTERED CASE, %	DOSE IN UNFILTERED CASE, %
Bone	150.	1.8×10^{-4}	0.016
Lung	75.	2.0×10^{-3}	0.19
Thyroid	300.	5.4×10^{-3}	5.4×10^{-3}
Whole Body	25.	4.7×10^{-4}	9.6×10^{-3}

The highest dose is 0.19% (0.14 rem) of the lung guideline dose which is not a significant hazard.

The increased radiation from the Booster target (about ten times that of the present target for the same operating conditions) while in operation or when shut down necessitates only minor changes in the main shield, and some changes in the target handling procedure. The increased radiation during operation will not cause any increase in groundwater activation above that of the present target.[10]

VIII. Neutronics and Power Densities

The complexity of the Booster target configuration suggests the application of a Monte Carlo code to the neutronic analysis, rather than a mesh-based analysis. We used Argonne's neutral particle radiation transport code VIM.[11] Since the Booster assembly is very small, it is intimately neutronically coupled to its environment. The spectrum in the target is very hard, but the surrounding media are mostly thermalizing, and contain large voids and localized strong absorbers, so there is no reliable way to postulate a fundamental mode neutron distribution to be used for multigroup cross section generation. VIM's use of combinatorial geometry and of detailed, composition- and spectrum- independent, continuous-energy cross sections and scattering distributions eliminates these problems altogether. Accordingly, we have used VIM for all neutronic design calculations, except for estimation of the prompt neutron generation time, for which we used KENO.

Having chosen from survey calculations the operating k_{eff} = .80 as providing approximately the desired design features, we have determined the required enrichment to be 77.5% from a series of eigenvalue calculations

performed for various values of enrichment. Subcriticality is assessed (and assured) in a variety of cases in which the Booster is completely surrounded by different materials which either are encountered during fabrication, transport and installation, or might be encountered in off-design circumstances. The ^{10}B decoupler layer in the vessel wall is assumed to remain in place for the purpose of these calculations. Table 3 shows the results. Since the Booster must pass through the beryllium outer reflector during insertion and removal, we have modeled these two situations in more realistic detail. These cases are conservative because the absorbing media associated with the moderator-reflector assembly and the iron constituting the main shield are represented as beryllium. As shown in Table 3, k_{eff} = 0.92 in both these cases, which differ in that in the removal case, we have accounted for the (estimated separately for 5 years operation at 20 μA, 500 MeV) 2.5% burnup of the ^{10}B decoupler.

Table 3

Booster Eigenvalues in Various Configurations

DESCRIPTION	k_{eff}
Bare	0.6660 ± 0.0034
Embedded in CH_4	0.7337 ± 0.0062
Embedded in H_2O	0.7523 ± 0.0046
Embedded in concrete	0.8119 ± 0.0060
Embedded in iron	0.8346 ± 0.0038
Embedded in natural uranium	0.8860 ± 0.0049
Embedded in graphite	0.8900 ± 0.0064
Embedded in beryllium	0.9362 ± 0.0051
During insertion	0.9200 ± 0.0035
During removal	0.9179 ± 0.0069

We calculate the power densities required for thermal-hydraulic, activation, and other analyses, using four radial bins in each disk. This is done in two steps; first using the High Energy Transport Code HETC[12] we simulate the transport and the heat generation of the incident protons, high energy fission and spallation processes. VIM then picks up the calculation for neutrons using the source site tape written by HETC, which contains the

spatial coordinates, energies and directions of all the neutrons born or downscattered below 15 MeV. About 30 additional generations (99.999%) of all neutrons born in subcritical multiplication are included in the VIM simulation. The resulting heat generation rates are the sum of the HETC estimates and the VIM fission rates, assuming 190. MeV is deposited at the fission site. Figure 14a shows the power density distribution. For these calculations we take the proton beam to have a full width at half maximum diameter of 3. cm, slightly larger than the radial mesh width of 1.27 cm. This radial peaking is evident when comparing the dominance of the fundamental mode axial profile in the outermost annulus to the front-peaked centerline profile. The rapid falloff of the power density in the downstream end of the target is due to the finite range of the protons. Figure 14b shows the two computational (and physical) components of the power density in the central zone: high energy interactions (HETC) and lower energy fissions (VIM). The fission rate density is peaked in the front due to the high density of source sites produced by high energy interactions (HETC), and its subsequent relaxation to the fundamental mode. We have found in a separate study that, in addition to producing more primary neutrons, higher energy protons excite the fundamental mode more efficiently than lower energy protons, and thus produce multiplied neutrons more than in proportion to the primary spallation yield.

The efficacy of the Booster has been demonstrated by calculating the neutron flux (track length) in a 1.4 cm-thick slab at the surface of a room temperature polyethylene moderator in position "C", on the side facing the neutron beam tube, and comparing the Booster with the present, depleted uranium target. Both calculations use the same HETC-generated primary neutron source, and employed modest splitting and Russian Roulette techniques to improve the efficiency of the calculation. Figure 15 shows that the shapes of the spectra are nearly identical, and larger in the Booster case than in the depleted target case by a factor of about 3.0.

We have used the Monte Carlo code KENO[13] for three purposes: (1) in safety-related assessments of the multiplication factor, for aggregations of free target disks and the assembled target in various media; (2) to determine the prompt-neutron generation time l_p and thus provide an estimate of the prompt pulse width $\tau \lesssim l_p/(1 - k_{eff})$); and (3) to perform check calculations of k_{eff} to compare with VIM results for several identical cases. The calculations show that subcriticality is guaranteed under all conditions of assembly, operation, and disposal. KENO is a criticality safety code,

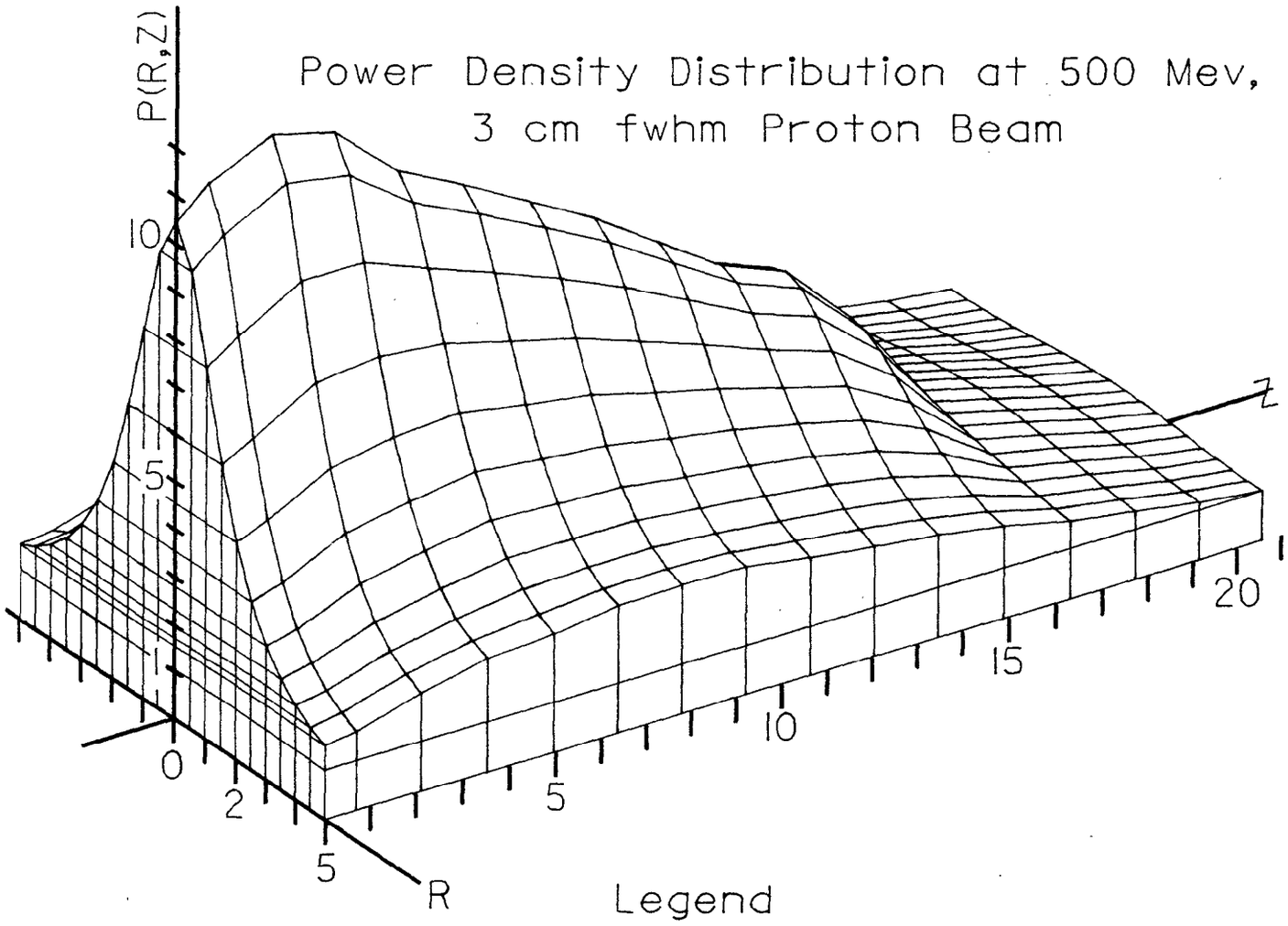

Legend

P(R,Z) - Power Density, watts/cc/μa

R - Radial Distance from Center Line of Target, cm

Z - Axial Distance from Front Face of Target, cm

Fig. 14a The Power Density Distribution in the Booster Target

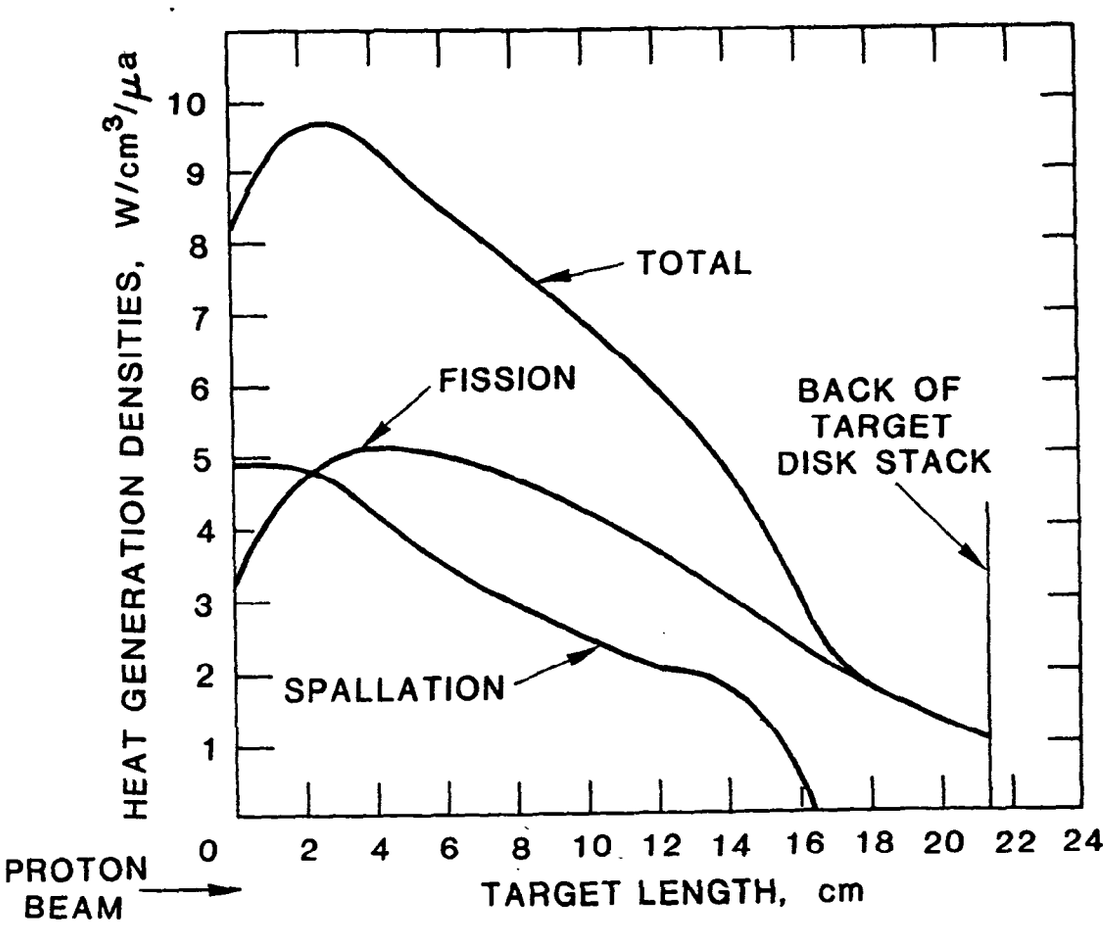

Fig. 14b Axial Centerline Profiles of the Internal Heat Generation in the Target Disks Due to Fission and Spallation and the Total

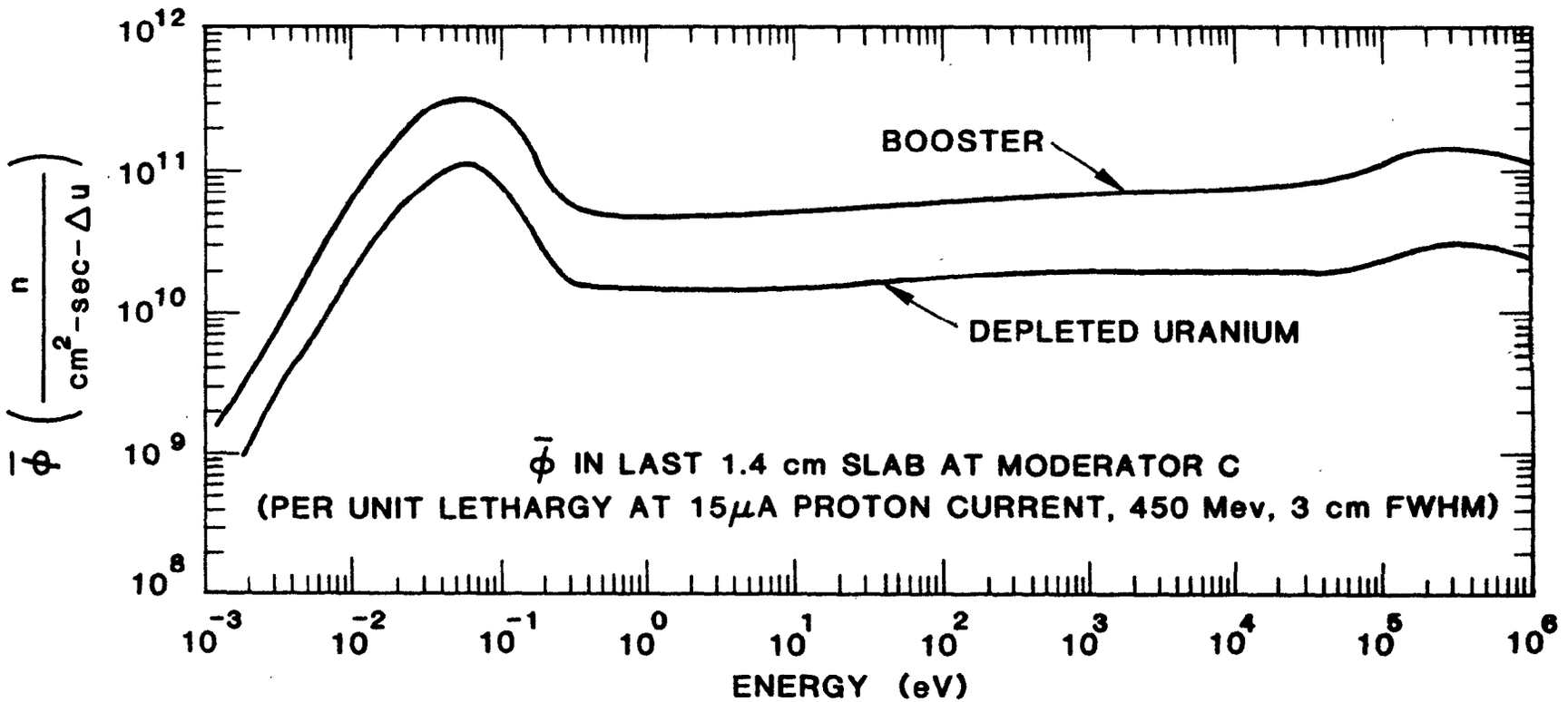

Fig. 15 Average Moderator Neutron Scalar Flux Spectra for the Depleted Uranium and the Booster Targets

which is known to be more conservative than VIM; as expected, the KENO k_{eff} values are always higher (Δk_{eff} = 0.01 - 0.03) than those from VIM. The prompt generation time is found to be 68. nanosec, and the Booster response time accordingly estimated to be 340. nanosec. This does not affect moderated neutron pulse widths significantly for energies below about 6. eV in a typical moderator. If the inner reflector were beryllium rather than graphite, and the coolant were D_2O rather than H_2O (design options that we have recognized but not employed for economic reasons) the Booster response time would be 43. nanosec., while the estimated pulse width would be 215 nanosec.

IX. Safeguards and Security

Because of its significant content of special nuclear material (^{235}U) and (eventually) of radioactive materials, the fabrication, operation and disposal phases of the Booster target are subject to safeguards and security regulations and controls. The design and operation of the target and supporting systems fully accommodate these regulations, and attention to them has been a substantial part of the design and planning activity. This aspect of the work has been facilitated by our continuous and early consideration of these issues.

X. Summary

We have described the design and evaluation of an enriched uranium booster target for IPNS. The new target will be installed in the near future, without extensive modification of the facility, and meets all the criteria for safe operation. The Booster will increase the intensities of the neutron beams, and therefore the effectiveness of IPNS by a factor of three.

Acknowledgement

We express our gratitude to M. H. Mueller, J. W. Richardson, Jr. (Argonne), D. G. Reichel, F. K. Ross and W. B. Yelon (Univ. of Missouri) for their excellent work on the neutron diffraction characterization of uranium. We thank T. Weincek and R. F. Domagala for development and production of the ^{10}B-Cu composite decoupler material.

REFERENCES

1. A. W. Schulke for the IPNS Enriched Uranium Booster Target Design Team, "IPNS Enriched Uranium Booster Target", ICANS VIII, Proceedings of the Eighth Meeting of the International Collaboration on Advanced Neutron Sources, Rutherford-Appleton Laboratory, July, 1985, Rutherford-Appleton Laboratory Report RAL-85-110, Volume I, 231, (1985).

2. D. J. Erickson, unpublished information, 1984.

3. "Flow of Fluids Through Valves, Fittings and Pipes" Technical Paper 409, Crane Company, 1942.

4. W. J. O'Donnell and B. F. Langer, "Fatigue Design Basis for Zircaloy Components", Nucl Sci & Eng 20, 112,(1964).

5. M. C. Billone personal communication to B. S. Brown.

6. B. A. Loomis personal communication to B. S. Brown.

7. M. H. Mueller and J. W. Richardson, personal communication.

8. D. R. Henley personal communication to A. E. Knox.

9. "Part 100--Reactor Site Criteria", U. S. Code of Federal Regulations, Chapter 10, Nuclear Regulatory Commission.

10. M. M. Barbier, unpublished information, 1984.

11. R. N. Blomquist, "VIM, A Continuous Energy and Photon Transport Code", Advances in Reactor Computations, Proceedings of a Topical Meeting, Salt Lake City, 28-31 March, 1983.

12. R. C. Chandler and T. W. Armstrong, "Operating Instructions for the High-Energy Nucleon-Meson Transport Code HETC", Oak Ridge National Laboratory report ORNL-TM-36607 (1972).

13. L. M. Petrie and N. M. Cross, "KENO IV--An Improved Monte Carlo Criticality Program", Oak Ridge National Laboratory report ORNL-4938 (1975).

ICANS IX

INTERNATIONAL COLLABORATION ON ADVANCED NEUTRON SOURCES

22-26 September, 1986

Studies of Low Enrichment Targets for ISIS

T.D. Beynon, D.J. Picton and T. Al-Sharify

Department of Physics, University of Birmingham,
Birmingham B15 2TT, England.

ABSTRACT

The paper concentrates on design options for a replacement to the current depleted uranium target on ISIS. The two options under consideration were the use of a variable enrichment to flatten power production, and a change in the shape of the target from a circular to a rectangular cross section.

The results for variably enriched targets must be judged by the available benefits to moderators, rather than overall gains in neutron production. "Flattening" power production by the use of axial enrichment variation would mainly benefit the "downstream" moderators possibly by a factor of two. In contrast, the use of a radially varying enrichment would enchance the performance of all moderators. It is clear that a combination of the two would be a desirable option.

The results for a target with a rectangular cross section were encouraging, in that substantial gains could be achieved at a far lower enrichment.

1. INTRODUCTION

Two basic options for enhancing the ISIS target station are currently under investigation. The present depleted uranium target could be replaced by an enriched target. The replacement target-moderator-reflector configuration would, in practice, be subject to a number of constraints; for example, the size and shape of the target pressure vessel could not be changed. The second option would involve the construction of a completely new target station, for which the conceptual design restrictions would of course be less severe.

This paper concentrates on design options relevant to the replacement of the existing target with an enriched uranium target of similar dimensions. As the title suggests, the concept of a highly enriched 'superbooster' within the available space is not realistic; a replacement target would have to have a relatively low average enrichment, and a peak power density of the same order of magnitude as the current target.

The three design options explored in this paper are: variable enrichment along the axis of the target cyclinder, radially varying enrichment, and a change in target geometry from the present cylinder of radius 4.5 cm to a slab-like target with a rectangular cross section (10x20 cm).

A variable enrichment is suggested because a flattening of power production would allow a target to produce a better neutron production within the constraint of a maximum peak fuel temperature. The use of a modified target shape, enlarged in one direction (without increasing the distance from the moderator to the centre of the proton beam) has a number of obvious advantages for any enriched target. In particular, the

degree of enrichment required can be considerably reduced, and (as will be demonstrated later) uniform flattening of power generation over the whole target would be far easier to achieve.

Section 2 presents results for a cylindrical target with axially varying enrichment, and section 3 presents similar results for a slab target. Section 4 contains calculation for a radial variation in enrichment in a cylindrical target.

2. AXIALLY VARIABLE ENRICHMENT IN A CYLINDRICAL TARGET

2.1 Calculational Details

Fig 1 shows the geometry specified for the variably enriched target. The target itself was represented as a cylinder of radius 4.5 cm and length 30 cm, enclosed in a 1 cm decoupler region (represented as 10^{22} atoms cm^{-3} of ^{10}B.) The decoupler was in turn surrounded by a 70 cm cube representing a D_2O cooled Be reflector and consisting of a homogeneous mixture (80% Be, 20% D_2O.)

The target region itself was divided into four zones for which differing degrees of ^{235}U enrichment could be specified. All four zones contained a homogeneous fuel-coolant mixture (80% uranium and 20% D_2O.)

All calculations were performed by the Monte Carlo code MORSE[1], using the DLC-37[2] coupled neutron-gamma library. The fixed source (representing all processes above 15 MeV) was based on a HETC[3] calculation for a pure ^{238}U target assuming a 7 cm proton beam diameter with a parabolic radial distribution. An adjustment was made for the reduced uranium density in this configuration.

In the heterogeneously enriched configuration here and in Section 3, enrichments were adjusted to flatten total neutron production (ignoring capture processes.) A more appropriate parameter to flatten would be the peak (i.e. centre line) power density. However, estimates of the peak power density based on the results in Section 4 suggest that a target with a uniform rate of neutron production per plate would also have a nearly uniform peak power density. This is due to the fact that the relatively flat spatial distribution of the fission source, compared with the primary source, compensates for the higher energy deposition per neutron.

All results presented in sections 2 and 3 consist of production rates in each target zone with the total primary source normalized to 1.0 for the whole target.

2.2 Results and Discussion

Results for the rate of neutron production in homogeneously enriched targets are shown in Fig. 1. It is clear that neutron production in such targets is very non-uniform, and a high proportion (about 45% for a ^{238}U target) are generated in the first 7.5 cm of the target.

Fig. 2 presents the calculated neutron production rates for the heterogeneous configuration designed to produce a uniform neutron production rate. A "flattened" result was found to be hard to achieve for the entire target - in fact the last quarter required an enrichment of 90% to match the performance of the 0% enriched first quarter!

Two parameters of greater importance are shown in Figs 3 and 4 for the heterogeneous target, clearly i.e. net neutron production and estimated power production. Here "net neutron production" exclued all neutrons list

in capture processes in the target, including fission capture. Power production was estimated as 30.2 MeV per neutron for the primary source and 61.3 MeV per neutron for the fission source[5]. (Note: for this non-thermal system, γ was calculated as 3.08 neutrons/fission.)

Two basic disadvantages of enriched targets are revealed here, and must always be taken into account. Fission deposits more energy per neutron produced than spallation, and also involves the capture of neutrons. Thus the ratio of power production to useful neutron production increases with enrichment, from about 40 MeV/neutron for pure ^{238}U to 100 MeV/neutron for ^{235}U.

The overall advantage the heterogeneous target as compared with a ^{238}U target is rather modest. Net neutron production is increased by only 52%, at the expense of a 135% increase in energy deposition. However, as previously mentioned, the performance of the rear moderaters would be considerably enhanced. A precise estimate of the gain must await calculations in which moderators are included.

3. AXIALLY VARIABLE ENRICHMENT IN A SLAB TARGET

3.1 Calculational Details

Fig. 6 shows the geometry specified for the slab target, which differed from the cylindrical target only in having a rectangular (20x10 cm^2) cross section.

Calculations were again performed by the code MORSE.

3.2 Results and dicussion

Neutron production rates for homogeneous enrichments are given in Fig 7, and results for two heterogeneous configurations in Fig. 8. Figs 9 and

10 contain net neutron production and estimated power production rates respectively.

The modified geometry exhibits the expected strong advantage over the cylindrical geometry. A relatively modest maximum enrichment (45% instead of 90%) is required to achieve a flattened neutron production rate over the whole target, and elsewhere in the target enrichments would be reduced in approximately the same proportion.

The minimally enriched heterogeneous configuration (enrichements 0, 10%, 22%, 45%) gives a 53% increase on net neutron production, at the expense of a 125% increase in power production, when compared with the homogeneous ^{238}U slab target. In this respect its performance is comparable with the heterogeneously enriched cylindrical target presented in section 2. The second configuration (enrichment 20%, 20%, 32%, 53%) increases net neutron production by a factor of 2.38 at the expense by a factor 4.19 in power production, again in comparison with a 0% enriched target.

Precise conclusions on the merits of a modified target geometry must involve a more detailed investigation in which a pure realistic design is adopted, and a full geometry calculation, including the moderators and reflector is performed.

4. INVESTIGATION OF RADIALLY VARYING ENRICHMENT

4.1 Calculational Details

The one dimensional S-N code ANISN[4] was used to calculate the performance of targets with a radially varying enrichment.

The material composition of the target, decoupler and reflector were as described in Section 2. The geometry of the system was similar to the MORSE geometry in Fig. 1, except that all components were represented as a set of concentric infinite cylinders or cylindrical shells.

The target was represented as a cylinder of radius 4.5 cm, subdivided into four zones of outer radii 1.125, 2.25, 2.375 and 4.5 cm. As for the MORSE calculations, the target was surrounded by a decoupler in the form of a 1 cm thick cylindrical shell. The reflector was represented by a cylinder of outer radius 35 cm.

The source used for these calculations had the same average radial distribution as in the MORSE calculations, and was normalized to 1 ns^{-1} cm^{-1}. The ratio of peak to average intensity used here was approximately 1.9. Care must be used in interpreting the results because in practice the source distribution broadens along the axis of the target. In the first few cm of the target the peak to average ratio is about 3 for a 7 cm diameter proton beam.

4.2 Results and discussion

Preliminary results indicated that the power densities in zones 1 and 2 ($0 < r < 1.125$ cm and $1.125 < r < 2.25$ cm) were nearly identical as was the enrichment required to produce a uniform power density throughout. A decision was therefore made to combine zones 1 and 2 in the analysis of results, and to specify the same level of enrichment for both.

Fig. 11 displays the total energy deposition in each target zone as a function of enrichment for uniformly enriched targets. Clearly the proportionate variation in power density is large at low enrichments,

(being dominated by the distribution of the primary source,) but becomes small at high enrichments (because of the presence of the reflector.)

Fig. 12 shows the results of a series of calculations in which the enrichments in different zones were adjusted to produce a uniform power density. The enrichments required (three values for zones 1 and 2 combined, zone 3 and zone 4) are plotted against the estimated power density in MeV cm^{-3}.

A similar pattern to fig. 11 is discernable, in that the variation in enrichment required to produce uniform power is larger at low enrichments.

Fig. 13 compares the net neutron production in the target for heterogeneously and homogeneously enriched configurations. Here the net leakage across the surface of the target is plotted against centre zone enrichment. In the absence of moderator calculations, this parameter is the best available indicator of target performance. However, a true comparison of the homogeneous and heterogeneous targets should be made at equal centre-line power densities, rather than enrichments. The slanted lines on Fig. 13, link points of equal power density in the centre zone.

As expected, the proportionate gain in neutron production is greatest at low enrichments. The heterogeneous configuration with zero enrichment at the centre shows a gain of about 25% in the homogeneous target (enrichment 3%) with the same centre zone power density. At higher enrichments, the available gains are relatively poor (about 15% for a centre line enrichment of 50%, falling to ~ 10% for a centre line enrichment of 60%.)

Finally, Fig 14 shows the total energy deposition as a function of centre - line enrichment. Again, the slanted lines link points of equal centre-zone power density.

5. GENERAL CONCLUSIONS

The results for an axially enriched cylindrical target suggest that an overall gain of 52% could be achieved over a ^{238}U target at the expense of an increase of power production from 230 to 540 kW. However, this could only be achieved with an unrealistically high enrichment of 90% for the last quarter of the target. As previously mentioned, the principal gain from the axially enriched target would be a considerably improved source for the rear moderators.

The use of a radially varying enrichment to flatten power production could also improve target performance. The source distribution used here predicts as 25% true gain (at constant peak power density) decreasing with increasing enrichment. However, a more appropriate source distribution would predict a higher available gain (by a factor of about two) near the front of the target. Thus axial and radial enrichment variation are to some extent complementary. The radial variation would mainly benefit the front end of the target, whereas the axial variation would benefit the rear end. Calculations will now be performed for a target which combines both types of enrichment variation. In principle the whole target could be flattened to give a power production of about 1.5 MW; however, a 1 MW target with power density flattened for the first 20 cm of uranium would be more realistic.

The results for a two dimensional target are interesting, in that the same level of neutron production can be achieved with about half the

enrichment. However, more detailed calculations are now needed to evaluate the neutron brightness available to the moderator.

Future calculations must also include a realistic moderator and reflector configuration. A major uncertainty must be resolved, i.e. the coupling efficiency of moderators to the fission source in an enriched target. For a number of reasons this source will be harder than the primary spallation source, and it can therefore be expected to couple less efficiently with moderators.

6. ACKNOWLEDGEMENTS

The authors wish to acknowledge the SERC for their financial support for this project.

7. REFERENCES

1. Taylor N.P. and Needham J (1983) Report AERE R104 (refers to MORSE-H version 2.7).

2. RSIC-DLC37F (1978). Radiation Shielding Information Center, O.R.N.L., Oak Ridge, Tenn.

3. HETC. RSIC Computer Code Collection no. CCC-178. Also see W.A. Coleman and T.W. Armstrong, ORNL-4606 (1970) and K.C. Chandler and T.W. Armstrong, ORNL-4744 (1972).

4. W.W. Engle Jr. O.R.N.L. Report no K1693 (1967).

5. "A theoretical study of a target reflector and moderator assembly for SNS," F. Atchison. RAL report RL-81-008, April 1981.

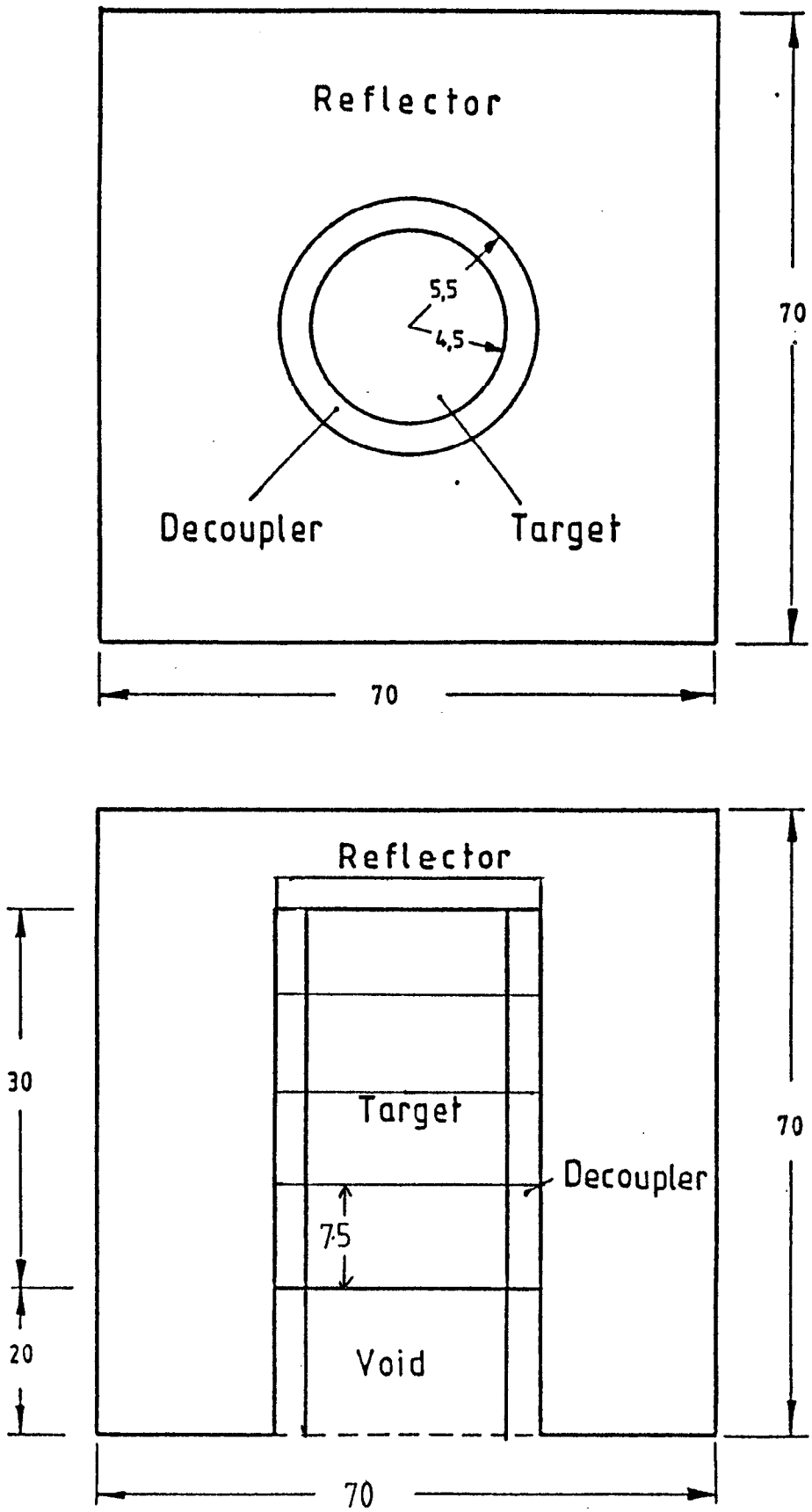

Fig. 1 Geometry specified for the cylindrical target configurations.

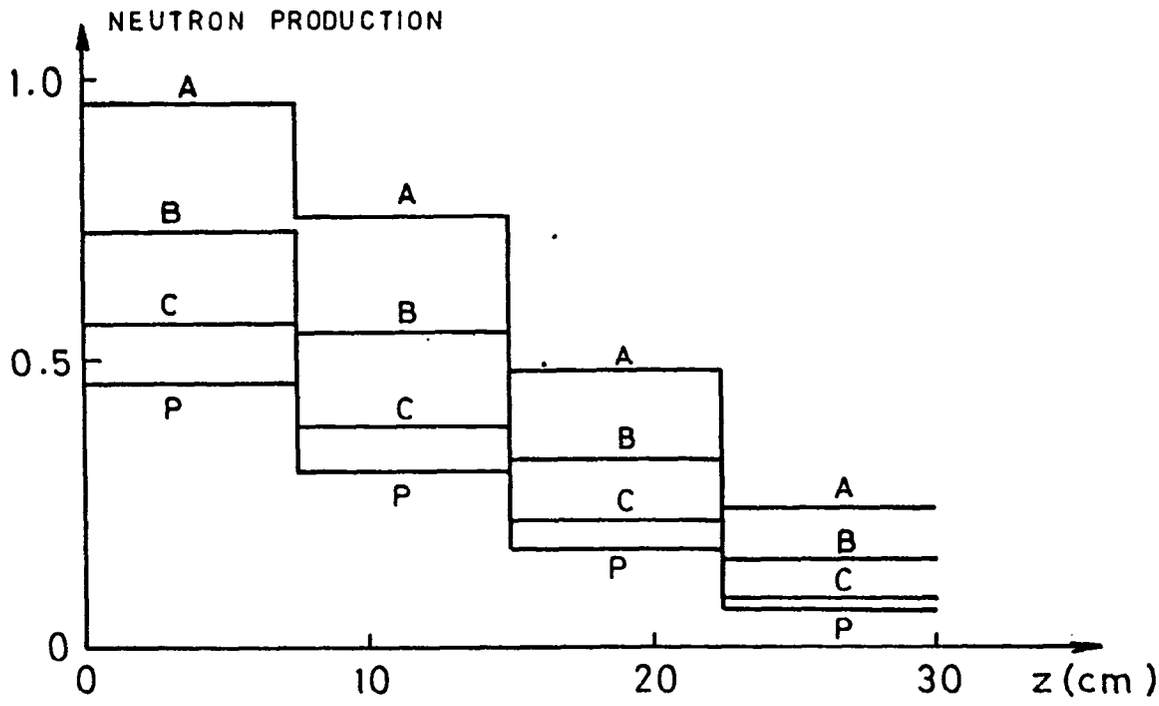

Fig. 2 Total neutron production (per target zone per unit primary source in whole target) in homogeneously enriched cylindrical targets. "P" represents the primary source (normalized to 1.0 for whole target.)

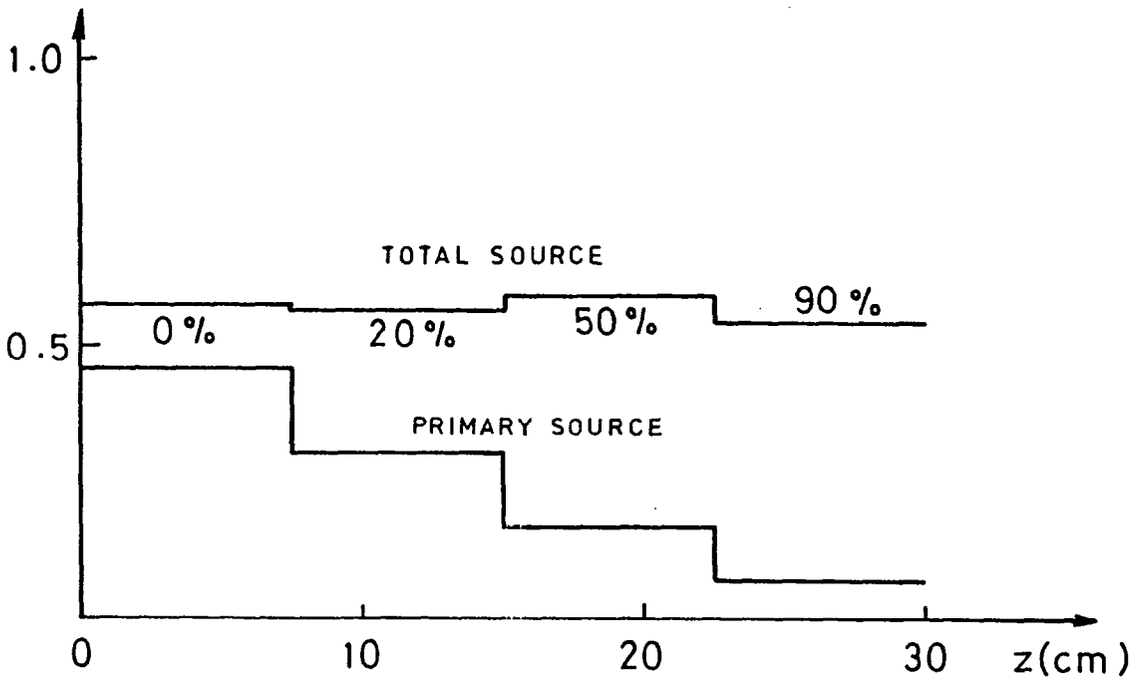

Fig. 3 Neutron production from the heterogeneously enriched cylindrical target. Enrichments are shown.

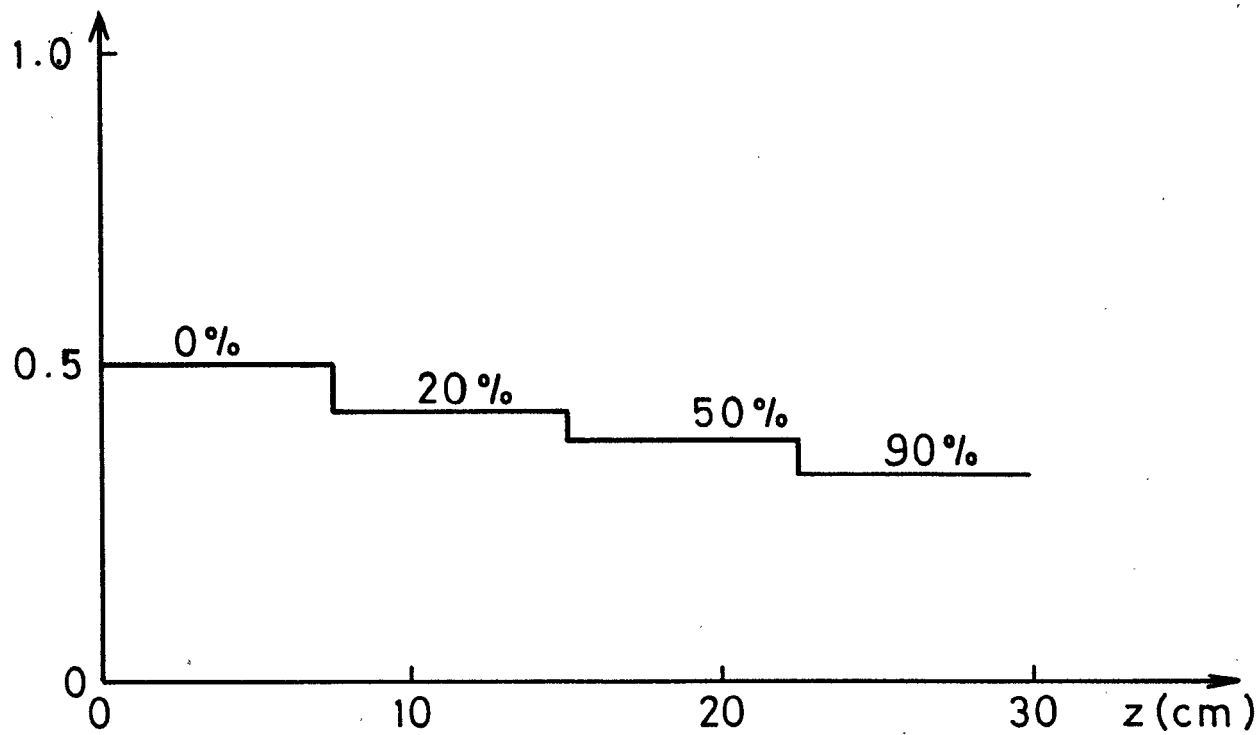

Fig. 4 Net neutron production in the heterogeneously enriched target. (per target zone per unit primary source in whole target)

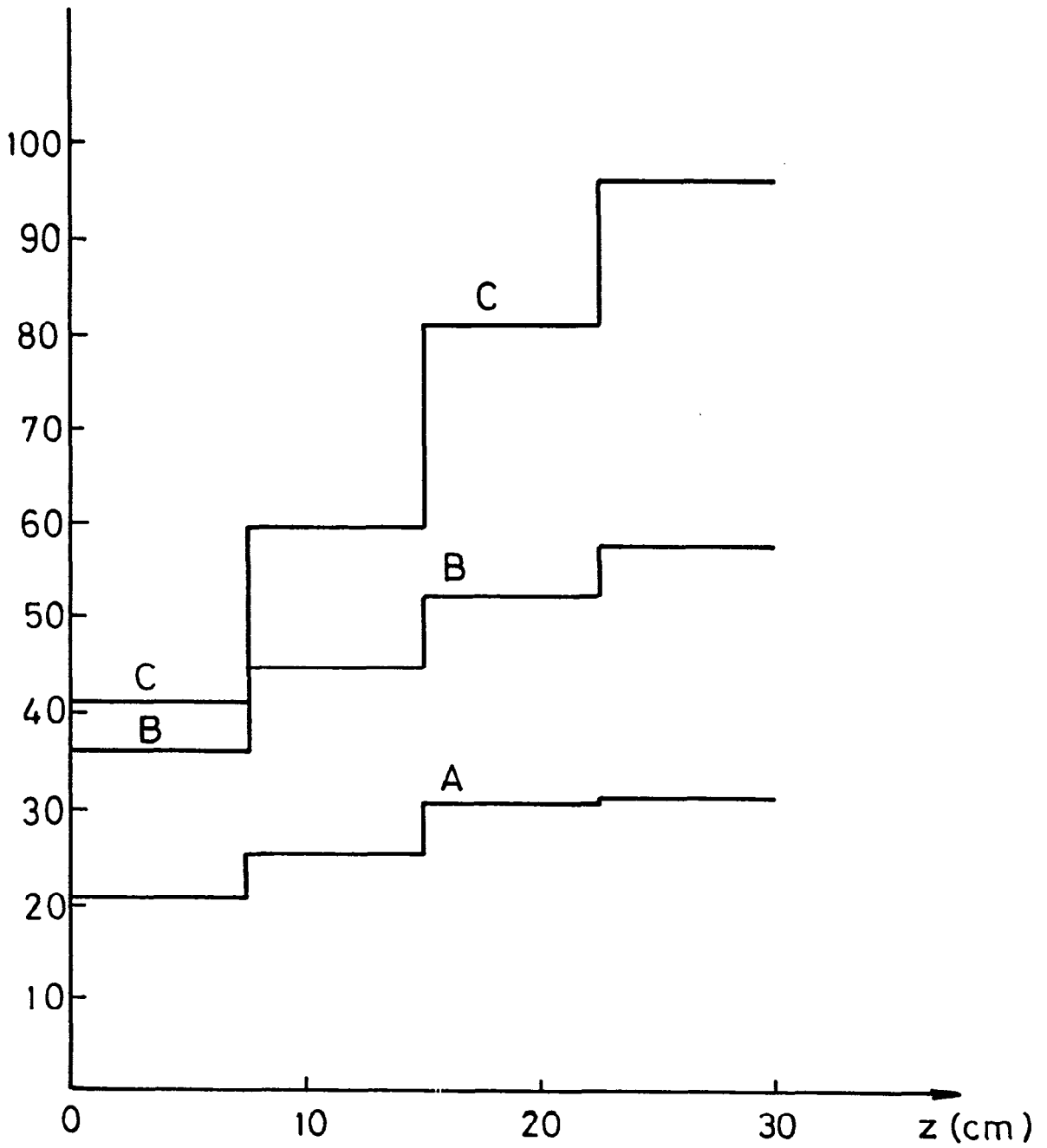

Fig. 5 Estimated power production (per target zone)

A. per unit primary source in whole target (1 MeV per primary neutron corresponds to 4.29 W at 200 μA beam current.)

B. per unit total source in target zone.

C. per unit net neutron production in target zone.

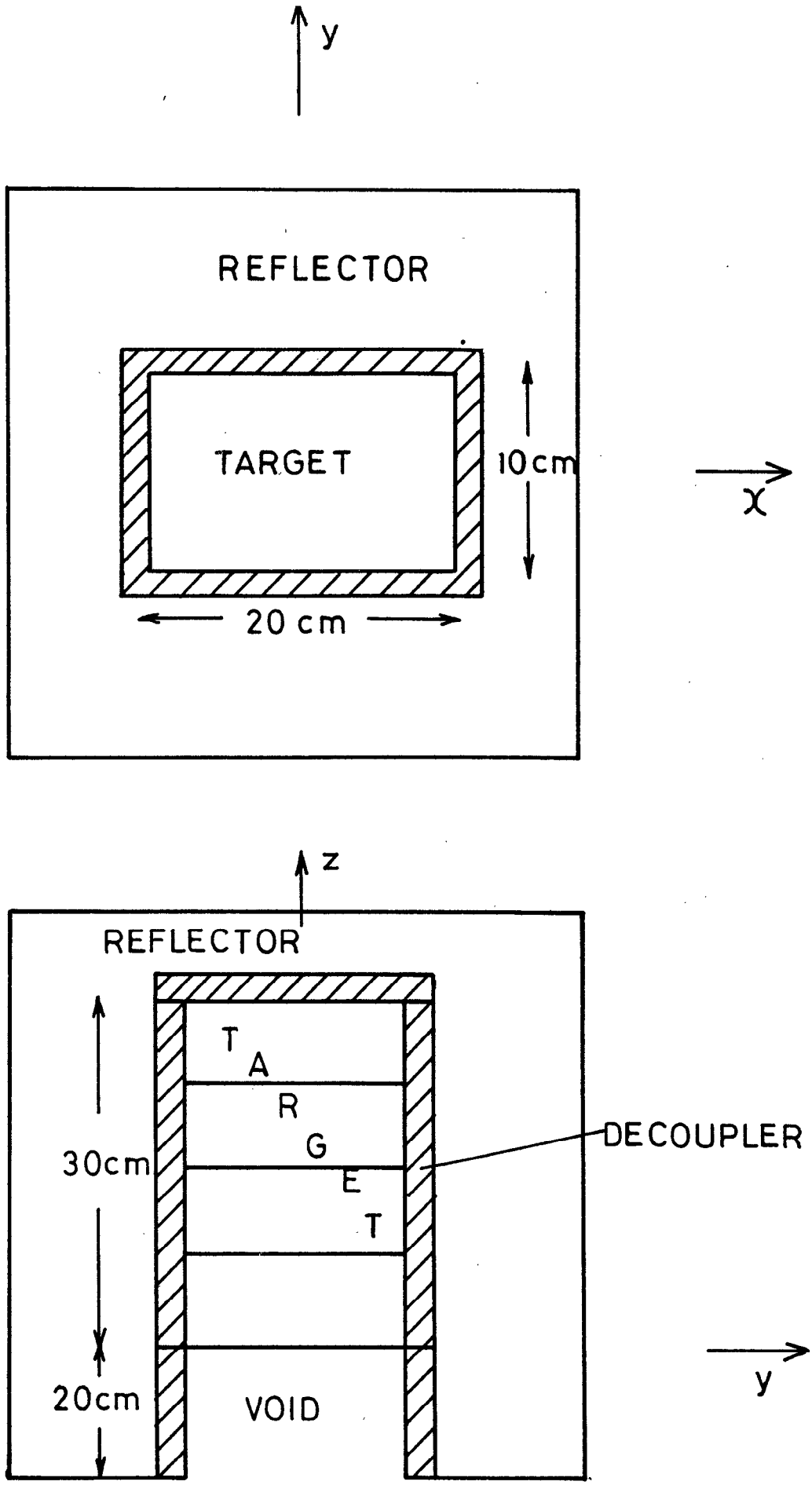

Fig. 6 Geometry of the slab target configuration.

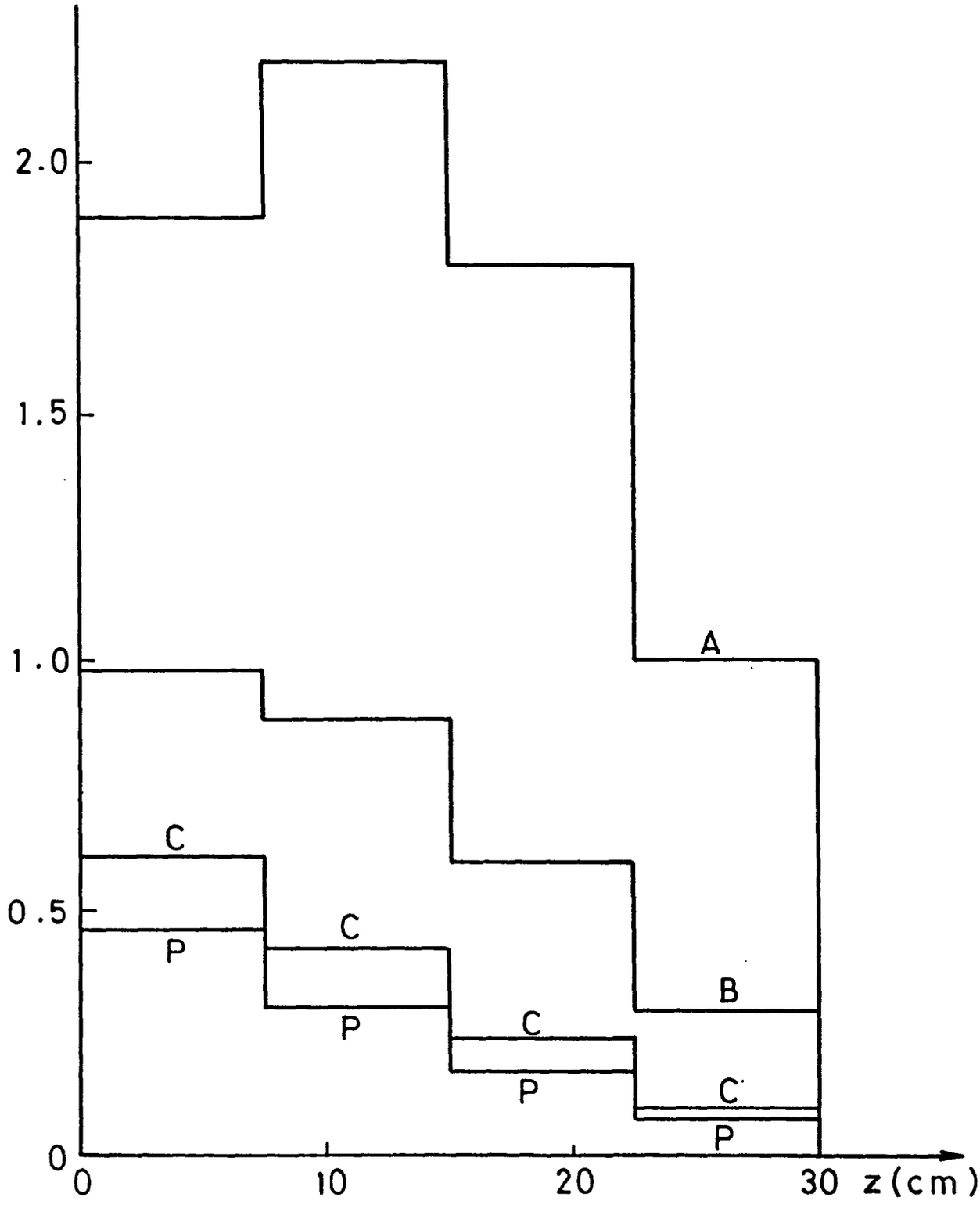

Fig. 7 Total neutron production per target zone in homogeneously enriched cases (per unit primary source in whole target)

A x = 40% B x = 20% C x = 0%

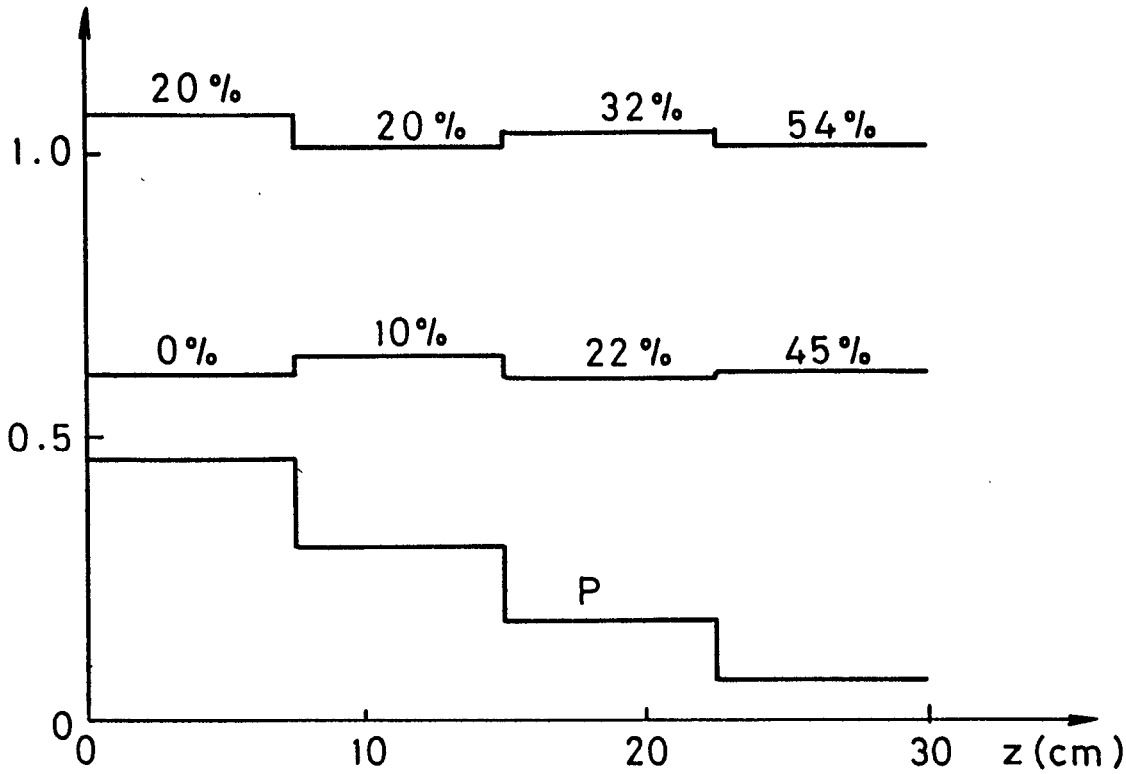

Fig. 8 Total neutron production per target zone in heterogenously enriched slab target configurations. Enrichments are as shown.

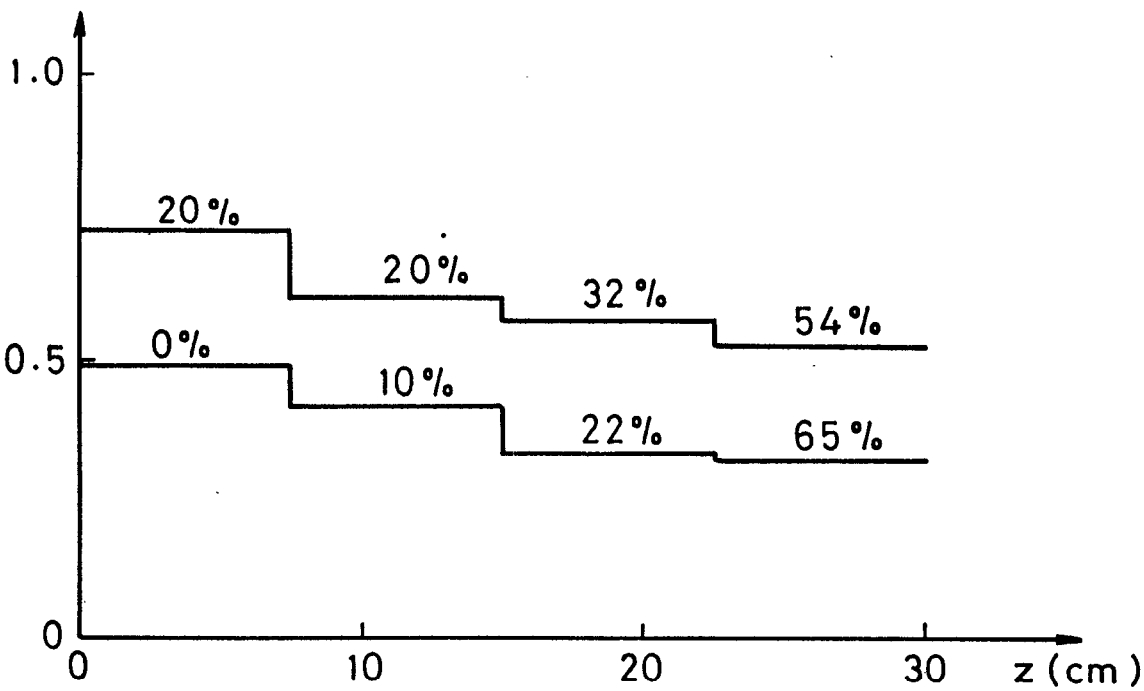

Fig. 9 Net neutron production (per target zone per unit primary source in whole target) for the heterogeneous slab targets.

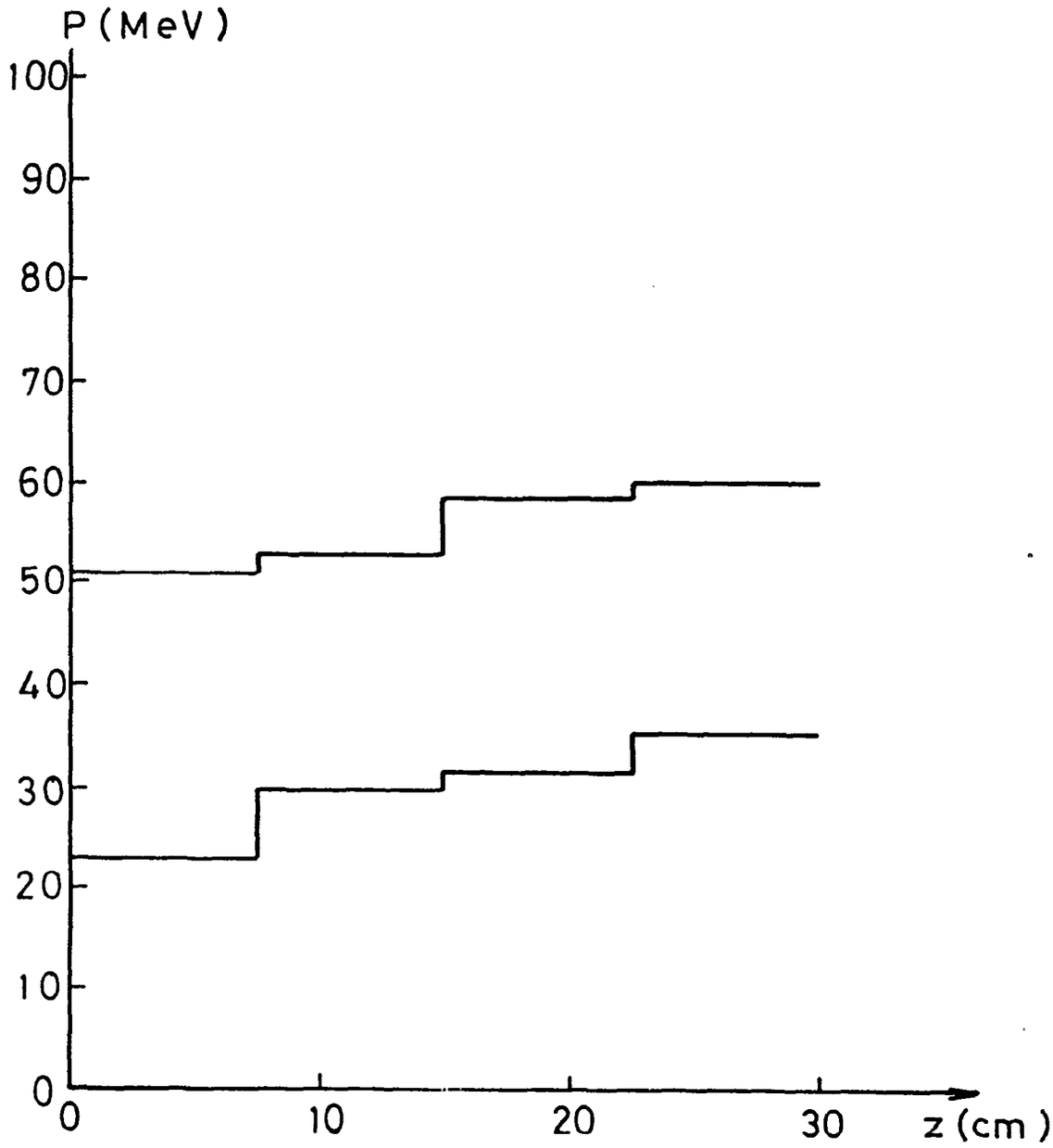

Fig. 10 Estimated power production in heterogeneously enriched slab targets (power in MeV per target zone per primary neutron in whole target.)

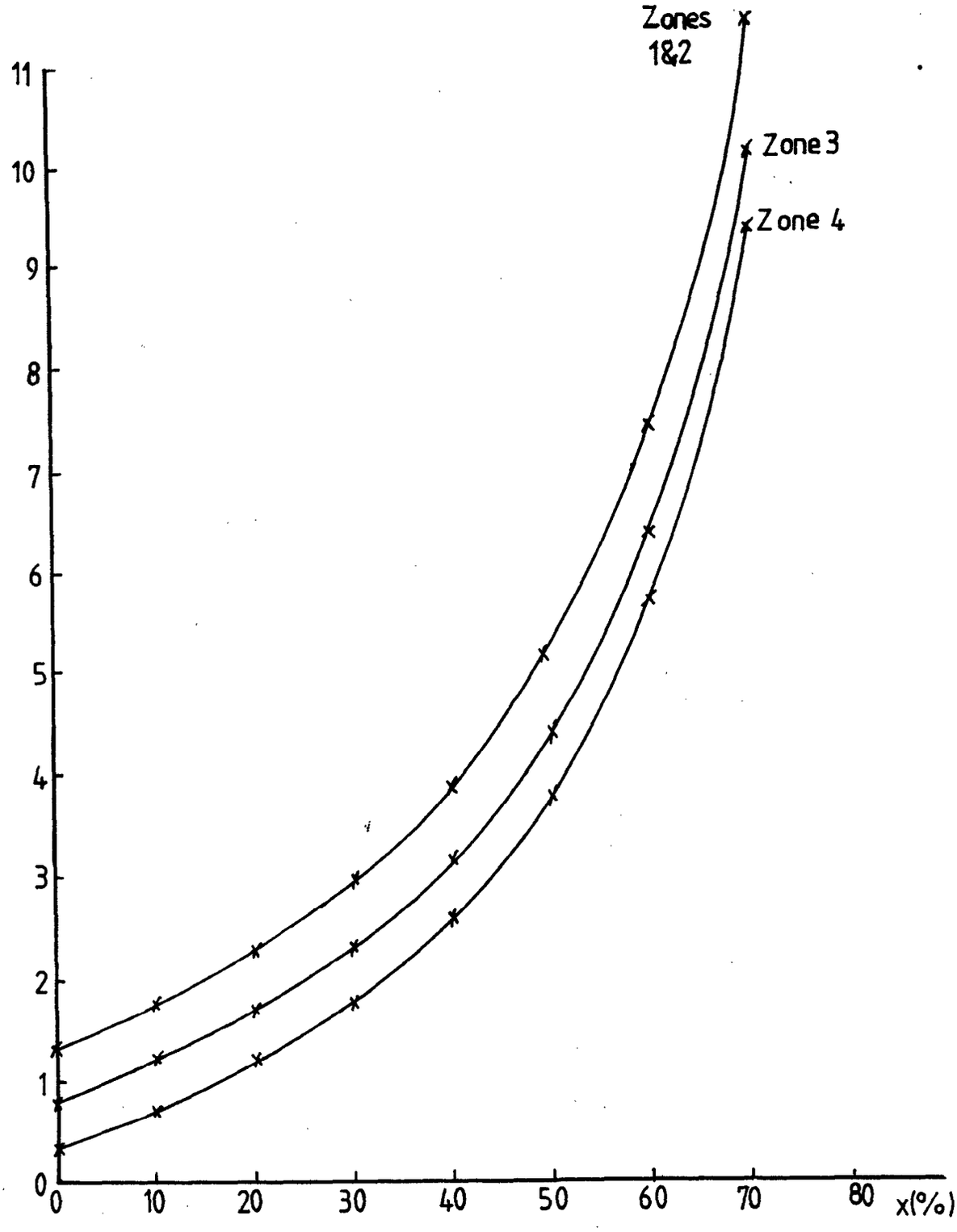

Fig. 11 Power density (in MeV per primary n) in homogeneously enriched targets.

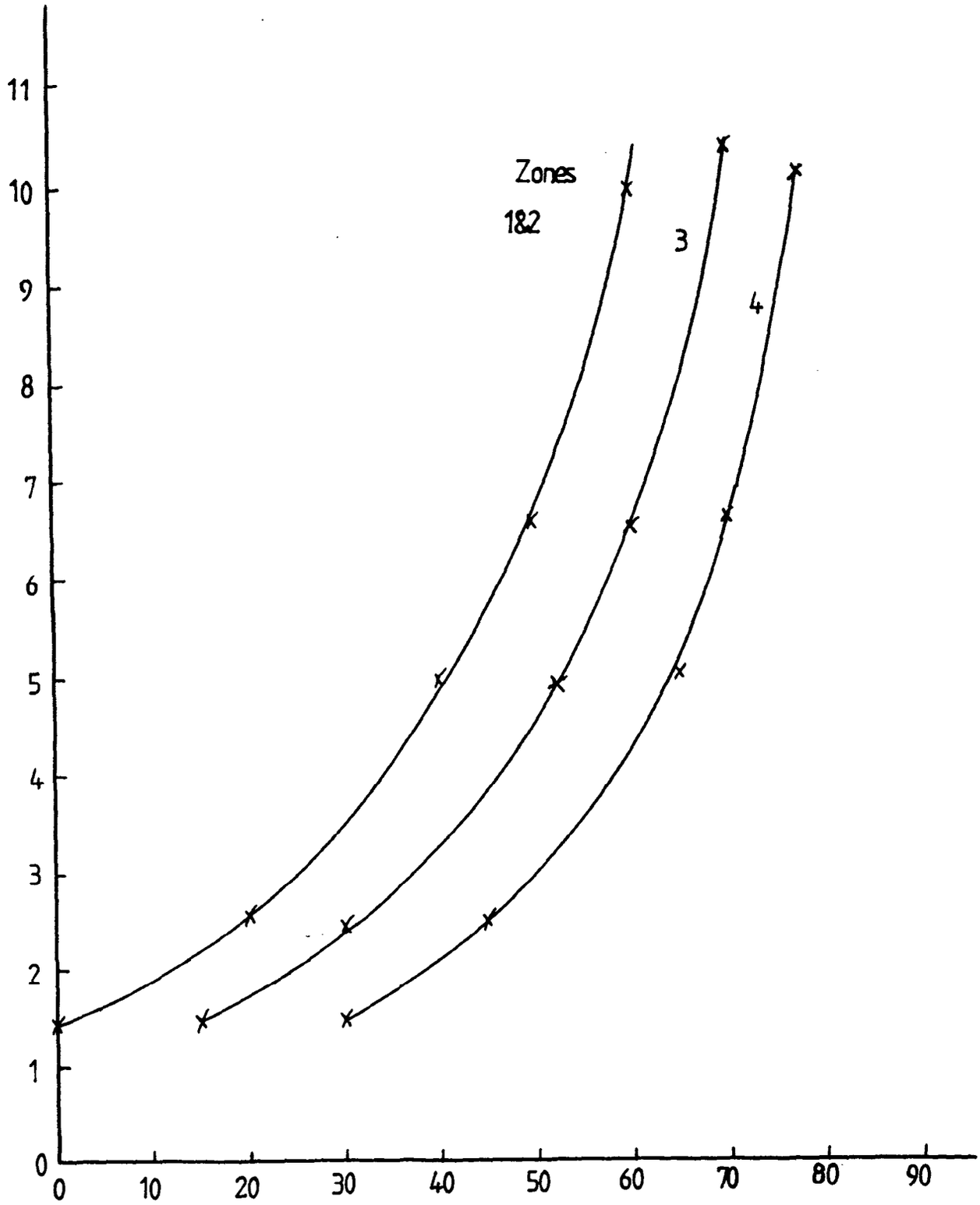

Fig. 12 Power density (MeV) vs enrichment in targets adjusted to produce a uniform power density.

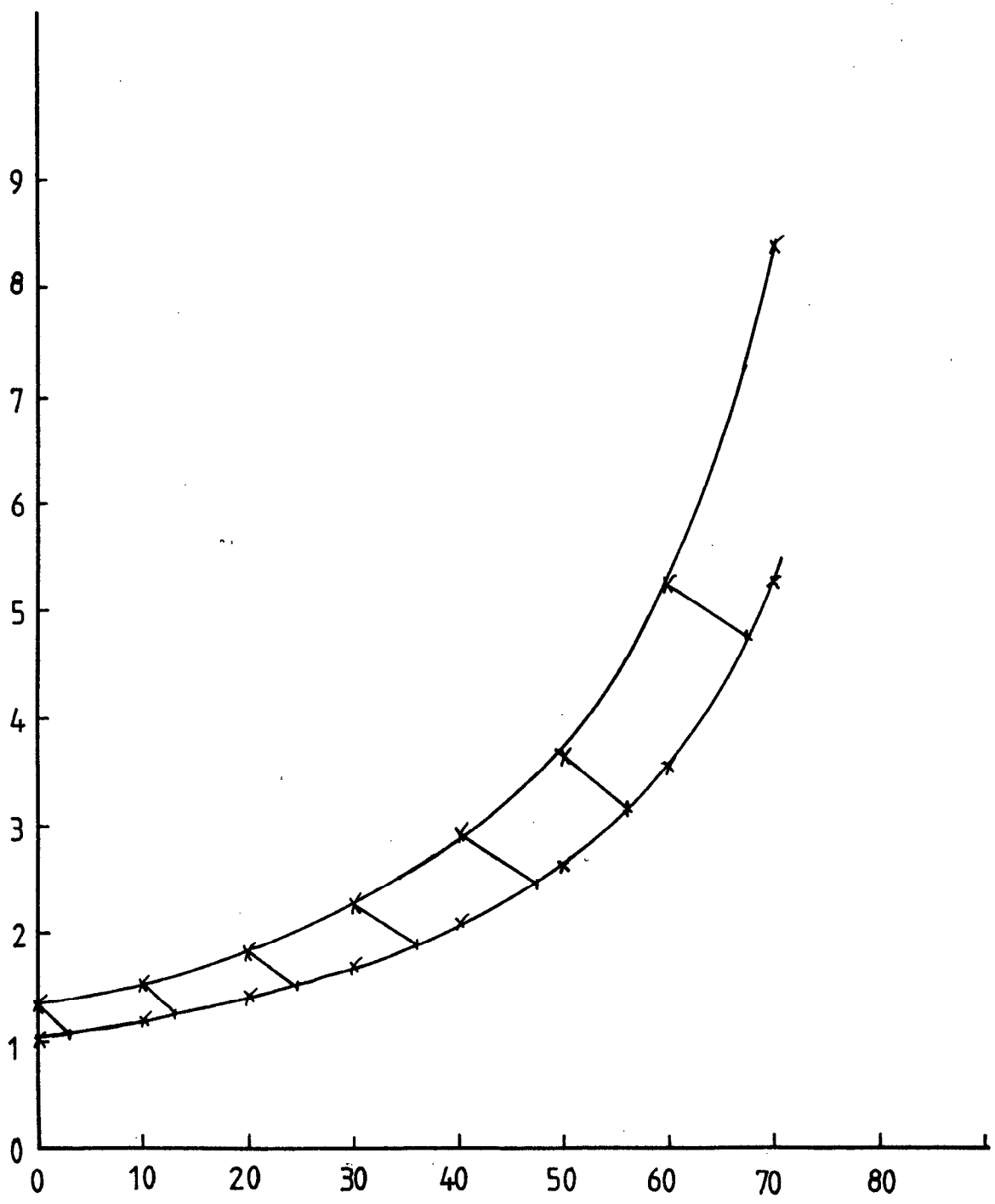

Fig. 13 Net neutron production (per primary neutron)

Upper curve: uniform power density and
Lower curve: uniform enrichment.

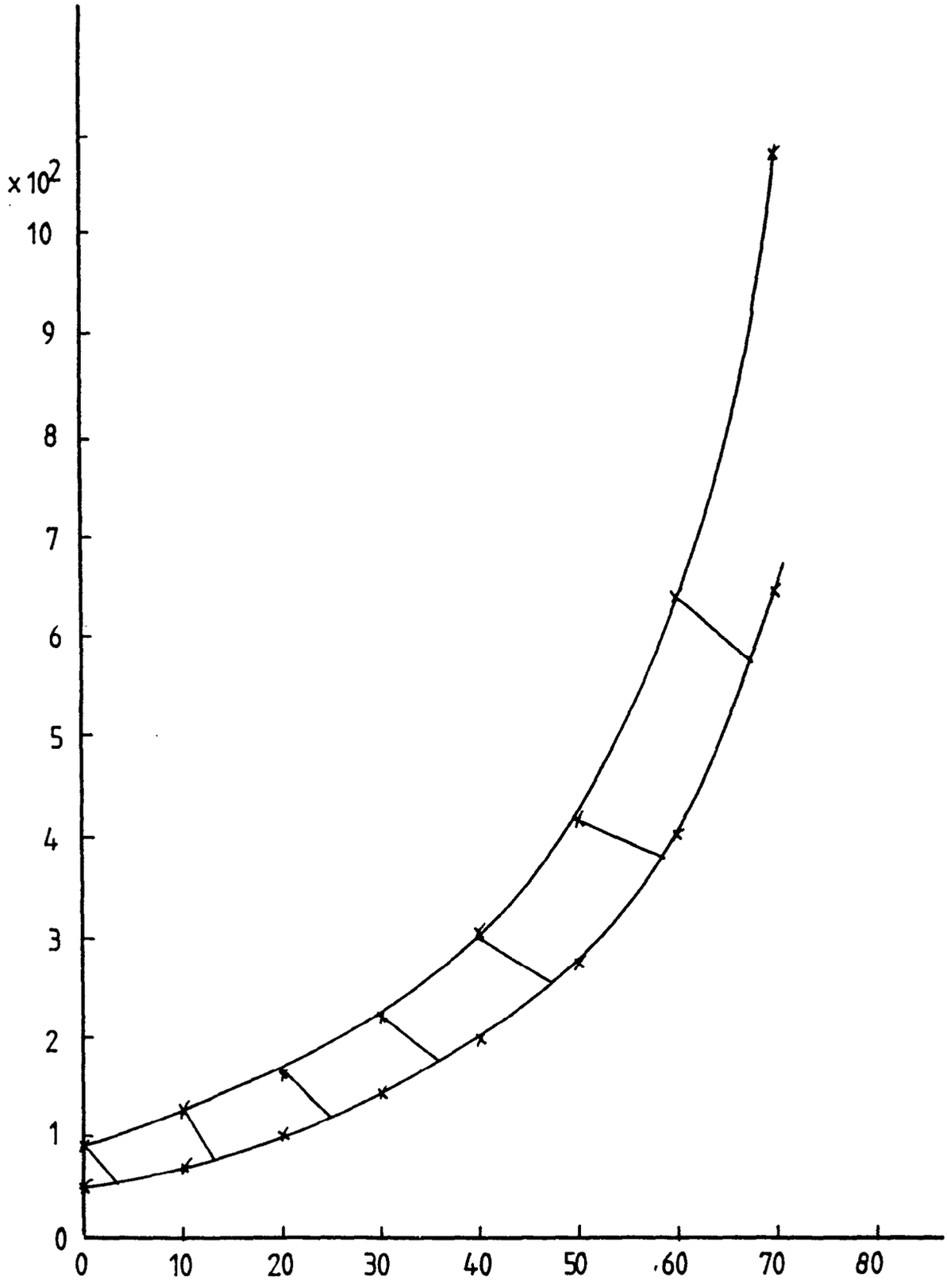

Fig. 14 Estimated power production (per primary neutron).

Upper curve: uniform power density.
Lower curve: uniform enrichment.

A CONCEPT FOR AN eV SPALLATION NEUTRON SOURCE

W. Fischer, SIN, Swiss Institute for Nuclear Research, CH-5234 Villigen

I. The Accelerator and its Beam Parameters

ASTOR is a proposal for an isochronous cyclotron, using the SIN-ring cyclotron as an injector[1]. The 590-MeV proton beam would be injected for further acceleration and be stored by means of the phase expansion effect. A continuous mode of operation without storage could also be provided. In the storage mode the ASTOR acts as an adiabatic debuncher. About 75 % of the circumference of the extraction orbit would be filled with protons in order to leave some time to excite the kicker magnet for a clean extraction of the bunches. The number of protons which can be stored is restricted by Liouvilles Theorem.

Let be:

$\Delta\psi_i$ the phase width of the injected micro-bunches.
$\Delta\psi_f$ the phase width at extraction from ASTOR $\Delta\psi_f < 360^o$.
a the filling factor of the circumference ($a \approx 0.75$).
ΔE_G the energy gain per turn at injection. It should be as low as possible, that is just high enough in order to clear the injection septum.
ΔE_f the total energy spread of the extracted beam

The number of particles which can be stored in one bunch is proportional to

$$N \simeq a \cdot \frac{\Delta\psi_f}{\Delta\psi_i} \cdot \frac{\Delta E_f}{\Delta E_G} \qquad (1)$$

Therefore, according to (1) the number of turns from the present SIN-cyclotron, which can be stacked into one bunch of ASTOR depends essentially on the energy spread, which can be tolerated in the extracted beam for a clean further transport and use of the beam. The peak intensity is thus determined by these conditions.

If we tolerate a momementum dispersion in the final proton beam of $\Delta p/p$ = 0.7 % we can stack 500 turns of the SIN-cyclotron into one bunch of ASTOR. The following beam parameters then follow:

Energy		2 GeV
Current (time averaged)		300 μA
Pulse length		240 nsec
Repetition rate		1.5 kHz
Peak intensity		$1.2 \cdot 10^{12}$ P/pls
Beam size:	radial	30 mm
	vertical	8 mm

The repetition rate can be decreased - however, only at the expense of time averaged current and hence not in favor of the peak intensity.

II. A "High" Energy Neutron Source and its Physics

If we insist to use the pulsed neutron source at ASTOR with the highest possible average beam current, we have to restrict the applications (and the optimization) of this facility to neutron energies $E \geqslant 1$ eV. According to the distance-time velocity plot (Fig. 1) for the neutrons, frame overlap problems for neutrons with lower energies are obvious. From the scientific point of view the following questions arise:

a) Are there any physics (or more generally - scientific experimental) investigations which should be treated preferentially with neutrons of energies $E \geqslant 1$ eV?

b) Are there - for such cases - simpler and/or more powerful alternatives?

An answer to the first question can be obtained by looking at the basic kinematics of a typical neutron scattering event[2]. Let be

E_0 the energy of the incident neutron
θ the scattering angle in the lab.-system
$\hbar\omega$ the energy transfer to the scattered neutron
Q the momentum transfer.

Then, we have

$$\frac{\hbar^2 Q^2}{2m} = 2E_0 + \hbar\omega - 2(E_0^2 + E_0\hbar\omega)^{1/2} \cos\theta \qquad (2)$$

From (2) we recognize that the access to regions of

a) high energy transfer and low momentum transfer

and

b) high momentum transfer

are favored by a high energy of the incident neutron. The first region is relevant for investigation of e.g. Phonon Dispersion, Molecular Vibrations and Magnetic Excitations. Measurements in the second region determine e.g. Short Range Correlations of scattering centers in liquids. The basic principles of neutron scattering for these domains are summarized in the tables I - III.

Figure 2 shows the kinematical regions (energy-momentum transfer), which can be investigated by the various methods applied for research of condensed matter. We observe that the region a) mentioned above is just enclosed by the regions which are considered to be favorably treated by means of light and X-ray scattering. Hence the application of neutron scattering in this domain is possibly in competition with corresponding experiments at synchrotron light sources. The competitivity depends then clearly on the qualities of the sources and on the state of the art of the instrumentation.

The development of scattering instruments using these higher energy neutrons is still in its infant stage. A typical type of instrument is the resonance spectrometer, which has been discussed at ICANS'meetings[3]. Therefore, instead of proceeding along that line we would rather like to make some guess, how a neutron source with high repetion rate could look like.

III. The Neutron Source

A 'low' frequency pulsed neutron source consists of a spallation target and a small moderator usually containing hydrogen. In order to increase the neutronic coupling between the target and the moderator, a reflector surrounds the latter. Normally the moderator is decoupled from the reflector suppressing the backflow of thermal neutrons into the moderator and hence dumping off the tail in the neutron pulses. Cooling of the moderator has two favored consequences:

a) The slowing down nature (1/E) of the neutron spectrum is extended to lower energies.
b) Neutron pulses become shorter for neutrons in the ambiant temperature region.

For a 'high' frequency pulsed source with emphasis of neutrons with higher energies (E>1 eV) the criterias are somewhat different. No thermal neutrons (not even lower epithermals) should be emitted by the moderator into the beam tubes. This can be achieved by the following means:
a) Encloser of the moderator (including the emitting surface) by proper absorbing materials. A sandwich of Au, Rh and Cd layers might be sufficient (Fig. 3).
b) The size of the moderator has to be carefully optimized for high leakage rate of neutrons with the wanted energy. That is the maxwellian has to be minimized - an absorbed neutron is a lost neutron and increases the energy deposition in the absorbing layer. The moderator will therefore be rather small.
c) Heterogeneous instead of surface absorption might be considered in order to deposit the resulting heat more evenly over the moderator volume.

1. Moderator Size

In order to estimate the size of a moderator let us make a guess of the migration area for a neutron which is slowed down to (say) 5 eV. The Fermi age can be written as[4]

$$\tau(E) = \frac{2}{\xi(1-2/3A)} \int_{E}^{E_Q} \lambda_S^2(E') \frac{dE'}{E'} \qquad (3)$$

ξ is the average log.-energy loss per collision, A the atomic mass of the moderator and λ_S the mean free path of the neutron. The average energy of the source neutrons is $E_Q \simeq 2$ MeV. The migration area is

$$r^2(E) = 6\ \tau(E) \qquad (4)$$

In the following table τ [cm^2] is given for an energy of E = 1.46 eV (Indium-resonance) and an estimate scaled up to E = 5 eV for various moderating materials

	E = 1.46 eV	E = 5 eV
H_2O	27 cm^2	22 cm^2
D_2O	109 cm^2	90 cm^2
Be	80 cm^2	66 cm^2
C	313 cm^2	258 cm^2

An estimate for the thickness of a slab formed moderator is

$$D \simeq (1/3\ r^2)^{1/2} \qquad (5)$$

That is 6.6 cm for H_2O - and 11.5 cm for Be. The surface of the moderator is given by the size of the beam tubes - 100 - 200 cm^2.

2. Moderation Time and Pulse Shape

An analytic solution of the slowing down integral equation can be given for the space independent case, that is far an infinite moderator medium. The corresponding pulse shape of the neutrons for an incident δ-shaped source pulse can serve as a guide line for our discussion.

The energy and time dependence of the pulse is given by[4)]

$$N(E,t) \simeq \frac{1}{2E} \frac{y^{2/\gamma}\, e^{-\gamma}}{\Gamma(2/\gamma)} \qquad (6)$$

where

$$\gamma = \begin{cases} 1 & \text{for atomic mass } A = 1 \\ \frac{4A}{3} & \text{for large atomic mass } A \end{cases}$$

and

$$y = \frac{\xi}{\gamma} N \cdot \sigma_{tot} \cdot (vt)$$

v = v(E) is the neutron velocity for energy E. The other parameters have the usual meaning. Figure 4 shows the pulses and their energy dispersion in a Be- and an H_2O-moderator. In view of the importance of the pulse width for the figure of merit in time of flight experiments it is likely that the moderator with a high hydrogen content will be favored.

For the H_2O-moderator the pulse width due to moderation is 1 μsec or longer. The contribution to the pulse length of the neutrons, due to the pulse width of the proton pulse (240 nsec), is therefore not significant.

3. Coupling of the moderator to the target

In order to keep the background of high energy neutrons as low as possible, a wing geometry for the target-moderator arrangement (Fig. 5a) is usually chosen. Due to the small thickness of our moderators their coupling to the target would be particularly weak, just for this geometry. A reflector surrounding the moderator could of course improve the coupling. However, the resulting pulse lengthening has, also carefully to be considered. Furthermore, if we want to avoid an increase of the moderating power of the system a heavy material has to be chosen as a reflector.

Let us make some estimates with a lead reflector. From the investigation for SNQ at mock-up experiments[5], we know that a lead reflector should have side length of 30-40 cm. We assume that the tail of the neutron pulse shows an exponential behaviour with a time constant essentially given by the reflector

$$\tau_R^{-1} = \alpha = v\Sigma a + DvB^2 \qquad (7)$$

B^2 is the buckling of the reflector

$$B^2 = \pi^2 \, [3(\tfrac{1}{\ell})^2] \qquad (8)$$

For the neutron velocity we chose $v \simeq 3.13$ cm/μs which corresponds to an energy of 5 eV. The diffusion constant is approximated by $D = 1/3\Sigma_S$ with $\Sigma_S \simeq 0.3\ cm^{-1}$. We then obtain a relaxation time for the reflector

$$t_R \simeq 15\ \mu s$$

Hence, an efficient reflector dominates the decay time of the neutron pulse and therewith spoils the resolution at the instrumentation. If we have to renounce a reflector, the only means to increase the target-moderator coupling is the choice of a slab geometry. With this arrangement the instruments view through the thin moderator directly onto the target. This leads to a rather untolerable background of high energy neutrons. A possible way out is the Flux Trap Geometry (Fig. 5b). This geometry has been proposed for LANSCE at Los Alamos[6]. This split target geometry increases the accepted solid angle for the moderators and therefore their coupling to the target, without suffering too much from penalties of background.

Of course, for a reasonable optimization of such a target-moderator system careful bench-marking - experimental as well as computational - is needed.

REFERENCES

1) W. Joho
Proceedings of Particle Accel. Conf. 1983
Santa Fe, USA

2) P. Egelstaff
Proc. ICANS VII 1983
Chalk River Nucl. Lab.

3) R.J. Newport, M.P. Pauli, V.T. Pugh, R.N. Sinclair
A.D. Taylor and W.G. Williams
Proc. ICANS VIII 1985

R.K. Crawford
The IPNS Resonance Detector Spectrometer
Proc. ICANS IX 1986 (in preparation)

4) K.H. Beckhurts, K. Wirtz
Neutron Physics
Springer Verlag 1964

5) Realisierungs-Studie zur Spallations-Neutronenquelle
Teil III; Band 2
Editor: G.S. Bauer

6) G.J. Russell, C.D. Bowman, E.R. Whitaker, H. Robinson
and M.M. Meier
Proc. ICANS VIII 1985 Vol. I
Rutherford-Appleton Lab.

X-RAYS	$\lambda \sim$ Å	$E \sim 100$ keV $\Delta E \sim$ meV-μeV	$\frac{\Delta E}{E} \sim 10^{-8}-10^{-11}$!
LIGHT	$\lambda \sim 10^{3}$ Å !	$\Delta E \sim$ meV-μeV	POSSIBLE
NMR RAMAN-SCATT.	LOCAL PROBING NO LONG RANGE CORRELATION		
NEUTRONS	$\lambda \sim$ Å	$E \sim 10$ meV $\Delta E \sim$ meV-μeV	$\frac{\Delta E}{E} \sim 10^{-1}-10^{-4}$ (OK)

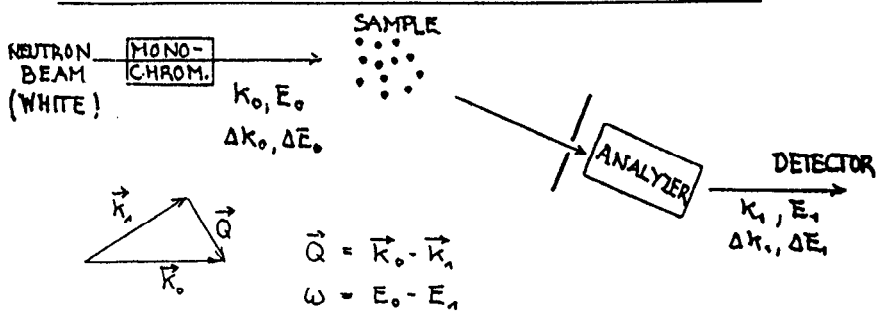

$$\vec{Q} = \vec{K}_0 - \vec{K}_1$$

$$\omega = E_0 - E_1$$

$$\boxed{\frac{d^2\sigma}{d\Omega\, dE_1} = \frac{K_1}{K_0} S(\vec{Q}, \omega)}$$

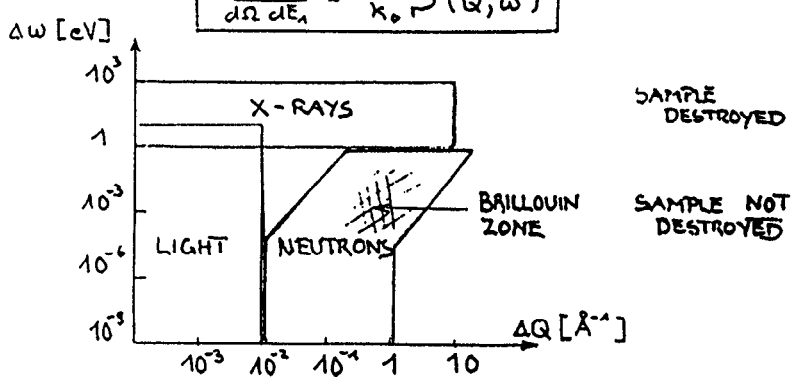

Table I

1) The wave length of X-rays is properly matched to the distance of atomic objects in condensed matter. Due to their high energies an incredilary high energy-resolution has, however, to be demanded for dynamical investigation of matter. For light scattering the energy resolution can be achieved but the wave length is matched to much bigger objects only. With thermal neutrons, both the wave length and the energy have the right order of magnitude in order to map the Brioullin-zone of solids.

2) The observable in a neutron scattering experiment is the differential cross section with respect to the scattering angle and the neutron energy. This cross section is proportional to a structure function of momentum- and energy-transfer, which contains all the information.

NEUTRON SCATTERING

A TOOL FOR CONDENSED MATTER RESEARCH

ESSENTIALS : L. van Hove Phys. Rev 95 (1954) 249

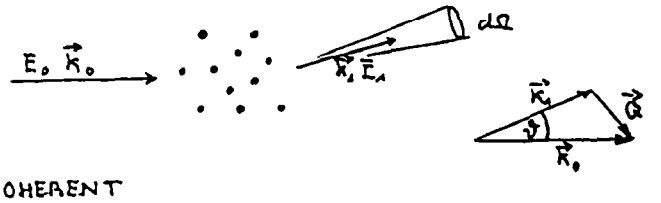

1) COHERENT

$$\frac{d^2\sigma_c}{d\Omega\, d\omega} = N \frac{k_1}{k_0} (\bar{b})^2\, S(Q,\omega)$$

2) INCOHERENT [ISOTOPES, SPIN-FLIP]

$$\frac{d^2\sigma_i}{d\Omega\, d\omega} = N \frac{k_1}{k_0} \left\{ \overline{b^2} - (\bar{b})^2 \right\} S_i(Q,\omega)$$

$$\frac{\hbar^2 Q^2}{2m} = 2E_0 + \hbar\omega - 2\left(E_0^2 + E_0\hbar\omega\right)^{1/2} \cos\vartheta$$

$$S(Q,\omega) = \frac{1}{2\pi} \int dt \int dx^3\, G(\vec{x},t)\, \exp[i(\vec{Q}\vec{x} - \omega t)]$$

$$S_i(Q,\omega) = \frac{1}{2\pi} \int dt \int dx^3\, G_s(\vec{x},t)\, \exp[i(\vec{Q}\vec{x} - \omega t)]$$

INFORMATION : $G_s(\vec{x},t)$ ATOMIC MOTION (DIFFUSION)

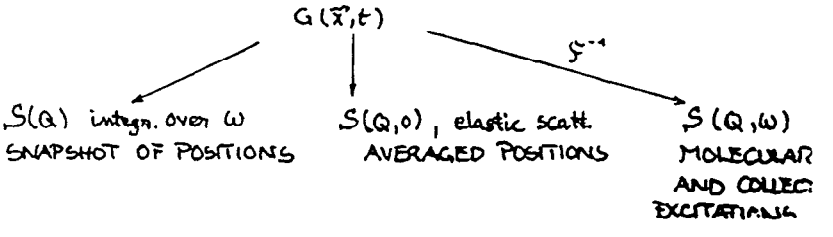

Table II

Since the elementary scattering length of neutron at different isotopes is usually different and also generally spin dependent, the scatter coherently as well as incoherently at condensed matter. Hence a coherent and an incoherent structure function can be defined. They contain different information. Both structure functions are the space-time Fourier transforms of correlation functions between the scattering centers.

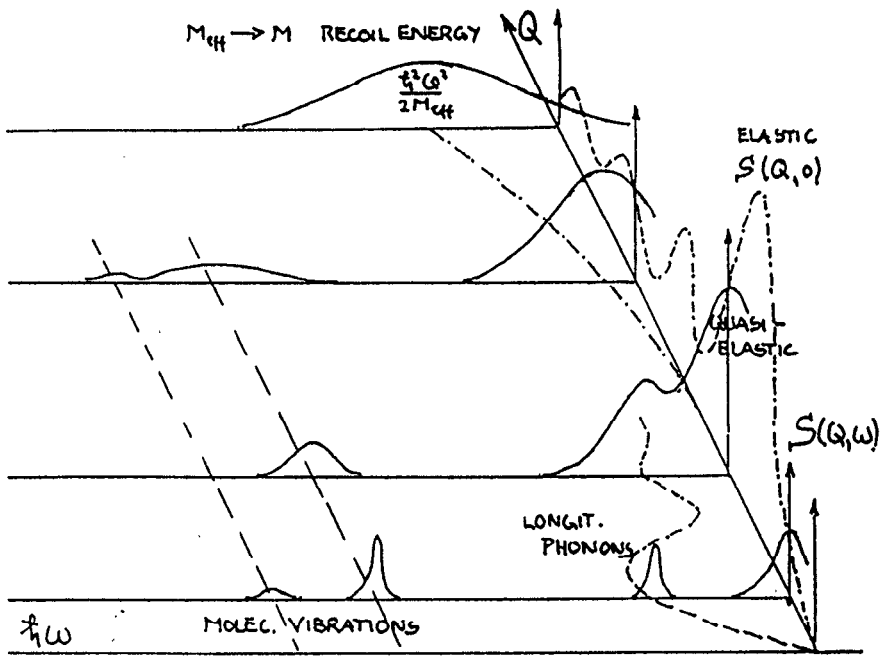

$$S(Q) = \int_{-\infty}^{+\infty} d\omega\, S(Q,\omega) \quad \text{———} \quad S(Q) = 1 + \frac{4\pi\rho}{Q}\int_0^\infty \{g(r)-1\}\, r \sin(Qr)\, dr$$

$$g(r) = 1 + \frac{1}{2\pi^2 N r}\int_0^\infty Q\,\{S(Q)-1\}\, \sin(Qr)\, dQ$$

SHORT RANGE CORRELATION } ——— DATA AT HIGH Q [RECOIL EFFECTS]

PHONON DISPERSION
MOLECULAR VIBRATION } ——— HIGH ENERGY TRANSFER ($\hbar\omega$) AT LOW Q

ALSO IN SOLIDS
MAGNETIC EXCITATION } MAGN. FORM FACTOR HIGH ENERGY TRANSFER

Table III

Those regions in the kinematical plane and the corresponding dynamical phenomena, which could favor higher energy (then thermal) neutrons for their investigation are emphasized.

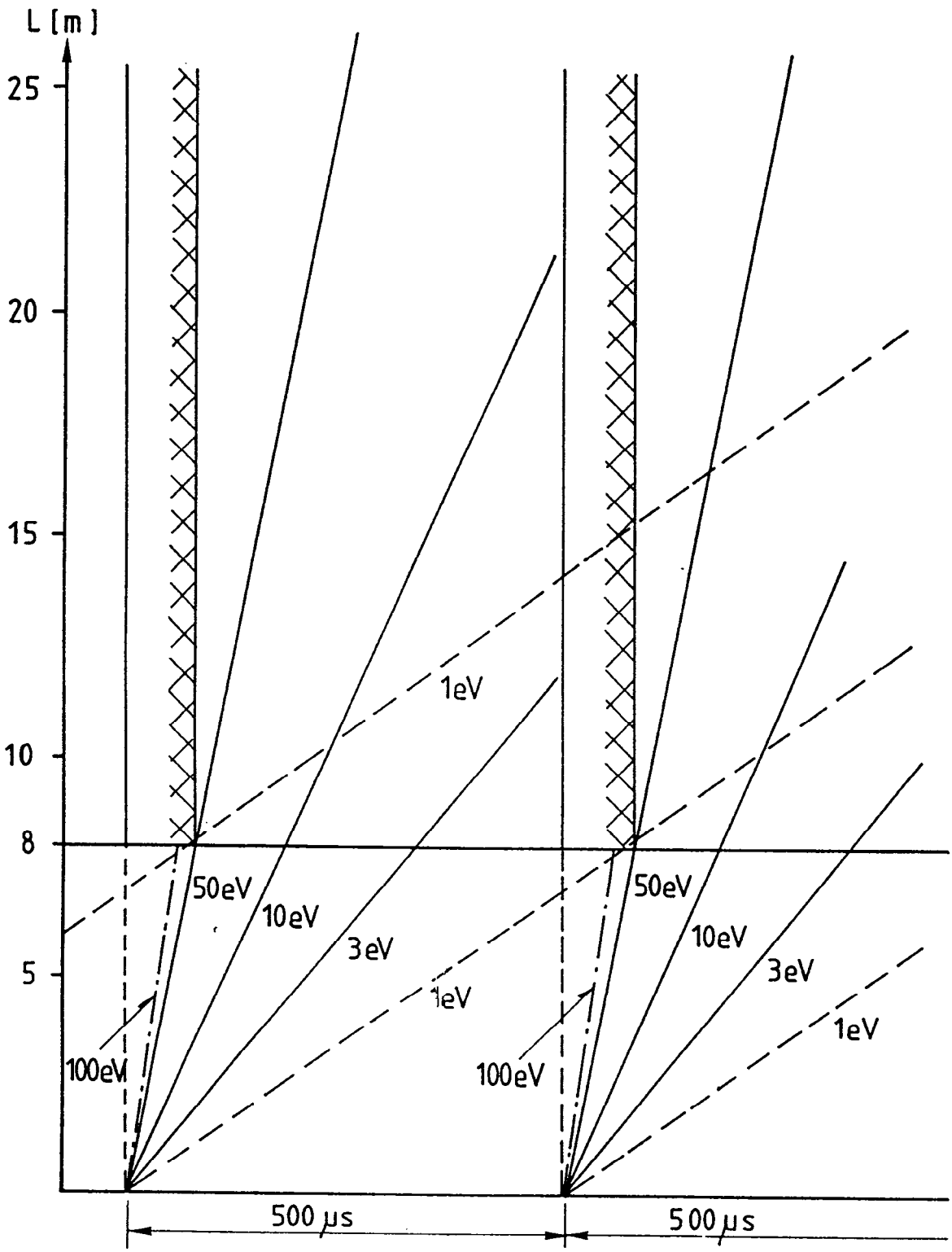

Fig. 1 Distance-time velocity plot for neutrons with a pulse repetition frequency of 2 kHz.

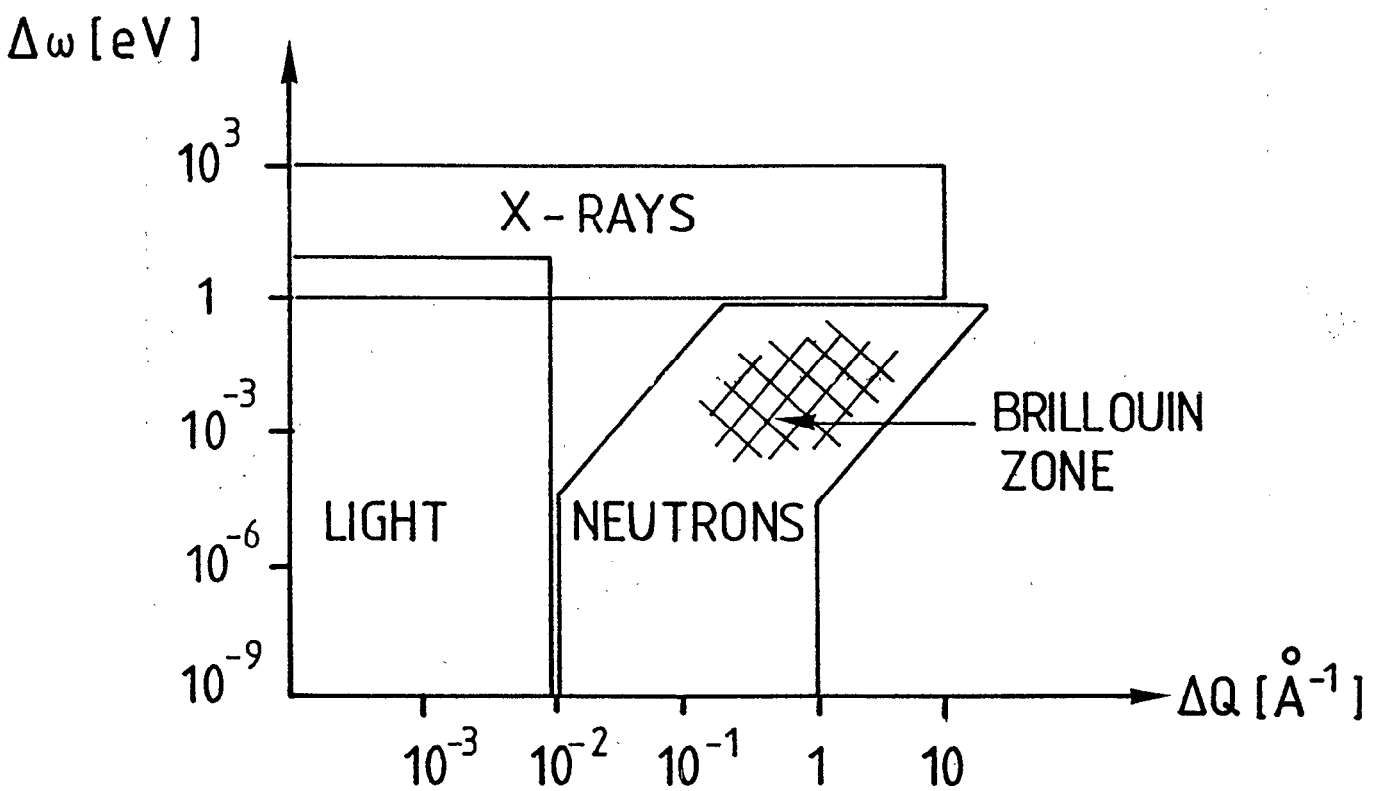

Fig. 2 Region of energy-momentum transfer favored by various experimental methods.

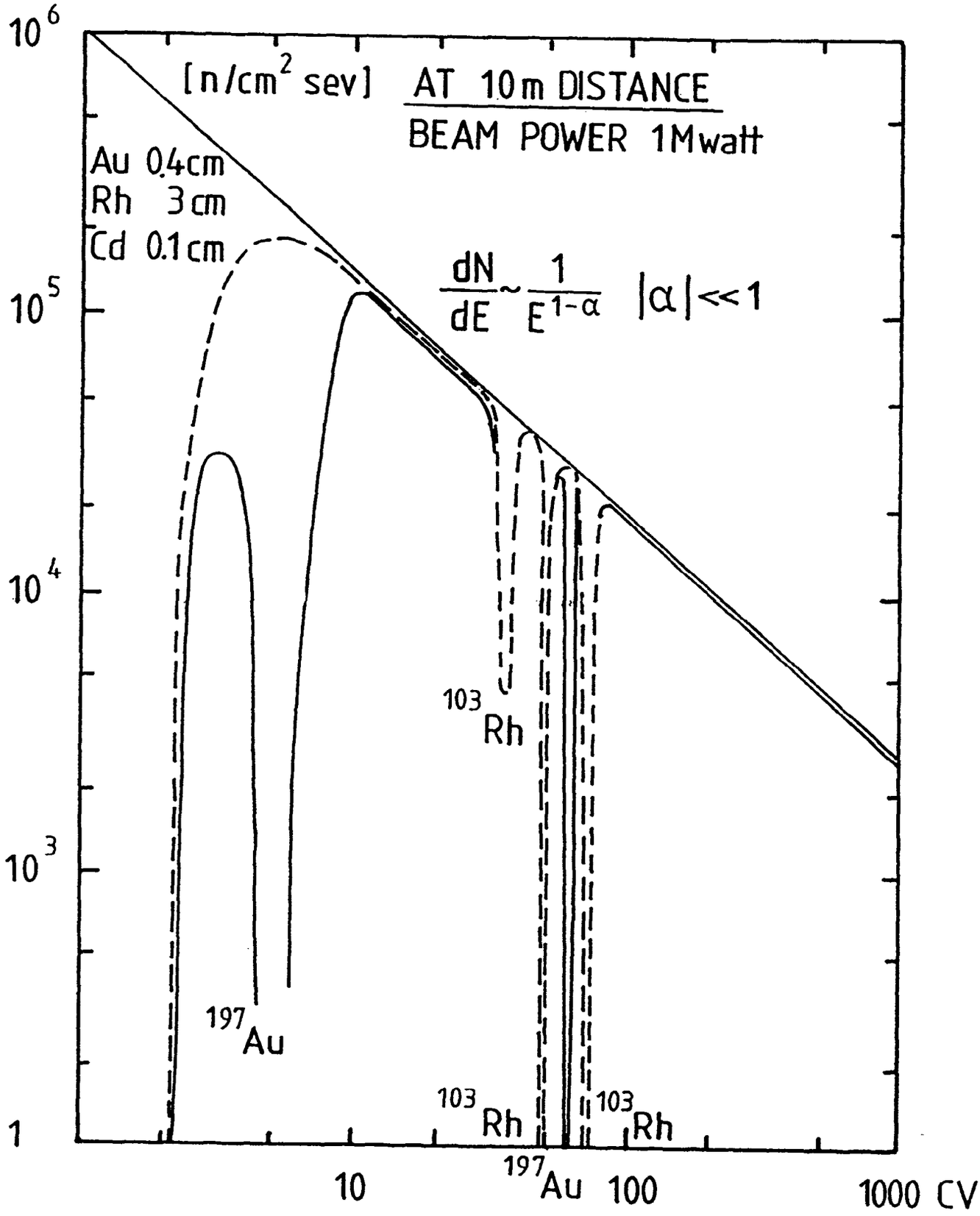

Fig. 3 Upper slowing down spectrum taylored by various absorbers.

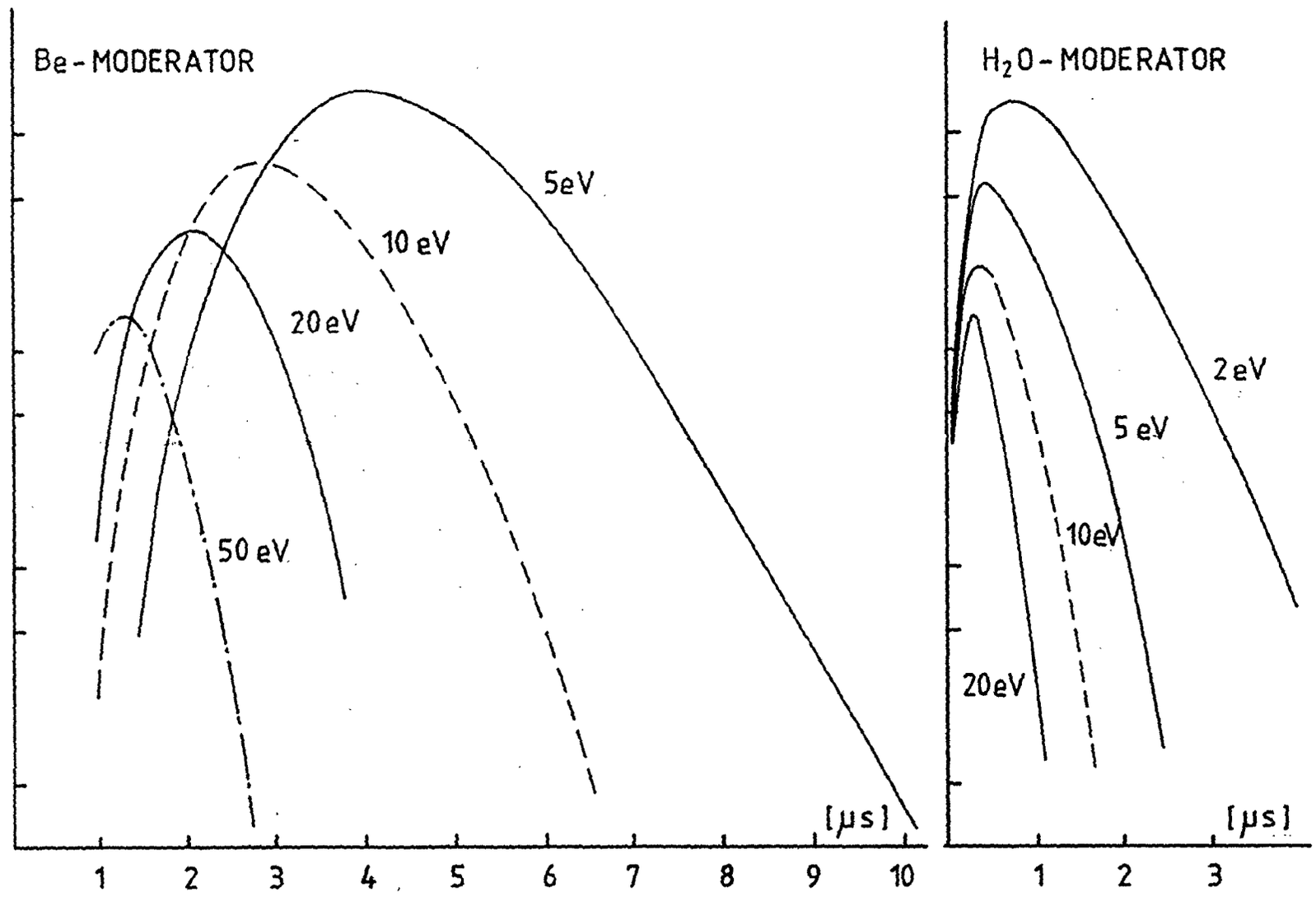

Fig. 4 Neutron pulses and their energy dispersion from a Be- and an H_2O-moderator.

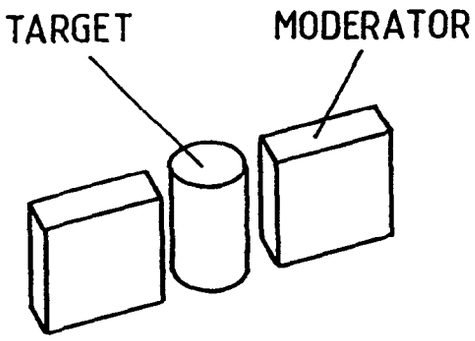
TARGET
MODERATOR

Fig. 5a

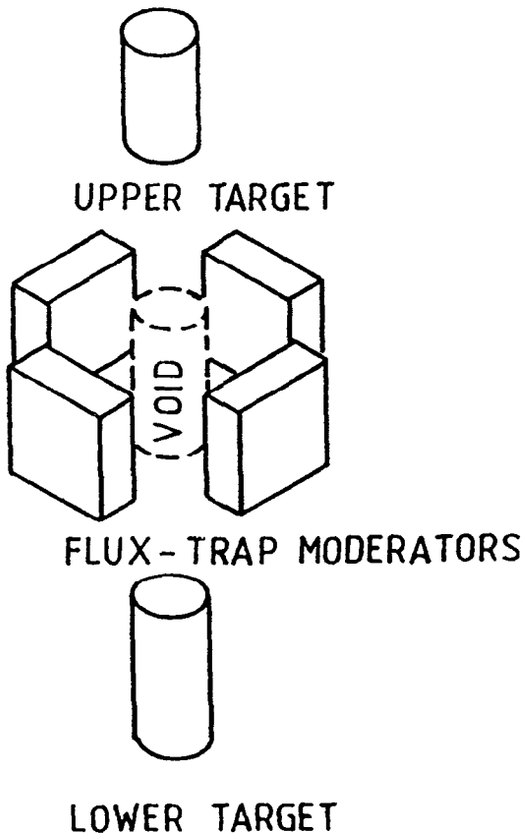
UPPER TARGET
VOID
FLUX-TRAP MODERATORS
LOWER TARGET

Fig. 5b

ICANS IX

INTERNATIONAL COLLABORATION ON ADVANCED NEUTRON SOURCES

22-26 September, 1986

EXPERIMENTAL AND THEORETICAL ANALYSIS OF THE HIGH ENERGY DEEP PENETRATION EXPERIMENT AT WNR - LOS ALAMOS (KFA/IRE - LANL/P9 COLLABORATION)

W.B. Amian, H. Schaal, V. Drüke, P. Cloth, D. Filges and N. Paul
Institut für Reaktorentwicklung, Kernforschungsanlage Jülich
Postfach 1913, D-5170 Jülich Germany

I. INTRODUCTION

In this paper a deep penetration experiment conducted at the Los Alamos WNR facility's Spallation Neutron Target /1/ is compared with calculations using the HETC/KFA-1 /2/, and ANISN /3/ codes installed at KFA-IRE.

For such problems the most reasonable technique to detect neutrons experimentally is by counting decaying residual nuclei of high energy interactions with suitable target materials. Especially for accelerator environments, spallation reactions on copper have been proposed by Routti /4/ as a means to extend the known threshold-foil technique to higher hadron energies. The yield cross sections for many spallation products have a threshold type energy dependence with threshold energies of tens or hundreds of MeV.

The problem with these reactions, however, is that the spallation yield cross sections are basically not known above 20 MeV. While the experiments can reveal clearly the exponential decrease of reaction rates with shielding thickness without any prior knowledge of cross sections, the quantitative comparison

between experiment and calculation suffers from the lack of reliable cross section data for these spallation yield cross sections.

We will demonstrate this deficiency by a comparison of experimental and theoretically determined production cross sections for some isotopes from natural copper. For more detailed information see Ref. /5/.

II. EXPERIMENTAL

Foils of 30 mm diameter and 1 mm thickness were irradiated inside the WNR target 1 bulk shield. They were imbedded into a stringer assembly that was inserted into flight path 5 of the facility. Foil materials studied were copper, cobalt, and nickel, all of natural isotopic composition. The stringer assembly loaded with iron foil containers and part of the WNR bulk shield are shown in Figure 1 and Figure 2, respectively.

During irradiations, ^{3}He-detector counts were recorded to correct for time variations of the proton-beam intensity and the resulting neutron-flux intensity. The ^{3}He detector was positioned in a polyethylene cylinder at the flight path's end (Fig. 1). This position was chosen to prevent interference from neighbouring experiments. The irradiations were performed with a tungsten target (4.45 cm diameter, 24 cm length) and a beryllium reflected water moderator assembly in place. Typical proton beam currents were approximately 3 μA.

After irradiations the reaction products in all foils were determined directly by counting in Ge(Li) gamma-ray spectrometers. All foil activities were corrected for self absorption in the foils, for decay during irradiation utilizing the recorded ^{3}He-detector counts, and for decay during counting. They

are for the time at the end of bombardment. The final reaction rates are normalized to the number of primary protons interacting in the target and the number of foil nuclei.

These reaction rates have been multiplied by the distance to the target squared and have been plotted versus depth in the shield. Results for some spallation reactions on copper are shown in Fig. 3 and 4.

III. HETC AND ANISN CALCULATIONS

Combined Monte Carlo and deterministic transport calculations were performed for the experimental arrangement of Fig. 2 to calculate the reaction rates for the measured reactions on copper. Two important simplifications can be done due to the fact that nearly all reactions used in the experiments have threshold energies above 15 MeV:

1. It is not necessary to follow neutrons in energy below 15 MeV, i.e. it is adequate to use only the Monte Carlo code HET/KFA-1 /2/ with a cut-off energy at 15 MeV and neglect subsequent low enery transport calculations.
2. It is allowed to simplify the complex moderator-reflector system surrounding the target (see Fig. 2) and simply describe it as a homogeneous beryllium cylinder, because in the shielding context the entire system is of interest only for removing high energy particles. The low energy particles stemming from moderations will not be measured by the threshold detectors and can therefore be neglected in the shielding calculations.

This simplifies our shielding calculation as compared to target calculations considerably.

Calculational Procedure

The particle histories were calculated with HET/KFA-1 down to the lower energy limit of 15 MeV. The histories were started by incoming protons of 800 MeV hitting the top surface of the cylindrical tungsten target (Fig. 5). The particle fluxes inside the shield were determined in two different ways:

1. Straight forward Monte Carlo with HETC and SIMPEL analysis. The code SIMPEL of the system /2/ derived neutron fluxes and proton fluxes at different depths inside the shield using track-length estimators.
2. HETC-ANISN surface coupling procedure via SIMPEL. Close to the inner surface of the bulk shield a spherical segment was defined serving as a coupling surface between SIMPEL and ANISN /3/. Here SIMPEL calculated a neutron surface source, which was handed over to the one-dimensional transport code ANISN. Starting with this source, ANISN calculated the neutron fluxes inside the shield in spherical geometry. The coupling procedure is described in /5/. The transport cross sections used for the calculations were taken from the LANL library /6/.

Both HETC and HETC-ANISN coupling calculated fluxes were folded with corresponding reaction cross sections to obtain reaction rates. Two sets of cross sections were generated using the RUDSTAM formulas /7/ and the code ALICE /8/, respectively.

Geometry

The geometrical layout for the HETC calculations was described using concentrical cylinders (see Fig. 5) with the following zones and materials:

Zone 1 was the tungsten target, zone 2 the beryllium reflector - the simplifying assumption for the moderator-reflector system. The radius of this reflector was set to the actual thickness in the line of sight in the experimental arrangement for FP5 from the target center to the surface of the stringer. Zone 3 is a void region and zone 4 is the shield which consists of a mixture of iron and concrete.

For the flux estimation from HETC histories SIMPEL used track length estimators which were rings of 20 cm heights and thicknesses of about 3 cm. These volume detectors are denoted A, B, C in Fig. 5. The advantage of such ring shaped detectors is the strongly enhanced statistics due to the azimuthal symmetry as compared to small detector boxes.

The coupling surface of the neutron surface source used by ANISN (denoted SQ in Fig. 5) was a spherical segment with radius 122 cm. This segment was placed entirely into the bulk shield. This geometry is not azimuthal symmetric. For the ANISN transport calculations beyond the coupling surface the bulk shield was assumed to be composed of iron only with nuclide density 8.44×10^{22} cm^{-3}. This is assumed to be the better approximation to the environment of the monitor foils inside the stringer than the iron/concrete mixture of the bulk shield.

IV. RESULTS

HETC and the HETC-ANISN coupling calculate particle fluxes for energies between 800 MeV and 15 MeV at different depths inside the shield. The proton flux is negligable as compared to the neutron flux as Table I shows. Therefore, protons have been neglected in all calculations following. Looking at the depth dependence in Table I, a comparison of the HETC-ANISN coupling and HETC results shows, that the high energy flux as calculated

by HETC is not decreasing as fast as predicted by the HETC-ANISN coupling while going further into the shield. The reason for this behaviour could be that for the HETC calculation a mixture of iron and concrete with an iron number density of 7.7×10^{22} cm^{-3} was assumed, while for the coupling calculation pure iron with a number density of 8.44×10^{22} cm^{-3} was used to account for the true material composition inside the stringer.

Flux Spectra

Fig. 6 shows a comparison of the flux spectra calculated by HETC at two different depths inside the shield. At 23 cm the spectrum is harder than at 103 cm depth. The reason could be that the mixture of iron and concrete acts as a moderator. But it should be mentioned that at 103 cm depth the fractional standard deviation values (FSD) for all energy groups of the spectrum are in the range of about 50 percent, indicating bad statistics. To compare the predictions of the spectral behaviour of both procedures the spectrum calculated by the HETC-ANISN coupling and the HETC spectrum are plotted in Fig. 7 at 23 cm depth. We have chosen this position because it is close to the coupling surface SQ in Fig. 5 and good statistics can be obtained with HETC itself. As expected, good agreement between both spectra is obtained. Fig. 8 gives the spectra calculated by the HETC-ANISN coupling at three different depth

In contrast to the spectrum behaviour calculated by HETC (Fig.6), the HETC-ANISN coupling spectrum is harder at 103 cm than at 23 cm depth. Furthermore, Fig. 8 shows that the spectra at 103 cm depth and in 203 cm are nearly identical. Therefore, it can be stated that the HETC-ANISN coupling spectra reach equilibrium very fast.

Reaction Rates

Calculated results that can be compared with the experiments are the threshold reaction rates. They were calculated by folding the group dependent neutron fluxes with reaction cross sections. Reaction rates were generated for two positions at 23 cm and 103 cm. In Table II the calculated and measured rates for the reactions on foils of natural copper are shown. Agreement within a factor of two between measured and calculated reaction rates is found for the Rudstam cross sections. It should be mentioned, however, that both the measured reaction rates and the calculated fluxes contain uncertainties of up to 50 percent (see spectrum results in Figs. 6-8). Much larger differences between measurement and calculation up to more than a factor of 10 are found if reaction cross sections generated by the code ALICE /8/ are used to calculate the reaction rates.

V. DISCUSSION

In comparing experiment and calculation the most serious source of uncertainty are the neutron cross sections for the production of residual nuclei in the monitor foils. It is simplistically assumed that at high energies (above 20 MeV) spallation cross sections for protons and neutrons are identical. The common description of this process as an intranuclear cascade and a subsequent evaporation process is in favour of this ide equal response to both nucleons. Therefore, cross sections for proton induced reactions which are much easier to obtain experimentally than neutron cross sections were compiled and treated like neutron cross sections to calculate the reaction rates at different positions in the shield. Sources of cross sections were the Rudstam /7/ formulas, which are semiempirical parameterizations of experimental results up to 1964, the modifications by Silberberg and Tsao /9/, more recent experiments on

copper targets reported by Orth /10/, Grüttner /11/, Williams /12/ and Greenwood /13/ and, finally, preequilibrium calculations with ALICE /8/.

For one example part of the compilations is shown in Fig. 9. The Silberberg/Tsao cross sections were not included in the plots because their general shape follows Rudstam's curves with up to 50% deviation to both sides. In Fig. 9 the agreement between experiments and ALICE calculations for the production of ^{57}Co from copper is reasonable close to the threshold energy. At higher energies they disagree significantly with ALICE predicting a steep decrease. Rudstam's curve is systematically too low, Silberberg/Tsao's prediction would hit the last point of Greenwood's experiment. The resulting large difference between the reaction rates calculated from both Rudstam's and ALICE's cross sections is found in Table II for ^{57}Co. The experimental reaction rate in Table II should be closer to the reaction rate obtained by folding the calculated neutron flux with ALICE's cross sections. But these cross sections seem to be the upper limits as compared to the more recent experimental cross sections.

The discussion shows that we can only argue within factors of two or three or more from these monitor reaction cross sections alone. The total disagreement between ALICE's and Rudstam's (or Silberberg/Tsao's) cross sections and experimental values makes any evaluation effort obsolete. ALICE seems to follow the general shape of the experimental results better than the Rudstam formulas, but still with large discrepancies. Under this aspect there is a strong need for cross section measurements especially above 70 MeV to produce a reliable data base. Not until cross sections have been obtained with reasonable uncertainties (of at least better than a factor of 2) and sufficiently narrow energy spacings at the threshold energies, more accurate comparisons between experiment and calculations cannot be expected.

VI. CONCLUSION

The deep penetration experiment at the WNR helped to generate an experimental data base for a well defined spallation physics environment to be compared with predictions of the HETC/KFA-1, SIMPEL and ANISN codes. The experiment's position perpendicular to the beam axis excluded primary protons and most of the high-energy neutrons beyond the evaporation neutron energies. This made especially the HETC calculations more elaborate, because most of the histories are in forward direction or are confined within the target/reflector volume. To get enough statistics perpendicular to the beam axis 122 cm away from the target calls certainly for more CPU time, but without making all simplifying assumptions and taking full advantage of the approximate symmetry of the WNR target, CPU time would be unreasonably large.

The direct comparison between experiment and calculation was based on the measured reaction rates, any unfolding of the experimental data would have introduced additional sources of uncertainty beyond cross sections. The agreement is not too satisfactory, but as the compilation of reaction cross sections for natural copper targets shows, cross sections for the production of nuclei in the detector foils alone are the largest source of uncertainty, larger than Monte Carlo statistics, coupling between codes or proton contributions. The results presented show that experiment and both HETC and ANISN calculations do compare to some extent, but the overall uncertainties introduced by the cross section for the specific reaction excludes conclusions as to how to improve the calculational model.

Basically one has to conclude that cross sections for the detection reactions studied have to be measured first with reasonable accuracy to provide a reliable base for comparing experiment and calculation. The lack of experimental cross sections above 20 MeV is certainly due to the fact that accelerators with variable particle energies between 1 GeV and 20 MeV are not available. The proposed COSY synchrotron that will produce protons between 2.5 GeV and 40 MeV would be the ideal facility to measure the required cross sections.

VII. REFERENCES

/1/ W. Amian, V. Drüke, N. Paul, G.J. Russell, P. Cloth, Dr. Filges, H. Schaal
Experiments and Theoretical Investigations for a High-Energy Source Shielding Experiment at the Los Alamos WNR Facility
Santa Fe Conference, May 13-17, 1985

/2/ P. Cloth, D. Filges, G. Sterzenbach, T.W. Armstrong, B.L. Colborn
The KFA-Version of the High-Energy Transport Code HETC and the generalized Evaluation Code SIMPEL
KFA-Report Jül-Spez-196, March 1983

/3/ W.W. Engle
ORNL-Report 1693, (1973)

/4/ J.T. Routti, J. Tapio
High-Energy Neutron Spectroscopy with Activation Detectors
UCRL-18514, 1969

/5/ KFA-Report, to be published

/6/ W.B. Wilson
LA-7159-T, 1978

/7/ G. Rudstam
Zeitschriften für Naturforschung 21, 1027, 1966
see also: J.T. Routti, J.V. Sandberg
Computer Physics Communications
23, 411, 1981

/8/ M. Blann
Phys.Rev.Lett. 27, 337, 1971
and UCID 19614, 1982

/9/ R. Silberberg, C.H. Tsao
The Astrophysical Journal Supplement
Series No. 220 (I), 25, 315&335, 1973

/10/ C.J. Orth et al.
Journal of Inorganic Nuclear Chemistry 38, 13, 1976

/11/ A. Grütter
Nucl.Phys. A 383, 98, 1982

/12/ I.R. Williams, C.B. Fulmer
Phys.Rev. 162, 1055, 1967

/13/ L.R. Greenwood, R.K. Smither
DOE-ER-0046/14, 1983

ACKNOWLEDGEMENTS

The authors would like to thank Richard Woods and all other members of his group for their kind hospitality and continuous support.

Special thanks to the operators and other personnel associated with the WNR facility for their assistance with the irradiations.

Table I: Total Flux per cm^2 and per incident proton

Depth in Shield	Position in Fig. 5	HETC protons	HETC neutron	HETC-ANISN coupling neutrons
23 cm	A	6.38×10^{-9}	1.48×10^{-6}	1.85×10^{-6}
103 cm	B	0	1.70×10^{-8}	8.60×10^{-9}
203 cm	C	0	0	1.90×10^{-11}

Table II: Comparison of calculated and measured reaction rates

Cu-nat	Experiment Run 1	Rudstam HETC-ANISN coupling	Rudstam HETC	ALICE HETC-ANISN coupling
		d = 23 cm		
Fe-59	2.1×10^{-33}	4.7×10^{-33}	3.5×10^{-33}	3.7×10^{-33}
Co-58	2.8×10^{-32}	4.5×10^{-32}	3.2×10^{-32}	9.3×10^{-32}
Co-57	1.4×10^{-32}	1.2×10^{-32}	0.8×10^{-32}	5.0×10^{-32}
Co-56	2.0×10^{-33}	2.4×10^{-33}	1.5×10^{-33}	16.0×10^{-33}
Mn-52	3.5×10^{-34}	6.3×10^{-34}	3.6×10^{-34}	60.0×10^{-34}
Mn-54	3.9×10^{-33}	5.3×10^{-33}	3.3×10^{-33}	14.0×10^{-33}
V-48	0.5×10^{-34}	1.0×10^{-34}	1.1×10^{-34}	20.0×10^{-34}
		d = 103 cm		
Fe-59	1.1×10^{-35}	2.7×10^{-35}	2.8×10^{-35}	1.8×10^{-35}
Co-58	1.8×10^{-34}	2.6×10^{-34}	2.5×10^{-34}	4.6×10^{-34}
Co-57	9.5×10^{-35}	7.5×10^{-35}	6.9×10^{-35}	27.0×10^{-35}
Co-56	1.7×10^{-35}	1.5×10^{-35}	1.3×10^{-35}	9.4×10^{-35}
Mn-52	2.8×10^{-36}	4.1×10^{-36}	3.2×10^{-36}	38.0×10^{-36}
Mn-54	3.2×10^{-35}	3.3×10^{-35}	2.8×10^{-35}	8.7×10^{-35}
V-48	1.0×10^{-36}	1.4×10^{-36}	0.9×10^{-36}	13.0×10^{-36}

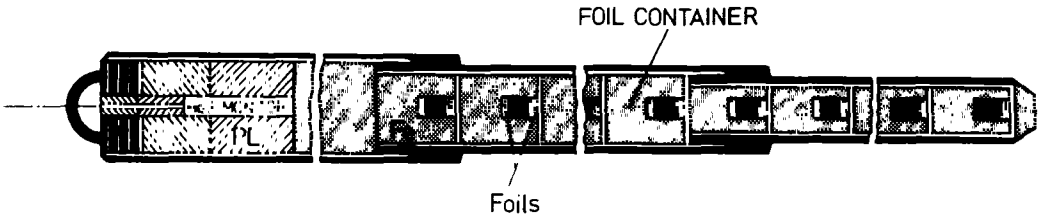

Fig. 1: The stringer assembly used to insert foil packages into the bulk shield of the WNR facility's Target I (LANSCE). Individual foil containers and foil positions are indicated. The ^{3}He monitor at the left is imbedded into PE rings and serves as a flux monitor.

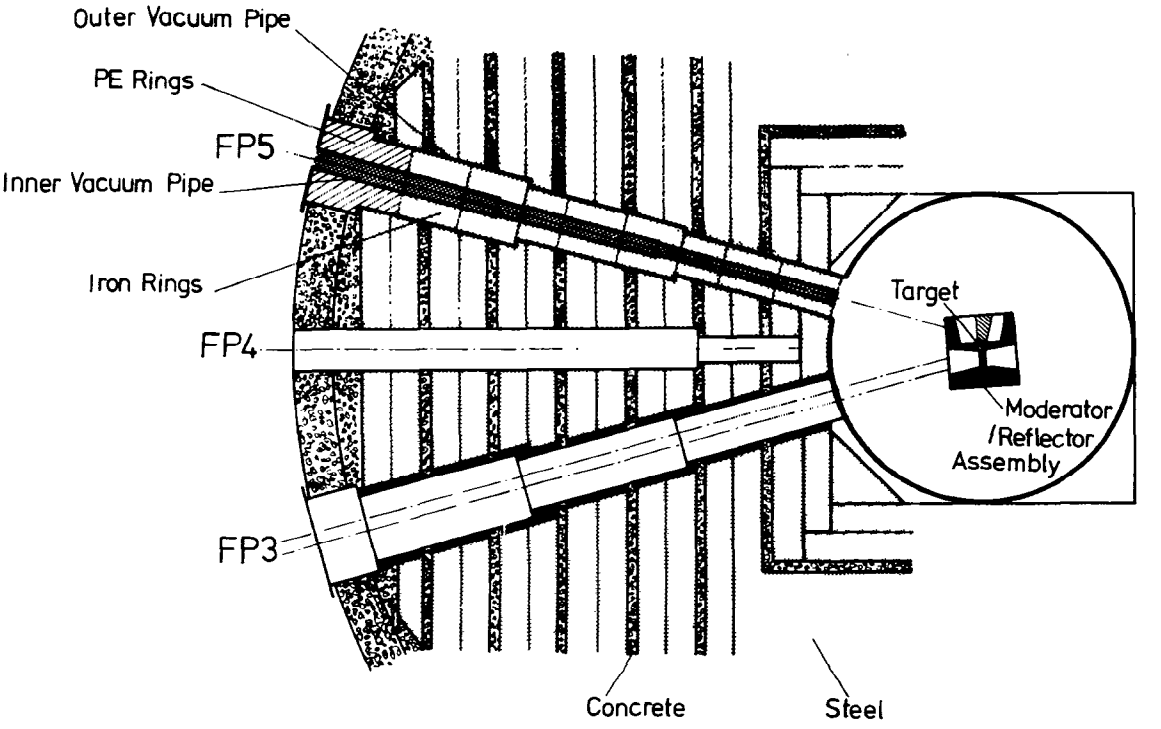

Fig. 2: Schematic scetch of the WNR target to the south. The stringer of Fig. 1 was inserted into Flight Path 5 (FP 5) for irradiations. Target, moderator and reflector are described in more detail in /5/

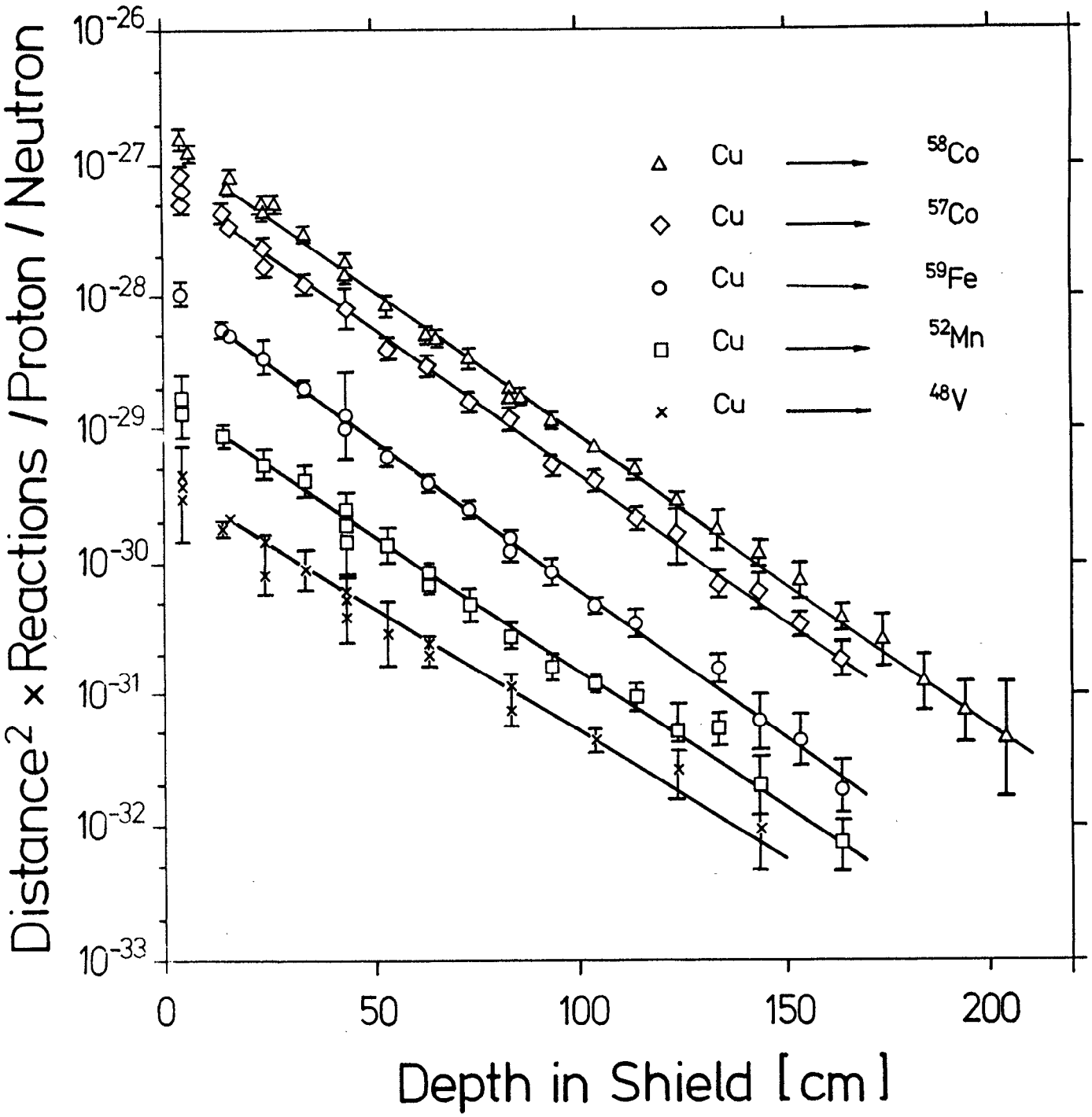

Fig. 3: Depth dependence of the reaction rates for some reactions on copper of natural isotopic composition. To eliminate solid angle dependence the reaction rates have been multiplied by the distance to the target center squared

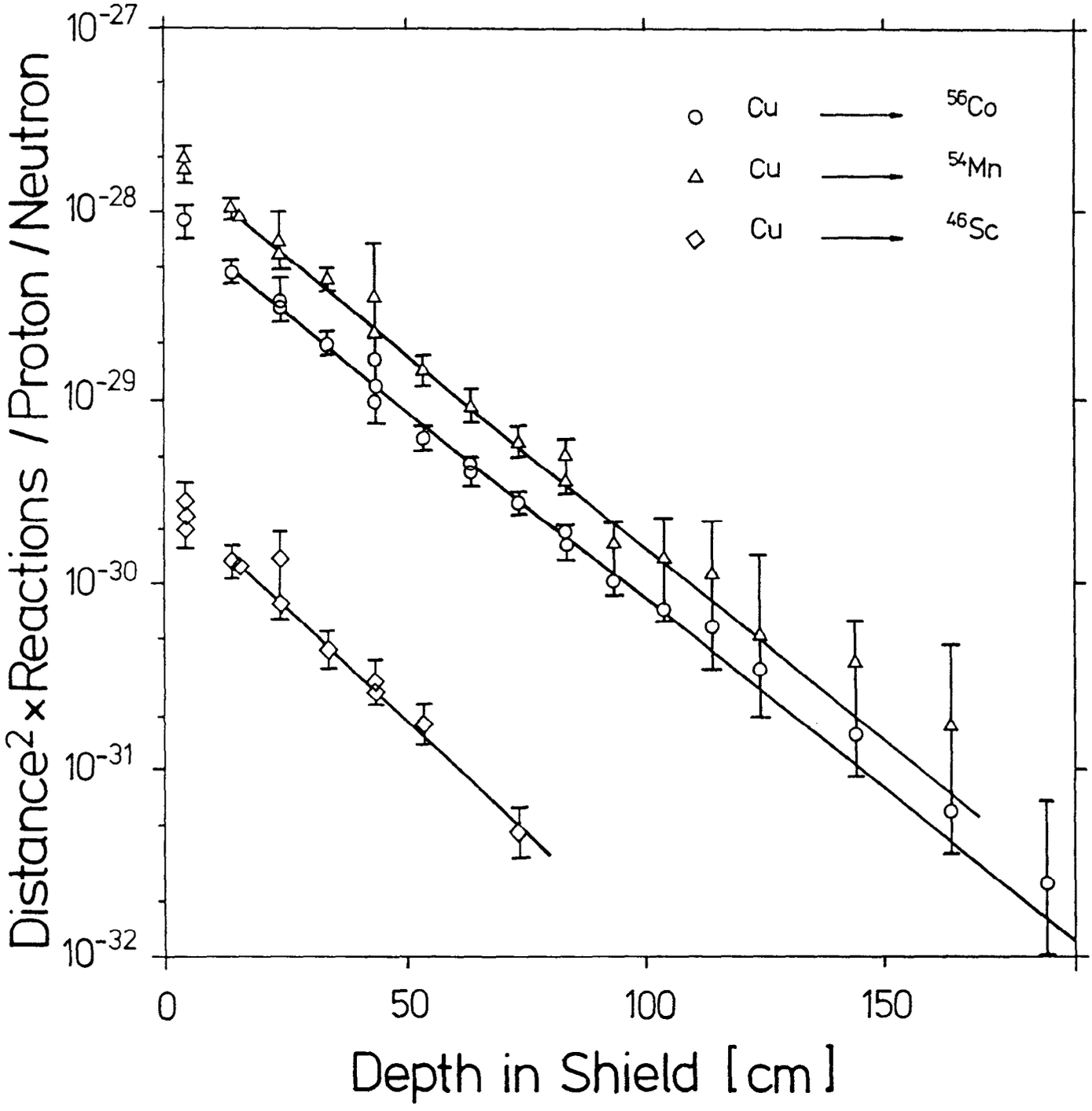

Fig. 4: Depth dependence of the reaction rates for some reactions on copper of natural isotopic compositions. To eliminate solid angle dependence the reaction rates have been multiplied by the distance to the target center squared

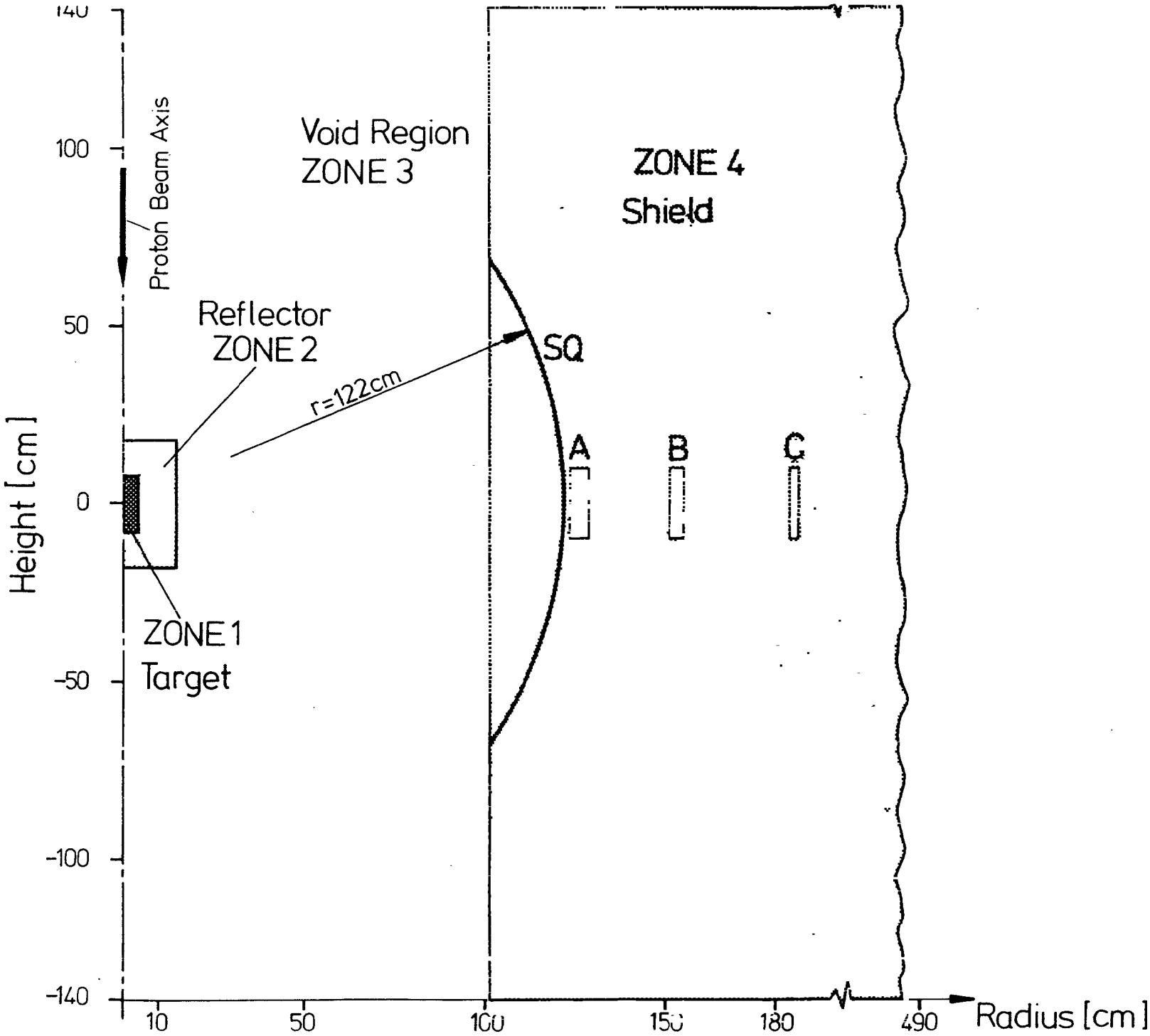

Fig. 5: Geometry

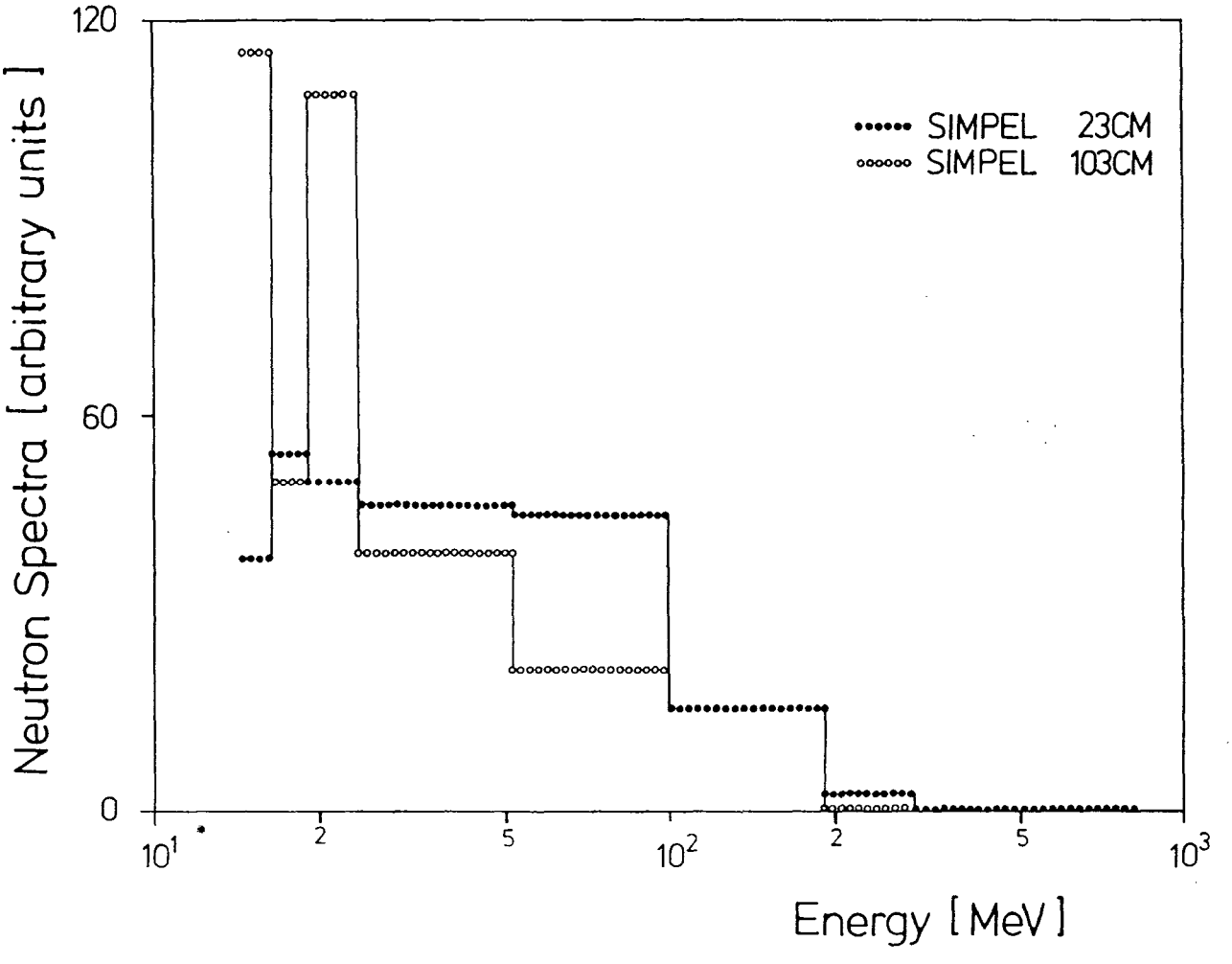

Fig. 6: HETC calculations

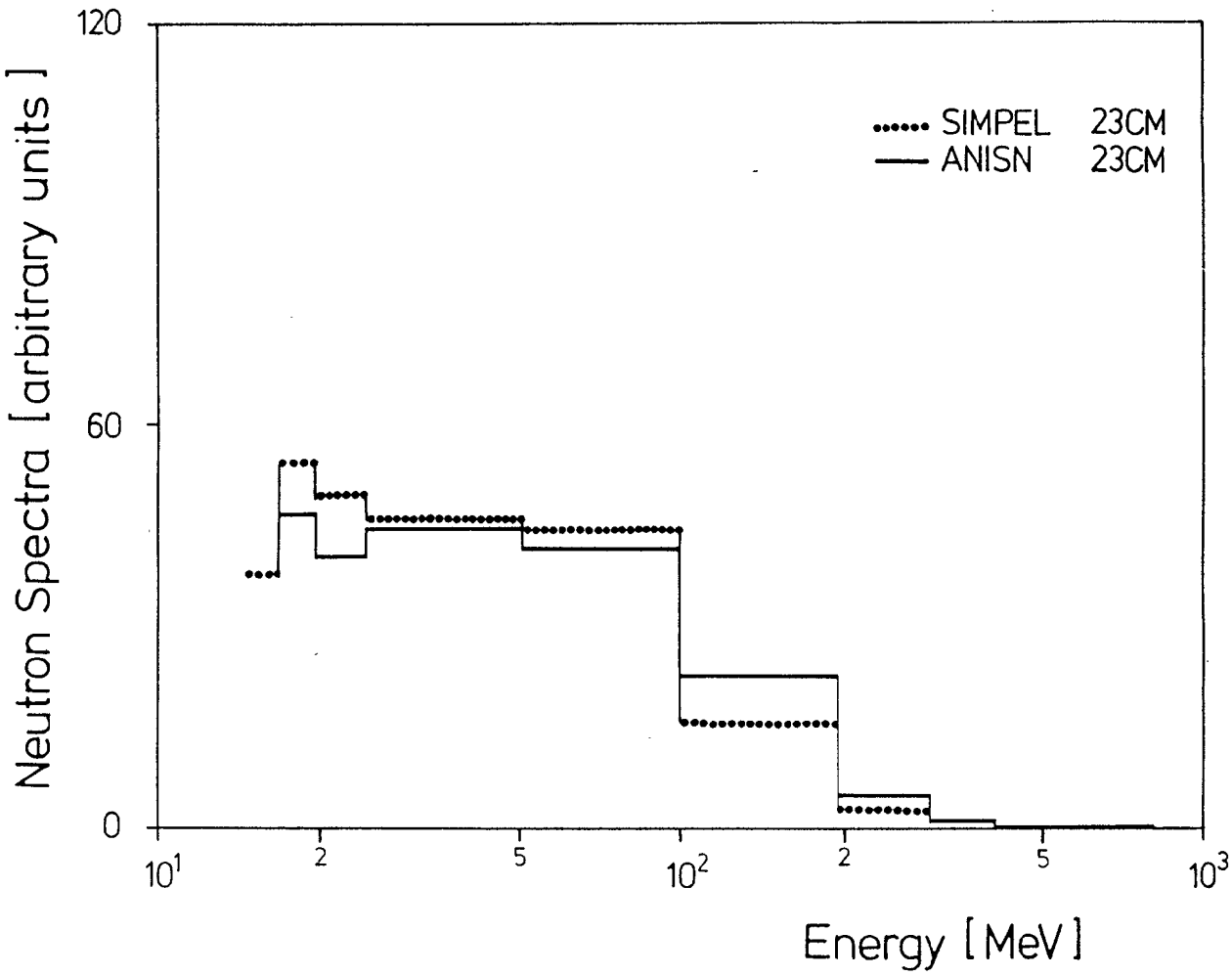

Fig. 7: Comparison of HETC-ANISN coupling and HETC calculations

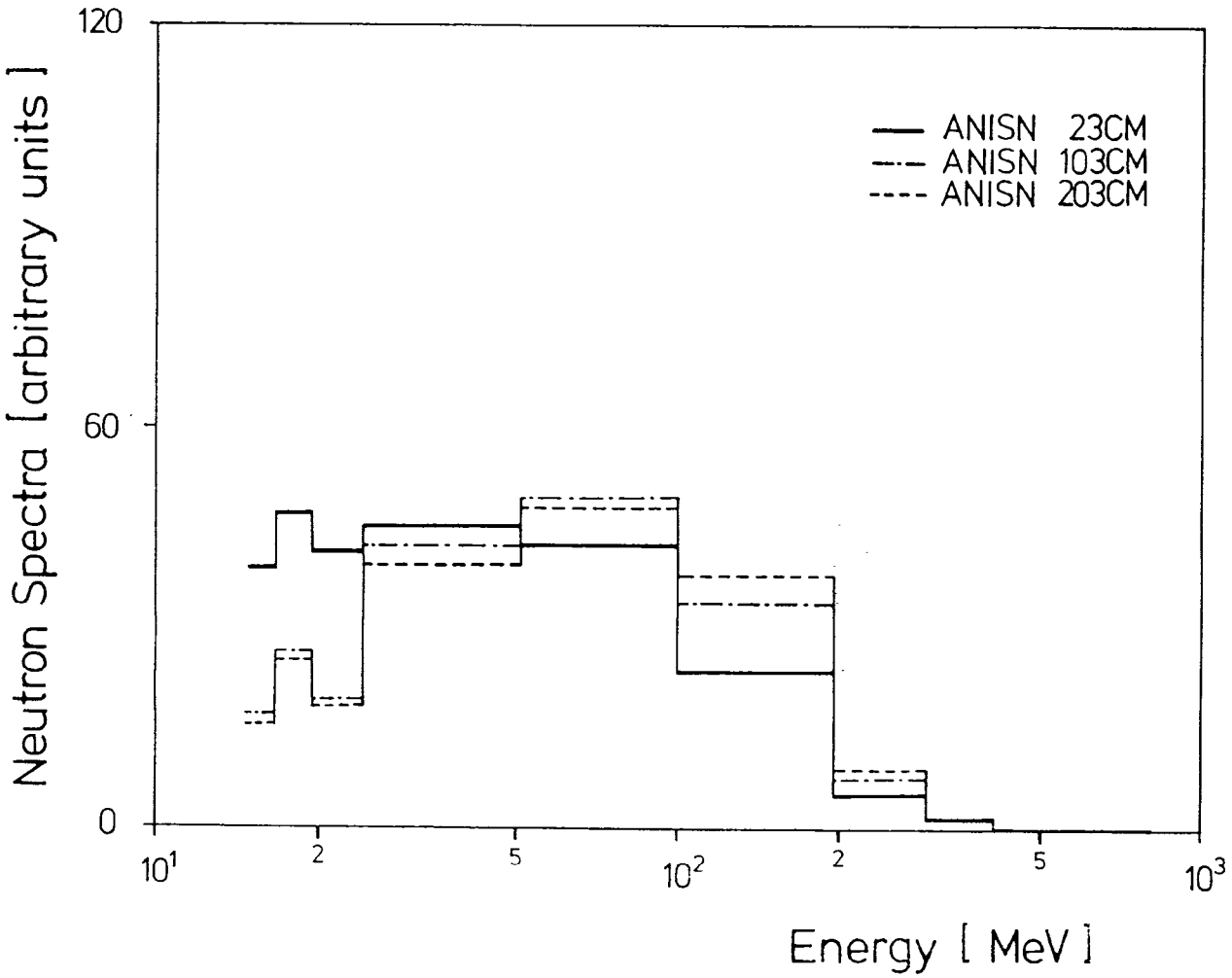

Fig. 8: HETC-ANISN coupling calculations

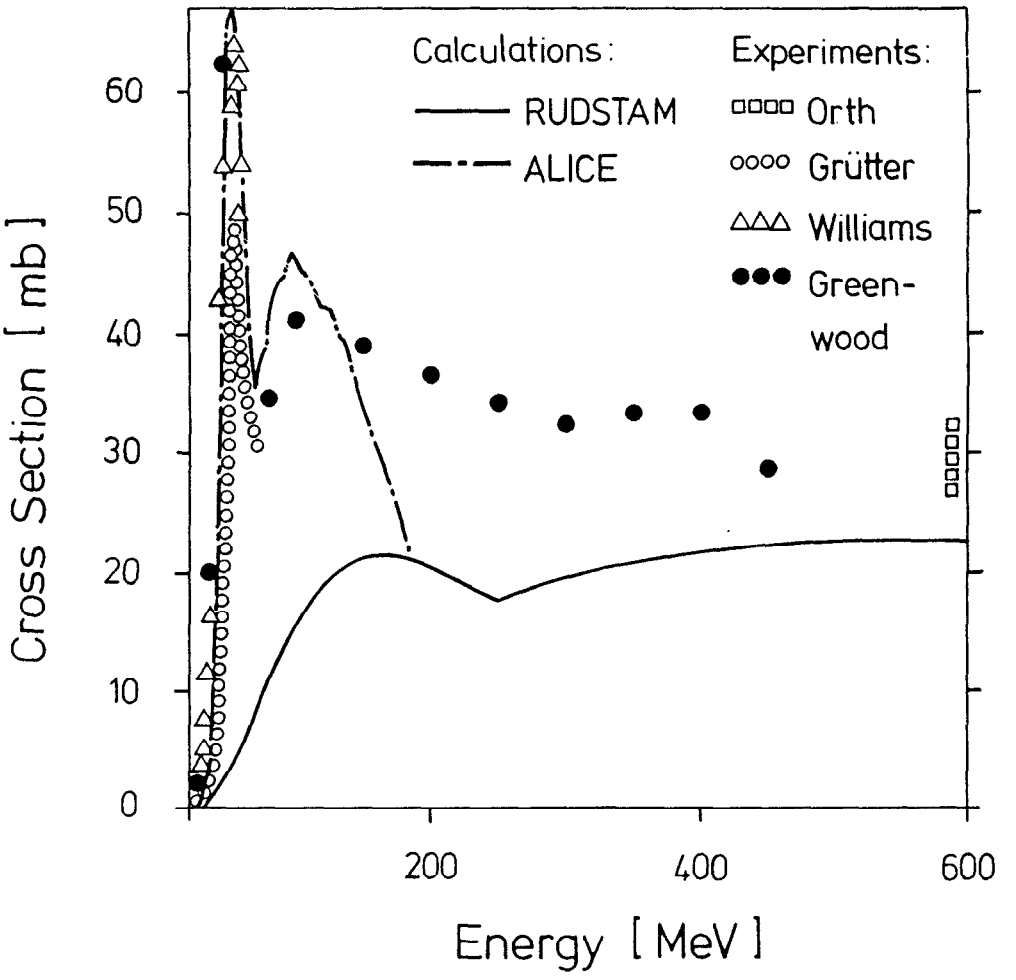

Fig. 9: Experimental cross sections /10-13/ and model calculations /7,8/ for the production of ^{57}Co from copper

ICANS IX

INTERNATIONAL COLLABORATION ON ADVANCED NEUTRON SOURCES

22-26 September, 1986

THE HIGH-ENERGY NEUTRON BACKGROUND AT SINQ

M. Pepin
SIN, Swiss Institute for Nuclear Research
CH-5234, Villigen, Switzerland

1. Introduction

The sources of high-energy (E_n > 15 Mev) neutron background at SINQ were reviewed by F. Atchison [1]. We now report the results of a study, using HET Monte-Carlo [2] and point-kernel methods, which was undertaken as a re-examination of these five sources of background, namely :

(1) The weakening of the iron bulk shield due to the beam tubes.

(2) The scattering of neutrons in the D_2O.

(3) The back-scattering of neutrons from the iron bulk shield.

(4) The scattering of neutrons in the windows at the beam tube tips.

(5) The penetration of the background neutrons into the monochromator shield, approximated by a large homogeneous block of iron.

Processes (1) to (4) contribute to the background at the monochromator, process (5) is relevant for the background further downstream. The geometry used in the study is a simplified SINQ arragement (see fig. 1).

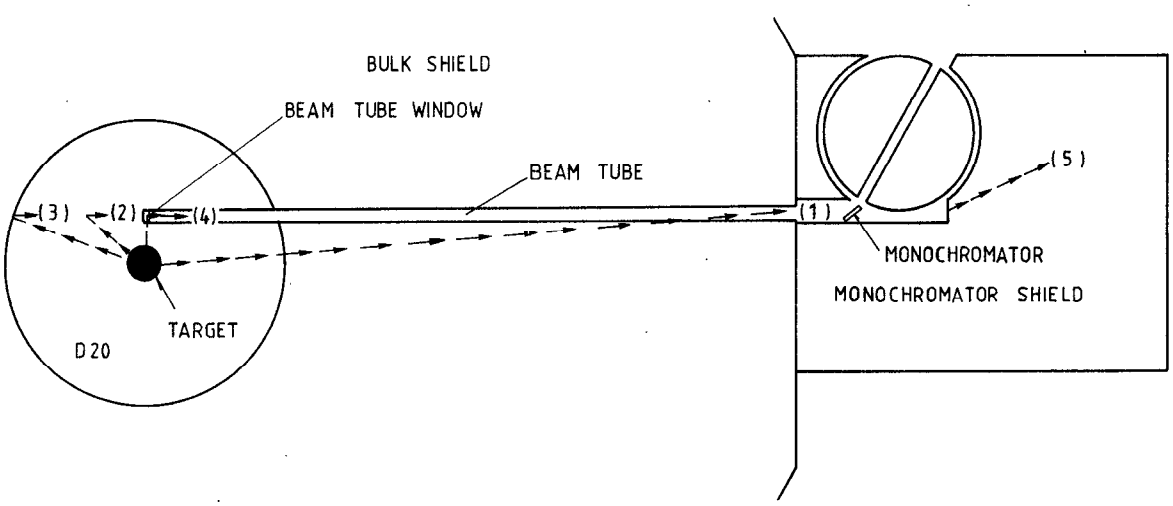

Fig. 1 Simplified geometry of the SINQ target and shielding, showing the investigated sources of high-energy neutron background.

The background was estimated as function of the radial distance of the beam tube tip from the centre of the target, and at two different values z_D = -1.5 cm and z_D = 21.5 cm for the level of the horizontal beam tubes with respect to the entrance face of the vertical target. The monochromator at D is taken on the beam tube axis. The beam tubes are 8 x 15 cm^2 in cross-section, 530 cm long, and are set in the tangential direction; their tips are covered by Al windows 5 mm thick.

2. Organisation of the study

The problem was treated in four main steps.

i) Lead-bismuth target and shield weakening. The cascades of 100 000 protons from the incoming beam were tracked through the target. The ca. 87 000 nucleons leaving the target were histogrammed and used as source term for a point-kernel calculation of the background due to the weakening of the bulk shield by the beam tubes.

ii) Scattering in the D_2O tank and bulk shield. A Monte-Carlo run was done for the continued propagation of the 87 000 escape particles through the D_2O tank and bulk shield, temporarily neglecting the beam tubes and their windows. The tangential neutron flux at the position foreseen for the beam tube window determines, by drift through vacuum, the contribution of scattering on D_2O and iron to the background at the monochromator. The component due to the iron was then deduced by examining the reflectivity of the bulk shield.

iii) Scattering in the beam tube windows. The flux observed in the D_2O at the position of the beam tube tips was used as source term for HET investigations of the Al window.

iv) Monochromator shield. The penetration of the high-energy background flux of neutrons into a massive, structureless monochromator shield of iron was studied by a joint Monte-Carlo and point-kernel method.

The following 3 sections of chapter 2 give more details about steps i) to iii). Chapter 3 presents the results for the high-energy background flux incident on the monochromator, and chapter 4 reports on the penetration of the flux into the monochromator shielding.

2.1 Shield Weakening

The particles escaping from the lead-bismuth target were histogrammed in the four variables energy, z, u = cos(ϕ), and w = cos(δ). The binning in the angular variables u and w comprises 25 bins and is illustrated in figs. 2a) and 2b). The choice of angular cooordinates relative to the normal to the target surface at the escape point P exploits the cylindrical symmetry of the situation.

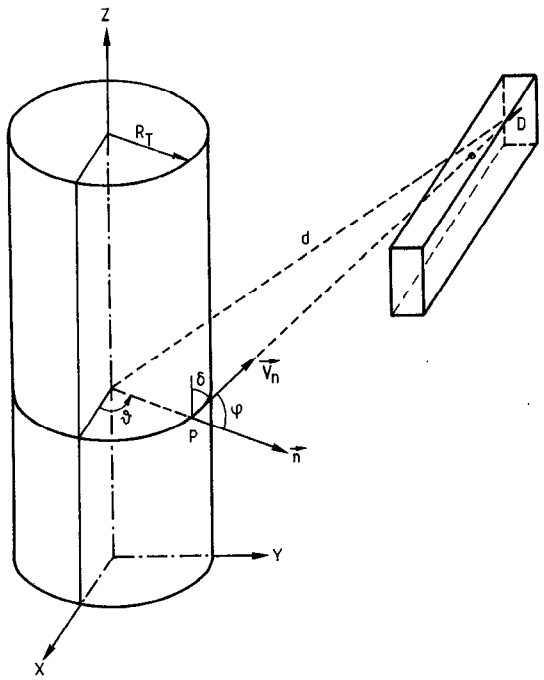

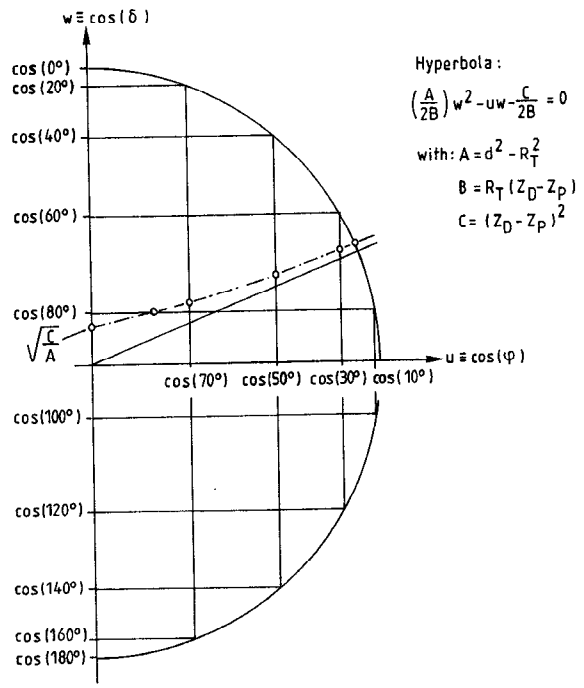

Fig. 2a Definition of the parameters used for the angular binning of the high-energy neutron escapes. $\vec{v}_n$ is the velocity vector of the neutron.

Fig. 2b Limits of the angular bins in (u,w) space, and the hyperbola engendered by the horizontal scan of the escape point P.

In the point-kernel calculation, the bins with $\phi > 70°$ (neutrons emitted nearly tangentially to the target surface) are affected with large errors (statistics of a few events), and enter the results with a large weight (near-parallelism to the beam tube). It is therefore necessary to calculate separately the contribution of each bin of the source histogram, in order to know which fraction of the resulting background is due to these potentially dangerous bins.

The contribution of each individual bin to the background at the monochromator position (point D) was obtained by numerical integration over those portions of the target surface which "see" the point D in the direction appropriate for the bin in consideration. The target surface was scanned at constant z and with varying azimuthal angle Θ for the escape point P. In this scan the straight segment from P to D determines a hyperbola in (u,w) space, whose intersections with the bin limits u=const, w=const, or $u^2+w^2=1$ were found (fig. 2b). These intersection points were then mapped back to give lower and upper limits for Θ. A constant worst-case attenuation length of 17.3 cm was taken for neutrons in iron, and a constant worst-case length of 75 cm was subtracted from the path to account for build-up. The D_2O was treated as vacuum.

The contribution of the bins with $\phi > 70°$ to the shield weakening depends strongly on the radial position of the beam tube tip. For radii at or beyond the position of the maximum thermal flux, the contributions of these bins no longer dominate, although they are still appreciable (up to 30%) in some cases.

2.2 D_2O Tank and Bulk Shield

The Monte Carlo runs which followed the cascades through D_2O tank and bulk shield were analysed as follows : for each combination of z and r values for the beam tube tip, the set of all possible azimuthal angles for the tip defines a ring-shaped volume of rectangular cross-section. Any portion of nucleon track within this "ring" is divided into elements of 1 cm length or less. Each track element makes a contribution of weight $\alpha/2\pi$ to the histogram of nucleons potentially entering a beam tube, where α is the angle defined by the start and end points of the track element, as seen from the target centre.

The high-energy background flux at the monochromator is essentially given by the number of neutrons entering the beam tube at a small angle relative to its axis. The results quoted in chapter 3 were obtained by assuming isotropic distribution over the solid angle, by taking drift in vacuum, and by normalization to an incoming proton current of 1 mA.

The number of high-energy nucleons back-scattered from the bulk shield in the range -9 cm $< z <$ 29 cm and in the approximate direction of the beam tube tips is 0.00025 nucleons per cm^2 per sterad and per 100 000 protons (very poor statistics). In vacuum, this would correspond to a few percent of the D_2O contribution. As the back-scatters still have a path of 100 cm through D_2O to cover before they enter the beam tube, and as most of them are of relatively low energy (15 to 30 MeV), the back-scattering from iron can safely be neglected.

2.3 Beam Tube Windows

The results of the HET run in D_2O were used to build maps of the neutron flux incident on the faces and edges of the Al windows. These maps gave the source terms for HET investigations of a system consisting only of the window itself.

For the neutrons incident on the faces of the Al windows, the histogram of the flux in D_2O is already available from section 2.2. There is an excess of typically 3 % between the number of high-energy neutrons escaping the windows within a 20° cone centered on the normal to the window, and the number of neutrons started within the same cone on the opposite face of the window. The results must be considered as upper values, as no corrections were made for the lost contributions of those volumes of D_2O which were replaced by aluminium.

For the neutrons incident on the window edges, the source term is determined by the neutrons penetrating into the "ring" defined by the window position. Each neutron entering this volume contributes with a weight of $\beta/2\pi$, where β is the angle subtended by 0.5 cm (i.e. the thickness of the window) at the radius of the entry point.

3. Results : Flux incident on Monochromator

The results for the processes mainly responsible for the high-energy background at the monochromator are shown in fig. 3. For comparison, the thermal fluxes calculated by F. Atchison [3] are also presented. The maximum thermal flux is reached at a radius of about 20 cm. The background due to the shield weakening is only given at one z-value, as the coarseness of the angular binning of the source term only very poorly resolves a height difference of 23 cm at 530 cm.

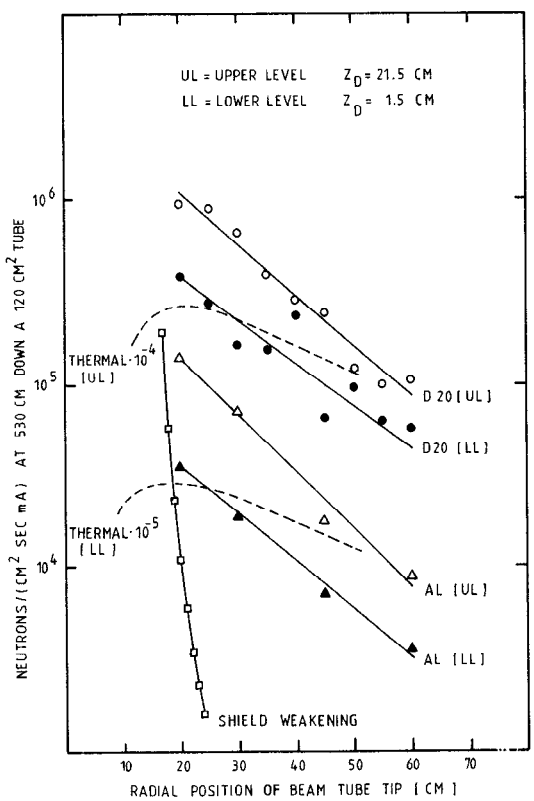

Fig. 3 Thermal neutron flux of ref. [3] and high-energy neutron background at the monochromator for scattering on D_2O and on the Al windows, at two beam tube levels. The shield weakening contribution is also shown.

Fig. 3 indicates that, for beam tube tip positions between 20 and 40 cm, the high-energy background flux is of the order of several 100 000 neutrons per second, cm^2 and mA. The D_2O scattering gives the greatest contribution to the background. The background flux is significantly higher for the upper level beam tubes and, as the thermal flux varies little with the beam tube level, the lower level tubes enjoy somewhat better signal to noise ratios.

Fig. 3 also shows that, as the beam tube tip moves outwards, the thermal flux decreases less rapidly than the background. A more favourable signal to noise ratio could therefore be achieved by placing the beam tubes at larger radii, however at the cost of a loss of thermal flux. The choice of the final value for the beam tube radii is therefore dependent on the answer to the question : "what is the highest tolerable high-energy background ?"

The decrease of the neutron flux through the shield is exponential, and the background due to shield weakening is very sensitive to variations of the beam tube geometry. For example, placing the monochromator at the worst edge of the tube, instead of on the tube axis, can increase this component of the high-energy background by a factor of several hundred. On the other hand the replacement of worst case attenuation coefficients and buildup factors by energy dependent ones [4],[5] decreases the background by an even greater factor. In any case, due to its very steep decrease with beam tip radius, the shield weakening becomes negligible at beam tip radii beyond the maximum of the thermal flux.

4. Monochromator Shield

The shape of the high-energy tail of the background neutrons incident on the monochromator is shown in fig. 4 for a typical beam tube position.

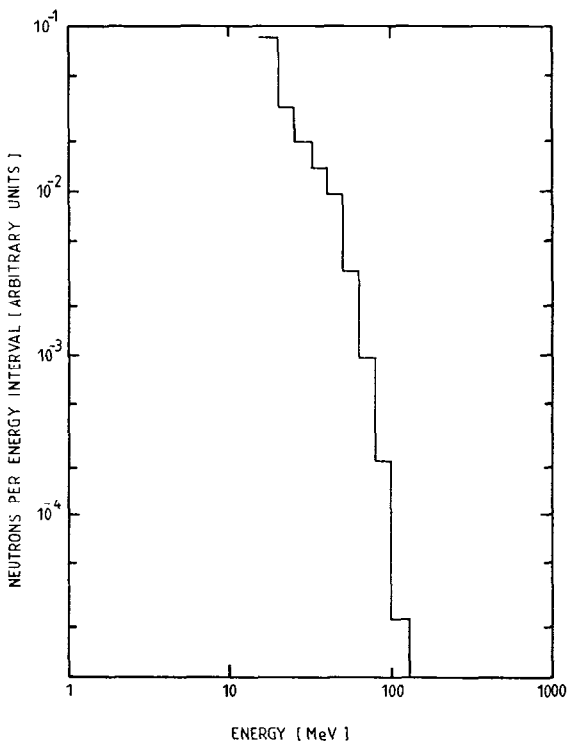

Fig. 4 Shape (in arbitrary units) of the energy spectrum of the combined Al and D_2O contributions to the high-energy background at the monochromator, and for a typical beam tube position.

The neutrons coming down the beam tube are highly directional, and for simplicity can be assumed along the central axis of the monochromator shield. Using the MECCRL code [6] for the intranuclear part of the HET cascades, the interaction cross-section σ_i and the differential cross -section $d^2\sigma/dEd\Omega$ for the production of nucleon secondaries by primary neutrons incident on iron were obtained at different energies. This information was then used to calculate the source of second-generation particles along the axis of the monochromator shield. The flux of high-energy nucleons in the monochromator shielding was then estimated by a point-kernel approximation.

The resulting flux map is shown in fig. 5 for the case of an 8 x 15 cm^2 beam tube with 300 000 high-energy neutrons/sec cm^2 coming down the tube (conditions prevalent at the lower level with a radial position of 25 cm for the beam tube tip). As must be the case, there is very good correlation with the energy deposition map obtained from HET/ENDEN5. This method, however, smooths out the large fluctuations observed with HET at the greater radii.

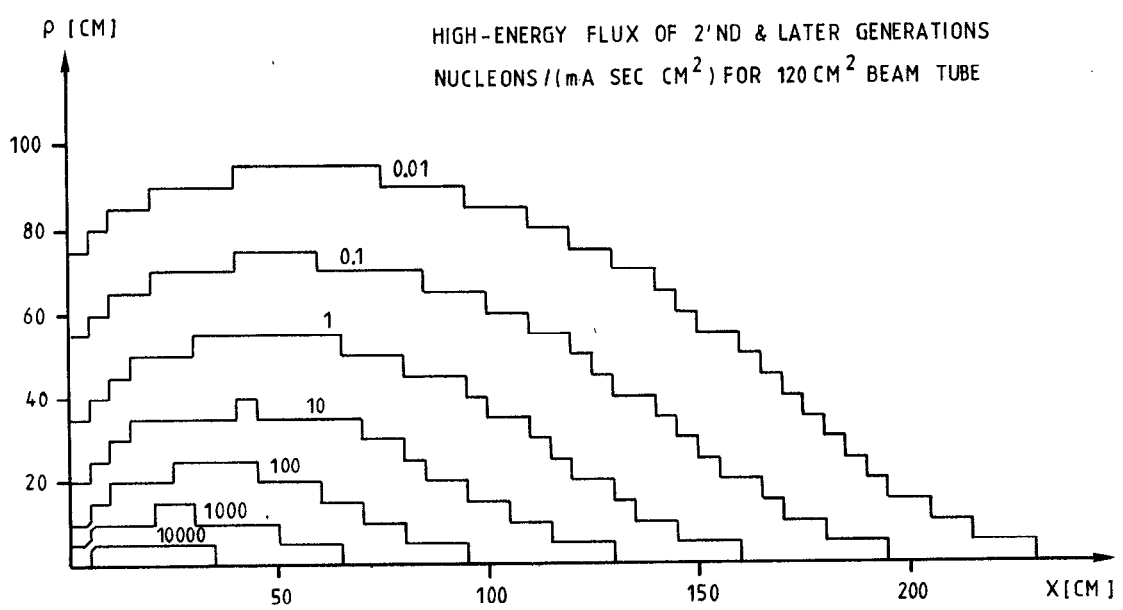

Fig. 5 Flux map of the high-energy background neutrons of the second and later generations in the monochromator shield. The cylindrical coordinates (x, ρ) give the prolongation of the beam tube axis into the monochromator shield and the distance normal thereto.

Aknowledgements

Francis Atchison emphasized the need and suggested the method for treating the point-kernel integration on a bin by angular bin basis, and communicated the build-up factors for neutrons in iron, which he had determined in an earlier study. The adaptations of the HET and MECCRL programmes to the SIN VAX system and the HET modifications which are necessary for treating deuterium are also due to him.

References

[1] F. Atchison "Considerations on Backgrounds at SINQ", ICANS-VIII Proceedings, Vol. 3, page 648.

[2] Radiation Shielding Information Centre code package CCC-178, HETC.

[3] F. Atchison "Poisoning Effects in Spallation Neutron Sources", ICANS-VIII Proceedings, Vol. 1, page 161.

[4] T. Broome, Rutherford lab. internal report No. SNS/TS/N1/81.

[5] F. Atchison, private communication.

[6] H.W. Bertini, M.P. Guthrie, and O.W. Hermann, ORNL-4564, (1971).

AUTHOR INDEX

Al-Sharify T. 591
Amian W.B. 627
Anderson I.S. 383
Armani R.J. 557
Bailey J.L. 557
Bauer G.S. 1, 141
Beynon T.D. 591
Blind B. 85
Blomquist R.N. 557
Bly M.J. 245
Boland B.C. 349, 529
Bowden Z.A. 349, 529
Bridge A. 177
Broome T.A. 245, 519
Brown B.S. 45, 557
Brumwell F. 113
Carne A. 551
Carpenter J.M. 45, 171, 271, 279, 315, 557
Cloth P. 627
Crawford R.K. 45, 365, 397, 431
Cudrnak S.S. 315
Cywinski R. 477
Davidson I. 529
DeCusatis C.M. 315
Drüke V. 627
Eaton G.H. 245
Endoh Y. 65, 457, 535
Filges D. 627
Fischer W.E. 101, 613
Fukunaga T. 539
Geick R. 389
Gray D.A. 23
Hardek T.W. 85
Hardekopf R.A. 85
Harris I.R. 477
Haumann J.R. 365
Henley D.R. 557
Hins A.G. 557
Hixon M. 477
Hughes K.J. 177
Inoue K. 65
Itoh S. 457
Jason A.J. 85
Johnson M.W. 449, 469
Jones T.J.L. 529
Knox A.E. 557
LaRock J. 383
Lawrence G.P. 85
Legate G.L. 177
Loomis B.A. 557
Lucas A.T. 305
Mayers J. 477
Mildner D.F.R. 279
Misawa M. 65, 539
Mitsuda S. 457
Morse F.A. 31
Neef R.D. 177
Ostrowski G.E. 365
Paul N. 627
Penfold J. 493, 505
Pepin M. 649
Picton D.J. 519, 591
Potts C.W. 45, 113
Price D.L. 365
Pulford W.C.A. 469
Quinton S.P.H. 469
Rauch H. 125
Rauchas A. 113
Robinson H. 177, 304
Rowe J.M. 383
Rush J.J. 383
Russell G.J. 177, 271, 304
Schaal H. 627
Schulke A.W. 557
Seeger P.A. 437
Sköld K. 365
Stipp V. 113
Takeda Y. 259
Taylor A.D. 167, 349, 519, 529, 535
Thresh H.R. 557
Tietze H. 389
Tomkinson J. 505
Trewhella J. 437
Udovic T.J. 383
Volk G. 113
Walter U. 279
Ward R.C. 493, 535
Watanabe N. 65, 535, 539
Whitaker E.R. 177
Williams A. 437
Williams W.G. 343, 477, 493, 535
Woods R. 177
Yamaguchi T. 539